Tobias Bruckmann
Andreas Pott   *Editors*

Cable-Driven Parallel Robots

Springer

Mechanisms and Machine Science

Volume 12

Series Editor

Marco Ceccarelli

Tobias Bruckmann · Andreas Pott
Editors

Cable-Driven Parallel Robots

Springer

Editors
Tobias Bruckmann
Universität Duisburg-Essen
Duisburg
Germany

Andreas Pott
Fraunhofer-Institut für Produktionstechnik
   und Automatisierung IPA
Stuttgart
Germany

Committee

General Chair

Andreas Pott, Fraunhofer IPA, Stuttgart, Germany
Tobias Bruckmann, University Duisburg-Essen, Germany

Honorary Chair

Manfred Hiller, University Duisburg-Essen, Germany

Scientific Committee

Sunil Agrawal, University of Delaware, United States
Clément Gosselin, Laval University, Québec, Canada
Marc Gouttefarde, LIRMM, Montpellier, France
Jean-Pierre Merlet, INRIA, Sophia Antipolis, France
Dieter Schramm, University Duisburg-Essen, Germany
Alexander Verl, University Stuttgart, Germany

Preface

Origins of cable-driven parallel robots lie in the late 1980s when first concepts of cranes, parallel kinematic manipulators, and cable-driven robotic devices were combined in the United States and in Japan.

Researchers all over the world started to work on these special robotic systems, most of them having a strong background in parallel kinematics: in contrast to conventional parallel and serial manipulators, cable-driven parallel robots promise a couple of unique advantages over other kinematic concepts. Cable robots allow for significant improvements in the size of the workspace, the maximum payload, and the dynamic capacities due to their superior efficiency in transmitting forces through cables. The research on cable robots led to a number of challenging scientific questions in the field of kinematics, statics, dynamics, control, and design. Due to the lack of a dedicated forum on cable robots, active researchers published their results, widely dispersed, in a broad range of robotic conferences and journals. Meanwhile, the number of contributions in this field was rapidly growing.

Recently, projects have started transferring the cable robot technology into practical application, e.g., in the fields of industrial large-scale material handling, intralogistics, and physiotherapy.

For the very first time, leading experts from three continents gather during the First International Conference on Cable-Driven Parallel Robots in Stuttgart, Germany. The conference allows the cable robot community to exchange ideas and to create new connections between active researchers around the world. The conference was organized under the patronage of International Federation for the Promotion of Mechanism and Machine Science (IFToMM).

Within this book, some of the most renowned experts present the state of the art, including both summarizing contributions as well as latest research results in key areas such as workspace, design, and control. The papers in this book cover classical topics such as motion planning, kinematics, dynamics, control, as well as design and their implications on cable robots. At the same time, practical issues such as components for cable robots, calibration, and prototyping are presented,

summarizing experiences from the increasing number of applications and prototypes.

We are most grateful for the authors for their outstanding contributions, for the reviewers for their critical but valuable feedback, and for the great support of the scientific committee that turned this conference into success. We would also like to extend our thanks to the staff at Springer for their support and patience during the preparation of the manuscripts.

Tobias Bruckmann
Andreas Pott
Editors

Introduction of the Honorary Chair

In the early 1990s, when we started cable-driven robot research at the Chair of Mechatronics at the University of Duisburg-Essen (formerly Gerhard-Mercator-University -GH- Duisburg), we were a very small community. Fascinated by the idea of manipulating objects through a simple system of connected wires, we were inspired by the theoretical challenges put forth in spite of the simplicity of the elementary mechanical setup based on cables and winches, as well as by the broad spectrum of applications deemed possible. Especially its application in the field of stage technology made us dream of the "flying carpet". In cooperation with Krupp Industrietechnik—a former German high-tech company—the first general concepts were laid out.

Nevertheless, nearly all research groups in the field of cable-driven robots focused on fundamental research funded by the state, and I would like to take this opportunity to thank the involved national and international funding organizations. World-wide, this has enabled the work which forms now the basis for the material presented in this conference and the accompanying book, reflecting the know-how and experience gathered from 25 years of research.

I am happy and proud to see that cable robots are mature enough now and ready to be proven in a number of upcoming application projects.

Besides several well-known experts, in this still new field, I am delighted to meet and welcome the newer colleagues from all over the world who have significantly contributed to the success of this conference. I am very optimistic that this conference will act as a foundation to integrate them into existing and newly created networks to cultivate and foster the scientific exchange.

I believe that this conference is the beginning of a new chapter in cable robots research and I am wishing all contributors a fruitful and memorable time at the "First International Conference on Cable-Driven Parallel Robots" 2012!

Manfred Hiller
Honorary Chair

Contents

Part VIII   Dynamics Modeling

Part I
Motion Planning

Global Planning of Dynamically Feasible Trajectories for Three-DOF Spatial Cable-Suspended Parallel Robots

Clément Gosselin

Abstract This paper addresses the dynamic trajectory planning of three-DOF spatial cable-suspended parallel robots. Based on a dynamic model of the suspended robot, a set of algebraic inequalities is obtained that represents the constraints on the cable tensions. Dynamic feasibility is then established using interval arithmetics on the latter inequalities in order to obtain global conditions on the trajectory parameters that can guarantee that the cable tensions remain positive throughout the trajectory. Such conditions are obtained for a variety of parametric trajectories. When periodic functions are used in the design of the trajectories, it is shown that special frequencies arise that are akin to natural frequencies of pendulum-type systems. These special frequencies can be used in practice to greatly simplify the trajectory planning. An experimental implementation on a three-dof cable-suspended prototype is presented. As demonstrated, the proposed trajectory planning approach can be used to plan dynamic trajectories that go beyond the static workspace of the mechanism, thereby opening novel applications and possibilities for cable-suspended robots.

1 Introduction

The dynamics of cable-driven parallel mechanisms has been a topic of interest since the introduction of the first designs. Indeed, cable-driven parallel mechanisms have the potential to produce very fast motions and the control of such motions requires a proper understanding of the dynamics of the mechanical system. In fully constrained cable-driven systems such as those presented in [13, 15, 22] (and many others), a dynamic model is highly relevant. In such mechanisms, very high speed motions can be generated due to the wrench closure property.

C. Gosselin (✉)

Département de Génie Mécanique, Université Laval, 1065 Avenue de la Médecine,
Québec, QC G1V 0A6, Canada
e-mail: gosselin@gmc.ulaval.ca

The dynamic modelling of fully constrained cable-driven parallel mechanisms was addressed in several publications. For instance, in [5, 7, 8], and [19], dynamic models are proposed for mechanisms with more cables than degrees of freedom. One important issue in this context is the optimization of the distribution of the tensions among the cables. This issue is investigated in more detail in [4, 9] and [16].

As opposed to fully constrained cable-driven parallel mechanisms, cable-suspended mechanisms use an external force—typically gravity—to maintain their cables in tension. They are not redundantly actuated, i.e., they include at most as many actuators as degrees of freedom. Cable-suspended parallel robots have been proposed in the literature as potential candidates for applications that require very large workspaces or as mechanisms that can provide effective payload to mass ratios. One of the first cable-suspended mechanisms that was built is the Robocrane [1], developed by NIST almost two decades ago. This six-degree-of-freedom robot was intended for crane-type operations in which the pose of the payload can be fully controlled. Other cable-suspended mechanisms have also been studied and prototypes were built to validate their performance (see for instance [10] and [20]).

Although cable-suspended mechanisms have been mostly considered as quasi-static devices, their dynamics has also been studied. Dynamic models of such mechanisms have been proposed for instance in [17, 24] and they have been used in the control of the devices. Closely related architectures are also studied in [3, 18] and others.

Many of the cable-suspended parallel mechanisms proposed or built in the past were designed to work in static or quasi-static conditions. The workspace of these devices can be determined based on the static equilibrium of the moving platform. The static workspace is defined as the set of platform poses for which static equilibrium can be obtained while maintaining tension in all cables. Techniques to determine the static workspace of cable-suspended robots were proposed in the literature, for instance in [21].

Cable-suspended robots can also be envisioned as dynamically controllable devices. In [6, 14, 23] and [25] dynamically controlled (pendulum-like) cable-suspended robots were proposed. By dynamically controlling the robots, their workspace can be extended beyond the static workspace and the notion of dynamic workspace [2] arises. The dynamic workspace is defined as the set of poses that the platform can reach with at least one kinematic state (position, velocity and acceleration). In other words, the platform can reach points beyond the static workspace with a controlled kinematic state (e.g. a zero velocity but non-zero acceleration).

The pendulum-like robots proposed in [6, 14, 23] and [25] are underactuated, i.e., they include fewer actuators than degrees of freedom. Therefore, the trajectory of their end-effector cannot be controlled exactly since the dynamics of the uncontrolled degree(s) of freedom must be accounted for. The techniques proposed in the latter references focus on the determination of actuator inputs that are capable of producing point-to-point motion between prescribed poses. Such techniques require the on-line numerical integration of the differential equation associated with the pendulum-like dynamics.

In [12], a fully actuated planar two-degree-of-freedom (2-dof) robot suspended on two cables was considered and global conditions were obtained for the feasibility of families of dynamic trajectories. In this paper, the same approach is applied to a spatial three-dof cable-suspended parallel mechanism. Families of Cartesian trajectories are prescribed globally in parametric form. Because the robot is not underactuated, it is possible to solve the dynamic model for the cable forces, for a given Cartesian trajectory (inverse dynamics). Based on the expressions of the cable forces, a set of inequalities that represent the constraints associated with the unilaterality of the forces in the cables of the robot is obtained, similarly to what was presented in [20]. By substituting the parametric form of the Cartesian trajectories into these inequalities, conditions on the global parameters of the trajectories are obtained that guarantee feasibility. It is shown that special frequencies akin to the natural frequency of pendulum-like systems can be used to better exploit cable-suspended robots. Means of transitioning smoothly between parametric trajectories are also developed. Finally, example trajectories are presented and an experimental validation is performed using a prototype.

Cable-suspended parallel robots that have the ability to operate beyond their static workspace could be used in applications where a large workspace is required and where the footprint to workspace ratio is smaller than one due to obstacles or other limitations.

2 Robot Architecture

A spatial three-degree-of-freedom (3-dof) cable-suspended robot is represented schematically in Fig. 1. The robot consists of three actuated spools mounted on a fixed structure which are used to control the extension of three cables. The cables are attached to a common end-effector which is considered as a point mass. By controlling the extension of the cables, the position of the point mass in a three-dimensional space can be controlled. The robot includes three actuators and three degrees of freedom and is therefore fully actuated. However, because cables can only work in tension (they cannot push), constraints must be imposed on the Cartesian trajectory prescribed at the end-effector in order to ensure that a given trajectory is feasible, i.e, that it does not require compression forces in the cables. The static workspace of the robot, i.e., the portion of the Cartesian space in which the end-effector can be brought to rest, is limited by the footprint of the robot. The latter workspace is in fact a prism of vertical axis and triangular section corresponding to the triangle defined by the projection of the cable attachment points onto a horizontal plane. However, by exploiting the dynamics of the cable-suspended robot, it is possible to produce trajectories that extend beyond the boundaries of the static workspace. Also, when dynamic trajectories are performed, the static workspace no longer defines the feasible workspace and the concept of dynamic workspace must be used [2]. Therefore, the unilaterality constraints associated with the forces in the cables are introduced using the dynamic model of the robot.

Fig. 1 Spatial three-degree-of-freedom cable-suspended robot
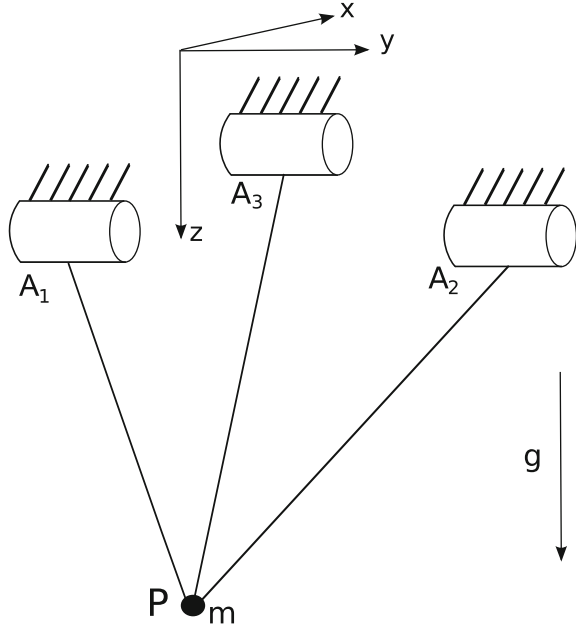
3 Kinematic and Dynamic Modelling

A fixed reference frame is first defined on the base of the robot, as illustrated in Fig. 1. The Z axis of the fixed reference frame is pointing downwards, i.e., in the direction of gravity. The points corresponding to the cable outputs of the spools are assumed to be fixed—in practice an eyelet or a pulley can be used—and are noted A_i, with $i = 1, 2, 3$. The vector connecting the origin of the fixed reference frame to point A_i is noted $\mathbf{a}_i$ and the position of the end-effector of mass m with respect to the origin of the fixed reference frame is noted $\mathbf{p} = [x, y, z]^T$. The cable lengths, which are used as joint coordinates, are respectively noted $\rho_i, i = 1, 2, 3$. The inverse kinematic equations can therefore be simply written as

$$\rho_i = \sqrt{(\mathbf{p} - \mathbf{a}_i)^T (\mathbf{p} - \mathbf{a}_i)}, \quad i = 1, 2, 3. \tag{1}$$

Since the mass of the cables is neglected, the dynamic model of the robot can be obtained by writing the force balance on the end-effector, which is considered as a point mass. One obtains

$$\sum_{i=1}^{3} \left(\frac{-F_i (\mathbf{p} - \mathbf{a}_i)}{\rho_i} \right) + m\mathbf{g} = m\ddot{\mathbf{p}} \tag{2}$$

where F_i is the tension in cable i and $\mathbf{g}$ is the vector of gravitational acceleration, namely $\mathbf{g} = [0, 0, g]^T$, in which g is the magnitude of the gravitational acceleration.

Equation (2) constitutes a system of three linear equations in three unknowns (tensions F_1, F_2 and F_3) that can be explicitly solved for F_1, F_2 and F_3 as

$$\mathbf{f} = m\mathbf{M}^{-1}(\mathbf{g} - \ddot{\mathbf{p}}) \tag{3}$$

where $\mathbf{f} = [F_1, F_2, F_3]^T$ and

$$\mathbf{M} = \left[\frac{1}{\rho_1}(\mathbf{p} - \mathbf{a}_1) \quad \frac{1}{\rho_2}(\mathbf{p} - \mathbf{a}_2) \quad \frac{1}{\rho_3}(\mathbf{p} - \mathbf{a}_3) \right]. \tag{4}$$

In order to obtain dynamically feasible trajectories, it must be ensured that the above solution yields tensions in the cables, i.e, it must be guaranteed that F_1, F_2 and F_3 are positive throughout the trajectory.

A generic form of the unilaterality constraints is obtained by rearranging the above equations. Unit vectors along the direction of the cables are first defined as

$$\mathbf{e}_i = \frac{\mathbf{p} - \mathbf{a}_i}{\| \mathbf{p} - \mathbf{a}_i \|} = \frac{1}{\rho_i}(\mathbf{p} - \mathbf{a}_i), \quad i = 1, 2, 3 \tag{5}$$

where $\mathbf{e}_i$ is a unit vector in the direction of the ith cable and oriented from the spool to the end-effector. Equation (2) can then be rewritten as

$$\mathbf{M}\tau = \mathbf{g} - \ddot{\mathbf{p}} \tag{6}$$

where

$$\mathbf{M} = [\mathbf{e}_1 \quad \mathbf{e}_2 \quad \mathbf{e}_3] \tag{7}$$

and

$$\tau = \frac{1}{m}\mathbf{f} = \frac{1}{m}[F_1 \quad F_2 \quad F_3]^T \tag{8}$$

is the vector of cable forces per unit mass of the end-effector. Using this notation, Eq. (3) can be rewritten as

$$\tau = \mathbf{M}^{-1}(\mathbf{g} - \ddot{\mathbf{p}}). \tag{9}$$

Referring to Eq. (7), the inverse of matrix $\mathbf{M}$ can be written as

$$\mathbf{M}^{-1} = \frac{\text{Adj}(\mathbf{M})}{\det(\mathbf{M})} \tag{10}$$

where $\text{Adj}(\mathbf{M})$ is the adjoint matrix of $\mathbf{M}$ and $\det(\mathbf{M})$ is its determinant. It can readily be observed that the determinant of $\mathbf{M}$ can be written as

$$\det(\mathbf{M}) = (\mathbf{e}_1 \times \mathbf{e}_2)^T \mathbf{e}_3 \tag{11}$$

and that this quantity is always strictly negative as long as the end-effector remains below the plane defined by the three attachment points A_1, A_2 and A_3. This assumption is used here and therefore it suffices to use the adjoint matrix in order to determine whether the tensions in the cables are positive. The adjoint matrix can be written as

$$\text{Adj}(\mathbf{M}) = \begin{bmatrix} (\mathbf{e}_2 \times \mathbf{e}_3)^T \\ (\mathbf{e}_3 \times \mathbf{e}_1)^T \\ (\mathbf{e}_1 \times \mathbf{e}_2)^T \end{bmatrix} \tag{12}$$

and hence the condition corresponding to positive tensions is written as

$$\tau \succeq 0 \tag{13}$$

where $\succeq$ stands for the componentwise inequality. Based on Eqs. (9) and (12) and noting that the determinant of $\mathbf{M}$ is always negative, the constraints then become

$$(\mathbf{e}_2 \times \mathbf{e}_3)^T (\ddot{\mathbf{p}} - \mathbf{g}) > 0 \tag{14}$$

$$(\mathbf{e}_3 \times \mathbf{e}_1)^T (\ddot{\mathbf{p}} - \mathbf{g}) > 0 \tag{15}$$

$$(\mathbf{e}_1 \times \mathbf{e}_2)^T (\ddot{\mathbf{p}} - \mathbf{g}) > 0. \tag{16}$$

The above inequalities represent the constraints to be satisfied in order to ensure that the cables are kept under tension. If these conditions are satisfied at all points of a given trajectory, then it can be guaranteed that the cables will remain under tension throughout the trajectory. These conditions are necessary and sufficient. Using Eq. (5), the inequalities can be written directly in terms of the position vector of the end-effector, which leads to

$$\left[\mathbf{p} \times (\mathbf{a}_2 - \mathbf{a}_3) + (\mathbf{a}_2 \times \mathbf{a}_3)\right]^T (\ddot{\mathbf{p}} - \mathbf{g}) > 0 \tag{17}$$

$$\left[\mathbf{p} \times (\mathbf{a}_3 - \mathbf{a}_1) + (\mathbf{a}_3 \times \mathbf{a}_1)\right]^T (\ddot{\mathbf{p}} - \mathbf{g}) > 0 \tag{18}$$

$$\left[\mathbf{p} \times (\mathbf{a}_1 - \mathbf{a}_2) + (\mathbf{a}_1 \times \mathbf{a}_2)\right]^T (\ddot{\mathbf{p}} - \mathbf{g}) > 0. \tag{19}$$

4 Trajectory Planning

The inequality constraints derived in the preceding section can be used to ensure that dynamic trajectories are feasible, i.e., that they can be performed while maintaining the cables under tension. Indeed, trajectories satisfying the tension constraints are automatically included in the *dynamic* workspace of the robot, which may extend beyond its *static* workspace.

In order to simplify the trajectory planning and to avoid having to consider the constraints in the control loop, feasible generic trajectories are now defined. Feasible trajectories are obtained by manipulating the inequality constraints to obtain

conditions on the global trajectory parameters that ensure positive cable tensions. In other words, the constraints are satisfied by trajectory design, which greatly simplifies the planning and control. To this end, a set of generic periodic trajectories is now analysed. It should be pointed out that the periodic trajectories defined below correspond to a *steady state* dynamic motion (e.g. vertical oscillations). In other words, the transition between the state of rest and a periodic trajectory—or between two periodic trajectories—is not considered and will be addressed in a separate section.

In order to provide physical insight, a specific robot architecture is used in this section. In this architecture, the three spools are located on the vertices of a horizontal equilateral triangle whose centroid is at the origin of the fixed reference frame. The geometry is therefore defined as

$$\mathbf{a}_1 = \left[\frac{a}{2}, -\frac{\sqrt{3}a}{6}, 0 \right]^T \tag{20}$$

$$\mathbf{a}_2 = \left[-\frac{a}{2}, -\frac{\sqrt{3}a}{6}, 0 \right]^T \tag{21}$$

$$\mathbf{a}_3 = \left[0, \frac{\sqrt{3}a}{3}, 0 \right]^T \tag{22}$$

where a is equal to the side of the equilateral triangle. Substituting the above geometric parameters into inequalities (17)–(19), the latter can be rewritten as

$$\sqrt{3}z\ddot{x} - z\ddot{y} + (\ddot{z} - g)\left(y - \sqrt{3}x - \frac{\sqrt{3}}{3}a \right) > 0 \tag{23}$$

$$-\sqrt{3}z\ddot{x} - z\ddot{y} + (\ddot{z} - g)\left(y + \sqrt{3}x - \frac{\sqrt{3}}{3}a \right) > 0 \tag{24}$$

$$z\ddot{y} + (g - \ddot{z})\left(y + \frac{\sqrt{3}}{6}a \right) > 0. \tag{25}$$

Parametric periodic trajectories are now defined and substituted into inequalities (23)–(25). Using interval arithmetics, i.e., the bounds of the trigonometric functions, conditions on the global trajectory parameters are obtained that ensure dynamic feasibility.

4.1 Vertical Oscillations

A simple vertical periodic oscillation is first studied. Although this trajectory is located inside the static workspace, the trajectory must still be planned such that

inequalities (23)–(25) are satisfied because the trajectory involves non-zero accelerations. A generic periodic trajectory along the Z axis—taking place along a vertical line passing through the centroid of the base triangle—is designed as follows:

$$x = y = 0, \quad z = z_0 + r\sin(\omega t), \quad z_0 > r \tag{26}$$

$$\dot{x} = \dot{y} = 0, \quad \dot{z} = r\omega\cos(\omega t) \tag{27}$$

$$\ddot{x} = \ddot{y} = 0, \quad \ddot{z} = -r\omega^2\sin(\omega t) \tag{28}$$

where z_0 is the centre of the vertical range of motion, r is one half of the total vertical range of motion, ω is the frequency of the periodic motion and t is the time. A complete oscillation is performed if $0 \le t \le 2\pi/\omega$. Substituting the above trajectory into inequalities (23)–(25) leads to one and the same condition for all three inequalities, namely

$$\ddot{z} - g < 0, \quad \text{or} \quad -r\omega^2\sin(\omega t) - g < 0. \tag{29}$$

Since one has $-1 \le \sin(\omega t) \le 1$, the above condition is satisfied for the global trajectory if

$$r\omega^2 < g. \tag{30}$$

When inequality (30) is satisfied, the above vertical trajectory can be performed while maintaining all cables in tension. Therefore, for a given vertical range of motion $2r$, the frequency ω can be adjusted to satisfy the tension constraints. Similarly, for a given frequency ω, the maximum feasible range of motion can be determined using inequality (30). The condition obtained is global and does not need to be verified for all trajectory points.

4.2 Horizontal Oscillations Along a Straight Line

A periodic horizontal motion along a straight line intersecting the vertical line passing through the centroid of the base triangle is now considered. The trajectory is designed as follows:

$$z = z_0, \quad x = r\cos\alpha\sin(\omega t), \quad y = r\sin\alpha\sin(\omega t), \quad z_0 > 0 \tag{31}$$

$$\dot{z} = 0, \quad \dot{x} = r\omega\cos\alpha\cos(\omega t), \quad \dot{y} = r\omega\sin\alpha\cos(\omega t) \tag{32}$$

$$\ddot{z} = 0, \quad \ddot{x} = -r\omega^2\cos\alpha\sin(\omega t), \quad \ddot{y} = -r\omega^2\sin\alpha\sin(\omega t) \tag{33}$$

where z_0 is the elevation of the horizontal trajectory, r is one half of the total horizontal range of motion, ω is the frequency of the periodic motion, α is the angle corresponding to the direction of the straight line in the horizontal plane and t is the time. Substituting the above parametric equations into inequalities (23)–(25) leads to three inequalities that can be written as

$$A_i \sin(\omega t) + B_i > 0, \quad i = 1, 2, 3 \tag{34}$$

where

$$A_1 = r(z_0\omega^2 - g)(\sin\alpha - \sqrt{3}\cos\alpha) \tag{35}$$

$$A_2 = r(z_0\omega^2 - g)(\sin\alpha + \sqrt{3}\cos\alpha) \tag{36}$$

$$A_3 = -r(z_0\omega^2 - g)\sin\alpha \tag{37}$$

$$B_1 = B_2 = \frac{\sqrt{3}}{3}ag \tag{38}$$

$$B_3 = \frac{\sqrt{3}}{6}ag. \tag{39}$$

Given the bounds on the sine function, the conditions given in Eq. (34) are satisfied throughout the trajectory if the following conditions are satisfied:

$$|A_i| < B_i, \quad i = 1, 2, 3. \tag{40}$$

When inequalities (40) are satisfied, the horizontal trajectory can be performed while maintaining all cables in tension. Since conditions (40) involve only the geometric parameters of the robot and the global parameters of the trajectory—elevation z_0, amplitude r, horizontal direction α and frequency ω—the parameters can be adjusted to produce feasible trajectories.

It can also be observed, from Eqs. (35)–(39) that when a frequency of

$$\omega_n = \sqrt{\frac{g}{z_0}} \tag{41}$$

is selected, inequalities (40) are always satisfied and arbitrary amplitudes of motion r can theoretically be produced. This is so because coefficients $B_i, i = 1, 2, 3$ are strictly positive quantities and the above frequency makes coefficients $A_i, i = 1, 2, 3$ equal to zero. This frequency, ω_n, can be thought of as a kind of *natural frequency* for the robot performing horizontal oscillations. It is remarkable that this frequency corresponds to the natural frequency of a single cable pendulum of length z_0. In practice, the existence of such a frequency can be exploited in order to maximize the effectiveness of the robot for lateral motions. Indeed, using this frequency for periodic horizontal motions guarantees that the cable tensions will always be positive, for any amplitude of motion r.

4.3 Circular Trajectories in a Horizontal Plane

Horizontal circular trajectories centred on a point $(0, 0, z_0)$ lying on the z axis can be designed using the following parametric equations:

$$z = z_0, \quad x = r\cos(\omega t), \quad y = r\sin(\omega t), \quad z_0 > 0 \tag{42}$$
$$\dot{z} = 0, \quad \dot{x} = -r\omega\sin(\omega t), \quad \dot{y} = r\omega\cos(\omega t) \tag{43}$$
$$\ddot{z} = 0, \quad \ddot{x} = -r\omega^2\cos(\omega t), \quad \ddot{y} = -r\omega^2\sin(\omega t) \tag{44}$$

where r is the radius of the circle, ω is the frequency of the rotating motion and t is the time. Substituting the above equations into inequalities (23)–(25) leads to three inequalities that can be written as

$$C_i \cos(\omega t) + D_i \sin(\omega t) + E_i > 0, \quad i = 1, 2, 3 \tag{45}$$

with

$$C_1 = -C_2 = \sqrt{3}r(g - z_0\omega^2) \tag{46}$$
$$C_3 = 0 \tag{47}$$
$$D_1 = D_2 = -r(g - z_0\omega^2) \tag{48}$$
$$D_3 = r(g - z_0\omega^2) \tag{49}$$
$$E_1 = E_2 = \frac{\sqrt{3}}{3}ag \tag{50}$$
$$E_3 = \frac{\sqrt{3}}{6}ag \tag{51}$$

Clearly, the expressions in Eq. (45) are periodic functions of time. Therefore, in order to ensure that these expressions are positive definite, it suffices to verify that all their extrema are positive. The extrema can be found by considering the partial derivatives of these expressions with respect to t. Substituting the conditions obtained by setting the partial derivatives to zero in the inequality constraints, a set of twelve conditions that are independent of time are obtained. The complete derivation is not given here because of space limitation. However, by inspection of Eqs. (46)–(51) it can be readily observed that the inequalities of Eq. (45) are automatically satisfied when one has

$$\omega = \omega_n = \sqrt{\frac{g}{z_0}}. \tag{52}$$

Similarly to what was observed for the straight line trajectories, arbitrarily large horizontal circles can be traced if the above frequency is used. It is again remarkable that the special frequency is equal to that of a single cable pendulum. This result is very useful in practice. Indeed, it makes the trajectory planning of horizontal

circular motions very simple, if the frequency ω_n given above is used. When other frequencies are needed, then the twelve conditions referred to above can be employed to determine the combinations of z_0, r and ω that lead to feasible trajectories, i.e., trajectories that can be performed while maintaining the tension in the cables.

4.4 Circular Trajectories in a Vertical Plane

Trajectories corresponding to circles centred on point $(0, 0, z_0)$ and traced in a vertical plane can be designed using the following parametric equations:

$$x = r \cos \beta \cos(\omega t), \quad y = r \sin \beta \cos(\omega t), \quad z = z_0 + r \sin(\omega t), \quad z_0 > r \quad (53)$$
$$\dot{x} = -r\omega \cos \beta \sin(\omega t), \quad \dot{y} = -r\omega \sin \beta \sin(\omega t), \quad \dot{z} = r\omega \cos(\omega t) \quad (54)$$
$$\ddot{x} = -r\omega^2 \cos \beta \cos(\omega t), \quad \ddot{y} = -r\omega^2 \sin \beta \cos(\omega t) \quad \ddot{z} = -r\omega^2 \sin(\omega t) \quad (55)$$

where r is the radius of the circle, ω is the frequency of the rotating motion, β is the angle defining the orientation of the vertical plane in which the trajectory is embedded and t is the time. Substituting the above equations into inequalities (23)–(25) leads to three inequalities that can be written exactly as in Eq. (45) but with

$$C_1 = C_2 = r(g - z_0\omega^2)(\sqrt{3}\cos \beta - \sin \beta) \quad (56)$$
$$C_3 = r \sin \beta (g - z_0\omega^2) \quad (57)$$
$$D_1 = D_2 = \frac{\sqrt{3}}{3} ar\omega^2 \quad (58)$$
$$D_3 = \frac{\sqrt{3}}{6} ar\omega^2 \quad (59)$$
$$E_1 = E_2 = \frac{\sqrt{3}}{3} ag \quad (60)$$
$$E_3 = \frac{\sqrt{3}}{6} ag. \quad (61)$$

The derivation of the global conditions ensuring the feasibility of this trajectory can be performed similarly to what was done for the preceding trajectory and a set of inequalities is obtained. The detailed expressions are not given here because of space limitations.

Similarly to what was observed above, the special frequency—ω_n, defined in Eq. (52)—appears in the equations. It can be readily shown that if the latter frequency is used, arbitrarily large vertical circles can be traced as long as they are contained below the attachment points of the mechanism (spool output points), i.e., as long as $z_0 > r$.

4.5 Spatial Trajectories on the Surface of a Cylinder of Vertical Axis

Trajectories embedded on the surface of a cylinder of vertical axis can be designed using the following parametric equations:

$$x = r\cos(\omega_1 t), \quad y = r\sin(\omega_1 t), \quad z = z_0 + h\sin(\omega_2 t), \quad z_0 > h \quad (62)$$

$$\dot{x} = -r\omega_1 \sin(\omega_1 t), \quad \dot{y} = r\omega_1 \cos(\omega_1 t), \quad \dot{z} = h\omega_2 \cos(\omega_2 t) \quad (63)$$

$$\ddot{x} = -r\omega_1^2 \cos(\omega_1 t), \quad \ddot{y} = -r\omega_1^2 \sin(\omega_1 t) \quad \ddot{z} = -h\omega_2^2 \sin(\omega_2 t) \quad (64)$$

where r is the radius of the cylinder, h is one half of the vertical range of motion, ω_1 is the frequency of the rotating motion, ω_2 is the frequency of the vertical oscillation and t is the time. If $\omega_1 > \omega_2$, the resulting trajectory will correspond roughly to circles going up and down the cylinder whereas if $\omega_2 > \omega_1$, the trajectory will correspond to a sine wave traced on the vertical cylinder.

Substituting the above equations into inequalities (23)–(25) leads to three inequalities which are not given here because of space limitations. Nevertheless, it can readily be observed from the expressions obtained that a special frequency for ω_1 appears again in the equations, namely

$$\omega_{1n} = \sqrt{\frac{g}{z_0}}. \quad (65)$$

Then, assuming that $\omega_1 = \omega_{1n}$ and that $\omega_2^2 = k\omega_1^2$, it can be shown that the trajectory will be feasible if the following global condition on the parameters is satisfied:

$$kh\left(r + \frac{\sqrt{3}}{6}a\right) < \frac{\sqrt{3}}{6}az_0 + hr. \quad (66)$$

4.6 Spatial Spherical Trajectories

Finally, trajectories defined on the surface of a sphere are designed using the following parametric equations

$$x = r\cos(\omega_1 t)\cos(\omega_2 t), \quad y = r\sin(\omega_1 t)\cos(\omega_2 t), \quad z = z_0 + r\sin(\omega_2 t) \quad (67)$$

where r is the radius of the sphere, t is the time and ω_1 and ω_2 are frequencies that can be modulated in order to obtain different types of trajectories. The time derivatives of the above parametric equations are rather cumbersome and are not given here because of space limitations. Nevertheless, they are readily obtained through straightforward differentiation.

Similarly to what was done for the other trajectories, the above parametric equations and their time derivatives are substituted into inequalities (23)–(25), which leads to rather lengthy expressions. However, it can be observed that special conditions on the frequencies can simplify the conditions greatly. For instance, using

$$(\omega_1^2 + \omega_2^2) = \frac{g}{z_0} \quad \text{and} \quad \omega_2 = k\omega_1 \tag{68}$$

it can be shown that the trajectory is feasible if the following global condition on the parameters is satisfied:

$$\omega_1^2 < \frac{\sqrt{3}ag}{r\left[\sqrt{3}ak^2 + (6 + 6\sqrt{3})z_0k + (6 + 6\sqrt{3})rk + (3 + 3\sqrt{3})r\right]}. \tag{69}$$

The latter condition can be used to plan spherical trajectories while ensuring that they are globally feasible.

4.7 Transition Trajectories

The periodic trajectories defined in the preceding subsections do not include points representing the state of rest, i.e., points of the trajectory where the velocity and acceleration are both equal to zero. Therefore, in order to start from rest and blend into one of the proposed periodic motions, transition trajectories are needed. Moreover, such trajectories can also be used to transit from one generic trajectory to another or simply to connect different points of the workspace.

The transition trajectories used in this work are obtained by progressively increasing the amplitude of motion—the amplitude of the oscillating motion, or the radius of the circle, cylinder or sphere—during the first phase of the trajectory, until the steady-state periodic trajectory is reached. The progressive increase of the amplitude of the trajectory is obtained using a polynomial. The technique is now briefly demonstrated for the vertical periodic motion described above. A similar approach is used for all other types of trajectories. The transition developed here connects an initial state of rest with the periodic trajectory. It is also possible to use a mirror image of the transition trajectory to end the periodic motion by connecting it to the state of rest.

Consider the vertical trajectory described in (26), (27) and (28). The transition trajectory can be designed as follows:

$$z = z_0 + \beta \sin(\omega t) \tag{70}$$

in which

$$\beta = rU(t), \ \ 0 \leq t < T \tag{71}$$
$$\beta = r, \ \ T \leq t \tag{72}$$

with

$$U(t) = 6\tau^5 - 15\tau^4 + 10\tau^3, \quad \tau = \frac{t}{T} \tag{73}$$

where r and ω are the parameters of the periodic trajectory (chosen to satisfy (30)) and T is the duration of the transition trajectory. When $t > T$, the periodic trajectory is used. The polynomial, $U(t)$, introduced here is often used in trajectory planning to match initial and final positions, velocities and accelerations [11]. Using this polynomial, the transition trajectory ensures continuity up to the acceleration level, thereby leading to continuous forces in the cables.

Differentiating (70) twice with respect to time, one obtains

$$\ddot{z} = -\beta\omega^2 \sin(\omega t) + \frac{2\omega r V(t) \cos(\omega t)}{T} + \frac{r W(t) \sin(\omega t)}{T^2} \tag{74}$$

where

$$V(t) = 30\tau^4 - 60\tau^3 + 30\tau^2 \tag{75}$$
$$W(t) = 120\tau^3 - 180\tau^2 + 60\tau. \tag{76}$$

Substituting the latter result into (29) then leads to

$$g + \beta\omega^2 \sin(\omega t) - \frac{2\omega r V(t) \cos(\omega t)}{T} - \frac{r W(t) \sin(\omega t)}{T^2} > 0. \tag{77}$$

Interval arithmetics can be applied to the expression appearing on the left hand side of (77) over the interval $t \in [0, T]$ in order to assess its behaviour. Noting that the sine and cosine functions are bounded in the interval $[-1, 1]$, it is readily found that the lowest value $e_{\min}$ that the above expression can possibly take in the interval $t \in [0, T]$ is given by

$$e_{\min} = g - r\omega^2 - \frac{15r\omega}{4T} - \frac{10\sqrt{3}r}{3T^2}. \tag{78}$$

Referring to (30)—which must be satisfied for the steady-state trajectory to be feasible—, it is clear that T can always be chosen large enough to ensure that (77) is satisfied, which demonstrates the feasibility of the proposed transition trajectory. In practice, however, it may be desirable to determine the minimum value of T that can be used while satisfying the constraints on the positive cable tensions. To this end, the time derivative of the expression appearing in inequality (77) is set to zero in order

Fig. 2 Prototype of a three-dof spatial cable-suspended robot
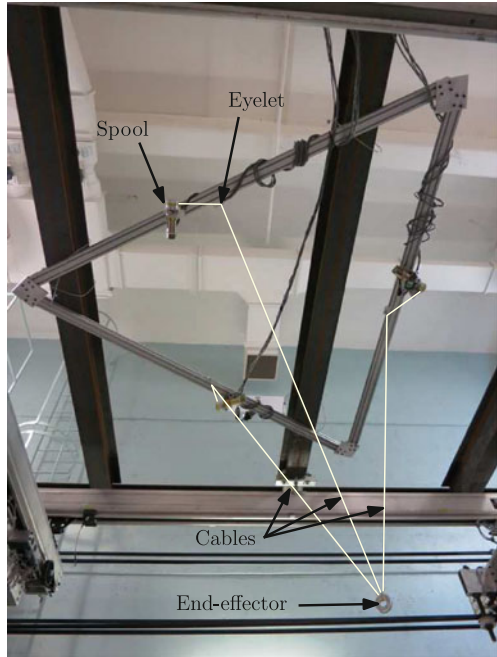
to determine the extrema. The resulting equation can be solved numerically in order to determine the values of t that correspond to extrema of the function. These values can then be substituted into (77) in order to determine the smallest value of T that can be used. Because of the periodic functions appearing in (77), its time derivative will have infinitely many roots (generally two per period). Therefore, roots can first be searched for in the interval defined as $t \in [0, \frac{2\pi}{\omega}]$. Moreover, good initial guesses are available by inspection of the intersections between the sine and cosine functions.

The approach described above for the planning of the transition trajectories can also be applied to the other generic trajectories with similar results.

5 Example Trajectories and Experimental Validation

A prototype of a three-dof spatial cable-suspended robot was built in order to validate the approach proposed in this paper. The prototype is shown in Fig. 2. The distance between the cable attachment points on the frame is $a = 1.03$ m and the mass of the end-effector is $m = 0.196$ kg. Three servo-controlled winches are used to control the length of the cables. Vertical, horizontal, circular, cylindrical and spherical trajectories were successfully demonstrated with the prototype. Large amplitudes of motion—bringing the end-effector beyond the static workspace—were produced
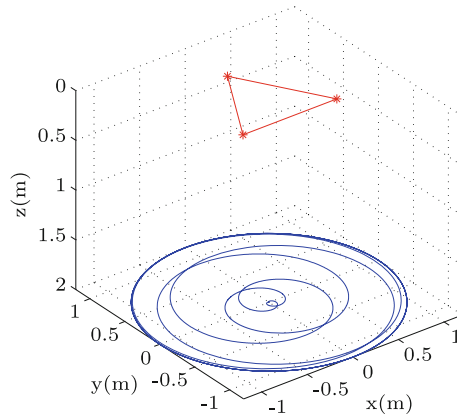
Fig. 3 Three-dimensional representation of the horizontal circular trajectory including the transition phase
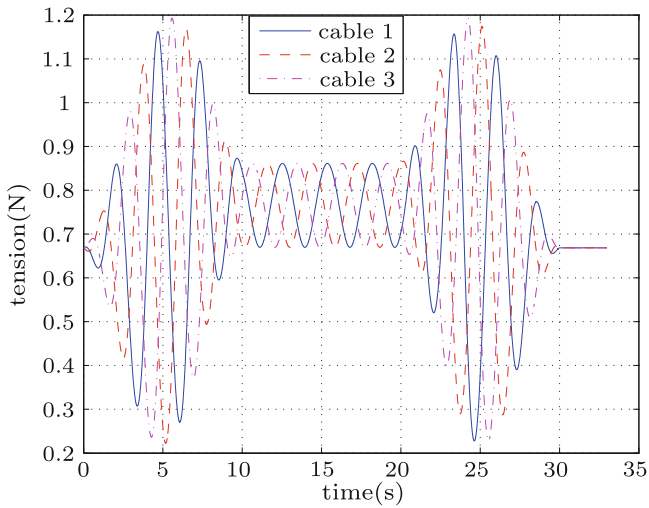
Fig. 4 Cable tensions in Newtons for the example of horizontal circular trajectory, with $m = 0.196\,\text{kg}$

using the 'natural' frequency, ω_n, defined in this paper. Example results are now presented.
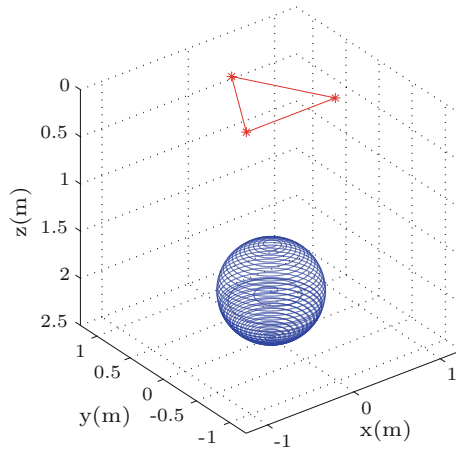
Fig. 5 Three-dimensional representation of the spherical trajectory
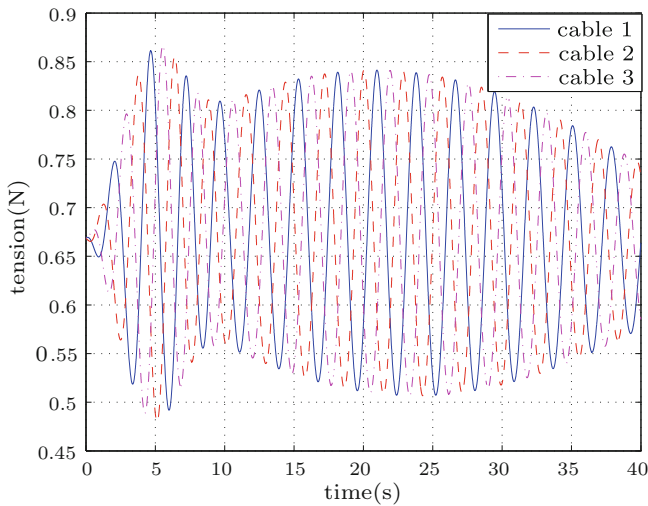
Fig. 6 Cable tensions in Newtons for the example of spherical trajectory, with $m = 0.196\,\text{kg}$

5.1 Horizontal Circular Trajectory

An example of a horizontal circular trajectory is first considered. The following parameters are chosen: $z_0 = 2\,\text{m}$ and $r = 1.2\,\text{m}$ (the circle is located beyond the static workspace). Moreover, the frequency is chosen as $\omega = \omega_n = 2.21 s^{-1}$ and the transition time is $T = 10\,\text{s}$. The resulting motion is illustrated schematically in Fig. 3, including the transition phase. The tensions in the cables are given in Fig. 4. It is readily verified that the cable tensions remain positive and continuous at all times.

5.2 Spherical Trajectory

An example of a spherical trajectory is now shown. The following parameters are chosen: $z_0 = 2$ m, $r = 0.5$ m, $\omega_1 = \omega_{1n} = 2.21s^{-1}$ and $\omega_2 = 0.039s^{-1}$ with a transition time of $T = 10$ s. The resulting motion is illustrated schematically in Fig. 5. The tensions in the cables is given in Fig. 6. It is readily verified that the cable tensions remain positive and continuous at all times. The duration of the trajectory is 180 s but only the first part of the trajectory is shown on the graph of Fig. 6 for better clarity.

6 Conclusion

In this paper, the performance of dynamically feasible trajectories with a three-dof spatial cable-suspended robot was investigated. Parametric Cartesian trajectories were proposed. By substituting these trajectories into the dynamic constraints—the constraints associated with the unilaterality of the cable forces—global conditions on the trajectory parameters were obtained. When these inequality conditions are satisfied, it can be ensured that all cables remain in tension throughout the trajectory. The advantage of this approach is that the results are global. Hence, there is no need to verify that the cable constraints are satisfied when performing the trajectory and no time discretization is necessary. The repertoire of trajectories investigated in this paper can easily be extended. Moreover, the basic trajectories studied here can be used as building blocks to construct more complex trajectories. The approach proposed in this work was validated experimentally on a three-dof prototype and some sample results are presented in the paper.

Remarkable special frequencies, akin to natural frequencies, were shown to have interesting properties for several of the periodic motions investigated. By exploiting the dynamic workspace, the approach proposed in this work opens the avenue for a variety of new applications of cable-suspended robots by allowing them to work outside of their static workspace. Further experimental investigations and the application of the technique to six-dof robots is the subject of ongoing work.

References

1. Albus, J., Bostelman, R., Dagalakis, N.: The NIST robocrane. J. Robot. Syst. **10**(5), 709–724 (1993)
2. Barrette, G., Gosselin, C.: Determination of the dynamic workspace of cable-driven planar parallel mechanisms. ASME J. Mech. Des. **127**(2), 242–248 (2005)
3. Behzadipour, S.: Kinematics and dynamics of a self-stressed Cartesian cable-driven mechanism. ASME, J. Mech. Des. 131, 061005-1-061005-10 (2009).
4. Borgstrom, P.H., Jordan, B.L., Sukhatme, G.S., Batalin, M.A., Kaiser, W.J.: Rapid computation of optimally safe tension distributions for parallel cable-driven robots. IEEE Trans. Robot. **25**(6), 1271–1281 (2009)
5. Brackbill, E.A., Mao, Y., Agrawal, S.K., Annapragada, M., Dubey, V.N.: Dynamics and control of a 4-dof wearable cable-driven upper arm exoskeleton. In: Proceedings of the IEEE International Conference on Robotics and Automation, pp. 2300–2305. Kobe, Japan (2009).
6. Cunningham D., Asada, H.: The Winch-Bot: a cable-suspended, under-actuated robot utilizing parametric self-excitation. In: Proceedings of the IEEE International Conference on Robotics and Automation, pp. 1844–1850 (2009).
7. Diao, X., Ma, O.: Workspace analysis of a 6-dof cable robot for hardware-in-the-loop dynamic simulation. In: Proceedings of the 2006 IEEE/RSJ International Conference on Intelligent Robots and Systems, pp. 4103–4108. Beijing, China (2006).
8. Fang, S., Franitza, D., Torlo, M., Bekes, F., Hiller, M.: Motion control of a tendon-based parallel manipulator using optimal tension distribution. IEEE/ASME Trans. Mechatron. **9**(3), 561–568 (2004)
9. Gosselin, C.: On the determination of the force distribution in overconstrained cable-driven parallel mechanisms. In: Proceedings of the Second International Workshop on Fundamental Issues and Future Research Directions for Parallel Mechanisms and Manipulators, pp. 9–17. Montpellier, France (2008).
10. Gosselin, C., Bouchard, S.: A gravity-powered mechanism for extending the workspace of a cable-driven parallel mechanism: application to the appearance modelling of objects. Int. J. Autom. Technol. **4**(4), 372–379 (2010)
11. Gosselin, C., Hadj-Messaoud, A.: Automatic planning of smooth trajectories for pick-and-place operations. ASME J. Mech. Des. **115**(3), 450–456 (1993)
12. Gosselin, C., Ren, P., Foucault, S.: Dynamic trajectory planning of a two-dof cable-suspended parallel robot. In: Proceedings of the IEEE International Conference on Robotics and Automation, pp. 1476–1481. St-Paul, Minnesota (2012).
13. Kawamura, S., Choe, W., Tanaka S., Pandian, S.: Development of an ultrahigh speed robot FALCON using wire drive system. In: Proceedings of the IEEE International Conference on Robotics and Automation, pp. 215–220 (1995).
14. Lefrançois, S., Gosselin, C.: Point-to-point motion control of a pendulum-like 3-dof underactuated cable-driven robot. In: Proceedings of the IEEE International Conference on Robotics and Automation, pp. 5187–5193 (2010).
15. Miermeister, P., Pott, A., Verl, A.: Dynamic modeling and hardware-in-the-loop simulation for the cable-driven parallel robot IPAnema. In: Proceedings of ISR/Robotik, pp. 1288–1295. Munich (2010).
16. Mikelsons, L., Bruckmann, T., Hiller, M., Schramm, D.: A real-time capable force calculation algorithm for redundant tendon-based parallel manipulators. In: Proceedings of the IEEE International Conference on Robotics and Automation, pp. 3869–3874. Pasadena, California (2008).
17. Oh, S.R., Ryu, J.C., Agrawal, S.K.: Dynamics and control of a helicopter carrying a payload using a cable-suspended robot. ASME J. Mech. Des. **128**, 1113–1121 (2006)
18. Oh, S.R., Mankala, K., Agrawal, S.K., Albus, J.S.: A dual-stage planar cable robot: dynamic modeling and design of a robust controller with positive inputs. ASME J. Mech. Des. **127**, 612–620 (2005)

19. Pham, C.B., Yang, G., Yeo, S.H.: Dynamic analysis of cable-driven parallel mechanisms. In: Proceedings of the 2005 IEEE/ASME International Conference on Advanced Intelligent Mechatronics, pp. 612–617. Monterey, California (2005).
20. Pusey, J., Fattah, A., Agrawal, S., Messina, E.: Design and workspace analysis of a 6–6 cable-suspended parallel robot. Mech. Mach. Theory **39**, 761–778 (2004)
21. Riechel, A.T. Ebert-Uphoff, I.: Force-feasible workspace analysis for underconstrained, point-mass cable robots. In: Proceedings of the IEEE International Conference on Robotics and Automation, pp. 4956–4962 (2004).
22. Tadokoro, S., Murao, Y., Hiller, M., Murata, R., Kohkawa, H., Matsushima, T.: A motion base with 6-dof by parallel cable drive architecture. IEEE/ASME Trans. Mechatron. **7**(2), 115–123 (2002)
23. Zanotto, D., Rosati, G., Agrawal, S.K.: Modeling and control of a 3-DOF pendulum-like manipulator. In: Proceedings of the IEEE International Conference on Robotics and Automation, pp. 3964–3969 (2011).
24. Zi, B., Duan, B.Y., Du, J.L., Bao, H.: Dynamic modeling and active control of a cable-suspended parallel robot. Mechatronics **18**, 1–12 (2008)
25. Zoso, N., Gosselin, C.: Point-to-point motion planning of a parallel 3-DOF underactuated cable-suspended robot. In: Proceedings of the IEEE International Conference on Robotics and Automation, pp. 2325–2330. St-Paul, Minnesota (2012).

Experimental Validation of a Trajectory Planning Approach Avoiding Cable Slackness and Excessive Tension in Underconstrained Translational Planar Cable-Driven Robots

Alberto Trevisani

Abstract The objective of this paper is providing the first experimental evidence of the effectiveness of an off-line trajectory planning approach developed to ensure positive and bounded cable tensions in under constrained planar two-degree-of-freedom translational cable robots. The hybrid (serial/parallel) topology of the investigated robot is general enough to ensure wide applicability of the proposed trajectory planning method, which translates the usual bilateral tensile cable force constraints into kinematic constraints on the velocity and acceleration of the robot tool center point along the desired path. Kinematic constraints are computed making use of the robot dynamic model and can then be incorporated in any trajectory planning algorithm. In this work a smooth trajectory planning algorithm based on quintic polynomials is adopted. The experimental setup is presented and the results obtained by applying the method to two sample paths are discussed.

1 Introduction

One essential requirement that has to be met in cable-direct-driven robots (CDDRs) is ensuring that tensile cable forces during the motion remain positive and bounded (i.e. below a maximum permissible tension depending on either the cable physical features or the actuator size). Such a problem is exacerbated in underconstrained and cable-suspended robots, where tensioning is provided by gravity (e.g. the Skycam [1], the RoboCrane [2] and the CSSR in [3]).

Given the importance of avoiding slackness in cables, several works have explicitly addressed the problems of predicting cable tensions [4] and workspace boundaries [5, 6] or of developing control schemes [7] and trajectory planning strategies [8] ensuring positive cable tensions during the motion. The techniques proposed to

A. Trevisani (✉)
DTG Università di Padova, Stradella S. Nicola 3, Vicenza 36100, Italy
e-mail: alberto.trevisani@unipd.it

date to guarantee positive cable tensions often rely on redundant cables [9]. Such an approach, however, has major limitations: given the higher number of wires and actuators, redundant CDDRs usually tend to obstruct the workspace, are more difficult to design (e.g. cable-interference can be hard to avoid) and more expensive to build and maintain than non-redundant CDDRs.

In order to overtake these limitations, and to specifically address both bilateral tensile cable force constraints (i.e. slackness and excessive tension in cables), in [10] an off-line trajectory planning method has been suggested to a-priori ensure positive and bounded cable tensions in underconstrained translational planar cable robots. By making use of dynamics modeling, the method translates the bilateral force constraints of the cables into kinematic constraints on the velocity and acceleration of the tool center point (TCP) along the desired path. Such an approach is here experimentally validated for the first time, by incorporating the kinematic constraints in a minimum time trajectory planning algorithm based on smooth quintic polynomials, which are particularly suitable for CDDRs, where the continuity of acceleration profiles is of paramount importance to prevent tracking errors and jerky motion due to cable elasticity. An underconstrained hybrid (serial/parallel) planar two-dof translational CDDR is studied: such a configuration has some peculiar advantages [10] and is more general than a purely parallel cable-suspended robot. Contrary to the hybrid robots presented in [11] and [12] no cable is here directly connected to the links but they are both connected to the end-effector. Additionally, both the revolute joints of the serial linkage are passive.

The studied CDDR is discussed in Sect. 2, then in Sects. 3 and 4 the analytical expressions of cable tensions are computed and employed to get the kinematic constraints to be satisfied at the trajectory planning stage. Subsequently, the use of quintic polynomials is discussed in Sect. 5, while the CDDR prototype and the experimental results from two different tests are presented in Sects. 6 and 7. Concluding remarks are finally provided in Sect. 8.

2 The Studied CDDR

The theory presented in this paper is explained and validated experimentally by applying it to the two-dof CDDR introduced in [10], where cables are combined with a linkage to produce a lightweight assembly. The CDDR is schematically depicted in Fig. 1. Table 1 explains the meaning of the symbols adopted in Fig. 1. The CDDR topology is hybrid, in the sense that the end-effector of the manipulator is driven by two coplanar cables (parallel topology) and it is also supported by a passive two-link serial manipulator in order to reduce out of the plane compliance. The end-effector can therefore translate in a vertical and planar workspace. A subset of the workspace is the rectangular base polygon shown in Fig. 1. The two driving cables wind around two motor-actuated pulleys. The studied translational planar two-dof CDDR is hence underconstrained since cable tensioning at rest can just be provided by gravity. In consequence of the presence of the passive serial manipulator, static cable tensioning

Fig. 1 Kinematic scheme of the planar CDDR with passive serial-link support
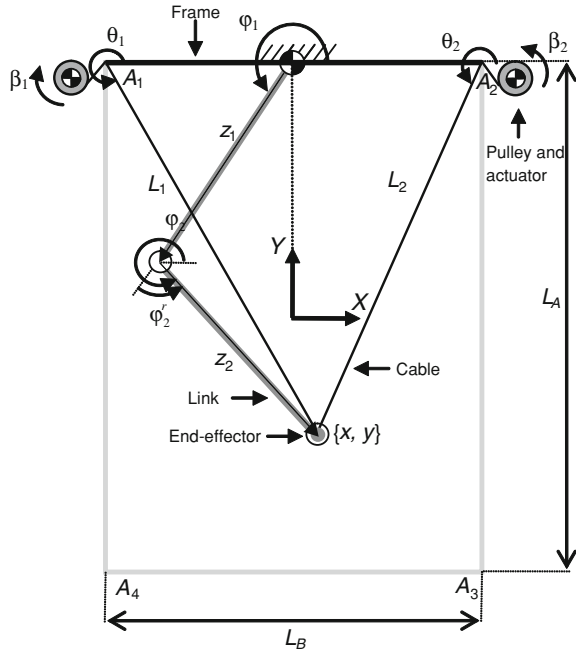
Table 1 Meaning of the symbols in Fig. 1

$\{X, Y\}$	Cartesian reference frame with origin at the centroid of the base polygon
$\{x, y\}$	Coordinates of the tool center point (TCP) of the end-effector
L_A, L_B	Fixed lengths of the base polygon sides
A_j	Vertices of the base polygon ($j = 1, ..., 4$)
L_i	Length of the ith cable, measured from vertex A_i to the TCP ($i = 1, 2$)
θ_i	Absolute ith cable angle ($i = 1, 2$)
β_i	ith pulley angle ($i = 1, 2$)
z_k	Fixed length of the kth link of the serial manipulator ($k = 1, 2$)
φ_k	kth link absolute angle ($k = 1, 2$)
φ_2^r	Relative angle between link 1 and link 2

is not possible in all the rectangular base polygon, but only in a part of it: the Static Equilibrium Workspace (SEW, [13]).

The proposed CDDR can approach the objects to manipulate from above, and leaves a completely unobstructed workspace below the end-effector. Therefore, it might be suitable for a wide range of industrial manipulations where over-the-belt mounting is required and also for applications where safe and comfortable man-robot interaction is needed, as for example in medical rehabilitation.

3 Computation of Cable Tensions

Cable tensions can be computed through the CDDR dynamic model. A suitable model has been developed in [10] starting from the one proposed in [9] for a similar but fully constrained CDDR. Here only the most significant model equations are recalled, slightly modified in the notation in order to improve clarity. The interested reader is referred to both the aforementioned references for further details. Henceforth boldfaced lower-case letters will be used to represent vectors while boldfaced upper-case letters will be reserved for matrices. The scalars and the entries of vectors and matrices will instead be denoted with lowercase italic letters.

Let cable elasticity be negligible. The two equilibrium equations for the end-effector may be stacked in the following matrix form:

$$\mathbf{f_T} + \mathbf{f_S} + \mathbf{p_E} = \mathbf{M}\ddot{\mathbf{x}} \tag{1}$$

where:

- $\mathbf{f_T}$ is the resultant force exerted by the cables on the end-effector. It can be computed through the matrix expression $\mathbf{f_T} = \mathbf{S}\boldsymbol{\tau}$, with $\boldsymbol{\tau}$ the vector of the tensions of the cables and $\mathbf{S}$ the pseudostatics Jacobian matrix whose elements are trigonometric functions of the cable angles [9]. Since the CDDR is underconstrained, $\mathbf{S}$ is a square matrix of order two and the computation of the cable tensions is straightforward;
- $\mathbf{f_S}$ is the force exerted by the passive serial support on the end-effector, which varies both in magnitude and direction during the motion;
- $\mathbf{p_E}$ is the weight force vector applied to the end-effector;
- $\mathbf{M}$ is the Cartesian mass matrix of the end-effector;
- $\ddot{\mathbf{x}}$ are the Cartesian accelerations of the end-effector (at the TCP).

In [10] it has been proved that when a two-link serial support is employed, it exerts a reaction force $\mathbf{f}_S$ which takes the following form:

$$\mathbf{f_S} = \mathbf{I_S}\ddot{\mathbf{x}} + \mathbf{N_S}(\mathbf{J_S^{-1}}\dot{\mathbf{x}})^2 + \mathbf{p_S} \tag{2}$$

where:

- $\dot{\mathbf{x}}$ and $\ddot{\mathbf{x}}$ are the end-effector (TCP) Cartesian velocities and accelerations;
- the elements of the matrices $\mathbf{I_S}$ and $\mathbf{N_S}$ depend on the inertial and geometrical properties of the serial support and on the positions of its links (and hence, in the end, on the Cartesian position $\mathbf{x}$ of the TCP);
- the elements of matrix $\mathbf{J_S}$ only depend on the lengths and the positions of the links;
- the elements of vector $\mathbf{p_S}$ account for the position-dependent gravitational effect introduced by the serial support.

Cable tensions can hence be computed as follows:

$$\boldsymbol{\tau} = \mathbf{S}^{-1}\left[(\mathbf{M} - \mathbf{I_S})\ddot{\mathbf{x}} - \mathbf{N_S}(\mathbf{J_S^{-1}}\dot{\mathbf{x}})^2 - (\mathbf{p_S} + \mathbf{p_E})\right] \tag{3}$$

A more compact expression for $\boldsymbol{\tau}$ can be obtained by setting $\mathbf{B} := \mathbf{S}^{-1}(\mathbf{M} - \mathbf{I_S})$, $\mathbf{C} := \mathbf{S}^{-1}\mathbf{N_S}$, and $\mathbf{d} := -\mathbf{S}^{-1}(\mathbf{p_S} + \mathbf{p_E})$:

$$\boldsymbol{\tau} = \mathbf{B}\ddot{\mathbf{x}} - \mathbf{C}\left(\mathbf{J_S}^{-1}\dot{\mathbf{x}}\right)^2 + \mathbf{d} \tag{4}$$

Equation (4) provides a set of two equations explicating the dependence of the cable tensions on the TCP Cartesian position, velocity and acceleration. Clearly, in order to get positive and bounded cable tensions, it is necessary that the chosen trajectory always satisfies the inequality:

$$0 \leq \mathbf{B}\ddot{\mathbf{x}} - \mathbf{C}\left(\mathbf{J_S}^{-1}\dot{\mathbf{x}}\right)^2 + \mathbf{d} \leq \boldsymbol{\tau}_{\max} \tag{5}$$

where $\boldsymbol{\tau}_{\max}$ is the vector of the maximum permissible cable tensions.

4 Kinematic Constraints to Trajectory Planning

A useful alternative expression of the inequality in Eq. (5) can be obtained by replacing Cartesian velocities and accelerations with expressions involving the magnitude and the direction of the velocity vector (which is tangent to the path followed by TCP) as well as the tangential and centripetal accelerations. Let:

- v and α be respectively the magnitude and the direction of the velocity vector,
- a and γ be respectively the magnitude of the tangential acceleration dv/dt, and the radius of curvature of the path,

  there follows that $\dot{\mathbf{x}} = \begin{Bmatrix} v\cos\alpha \\ v\sin\alpha \end{Bmatrix}$ and $\ddot{\mathbf{x}} = \left\{ a\cos\alpha - \frac{v^2}{\gamma}\sin\alpha \;\; a\sin\alpha + \frac{v^2}{\gamma}\cos\alpha \right\}^T$,

  hence, referred to the ith cable ($i = 1, 2$), Eq. (5) takes the following form:

$$0 \leq \tau_i := p_i a + (q_i/\gamma - c_i)v^2 + d_i \leq \tau_{i\,\max} \tag{6}$$

where:

- c_i is the ith row element of vector $\mathbf{C}\left(\mathbf{J_S}^{-1}\begin{Bmatrix} \cos\alpha \\ \sin\alpha \end{Bmatrix}\right)^2$,
- d_i is the ith row element of vector $\mathbf{d}$,
- p_i and q_i are the ith row elements of vectors $\mathbf{B}\begin{Bmatrix} \cos\alpha \\ \sin\alpha \end{Bmatrix}$ and $\mathbf{B}\begin{Bmatrix} -\sin\alpha \\ \cos\alpha \end{Bmatrix}$.

Based on these definitions:

- d_i only depends on the robot position. d_i is the ith cable tension in static conditions, hence d_i is always positive in the SEW;
- c_i, p_i, and q_i depend on the robot position and on the velocity vector direction;

Equation (5) can be translated into four explicit constraints: a lower and an upper bound for both cable tensions. In turn, cable force constraints can be translated into kinematic constraints on the velocity and acceleration of the robot TCP along the path. Two paths typically adopted in industry are addressed here: the straight line path and the circular path.

4.1 Straight Line Path

In straight line paths, α is constant, the centripetal acceleration is null, and, for each ith cable ($i = 1, 2$), the condition $0 \leq \tau_i$ can be rewritten in the form $p_i a \geq c_i v^2 - d_i$. Let $v_{\lim}$ be the limit TCP velocity along the path (a more descriptive definition of $v_{\lim}$ is provided below). Since d_i is always positive in the SEW and v is bounded between 0 and $v_{\lim}$, the maximum values of $c_i v^2 - d_i$ only depend on the sign of c_i. Indeed, if $c_i > 0$ $\max(c_i v^2 - d_i) = c_i \max(v^2) - d_i = c_i v_{\lim}^2 - d_i$, while if $c_i \leq 0$ $\max(c_i v^2 - d_i) = c_i \min(v^2) - d_i = -d_i$. It is therefore useful to define a function $u_i = u_i(c_i)$ only taking two values:

$$u_i(c_i) = \begin{cases} c_i v_{\lim}^2 - d_i & \text{if } c_i > 0 \\ -d_i & \text{if } c_i \leq 0 \end{cases} \tag{7}$$

By means of this new function, the condition $0 \leq \tau_i$, referred to the ith cable, can be rewritten in the more restrictive form: $p_i a \geq u_i$. If it is possible to choose an upper bound of the TCP velocity (i.e. $v_{\lim}$, in general not coinciding with the maximum permissible velocity actually achievable) so that the u_i function takes negative values along the straight line path, the inequality $p_i a \geq u_i$ allow getting positive upper bounds (a_{sup}^u) and negative lower bounds (a_{inf}^u) for the acceleration. As a consequence, as long as $v \leq v_{\lim}$, it is possible to identify an admissible interval of the TCP acceleration a ($a_{inf}^u \leq a \leq a_{sup}^u$) ensuring positive cable tensions along the whole straight path. The different cases that can be discriminated on the basis of the sign of p_i are reported in Table 2, row 1.

A similar reasoning allows inferring the acceleration bounds introduced by the constraint on the maximum permissible tension $\tau_i \leq \tau_{i\,\max}$: $p_i a \leq c_i v^2 - d_i + \tau_{i\,\max}$, where the sum of the terms $-d_i + \tau_{i\,\max}$ is always positive (alternatively, cable tensions in static conditions would overcome the maximum tensions). The minimum values of $c_i v^2 - d_i + \tau_{i\,\max}$ only depend on the sign of c_i; it is therefore useful to introduce the function $s_i = s_i(c_i)$ which can only take the following two values:

$$s_i(c_i) = \begin{cases} c_i v_{\lim}^2 - d_i + \tau_{i\,\max} & \text{if } c_i < 0 \\ -d_i + \tau_{i\,\max} & \text{if } c_i \geq 0 \end{cases} \tag{8}$$

By means of s_i it is possible to introduce the following more restrictive condition for permissible tensions: $p_i a \leq s_i$. Positive upper bounds (a_{sup}^s) and negative lower bounds (a_{inf}^s) for the TCP acceleration can be computed if s_i takes positive values

Table 2 Upper and lower acceleration bounds for positive and bounded cable tensions along a straight line path

If $p_i > 0 \Rightarrow a^u_{inf\ i} = u_i / u_i\, p_i$	If $p_i < 0 \Rightarrow a^u_{sup\ i} = u_i / p_i$
$a^u_{inf} = \max(a^u_{inf\ i})\ i = (1, 2)$	$a^u_{sup} = \min(a^u_{sup\ i})\ i = (1, 2)$
If $p_i < 0 \Rightarrow a^s_{inf\ i} = s_i / p_i$	If $p_i > 0 \Rightarrow a^s_{sup\ i} = s_i / p_i$
$a^s_{inf} = \max(a^s_{inf\ i})\ i = (1, 2)$	$a^s_{sup} = \min(a^s_{sup\ i})\ i = (1, 2)$
$a_{inf} = \max(a^u_{inf}, a^s_{inf})$	$a_{sup} = \min(a^u_{sup}, a^s_{sup})$

along the straight line path. A suitable $v_{\lim}$ value (in general not coinciding with the one ensuring $u_i < 0$) should be chosen. The different cases that can be discriminated on the basis of the sign of p_i are shown in Table 2, row 2.

In conclusion, once an upper bound $v_{\lim}$ is found which ensures both negative u_i and positive s_i functions, there always exist an upper (a_{sup}) and a lower (a_{inf}) bound for the acceleration (see Table 2, row 3), guaranteeing that, if the kinematic constraints $a_{inf} \le a \le a_{sup}$ and $v \le v_{\lim}$ are satisfied, cable tensions are simultaneously positive and below the maximum permissible values. In general, a_{sup} and a_{inf} are not constant but vary along the path. They should hence be computed as functions of a path coordinate (l) by adopting a suitable discretization of the path.

Equations (7) and (8) show that a $v_{\lim}$ simultaneously ensuring $u_i < 0$ and $s_i > 0$ always exists in the SEW. The choice of $v_{\lim}$ has a considerable impact on the computation of the acceleration bounds and consequently on the minimum traversal time. An inappropriate choice, may lead to overconservative trajectory planning. Generally speaking, either a single $v_{\lim}$ value holding for the whole SEW (or for a subset of it) may be used or a different (variable or constant) $v_{\lim}$ may be adopted for each given path. Such a choice is still a matter of investigation and will be addressed in future works. Admittedly, whichever the choice, as long as $u_i < 0$ and $s_i > 0$ positive and bounded tensions are ensured.

4.2 Circular Path

In case of circular paths of the TCP, the seek for kinematic bounds can be done following an approach almost identical to the one discussed in the previous section. It is only necessary to apply the reasoning to circular path geometrical and kinematic parameters: let R be the radius of the path and ϕ the angular coordinate ($0 \le \phi \le 2\pi$), let α be the direction angle of the velocity vector v, which is now tangent to the circular path. Hence, $\alpha = \phi + \pi/2 \Rightarrow \phi = \alpha - \pi/2, v = R\dot{\alpha}, a = R\ddot{\alpha}$ and Eq. (6) becomes: $0 \le \tau_i = p_i R\ddot{\alpha} - R(Rc_i - q_i)\dot{\alpha}^2 + d_i \le \tau_{i\,\max}$ ($i = 1, 2$), which can be split into two inequalities for each CDDR cable. In particular, by replacing $p_i R$ with p^*_i and

$R(Rc_i - q_i)$ with c_i^* it is possible to write $u_i^* \le p_i^* \ddot{\alpha} \le s_i^*$ where

$$u_i^* = \begin{cases} c_i^* \dot{\alpha}_{\text{lim}}^2 - d_i & \text{if } c_i^* > 0 \\ -d_i & \text{if } c_i^* \le 0 \end{cases} \quad \text{and} \quad s_i^* = \begin{cases} c_i^* \dot{\alpha}_{\text{lim}}^2 - d_i + T_{\text{max}} & \text{if } c_i^* < 0 \\ -d_i + T_{\text{max}} & \text{if } c_i^* \ge 0 \end{cases}$$

These definitions of u_i^* and s_i^* should be compared to those in Eqs. (8) and (9): it is apparent that the considerations made for establishing bilateral constraints on the acceleration a along a straight line path can be immediately extended to the angular acceleration $\ddot{\alpha}$. In particular, a limit angular velocity $\dot{\alpha}_{\text{lim}}$ needs to be found within the interval $0 \le \phi \le 2\pi$ so that $u_i^* < 0$ and $s_i^* > 0$. The dependence of c_i^* on q_i makes it extremely difficult, if not impossible, to find a single $\dot{\alpha}_{\text{lim}}$ holding for the whole SEW, or for a sufficiently wide subset of it. Hence path-specific $\dot{\alpha}_{\text{lim}}$ values should be generally employed.

5 Trajectory Planning with Quintic Polynomials

Let us first denote with l the path coordinate: $\dot{l}$ and $\ddot{l}$ coincides with respectively v and a in the case of straight paths, and with $\dot{\alpha}$ and $\ddot{\alpha}$ in the case of circular paths. Coherently, henceforth kinematic constraints on velocity and acceleration will be denoted with the symbols $\dot{l}_{\text{lim}}$, $\ddot{l}_{inf}$, and $\ddot{l}_{sup}$. Any trajectory planning method yielding a trajectory in time $l(t)$ meeting the velocity and acceleration constraints defined for $\dot{l}$ and $\ddot{l}$ in either Sect. 4.1 or Sect. 4.2 can assure that cable tensions are always positive and below the maximum permissible values along the path. Minimun-time trajectory planning methods should be usually preferred in industrial robotics, since they allow increasing productivity and minimizing costs. However, since the scope of this work is proving the effectiveness of the proposed method for avoiding slackness and excessive tension in cables, a planning method leading to smooth trajectories is preferred. Quintic polynomial trajectories are adopted for point-to-point planning. Quintic polynomial trajectories are suitable to CDDR trajectory planning because they are characterized by continuous velocity, acceleration and jerk profiles. Hence they are smooth enough not to excite vibrational phenomena induced by cable elasticity. Additionally, minimum-time trajectories can be easily computed. Clearly, the time computed is not the absolute minimum for a given point-to-point motion [8].

Let us express the path coordinate l through the following polynomial:

$$l(t) = b_0 + b_1 t + b_2 t^2 + b_3 t^3 + b_4 t^4 + b_5 t^5 \tag{9}$$

It holds $0 \le l \le L_t$, where L_t is the path length. Let 0 and t_f be respectively the initial and final trajectory time and let impose zero velocity and acceleration at 0 and t_f. It is well known that the coefficients satisfying such boundary conditions are: $b_0 = 0, b_1 = 0, b_2 = 0, b_3 = 10 \left(L_t / t_f^3 \right), b_4 = 15 \left(-L_t / t_f^4 \right)$ and $b_5 = 6 \left(L_t / t_f^5 \right)$. The corresponding trajectory is symmetric with respect to the mean time $t_m = t_f / 2$,

where the maximum velocity $\dot{l}_{\max} = 15L_t / \left(8t_f\right)$ is achieved and the acceleration is zero. In the first half of the trajectory the acceleration is always positive while in the second half the acceleration is always negative. As a consequence of the trajectory symmetry, the maximum acceleration and deceleration are identical in absolute value: $\ddot{l}_{\max} = 10L_t / \left(t_f^2 \sqrt{3}\right)$.

In order to meet both the velocity and the acceleration constraints t_f can be chosen so that $\dot{l}_{\max} \leq \dot{l}_{\lim}, \ddot{l}_{\max} \leq \min(\min(\ddot{l}_{sup}\big|_0^{\frac{L_t}{2}}), \left|\max(\ddot{l}_{inf}\big|_{\frac{L_t}{2}}^{L_t})\right|)$. The minimum travel time t_f can hence be obtained:

$$t_f = \max\left(\sqrt{10L_t / \left(\ddot{l}_{\max}\sqrt{3}\right)}, 15L_t / \left(8\dot{l}_{\max}\right)\right) \qquad (10)$$

Admittedly, any travel time longer than t_f can be adopted without violating the kinematic constraints: the scaled trajectory $l(t_s)$ can be computed by just introducing the scaled time variable t_s defined as $t_s = t/\lambda$, where $\lambda > 1$ is the scaling factor, i.e. the ratio between the desired travel time t_d ($t_d > t_f$) and t_f: $\lambda = t_d/t_f$.

6 The Experimental Setup

A picture of the two-cable, two-dof CDDR with passive serial support commissioned to validate the theory presented above is shown in Fig. 2. The robot is driven by two Dyneema® cables (Young's modulus $\approx$100 GPa, yield stress $\approx$3 GPa) directly connected to the free end of the passive serial manipulator. The cables are forced to pass through the two fixed vertices A_1 and A_2 (see Fig. 1 and Table 1) at the top of the base polygon by means of guide pulleys and are wound into screw threads machined on the drive pulley surfaces. The drive pulleys are directly driven by two Siemens 1FT6 brushless motors (rated torque 2.15 Nm, maximum torque 10 Nm, rated speed 3,000 rpm) with Simodrive 611U servodrives. Torque control with analog interface is the operating mode selected for both the motors. Additionally, TTL 2,048-line encoder emulation has been chosen to get a direct measurement of motor shaft position, and hence of the pulley angles β_i. The positions of the aluminum links have instead been measured by two 5,000-line Eltra incremental encoders, one measuring the absolute rotation of link 1 (φ_1), the other the relative angle between link 1 and 2 (φ_2^r). The robot trajectory planning and control algorithms have been implemented in a multitasking controller developed using Simulink models and the XPc target real time operating system. Measurement Computing PCIM-DDA06/16 and PCI QUAD/04 boards have been employed to manage signal generation and acquisition. The trajectory planning strategy implemented in the controller puts into action the achievements discussed in Sects. 4 and 5, whilst the control algorithm developed is based on the centralized controller proposed in [9], which makes use of a complete dynamic model of the CDDR for performing feedback linearization.

Fig. 2 Prototype of the planar
CDDR

Table 2 collects the chief kinematic and inertial features of the CDDR. L_A, L_B
and z_k, are defined in Table 1, while, coherently with the notation in [10]:

- z_{Gk} is the distance of the center of gravity G_k of the kth link ($k = 1, 2$) from the
  origin of vector z_k fixed to the link (see Fig. 1)
- m_k is the mass of the kth link ($k = 1, 2$)
- m_{enc2} is the concentrated mass accounting for the presence of the encoder at the
  kinematic coupling between link 1 and 2
- I_k^{δ} is the moment of inertia of the kth link about the orthogonal axis through point δ
- r_i is the radius of the ith drive pulley ($i = 1, 2$)
- J_i is the lumped rotational inertia of the ith drive pulley, also including the moment
  of inertia of the rotor and of the brake of the motor
- c_{vi} is the rotational viscous damping coefficient estimated at the ith drive pulley
- M is the mass of the payload (and of the end-effector, if it is present).

Fig. 3 The load fitted at the
CDDR tip
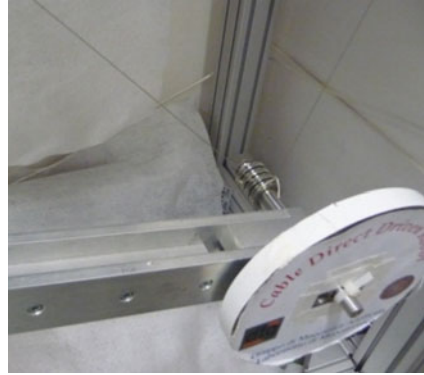
Fig. 4 The CDDR SEW
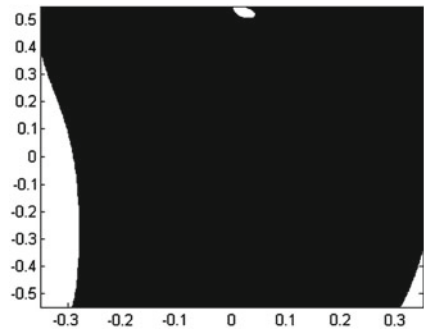
In the experiments, a load of mass M has been introduced through a steel disk (see
Fig. 3) pivoting about the thin shaft at the free end of the serial manipulator. The
presence of such a payload makes the SEW take the shape shown in Fig. 4: static
cable tensioning is not possible in all the rectangular workspace but only in the sub
area filled in black.

7 Experimental Results

Two experiments have been carried out. In the first one (T1) the CDDR TCP (assumed
coinciding with the point where cables converge, or, which is the same, with the
intersection point between the axis of the thin shaft at the tip of the serial manipulator
and the plane of motion) is made perform a straight line path in the plane of motion.
In the second experiment (T2) a circular path is executed (Table 3).

Identical maximum permissible tensions $\tau_{i\,max}$ have been set for the both the
cables: $\tau_{i\,max} = 200$ N. This is a quite conservative choice coherent with the cable
material properties and the motor deliverable torques.

Table 3 Physical features of the CDDR

Parameter	Value	Units
L_A	1.108	m
L_B	0.712	m
$z_k \ (k = 1, 2)$	0.622	m
z_{G1}	0.2741	m
z_{G2}	0.3261	m
m_1	2.045	kg
m_2	1.793	kg
m_{enc2}	0.330	kg
I_1^0	0.23434	kg $\cdot$ m^2
I_2^{G2}	0.08005	kg$\cdot$ m^2
$r_i \ (i = 1,2)$	$3.8253 \cdot 10^{-2}$	m
$J_i \ (i = 1,2)$	$6.8414 \cdot 10^{-4}$	kg$\cdot$ m^2
$c_{vi} \ (i = 1,2)$	$0.4 \cdot 10^{-4}$	N$\cdot$ m$\cdot$ s
M	1.977	kg

In both the experiments, the planned TCP Cartesian displacements and velocities have been compared with the actual TCP displacements and velocities computed by direct kinematics from the joint displacements measured by the two encoders fitted on the serial manipulator. Such measurements are not affected by cable elasticity as would be those based on motor encoder recordings. An accurate tracking of the desired trajectory by the CDDR TCP is by itself a proof that proper cable tensioning has been ensured along the whole path. In particular, it is apparent that significant discrepancies would arise in case one or both cables were slack.

Estimates of cable tensions along the paths have been inferred (and plotted) from the torque measurements provided by the motor drives. Such estimate confirm that cable tensions are safely kept within the desired bounds in both the experiments.

7.1 Test 1 (T1): Straight Line Path

A straight line path between two generic points in the SEW has been first executed. The starting point coordinates in the reference frame $\{X, Y\}$ are $(0, -0.554\,\text{m})$. The ending point coordinates are $(0.3, 0.046\,\text{m})$. Hence, the length L_t of the path is $0.6708\,\text{m}$. The limit velocity $\dot{l}_{\text{lim}}$ selected to ensure $u_i < 0$ and $s_i > 0$ is $1.5\,\text{m/s}$, from which bilateral constraints $\ddot{l}_{inf}$ and $\ddot{l}_{sup}$ have been computed as functions of l. Such kinematic constraints are shown in Fig. 5 (thin lines), where the planned velocity and acceleration profiles are also plotted (bold lines). The most stringent constraint is $\ddot{l}_{inf}$ ($\ddot{l}_{inf} = -4.32\,\text{m/s}^2$) close to the end of the path ($l = 0.626\,\text{m}$). The minimum traversal time t_f achievable with such an $\ddot{l}_{inf}$ is $0.95\,\text{s}$. The CDDR position tracking capability can be evaluated in Fig. 6, where, in the two plots at the top of the figure, the planned TCP Cartesian displacements are compared with the
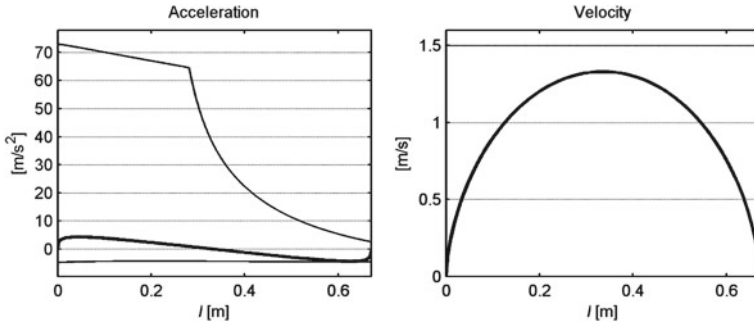
Fig. 5 T1: Velocity and acceleration constraints and planned profiles
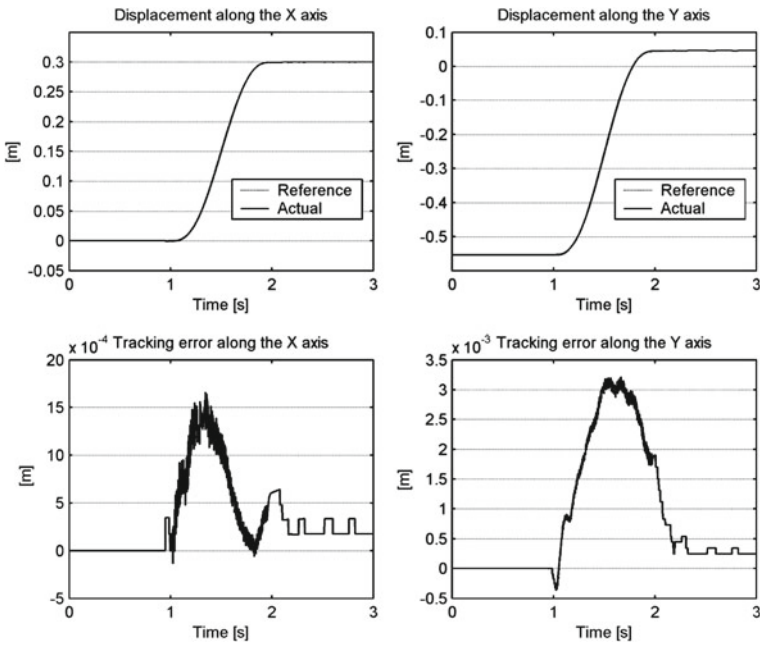
Fig. 6 T1: Comparison between planned and actual Cartesian displacements

actual displacements. The resulting tracking errors along each axis are shown in the two plots at the bottom of Fig. 6. Tracking velocity capabilities can instead be appreciated in Fig. 7, where the planned and actual TCP velocities are plotted. Finally, the measured motor torques and the estimated cable tensions are shown in Fig. 8, respectively in the two plots at top and at the bottom of the figure. It is apparent that all the physical constraints involving cable tensions motor torques are satisfied. As it was expected the tension in one cable (cable 2) tends to take a minimum value
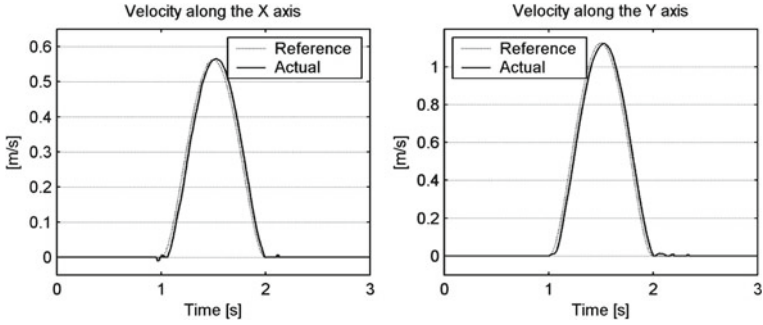
Fig. 7 T1: comparison between planned and actual Cartesian velocities
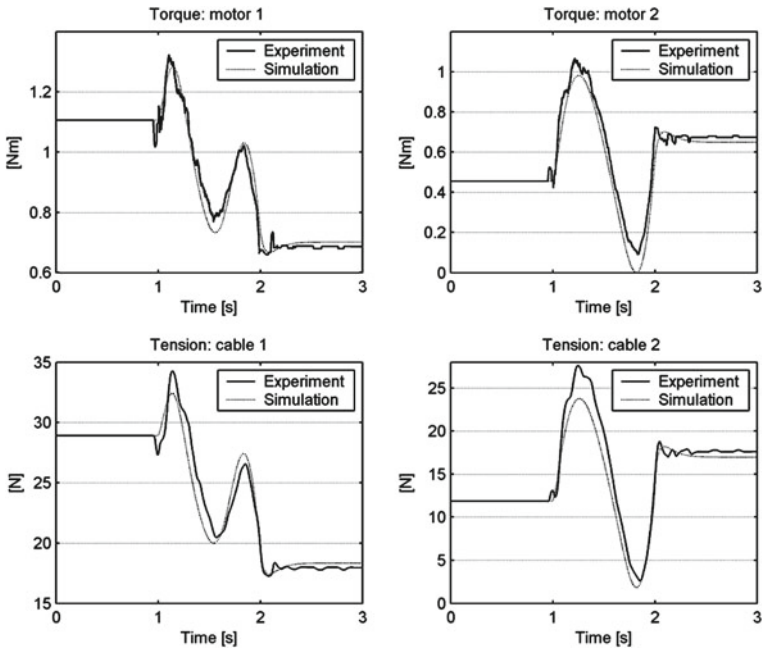
Fig. 8 T1: Numerical and experimental motor torques and cable tensions

close to zero when the TCP approaches the end of the path (see the $\ddot{l}_{inf}$ constraint in Fig. 5): it is intuitive that the upwards motion of the TCP makes the end-effector deceleration phase much more critical, in terms of cable tensions, than the acceleration phase. Additionally, in Fig. 8 experimental cable tensions and motor torques are compared with simulated outcomes to prove the accuracy of the underlying dynamic model.
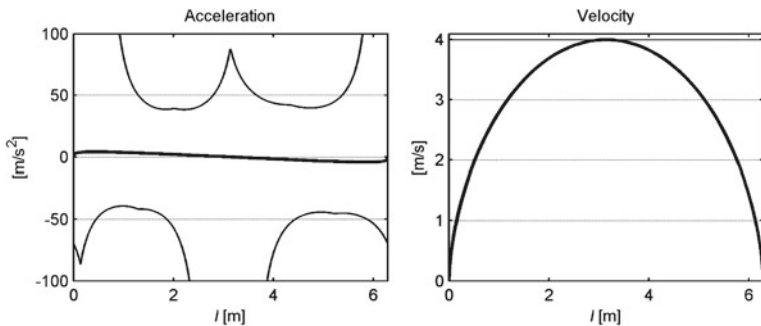
Fig. 9 T2: Velocity and acceleration constraints and planned profiles

7.2 Test 2 (T2): Circular Path

The center of the circular path is at point $(0.1, -0.1\,\text{m})$ in the reference frame $\{X, Y\}$ while the circle radius R is $0.1\,\text{m}$. Hence, the length L_t of the path is $0.6283\,\text{m}$. The starting point is at $(0.25, -0.1\,\text{m})$ and motion direction is counterclockwise.

The limit angular velocity $\dot{l}_{\text{lim}}$ selected for the path is $4\,\text{rad/s}$, which is slightly below the value concurrently satisfying $u_i^* < 0$ and $s_i^* > 0$ along the whole path. The resulting bilateral constraints $\ddot{l}_{inf}$ and $\ddot{l}_{sup}$ on the angular acceleration $\ddot{\alpha}$ take the shape shown in Fig. 9 (thin lines). It is apparent that the velocity constraint is the most stringent one. The minimum traversal time t_f achievable with such an $\dot{l}_{\text{lim}}$ is $2.94\,\text{s}$, the corresponding velocity and acceleration profiles of the trajectory planned are shown in Fig. 9 too (bold lines). At the top of Fig. 10 the planned TCP Cartesian displacements are compared with the actual displacements while tracking errors are plotted at the bottom of the same figure. Planned and actual TCP velocities are shown in Fig. 11, while the measured motor torques and the estimated cable tensions are shown in Fig. 12. Also in this test, the physical constraints in terms of cable tensions and motor torques are satisfied.

8 Conclusions

Lack of cable redundancy in underconstrained cable-driven robots makes keeping positive and bounded cable tensions a critical issue. In this paper an approach is discussed and validated experimentally which translates such requirements into kinematic constraints to be met by the TCP trajectory at the planning stage. The computation of the constraints accounts for robot dynamics: basically, the method leads to the definition of bounds on the first and second derivatives of the TCP path coordinate. If the robot trajectory planner allows managing trajectories defined in terms of a path coordinate and with constraints on both velocity and acceleration, the proposed
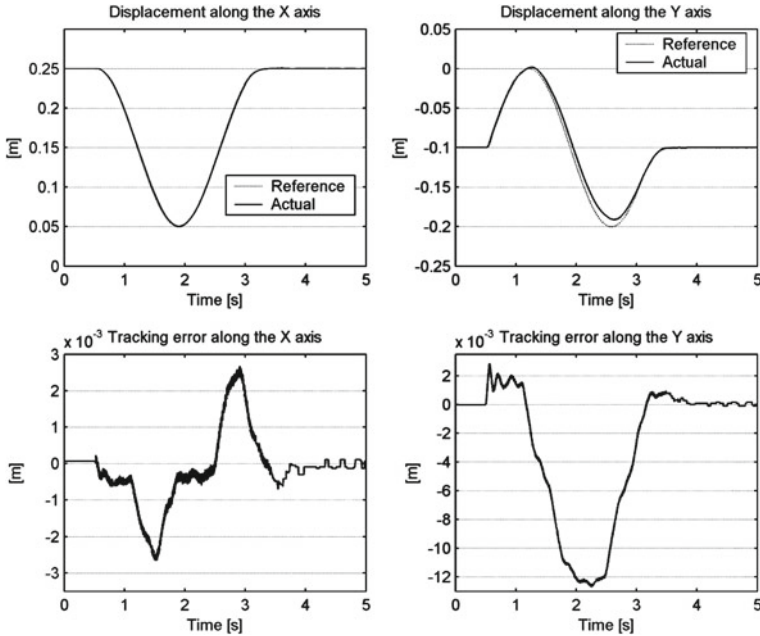
Fig. 10 T2: Comparison between planned and actual Cartesian displacements
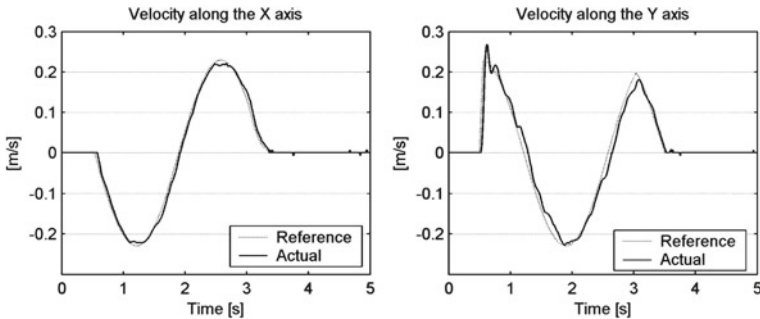
Fig. 11 T2: comparison between planned and actual Cartesian velocities

method ensures that cable tensions neither drop to zero nor exceed the maximum permissible tension during the motion. Clearly, the robot controller must also ensure limited tracking error, which is however a conventional specification. Given the kinematic constrains, minimum time trajectories should be chosen, yet this aspect is marginally discussed being out of the paper scope.

A two-dof fully actuated hybrid planar cable robot has been used to introduce many of the aspects of the proposed method; nonetheless, it is believed that the concepts and the approach can be extended to more general and complex systems.
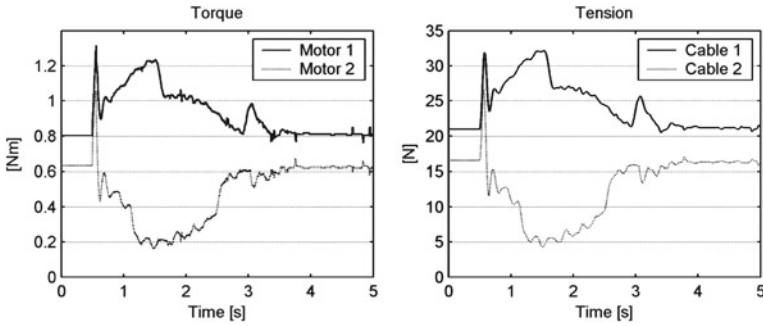
Fig. 12 T2: Motor torques and cable tensions

References

1. Cone, L.L.: Skycam: an aerial robotic camera system. Byte **10**(10), 122–32 (1985)
2. Albus, J.S., Bostelman, R., Dagalakis, N.G.: The nist robocrane. J. Robot Syst. **10**(5), 709–724 (1993)
3. Castelli, G., Ottaviano, E., González, A.: Analysis and simulation of a new Cartesian cable-suspended robot. Proc. Inst. Mech. Eng. Part C J. Mech. Eng. Sci. **224**(8), 1717–1726 (2010)
4. Roberts, R.G., Graham, T., Lippitt, T.: On the inverse kinematics, statics, and fault tolerance of cable-suspended robots. J. Robot. Syst. **15**(10), 581–597 (1998)
5. Barrette, G., Gosselin, C.M.: Determination of the dynamic workspace of cable-driven planar parallel mechanisms. J. Mech. Design 127(2), 242 (7 pages) (2005).
6. Stump, E., Kumar, V.: Workspaces of cable-actuated parallel manipulators. J. Mech. Design **128**, 159–167 (2006)
7. Oh, S.-R., Agrawal, S.K.: Cable-suspended planar parallel robots with redundant cables: controllers with positive cable tensions, In: Proceedings of IEEE International Conference on Robotics and Automation, pp. 3023–3028 (2003).
8. Behzadipour, S., Khajepour, A.: Time-optimal trajectory planning in cable-based manipulators. IEEE Trans. Robot. **22**(3), 559–563 (2006)
9. Trevisani, A., Gallina, P., Williams II, R.L.: Cable-direct-driven robot (CDDR) with passive SCARA support: theory and simulation. J. Intell. Robot. Syst. **46**, 73–94 (2006)
10. Trevisani, A.: Underconstrained planar cable-direct-driven robots: a trajectory planning method ensuring positive and bounded cable tensions. Mechatronics **20**, 113–127 (2010)
11. Notash, L., Kamalzadeh, A.: Inverse dynamics of wire-actuated parallel manipulators with a constraining linkage. Mechanism Mach. Theor. **42**(9), 1103–1118 (2007)
12. Kino, H., Kawamura, S.: Development of a serial link structure/parallel wire system for a force display. In: Proceedings of the 2002 IEEE International Conference on Robotics and Automation, pp. 829–834 (2002).
13. Riechel, A.T., Ebert-Uphoff, I.: Force-feasible workspace analysis for underconstrained point-mass cable robots. In: Proceedings of the 2004 IEEE International Conference on Robotics and Automation, pp. 4956–4962 (2004).

Time-Energy Optimal Trajectory Planning of Cable-Suspended Manipulators

Mahdi Bamdad

Abstract This paper addresses the problem of time-energy optimal control of cable robot with the trajectory planning as the overall mission. The final dynamic equations were organized in a closed form similar to serial manipulator equations. Thus, employing the Pontryagin maximum principle, it was verified that the optimal motions are all bang–bang controls with bounded control torque on the winches. This consists of minimizing a cost function, considering dynamic equations of motion as well as bounds on joint torques. Here, the cost function was chosen as a weighted balance of traveling time and mechanical energy of the actuators. The approaches of solving concrete optimal control laws based on Two-Point Boundary Value Problems were provided in this paper and the algorithm was tested in simulation yielding acceptable results.

1 Introduction

In large scale industries, i.e. material handling, the RoboCrane is known as one of the earliest works in cable-driven manipulators. Having been developed based on the Stewart platform parallel link manipulator, it provides precise six degree of freedom control of loadsy [1]. In long reach industrial robotics, one wants to generate a continuous intersection-free motion of the robot manipulator connecting the two given points of the workspace. The resulting motion along the planned path must be consistent with the dynamic equations of the system and the other constraints acting on the mechanical system. Therefore, optimal time-energy has been an important performance index in industrial application that require saving energy. Nonethe-

M. Bamdad (✉)
Mechatronic Research Laboratory, College of Mechanical Engineering,
Shahrood University of Technology, Shahrood, Iran
e-mail: Bamdad@shahroodut.ac.ir

less, to keep smooth trajectories, trajectory planning should include the energetic criteria [2].

Amongst all the trajectory planning techniques proposed in the scientific literature, minimum-time algorithms were the very firsty [3–5]. What has been a multi-dimensional control problem has turned into a bi-dimensioanl one. The manipulator dynamics is described and input torque/force constraints are taken into account using parametric functions which represent geometric path constraints to be satisfied. Finally, the minimum-time solution for the optimal path tracking problem is found using phase plane techniques [3–5]. In most of the motions optimization has focused on minimizing motion time of manipulators, the control inputs are physically unrealizable due to the typical discontinuities at the switching times [4].

Previous efforts for solving the energy optimization problem include a dynamic programming search in the state space for point to point motions [7] and for motions along specified paths [8, 9].

Cable driven manipulator motions are investigated in several dynamical criteria [10]. Much of this prior work aims to minimize the execution time of a desired trajectory, which often adversely affects energy efficiency [11–13]. Meanwhile, in [14] experimental results on a three cable robot show substantial reductions in energy consumption as compared to linear trajectories.

The time-optimal trajectory-planning is studied on a high-speed cable-based parallel manipulators for a given geometrical Path [12] and the results of this technique are evaluated experimentally. In a relevant study [13], time optimal trajectory tracking of spatial cable suspended robots is addressed. Both cable tensions and cable velocities are considered to be limited [13]. The method was similar to that described in [4] by assuming bang–bang control, also based on the concepts of characteristic switching points and limit curves.

This paper considers a time-energy cost function. The representative work can be found for articulated systems moving along specified paths [15]. The cable suspended manipulators are studied providing a background on dynamic analysis. Consequently, since [3, 4] ignored the issue of singular control, assuming bang–bang acceleration along the path, in this work a more general necessary condition for singular control is given. The state constraints are solved by determining the upper and lower bounds. Using the Pontryagin's Minimum Principle (PMP), the optimal trajectory is shown to be continuous in smooth velocity profiles. The optimal trajectory is computed by numerically solving a two point boundary value problem and the method is demonstrated numerically for a 6 DOF spatial cable manipulator.

2 Kinematic and Dynamic modeling

In a general model of a cable-suspended with m cables, the motion of the end effector $\mathbf{x} = [x, y, z, \theta_x, \theta_y, \theta_z]^T$ can be derived from the Newton–Euler equation [10, 16].

$$D(\mathbf{x})\ddot{\mathbf{x}} + C(\mathbf{x}, \dot{\mathbf{x}}) + g(\mathbf{x}) = -\boldsymbol{J}^T T \tag{1}$$

where $D(\mathbf{x})$ is the inertia matrix, $C(\mathbf{x}, \dot{\mathbf{x}})$ is the vector of velocity terms and $g(\mathbf{x})$ is the gravity vector. The conventional parallel manipulator Jacobian J is defined as the matrix that transforms the end-effector velocity in the inertial coordinates to the joint rates of the actuator. The vector of cable lengths and cable tensions are $\mathbf{q} = [l_1, l_2, \ldots, l_m]^T$, $T = [T_1, T_2, \ldots, T_m]^T$ respectively.

Let Ω be the set of the admissible control torques. The optimization problem is to find the control $U \in \Omega$ which limit the motor torques. Here, the optimization method would take into account the complete system dynamics and all the constraints. The combined dynamic effects of the motor, the cable pulley and the end effector resulted in manipulator dynamic modeling.

$$D(\mathbf{x})\ddot{\mathbf{x}} + C(\mathbf{x}, \dot{\mathbf{x}}) + g(\mathbf{x}) = \frac{1}{r}\boldsymbol{J}^T (U_{vel} - U) \tag{2}$$
$$U_{vel} = J_A\ddot{\beta} + C_A\dot{\beta}$$

where J_A and C_A are diagonal matrices with rotational inertia and rotational viscous damping coefficients [17]. The vector of pulley angles with pulley radii r is denoted by β. The dynamic equation is organized in a typical closed form

$$D_{eq}(\mathbf{x})\ddot{\mathbf{x}} + C_{eq}(\mathbf{x}, \dot{\mathbf{x}}) + G_{eq}(\mathbf{x}) = -\boldsymbol{J}^T U \tag{3}$$

where

$$D_{eq}(\mathbf{x}) = r D(\mathbf{x}) + \frac{1}{r}\boldsymbol{J}^T J_A J$$
$$C_{eq}(\mathbf{x}, \dot{\mathbf{x}}) = r C(\mathbf{x}, \dot{\mathbf{x}}) + \frac{1}{r}\boldsymbol{J}^T J_A \frac{d\boldsymbol{J}}{dt}\dot{\mathbf{x}} + \frac{1}{r}\boldsymbol{J}^T C_A J\dot{\mathbf{x}} \tag{4}$$
$$G_{eq}(\mathbf{x}) = r g(\mathbf{x})$$

The equations are rewritten as an equivalent system and the state variables represent the system's displacements and velocities.

$$X = [X_1 \quad X_2]^T = [\mathbf{x} \quad \dot{\mathbf{x}}]^T \tag{5}$$

Equation (5) can be rewritten in state space form as

$$\dot{X} = [\dot{X}_1 \quad \dot{X}_2]^T = [X_2 \quad N(X) + Z(X)U]^T \tag{6}$$

where $N \in R^m$ and $Z \in R^{m \times m}$.

$$N(X) = -D_{eq}^{-1}(\mathbf{x})\left(C_{eq}(\mathbf{x}, \dot{\mathbf{x}}) + G_{eq}(\mathbf{x})\right) \tag{7}$$
$$Z(X) = -D_{eq}^{-1}(\mathbf{x})\boldsymbol{J}^T$$

The vector $\mathbf{x}(\mathbf{s})$ represents the position and the orientation of the moving frame along path and s is the path parameter.

$$\mathbf{x}(\mathbf{s}) = F(s) = [f_1(s), f_2(s), f_3(s), f_4(s), f_5(s), f_6(s)]^T \tag{8}$$

A trajectory is completely determined by the initial state of the robot (position and velocity) and subsequent sequence of accelerations. The velocities and accelerations as functions of the parameter s and its time derivatives (prime denotes s derivative) can be obtained as

$$\dot{X} = \begin{bmatrix} f'\dot{s} & f''\dot{s}^2 + f'\ddot{s} \end{bmatrix}^T, \quad \ddot{s} = \left(\frac{d\dot{s}}{ds}\right)\dot{s} \tag{9}$$

The dynamic model is rearranged in the following manner to show along the path [13].

3 Formulation of Energy Efficient Problem

In order to increase the manipulator performances, it is highly desirable to control the dynamic system taking into account technological, geometrical and environmental constraints as well as any other constraints inherent both to the robot design and to the nature of the task to be executed. The actual DC motor is not a loss-less transducer, having resistance at the rotor windings, and the commutation mechanism. The actuator torque as the realistic constraints posed a limitation on motion. The dynamic equilibrium should be maintained during the whole motion; therefore, there must only be a positive force in the cables.

In the permanent magnet DC motors, the torque U is in general proportional to the current I flowing to the rotor windings.

$$U = K_T I(t) \tag{10}$$

The energy loss associated with executing a trajectory can be found by integrating the loss over the duration of the trajectory.

$$E = K_T{}^2 R \int_{t_0}^{t_f} \|U(t)\|^2 \partial t \tag{11}$$

The torque speed characteristic curves of such DC motors may be represented by linear equation and the bounds on the control input, U^- and U^+ are

$$\begin{aligned} U^+ &= K_1 - K_2\dot{\beta} \\ U^- &= -K_1 - K_2\dot{\beta} \end{aligned} \tag{12}$$

where $K_1 = [\tau_{s1} \quad \tau_{s2} \cdots \tau_{\text{sm}}]^{\mathrm{T}}$, $K_2 = dig\,[\tau_{s1}/\omega_1 \cdots \tau_{\text{sm}}/\omega_{\text{m}}]$, τ_s is the stall torque and ω is the maximum no load speed [10].

4 Optimality Equations

The Hamiltonian function of the problem is determined and then PMP derive the optimality conditions. The optimal solution (indicated here by *) must satisfy the following conditions

$$\dot{X}^* = \partial H / \partial \psi \tag{13}$$

$$\dot{\psi}^* = -\partial H / \partial X \tag{14}$$

$$H(X^*, \psi^*, U^*) \leq H(X^*, \psi^*, \bar{U}). \tag{15}$$

where U^* is optimal control and $\bar{U}$ is all admissible control and $\psi = \begin{bmatrix} \psi_1^T & \psi_2^T \end{bmatrix}^T$ is the vector of costates.

The performance index now looks like

$$\underset{U(t)}{Minimize}\, J_0 = \int_{t_0}^{t_f} L(X, U, t)dt \tag{16}$$

where

$$L(X, U, t) = 1 + \varepsilon^2 \left(\|X_1\|_{W_1}^2 + \|X_2\|_{W_2}^2 + \|U\|_R^2 \right). \tag{17}$$

Integrand L (.) is a smooth, differentiable function in the arguments, $\|X\|_K^2 = X^{\mathrm{T}}KX$ is the generalized squared norm, W_1 and W_2 are symmetric, positive semi-definite (m×m) weighting matrices and R is symmetric, positive definite (m×m) matrices. The time-energy objective function consists of an ε-weighted combination of the time. The state departs from the initial conditions and reaches the terminal conditions at the unspecific terminal time.

The objective function provides the possibility for the designer to decide on the state priority and torque control efforts by the numerical choice of W_1, W_2, and R. These matrices can be used to convert the dimensions of the terms to consistent units and the Hamiltonian function is defined as

$$H(X, U, \psi) = L(X, U, t) + \psi_1^T X_2 + \psi_2^T [N(X) + Z(X)U]. \tag{18}$$

The optimality conditions can be obtained by differentiating the Hamiltonian function with respect to states, costates and control as follows

$$\begin{bmatrix} \dot{X}_1 & \dot{X}_2 \end{bmatrix}^T = [X_2 \quad N(X) + Z(X)U]^{\mathrm{T}} \tag{19}$$

$$\begin{bmatrix} \dot{\psi}_1 & \dot{\psi}_2 \end{bmatrix}^T = -\begin{bmatrix} \partial H/\partial X_1 & \partial H/\partial X_2 \end{bmatrix}^T \tag{20}$$

$$\varepsilon^2 R U + Z^T \psi_2 = 0. \tag{21}$$

For the cable driven robots there must always be positive torque in the system, so the lower bound must be greater than zero. Unlike the manipulators that have their motors work in a symmetric bound, these could be efficient only in the positive bound of the motor limitation. Control values are limited with upper and lower bounds, so using Eq. (21) the optimal control is given by

$$U = \begin{cases} U^+ & -R^{-1}Z^T\psi_2 > U^+ \\ -\dfrac{R^{-1}Z^T\psi_2}{\varepsilon^2} & U^- < -R^{-1}Z^T\psi_2 < U^+ . \\ U^- & -R^{-1}Z^T\psi_2 < U^- \end{cases} \tag{22}$$

The non-saturating actuator torques governed by the control law shall set the platform in motion from point-to-point along a prescribe path with minimal time-energy cost. In this formulation, the differential equations are used to determine the state and costate variables. The set of differential equations Eqs. (19) and (20), the control law, and the boundary conditions construct a standard form of Two Point Boundary Value Problem (TPBVP). The algorithm iterates on the initial values of the costate until the final boundary conditions are satisfied. The used function produces a solution that is continuous on workspace area in duration of the motion. The standard form of TPBVP by MATLAB command is supplied. Bvp4c is a finite difference code that implements the 3-stage Lobatto IIIa formula. This is a collocation formula and the collocation polynomial provides a C^1-continuous solution that is fourth-order accurate uniformly in the interval of integration. Mesh selection and error control are based on the residual of the continuous solution. The collocation technique uses a mesh of points to divide the interval of integration into subintervals.

The algorithm will be repeated awaiting the desired degree of accuracy in TPBVP solving:

$$\frac{1}{2}\left\| X_1(t_f) - X_{1f} \right\|_{W_p}^2 + \frac{1}{2}\left\| X_2(t_f) - X_{2f} \right\|_{W_v}^2 \leq \delta \tag{23}$$

The component of W_p and W_v can be changed for achieving the relative importance of position and velocity errors of end effector during the trajectory. The final error obtained must be less than the desired accuracy δ. The points of the initial mesh as well as an initial approximation of the solution should be provided. If the solution does not satisfy the tolerance criteria, the algorithm adapts the mesh and repeats the procedure.

Fig. 1 A spatial 6-cable-
suspended manipulator
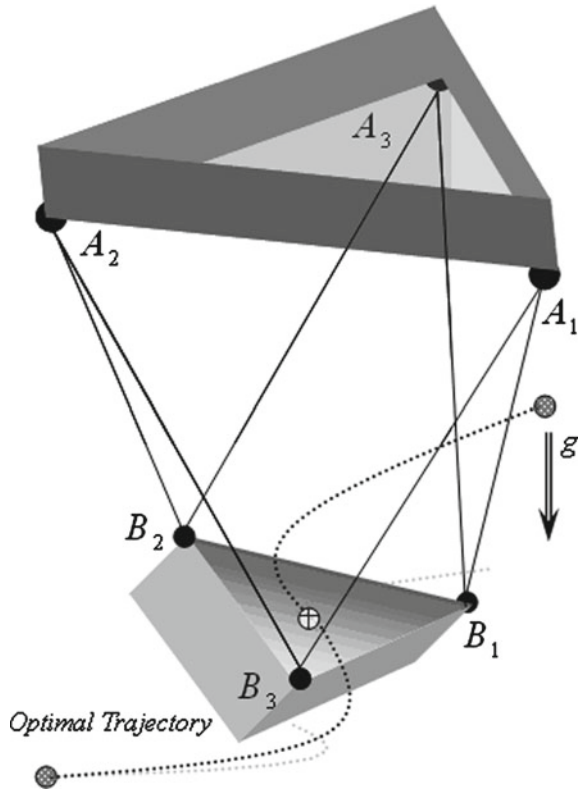
Table 1 Simulation
parameters for actuators

Value	Parameter
Pulley radius	$r = 5 \times 10^{-2}$ m
Motor shaft viscous damping coefficient	$c = 0.02$ N.m.s
Lumped actuator rotational inertia	$J = 10^{-3}$ Kg.m^2
Stall torque	$\gamma_{stall} = 410$ oz.in
Maximum no-load speed	$\omega_m = 3211$ rpm

5 Simulation Studies

In this section, a three-dimensional manipulator with six cables is considered. The
end effector is kinematically constrained by maintaining tension in all six support-
ing cables. The suspended movable platform and the overhead support are typi-
cally two equilateral triangles shown in Fig. 1. The penalty matrices are $W_1 = [0]$,
$W_2 = [0]$ and $R = \text{diag}(1)$. The initial and terminal configuration is given
$X_{10} = [-0.1, -0.1, 1.5, 0, 0, 0]$ and $X_{1f} = [0.1, 0.1, 1.8, 0, 0, 0]$ respectively, and
the states are constant $(X_{20} = X_{2f} = [0])$.

Fig. 2 The endpoints of a
specified path
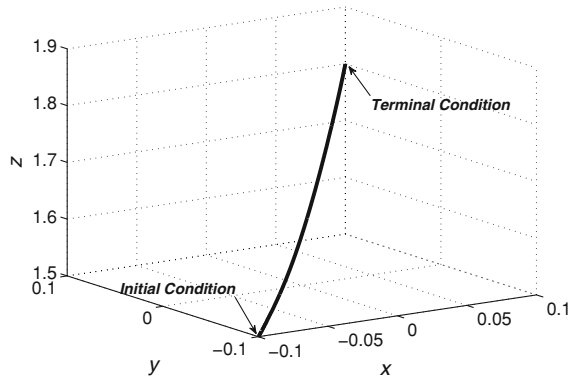
Fig. 3 The endpoints of a
specified path
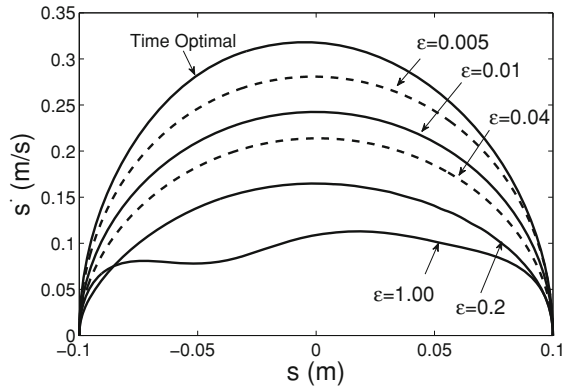
The side lengths, base and movable platforms are 0.6 m. Motor is a brush com-
mutated DC motors (Pittman 14207S007). The characteristics of the winches have
been presented in the Table 1.

In the proposed algorithm, desired accuracy is $\delta = 0.01$ and $W_p = W_v = diag(1)$. The payload attached to movable platform is 22.9 Kg. The motion planning
is applied from point-to-point along a prescribe path illustrated in Fig. 2.

In Fig. 3 the path velocity function of path parameter for various values of ε is
shown. In phase plane, the path velocity at each point along the path increase as ε is
reduced. By reduction to zero, the minimum time velocity profile is reached.

The required torque for all 6 motors to carry the maximum payload is shown in
Fig. 4. The upper limits of motor torque are presented with dashed lines. It can be
shown that decreasing ε makes more required torque and the curves lay on their own
saturation limit.

One of the key points in cable robots is that, the cable forces should always be
positive. Due to optimization procedure, the cable forces for $\varepsilon = 1.00$ is displayed in
Fig. 5. The demonstration of tensionability in results can be used as a proof for con-
straint consistency which leads to the appropriateness of the control motor torques.
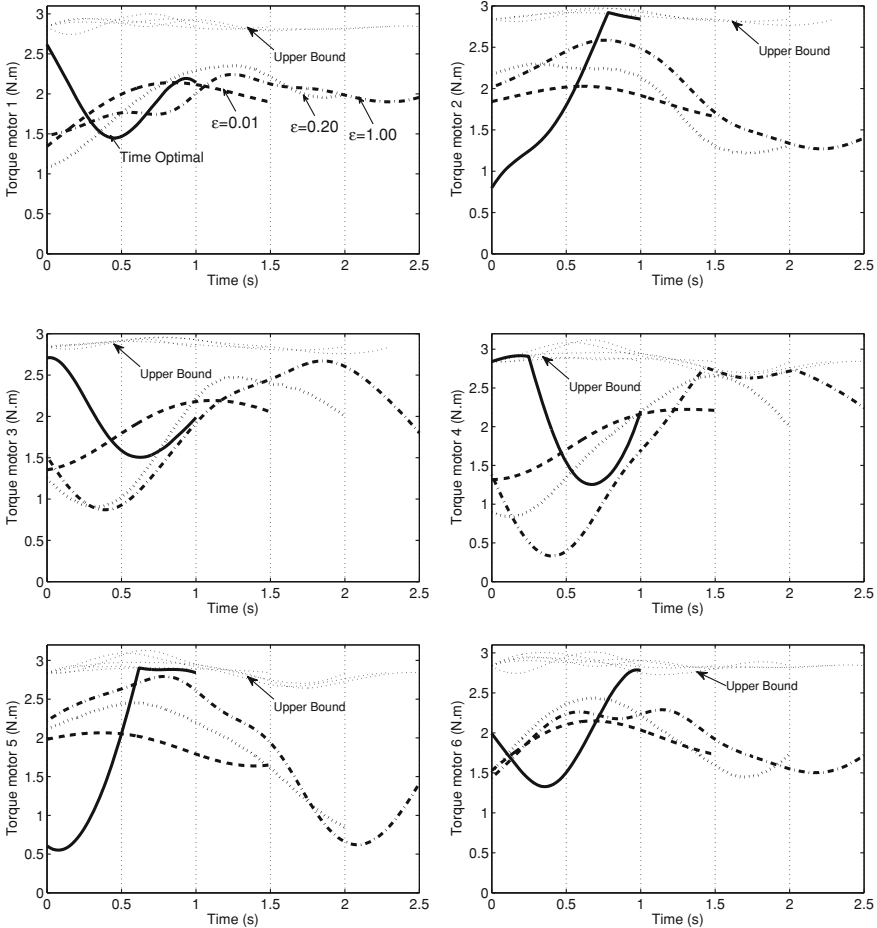
Fig. 4 All Motor torques versus time for $\varepsilon = 0, 0.01, 0.20, 1.00$

6 Conclusion

The motion planning problem for cable-suspended parallel manipulators is investigated via a computational algorithm on the basis of the optimal control approach. Hence, the optimal traveling time and the minimum mechanical energy of the actuators are considered together. The physical constraints in this optimization matter include input force/torque constraints. The algorithm in the present work has been out-lined, which covers the formation of manipulation mechanism functional movements and calculation of driving torques and all relevant energy parameters that are necessary for the adequate choice of the actuation system.

Fig. 5 Cable tensions versus time for $\varepsilon = 1.00$
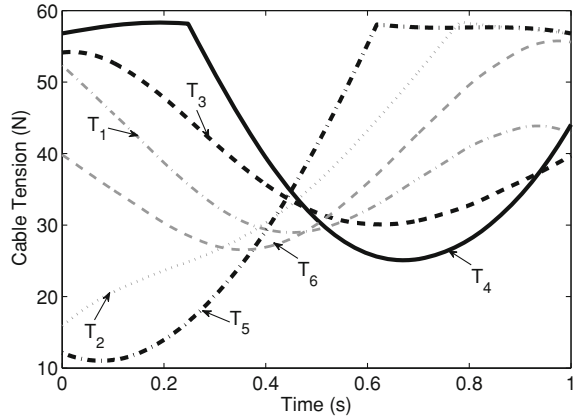
The optimal solutions with bang–bang controls are found by solving the corresponding nonlinear TPBVP. The complete form of the obtained nonlinear dynamic equations of the motion is used, and the procedure is capable to determine the states, costates, and the switching functions with a high numerical accuracy. The strategy cause the motors operated with the maximum torques to change directions at the switching time. In the simulation section the optimal trajectories for a 6-cable spatial manipulator are described in detail. With minimal time-energy cost, the non-saturating actuator torques governed by control law determines a point-to-point motion along a prescribe path.

References

1. Albus, J., Bostelman, R., Dagalakis, N.: The Nist Robocrane. J. Rob. Syst. **10**, 709–724 (1993)
2. Gasparetto, A., Zanotto, V.: A technique for time-jerk optimal planning of robot trajectories. Robot. Comput. Integr. Manuf. **24**, 415–426 (2008)
3. Shin, K.G., McKay, N.D.: Minimum-time control of robotic manipulators with minimum-time control of robotic manipulators with geometric path constraints. IEEE Trans. Autom. Control **30**, 531–541 (1985)
4. Bobrow, J., Dubowsky, S., Gibson, J.: Time-optimal control of robotic manipulators along specified paths. Int. J. Robot. Res. **4**, 3–17 (1985)
5. Huang, H.P., McClamroch, N.H.: Time-optimal control for a robotic contour following problem. IEEE J. Robot. Autom. **4**, 19–28 (1988)
6. Gregory, J., Olivares, A., Staffetti, E.: Energy-optimal trajectory planning for robot manipulators with holonomic constraints. Syst. Control Lett. **61**, 279–291 (2012)
7. Vukobratovic, M., Kircanski, M.: A method for optimal synthesis of manipulation robot trajectories. J. Dyn. Syst. Meas. Control **104**, 188–193 (1982)
8. Singh, S., Leu, M.C.: Optimal trajectory generation for robotic manipulators using dynamic programming. J. Dyn. Syst. Meas. Control **109**, 88–96 (1987)
9. Pfeiffer, F., Johanni, R.: A Concept for Manipulator Trajectory Planning. IEEE Trans. Robot. Autom. **3**, 115–123 (1987)

10. Korayem, M.H., Bamdad, M.: Dynamic load carrying capacity of cable-suspended parallel manipulators. Int. J. Adv. Manuf. Technol. **44**, 1133–1143 (2009)
11. Hiller, M., Fang, S., Mielczarek, S., Verhoeven, R., Franitza, D.: Design, analysis and realization of tendon-based parallel manipulators, mechanism and machine theory. In: IEEE International Conference on Robotics and Automation ICRA'04, New Orleans (2004).
12. Behzadipour, S., Khajepour, A.: Time optimal trajectory planning in cable-based manipulator. IEEE Trans. Robot. **22**, 559–563 (2006)
13. Fahham, H.R., Farid, M.: Minimum-time trajectory planning of spatial cable-suspended robots along a specified path considering both tension and velocity constraints. Eng. Optim. **42**, 387–402 (2010)
14. Borgstrom, P.H., Stealey, M.J., Batalin, M.A., Kaiser, W.J.: NIMS3D: A novel rapidly deployable robot for 3-dimensional applications. In: Proceedings IEEE/RSJ Internationl Conference on Intelligent Robots and Systems, pp. 3628–3635, (2006).
15. Shiller, Z.: Time-energy optimal control of articulated systems with geometric path constraints. Trans. ASME J. Dynam. Syst. Meas. Control **118**, 139–43 (1996)
16. Alp, A.B., Agrawal, S.K.: Cable-suspended robots: design, planning and control. In: IEEE International Conference on Robotics and Automation, Washington D.C., pp. 4275–4280, (2002).
17. Williams II, R.L., Gallina, P.: Planar translational cable-direct-driven robots: design for wrench exertion. J. Intell. Robot. Syst. **35**, 203–219 (2002)

Navigating the Wrench-Feasible C-Space of Cable-Driven Hexapods

Oriol Bohigas, Montserrat Manubens and Lluís Ros

Abstract Motion paths of cable-driven hexapods must carefully be planned to ensure that the lengths and tensions of all cables remain within acceptable limits, for a given wrench applied to the platform. The cables cannot go slack—to keep the control of the platform—nor excessively tight—to prevent cable breakage—even in the presence of bounded perturbations of the wrench. This paper proposes a path planning method that accommodates such constraints simultaneously. Given two configurations of the platform, the method attempts to connect them through a path that, at any point, allows the cables to counteract any wrench lying inside a predefined uncertainty region. The resulting C-space is placed in correspondence with a smooth manifold, which allows defining a continuation strategy to search this space systematically from one configuration, until the second configuration is found, or path non-existence is proved by exhaustion of the search. The approach is illustrated on the NIST Robocrane hexapod, but it remains applicable to general cable-driven hexapods, either to navigate their full six-dimensional C-space, or any of its slices.

O. Bohigas (✉) · M. Manubens · L. Ros
Institut de Robòtica i Informàtica Industrial, Barcelona, Spain
e-mail: obohigas@iri.upc.edu

M. Manubens
e-mail: mmanubens@iri.upc.edu

L. Ros
e-mail: lros@iri.upc.edu

1 Introduction

In recent years, cable-driven parallel mechanisms have been increasingly studied and applied to more and more relevant tasks, such as manipulation of heavy loads [7, 20], high-precision positioning [18], monitoring of aquatic environments [4, 13], automated construction of civil structures [5], rescue systems [19], or motion simulators [28], among others. Their generally simple design, consisting of a moving platform connected to a fixed base by means of cables that wind up on winches, results in manipulators with low weight but high load capacity. These advantages, together with the fact that they can usually achieve larger workspaces than their counterparts with rigid-limb legs, make cable-driven manipulators very energy-efficient and appropriate to maneuver heavy loads. However, additional constraints apply: their cables can pull but are unable to push the platform, which obliges to keep the tensions in all cables positive during normal operation.

The workspace of a cable-driven manipulator is limited by a number of hypersurfaces where the control of the manipulator is compromised [29], corresponding to configurations where the tension of some cable is either zero, for which the cable goes slack and control of one degree of freedom is lost, or goes to infinity, which indicates that the mechanism is on a singular configuration and the cable can break. In practice, it is important to prevent both extreme situations, and ensure that the cables work within a predefined range of admissible tensions for a given wrench applied on the platform, subject to bounded perturbations in all directions. Several authors have proposed strategies for the determination of wrench-feasible workspaces [6, 12, 23, 27, 29, 30], but the problem of planning paths between two configurations in such spaces has not been intensively studied. Some algorithms exist that try to avoid the singular configurations where forces tend to infinity, but they are mainly tailored to classical Stewart platforms with UPS legs [2, 9, 10, 26], and their application to cable-driven manipulators is not straightforward because they do not account for the positivity constraint on the leg tensions. Moreover, these algorithms measure the clearance of the path relative to the singularity locus using the determinant or the condition number of the Jacobian matrix, which, as noted in [31], lack physical significance. While some approaches indeed exist for cable-driven manipulators [11, 15, 17], the path they compute is evaluated for feasibility at discrete points only, and the fulfillment of all constraints along the whole path is not guaranteed.

This paper provides a method for planning paths on the wrench-feasible C-space of cable-driven hexapods, also called tendon-based Stewart platforms. This C-space is defined following the spirit of [6], as the one that results from only allowing wrench-feasible configurations; i.e., those on which the cable tensions remain within the allowed limits, for any platform wrench belonging to a prescribed six-dimensional region (Sect. 2). The method relies on defining a system of equations whose solution manifold corresponds to the wrench-feasible C-space of the hexapod, so that maneuvering through such manifold guarantees singularity avoidance at all times, while maintaining cable tensions and lengths within their allowable bounds (Sect. 3). This manifold, as well as any of its slices obtained by fixing some of the pose parameters,

can be proved to be smooth everywhere, which allows defining a systematic higher-dimension continuation strategy to explore the manifold from a start configuration, until a path to a goal configuration is found, or path non-existence is proved (Sect. 4). The approach has been implemented and validated on several experiments (Sect. 5), and points for future attention have been identified (Sect. 6).

2 Problem Statement

A cable-driven hexapod consists of a moving *platform* suspended from a fixed *base* by means of six cables, winding around independent winches (Fig. 1). When all cables are in tension, which can be achieved by the action of gravity, their lengths determine a locally unique pose for the platform, so that it is possible to control the six degrees of freedom of the platform by actuating the winches.

Let $OXYZ$ and $PX'Y'Z'$ be fixed and moving reference frames respectively attached to the base and the platform (Fig. 1). Any configuration of the platform can be uniquely represented by a pair $q = (p, R) \in SE(3)$, where $p = [x, y, z]^T$ is the position vector of point P in the fixed frame, and R is a 3×3 rotation matrix providing the orientation of $PX'Y'Z'$ relative to $OXYZ$. However, the entries of R are not independent, since they must define an orthogonal matrix of positive determinant. Such a constraint can be defined in a variety of ways, e.g. by establishing appropriate dot- and cross-product equations on the columns of R, but more intuitive representations of the orientation are obtained when three-parameter expressions for R are adopted. Due to its attractive properties, we will use here the parameterization provided by tilt-and-torsion angles [16], $\tau = \{\phi, \theta, \sigma\}$, for which

$$R = R_z(\phi)\, R_y(\theta)\, R_z(\sigma - \phi), \tag{1}$$

but any other parameterization could be used if desired.

In practice, not all configurations can be reached, because the cable lengths ρ_i are constrained to lie within the range $(\underline{\rho_i}, \overline{\rho_i})$ of allowable values, with $\underline{\rho_i} > 0$. Thus, if a_i and b_i denote the position vectors of the anchor points A_i and B_i of the ith leg (Fig. 1), expressed in $OXYZ$ and $PX'Y'Z'$ respectively, and u_i is the vector $B_i - A_i$ expressed in $OXYZ$, the configuration will only be valid if it satisfies

$$p + Rb_i - u_i - a_i = 0, \tag{2}$$

$$u_i^T u_i - \rho_i^2 = 0, \tag{3}$$

with

$$\rho_i \in (\underline{\rho_i}, \overline{\rho_i})$$

for $i = 1, \ldots, 6$.
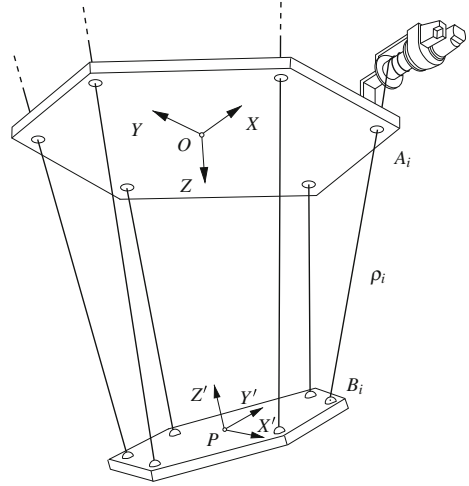
Additionally, any configuration must be *wrench-feasible*, in the sense that it must allow the platform to equilibrate any external wrench $\hat{\boldsymbol{w}}$ acting on it, subject to lie inside a prescribed six-dimensional region $\mathscr{W} \subset \mathbb{R}^6$. The significance of $\mathscr{W}$ depends on the particular context of application but, typically, $\mathscr{W}$ is determined by the gravitational wrench $\hat{\boldsymbol{w}}_0$ acting on the platform, and by bounds on the perturbations introduced by inertia forces or external agents like the wind, for instance. Specifically, the wrench-feasibility requirement on a given $\boldsymbol{q}$ implies that for each wrench $\hat{\boldsymbol{w}} \in \mathscr{W}$ there must be a vector

$$\boldsymbol{f} = [f_1, \ldots, f_6]^\mathsf{T} \in \mathscr{D} = (\underline{f_1}, \overline{f_1}) \times \cdots \times (\underline{f_6}, \overline{f_6})$$

of cable tensions satisfying

$$\boldsymbol{J}(\boldsymbol{q}) \cdot \boldsymbol{f} = \hat{\boldsymbol{w}},$$

where $\boldsymbol{J}(\boldsymbol{q})$ is the 6×6 screw Jacobian of the manipulator at $\boldsymbol{q}$, and $(\underline{f_i}, \overline{f_i})$ is the range of cable tensions that can be resisted by the ith cable, with $\underline{f_i} > 0$. Here, $\hat{\boldsymbol{w}}$, $\hat{\boldsymbol{w}}_0$, and $\boldsymbol{J}(\boldsymbol{q})$ will be assumed to be given in a frame $PXYZ$ centered in P and parallel to $OXYZ$, although any other frame could be assumed if desired, and $\mathscr{W}$ will be a six-dimensional ellipsoid defined as

$$(\hat{\boldsymbol{w}} - \hat{\boldsymbol{w}}_0)^\mathsf{T} \boldsymbol{E} \, (\hat{\boldsymbol{w}} - \hat{\boldsymbol{w}}_0) \le 1,$$

where $\boldsymbol{E}$ is a constant 6×6 positive-definite symmetric matrix. In practice, this ellipsoid can be constructed by propagating known bounds on other variables related to $\hat{\boldsymbol{w}}$, using the tools of an ellipsoidal calculus [24], for example.

Now, let us define the *wrench-feasible C-space* of the manipulator, $\mathscr{C}$, as the set of $\boldsymbol{q} \in SE(3)$ for which the platform is able to counteract all $\hat{\boldsymbol{w}} \in \mathscr{W}$ with $\rho_i \in (\underline{\rho_i}, \overline{\rho_i})$

and $f \in \mathcal{D}$. Given two configurations in $\mathcal{C}$, q_1 and q_2, the goal of this paper is to provide an algorithm for computing a path on $\mathcal{C}$ connecting them, if one exists, or to determine path non-existence otherwise. To this end, we next define a system of equations that are suitable to compute such path using a continuation approach.

3 Equations of the Wrench-Feasible C-Space

Let f_0 be the vector of cable tensions corresponding to a given $\hat{w}_0 \in \mathcal{W}$, i.e.,

$$J(q) \cdot f_0 = \hat{w}_0. \tag{4}$$

By noting that $J(q)(f - f_0) = \hat{w} - \hat{w}_0$, it is easy to see that, for a given q, the set $\mathscr{F}(q)$ of cable tensions f corresponding to all $\hat{w} \in \mathcal{W}$ is the ellipsoid given by

$$(f - f_0)^\mathsf{T} B \, (f - f_0) \leq 1,$$

where $B = J(q)^\mathsf{T} E \, J(q)$. This ellipsoid will be bounded in all directions or unbounded in some, depending on whether $det(J(q)) \neq 0$ or not. However, it is not difficult to see that $J(q)$ is non-singular for all $q \in \mathcal{C}$ (Appendix A), so that $\mathscr{F}(q)$ will always be a bounded ellipsoid in our case.

Now, for q to be wrench-feasible, we must have $\mathscr{F}(q) \subseteq \mathcal{D}$, which can be checked as follows. For each $i = 1, \ldots, 6$, let $v_i \in \mathbb{R}^6$ be a vector satisfying

$$\left. \begin{array}{c} v_i^\mathsf{T} B \, v_i = 1 \\ B^i v_i = 0 \end{array} \right\}, \tag{5}$$

where B^i stands for the matrix B with its ith row removed. Observe that if $J(q)$ is non-singular, then B and B^i are full row rank, and if the ith component of v_i, $v_{i,i}$, is chosen non-negative, then there is exactly one vector v_i satisfying Eq.(5). Using Lagrange multipliers, it can be shown that, for the solutions v_i of Eq.(5) with $v_{i,i} \geq 0$, $f_0 - v_i$ and $f_0 + v_i$ are the vectors in $\mathscr{F}(q)$ attaining the smallest and largest value along the ith coordinate. Hence, when $det(J(q)) \neq 0$, $\mathscr{F}(q) \subseteq \mathcal{D}$ if, and only if,

$$f_{0,i} - v_{i,i} > \underline{f_i},$$

and

$$f_{0,i} + v_{i,i} < \overline{f_i},$$

for $i = 1, \ldots, 6$. These two conditions are equivalent to imposing

$$(f_{0,i} - v_{i,i} - \underline{f_i}) \cdot s_i = 1, \tag{6}$$

$$(\overline{f_i} - f_{0,i} - v_{i,i}) \cdot t_i = 1, \tag{7}$$

together with the inequalities $s_i \geq 0$, and $t_i \geq 0$, where s_i and t_i are newly-defined auxiliary variables. Looking at the first equation, for instance, it is clear that neither $f_{0,i} - v_{i,i} - \underline{f_i}$ nor s_i can be zero, so that for any $s_i \geq 0$, it will always be $f_{0,i} - v_{i,i} > \underline{f_i}$ as desired. In a similar way, the cable-length constraints $\rho_i \in (\underline{\rho_i}, \overline{\rho_i})$ are equivalent to imposing

$$(\rho_i - \underline{\rho_i}) \cdot (\overline{\rho_i} - \rho_i) \cdot g_i = 1, \tag{8}$$

in conjunction with the inequality constraint $g_i \geq 0$ acting on the new variable g_i.

At this point, let us consider the system formed by Eqs. (1–8), which we will write compactly as

$$F(x) = 0, \tag{9}$$

where x refers to an n_x-vector encompassing all of its variables, and let us distinguish between the solution set of Eq. (9),

$$\mathcal{M} = \{x : F(x) = 0\},$$

and the set

$$\mathcal{M}^+ = \{x \in \mathcal{M} : v_{i,i} \geq 0, \ s_i \geq 0, \ t_i \geq 0, \ g_i \geq 0, \quad \text{for } i = 1, \ldots, 6\}.$$

Note that every configuration $q \in \mathcal{C}$ has a corresponding point $x \in \mathcal{M}^+$ and, conversely, each point in $\mathcal{M}^+$ projects down to one $q \in \mathcal{C}$. Moreover, any continuous path in $\mathcal{C}$ will also be represented by a continuous path in $\mathcal{M}^+$ and viceversa, so that the original problem of computing a wrench-feasible path in $\mathcal{C}$ from q_1 to q_2 can be reduced to that of computing a path in $\mathcal{M}^+$ connecting points x_1 and x_2 corresponding to q_1 and q_2.

Two properties can be exploited regarding the structure of $\mathcal{M}$ and $\mathcal{M}^+$ (Appendix A), which allow to apply a continuation strategy to connect x_1 and x_2 using Eq. (9). It is easy to see, first, that $v_{i,i}$, s_i, t_i, and g_i never vanish on $\mathcal{M}$, so that there does not exist any path traversing from $\mathcal{M}^+$ to its complement $\mathcal{M} \setminus \mathcal{M}^+$. Thus, if x_1 and x_2 are chosen with positive values for $v_{i,i}$, s_i, t_i, and g_i, then any continuous path on $\mathcal{M}$ connecting x_1 and x_2 will entirely lie on $\mathcal{M}^+$, and it will correspond to a path on $\mathcal{C}$ therefore. In other words, when trying to connect x_1 and x_2 by continuation on $\mathcal{M}$, the positivity constraints on $v_{i,i}$, s_i, t_i, and g_i will be implicitly fulfilled, and they can be safely neglected. Second, it can be shown that $\mathcal{M}$, and in particular $\mathcal{M}^+$, is a six-dimensional smooth manifold everywhere, so that every point x has a well-defined tangent space $T_x\mathcal{M}$, which facilitates the application of the following continuation strategy to connect x_1 and x_2, because no bifurcations, sharpnesses, or dimension changes will be found when traversing $\mathcal{M}$.
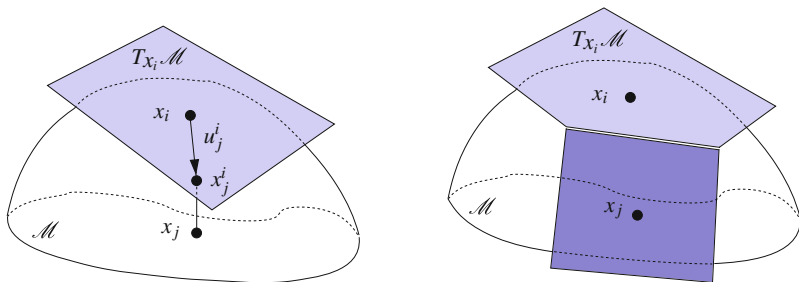
Fig. 2 The higher-dimensional continuation method applied to a 2-dimensional manifold in $\mathbb{R}^3$

4 Exploring $\mathscr{M}$ for a Connecting Path

To determine a path on $\mathscr{M}$ connecting two points x_1 and x_2 we can gradually construct an atlas of $\mathscr{M}$, i.e., a collection of charts where each chart C_i defines a local map from a domain $\mathscr{P}_i \subset \mathbb{R}^6$ to an open set of $\mathscr{M}$ around a point $x_i \in \mathscr{M}$, initially x_1. The atlas will be computed using the higher-dimensional continuation approach proposed in [14], which defines the local map for chart C_i using $\boldsymbol{\Psi}_i$, an orthonormal basis of $T_{x_i}\mathscr{M}$. The map is defined by first selecting a vector $\boldsymbol{u}^i_j \in \mathbb{R}^6$ of parameters (Fig. 2, left), which is used to generate a point $\boldsymbol{x}^i_j \in \mathbb{R}^{n_x}$ in the neighborhood of x_i, using $\boldsymbol{x}^i_j = x_i + \boldsymbol{\Psi}_i \boldsymbol{u}^i_j$. Then, a point $x_j \in \mathscr{M}$ corresponding to the projection of $\boldsymbol{x}^i_j$ on $\mathscr{M}$ is computed, by solving the system formed by $\boldsymbol{F}(x_j) = \boldsymbol{0}$ and $\boldsymbol{\Psi}_i^{\mathsf{T}}(x_j - \boldsymbol{x}^i_j) = \boldsymbol{0}$ using a Newton method initialized at $\boldsymbol{x}^i_j$.

Each point x_j is the potential center of a new chart (Fig. 2, right), and a method due to Henderson can be used to decide where to place the chart centers so as to ensure a good coverage of the manifold [14]. In his approach, the domain $\mathscr{P}_i$ of chart C_i is initialized as a 6-dimensional hypercube enclosing a ball $\mathscr{B}_i$ of radius r, both defined in $T_{x_i}\mathscr{M}$, as illustrated in Fig. 3, left. A vertex of $\mathscr{P}_i$ exterior to $\mathscr{B}_i$, with position vector $\boldsymbol{s}$, is used to generate a point $\boldsymbol{x}^i_j$, with $\boldsymbol{u}^i_j = \alpha \cdot \boldsymbol{s}/\|\boldsymbol{s}\|$, where α is initialized to r. If the projection of $\boldsymbol{x}^i_j$ to $\mathscr{M}$ does not converge, or if the new chart C_j at x_j is too far or too different from C_i, i.e., if

$$\|x_j - \boldsymbol{x}^i_j\| > \varepsilon, \quad \text{or} \quad \|\boldsymbol{\Psi}_i^{\mathsf{T}}\boldsymbol{\Psi}_j\| < 1 - \varepsilon,$$

for a given threshold ε, the new chart is discarded and a new attempt of chart generation is performed with a smaller α, allowing to adapt the size of the area covered by each chart to the local curvature of the manifold. When C_j is valid, it is used to crop $\mathscr{P}_i$ from the intersection between $\mathscr{B}_i$ and C^i_j, the projection on $T_{x_i}\mathscr{M}$ of the part of the manifold covered by C_j. This projection is approximated by a ball $\mathscr{B}^i_j$ of radius r in $T_{x_i}\mathscr{M}$, centered at the point given by $\boldsymbol{u}^i_j$, as shown in Fig. 3, right. The intersection of $\mathscr{B}_i$ and $\mathscr{B}^i_j$ defines a new face for $\mathscr{P}_i$ that eliminates some of its
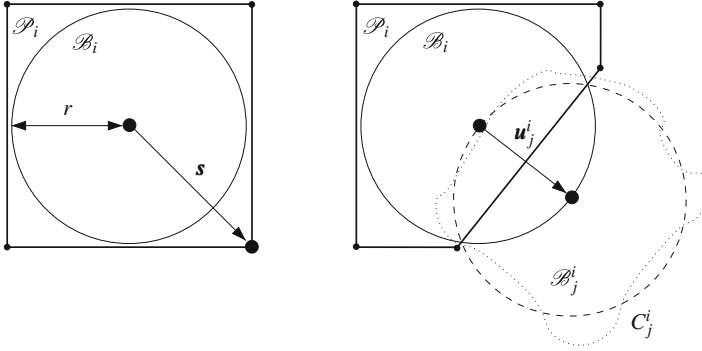
Fig. 3 The process of chart construction

vertices (in particular the one given by s) and generates new ones. Symmetrically, the polytope $\mathscr{P}_j$ associated with C_j is cropped using C_i. When C_i is surrounded by other charts, $\mathscr{P}_i$ becomes a convex polytope included in $\mathscr{B}_i$, and C_i is considered to be *closed*, meaning that no further expansion of the atlas needs to be attempted from that chart. In practice, as $\mathscr{M}^+$ is unbounded in the directions s_i, t_i, and g_i, we impose an upper bound on these variables in order to ensure the termination of the atlas expansion. The charts generated outside these bounds are also considered to be closed. When all charts are closed, the connected component of $\mathscr{M}$ containing the initial point x_1 gets fully covered. If a path exists from x_1 to x_2, x_2 must be included in one of the charts of the atlas and, thus, a solution path can be determined by searching on the graph implicitly defined by the chart centers and their neighborhood relations. In practice, however, the expansion of the charts is performed according to an A* search strategy using an admissible heuristic [25], so that the path is returned as soon as it is found without computing the whole atlas, and it is guaranteed to be the shortest possible on $\mathscr{M}$. If x_2 is not included in any of the charts in the end, path non-existence is established at the considered value for r. A detailed analysis of the cost of the algorithm can be found in [21].

5 Experiments

The method has been implemented in C, and run on a MacBook Pro equipped with a 2.66 GHz Intel Core i7 processor. To verify its performance on a realistic situation, the geometric parameters of the NIST Robocane manipulator have been used [1] (Fig. 4). This manipulator follows an octahedral design where both the base and the platform are equilateral triangles of sides $2b$ and $2a$, respectively. The fixed reference frame $OXYZ$ is defined with the Z axis pointing downwards, and a mobile reference frame $PX'Y'Z'$ is attached to the platform. The coordinates of the vertex points of the base, expressed in $OXYZ$, are $A_1 = (-b, -b\sqrt{3}/3, 0)$, $A_2 = (b, -b\sqrt{3}/3, 0)$,
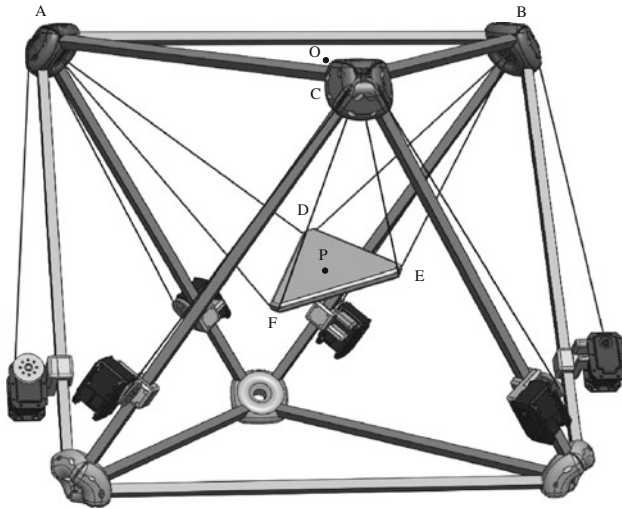
Fig. 4 CAD Model of the cable-driven hexapod under construction at Institut de Robòtica i Informàtica Industrial (IRI), inspired in the NIST Robocrane [1] (courtesy of P. Grosch)

and $A_3 = (0, 2b\sqrt{3}/3, 0)$, and those of the platform, expressed in $PX'Y'Z'$, are $B_1 = (0, -2a\sqrt{3}/3, 0)$, $B_2 = (a, a\sqrt{3}/3, 0)$, and $B_3 = (-a, a\sqrt{3}/3, 0)$.

In all experiments, the platform is required to withstand a weight of m Newtons applied at a point $P_m = (\frac{a}{5}, \frac{a}{5}, 0)$ in $PX'Y'Z'$. Since the weight always points downwards, this corresponds to a wrench $\hat{\boldsymbol{w}}_0 = [0, 0, m, 0, 0, 0]^\mathsf{T}$ that is constant in a reference frame parallel to $OXYZ$ translating with P_m. For simplicity, the small variations that may be introduced by inertia forces or external agents are represented by the ellipsoid $\mathscr{W}$ centered in $\boldsymbol{w}_0$ defined by $\boldsymbol{E} = 10^4 \cdot \boldsymbol{I}_6$, which is a six-dimensional sphere of radius 10^{-2}, and the forces and lengths for all cables are set to remain positive but lower than $\overline{f_i} = m$ N and $\overline{\rho_i} = 5a$, respectively.

To illustrate the complexity of the path planning problem, Fig. 5 shows several slices of the wrench-feasible C-space $\mathscr{C}$ of the manipulator, computed in Matlab using discretization with $a = 1$, $b = 2$, and $m = 1$. The configurations that cannot be reached due to either cable lengths or forces out of range are represented by the red and blue areas, respectively, while those corresponding to $\mathscr{C}$ are indicated in green. The figure also shows the singularity curves where $det(\boldsymbol{J}(\boldsymbol{q})) = 0$, in red, computed with the method in [3] under no constraints on the cable tensions or lengths. It can be observed that the wrench-feasible C-space naturally avoids crossing singularities, although in some zones this point may not be clear due to the resolution of the discretization, and to the small size of the figures. The top row of Fig. 5 corresponds to slices where the point P and the torsion σ are held fixed. In the bottom row, the whole orientation $\boldsymbol{\tau}$ of the platform and one of the coordinates of P are held fixed. As it can be seen from the figures, the navigation between two configurations of $\mathscr{C}$ is not a trivial task. In particular, evaluating the wrench-feasibility conditions on discrete
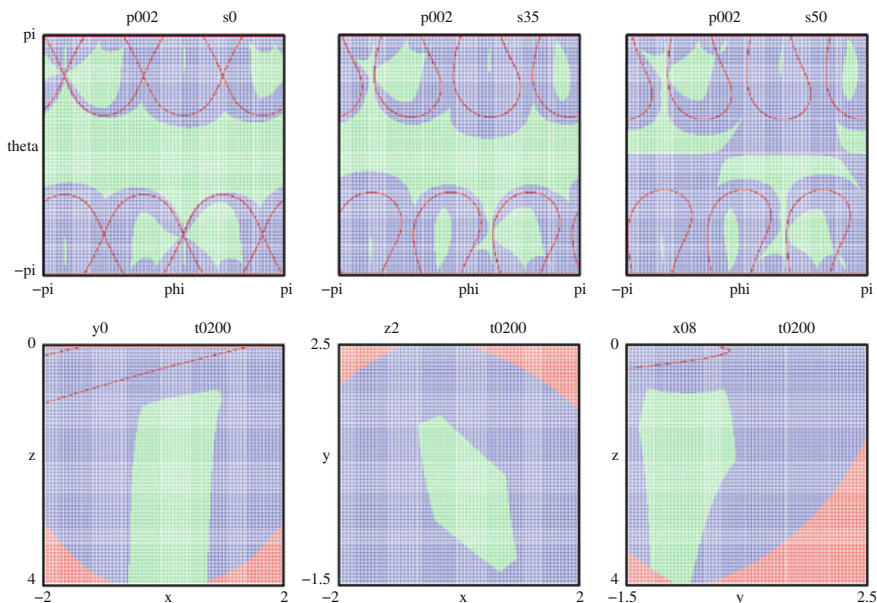
Fig. 5 Slices of the wrench-feasible C-space obtained by discretization. *Blue*, *red* and *green* zones correspond to configurations where some force is out of range, configurations not attainable due to cables length, and configurations belonging to the wrench-feasible C-space, respectively

points along a path could result in erroneous paths that, for example, could join points belonging to different connected components of $\mathscr{C}$. The method presented in this paper is able to solve such hard planning queries, even when permitting the variation of all pose parameters. However, due to illustration limitations, the performance of the method is demonstrated here by means of two experiments where four and three pose parameters are held fixed.

In the first experiment, we compute two different paths on the top-center slice of $\mathscr{C}$ shown in Fig. 5, where $p = [0, 0, 2]^{\mathsf{T}}$ and $\sigma = 35°$. Using the start q_1 and goal q_2 configurations defined by $\tau_1 = \{-0.5, 0.9, \frac{7}{36}\pi\}\ rad$ and $\tau_2 = \{2, 0.9, \frac{7}{36}\pi\}\ rad$, respectively, the resulting path is computed in 20 s. Figure 6, top, shows this path in red together with the atlas corresponding to the whole connected component of $\mathscr{C}$ accessible from the start configuration (shown as a green mesh), and the region explored by the algorithm (shaded in grey). In order to evaluate the performance of the method on a more challenging situation, a second path is computed between configurations q_3 and q_4 given by $\tau_3 = \{0.8, -2.4, \frac{7}{36}\pi\}\ rad$ and $\tau_4 = \{-2.4, 2.4, \frac{7}{36}\pi\}\ rad$. In this case the path is computed in 280 s and the region explored is shaded in green (Fig. 6, top). On both planning queries, note that the interpolated path between the start and goal configurations would violate some of the constraints of $\mathscr{C}$, giving rise to uncontrollable motions of the platform, or to breakage of some of the cables, but the computed paths correctly avoid these sit-
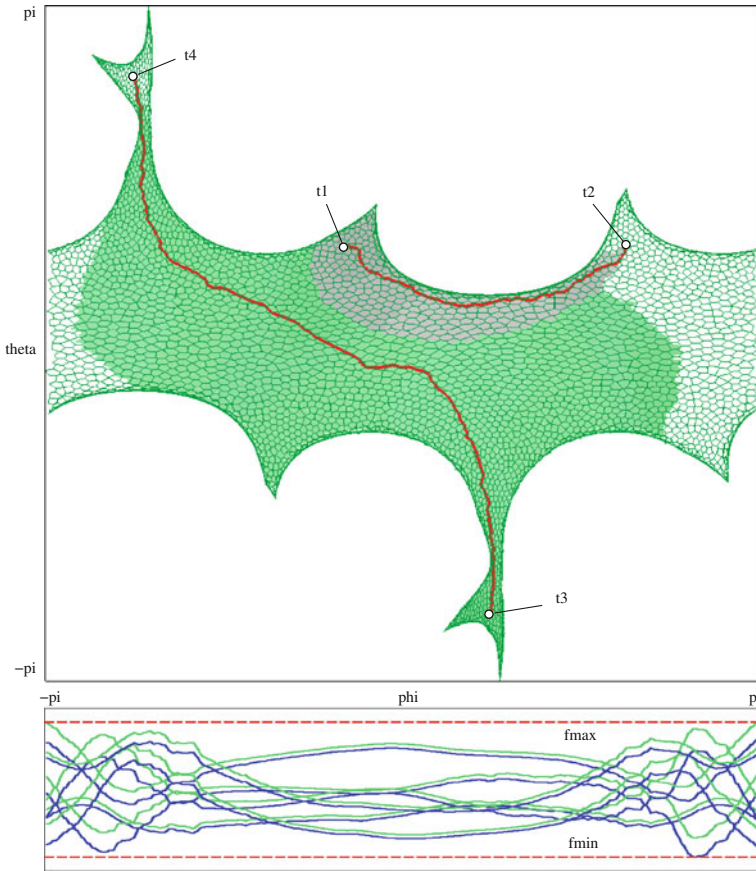
Fig. 6 *Top*: Two paths and the areas of $\mathscr{C}$ explored to compute them, on the slice of the wrench-feasible C-space corresponding to $\boldsymbol{p} = [0, 0, 2]^\mathsf{T}$ and $\sigma = 35°$. *Bottom*: evolution of the maximum (*green*) and minimum (*blue*) possible tensions for each cable, along the path from $\boldsymbol{q}_3$ to $\boldsymbol{q}_4$

uations. Indeed, an advantageous property of the continuation strategy employed, which cannot be ensured by methods relying on discretization, is that the computed path will not jump between distinct connected components of $\mathscr{C}$, even when such components are close to each other, thus ensuring that the forces on all cables keep within the prescribed ranges along the whole path. As an example, these forces can be seen in Fig. 6, bottom, for the path from $\boldsymbol{q}_3$ to $\boldsymbol{q}_4$. The evolution along this path of the maximum and minimum tensions on each cable are plotted in green and blue, respectively. Towards the end of the path, some cable may attain a near-zero tension, but this can be easily avoided if desired, by simply setting a higher value of $\underline{f}_i$.

On the second experiment, only three pose variables are held fixed, namely $x = 0$, $y = 0$, and $\sigma = 35°$, giving rise to a three-dimensional slice of the wrench-feasible C-space $\mathscr{C}$. Here, the start and goal configurations, $\boldsymbol{q}_5$ and $\boldsymbol{q}_6$, are given by $\boldsymbol{p}_5 =$
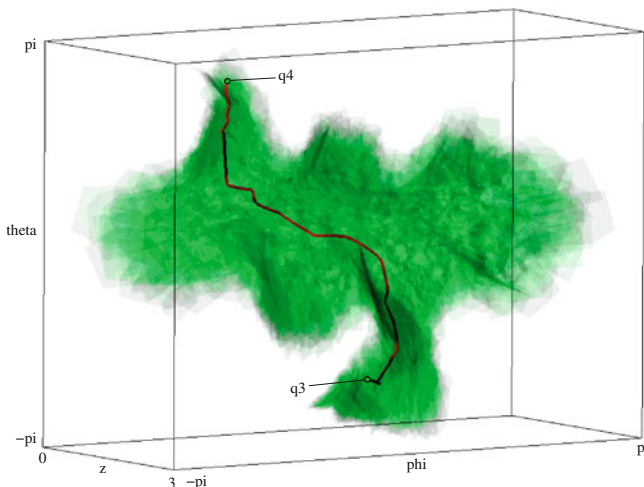
Fig. 7 A path on a three-dimensional slice of the wrench-feasible C-space with $x = 0$, $y = 0$ and $\sigma = 35°$. The *green volume* corresponds to the portion of $\mathscr{C}$ explored by the algorithm, which is here visualized by projecting the chart polytopes $\mathscr{P}_i$ to the space of z, ϕ, and θ, and representing their faces as semi-transparent walls, in order to visualize the computed path in the interior

$[0, 0, 1.2]^{\mathsf{T}}$, $\boldsymbol{\tau}_5 = \{0.8, -2.6, \frac{7}{36}\pi\}$ *rad* and $\boldsymbol{q}_6 = \boldsymbol{q}_4$. The resulting path can be seen in Fig. 7 in red, together with the atlas generated by the algorithm in green. This case represents a hard planning query and, therefore, the computation time increases significantly. However, once a partial atlas is computed, all planning queries between configurations covered by such atlas can be solved in a few milliseconds.

6 Conclusions and Future Work

This paper has presented a path planning method for computing wrench-feasible paths on cable-driven hexapods, i.e., configuration paths that guarantee the resolvability of a six-dimensional set of wrenches at any point on the path. As a by product, the method implicitly ensures that the screw Jacobian of the manipulator will be non-singular along the path, thus allowing a full control of the platform motions at all times. The method has been tested successfully on several cases of increasing complexity, though only cases where three or four pose variables are held fixed have been shown due to illustration limitations.

The presented approach allows extensions in several possible ways. For example, some additional constraints could be considered, like enforcing a certain degree of positioning accuracy of the platform, or the avoidance of platform collisions (cable-platform or cable-cable collisions, or even those with the environment). While the former constraints can in principle be incorporated using dual developments to those

herein presented, the latter require investigating the possibility of randomizing the planner, in the spirit of [8] or [22].

Appendix: Properties of $\mathcal{M}$

This appendix is devoted to the proof of two properties that are essential in order to apply the continuation strategy described in Sect. 4. The first one is the non-nullity of s_i, t_i, g_i and $v_{i,i}$, and the second one is smoothness of the six-dimensional manifold $\mathcal{M}$. A by-product of the second property is the fact that $J(q)$ is non-singular for all $q \in \mathcal{C}$.

From Eqs. (6–8) it follows directly that s_i, t_i and g_i can never be zero on $\mathcal{M}$. The same property for $v_{i,i}$ can be proved by contradiction. Let us assume that $v_{i,i} = 0$ for some i. If we consider Eq. (5), then, by replacing $B^i v_i = 0$ into $v_i^\mathsf{T} B\, v_i = 1$, we obtain the dot product of two vectors: v_i^T, with $v_{i,i} = 0$, and the vector $B v_i$, whose components are all zero except that in position i. The result of this dot product is 0, which contradicts Eq. (5), as it should be 1. As a result, the set $\mathcal{M}^+$ and its complement $\mathcal{M} \setminus \mathcal{M}^+$ are disconnected.

Let us now prove the smoothness of $\mathcal{M}$. If we can verify that $F(x)$ is a differentiable function with full rank differential F_x, then the smoothness of $\mathcal{M}$ will follow from the implicit function theorem. By construction, all functions intervening in $F(x)$ are differentiable all over $\mathcal{M}$, and the differential matrix F_x can be expressed in the following block-triangular form after re-organizing some equations and variables

$$
F_x = \begin{pmatrix}
\Phi_y & & & & & \\
* & J(q) & & & & \\
& & \begin{matrix} 2v_1^\mathsf{T} B \\ B^1 \end{matrix} & & & \\
* & & & \ddots & & \\
& & & & \begin{matrix} 2v_6^\mathsf{T} B \\ B^6 \end{matrix} & \\
& * & & * & & S \\
& * & & * & & T
\end{pmatrix},
$$

where empty blocks represent zero-matrices and asterisks indicate non-zero blocks.

Due to the triangular structure of F_x it suffices to verify that the five blocks in the diagonal are full-rank in order to prove the smoothness of $\mathcal{M}$. The first block is

$$
\boldsymbol{\Phi_y} = \begin{pmatrix} * & \boldsymbol{I}_9 & & & \\ & * & * & -\boldsymbol{I}_{18} & & \\ & & & * & -2\boldsymbol{L} & \\ & & & & * & \boldsymbol{G} \end{pmatrix},
$$

which is the differential matrix of the system $\boldsymbol{\Phi}(\boldsymbol{y}) = \boldsymbol{0}$ formed by Eqs. (1–3) and (8) with respect to $\boldsymbol{y} = (\boldsymbol{\tau}, \boldsymbol{p}, \boldsymbol{R}, \boldsymbol{u}_i, \rho_i, g_i)$. Here $\boldsymbol{L}$ and $\boldsymbol{G}$ are 6×6 diagonal matrices with diagonal elements ρ_i and $(\rho_i - \underline{\rho_i}) \cdot (\overline{\rho_i} - \rho_i)$, respectively. To see that $\boldsymbol{\Phi_y}$ is full rank, observe that its last four block-columns comprise a non-singular square submatrix of maximum size, as its diagonal elements do not vanish over $\mathcal{M}$ by virtue of Eq. (8) and the fact that $\underline{\rho_i} > 0$.

The remaining four diagonal blocks of $\boldsymbol{F_x}$ are the differential matrices of Eqs. (4–7) with respect to the variables $\boldsymbol{f}_0$, $\boldsymbol{v}_i$, s_i and t_i, respectively, where the blocks $\boldsymbol{S}$ and $\boldsymbol{T}$ are 6×6 diagonal matrices with elements $f_{0,i} - v_{i,i} - \underline{f_i}$ and $\overline{f_i} - f_{0,i} - v_{i,i}$, respectively. The screw Jacobian $\boldsymbol{J}(\boldsymbol{q})$ can be shown to be full rank over $\mathcal{M}$ by contradiction. Indeed, if $\boldsymbol{J}(\boldsymbol{q}_s)$ were rank deficient for some $\boldsymbol{q}_s$, then so would be $\boldsymbol{B}$, and therefore ker $\boldsymbol{B}$ would contain non-zero vectors. In such case, for some i all solutions of $\boldsymbol{B}^i \boldsymbol{v}_i = \boldsymbol{0}$ would satisfy $\boldsymbol{v}_i \in \ker \boldsymbol{B}$ and, thus, it would be $\boldsymbol{v}_i^{\mathsf{T}} \boldsymbol{B} \boldsymbol{v}_i = 0$, which contradicts Eq. (5) and, hence, $\boldsymbol{J}(\boldsymbol{q})$ cannot be rank deficient over $\mathcal{M}$. The 6×6 block matrices involving $\boldsymbol{B}$ and $\boldsymbol{B}^i$ can only be rank deficient if $v_{i,i} = 0$, but this can never happen as we have already seen. All these blocks are therefore full rank over $\mathcal{M}$. Finally, it is clear that $\boldsymbol{S}$ and $\boldsymbol{T}$ are also full rank over $\mathcal{M}$, since their diagonal elements never vanish due to Eqs. (6–7), and this completes the proof of the smoothness of $\mathcal{M}$ and, in particular, that of $\mathcal{M}^+$.

It is worth mentioning that not only $\mathcal{M}$ and $\mathcal{M}^+$ are smooth, but also any slice taken as a combination of the angular and position parameters, $\boldsymbol{\tau}$ and $\boldsymbol{p}$. Indeed, taking any of these slices implies only the removal of some columns amongst the first two blocks of $\boldsymbol{\Phi_y}$, which does not change the global rank of the differential $\boldsymbol{F_x}$ corresponding to the considered slice.

References

1. Albus, J., Bostelman, R., Dagalakis, N.: The NIST Robocrane. J. Robot. Syst. **10**(5), 709–724 (1993)
2. Bhattacharya, S., Hatwal, H., Ghosh, A.: Comparison of an exact and an approximate method of singularity avoidance in platform type parallel manipulators. Mech. Mach. Theory **33**(7), 965–974 (1998)
3. Bohigas, O., Zlatanov, D., Ros, L., Manubens, M., Porta, J.: Numerical computation of manipulator singularities. Proceedings of the IEEE Internatioanl Conference on Robotics and Automation, In (2012)
4. Borgstrom, P., Jordan, B., Borgstrom, B., Stealey, M., Sukhatme, G., Batalin, M., Kaiser, W.: Nims-pl: a cable-driven robot with self-calibration capabilities. IEEE Trans. Robot. **25**(5), 1005–1015 (2009)
5. Bosscher, P., Williams II, R.L., Bryson, L.S., Castro-Lacouture, D.: Cable-suspended robotic contour crafting system. Autom. Constr. **17**(1), 45–55 (2007)

6. Bosscher, P., Riechel, A., Ebert-Uphoff, I.: Wrench-feasible workspace generation for cable-driven robots. IEEE Trans. Robot. **22**(5), 890–902 (2006)
7. Cheng, P., Fink, J., Kim, S., Kumar, V.: Cooperative towing with multiple robots. In: Chirikjian, G., Choset, H., Morales, M., Murphey, T. (eds.) Algorithmic Foundation of Robotics VIII, Springer Tracts in Advanced Robotics, vol. 57, pp. 101–116. Springer, Berlin (2009)
8. Cortés, J., Siméon, T.: Probabilistic motion planning for parallel mechanisms. In: Proceedings of the IEEE International Conference on Robotics and Automation, vol. 3, pp. 4354–4359 (2003).
9. Dasgupta, B., Mruthyunjaya, T.: Singularity-free path planning for the Stewart platform manipulator. Mech. Mach. Theory **33**(6), 711–725 (1998)
10. Dash, A.K., Chen, I.M., Yeo, S.H., Yang, G.: Workspace generation and planning singularity-free path for parallel manipulators. Mech. Mach. Theory **40**(7), 776–805 (2005)
11. Fang, S., Franitza, D., Verhoeven, R., Hiller, M.: Proceedings of the 11th IFToMM World Congress in Mechanism and Machine Science. China Machinery Press, Tianjin (2003)
12. Gouttefarde, M., Daney, D., Merlet, J.P.: Interval-analysis-based determination of the wrench-feasible workspace of parallel cable-driven robots. IEEE Trans. Robot. **27**(1), 1–13 (2011)
13. Harmon, T., Ambrose, R., Gilbert, R., Fisher, J., Stealey, M., Kaiser, W.: High-resolution river hydraulic and water quality characterization using rapidly deployable networked infomechanical systems (NIMS RD). Environ. Eng. Sci. **24**(2), 151–159 (2007)
14. Henderson, M.E.: Multiple parameter continuation: Computing implicitly defined k-manifolds. Int. J. Bifurcation Chaos **12**(3), 451–476 (2002)
15. Hiller, M., Fang, S., Mielczarek, S., Verhoeven, R., Franitza, D.: Design, analysis and realization of tendon-based parallel manipulators. Mech. Mach. Theory **40**(4), 429–445 (2005)
16. Bonev, I.A., Zlatanov, D., Gosselin, C.: Advantages of the modified Euler angles in the design and control of PKMs. In: Parallel Kinematic Machines International Conference, Chemnitz, April 23–25, pp. 171–188 (2002).
17. Lahouar, S., Ottaviano, E., Zeghoul, S., Romdhane, L., Ceccarelli, M.: Collision free path-planning for cable-driven parallel robots. Robot. Auton. Syst. **57**(11), 1083–1093 (2009)
18. Lytle, A.M., Saidi, K.S., Bostelman, R.V., Stone, W.C., Scott, N.A.: Adapting a teleoperated device for autonomous control using three-dimensional positioning sensors: experiences with the NIST RoboCrane. Autom. Constr. **13**, 101–118 (2004)
19. Merlet, J.P., Daney, D.: A portable, modular parallel wire crane for rescue operations. In: Proceedings of the IEEE Internationl Conference on Robotics and Automation, pp. 2834–2839 (2010).
20. Oh, S.R., Ryu, J.C., Agrawal, S.K.: Dynamics and control of a helicopter carrying a payload using a cable-suspended robot. J. Mech. Des. **128**(5), 1113–1121 (2006)
21. Porta, J., Jaillet, L., Bohigas, O.: Randomized path planning on manifolds based on higher-dimensional continuation. Int. J. Robot. Res. **31**(2), 201–215 (2012)
22. Porta, J.M., Jaillet, L.: Path planning on manifolds using randomized higher-dimensional continuation. In: Hsu, D., Isler, V., Latombe, J.C., Lin, M. (eds.) Algorithmic Foundations of Robotics IX, Springer Tracts in Advanced Robotics, vol. 68, pp. 337–353. Springer, Berlin (2011)
23. Pusey, J., Fattah, A., Agrawal, S., Messina, E.: Design and workspace analysis of a 6–6 cable-suspended parallel robot. Mech. Mach. Theory **3**, 761–778 (2004)
24. Ros, L., Sabater, A., Thomas, F.: An ellipsoidal calculus based on propagation and fusion. IEEE Trans. Syst. Man Cybern. Part B Cybern. **32**(4), 430–442 (2002)
25. Russell, S.J., Norvig, P.: Artificial Intelligence: A Modern Approach. Prentice Hall, Upper Saddle River (2003)
26. Sen, S., Dasgupta, B., Mallik, A.K.: Variational approach for singularity-free path-planning of parallel manipulators. Mech. Mach. Theory **38**(11), 1165–1183 (2003)
27. Stump, E., Kumar, V.: Workspaces of cable-actuated parallel manipulators. J. Mech. Des. **128**(1), 159–167 (2006)
28. Tadokoro, S., Matsushima, T., Murao, Y., Kohkawa, H.: A parallel cable-driven motion base for virtual acceleration. In: Proceedings of the IEEE/RSJ International Conference on Intelligent Robots and Systems, vol. 3, pp. 1700–1705 (2001).

29. Verhoeven, R.: Analysis of the workspace of tendon based Stewart platforms. Ph.D. Thesis, Universität Duisburg-Essen (2004).
30. Verhoeven, R., Hiller, M., Tadokoro, S.: Workspace of tendon-driven Stewart platforms: Basics, classification, details on the planar 2-dof class. In: Proceedings of the 4th International Conference on Motion and Vibration, Control, pp. 871–876 (1998).
31. Voglewede, P., Ebert-Uphoff, I.: Overarching framework for measuring closeness to singularities of parallel manipulators. IEEE Trans. Robot. **21**(6), 1037–1045 (2005)

Part II
Force Distribution

A Tension Distribution Method with Improved Computational Efficiency

Johann Lamaury and Marc Gouttefarde

Abstract This paper introduces a real-time capable tension distribution algorithm for n degree-of-freedom cable-driven parallel robots (CDPR) actuated by $n+2$ cables. It is based on geometric considerations applied to the two-dimensional convex polytope of feasible cable tension distribution. This polytope is defined as the intersection between the set of inequality constraints on the cable tension values and the affine space of tension solutions to the mobile platform static or dynamic equilibrium. The algorithm proposed in this paper is dedicated to n degree-of-freedom CDPR actuated by $n + 2$ cables. Indeed, it takes advantage of the two-dimensional nature of the corresponding feasible tension distribution convex polytope to improve the computational efficiency of a tension distribution strategy proposed elsewhere. The fast computation of the polytope vertices and of its barycenter made us successfully validate the real-time compatibility of the presented algorithm.

1 Introduction

A cable-driven parallel robot (CDPR) mainly consists of a base, a mobile platform connected in parallel to the base through flexible cables and motorized winches. The cable lengths can be modified by means of the winches thereby allowing the motion control of the platform. Contrary to common parallel robot architectures, CDPR with large to very large workspaces can be designed as cables can be unwound over great lengths. Moreover, their light weight, fast motion, heavy payload capabilities and high reconfigurability potential make these robots good candidates for large-

J. Lamaury (✉) · M. Gouttefarde
Laboratoire d'Informatique, de Robotique et de Micro-électronique de Montpellier,
161 rue Ada, 34392 Montpellier Cedex 5, France
e-mail: johann.lamaury@lirmm.fr

M. Gouttefarde
e-mail: marc.gouttefarde@lirmm.fr

dimension applications, for example pick-and-place tasks across a manufacturing plant.

CDPR are generally classified as fully constrained or else under-constrained. Examples of fully constrained CDPR are the FALCON robot [6], the SEGESTA [4] and the KNTU [10]. A well-known under-constrained CDPR is the NIST ROBOCRANE [1]. In both cases, the number of cables driving the mobile platform can be greater than its number of degrees of freedom (DOF). When controlling such redundantly actuated CDPR, the issue of cable tension distribution is to be dealt with. Indeed, at any point along a trajectory, there exists an infinity of possible sets of cable tensions and one generally wants to find a feasible one, possibly satisfying some optimality criterion. A cable tension vector is feasible when all its components are contained between minimal and maximal tension values t_{min} and t_{max}. The maximum t_{max} is notably given by the maximal admissible cable strain whereas t_{min} is usually set as the lowest acceptable tension with the goal of avoiding slack cables ($t_{min} \geq 0$).

Several methods have been proposed, mainly for fully constrained CDPR, in order to find (optimal) feasible tension distributions among the infinite number of possible ones. Fang et al. [4] put forward an optimal tension distribution algorithm that uses a 1-norm linear programming method (LPM) for configuration with one degree of redundancy (DOR), i.e. in the case $m = n + 1$ where m and n are the number of cables and of DOF, respectively. LPM was also used to solve higher DOR in [2, 10]. However, LPM does not guarantee the continuity along a given trajectory which may result in high mechanical loads and vibrations. To avoid them, quadratic programming methods (QPM) may be used [3, 5] but they are suffering from non-predictable worst-case runtime as specified in [3]. For suspended CDPR, Oh and Agrawal [8] proposed to plan the robot trajectory to stay into the feasible tension space by describing this latter as a set of linear inequalities. Yu et al. [11] applied QPM for the control of suspended CDPR with redundant cables, coupling basic tension optimization problem to an active stiffness control scheme.

Nevertheless, all these methods are using optimization procedures, which are most of the time expensive in terms of computation time and against real-time control constraints because of their iterative nature. Consequently, for real-time control needs, a deterministic non-iterative method is highly preferable. Mikelsons et al. [7] proposed such a method in which the barycenter of the *polytope of feasible tension distributions* is determined. To deal with the case of redundant under-constrained CDPR (crane-like configuration), the method proposed in [7] has the additional interest of providing a tension vector contained within the polytope of feasible tension distributions "far" from the polytope boundaries. However, this method requires the computation of all the vertices of this polytope which takes a lot of time if a brute force method, such as the one proposed in [7], is used.

The contribution of this paper is a fast algorithm aiming at a real-time implementation of the barycentric approach proposed in [7]. The proposed algorithm is dedicated to CDPR with two DOR, i.e., actuated by $m = n+2$ cables. Indeed, it takes advantage of the two-dimensional nature of the corresponding polytope of feasible tension distributions which is in fact a convex polygon. The idea consists essentially

in computing a first vertex of this polygon and, then, in finding the others by "moving" from one vertex to the next one while following the polygon one-dimensional boundary which is made of straight line segments. Once all the polygon vertices are determined, the barycenter (centroid) is simply obtained by well-known closed-form formulas. Therefore, in the case of CDPR with two DOR, this paper complements [7] by providing an efficient means of implementing the tension distribution strategy proposed therein.

This paper is organized as follows. Section 2 details the proposed real-time capable algorithm. A brief description of our prototype is given in Sect. 3. Some preliminary simulation results are reported in Sect. 4. Finally, conclusions and future works are addressed in the last section.

2 A Fast Tension Distribution Algorithm

2.1 Mikelsons' Barycenter Approach

The wrench $\mathbf{f}$ applied by the cables on the mobile platform is given by [9]

$$\mathbf{Wt} = \mathbf{f} \tag{1}$$

where $\mathbf{W}$ is the wrench matrix and $\mathbf{t} = [t_1, ..., t_m]^T \in \mathbb{R}^m$ is the cable tension vector. The challenge lies in the cable inability to transmit compressive forces, which means that $\mathbf{t}$ has to remain non-negative. This paper deals with n-DOF CDPR driven by $m = n + 2$ cables, i.e., with $r = 2$ DOR. Consequently, the $n \times m$ wrench matrix $\mathbf{W}$ is non-square and, assuming that $\mathbf{W}$ has full rank, (1) is equivalent to

$$\mathbf{t} = \mathbf{W}^+ \mathbf{f} + \mathbf{N}\boldsymbol{\lambda} = \mathbf{t}_p + \mathbf{t}_n \tag{2}$$

where $\mathbf{W}^+$ is the Moore-Penrose pseudo-inverse of the wrench matrix, $\mathbf{N} = null(\mathbf{W})$ $= [\mathbf{k}_1 \ \mathbf{k}_2]$ is a full rank $m \times 2$ matrix and $\boldsymbol{\lambda} = [\lambda_1 \ \lambda_2]^T$ is an arbitrary 2-dimensional vector. The two columns of $\mathbf{N}$ form a basis of the nullspace of $\mathbf{W}$. $\mathbf{t}_p$ is the particular minimum-norm solution of (1) and $\mathbf{t}_n$ is the homogeneous solution that maps λ to the nullspace of $\mathbf{W}$.

Let us define $\Sigma \subset \mathbb{R}^m$ the r-dimensional affine space ($r = 2$ in this paper) of the solutions to (1)

$$\Sigma = \{\mathbf{t} \mid \mathbf{Wt} = \mathbf{f}\} \tag{3}$$

whose points are given by (2). Let us also define $\Omega \in \mathbb{R}^m$ as the m-dimensional hypercube of feasible cable tensions

$$\Omega = \{\mathbf{t} \mid t_i \epsilon \, [t_{\min}, t_{\max}], \ 1 \le i \le m\} \tag{4}$$
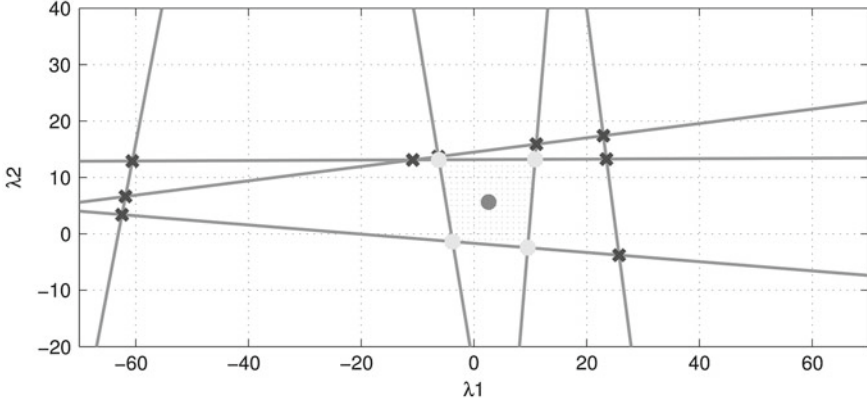
Fig. 1 Preimage of Λ in the plane (λ_1, λ_2) for the pose $[0.9 \quad 1.2 \quad 1 \quad 10 \quad 10 \quad 20]^T$ (units: meters and degrees) with a 6.34 kg total mass (XYZ Euler angle convention)

where we assume that the $t_{\min}$ and $t_{\max}$ limiting tension values are the same for the m cables. The intersection $\Lambda = \Omega \cap \Sigma$ of the hypercube Ω and the affine space Σ is a convex polytope [12]. This *feasible tension distribution polytope* Λ represents the set of tension solutions $\mathbf{t}$ to (1) satisfying the inequalities $t_{\min} \leq t_i \leq t_{\max}$. The preimage of Λ under the affine mapping $(\mathbf{N}, \mathbf{t}_p)$ is also a convex polytope which, according to (2), is defined by the following set of $2m$ linear inequalities

$$\mathbf{t}_{\min} - \mathbf{t}_p \leq \mathbf{N}\boldsymbol{\lambda} \leq \mathbf{t}_{\max} - \mathbf{t}_p \tag{5}$$

In this paper, since $r = 2$, the feasible tension distribution convex polytope Λ is two-dimensional and its preimage under the affine mapping $(\mathbf{N}, \mathbf{t}_p)$ is thus a convex polygon.

For example, Fig. 1 shows the preimage of Λ obtained for a static equilibrium pose of the mobile platform of ReelAx8, a CDPR prototype briefly described in Sect. 3. In (5), each of the $2m$ inequalities defines an halfplane. Each of the $2m$ lines bounding these halfplanes corresponds to values of $\boldsymbol{\lambda}$ for which one of the cable tension is equal to $t_{\min}$ or to $t_{\max}$. Figure 1 shows some of these lines together with the preimage of Λ.

In order to select a "safe" tension distribution, i.e. one which is far from the boundaries of the polytope Λ, Mikelsons et al. [7] proposed to find Λ barycenter. Their method consists essentially in computing all the vertices of the preimage of Λ. To this end, all the 2×2 subsystems of linear equations obtained by selecting two of the $2m$ inequalities of (5) are solved. A solution $\boldsymbol{\lambda}$ of one of these systems is a vertex if it verifies (5). Once all the vertices of the preimage of Λ are known, in [7], its barycenter $\boldsymbol{\lambda}_c$ is determined by means of a triangulation. Finally, the barycenter of Λ is calculated as the image of $\boldsymbol{\lambda}_c$ under the affine mapping $(\mathbf{N}, \mathbf{t}_p)$, i.e., as $\mathbf{t}_p + \mathbf{N}\boldsymbol{\lambda}_c$.

The computational burden of the method presented in [7] is thus mainly determined by the number of non-singular 2×2 subsystems of linear equations drawn from (5). In the case $n = 6$ and $m = 8$, there are $C_{16}^2 = 120$ such subsystems. But, as noted in [2], since each line of (5) defines two halfplanes bounded by two parallel lines, the number of non-singular ones is equal to $C_{16}^2 - 8 = 112$.

The method of Mikelsons et al. provides a continuous tension distribution with a predictable worst-case runtime. However, because of the high number of linear systems that must be solved, the computation time is too high to fit our real-time controller loop time so that we were not able to implement it on our prototype ReelAx8. Besides, to the best of our knowledge, no real-time implementation of this method has been reported.

The present paper proposes a strong decrease of the computational time of this method by finding a first vertex of the convex polytope Λ and then moving along the polytope hull in order to determine the other vertices. An efficient implementation of this idea is discussed in Sect. 2.2. It is dedicated to CDPR with 2 DOR as it requires the feasible tension distribution convex polytope to be two dimensional. Simulation results show that the proposed improvement provides a real-time compatibility.

2.2 Detailed Description of the Proposed Algorithm

2.2.1 Initialization

Let us consider the intersection point, represented by the two-dimensional column vector λ_{ij}, between two lines L_{i_b} and $L_{j_b}, \{i, j\} \in \{1, \ldots, m\}, i \neq j$. L_{i_b} and L_{j_b} are obtained by taking two inequalities among the $2m$ of (5) and replacing the inequality signs by equalities. These two lines are thus defined by the following equations

$$\begin{cases} b_i - t_{p_i} = \mathbf{n}_i \lambda_{ij} \\ b_j - t_{p_j} = \mathbf{n}_j \lambda_{ij} \end{cases} \tag{6}$$

where each one of b_i and b_j is equal either to $t_{\min}$ or to $t_{\max}$ depending on which inequalities are being considered. The two-dimensional line vectors $\mathbf{n}_i$ and $\mathbf{n}_j$ denote the lines i and j of $\mathbf{N}$, respectively. Examples of such L_{i_b} and L_{j_b} lines and intersection points λ_{ij} can be seen in Fig. 1. Furthermore, λ_{ij} is a vertex $\mathbf{v}_{ij}$ of the preimage of Λ if

$$\mathbf{t}_{\min} - \mathbf{t}_p \leq \mathbf{N}\lambda_{ij} \leq \mathbf{t}_{\max} - \mathbf{t}_p \tag{7}$$

which means that λ_{ij} is included into Ω. The algorithm proposed in this paper consists in first finding a vertex $\mathbf{v}_{init}$ of the preimage of Λ, which is a convex polygon, and, then, in *moving* along one of the two lines L_{i_b} or L_{j_b} intersecting at $\mathbf{v}_{init}$ until a new vertex of the polygon is reached. This process continues until it reaches the polygon

vertex which belongs to the other line intersecting at $\mathbf{v}_{init}$, i.e, when all the vertices
of the convex polygon have been found.

The first step is thus the calculation of the first vertex $\mathbf{v}_{init}$. To this end, we are
looking for an intersection point λ_{ij} which satisfies the following requirements

$$\begin{cases} b_i - t_{p_i} = \mathbf{n}_i \lambda_{ij} \\ b_j - t_{p_j} = \mathbf{n}_j \lambda_{ij} \\ \mathbf{t}_{\min} - \mathbf{t}_p \leq \mathbf{N}\lambda_{ij} \leq \mathbf{t}_{\max} - \mathbf{t}_p \end{cases} \tag{8}$$

By taking a couple i and j of cables among the C_m^2 available and taking $t_{\min}$ or $t_{\max}$
as the value of b_i and of b_j, the two equalities of (8) are solved (if the corresponding
linear system is not singular), and the resulting vector λ_{ij} is the searched $\mathbf{v}_{init}$ vertex
if the two inequalities of the last line of (8) are verified. From a general point of view,
it may be necessary to consider many couples i and j of cables and combinations of
$t_{\min}$ and $t_{\max}$ values before such a first vertex of the polygon can be found. However, in
practice, let us note that the computation of the first vertex $\mathbf{v}_{init}$ should generally not
be an issue since the first point of a trajectory is generally a known (static equilibrium)
mobile platform pose at which the preimage of Λ is already determined. Indeed, this
first pose is typically either the home starting pose of the CDPR for which all the
computations can be done offline and once and for all, or else the end point of a
previous trajectory for which the preimage of Λ has been calculated previously. For
any other point of the trajectory at hand, since the preimage of Λ evolves continuously
in time, the first vertex $\mathbf{v}_{init}$ is easily obtained from the first vertex or any of the other
vertices of preimage of Λ associated with the previous point of the trajectory.

2.2.2 From One Vertex to the Next One

Once the first vertex $\mathbf{v}_{init}$ is known, the second step consists in moving along one of
the two lines L_{i_b} or L_{j_b} intersecting at $\mathbf{v}_{init}$ until a new vertex $\mathbf{v}$ of the convex polygon
(preimage of Λ) is found. Let us arbitrarily choose L_{i_b}. The points $\mathbf{p}$ belonging to
this line are given by

$$\mathbf{p} = \mathbf{v}_{init} + \alpha \mathbf{n}_{i_\perp}^T \tag{9}$$

where α is a scalar and $\mathbf{n}_i \cdot \mathbf{n}_{i_\perp}^T = 0$, i.e., the line vector $\mathbf{n}_{i_\perp}$ is orthogonal to $\mathbf{n}_i$ and
thus defines the direction of the line L_{i_b}. With $\mathbf{n}_i = [a \ b]$, there exists two possible
vectors $\mathbf{n}_{i_\perp}$ which are $\mathbf{n}_{i_{\perp 1}} = [b \ -a]$ and $\mathbf{n}_{i_{\perp 2}} = [-b \ a]$. Care must be taken in
the choice between these two possible vectors. Indeed, the goal is to move along
the boundary of the convex polygon and not to follow L_{i_b} while moving away from
the polygon. Let us decide that $\alpha \geq 0$ in (9) so that $\mathbf{n}_{i_\perp}$ must be directed toward the
interior of the polygon in order to move along the polygon boundary. Two cases have
to be distinguished.

- Case 1: $b_j = t_{\min}$. In this case, moving along line L_{i_b} from its intersection point with line L_{j_b} while staying on the polygon boundary requires

$$t_{\min} - t_{p_j} \leq \mathbf{n}_j \mathbf{p} \Leftrightarrow t_{\min} - t_{p_j} \leq \mathbf{n}_j \mathbf{v}_{init} + \alpha \mathbf{n}_j \mathbf{n}_{i_\perp}^T$$
$$\Leftrightarrow \qquad \mathbf{n}_j \mathbf{n}_{i_\perp}^T \geq 0 \tag{10}$$

The last equivalence is true because $\alpha \geq 0$ and also because, $\mathbf{v}_{init}$ lying on line L_{j_b}, we have $t_{\min} - t_{p_j} = \mathbf{n}_j \mathbf{v}_{init}$. Therefore, among the two possible vectors $\mathbf{n}_{i_\perp}$, the good choice in order to stay on the polygon boundary is the one such that $\mathbf{n}_j \mathbf{n}_{i_\perp}^T \geq 0$.

- Case 2: $b_j = t_{\max}$. In this second case, moving along line L_{i_b} from its intersection point with line L_{j_b} while staying on the polygon boundary requires

$$\mathbf{n}_j \mathbf{p} \leq t_{\max} - t_{p_j} \Leftrightarrow \mathbf{n}_j \mathbf{v}_{init} + \alpha \mathbf{n}_j \mathbf{n}_{i_\perp}^T \leq t_{\max} - t_{p_j}$$
$$\Leftrightarrow \qquad \mathbf{n}_j \mathbf{n}_{i_\perp}^T \leq 0 \tag{11}$$

since $\alpha \geq 0$ and $\mathbf{n}_j \mathbf{v}_{init} = t_{\max} - t_{p_j}$. This time, among the two possible vectors $\mathbf{n}_{i_\perp}$, the good choice is the one such that $\mathbf{n}_j \mathbf{n}_{i_\perp}^T \leq 0$.

Now that we know along which direction to move along line L_{i_b} in order to follow the polygon boundary from vertex $\mathbf{v}_{init}$, we aim at finding the other polygon vertex $\mathbf{v}$ belonging to L_{i_b}. In fact, this other vertex is the point $\mathbf{p}$ in (9) corresponding to the maximal value of $\alpha \geq 0$ such that all the inequalities of (5) are verified. Equivalently, this maximal value is equal to the smallest $\alpha \geq 0$ such that one of the inequalities of (5) apart from inequalities i and j becomes an equality. Therefore, let us consider line k of (5), $k \in \{1, \ldots, m\} \setminus \{i, j\}$, and let us substitute λ by the point $\mathbf{p}$ of L_{i_b} given by (9), i.e.

$$\begin{cases} t_{\min} - t_{p_k} \leq \mathbf{n}_k \mathbf{p} \leq t_{\max} - t_{p_k} \\ \mathbf{p} = \mathbf{v}_{init} + \alpha \mathbf{n}_{i_\perp}^T \end{cases} \tag{12}$$

which is equivalent to

$$t_{\min} - t_{p_k} \leq \mathbf{n}_k \mathbf{v}_{init} + \alpha \mathbf{n}_k \mathbf{n}_{i_\perp}^T \leq t_{\max} - t_{p_k} \tag{13}$$

Let us assume that none of the two L_{k_b} lines, the two lines bounding the halfplanes defined by the two inequalities of line k of (5), crosses line L_{i_b} at $\mathbf{v}_{init}$. This amounts to assuming that

$$t_{\min} - t_{p_k} < \mathbf{n}_k \mathbf{v}_{init} < t_{\max} - t_{p_k} \tag{14}$$

The particular case in which three lines are crossing at the same point (here lines L_{i_b}, L_{j_b} and L_{k_b} crossing at the current vertex) is addressed in Sect. 2.3.

Now, let us consider (13) and (14).

- If $\mathbf{n}_k\mathbf{n}_{i_\perp}^T = 0$ then $\forall\alpha \geq 0$ the inequalities of the system (12) cannot become equalities (which means that L_{i_b} is parallel to the two L_{k_b} lines).
- If $\mathbf{n}_k\mathbf{n}_{i_\perp}^T > 0$ then $\forall\alpha \geq 0$,

$$\mathbf{n}_k\mathbf{v}_{init} + \alpha\mathbf{n}_k\mathbf{n}_{i_\perp}^T \geq \mathbf{n}_k\mathbf{v}_{init} > t_{\min} - t_{p_k} \tag{15}$$

Consequently, (13) could only become an equality by its right side when $\alpha \geq 0$, i.e., $\mathbf{n}_k\mathbf{v}_{init} + \alpha\mathbf{n}_k\mathbf{n}_{i_\perp}^T = t_{\max} - t_{p_k}$, which is satisfied by the following value of $\alpha \geq 0$

$$\alpha_k = \frac{t_{\max} - t_{p_k} - \mathbf{n}_k\mathbf{v}_{init}}{\mathbf{n}_k\mathbf{n}_{i_\perp}^T} \tag{16}$$

- If $\mathbf{n}_k\mathbf{n}_{i_\perp}^T < 0$ then $\forall\alpha \geq 0$,

$$\mathbf{n}_k\mathbf{v}_{init} + \alpha\mathbf{n}_k\mathbf{n}_{i_\perp}^T \leq \mathbf{n}_k\mathbf{v}_{init} < t_{\max} - t_{p_k} \tag{17}$$

Consequently, (13) could only become an equality by its left side when $\alpha \geq 0$, i.e., $\mathbf{n}_k\mathbf{v}_{init} + \alpha\mathbf{n}_k\mathbf{n}_{i_\perp}^T = t_{\min} - t_{p_k}$, which is satisfied by

$$\alpha_k = \frac{t_{\min} - t_{p_k} - \mathbf{n}_k\mathbf{v}_{init}}{\mathbf{n}_k\mathbf{n}_{i_\perp}^T} \tag{18}$$

As a consequence, the sign $s_k = Sign(\mathbf{n}_k\mathbf{n}_{i_\perp}^T)$ indicates which side of inequality (13) can become an equality for $\alpha \geq 0$. Moreover, since $\mathbf{v}_{init}$ is the intersection of lines L_{i_b} and L_{j_b}, the line L_{k_b} must be found for k belonging to the index set $\{1,\ldots,m\}\setminus\{i,j\}$ that leaves $2(m-2)$ possibilities (two possible line equations per line of (5)). By computing s_k, the previous analysis allows us to reduce this number to $m-2$ possibilities.

In order to find the next vertex of the polygon, i.e., the second polygon vertex belonging to L_{i_b}, the m α_k are thus computed by means of (16) or (18) and the one, denoted α_v, which will determine the next vertex is the smallest, that is

$$\alpha_v = \min_{k,\mathbf{n}_k\mathbf{n}_{i_\perp}^T \neq 0}\left(\frac{b_k - t_{p_k} - \mathbf{n}_k\mathbf{v}_{init}}{\mathbf{n}_k\mathbf{n}_{i_\perp}^T}\right) \tag{19}$$

where $b_k = t_{\min}$ or $t_{\max}$ despite of the value of s_k. The next vertex $\mathbf{v}$ is thus given by

$$\mathbf{v} = \mathbf{v}_{init} + \alpha_v\mathbf{n}_{i_\perp}^T \tag{20}$$

and the line L_{l_b} which crosses L_{i_b} at $\mathbf{v}$ while supporting the polygon along one of its edge is the set of point $\mathbf{p}$ verifying $b_l - t_{p_l} = \mathbf{n}_l\mathbf{p}$ where $b_l = t_{\max}$ if $\mathbf{n}_l\mathbf{n}_{i_\perp}^T > 0$ and $b_l = t_{\min}$ if $\mathbf{n}_l\mathbf{n}_{i_\perp}^T < 0$ and

$$l = \operatorname*{argmin}_{k, \mathbf{n}_k \mathbf{n}_{i_\perp}^T \neq 0} \left(\frac{b_k - t_{p_k} - \mathbf{n}_k \mathbf{v}_{init}}{\mathbf{n}_k \mathbf{n}_{i_\perp}^T} \right) \tag{21}$$

Starting from this newly found polygon vertex $\mathbf{v}$, which is the intersection point between L_{i_b} and L_{l_b}, and moving along line L_{l_b} (in the appropriate direction), the next polygon vertex is found in exactly the same way as vertex $\mathbf{v}$ has been found. This process continues until the newly found vertex lies on the same line as $\mathbf{v}_{init}$ (L_{j_b} in our example), at which point the research stops since all the vertices of the convex polygon, preimage of Λ, have been determined.

2.2.3 The Barycenter Calculation

The final step is the calculation of the barycenter $\mathbf{v}_c$ of the preimage of Λ whose q vertices $\mathbf{v}_p = [v_{p_1} \ v_{p_2}]^T$, $p \in \{1, \dots, q\}$ have just all been determined. The preimage of Λ is a convex polygon which is not self-intersecting. Therefore, its centroid $\mathbf{v}_c = [v_{c_1} \ v_{c_2}]^T$ is given by the following well-known formulas

$$\begin{cases} v_{c_1} = \frac{1}{6A} \sum_{p=0}^{q-1} (v_{p_1} + v_{(p+1)_1})(v_{p_1} v_{(p+1)_2} - v_{(p+1)_1} v_{p_2}) \\ v_{c_2} = \frac{1}{6A} \sum_{p=0}^{q-1} (v_{p_2} + v_{(p+1)_2})(v_{p_1} v_{(p+1)_2} - v_{(p+1)_1} v_{p_2}) \end{cases} \tag{22}$$

where A is the area of the polygon given by

$$A = \frac{1}{2} \sum_{p=0}^{q-1} (v_{p_1} v_{(p+1)_2} - v_{(p+1)_1} v_{p_2}) \tag{23}$$

Finally, the polygon barycenter $\mathbf{v}_c$ is mapped into $\mathbb{R}^m$ in order to find $\mathbf{t}_c = \mathbf{t}_p + \mathbf{N}\mathbf{v}_c$, the barycenter of Λ which is the desired feasible cable tension distribution.

As an example, Fig. 1 shows $\mathbf{v}_c$ as the dark dot into the polygon. The points indicated with crosses correspond to some intersection points between lines bounding the halfplanes defined in (5). The four clear dots are the vertices of the preimage of Λ.

2.3 Case of Three (Ore More) Concurrent Lines

In the algorithm proposed in Sect. 2.2, let us assume that we have to move from a vertex $\mathbf{v}_{ij}$ to the next one $\mathbf{v}_{jk}$ along line j. In order to compute $\mathbf{v}_{jk}$, the algorithm calculates $m - 2$ values of α as given by (16) or (18) and retains the minimal one. If this minimal value of α is obtained for two indices k and l [i.e., both k and l

Fig. 2 Illustration of the case
of *three concurrent lines*
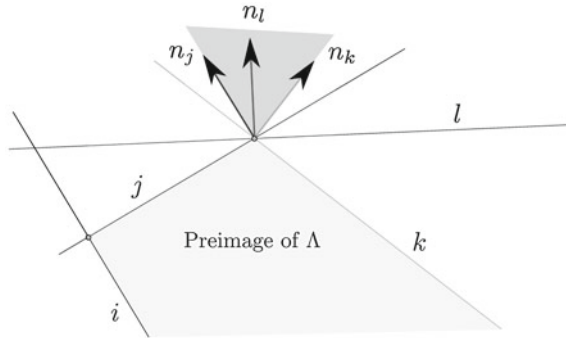
verify (21)], it means that the vertex $\mathbf{v}_{jk}$ is the intersection of three concurrent lines
(here, lines j, k and l). This particular case is illustrated in Fig. 2. In such a case,
the determination of the vertex $\mathbf{v}_{jk}$ is not a problem but care must be taken in the
determination of the next line that will be followed in order to find a new polygon
vertex. Indeed, this next line has to support the polygon along one of its edges and
not only at $\mathbf{v}_{jk}$. As illustrated in Fig. 2, moving from $\mathbf{v}_{jk}$ along line l instead of line k
is a bad choice as we then leave the polygon boundary. Consequently, the algorithm
must be able to select the edge supporting line which is either line k or else line l.
As along a trajectory new polygon vertices are generally coming with this particular
case, it should be addressed in order to ensure robustness of the algorithm.

In order to select the appropriate edge supporting line, a simple geometric analysis
can be used. Vector $\mathbf{n}_j$ is normal to line j and chosen to be directed outward of the
polygon. In our current implementation of the algorithm detailed in Sect. 2.2, as
soon as two equal α are calculated, say α_k and α_l, the vectors $\mathbf{n}_k$ and $\mathbf{n}_l$ are drawn
from lines k and l of $\mathbf{N}$ and chosen to be directed outward of the polygon. Then, we
check if $\mathbf{n}_l$ is included in the cone spanned by $\mathbf{n}_j$ and $\mathbf{n}_k$ as shown in Fig. 2. If $\mathbf{n}_l$
is strictly included inside this cone, line l supports the polygon at a vertex only. It
is thus discarded and line k is selected as the next line to follow since it is an edge
supporting line of the polygon. This is the case illustrated in Fig. 2. Otherwise, when
$\mathbf{n}_l$ is not included inside the cone spanned by $\mathbf{n}_j$ and $\mathbf{n}_k$, line l supports the polygon
along one of its edge and it will be the next line followed in the quest of a new vertex.
Note that in the very particular case in which $\mathbf{n}_l$ and $\mathbf{n}_k$ are collinear, any of the two
lines k or l can be followed.

Finally, in the cases in which more than three lines, say $h > 3$ lines, are all concur-
rent at the same vertex of the polygon, the determination of the edge supporting line
to be followed during the next algorithm step can be done by sequentially considering
sets of three lines among the h concurrent ones and, for each such set, discarding
one of the three lines as explained in the previous paragraph.
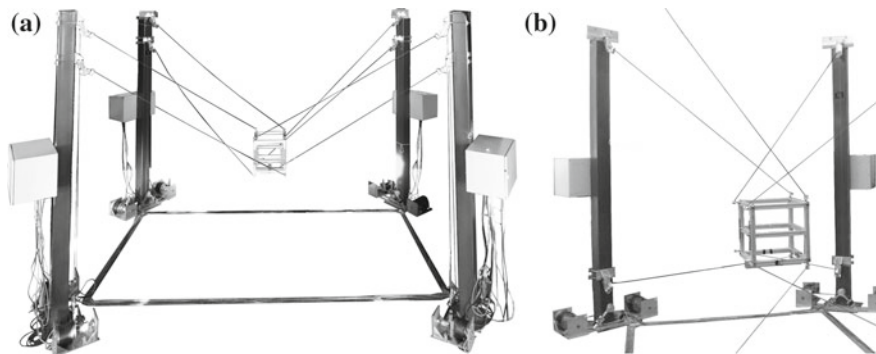
Fig. 3 The prototype ReelAx8 in suspended under constrained (**a**) and fully constrained (**b**) configurations

Fig. 4 Suspended ReelAx8 basic PID-control scheme
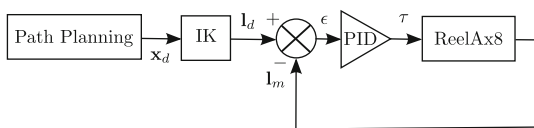
3 ReelAx8 Prototype

The prototype ReelAx8 has 6-DOF and is driven by 8 cables so that it is *redundantly actuated* with two 2 extra cables (2 DOR). These two extra cables significantly improve the ratio between the workspace and the whole robot footprint. The workspace is defined as the set of feasible static equilibrium mobile platform poses. A pose is said to be feasible when there exists a set of non-negative cable tensions satisfying the platform equilibrium and when there are no cable interferences. Two different configurations have been experimented: suspended and fully constrained, shown in Fig. 3a and b, respectively.

Let us note that redundantly actuated suspended (under constrained) CDPR have rarely been studied [8, 11]. However, this configuration may be required in some situations as all the cable drawing points are located above the workspace. Consequently, the space located below the mobile platform is free of cables. Suspended CDPR have thus the potential of operating in presence of human workers and good transits and are suitable for crane-like applications. ReelAx8 is currently set in its suspended configuration shown in Fig. 3a. As we have not yet implemented an effective control scheme able to use tension distribution strategies for this suspended configuration, the next section gives some preliminary simulation results. Therefore, the real-time compatibility has been established by executing on the real-time controller the algorithm proposed in Sect. 2.2 in parallel of the basic articular PID control scheme, shown in Fig. 4, presently in used on ReelAx8.
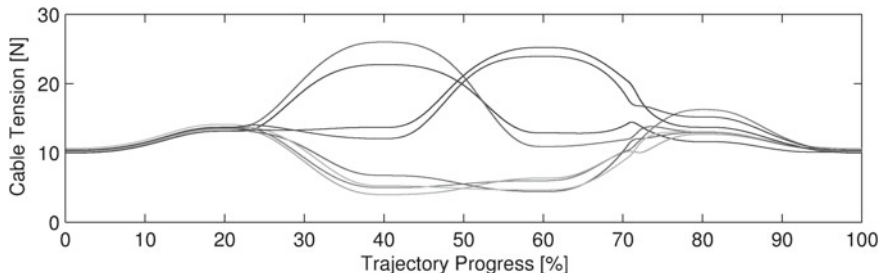
Fig. 5 Cable tensions obtained with the proposed algorithm for ReelAx8 in suspended configuration
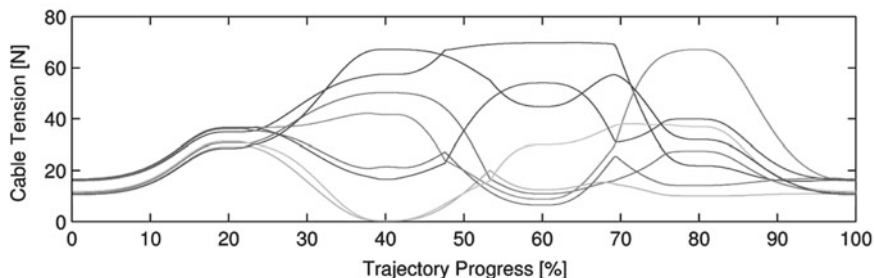
Fig. 6 Cable tensions obtained with the proposed algorithm for ReelAx8 in fully constrained configuration

4 Simulation Results

Figure 5 shows the evolution of the tension into the cables, obtained by means of the algorithm introduced in Sect. 2.2, of the suspended ReelAx8 (Fig. 3a) for a given trajectory of the mobile platform. The trajectory starts at the platform reference pose $[0\ 0\ 0.25\ 0\ 0\ 0]^T$, goes up to $[0.8\ (-0.9)\ 1\ 0\ 0\ 0]^T$, passes through $[0.9\ 0.9\ 1\ 0\ 0\ 0]^T$ and $[0\ 0\ 1\ 0\ 0\ 45]^T$, where a non-zero orientation is accomplished, and finally returns to the reference pose (units are meters and degrees; XYZ Euler angle convention is used to define the platform orientation). Figure 6 shows the evolution of the cable tensions of ReelAx8 in fully constrained configuration (Fig. 3b) along the same trajectory. As observed, all cables are tensed along the whole trajectory and the tension curves are continuous. Let us note that in fully constrained configuration, the choice of the polytope centroid may results in high tension values.

In MATLAB simulations along the same trajectory, the use of the brute force method suggested in [7] which consists in computing all the intersection points between all the lines drawn from (5) results in an average computation runtime of 1.9152 ms against 0.638 ms with our algorithm. This significant improvement should make our algorithm suitable for a future real-time use on ReelAx8.
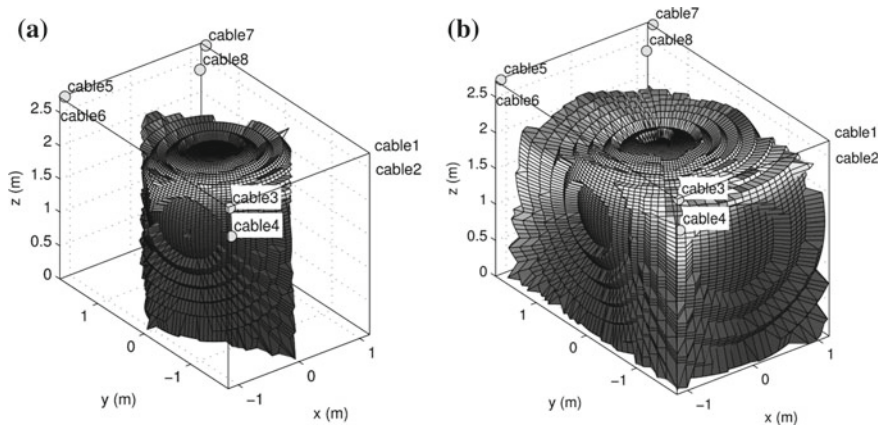
Fig. 7 Workable part of the constant-orientation static workspace of ReelAx8 without and with a tension distribution algorithm. **a** Without any tension distribution. **b** With the barycenter tension distribution strategy

Furthermore, in order to apply the proposed method experimentally on ReelAx8, the currently used basic control scheme has to be improved. Meanwhile, the algorithm of Sect. 2.2 has been compiled and tested in real-time in parallel of our current control scheme on a target computer using MATLAB/Simulink language. It appeared to be real-time compatible with an average Task Execution Time of 0.156 ms.

Let us note that, compared to the basic PID control of Fig. 4, which outputs negative tension set points in a large part of ReelAx8 workspace, the barycenter tension distribution strategy should increase the practical workspace of ReelAx8 in suspended configuration from 7.58 to 18.9 m³, i.e. 78.18 % of the overall robot occupied volume, as shown in Fig. 7b. These values are obtained for the unloaded platform mass which is of 6.34 kg. The influence of the total mass (loaded platform) on the workspace volume is depicted in Fig. 8. The maximum cable tension considers in this figure is 350 N.

5 Conclusions and Future Works

A real-time capable algorithm for tension distribution of cable-driven parallel robots was presented in this paper. This algorithm efficiently implements the barycenter approach of [7] which leads to safe and continuous cable tension distribution. Simulation results showed that it is faster than a brute force implementation of the barycenter approach. The proposed algorithm is dedicated to n-DOF parallel robots driven by $n + 2$ cables as it takes advantage of the 2-dimensional nature of the polytope of feasible tension distributions.
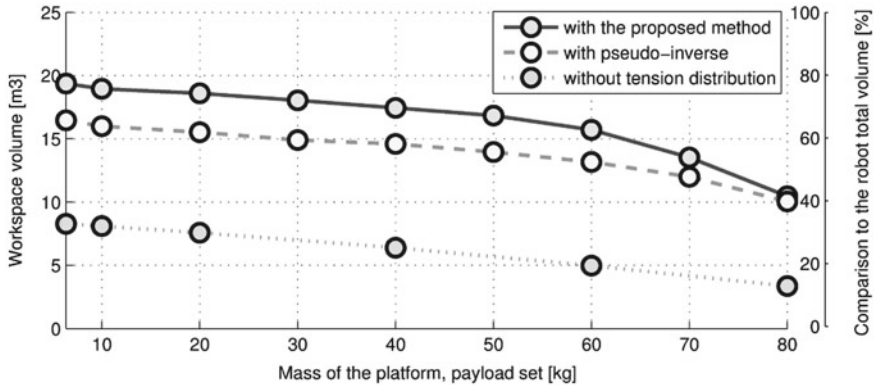
Fig. 8 Influence of the platform and payload total mass on the suspended ReelAx8 workable workspace volume

We believe that the barycenter cable tension distribution approach is appropriate to deal with the case of redundantly actuated suspended (under constrained) cable-driven parallel robots since it provides a tension distribution set point far from the boundaries of the polytope of feasible tension distributions. However, in the case of fully constrained robots, using the centroid of this polytope as the desired cable tension distribution might not be the better choice as it can lead to large cable tensions and consequently limit the robot workspace and leads to high energy consumption.

The proposed algorithm, tested in real-time on our embedded computer in parallel of our current basic control scheme, must now be implemented within a suitable control scheme. The realization of this latter is part of our future works.

References

1. Albus, J., Bostelman, R., Dagalakis, N.: The NIST robocrane. J. Robot. Syst. **10**(2), 709–724 (1993)
2. Borgstrom, P.H., Jordan, B.L., Sukhatme, G.S., Batalin, M.A., Kaiser, W.J.: Rapid computation of optimally safe tension distributions for parallel cable-driven robots. IEEE Trans. Robot. **25**(6), 1271–1281 (2009)
3. Bruckmann, T., Andreas, P., Hiller, M., Franitza, D.: A modular controller for redundantly actuated tendon-based stewart platforms. EuCoMeS, Obergurgl, Austria, In (2006)
4. Fang, S., Franitza, D., Torlo, M., Bekes, F., Hiller, M.: Motion control of a tendon-based parallel manipulator using optimal tension distribution. IEEE/ASME Trans. Mechatron. **9**, 561–568 (2004)
5. Hassan, M., Khajepour, A.: Analysis of bounded cable tensions in cable-actuated parallel manipulators. IEEE Trans. Robot. **27**(5), 891–900 (2011)

6. Kawamura, S., Kino, H., Won, C.: High-speed manipulation by using parallel wire-driven robots. Robotica **18**, 13–21 (2000)
7. Mikelsons, L., Bruckmann, T., Hiller, M., Schramm, D.: A real-time capable force calculation algorithm for redundant tendon-based parallel manipulators. IEEE International Conference on Robotics and Automation, May, In (2008)
8. Oh, S.-R., Agrawal, S.K.: Controllers with positive cable tensions. IEEE International Conference on Robotics and Automation, Cable-Suspended Planar Parallel Robots with Redundant Cables, In (2003)
9. Roberts, R.G., Graham, T., Lippitt, T.: On the inverse kinematics, statics, and fault tolerance of cable-suspended robots. J. Robot. Syst. **15**(10), 581–597 (1998)
10. Vafaei, A., Aref, M.M., Taghirad, H.D.: Integrated controller for an over constrained cable driven parallel manipulator: KNTU CDRPM. In IEEE 2010 International Conference on Robotics and Automation, pp. 650–655. Anchorage, Alaska, USA (2010).
11. Yu, K., Lee, L., Krovi, V.N.: Simultaneous trajectory tracking and stiffness control of cable actuated parallel manipulator. International Design Engineering Technical Conference and Computers and Information in Engineering Conference, In (2009)
12. Ziegler, G.: Letures on Polytopes. Springer, Heidelberg (1994)

Optimal Force Distribution Based on Slack Rope Model in the Incompletely Constrained Cable-Driven Parallel Mechanism of FAST Telescope

Hui Li, Xinyu Zhang, Rui Yao, Jinghai Sun, Gaofeng Pan and Wenbai Zhu

Abstract This paper addressed the determination of the tension distribution in the slack steel wires of the incompletely constrained cable-driven parallel mechanism of FAST telescope. Slack rope hung with piecewise uniform mass is specially investigated. First, the general formulation based on the wrench matrix was derived. Then the analytical model of slack rope was built to give the quantized relation between direction and amplitude of tension vector. The wrench matrix is not only platform pose dependent but influenced by rope geometry. Finally, a performance index based on minimal tension variance is selected to optimize the tension distribution among steel wires. Levenberg-Marquardt method is applied to solve the quadratic program and a discrete-mesh plan is proposed for the whole focal surface. An example of computation is given to verify the effect of the resolution.

1 Introduction

Cable-driven parallel mechanisms have many important applications over the past decade. One is verified in the Five-hundred-meter Aperture Spherical radio Telescope (FAST) which is being built in southwest China [1]. The giant telescope has a relatively light airborne focus cabin carrying the precise expensive feed receivers to observe stars in the sky. Because of its large size, it is very difficult to build a solid support structure between the cabin and the ground. Ropes, however, provide the possibility and further conveniences beyond other means: light weight, very large ranges of motion and little inertia. The cable-driven parallel mechanism used in the FAST telescope might be the largest robot over the world, as shown in Fig. 1. As the mobile platform, the 30-ton focus cabin is supported and driven by 6 parallel steel

H. Li (✉) · X. Zhang · R. Yao · J. Sun · G. Pan · W. Zhu
National Astronomical Observatories, Chinese Academy of Sciences,
20A Datun Road, Chaoyang District, Beijing 100012, China
e-mail: lihui@nao.cas.cn
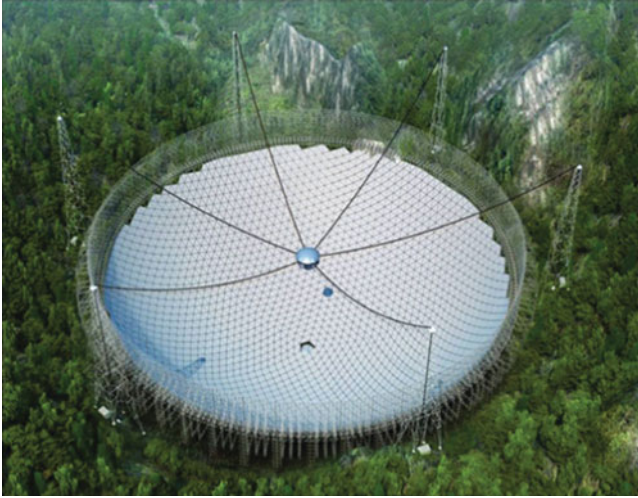
Fig. 1 An overlook of FAST telescope

wires so that it can move in a large calotte, so called focal surface, which is about 206 m in aperture. The 6 steel wires are respectively suspended by 6 steel towers more than 100 m high and equally spaced on a circle of 600 m in diameter. Each is driven by a capstan motor with the common tension force reaching tens of tons.

The FAST cable-driven parallel mechanism is a typical incompletely restrained parallel mechanism (IRPM). The gravity plays as the seventh rope to fully constrain the 6-degree-of-freedom (6-DOF) mobile platform. More details of explanation are given in Sect. 3. Furthermore, electric cables or optical fiber cables are also suspended under each steel wire for the power supply and signal transmission into the cabin, as shown in Fig. 5 [2]. Their lengths are self-adaptive to the 6 steel wires as the cabin drifts within the focal surface. The redundant parts of these power/signal lines therefore have to pile up in middle lines of the steel wires. Obviously in this case the sagging effect should not be neglected for the 6 steel wires. Besides, as the ropes can only exert tension forces, the design of the FAST rope system are quite challenging.

One important issue on cable-driven parallel mechanisms is the determination of workspace, as investigated in quite a few literatures [3–6]. For the FAST cable-driven parallel mechanism, the required workspace is certain as the focal surface. The main problem is then to analyze whether or not the focal surface belongs to the wrench-feasible and controllable workspace. Unfortunately, the former researches seem inapplicable because the analysis of rope sag is rarely involved. On the other hand, the FAST IRPM is often redundantly actuated because of the inability of the ropes to work in compression. For a given wrench on certain position, the rope forces may not have the unique solution. However, large force variance is not acceptable for the rope-driving capstans in that the maximal force is often one of calculation bases in the power layout of electric motors. Thus a reasonable design concept of force
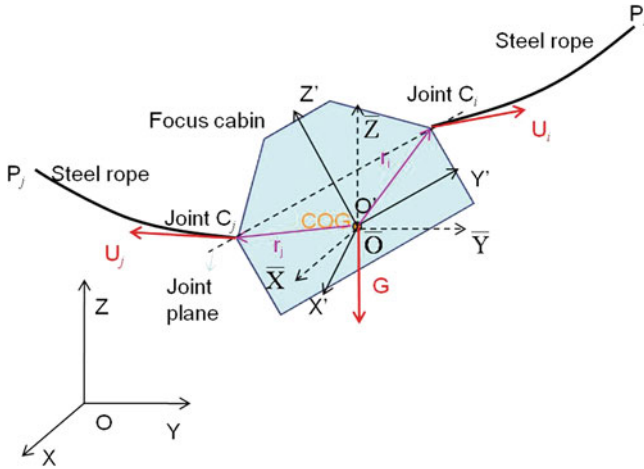
Fig. 2 Mechanism configuration of FAST IRPM

distribution based on slack rope model is not only the key to evaluate workspace but also the way to optimize the energy consumption.

This paper first addresses the modelling of slack rope, trying to construct the mapping relation between rope tension and rope geometry. Based on the results obtained, static equilibrium model is derived for the focus cabin. Then the paper devotes to the optimal force distribution among the 6 ropes of the FAST IRPM. This problem is generally treated in the literature by minimizing the Euclidean norm of the forces in the ropes. Finally the optimal forces are solved in the whole focal surface. As the direct consequence the cabin orientations corresponding to these optimal forces are also analyzed schematically.

2 Mechanism Configuration

2.1 Notation

The kinematic diagram of the FAST IRPM is represented in Fig. 2. The focus cabin is assumed as the moving rigid platform connected to the base by a set of 6 steel wires attached to the platform and to a fixed pulley on which the ropes are wound. By controlling the extension of the ropes, the position and orientation of the platform can be controlled.

Referring to Fig. 2, a fixed reference frame, noted **OXYZ**, is attached to the center of the focal surface and is regarded as the base frame. A moving reference frame, noted **O′X′Y′Z′**, is attached on the focus cabin, where the reference point O is also the center of gravity (COG) to be positioned by the focus cabin. Besides, the
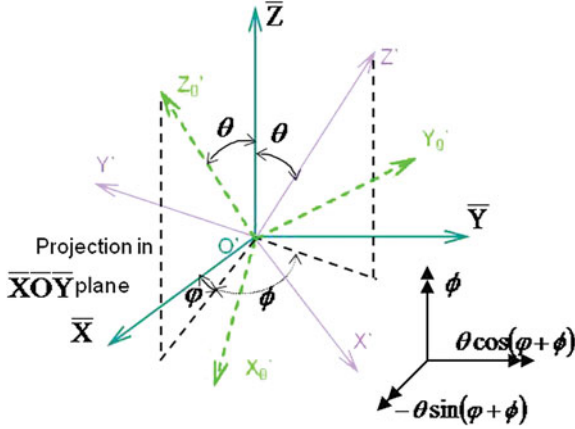
Fig. 3 3D rotations of the cabin frame and orientation angle

reference frame, noted $\overline{\mathbf{OXYZ}}$, is parallel to the base frame, but has the same origin as the frame $\mathbf{O'X'Y'Z'}$. The orientation of the moving frame with respect to the base frame, represented by the rotation matrix $\mathbf{R}$, describes the cabin pose with respect to the base of the mechanism. The joint $C_i (i = 1, 2, \ldots, 6)$ at which the ith steel wire enters the spool, is assumed to be fixed on the focus cabin. Furthermore, another end of the ith steel wire is attached to the point P_i which is assumed to be fixed relative to the base frame. The ith steel wire then connects point C_i with P_i, both of which are modeled as spherical joints. Then the vector $\mathbf{r}_i$ is defined as the radial vector connecting the origin O' to the joint C_i. The unit vector $\mathbf{U}_i$ represents the tension direction of the ith steel wire acting on the joint C_i. As the rope curve is not necessarily straight, $\mathbf{U}_i$ is parallel to its tangential direction. Finally the vector $\mathbf{G}$ represents the gravity of the focus cabin, always vertically acting on its COG.

The rotation matrix $\mathbf{R}$ includes the information of 3 independent orientation angles defined as shown in Fig. 3. Here angle θ represents the cabin tilt, φ the azimuth angle and ϕ the spin angle. The coordinate frame $\overline{OXYZ}$ first rotates the tilt θ around a horizontal axis perpendicular to the angle φ, which yields the interim frame $O'X_0Y_0Z_0$. Then it rotates the angle ϕ around the axis $\overline{Z}$, which forms the final frame $\mathbf{O'X'Y'Z'}$. The rotation matrix $\mathbf{R}$ can therefore be written as [7]:

$$\mathbf{R} = \begin{bmatrix} S_\varphi S_{\varphi+\phi} + C_\theta C_\varphi C_{\varphi+\phi} & -S_\varphi C_{\varphi+\phi} + C_\theta S_{\varphi+\phi} C_\varphi & -S_\theta C_\varphi \\ S_\varphi C_{\varphi+\phi} C_\theta - S_{\varphi+\phi} C_\varphi & C_\theta S_{\varphi+\phi} S_\varphi + C_\varphi C_{\varphi+\phi} & -S_\theta S_\varphi \\ S_\theta C_{\varphi+\phi} & S_\theta C_{\varphi+\phi} & C_\theta \end{bmatrix}^{\mathrm{T}}, \quad (1)$$

where the symbol C represents the cosine function and S the sine function.

2.2 Wrench Matrix

When tension is maintained in all ropes, the ith rope exerts a pure force at point C_i on the mobile platform. The latter force can be written as $t_i U_i$, where t_i is the tension in the ith rope. By definition, t_i is always nonnegative. This pure force generates a moment $\mathbf{r}_i \times t_i U_i$ at the COG of the mobile platform and the wrench (force/moment pair) applied at C_i by the ith rope is therefore $t_i W_i$, with wrench W_i defined as:

$$W_i = \begin{bmatrix} U_i \\ \mathbf{r}_i \times U_i \end{bmatrix}, \tag{2}$$

where W_{COG} denotes the wrench applied at the COG by all 6 ropes of the mechanism and the cabin gravity. Since W_{COG} is the sum of the rope wrenches $t_i W_i$, the relationship between the tension t_i in the ropes and the wrench W_{COG} can be written in matrix form as:

$$W\mathbf{t} = W_{\text{COG}}, \tag{3}$$

with

$$W = [[W_1 \quad W_2 \quad \dots \quad W_6], W_G], \tag{4}$$

and

$$\mathbf{t} = [[t_1 \quad t_2 \quad \dots \quad t_6], t_G]^{\mathrm{T}}, \tag{5}$$

where t is the vector of rope tensions and W the 6×7 wrench matrix. The superscript T means transposition of matrix and the subscript G means the gravity of the focus cabin.

2.3 Modelling of Slack Rope

In the case of the FAST IRPM where rope sag has to be taken into account, the wrench matrix W is not only platform pose dependent but influenced by rope geometry. In the mean time rope geometry is in turn influenced by rope tension. Mathematically this type of mapping relation can be built under the assumption that steel wire should be perfectly flexible, tension-only and unstretchable material.

Referring to Fig. 4, a separate equilibrium analysis is given for the ith suspension rope imposed by homogenous vertical load q along the curve. Here the tension vector $\mathbf{T}_i$ of the ith steel wire has a vertical component V_i and horizontal component H_i respectively. The angle β_i forms between the vector $\mathbf{T}_i$ and the horizontal plane. The rope has a horizontal span of a_i and vertical height of h_i. Let's set the origin of the local coordinate frame on the lower endpoint, the plane XOY parallel to the suspension rope and X axis along the horizontal direction. Then we get the following differential equation:

Fig. 4 Equilibrium of suspension rope under the gravity
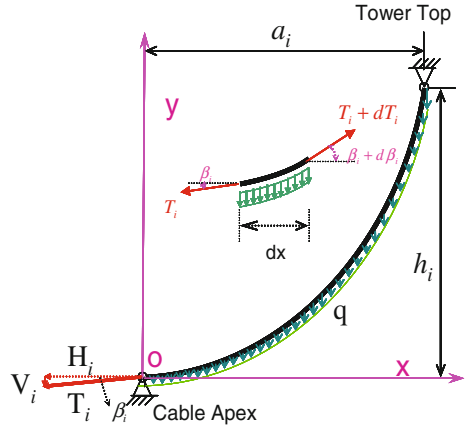
$$y'' = \frac{q}{H_i}\sqrt{1 + (y')^2},\tag{6a}$$

with

$$y(0) = 0 \quad \text{and} \quad y(a_i) = h_i.\tag{6b}$$

Solving it yields the following hyperbolic cosine curve to exactly describe the rope curve:

$$y(x) = \frac{H_i}{q}\cosh\left(\frac{qx}{H_i} + A_i\right) + B_i; \quad (i = 1, 2, \ldots, 6),\tag{7a}$$

where the constants A_i and B_i are expressed as:

$$\begin{cases} A_i = \log\left[\left(\frac{qh_i}{H_i} + \sqrt{\left(\frac{qh_i}{H_i}\right)^2 + 4\sinh^2\left(\frac{qa_i}{2H_i}\right)}\right) \Big/ \left(\exp\left(\frac{qa_i}{H_i}\right) - 1\right)\right] \\ B_i = -H_i\cosh(A_i)/q \end{cases}\tag{7b}$$

Equation (7a) obviously shows that the ith rope curve is only determined by the force H_i once load q is known. Differentiating Eq. (7a) with respect to x at 0 yields a function to describe the variables H_i and β_i as:

$$\tan(\beta_i(H)_i) = y_i'(0) = \sinh(A_i).\tag{8}$$

Here Eq. (8) indicates the relation between the direction of rope tension at the cabin joint and the rope curve.

The case of FAST IRPM, however, is more complicate due to the redundant length of power/signal cables hung on steel wire, as shown in Fig. 5. These cables are fixed on steel wire via equally spaced connectors in the line segment d_1, but can slide in the line segment d_2 and d_3 as they are on mobile trolleys. The length of line segment
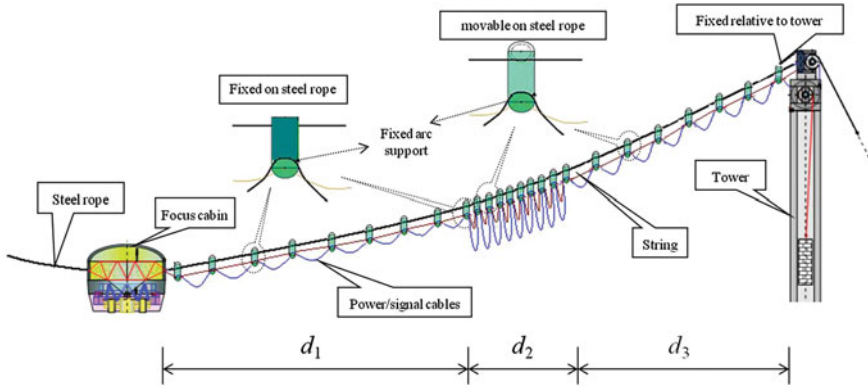
Fig. 5 Power/signal lines hung under steel wire
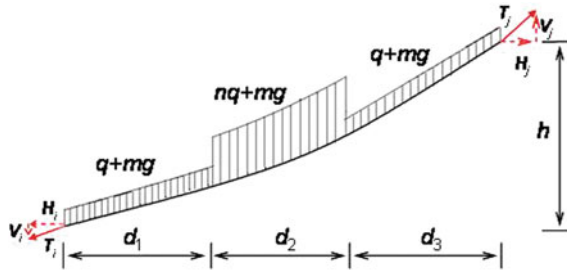
Fig. 6 Analytic sketch of steel wire hung with power/signal cables

d_1 is always never changed given any cabin position in the focal surface. It keeps the redundant cables far away from the cabin in order to avoid collision. There is a minimal and a maximal space between two neighbor trolleys. Once the focus cabin moves in the focal surface so that the rope length reaches its minimum, the mobile trolleys are crowded one by one in the minimal space with d_3 equal to 0. On the contrary once the rope length reaches its maximum, the mobile trolleys arrange in the maximal space with d_2 equal to 0 and the lower hung cables are completely extended, i.e., no accumulation happens.

At analytic convenience the steel wire hung with power/signal cables is simplified as a combination of 3 similar curves, as shown in Fig. 6 [2]. Here the symbol 'mg' represents the linear weight of steel wire, 'q' the linear weight of normally stretched cables, 'n' the ratio of the linear density of accumulated cables to that of normally stretched cables.

Based on the above assumption an approximate length estimation of line segment d_1 comes as follows:

$$\begin{cases} S_{\min} = S_1 + S_T \\ S_{\max} = S_1 + n \cdot S_T \end{cases}. \tag{9a}$$

Here S_1 is the fixed curve length of the segment d_1. $S_{\min}$ and $S_{\max}$ are respectively the minimal and maximal rope lengths wherever the cabin moves in the focal surface. S_T is the sliding length for the mobile cable trolleys. It is only the curve length of the segment d_2 when the total rope length reaches its minimum. Here d_3 varnishes as aforementioned and all redundant power/signal cables are overcrowded on the segment d_2. When the maximum $S_{\max}$ is got, however, the same cables are fully extended and d_2 varnishes. Therefore we get the sliding length of $n \cdot S_T$ at $S_{\max}$. Equation (9a) can be further written as follows:

$$d_1 \approx S_1 \cos(\beta) = \left(\frac{n S_{\min} - S_{\max}}{n - 1} \right) \cos(\beta). \tag{9b}$$

Constructing 3 local coordinate frames with their origins located on the left end of each catenary and their x axes pointing horizontally to the right respectively, we obtain 3 separate curve segments mathematically expressed as the following:

$$y_j(x) = \frac{H}{q_j} \cosh \left(\frac{q_j x}{H} + A_j \right) + B_j \quad (j = 1, 2, 3), \tag{10a}$$

with

$$\begin{cases} A_j = \log \left[\left(\frac{q_j h_j}{H} + \sqrt{\left(\frac{q_j h_j}{H} \right)^2 + 4 \sinh^2 \left(\frac{q_j d_j}{2H} \right)} \right) \Big/ \left(\exp \left(\frac{q_j d_j}{H} \right) - 1 \right) \right]. \\ B_j = -H \cosh(A_j) / q_j \end{cases} \tag{10b}$$

Here the 3 linear weights have the relations such as $q_1 = q_3 = q + mg$ and $q_2 = q + n * mg$. The symbol h_j represents the height of jth curve segment. As the total curve is regarded continuous and differentiable at least in the first order, the following boundary conditions exist:

$$\begin{cases} y_1(d_1) + y_2(d_2) + y_3(d_3) = \sum_{j=1}^{3} \left[\frac{H}{q_j} \cosh \left(\frac{q_j d_j}{H} + A_j \right) + B_j \right] = h \\ y_1'(d_1) = y_2'(0) \Rightarrow \sinh \left(\frac{q_1 d_1}{H} + A_1 \right) = \sinh(A_2) \\ y_2'(d_2) = y_3'(0) \Rightarrow \sinh \left(\frac{q_2 d_2}{H} + A_2 \right) = \sinh(A_3) \end{cases} . \tag{11}$$

Equation (10b) provides the relation between A_i and B_i ($i = 1, 2, 3$) of 3 curves. So the combination of Eqs. (10b) and (11) gives 6 independent equations and 6 independent variables. Substituting the 3 curve equations represented by Eq. (10b) into Eq. (11) and considering the properties of parabolic sine function yield:

$$\begin{cases} \sum_{j=1}^{3} \left[\dfrac{1}{q_j} \cosh\left(\dfrac{q_j d_j}{H} + A_j \right) - \dfrac{1}{q_j} \cosh(A_j) \right] = \dfrac{h}{H} \\[2ex] \dfrac{q_1 d_1}{H} + A_1 = A_2 \\[2ex] \dfrac{q_2 d_2}{H} + A_2 = A_3 \end{cases} . \tag{12}$$

Equation (12) can further change via elimination of A_2 and A_3 as follows:

$$\frac{q_2 - q_1}{q_1 q_2} \cosh\left(\frac{q_1 d_1}{H} + A_1 \right) + \frac{q_3 - q_2}{q_2 q_3} \cosh\left(\frac{q_1 d_1 + q_2 d_2}{H} + A_1 \right)$$

$$+ \frac{1}{q_3} \cosh\left(\frac{q_1 d_1 + q_2 d_2 + q_3 d_3}{H} + A_1 \right) - \frac{1}{q_1} \cosh(A_1) = \frac{h}{H}. \tag{13}$$

Solving Eq. (13) for the constant A_1 and substituting it into Eq. (8) yield a similar function of the angle β where the horizontal component of rope tension H is the only independent variable.

$$\beta(H) = a \tan\left[\sinh(A_1(H))\right]. \tag{14}$$

The tension vector of the ith steel wire at the cabin joint can be written as

$$\mathbf{U}_i = \cos(\beta_i) \left[\cos(\alpha_i) \ \sin(\alpha_i) \ \tan(\beta_i) \right]^{\mathrm{T}}, \tag{15}$$

where the angle α forms between the horizontal projection of steel wire and the X axis of the global coordinate frame. Substituting Eqs. (14) and (15) into Eqs. (2) and (3) shows that the wrench matrix W is the function of the 6 horizontal components of rope tensions.

3 Problem Formulation and Resolution

3.1 Minimization of the Force Variance

In view of static equilibrium, the determination of the tensions in the ropes of the mechanism can be formulated as follows:

For a given external wrench applied on the platform, $-W_{\mathrm{COG}}$, find a vector of positive rope tensions $\mathbf{t}$ and pose vector $[\theta, \varphi, \phi]^{\mathrm{T}}$ that satisfies Eq. (3).

Here for the FAST IRPM, the only completely known external wrench is the gravity-induced W_{G}. The other wrenches are yet dependent on the pose of the platform because unit vector $\mathbf{U}$ may change with joint position as shown in Fig. 2. Obviously there may be infinitely many solutions according to the above problem. Therefore, in order to obtain an optimal unique solution, a performance index is

usually optimized while using the above condition as a constraint. In order to ensure a balance of force distribution among the 6 steel wires, the force variance is selected. Mathematically, the problem can then be formulated as follows:

$$\min_t \Pi = \min_t \left\| \mathbf{t} - \bar{t}\mathbf{I} \right\|_2 = \min_t \left\| \mathbf{t} - \frac{1}{6} \sum_{i=1}^{6} t_i \cdot \mathbf{I} \right\|_2 \tag{16}$$

subject to Eq. (3) and the following inequality constraints

$$t_i \geq 0, \quad i = 1, 2, \ldots, 6. \tag{17}$$

Here the symbol $\mathbf{I}$ represents the 6-dimension vector and $\mathbf{I} = [1, 1, \ldots, 1]^{\mathrm{T}}$.

3.2 Optimization of Quadratic Program

Mathematically, the above optimization problem is known as quadratic programming due to the quadratic nature of the performance index. The unknowns to be optimized are the 6 rope tensions (H_i, $i = 1, 2, \ldots, 6$) and the rotation matrix R represented by 3 orientation angles, namely. An efficient iterative algorithm called Levenberg-Marquardt method [8, 9] is applied for the resolution of this 9-variable quadratic program. A resolution plan is shown in Fig. 7.

The resolution of this quadratic program can be applied repeatedly to an arbitrary point of the focal surface. An effective discretization mesh is shown in Fig. 8. Due to the symmetry of FAST IRPM, only one sixth of the focal surface is considered. All the triangle vertexes of the mesh are the points where the resolution is done. These points begin from the center of the focal surface and arrange at equal space along several latitudinal lines. The resolution process repeats independently at each position point until all are finished.

However, as the constraints represented by Eq. (3) are actually nonlinear in the case of FAST IRPM, it should be careful in selecting the initial value for the iterative computations. An effective proposal is to begin the resolution from the center of mesh where the cabin has the simplest horizontal orientation and the 6 rope forces are set equal. Then the next point extends outward one by one along latitudinal line and the solution of the former point is set as the initial value of the next.
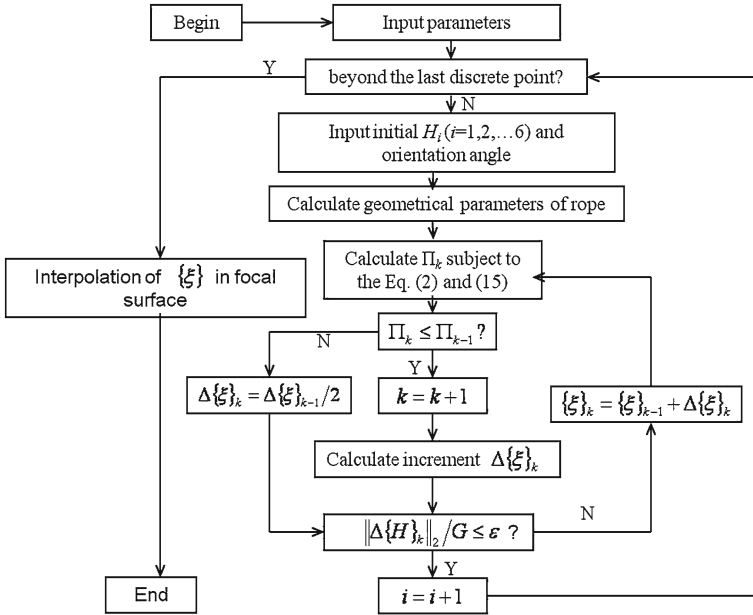
Fig. 7 Block diagram of the optimization program
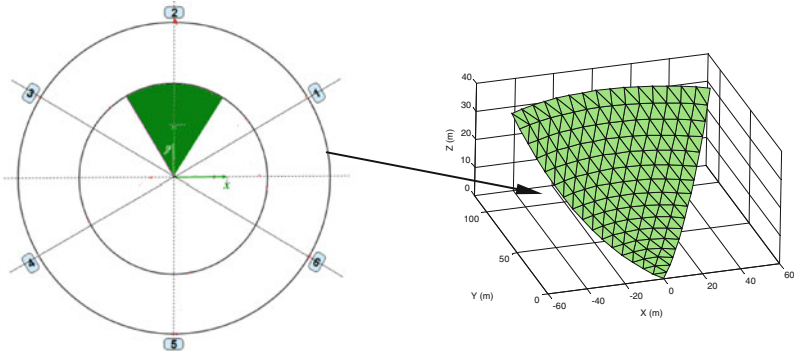
Fig. 8 Geometric parameters of FAST IRPM: **a** plan view, **b** cross sectional view

4 Results

4.1 Description of Mechanism Parameters

The optimization results are greatly influenced by a series of geometric parameters as shown in Fig. 9. Besides, other important parameters are listed in Table 1.
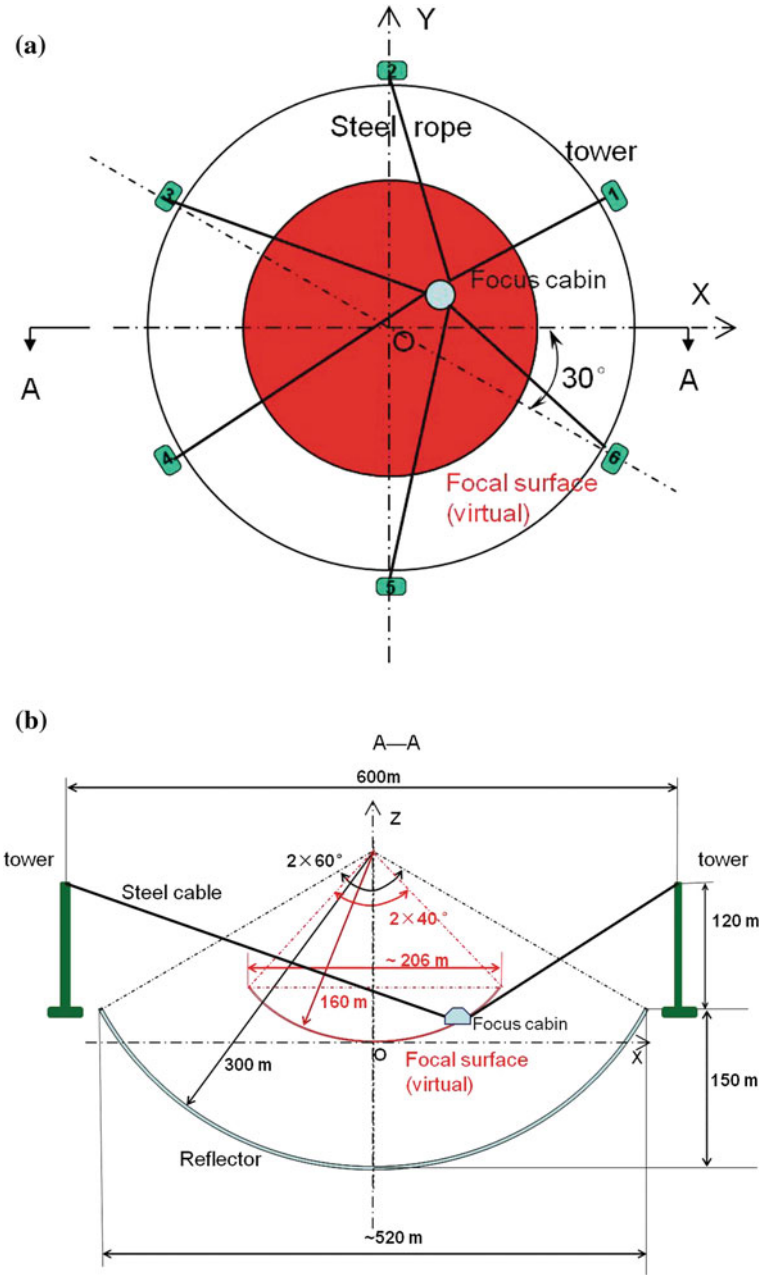
Fig. 9 Discrete mesh of 1/6 focal surface
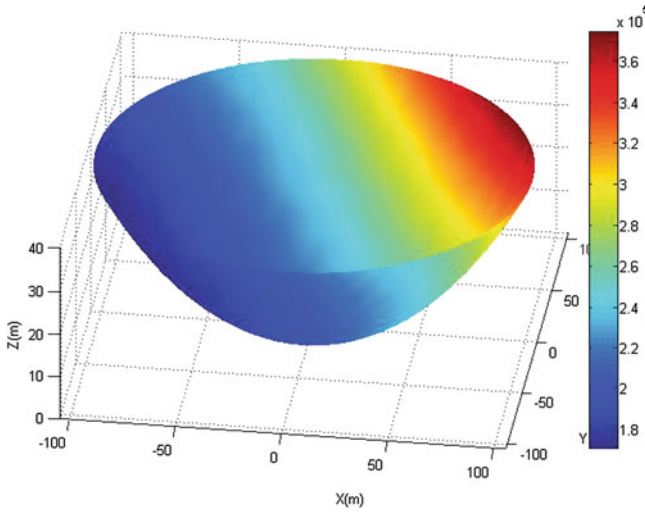
Fig. 10 Distribution of rope tension t_2 (N) (at the end P_2) on the focal surface

Table 1 Some important parameters in the computation

Symbol	Description	Value
q_1 & q_3	Linear weight of steel wire hung with normally stretched cables	176.40 N/m
q_2	Linear weight of steel wire hung with accumulated cables	323.89 N/m
n	Linear mass ratio of accumulated cables to normally stretched cables	3.15
r_i	Projection length of the vector $\mathbf{r}_i$ ($i = 1, 2, \ldots, 6$) in the joint plane	6.40 m
G	Total weight of focus cabin	3.0×10^5 N
δ	Distance of COG to the joint plane (as shown in Fig. 2)	0.246 m

4.2 Display of Results

The optimal distribution of 6 rope tensions is calculated over the whole focus surface. Figure 10 draws the case of rope 1 where the colors represent the different tension values, and yet due to the symmetry we can easily obtain a similar tension distribution of rope 2, 3, 4, 5 and 6 by simply rotating the figure in counter-clockwise direction with 60, 120, 180, 240 and 300° respectively. The figure shows that the rope tensions vary continuously and smoothly within a range of about 180–380 KN, which is an input base for the future design of steel wire and the corresponding capstan motors.

The optimization results then give the variation of 3 orientation angles. Figure 11 draws the change of natural tilt as the cabin moves in the focus surface. The optimal tilt is almost perfectly axisymmetric in a range of 0–15°.

When the FAST telescope works, the desired pointing of the focus cabin demands that the tilt direction and the symmetric axis of the focal surface should be coplanar. The tilt direction is indicated in the angles φ and ϕ, so the desired pointing actually
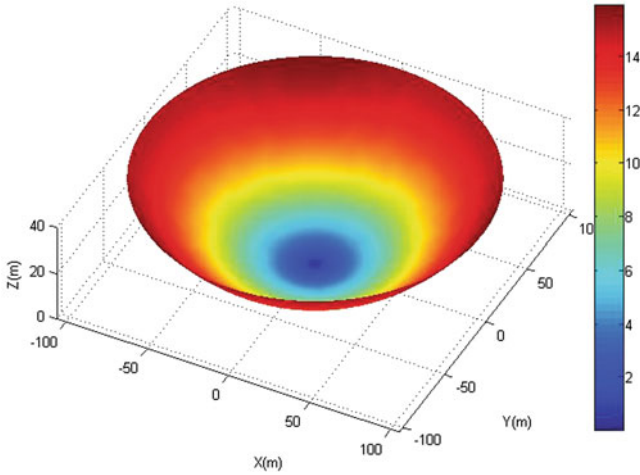
Fig. 11 Distribution of cabin tilt θ (°) on the focal surface
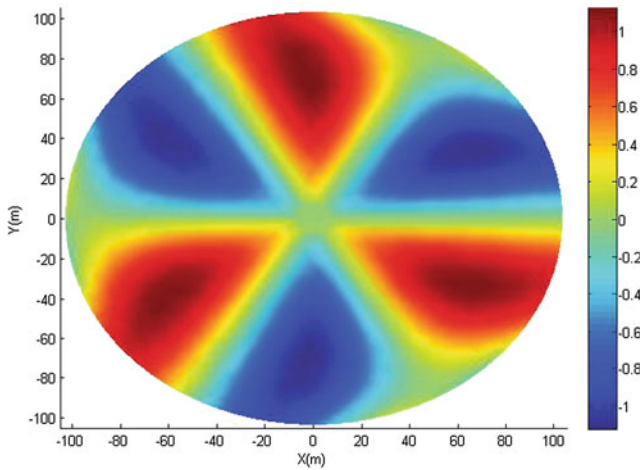
Fig. 12 Variance of φ (°) (computation value vs. ideal pointing) on the focal surface

requires that the ideal φ is always along the radial direction and the ideal ϕ equal to 0. Figures 12 and 13 respectively draw the distribution of this kind of variance between the computation value and the ideal value. Both two figures are almost perfectly symmetric and they verify that the maximal absolute variance is not more than 1°. These facts show that the FAST IRPM has good consistency with the ideal pointing.
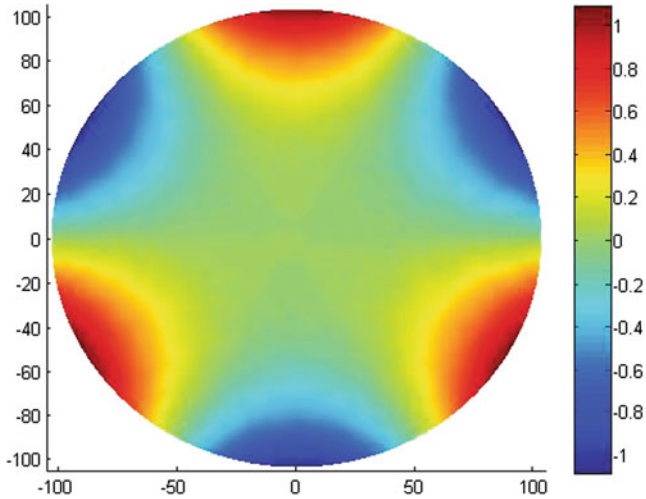
Fig. 13 Variance of ϕ (°) (computation value vs. ideal pointing) on the focal surface

5 Conclusion

A kind of incompletely restrained cable-driven parallel mechanism is introduced and studied on the optimal tension distribution. Due to its huge size, slack-rope model hung with piecewise uniform mass is specially investigated to build a dual-parameter-dependent wrench matrix, i.e., both platform pose and rope geometry dependent. The performance index based on force variance is proposed to optimize the force distribution among slack ropes. The computation results show good consistency with the ideal pointing of the telescope.

References

1. Nan, R.D.: Five-hundred-meter aperture spherical radio telescope (FAST). Sci. China Ser. G Phys. Mech. Astron. 49(2), 129–148 (2006).
2. Li, H., Zhu, W., Pan, G.: Equilibrium analysis of FAST rope-drive parallel manipulator based on rope force optimization. Eng. Mech. 28(4), 185–193 (2010) (in Chinese).
3. Barrette, G., Gosselin, C.: Determination of the dynamic workspace of cable-driven planar parallel mechanisms. ASME J. Mech. Des. **127**(2), 242–248 (2005)
4. Bosscher, P., Ebert-Uphoff, I.: Wrench-based analysis of cable-driven robots. In: Proceedings of the 2004 IEEE International Conference on Robotics and Automation, pp. 4950–4955, New Orleans, LA, USA (2004).

5. Verhoeven, R., Hiller, M.: Estimating the controllable workspace of tendon-based Stewart platforms. In: Lenarcic, J., Stanisic, M.M. (eds.) Advances in Robot Kinematics, pp. 277–284. Kluwer Academic, Dordrech (2000)
6. Riechel, A.T., Ebert-Uphoff, I.: Force-feasible workspace analysis for underconstrained point-mass cable robots. In: Proceedings of the 2004 IEEE International Conference on Robotics and Automation, pp. 4956–4962, New Orleans, LA, USA (2004).
7. Li, H., Nan, R., Kärcher, H., et al.: Working space analysis and optimization of the main positioning system of FAST cabin suspension. In: Proceedings of SPIE, Astronomical Instrumentation, Ground-Based and Airborne Telescopes II, Marseille, vol. 70120T(1–11) (2008).
8. Levenberg, K.: A method for the solution of certain non-linear problems in least squares. . Q. Appl. Math. **2**(2), 164–168 (1944)
9. Marquardt, D.W.: An algorithm for the least-squares estimation of nonlinear parameters. SIAM J. Appl. Math. **11**(2), 431–441 (1963)

Investigation of the Influence of Elastic Cables on the Force Distribution of a Parallel Cable-Driven Robot

Werner Kraus, Philipp Miermeister and Andreas Pott

Abstract Cable-driven parallel robots rely on cables instead of rigid links to manipulate the endeffector in the workspace. The cable force distribution is the result of cable elongation and the force coupling at the endeffector. In this paper, the experimental investigation of the force coupling is presented. In the experiment, the cable length in each individual cable was varied, and the resulting progression of the force distribution and the deflection were measured. With this approach, the steady state gain matrix for the transfer function between a delta in cable length and the resulting changes in the cables forces can be determined. Furthermore, the impact of the observed force coupling on cable force control is discussed.

1 Introduction

1.1 Motivation

In the recent years, cable-driven parallel robots have attracted several researchers due to their positive properties like scalability, high dynamic and a good payload-weight ratio (see e.g. [3, 5, 6, 8]). A typical control architecture for a cable robot is presented by Shiqing et al. in [7]. As cables can only transmit pull forces, the

---

W. Kraus (✉) · P. Miermeister · A. Pott
Fraunhofer Institute for Manufacturing Engineering and Automation IPA, Stuttgart, Germany
e-mail: Werner.Kraus@ipa.fhg.de

P. Miermeister
e-mail: Philipp.Miermeister@ipa.fhg.de

A. Pott
e-mail: Andreas.Pott@ipa.fhg.de

robot controller must ensure that during operation all cables are under tension. The cable force is the result of the elongation of the elastic cable. Therefore, the output of force controllers are cable lengths. As the cables are all connected to the moving platform, the controlled system is coupled and non-linear. The knowledge of these dependencies is necessary to design a force controller. For this reason, we discuss in this paper experimental results which deliver insight to the influence of elastic cables to the force distribution.

The paper is organized as followed. At first, we briefly introduce in the robot kinematics, the determination of feasible force distributions and the stiffness analysis. In the next section, the experimental setup and test procedure is described. Then the experimental results regarding the progression of the force distribution and the deflection of the platform are presented. The results are discussed regarding the requirements to a cable length-based force control.

2 Model of the Cable Robot

2.1 Robots Kinematic

The geometry of the robot is described by proximal anchor points on the robot base $\mathbf{a}_i$ and the distal anchor points on the endeffector $\mathbf{b}_i$. The index i denotes the cable number and m is the absolute number of cables. By applying a vector loop as shown in Fig. 1 the cable vector $\mathbf{l}_i$ follows as

$$\mathbf{l}_i = \mathbf{a}_i - \mathbf{r} - \mathbf{R}\,\mathbf{b}_i. \tag{1}$$

The structure equation

$$\underbrace{\begin{bmatrix} \mathbf{u}_1 & \cdots & \mathbf{u}_m \\ \mathbf{b}_1 \times \mathbf{u}_1 & \cdots & \mathbf{b}_m \times \mathbf{u}_m \end{bmatrix}}_{\mathbf{A}^T(\mathbf{r},\mathbf{R})} \underbrace{\begin{bmatrix} f_1 \\ \vdots \\ f_m \end{bmatrix}}_{\mathbf{f}} = - \underbrace{\begin{bmatrix} \mathbf{f}_p \\ \boldsymbol{\tau}_p \end{bmatrix}}_{\mathbf{w}} \quad \text{where } \mathbf{u}_i = \mathbf{l}_i \|\mathbf{l}_i\|^{-1}. \tag{2}$$

results from the force and torque equilibrium of the robot's endeffector. The wrench $\mathbf{w}$ consists of external forces $\mathbf{f}_p$ and torques $\boldsymbol{\tau}_p$.

2.2 Cable Force Distribution

To compute a force distribution $\mathbf{f}$, which solves the structure equation (Eq. 2) under the constraint $f_{min} \leq f_i \leq f_{max}$, the Dykstra alternating projection solution presented by Hassan and Khajepour is used [4]. The advantage of this approach is, that it

Fig. 1 Robot kinematic
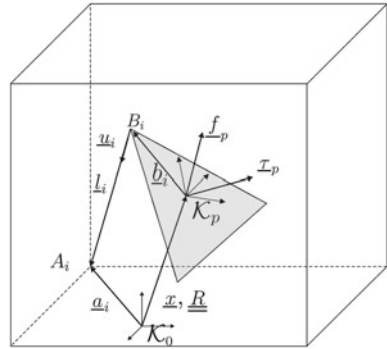
minimizes the 2-norm of the force distribution and delivers a feasible solution if it exists. The algorithm starts with a zero force vector. In each iteration, the force vector $\mathbf{f}$ is first projected on the nullspace of $\mathbf{A}^T$ translated by $-\mathbf{A}^{+T}\mathbf{w}$

$$proj_A(\mathbf{f}) = (\mathbf{I} - \mathbf{A}^{+T}\mathbf{A}^T)\mathbf{f} - \mathbf{A}^{+T}\mathbf{w} \qquad (3)$$

where $\mathbf{A}^{+T}$ denotes the Moore-Penrose matrix inverse, and afterwards the resulting force vector is projected on the bounds of the cable forces

$$proj_C(\mathbf{f}) = [\overline{f}_1 \cdots \overline{f}_m]^T : \overline{f}_i = \begin{cases} f_{min}, & f_i < f_{min} \\ f_i, & f_{min} \leq f_i \leq f_{max} \\ f_{max}, & f_i > f_{max} \end{cases}. \qquad (4)$$

The algorithm iterates until the two projections converge. The force distribution is valid, when the two projection converged to the same point. Otherwise there exist no feasible force distribution.

2.3 Stiffness

The stiffness of cable robots is discussed in detail in [2, 8, 9]. Here we give a short overview. The Cartesian stiffness matrix $\mathbf{K}_x$ describes the linear relation

$$\delta\mathbf{w} = \mathbf{K}_x\delta\mathbf{x} \qquad (5)$$

between an infinitesimal wrench $\delta\mathbf{w}$ and deflection $\delta\mathbf{x}$. For the analytic expression for $\mathbf{K}_x$ we have to differentiate the structure equation (Eq. 2), which yields to

$$d\mathbf{w} = -\frac{\partial\mathbf{A}^T}{\partial\mathbf{x}}dx\mathbf{f} - \mathbf{A}^T d\mathbf{f} \qquad (6)$$

where $d\mathbf{A}^T$ is the derivation of the structure matrix by the generalized coordinates $\mathbf{x} = [r_x, r_y, r_z, \theta_x, \theta_y, \theta_z]^T$. The relation between the incremental cable forces and an incremental change in cable length for a linear spring model can be expressed by

$$\delta\mathbf{f} = \mathbf{K}_l \delta\mathbf{l} \tag{7}$$

where $\mathbf{K}_l$ is the joint space stiffness matrix with the stiffness of each cable on the diagonal. Incremental changes in the platform pose $\delta\mathbf{x}$ are transformed to the endeffector space with

$$\delta\mathbf{l} = -\mathbf{A}\delta\mathbf{x}. \tag{8}$$

With Eqs. 5, 7 and 8 one receive from Eq. 6

$$\mathbf{K}_x d\mathbf{x} = \underbrace{-\frac{\partial \mathbf{A}^T}{\partial \mathbf{x}}\mathbf{f}\,d\mathbf{x}}_{\mathbf{K}_g} + \underbrace{\mathbf{A}^T \mathbf{K}_l \mathbf{A}\,d\mathbf{x}}_{\mathbf{K}_c}. \tag{9}$$

This equation shows, that the stiffness is based on two separated effects. The stiffness $\mathbf{K}_g$ results from the change of the Jacobian when deflecting the platform. Beside geometrical parameters, the height of this part depends on the height of the force distribution. The second term of Eq. 9 results from cable stiffness.

3 Experimental Evaluation

3.1 Test Setup

The experiments were performed on the cable robot IPAnema 2. The test environment is shown in Fig. 2. Its geometrical parameters are shown in Table 1. For the force measurement the robot is equipped with 8 cable force sensors at the endeffector. The sensors have a resolution of 0.13 N and a measurement range of ±2,000 N. The analog output signal of the force sensors is digitialized and sent via the field bus in real-time to the PLC. The deflection of the platform is measured with a Leica Laser Tracker. It can determine the absolute position of the reflector mounted in the center of the endeffector with an accuracy of ±15 µm+6 µm/m. For the synchronization between the robot control and the position measurement, the Laser Tracker is triggered by an output of the robot control.

The cable type is LIROS D-Pro 01505-0250 based on Dyneema SK 75 fibre (Polyethylene) with a diameter of 2.5 mm. The specific stiffness k' is 120,000 N.
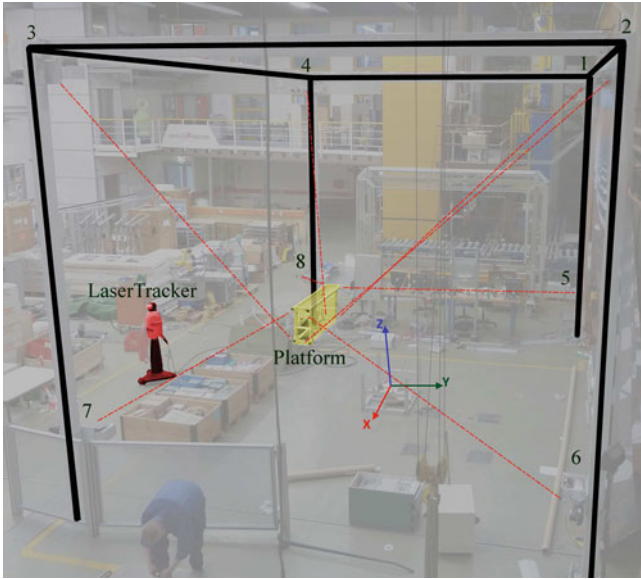
Fig. 2 Test environment with cable robot IPAnema 2 and Laser Tracker

Table 1 Robot Geometrical Parameters: base vector $\mathbf{a}_i$ and platform vector $\mathbf{b}_i$

Cable i	Base vector $\mathbf{a}_i$ in [m]			Platform vector $\mathbf{b}_i$ in [m]		
	x	y	z	x	y	z
1	[−4.277	2.950	4.604]^T	[−0.653	0.201	−0.085]^T
2	[4.335	2.951	4.480]^T	[0.641	0.196	−0.102]^T
3	[4.029	−2.736	4.609]^T	[0.639	−0.052	−0.092]^T
4	[−3.967	−2.733	4.737]^T	[−0.634	−0.117	−0.058]^T
5	[−4.346	2.902	0.515]^T	[−0.759	0.200	0.410]^T
6	[4.255	2.925	0.372]^T	[0.763	0.192	0.402]^T
7	[3.952	−2.766	0.424]^T	[0.756	−0.014	0.406]^T
8	[−4.033	−2.766	0.573]^T	[−0.750	−0.012	0.423]^T

3.2 Test Procedure

The test procedure is shown in the flow diagram in Fig. 3. The positioning of the endeffector to the four positions is made by a position control based on the inverse kinematic. For an automated workflow, the following test procedure is completely implemented in the PLC. Next, a simple force control based on cable lengths is applied, to receive the desired force distribution. The four force distributions are precalculated with the Dykstra-algorithm assuming a gravity wrench of −200 N. The real values are gained from the cable force sensors. Based on this set of cable lengths the experiment is performed. One after the other cable is tensioned with a

Positionate the endeffector to the pose, controlled by the inverse kinematic

Loop for tension niveau: $j=1{:}4$

Control the cable forces to a precalculated force distribution j

Loop for 3x repetition

Loop for varied cable: $i=1{:}8$

Phase 1: tense cable *i with stepwidth* Δl from $q_i=q_{i0}$ to $q_i=q_{i0}+\Delta l_{max}$
After each step:
- Save the actual cable forces
- Trigger LaserTracker

Phase 2: relax cable *i with stepwidth* Δl from $q_i=q_{i0}+\Delta l_{max}$ to $q_i=q_{i0}$
After each step:
- Save the actual cable forces
- Trigger LaserTracker

Finish

Fig. 3 Test procedure

stepwidth Δl is 0.5 mm to Δl_{max} of 15.0 mm and afterward relaxed to the initial length. As the forward and backward movement (Phase 1 and 2) is logged, one receive 61 values for the variation of one cable and 488 datasets in total for one tension niveau. This cycle is performed three times in succession. The first run is dropped, because it is influenced by settlement of the cables on the drum and leads to non-repeatable results. To receive insight in the pose-dependency of the force coupling, four different poses are examined. Their position is listed in Table 2 and they are visualized in Fig. 4.

Table 2 Investigated poses and resulting cable lengths in [mm]

Pose	x	y	z	l_1	l_2	l_3	l_4	l_5	l_6	l_7	l_8
P_1	−1200	−1000	3000	4736.5	6419.7	5213.4	3243.0	5265.4	6786.2	5631.0	3935.5
P_2	0	−1000	3000	5456.3	5539.8	4200.9	4107.0	5903.5	5985.7	4739.8	4649.4
P_3	0	0	3000	4837.2	4931.3	4715.0	4631.1	5335.6	5422.4	5205.9	5123.6
P_4	0	0	1800	5372.2	5455.2	5279.6	5208.8	4787.3	4877.0	4637.6	4555.0
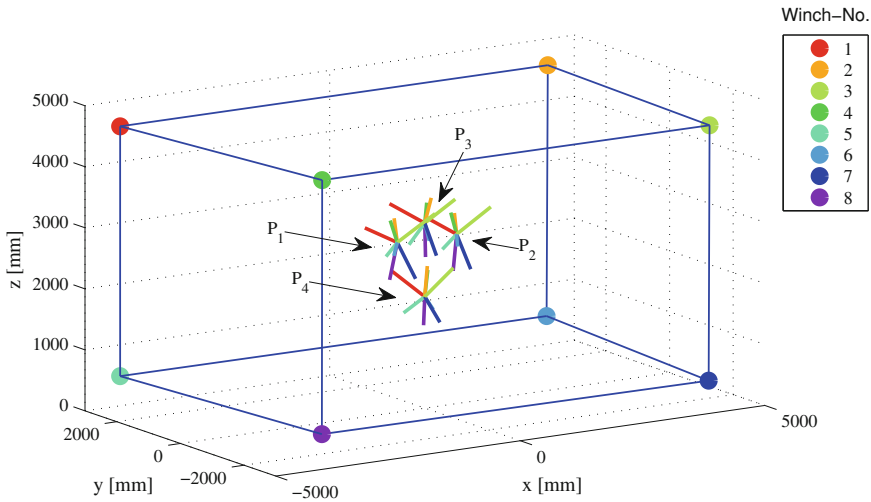
Fig. 4 Deflection of the platform for $\Delta q = 15$ mm

3.3 Experimental Results: Force Distribution

The initial force distributions measured with the force sensors are exemplary for Pose 2 shown in Table 3. The mean forces $\bar{\mathbf{f}}$ are evenly distributed with a distance of about 50 N.

The force progression is shown in Fig. 5, where based on the tension niveau 4 cable 1 is tensed by 15 mm. Each point marked with a cross represents a measurement and the straight shows in each case the linearization. It is important to notice, that the progression of the cable forces is linear. The diagram also reveals that the force in one single cable influences strongly the other cables. As expected, the cable forces rise in some cable during in others decrease. For illustration, the pose and the corresponding stiffness model are visualized in Fig. 6.

This correlation can be expressed generalized for m cables in form of the steady state gain matrix G

Table 3 Measured force distribution $\mathbf{f}$ and mean force $\bar{\mathbf{f}}$ in pose 2 for the 4 tension niveaus in [N]

Tension niveau	f_1	f_2	f_3	f_4	f_5	f_6	f_7	f_8	$\bar{\mathbf{f}}$
T_1	171.7	176.4	247.5	242.5	41.6	20.5	85.9	64.2	131.3
T_2	221.0	229.0	326.9	320.0	72.3	46.8	137.6	114.8	183.5
T_3	272.8	281.4	412.1	401.6	104.8	73.5	192.9	168.2	238.4
T_4	317.7	327.3	483.6	474.6	132.2	96.9	241.3	213.2	285.8
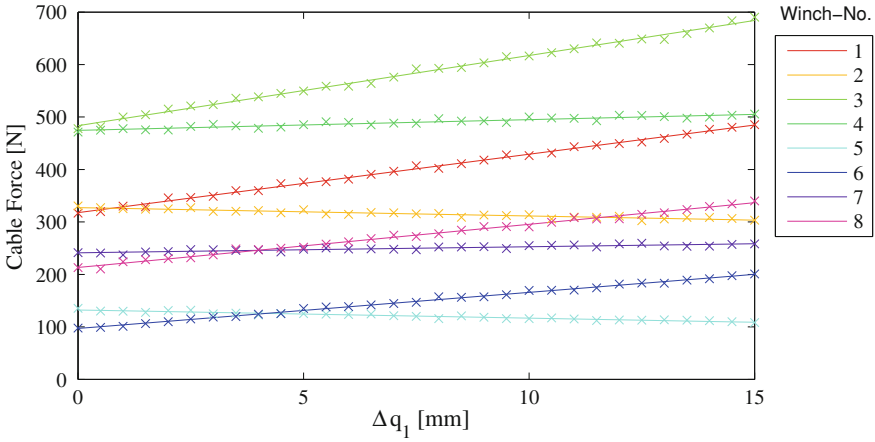
Fig. 5 Progression of the force distribution for tension niveau 4 in pose 2 while tensioning cable 1

$$f_i = k\Delta l = k'|l_i|(|l_{i0}| - |l_i|)$$
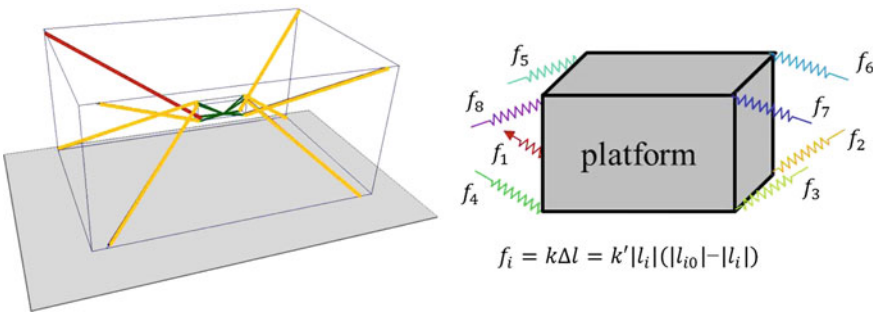
Fig. 6 Stiffness model of the cable robot

$$G = \begin{bmatrix} \frac{\partial f_1}{\partial q_1} & \cdots & \frac{\partial f_1}{\partial q_m} \\ \vdots & \ddots & \vdots \\ \frac{\partial f_m}{\partial q_1} & \cdots & \frac{\partial f_m}{\partial q_m} \end{bmatrix}. \tag{10}$$

It represents the transfer function between changes in cable lengths Δq and the corresponding change in cable force Δf

Table 4 Steady gain matrix in pose 2 for the tension niveau 4 in [N/mm]

	Δq_1	Δq_2	Δq_3	Δq_4	Δq_5	Δq_6	Δq_7	Δq_8
Δf_1	11.1	−1.6	13.4	2.0	−1.6	6.9	1.1	8.2
Δf_2	−1.2	10.1	2.2	11.3	6.8	−1.5	7.9	1.5
Δf_3	11.0	2.5	15.4	7.0	1.3	6.3	4.4	9.7
Δf_4	2.4	11.5	6.6	14.9	7.3	0.6	9.8	4.5
Δf_5	−1.3	7.6	1.6	8.2	6.4	−2.4	6.5	−0.2
Δf_6	7.3	−1.3	6.4	0.9	−2.6	5.4	−0.5	6.2
Δf_7	1.4	7.9	5.4	10.0	6.1	−0.6	8.1	2.0
Δf_8	8.3	1.4	10.6	4.3	−0.5	5.9	2.2	8.2

Table 5 Comparision between the measured stiffness $k_{measured}$ and the cable stiffness k_{cable} in pose 2 for the tension niveau 4

	1	2	3	4	5	6	7	8
$k_{measured}\left[\frac{N}{mm}\right]$	11.1	10.1	15.4	14.9	6.4	5.4	8.1	8.2
$k_{cable}\left[\frac{N}{mm}\right]$	22.0	21.7	28.6	29.2	20.3	20.0	25.3	25.8
$\frac{k_{measured}}{k_{cable}}[\%]$	50.6	46.8	53.8	50.8	31.4	27.0	31.8	31.9

$$\Delta f = G(x, f)\Delta q. \tag{11}$$

This matrix can be evaluated from the experiment, as the entries are the slope of interpolated straights from the progression of the force distribution. Exemplary, the steady state matrix for the highest tension niveau in pose 2 is shown in Table 4. The diagonal entries can be interpreted as the stiffness of each cable under consideration, that the platform has also a stiffness. If the platform is fixed, the gain matrix is a diagonal matrix corresponding to $\mathbf{K}_l$. The force coupling is expressed by the non-diagonal entries of the gain matrix. The measured values reveal that the interaction between the cables is significant. For example, a change in the length of cable 1 causes approximately the same change in cable force in cable 3.

The effect of the force coupling can also be seen, when comparing the cable stiffness $k_{cable,i} = \frac{k'}{l_i}$ with the measured stiffness $k_{measured}$ as shown in Table 5. It also reveals, that the proportion between the two sizes depends strongly on the cable.

To evaluate the pose-dependency of the gain matrix, the range for each element over the four poses is determined according to

$$\Delta g_{i,j} = max(g_{i,j}(x = P_1 : P_4, f = T_2)) - min(g_{i,j}(x = P_1 : P_4, f = T_2)). \tag{12}$$

The result is shown in Table 6. It reveals, that both the diagonal and non-diagonal entries underly a significant dependency on the pose.

The gain matrix depends also on the tension niveau. For illustration, the diagonal entries of the gain matrix for the four tension niveaus shown in Table 7. The compari-

Table 6 Range of the gain matrix over all 4 poses for tension niveau 2 [N/mm]

	Δq_1	Δq_2	Δq_3	Δq_4	Δq_5	Δq_6	Δq_7	Δq_8
Δf_1	3.1	4.9	3.0	8.7	2.8	2.8	0.6	0.3
Δf_2	5.1	4.1	4.7	3.2	2.8	2.8	1.8	3.6
Δf_3	3.1	4.5	5.5	9.1	0.3	2.0	3.4	1.5
Δf_4	8.6	3.2	9.4	6.8	0.9	0.6	1.6	7.0
Δf_5	3.9	2.9	2.1	0.6	5.9	5.3	4.4	4.4
Δf_6	2.7	3.9	1.9	0.6	6.0	4.8	5.1	4.5
Δf_7	2.3	2.1	3.9	1.5	4.8	4.2	3.7	4.5
Δf_8	0.4	1.2	1.9	7.5	4.2	4.9	4.0	3.1

Table 7 Diagonal elements of the gain matrix for the 4 tension niveaus in pose 2 [N/mm]

	Δq_1	Δq_2	Δq_3	Δq_4	Δq_5	Δq_6	Δq_7	Δq_8
T_1	9.0	8.4	13.0	12.8	4.5	4.3	6.8	6.2
T_2	10.2	9.4	14.2	13.7	5.6	4.8	7.3	7.2
T_3	10.8	9.9	14.8	14.4	6.1	5.2	7.8	7.8
T_4	11.1	10.1	15.4	14.9	6.4	5.4	8.1	8.2

Table 8 Deflection of the platform in mm for $\Delta q_i = 15$ mm in winch i

Tension niveau	$|\Delta \mathbf{r}|_1$	$|\Delta \mathbf{r}|_2$	$|\Delta \mathbf{r}|_3$	$|\Delta \mathbf{r}|_4$	$|\Delta \mathbf{r}|_5$	$|\Delta \mathbf{r}|_6$	$|\Delta \mathbf{r}|_7$	$|\Delta \mathbf{r}|_8$	$\overline{|\Delta \mathbf{r}|}$
T_1	6.707	7.138	7.830	7.794	4.454	3.270	6.223	6.001	6.177
T_2	6.536	6.700	7.851	7.823	3.803	3.465	6.229	6.316	6.090
T_3	6.483	6.581	7.791	7.783	3.553	3.412	6.286	6.241	6.016
T_4	6.512	6.618	7.762	7.702	3.730	3.461	6.148	6.100	6.004
$\Delta \overline{r}$	6.560	6.759	7.808	7.776	3.885	3.402	6.222	6.165	6.072
σ	0.101	0.258	0.040	0.052	0.394	0.091	0.056	0.141	

son reveals, that the effective stiffness rises proportional with the tension niveau. The coupling between cable length and force has therefore a progressive characteristic.

3.4 Experimental Results: Deflection of the Endeffector

During the experiment also the deflection of the endeffector is measured. Exemplary for pose 2 the resulting deflection for a change in cable length of 15 mm are visualized in Fig. 7. The length of the deflection for the four tension niveaus is listed in Table 8. The size of the deflection depends mainly on the considered cable. For example cable 6 is relative long and has therefore a small cable stiffness, what results in a litte deflection of the platform. The relation between the stiffness of the cable and the stiffness of the anchor point seems to be constant for different tension niveaus. The
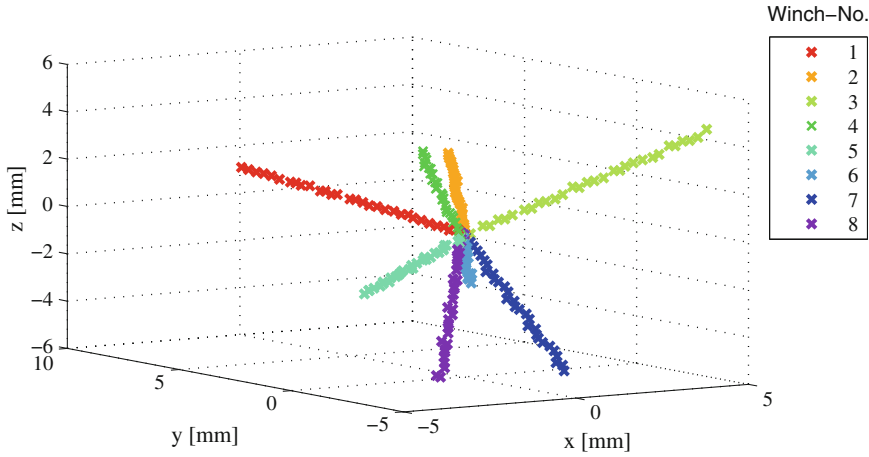
Fig. 7 Deflection of the platform for $\Delta q = 15\,\text{mm}$

Table 9 Relative Gain Array $\Lambda(s)$ for tension niveau 4 in pose 2

−21.0	4.7	−8.8	1.2	−7.1	39.3	0.1	−7.4
14.3	−239.3	−14.3	62.3	186.2	−39.2	25.8	5.2
−40.8	−22.3	−36.4	19.0	11.9	43.8	4.0	21.8
14.6	146.6	24.8	−35.5	−106.1	−8.5	−23.4	−11.5
−8.6	100.0	5.3	−29.4	−85.7	33.0	−13.9	0.4
−18.6	9.6	−16.6	1.5	−20.1	35.8	−0.7	10.2
−1.7	−22.1	−4.7	3.1	12.6	−1.3	13.4	1.6
62.8	23.9	51.7	−21.2	9.3	−101.9	−4.3	−19.3

standard deviation for the deflection regarding the tension niveaus is smaller than 0.394 mm.

4 Discussions

4.1 Effects on Force Control

The performed investigation showed, that one single cable force significantly affects the whole force distribution. This coupling has to be taken into account while controlling the cable force based on changes in cable lengths. For decoupling, a typical approach is based on the singular value decomposition. Based on the static gain matrix G the relative gain array (RGA) $\Lambda(s)$ yields with a element-by-element multiplication ($\times$) to

$$\Lambda(s) = G(s) \times (G(s)^T)^{-1} \tag{13}$$

which gives a scaling- and controller-independent insight in the behaviour of the controlled system [1]. The RGA for tension niveau 4 in pose 2 (Gain matrix in Table 4) is shown in Table 9. The matrix is far away from the identity matrix, what confirms the strong coupling. The transformation of the system into a single input single output system is therefore not feasible and has to be handled as multivariable control problem.

4.2 Outlook

The measurement of the endeffector's deflection is actual conducted with a Laser Tracker, which can only capture the position of one single point, but not the orientation of the endeffector. For more detailed investigation on the deflection, it would be desirable to repeat the experiments with a 6-DOF measurement system. Another approach could be to repeat the same experiment with different measured points on the platform. The received data would allow to extract also the change in orientation.

The received measurement results showed, that the force coupling has a strong influence on the system behaviour and should be included into the force controller. Therefore, a simulation model has to be developed and verified. In the next step, a computationally efficient implementation should be found to enable an adaptive controller.

5 Conclusions

In this paper, a brief introduction into the stiffness analysis for cable robots is given. Then the experimental setup for the investigation of the force coupling is described. Subsequently, the measurement results were presented and discussed regarding the properties of the force distribution and the deflection of the endeffector under the change in length of one cable. After that, the effects of the gained insight of the force coupling on the force control are considered.

References

1. Albertos, P., Sala, A.: Multivariable control systems: an engineering approach. Springer, Spain (2004)
2. Behzadipour, S., Khajepour, A.: Stiffness of cable-based parallel manipulators with application to stability analysis. J. Mech. Des. Trans. ASME **128**, 303–310 (2006)

3. Gouttefarde, M., Merlet, J.P., Daney, D.: Wrench-feasible workspace of parallel cable-driven mechanisms. In: ICRA, pp. 1492–1497. Roma and Italy (2007).
4. Hassan, M., Khajepour, A.: Analysis of bounded cable tensions in cable-actuated parallel manipulators. IEEE Trans. Robot. **27**, 891–900 (2011)
5. Hiller, M., Fang, S., Mielczarek, S., Verhoeven, R., Franitza, D.: Design, analysis and realization of tendon-based parallel manipulators. Mech. Mach. Theory **40**, 429–445 (2005)
6. Merlet, J.P., Daney, D.: A new design for wire-driven parallel robot. In: 2nd International Congress, Design and Modelling of Mechanical Systems (CMSM 2007). Monastir, Tunesia (March, 2007).
7. Shiqing, F., Franitza, D., Marc, T., Frank, B., Hiller, M.: Motion control of a tendon-based parallel manipulator using optimal tension distribution. IEEE/ASME Trans. Mechatron. **9**, 561–568 (2004)
8. Verhoeven, R.: Analysis of the workspace of tendon-based stewart platforms. Ph.D. thesis, University of Duisburg-Essen, Duisburg (2004).
9. Yu, K., Lee, L., Krovi, V., Tang, C.: Enhanced trajectory tracking control with active lower bounded stiffness control for cable robot. In: IEEE International Conference on Robotics and Automation, pp. 669–674 (2010).

Part III
Application and Protoypes

IPAnema: A family of Cable-Driven Parallel Robots for Industrial Applications

Andreas Pott, Hendrick Mütherich, Werner Kraus, Valentine Schmidt, Philipp Miermeister and Alexander Verl

Abstract Nowadays there are very little robot systems in operation in the field of medium to large-scale handling and assembly mostly due to lack of repetitive processes or shortcomings in programming and configuring such robots. In this paper we introduce a family of cable-driven parallel robot called IPAnema that are designed for industrial processes. We address the system architecture, key components such as winches and controller, as well as design tools. Furthermore, some experimental data from the evaluation are presented to illustrate the performance of cable robots.

1 Introduction

Industrial robots were successfully applied to a number of industrial processes including handling, welding, and assembly. After decades of research on serial industrial robots it seems that the major potential for performance improvement are exhausted. Is seems that only limited gains in the robot performance can be expected from further optimization of the mechanical construction, the drive-trains, and controllers. Contrary, cable-driven parallel robots promise to increase the three performance—criteria payload, workspace, and dynamics—by one to two orders of magnitude compared to industrial robots. Furthermore, these performance criteria are mostly decoupled in the design. The key components in the design of cable robots are its winches. The maximum size of the workspace is primary given by the capacity of the winch's drum. Tiny winches can have a stroke of some millimeters while industrial large scale winches can coil several kilometers of cable. The product of dynamic performance and payload follows from the power of the actuator as well as from the chosen gearboxes. Industrial grade components are widely available. The range of electrical motors starts below one Watt and ends in the scale of Megawatt. Effective

A. Pott (✉) · H. Mütherich · W. Kraus · V. Schmidt · P. Miermeister · A. Verl
Fraunhofer IPA, Nobelstr. 12, D-70569 Stuttgart, Germany
e-mail: andreas.pott@ipa.fraunhofer.de

forces in the cables can range from below one Newton up to several tons as is routinely done in conventional crane applications. Summing up one can observe that payload, dynamics performance, and size of the workspace can all be designed in a range of at least six orders of magnitude—a dimension that cannot be achieved with other kind of robotic systems.

So far, although cable robots are hardly used in practical applications there are a number of prototypes. In the following an overview of active research centers is given. As far as possible the targeted application and related literature is presented. Clearly, the overview is concise but omits details due to limited space here. The first prototypes were develop in the United States and in Japan. As early as 1989 the RoboCrane system at NIST was presented and it seems to be the first prototype. It was evaluated for large-scale handling [1, 5]. Later Kawamura's Falcon was design for fast pick-and-place [10] and Tadokoro developed a mobile cable robot system for rescue after earthquakes [13, 27].

With the turn of the century the research on cable robots broadened. Lafourcade applied the ultra-light structure of a cable robot for motion generation in wind tunnels [11, 12]. A lightweight prototype named Segesta was developed at the University of Duisburg-Essen, Germany [4, 6, 9, 28] as a research system for kinematics, control, and design studies. At the same time the under-constraint robot Cablev was developed as scaled prototype for handling and automated cranes at the University of Rostock, Germany [8, 14]. A bit later the robot String-Man was used at Fraunhofer IPK (Berlin, Germany) for gait-rehabilitation with focus on force control and safety considerations [25, 26]. At INRIA in France, the robot family Marionet includes a small size prototype for high-speed applications, a portable crane for rescue, and components for person assistance [15]. There were a couple of recent work from Canada where Otis developed a locomotion system [17, 18]. A motion simulator for sport devices was developed at the ETH Zurich, Switzerland [24, 29, 30]. In China researchers are planning to built the world largest cable robot for positioning of the reflector of the telescope FAST [3]. In Iran the KNTU cable robots were studied [2]. Beside these many other prototypes have been developed that we cannot name here.

Since 2006 our group at Fraunhofer IPA develops a family of robots named IPAnema for medium to large-scale inspection, handling, and assembly operations [21, 23]. A major goal of the ongoing research projects is the development of a cable robot based on industrial grade components. On the one hand, this approach shall lead to high robustness and reliability of the system by making use of state-of-the-art components for motors, amplifiers, and control components. On the other hand, these field-tested components put large restriction on the development of control algorithms since advanced numerical methods are difficult to integrate into a mostly closed real-time system, and refactoring algorithms that have been easily developed in scientific tools such as Matlab/Simulink, Maple, or Mathematica can hardly be implemented in robot controllers and PLC due the lack of numerical libraries and real-time constraints. Therefore, our applied research aims at finding acceptable compromises between mathematical complexity that can often be found in literature and ways of implementation on robust, dependable but relatively simple controller hardware.
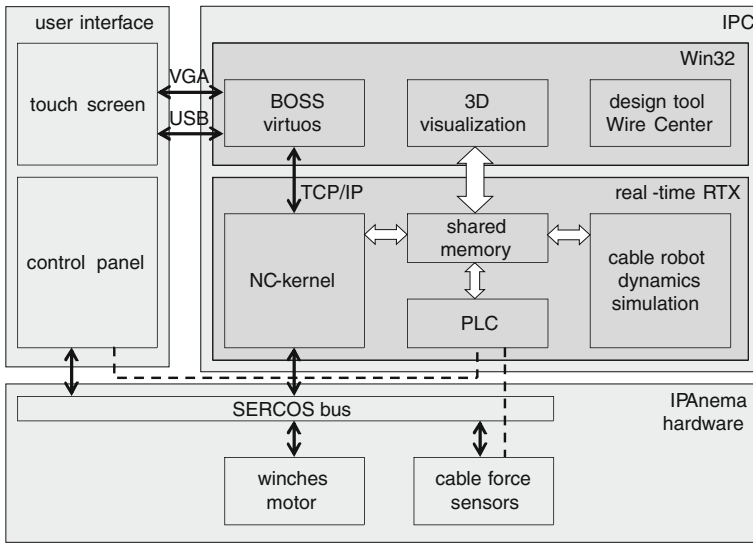
Fig. 1 System structure for the cable robot IPAnema

This paper presents the basic technology used for the cable robot family IPAnema [20, 22]. The rest of the paper is structured as follows. The system architecture and majors components of the IPAnema system family is introduced in Sect. 2. In Sect. 3 we present our test-beds that are currently used for experimental evaluations, where some experimental results are examined in Sect. 4. The papers closes with some conclusions and outlook.

2 Cable-Driven Parallel Robot IPAnema

In this section we give an overview of the IPAnema system family. The IPAnema family consists of three types of cable-robots. Firstly, we have a modular spatial cable robot with currently up to eight winches. Secondly, a medium-size planar robot is composed of four linear direct driven allowing for a 2-D motion. Finally, a passive cable system is built from six cable-length sensors allowing to measure the position of the mobile platform with the encoders. In the following sections the system architecture of the IPAnema cable robot family is given and an overview of the components is presented (Fig. 1).

2.1 System Architecture

The development of a robust control system architecture presents neither new insights nor can it be solved with reasonable research budgets. The manufacturer of the

NC-controller used for the IPAnema robots estimate around 100 person-years of development efforts to make the NC-controller software industrial grade. Therefore, this existing structure was adapted as basis for the controller architecture. The motors in the winches are connected through a SERCOS or EtherCAT interface and set-point values are currently transferred with a cycle time of 2 ms to the amplifiers. The bus system and the NC-kernel can probably achieve a cycle frequency of up to 10 kHz where some of the currently used cable-robot specific control algorithms are not yet fast enough to provide the data in such small time slots.

The control system and the drive amplifiers can command either position, velocity, or torque set values for the motors. The low level force and current control loops are embedded in standard amplifiers. The controllers show excellent performance in terms of position accuracy which is for a machine tool typically below 10 μm. The kernel of the control system is implemented into a PC-based real-time operating system. By use of an industrial PC two important design goals are achieved. Firstly, the reliability and availability of the control system is adequate for industrial applications. Secondly, the control system is nearly as fast as current desktop computers.

A software PLC is coupled to the NC-kernel in full cycle time. One of the major challenges in the development of the controller system is to integrate the kinematic transformation. For path generation it is necessary to calculate the set-point values for the cable length from given Cartesian coordinates in real-time and to allow supervision and correction of the generated set-point values. The Cartesian coordinates of the mobile platform are generated from a NC-program written in G-Code (DIN 66025). At the same time, the actual values measured by multi-turn absolute encoders inside the winches have to be transformed into the current pose of the end-effector. The latter transformation is by far the more complicated one: for our robot it involves solving an over-constrained nonlinear system of equations. Other robot design with fewer cable that degrees-of-freedom might need to solve constrained optimization problems. The existing implementation [23] allows to perform that task in real-time within 1 ms. To ensure the reliable operation of the cable robot system, the tension in the cables is monitored. This is done in two different ways: firstly, tension can be estimated from the current in the motors. This kind of measurement is integrated into the motors. However, a more accurate measurement is received from forces sensors which are integrated into proximate or distal anchor points of the cables.

2.2 Design of Winches

The mechanical design of the current winches is derived from crane winches. However, some additional requirements have to be taken into account to control and operate cable-driven parallel robots. The first requirement for permanent operation of cable robots, without excessive wear of the cables, is maintaining the bend radius experienced by the cables. This must be significantly larger than the the diameter of the cables. Secondly, the direction of the cables changes continuously during

Fig. 2 Concept for servo-controlled winch for cable robot IPAnema
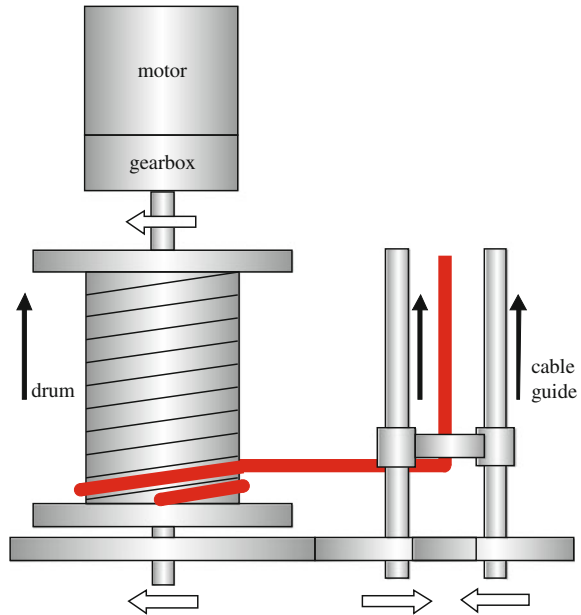
operation of the cable robot. Therefore, it is necessary to include an omnidirectional guidance pulley into the winch. The concept of the winches is shown in Fig. 2.

A synchronous servo motor IndraDyn S with integrated multi-turn absolute encoders by Bosch-Rexroth is coupled to a planetary gearbox with transmission ratio of $i = 3$ or $i = 12$. This drive train is connected to a drum with a diameter $d = 100$ m that can store a cable length of up to $l_{max} = 6$ m. The power train is connected to an additional gearing that moves a cable guidance in parallel to the drum. Due to equal pitch of the drum and the spindle the relative direction of the coiled cable is constant allowing for reliable coiling and uncoiling of the cable. This is especially important since the velocities and accelerations of the cables are very high for cable robots.

The guidance includes a pulley that redirects the cable in parallel to the axis of the motor. At the end of the guidance another pulley mechanism allows for an omnidirectional redirection of the cable into the inner workspace of the cable robot.

Currently, a new winch generation is under development to extend the maximum feasible cable length l_{max} greatly, as well as the maximum cable forces f_{max} (Fig. 3). Beside the improvement of the technical parameters the new winch is designed for lower production costs due to less components and simpler manufacturing technology. Furthermore, it is possible to integrate a force sensors and a redundant brake.
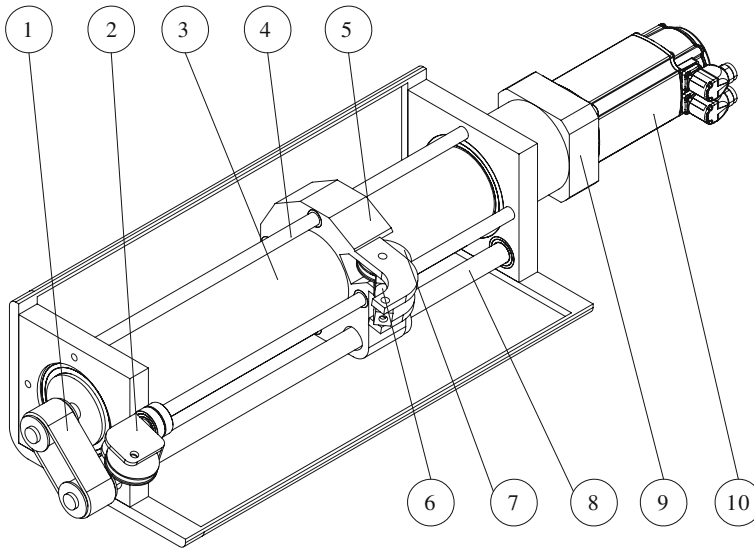
Fig. 3 Concept for new servo-controlled winch with integrated force sensing: (1) transmission belt, (2) guiding pulley, (3) drum, (4) linear guiding, (5) spooling unit, (6) force sensor, (7) guiding pulley, (8) spindle, (9) planetary gearbox, (10) servo motor

2.3 Control Software and Kinematic Transformation

The control system of the cable robot consists of closed-loop position control algorithms which are integrated into the axis modules for each winches. On the position level, state-of-the-art servo-controller from Bosch-Rexroth are used to execute the motion commands which are sent through the SERCOS bus by the NC-kernel. The cascaded closed-loop position and current control for each servo motor can be tuned individually within the framework of the servo-controller.

The NC-kernel runs within the real-time extension RTX of the Windows XP operating systems. The NC-kernel interprets robot programs written in G-Code and generates smooth trajectories according to the G-Code program in world coordinates. To translate the desired motion of the mobile platform to cable lengths and then to set values of the servo motors, a kinematic transformation is used [21]. In addition, the measured cable length is read from the absolute encoders of the winches in order to estimate the current position of the mobile platform. The latter is done by a real-time capable forward transformation. Since most cable robots are over-constrained with respect to forward kinematics an approach based on minimizing the energy is used. The kinematic code solves the optimization problem with sufficient accuracy in real-time [21].

For interfacing with standard industrial equipment, a programmable logic controller (CoDeSys PLC by 3S-Smart Software Solutions) is coupled with the NC-kernel through a shared memory interface. The data exchange is performed

Table 1 IPAnema 1 geometrical parameters: platform vectors b and base vectors a

Cable i	Base vector a_i	Platform vector b_i
1	$[-1.8, 1.5, 2.0]^{\mathrm{T}}$	$[-0.1, 0.1, 0.0]^{\mathrm{T}}$
2	$[1.8, 1.5, 2.0]^{\mathrm{T}}$	$[0.1, 0.1, 0.0]^{\mathrm{T}}$
3	$[1.8, -1.5, 2.0]^{\mathrm{T}}$	$[0.1, -0.1, 0.0]^{\mathrm{T}}$
4	$[-1.8, -1.5, 2.0]^{\mathrm{T}}$	$[-0.1, -0.1, 0.0]^{\mathrm{T}}$
5	$[-2.0, 1.3, 0.0]^{\mathrm{T}}$	$[-0.1, 0.1, 0.2]^{\mathrm{T}}$
6	$[2.0, 1.3, 0.0]^{\mathrm{T}}$	$[0.1, 0.1, 0.2]^{\mathrm{T}}$
7	$[2.0, -1.3, 0.0]^{\mathrm{T}}$	$[0.1, -0.1, 0.2]^{\mathrm{T}}$
8	$[-2.0, -1.3, 0.0]^{\mathrm{T}}$	$[-0.1, -0.1, 0.2]^{\mathrm{T}}$

at every interpolation cycle time of 2 ms. The integration of additional sensor data, i.e. the cable forces read from the force sensors are processed in the PLC. Furthermore, the PLC can interface with additional IT-infrastructure such as a manufacturing execution system.

The user interface of the robot consists of two main components. Firstly, a touchscreen with a graphical user interface (GUI), which is implemented in the Windows XP operating system and allows for visualization of complex data structures. Secondly, a control panel is integrated to provide hardware buttons to switch operations modes, unlock the drives, and provide an emergency stop button. A non realtime data exchange is possible between the GUI and the NC-kernel where the latency of the Windows system is in average smaller than the 60 Hz refresh rate of the monitor. The data exchange between the user interface and the NC-kernel is realized through a TCP/IP channel. The control panel is coupled with the SERCOS bus allowing direct interaction with the NC-kernel and the PLC.

2.4 Dynamics Simulation

A mechatronic, multi-physics simulation of the cable robot dynamics is presented in another paper [16]. The cable robot is a mechatronic system consisting of a mechanical part and an electrical part (Fig. 4). The mechanical parts includes the mobile platform that is connected by m cables to the winches. The electrical part consists of m servo motors and position controllers. The governing numerical control is not further modeled. Instead, we refer to Sect. 2.3 for the details. Its generated set-point position signal θ_i with $i = 1, \ldots, m$ is used as reference signal for the cascaded controller.

The dynamic behavior of the subsystems of a cable robot can be described by ordinary differential equations (ODEs) of first or second order. For simulation and numerical integration the equivalent state space representation is obtained by transforming the high order differential equations into a system of first order ordinary differential equations. The overall system structure with its forward dynamics, inverse
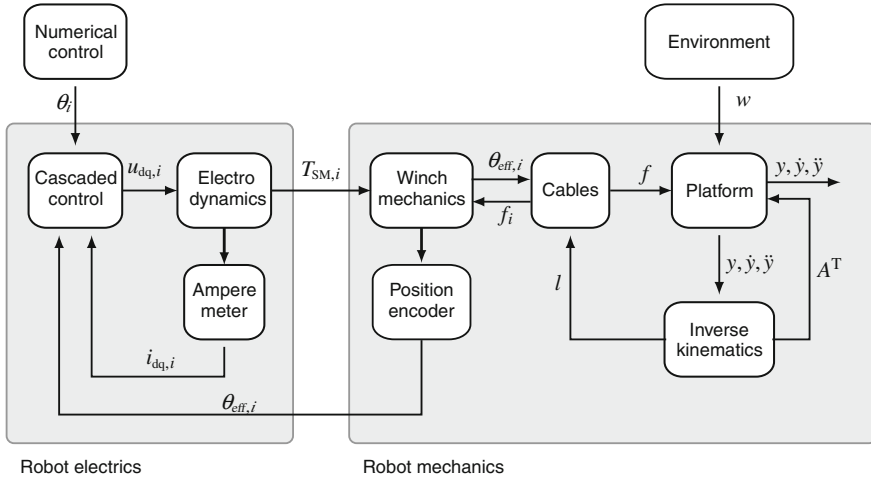
Fig. 4 Structure and interfaces of the mechatronic model for a cable-driven parallel robot
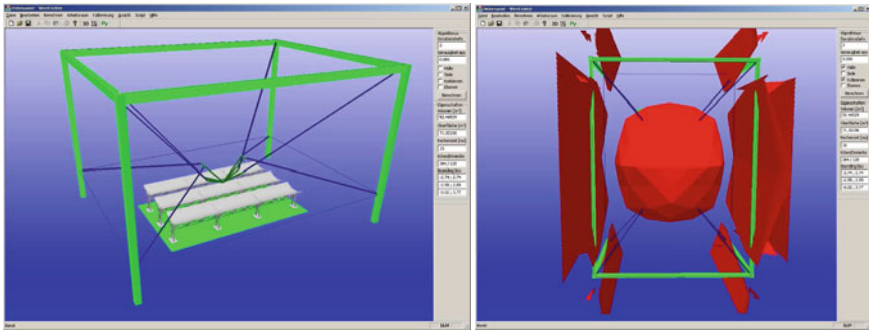
Fig. 5 Design tool for cable robots. *Left* Constant orientation workspace study for IPAnema 2 for a handling application. *Right* IPAnema robot: Interference between cables (*red region* around the machine frame) only occurs outside the workspace (*round region* in the center)

kinematics, and the modeled subsystems with their associated input and output quantities is shown in Fig. 4. The model was developed using the Matlab/Simulink toolchain. The resulting model was then implemented into the controller real time system RTX for validation. When considering the architecture as presented above the simulation of the robot dynamics can be exchanged with the real robot hardware for testing purpose (see Fig. 4). This hardware-in-the-loop simulation is used to verify and evaluate large-scale robots as well as to design the control system. Especially, the design of the force control of the cable robots is largely simplified if it can be optimized with a simulation model.

2.5 Design Tools

For cable-driven parallel robots the workspace of the robot and its geometry are coupled in a complicated and non-intuitive way. Therefore, a sophisticated design approach is needed to construct a cable robot with pre-described properties. The most important criterion for the workspace is controllability, i.e. the ability of the robot to create positive forces in the cables. In the literature, there are different criteria to check whether a pose of the robot belongs to the workspace [7, 22, 28]. Here, the algorithms for feasible workspace determination [28] and optimal closed-form force distribution [20, 22] are integrated into the interactive planning tool WireCenter (Fig. 5). The tool can calculate the hull of the workspace quickly, allowing for manual optimization of robot geometry. Furthermore, the robot geometry is checked for interference between cables following the geometric approach [19]. The region of cable interference for the current design of the IPAnema 1 system is depicted in Fig. 5. It can be seen that no intersection between the region of interference and the workspace occurs. Note, that the upper and lower cables are crossed in the workspace, i.e. the upper winches are connected to the lower platform level and the lower winches are connected to a higher platform level. This design allows for improved stiffness and reduction of cable-environment collisions. Still no cable-cable collisions occur inside the machine frame and thus inside the workspace of the robot.

3 IPAnema System Family Demonstrators

3.1 Spatial Cable Robot IPAnema 1

Based on the IPAnema winch design two generations of cable robots were developed in the last years. The first generation was built from an aluminum frame with the geometric parameters as given in Table 1 and is depicted in Fig. 6. The IPAnema 1 setup used the winches with gearboxes with a transmission ratio of $i = 3$. Therefore, the payload of the robot was in the range of up to 3 kg with a maximum velocity $v_{max} = 10$ m/s and a maximum acceleration $a_{max} = 100$ m/s^2.

3.2 Robot and End-Effector Design for IPAnema 2

When moving from the first to the second generation, the robots property to be quickly reconfigurable was proven. In less than one week the experimental setup was disassembled and the the new robot design was put into operation. By changing the gearboxes from $i = 3$ to $i = 12$, and using the second generation machine frame and mobile platform all relevant robot properties were changed: The workspace and

Fig. 6 Cable-driven parallel robot IPAnema 1 and IPAnema 2

Table 2 IPAnema 2 geometrical parameters: platform vectors b and base vectors a

Cable i	Base vector a_i	Platform vector b_i
1	$[-4.0, 3.0, 5.0]^{\mathrm{T}}$	$[-0.65, 0.125, 0.25]^{\mathrm{T}}$
2	$[4.0, 3.0, 5.0]^{\mathrm{T}}$	$[0.65, 0.125, 0.25]^{\mathrm{T}}$
3	$[4.0, -3.0, 5.0]^{\mathrm{T}}$	$[0.65, -0.125, 0.25]^{\mathrm{T}}$
4	$[-4.0, -3.0, 5.0]^{\mathrm{T}}$	$[-0.65, -0.125, 0.25]^{\mathrm{T}}$
5	$[-4.0, 3.0, 1.0]^{\mathrm{T}}$	$[-0.75, 0.100, 0.75]^{\mathrm{T}}$
6	$[4.0, 3.0, 1.0]^{\mathrm{T}}$	$[0.75, 0.100, 0.75]^{\mathrm{T}}$
7	$[4.0, -3.0, 1.0]^{\mathrm{T}}$	$[0.75, -0.100, 0.75]^{\mathrm{T}}$
8	$[-4.0, -3.0, 1.0]^{\mathrm{T}}$	$[-0.75, -0.100, 0.75]^{\mathrm{T}}$
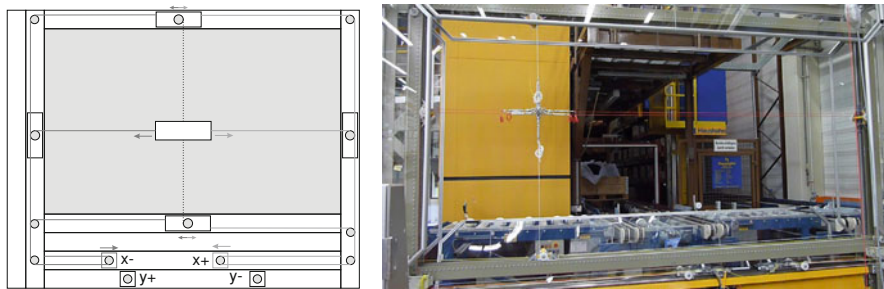
Fig. 7 2D IPAnema 2. *Left* Kinematic concept for the decoupled motion of the mobile platform. *Right* prototype with orthogonal cable arrangement

payload were increased by factors of ten, where the velocity and acceleration were decreased by a factor of four. Cables, controllers, and winches are left unchanged.

The robot frame has a size of $8 \times 6 \times 5$ m and the end-effector was designed to match the footprint of the collector modules. The design parameter of the IPAnema 2 system are given in Table 2. A gripper system is integrated with end-effector to handle

the collectors and to perform the required assembly by installing the collectors into the pylons.

3.3 Planar Cable Robot 2-D IPAnema 2

In a couple of applications such as warehousing a robotic systems is needed that performs a planar motion. For that purpose the 2-D IPAnema 2 system was designed using four linear direct drives to actuate the platform (Fig. 7). The open space in the robot frame has a width of 4 m and a height of 2 m. All four linear actuators are placed in the lower part of the frame and the cables are guided by pulleys through the frame structure. This compact layout allows for flexible design of the rest of the frame. Furthermore, the center of gravity is close to the floor giving the robot a solid stability. Two arrangements for the cables are possible. In the conventional design the cable are guided around four winches that are placed in the corners of the machine frame. This kind of design was largely studied as planar robot. In the second design the pulleys are located on trolleys that can move along a linear guiding on the inner side of the robots frame. In this setting two pairs of the motors operate antagonistic by generating one translational degree-of-freedom at the end-effector. The trolleys are connected to the motors by additional cables such that the vertical trolley movement is mechanically coupled to the end-effector motion. Thus, one receives a cable-driven parallel robots with decoupled Cartesian motion.

For the orthogonal arrangement of the cables the kinematic transformation becomes trivial since the kinematic Jacobian of the robot is isotropic in any tensed configuration. The motion of the actuator is mapped one by one to the horizontal or vertical motion of the platform. To improve the motion of the platform we apply a force control to the pairs of actuators which is also very simple since the motor pairs are each directly coupled. The orthogonal robot design has a rectangular workspace allowing to the cable robot to reach the very corners of the robot frame. Therefore, the robot has an excellent ratio when comparing the workspace to the overall robot size. This shape of the workspace is highly favorable for warehousing applications.

3.4 IPAnema 2 Measurement Device

A cable-based 6-D pose measurement systems completes the IPAnema system family. The measurement system was build from industry standard cable length measurement sensors that were arranged on a simple planar frame. The drums are equipped with passive springs to keep tension on the cables and with optical absolute encoders with a position accuracy of around 0.05 mm and a maximum cable length of $l_{max} =$ 7.5 m. The length measurement can be taken from the encoders with a frequency of 1 kHz. The embedded IPC records and evaluates the measured length in a PLC.

Fig. 8 IPAnema 2 Measurement Device: Cable sensor based 6-D-pose measurement system applied to measure the pose of an industrial robot: (1) base with winch arrangement, (2) cable length sensors, (3) mobile platform, (4) embedded IPC with real-time pose estimation
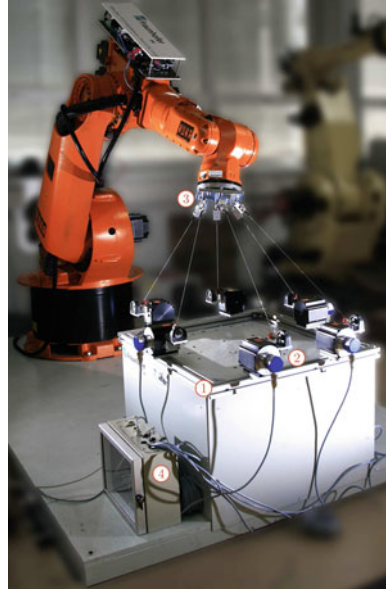
The CoDeSys PLC by S3 is one of our target hardware platform that have to run the forward kinematic codes as presented in [21] (Fig. 8).

4 Performance and Results

The demonstrator system IPAnema 1 is depicted in Fig. 6. The hardware of the robot was used for experimental evaluation of the system. Due to space limitations in this paper, we can only report a selection of measurements that were recorded using the IPAnema system.

4.1 Repeatability

Here, we focus on some tests according the norm ISO 9283, which describes performance criteria for robots and which are important to evaluate if the robot's technique is adequate for assembly operations. The measurements were performed using a Leica Absolute Laser Tracker AT901-MR with a certified absolute accuracy of less than $10\,\mu\mathrm{m}$.

As an example, the definition of the position repeatability is shown in Fig. 9. Similar definitions are detailed in ISO 9283 for the path repeatability and for the distance repeatability. Following the evaluation procedure given in the norm 30 single

Fig. 9 Definition of the position repeatability
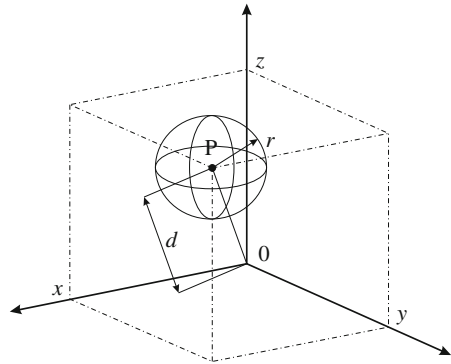
measurements were taken at different velocities of the robot ($v_1 = 0.5$ m/s, $v_2 = 2.5$ m/s, $v_3 = 5$ m/s). The pose repeatability was found to be smaller than $r_{\text{Pose}} = 0.75$ mm for all velocities where it largely depends on the nominal velocity. Interestingly, it was found that the best values could be achieved with highest velocity of the cable robot where a repeatability better than $r_{\text{Pose}}^{(3)} = 0.35$ mm was determined. For the distance repeatability a value better than $r_{\text{Dis}} = 0.2$ mm was determined. For distance repeatability we measured better values at lower velocities were good values of less than $r_{\text{Dis}}^{(1)} = 0.06$ mm were measured for v_1. Finally the path repeatability was investigated and the experiment yields a value than $r_{\text{Path}} = 0.5$ mm. Again, the best values were measured for v_1 where the repeatability was $r_{\text{Path}}^{(1)} = 0.17$ mm.

The experimental evaluation of the cable robot yields encouraging results to underline that the cable robot technology seems capable of performing the required assembly operations. It is expected that additional efforts in terms of calibration and improvements on the kinematic model can further increase the performance of the robot.

4.2 Stiffness Evaluation

In the following we present some experimental data for the cable robot IPAnema 1, which parameters are listed in Table 1. In the experimental setup, cables made from Dyneema were used. The diameter of the cables was $d = 1.5$ mm. The platform was moved to the measurement positions p. Then an additional cable was connected to a mass element of $m = 10$ kg by means of a pulley. Therefore, a static forces $f = gm$ was exerted on the mobile platform. For each measurement position p the pulley was located so that the force acts along each coordinate axis, both in positive and negative direction. For the measurement positions 4–7, it was not possible to fix the pulley above the platform. Therefore, in these cases only five rather than six forces were exerted on the platform. The Cartesian displacement δr of the platform

Table 3 Experimental determination of the stiffness and compliance matrix for the IPAnema 1 prototype

Position	r (mm)	Compliance matrix C (μm/N)	Stiffness matrix K (N/μm)
1	$\begin{pmatrix} 0 \\ 0 \\ 1500 \end{pmatrix}$	$\begin{pmatrix} 7.28 & 1.08 & -0.69 \\ -0.07 & 9.33 & 0.00 \\ 0.37 & 0.00 & 24.70 \end{pmatrix}$	$\begin{pmatrix} 0.137 & -0.015 & 0.003 \\ 0.001 & 0.107 & 0.000 \\ -0.002 & 0.000 & 0.040 \end{pmatrix}$
2	$\begin{pmatrix} 0 \\ 0 \\ 500 \end{pmatrix}$	$\begin{pmatrix} 6.88 & 1.17 & -0.62 \\ -0.08 & 12.05 & 0.16 \\ 0.70 & 1.42 & 22.10 \end{pmatrix}$	$\begin{pmatrix} 0.144 & -0.014 & 0.004 \\ 0.001 & 0.082 & -0.000 \\ -0.004 & -0.004 & 0.045 \end{pmatrix}$
3	$\begin{pmatrix} 0 \\ 0 \\ 1000 \end{pmatrix}$	$\begin{pmatrix} 6.57 & 1.19 & -1.03 \\ -0.05 & 9.81 & -0.11 \\ -0.28 & 1.70 & 22.31 \end{pmatrix}$	$\begin{pmatrix} 0.152 & -0.019 & 0.006 \\ 0.000 & 0.101 & 0.000 \\ 0.001 & -0.008 & 0.044 \end{pmatrix}$
4	$\begin{pmatrix} -1200 \\ 0 \\ 1000 \end{pmatrix}$	$\begin{pmatrix} 10.89 & 7.92 & -1.71 \\ -0.55 & 15.91 & -0.36 \\ -4.30 & -0.26 & 20.49 \end{pmatrix}$	$\begin{pmatrix} 0.092 & -0.045 & 0.006 \\ 0.003 & 0.061 & 0.001 \\ 0.019 & -0.008 & 0.050 \end{pmatrix}$
5	$\begin{pmatrix} -800 \\ -300 \\ 600 \end{pmatrix}$	$\begin{pmatrix} 7.04 & 2.17 & -0.66 \\ -2.38 & 12.59 & 0.29 \\ -1.27 & 0.57 & 21.92 \end{pmatrix}$	$\begin{pmatrix} 0.134 & -0.023 & 0.004 \\ 0.025 & 0.075 & -0.000 \\ 0.007 & -0.003 & 0.045 \end{pmatrix}$
6	$\begin{pmatrix} -800 \\ -600 \\ 1400 \end{pmatrix}$	$\begin{pmatrix} 7.56 & 0.15 & -0.74 \\ -4.52 & 11.24 & 2.04 \\ -2.00 & 2.14 & 21.77 \end{pmatrix}$	$\begin{pmatrix} 0.131 & -0.002 & 0.004 \\ 0.051 & 0.089 & -0.006 \\ 0.007 & -0.009 & 0.047 \end{pmatrix}$
7	$\begin{pmatrix} 0 \\ -900 \\ 1000 \end{pmatrix}$	$\begin{pmatrix} 6.43 & 0.47 & 0.36 \\ 0.64 & 13.79 & 3.03 \\ 0.19 & 2.78 & 20.06 \end{pmatrix}$	$\begin{pmatrix} 0.156 & -0.004 & -0.002 \\ -0.007 & 0.075 & -0.011 \\ -0.000 & -0.010 & 0.051 \end{pmatrix}$

For seven poses of the platform the translational stiffness was determined by applying a load to the platform. Measurements were taken with and without the load. The load was applied through an attached cable with a mass element as counter weight. The Euclidian displacement of the platform was measured with a laser tracker with a very high accuracy

was measured using the same a Leica Absolute Tracker. For different magnitudes of the force, different directions, and different displacements the stiffness matrix was measured. The results of the stiffness determination are shown in Table 3.

5 Conclusions

In this paper we give a brief overview of the state of the art at the Fraunhofer IPA. We introduce the IPAnema family of cable robots, which are highly versatile. Furthermore, details on the methods for planning and simulation of the cable robot were presented. Finally, the cable robot IPAnema was evaluated based on ISO 9283. The experimental results indicate that the cable robot technology is feasible for handling and assembly operations.

References

1. Albus, J.S., Bostelman, R.V., Dagalakis, N.G.: The nist robocrane. J. Res. Nat. Inst. Stand. Technol. **97**(3), 373–385 (1992)
2. Aref, M.M., Taghirad, H.D., Barissi, S.: Optimal design of dexterous cable driven parallel manipulators. Int. J. Robotics **1**, 29–47 (2009)
3. Baoyan, D., Qiu, Y-Y., Fushun, Z., Zi, B.: Analysis and experiment of the feed cable-suspended structure for super antenna. In: IEEE/ASME International Conference on Advanced Intelligent Mechatronics, AIM 2008, pp. 329–334 (2008).
4. Bruckmann, T.: Auslegung und Betrieb redundanter paralleler Seilroboter. Universität Duisburg-Essen (2010).
5. Dagalakis, N.G., Albus, J.S., Wang, B.-L., Unger, J., Lee, J.D.: Stiffness study of a parallel link robot crane for shipbuilding applications. ASME J. Mech. Des. **111**(3), 183–193 (1989)
6. Fang, S.: Design, Modeling and Motion Control of Tendon-Based Parallel Manipulators. Fortschritt-Berichte VDI, Reihe 8, Nr. 1076. VDI Verlag, Düsseldorf (2005).
7. Gouttefarde, M., Merlet, J.P., Daney, D.: Wrench-feasible workspace of parallel cable-driven mechanisms. In: ICRA, pp. 1492–1497. Rome, Italy (2007).
8. Heyden, T.: Bahnregelung eines seilgeführten Handhabungssystems mit kinematisch unbestimmter Lastführung. Fortschritt-Berichte VDI, Reihe 8, Nr. 1100. VDI Verlag, Düsseldorf (2006).
9. Hiller, M., Fang, S., Mielczarek, S., Varhoeven, R., Franitza, D.: Design, analysis and realization of tendon-based parallel manipulators. Mech. Mach. Theor. **40**(4), 429–445 (2005)
10. Kawamura, S., Tanaka, W.S., Pandian, S.R.: Development of an ultrahigh speed robot falcon using wire drive system. In: IEEE International Conference on Robotics and Automation, pp. 1764–1850 (1995).
11. Lafourcade, P., Llibre, M., Reboulet, C.: Design of a parallel wire-driven manipulator for wind tunnels. In: Gosselin, C.M. Ebert-Uphoff, I. (eds.) Workshop on Fundamental Issues and Future Research Directions for Parallel Mechanisms and Manipulators, Quebec City and Canada (2002).
12. Lafourcade, P., Zheng, Y-Q., Liu, X.: Stiffness analysis of wire-driven parallel kinematic manipulators. In: Proceedings 11th World Congress on Theory of Machines and Mechanisms, IFToMM, Tianjin and China (2003).
13. Maeda, K., Tadokoro, S., Takamori, T., Hiller, M., Verhoeven, R.: On design of a redundant wire-driven parallel robot warp manipulator. In: Proceedings of IEEE International Conference on Robotics and Automation, pp. 895–900. Detroit and MI and USA (1999).
14. Maier, T.: Bahnsteuerung eines seilgeführten Handhabungssystems. Fortschritt-Berichte VDI, Reihe 8, Nr. 1047. VDI Verlag, Düsseldorf (2004).
15. Merlet, J.P.: Kinematics of the wire-driven parallel robot marionet using linear actuators. Proceedings of the IEEE International Conference on Robotics and Automation, Pasadena and CA and USA, In (2008)
16. Miermeister, P., Pott, A., Verl, A.: Dynamic modeling and hardware-in-the-loop simulation for the parallel cable robot ipanema. In: ISR/Robotik 2010, Munich and Germany (2010).
17. Otis, M.J.-D., Comtois, S., Laurendeau, D., Gosselin, C.M.: Human safety algorithms for a parallel cable-driven haptic interface. Adv. Intell. Soft Comput. **83**, 187–200 (2010)
18. Otis, M.: J-D., Perreault, S., Dang, T-L. N., Lambert, P., Gouttefarde, M., Laurendeau, D., Gosselin, C.M.: Determination and management of cable interferences between two 6-dof foot platforms in a cable-driven locomotion interface. Man. Cybern. Syst. **39**(3), 528–544 (2009)

19. Perreault, S., Cardou, P., Gosselin, C.M., Otis, M. J-D.: Geometric determination of the interference-free constant-orientation workspace of parallel cable-driven mechanisms. ASME J. Mech. Rob. 2(3) (2010).
20. Pott, A.: Forward kinematics and workspace determination of a wire robot for industrial applications. In: ARK, pp. 451–458, Springer, Baz-sur-Mer and France (2008).
21. Pott, A.: An algorithm for real-time forward kinematics of cable-driven parallel robots. In: 12th International Symposium on Advances in Robot Kinematics, Springer, Piran Portoroz and Slovenio (2010).
22. Pott, A., Bruckmann, T., Mikelsons, L.: Closed-form force distribution for parallel wire robots. In: Computational Kinematics, pp. 25–34, Springer, Duisburg and Germany (2009).
23. Pott, A., Meyer, C., Verl, A.: Large-scale assembly of solar power plants with parallel cable robots. In: Robotics (ISR), 2010 41st International Symposium on and 2010 6th German Conference on Robotics (ROBOTIK), pp. 1–6 (2010).
24. Rauter, G., von Zitzewitz, J., Duschau-Wicke, A., Vallery, H., Riener, R.: A tendon-based parallel robot applied to motor learning in sports. In: Proceedings of the 2010 3rd IEEE RAS and EMBS, Tokyo and Japan (2010).
25. Surdilovic, D., Bernhardt, R.: String-man: a new wire robot for gait rehabilitation. In: Proceedings of IEEE International Conference on Robotics and Automation, pp. 2031–2036. New Orleans (2004).
26. Surdilovic, D., Jinyu, Z., Bernhardt, R.: String-man: Wire-robot technology for safe, flexible and human-friendly gait rehabilitation. In: IEEE 10th International Conference on Rehabilitation Robotics, ICORR 2007, pp. 446–453 (2007).
27. Tadokoro, S., Verhoeven, R., Hiller, M., Takamori, T.: A portable parallel manipulator for search and rescue at large-scale urban earthquakes and an identification algorithm for the installation in unstructured environments. In: Proceedings of International Conference on Intelligent Robots and Systems IROS 1999, Kyongju and South Korea (1999).
28. Verhoeven, R.: Analysis of the Workspace of Tendon-based Stewart Platforms. PhD thesis, University of Duisburg-Essen, Duisburg (2004).
29. von Zitzewitz, J., Rauter, G., Steiner, R., Brunschweiler, A., Riener, R.: A versatile wire robot concept as a haptic interface for sport simulation. In: Proceedings of the 2009 IEEE International Conference on Robotics and Automation (ICRA), Tokyo and Japan (2009).
30. von Zitzewitz, J., Rauter, G., Vallery, H., Morger, A., Riener, R.: Forward kinematics of redundantly actuated, tendon-based robots. In: Proceedings of the 2010 IEEE/RSJ International Conference on Intelligent Robots and Systems (IROS) (2010).

A Reconfigurable Robot for Cable-Driven Parallel Robotic Research and Industrial Scenario Proofing

Jean-Baptiste Izard, Marc Gouttefarde, Micaël Michelin,
Olivier Tempier and Cedric Baradat

Abstract Picturing the interest of research institutions and industrial actors, the list of research and demonstration parallel cable-driven robot prototypes is growing by the day. LIRMM and Tecnalia have decided to put knowledge in common in order to develop novel concepts for cable-driven parallel robotics and demonstrate its capabilities in industrial tasks. We have developed together a reconfigurable cable robot for this purpose. The robot main characteristics, e.g. footprint, mobile platform geometry and drawing point layout can be modified at will, making it particularly suitable for studying in good conditions new configurations or novel control laws, as well as any scenario suggested by our partners. The present paper first provides an overview of the robot. Afterwards, a more specific view on the different components and the capabilities of reconfiguration are presented, as well as examples of layouts meant for various research and industrial projects.

1 Introduction: Previous Art

The different scientific developments that occurred in the past years in cable-driven parallel robotics have brought today the introduction of these concepts in factories, civil work sites, buildings and warehouses just a step away. Scientific developments are still underway, e.g. on the control of cable-driven parallel robots in crane-like configurations, a promising branch of parallel cable-driven robotics in terms of applications. One of the major limitations to transposing cable-driven robots to industry is however them being accepted for carrying out real world applications. Parallel

J-B Izard (✉) · M. Michelin · C. Baradat
Tecnalia France MIBI, 672 rue du Mas de Verchant, 34000 Montpellier, France
e-mail: jeanbaptiste.izard@tecnalia.com

M. Gouttefarde · O. Tempier
LIRMM, UMR 5506, CC 477, 161 rue Ada, 34095 Montpellier Cedex 5, France

cable-driven robot reconfigurability is probably a key to this issue especially when various tasks are assigned to the robot.

Since the development of the FALCON [1] and of the Robocrane [2], which were among the first proofs of operability with good performances for fast manipulations, numerous contributors have developed various options for operation of cable-driven parallel robots. Applications requiring movements in a large workspace for crane-like applications [2], emergency deployable robots [3, 4], giant telescopes [5], aerial cameras [6, 7], service robotics [4] and positioning and measuring systems in wind tunnels [8] may be cited. Several others parallel cable-driven robots for research have been developed, e.g. the SEGESTA [9] and IPAnema [10].

Each of the aforementioned applications has specific requirements, which lead to different parallel cable robot configurations. At LIRMM and Tecnalia, we have considered the recent constraints in academic research that urged to develop new technical concepts, such as specific control laws and cable models, and on the other hand the pressing need by potential end users of cable-driven robots to have at their disposal a parallel cable-driven robot prototype. The main goal is to test different scenarios and different robot configurations: different operational spaces (e.g. planar, spatial, with different numbers of degrees of freedom), various platform configurations (flat, single point, spatial), different cable layouts (crane-type suspended configurations, fully constrained designs) and different constraints on the design due to the objectives of the scenario at hand. As a result, we have carried out research on choosing the optimal configuration for a specific scenario, but we also developed a parallel cable-driven prototype that is easily reconfigurable. This prototype is called ReelAx. The purpose of this paper is to describe the main components of ReelAx and the various configurations that have been tested so far.

2 Specifications

Geometry specifications are based on the positions of the cable output points, which are the points at which the cable are drawn out from the base frame, and the attachment points, where the cables are attached to the mobile platform. The first geometrical requirement of ReelAx is reconfigurability. It should be possible to easily modify the positions of the output points and of the attachment points, and also the cable connection between them.. In addition, the different elements of the cable robots should be easily transported. The maximum number of cables is 8.

The size of the maximum workspace of the robot is limited by the total length of each cable. This length has been set at 6.6 m to be able to cross the diagonal of a 4 m edge cube, and thus in order to be able to sweep through a workspace larger than that of most serial robot. The height of the output points shall be up to 3 m above the ground.

The platform maximum load is 25 kg. It has been decided that the cables should be able to resist the full weight of the platform each with some margin, that lead to
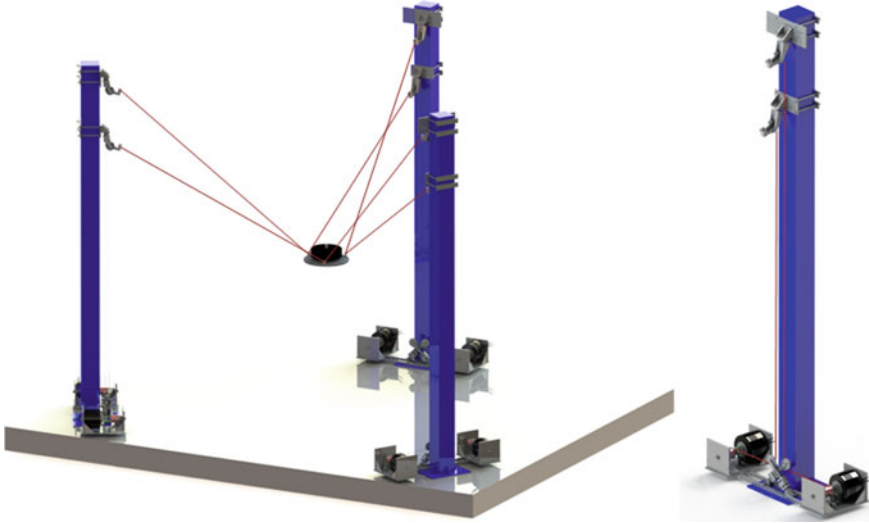
Fig. 1 *Left* general view of the suspended ReelAx6 configuration with three posts and six cables. *Right* view of a single post

a maximum tensile force in the cable of 300 N. Typical mobile platform velocities imply cable length modification speeds up to 1.5 m/s.

The cable routing between the drum and the output point should include a force sensor in a way that cable tension can be measured. In addition, in order to avoid any perturbation on the geometrical model of the robot, the routing path of the cable should be of the same length whatever the length of cable reeled in.

3 ReelAx Design Description

3.1 General Layout

A base frame must be built in order to assemble the various components of the cable-driven robot. This structure has to withstand the forces applied by the components which are due to the loading of the cables, whose sum is equal to the weight of the platform and the dynamic forces it undergoes. In the case of the robot ReelAx, the structure is composed of up to 4 steel posts that are 3 m high, with 2 cables being attached to each post (Fig. 1).

With these 4 posts, the reconfigurability is typically carried out in three steps:

- The first one is the selection of the number and of the positions of the posts around the workspace. It sets the horizontal dimensions of the maximal workspace and the number of cables.

- Second, the position of each post output points are configured, moving a block which redirects the cable. Indeed, each output point block can be clamped anywhere on the post, and the user is free to set the horizontal spacing between the output points (within a limited range).
- Third, the platform is designed to have the dimensions that are required by the application at hand, and built on purpose with standard interfaces for cables.

The winches are placed at the bottom of the posts. They cannot be moved. The cable goes out of the winch at the same position whatever the angular position of the drum and is then directed towards a vertical pulley, which deflects it to the output point block with a constant 90° angle. The vertical pulley is fitted with a force sensor that measures the effort on the pulley, thanks to the constant angle between the in and out portions of the cable in the pulley.

The robot is controlled using a MathWorks xPC Target based controller. As a result, control laws are designed using MATLAB and Simulink. The robot controller is connected to the posts using a real-time Ethernet bus, based on EtherCAT protocol, to which the drives of the motors are connected as well. Using this protocol, the posts can be up to 100 m apart from each other. Each post is equipped with one AccurET drive from ETEL Motion Technology that is able to control the two winches of the post. These latter are actuated by brushless direct-drive servo motors. Each drive also gathers the outputs of the force sensors to send them to the controller. Between each post run the power line and an emergency stop signal pair as well.

During an initialization phase, the cable tensions are brought to levels set by the user using a basic force control loop on the winches. The controller switches to a position or to a hybrid force/position feedback control loop once the cable lengths are initialized. The tensions in the cables should be high enough for the cables to be straight. During the initialization, it may be necessary to fix the platform to the ground or, in case of fully constrained configuration, to a collapsible stand (if the platform mass is too low, for example). Let us note that this initialization phase may be simplified if absolute multi-turn encoders are used. It is not currently the case for ReelAx which uses incremental encoders.

As the first reconfiguration step implies moving the posts, it should not be carried out very frequently since the posts must be either attached to the ground or attached to ballast at its base.

The two other reconfiguration steps can be more easily carried out, and will be used extensively as illustrated in the last section of this paper, in which the different configurations that have been tested with ReelAx are presented.

3.2 Winches

The main constraint on the design of the winches was to be able to reel in and out the cable without modifying the position of the point at which the cable is drawn out from the drum. In order to fulfill this requirement, the winches have been
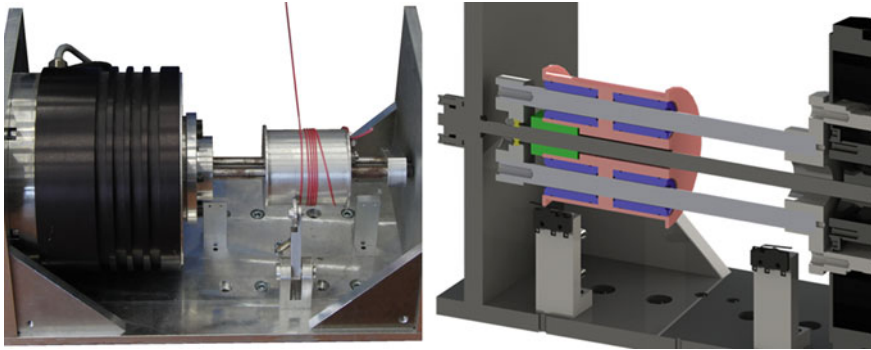
Fig. 2 Views of the first version of the winches. *Right* is a cut CAD view, with the drum part in *red*, the cylindrical bearings in *blue*, the screw nut in *green* and other turning parts in *grey*

designed with a drum having a combined translational and rotational movement so that, when the cable is wound or unwound on the drum, its exit point is kept at the same position. Several kinematic solutions have been studied, all of them using a screw/nut joint to generate the combined translational-rotational movement of the drum from the rotation of the motor. The solution has been chosen in order to optimize the compactness of the winch, regarding both the length of the winch with respect of that of the drum and the diameter of the drum. Simplicity of realization was also a concern that led to the actual design of the winch.

As shown in Fig. 2, the mechanism set in motion by the direct-drive motor uses two shafts on which sits the drum by means of two cylindrical bearings. The drum both sits on these bearings and on the nut of a ball screw, the screw being fixed to the main frame of the mechanism. As a result, the rotational motion of the motor is transmitted to the drum through the two shafts and cylindrical bearings, this rotational motion being transformed in a combined translational-rotational motion by the screw/nut joint.

Given the maximal tension in the cable of 300 N, the different parts have been dimensioned. Using a ball screw with a restrained cost implies a quite large nut, which forces the diameter of the drum up to 65 mm. Given this diameter, the motor should run at 440 rpm with a torque up to 10 Nm, preferably in direct drive: The ETEL Motion Technology direct-drive motor RTMB-140-070 has been selected. This motor has the advantage of having a hollow shaft so that the screw can run across the whole mechanism and the motor. 300 N corresponds to the maximum recommended tension in a Ø1 mm steel wire with 1780 MPa tensile strength (50 % of the breaking load), therefore the pitch of the screw has been set at 2 mm. The maximum cable diameter that may be used in ReelAx will therefore be Ø2 mm, made of steel or other cable material such as Dyneema. With a 63 mm long drum, this corresponds to more than 6 m of cable that can be reeled in.

As shown in Fig. 3, a second version of the winch has been designed based on the experience of the first one. Indeed, the juxtaposition of the two sets of cylindrical ball
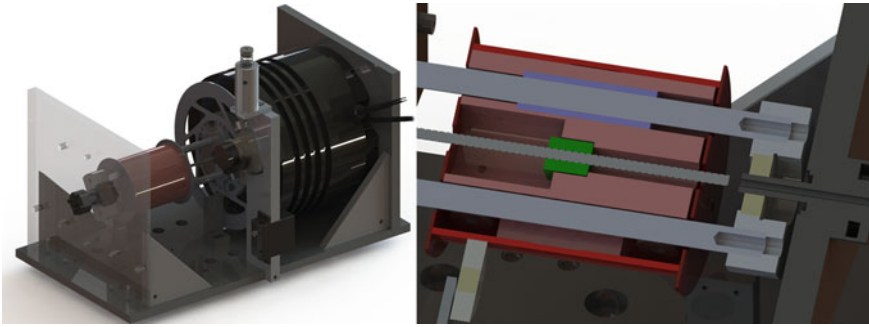
Fig. 3 *Left* CAD view of the final version of the winches; *Right* close-up on the cut view of the drum (same color coding as in Fig. 2)

bearings and the ball screw leads to an overconstrained design that induces internal forces in the mechanism and additional friction. In the second version, one of the rods is fitted with a pair of bronze bushings, while the other is held by a pair of rollers on the pulling side of the drum and a PTFE cushion on the other side, with a clearance of 0.5 mm. Using smaller rods, this could have led to smaller drums; however, we chose to keep same drum outer diameter than the previous design in order not to change the speed and torque of the motor for a given tension and speed at the level of the cable. The ball screw has been replaced by a smaller screw with a low-friction Haydon-Kerk nut. In this second version of the winches, a notable difference is that the screw does not run through the whole mechanism. It is held on the side of the motor only. Misalignment is therefore compensated for by the flexibility of the screw induced by the long cantilever arm between the nut and the screw holding position (at least 170 mm) and the screw small diameter (Ø3.3 mm). These nuts also exist in 1 and 0.5 mm pitch, which would allow reeling in longer cables if needed in future applications, with the constraint of using smaller cables. In addition, changing the screw pitch in the assembly requires little investment.

Moreover, a current loss brake system has been set in place for all of the winches. In addition, considering the poor behavior of Dyneema cables under stress (creeping, low breaking force when loaded for several hours) and in order to test the effect of sagging cables, the cables have been replaced by steel cables with a diameter of 1 mm and a breaking load of 600 N.

3.3 Output Blocks: Cable Exit Points

The output blocks shown in Fig. 4 have been designed with the following objectives: to provide a wide range of possibilities for the positioning of the output points for reconfigurability, to ensure that the positions of the output points do not change over
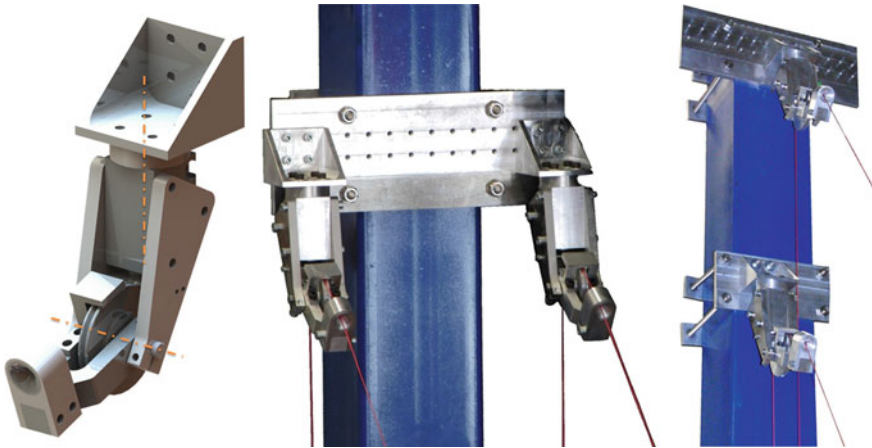
Fig. 4 *Left to right* CAD view of the output blocks, with *orange lines* showing the axes of rotation set by the user; two different configurations of the output blocks

time and to maintain the cable routing steady whatever the position and orientation of the robot mobile platform.

The reconfigurability constraint has been addressed by designing a generic output block that may be placed wherever it is needed on the post. In order to fix it, milled plates have been designed with an array of holes for placing and maintaining in place the output block. On each post, it is possible either to place the two pulleys on the same plate, thereby positioning the two output points at the same height separated by a distance from 75 to 300 mm (central picture in Fig. 4), or else to place them on different plates that may be clamped anywhere along the post, up to 3 m high (right picture in Fig. 4).

In each output block, the cable first comes in contact with a freewheeling pulley. This pulley is fixed on a part which can be turned around an axis materialized by the vertical part of the cable coming from the drum. The orientation of this rotating part is set by the user and held in place by a set of screws. The cable is then redirected toward any point in the workspace by means of an eyelet. This latter is a part having a pseudosphere shape obtained by revolving a portion of circle around its tangent, the tangent being the axis of the cable coming from the pulley. The cable sits and slides on this pseudosphere shaped part when pulled. The output point is considered to be where the axis of the cable and the circle generating the pseudosphere intersect (Fig. 5). In order to optimize the output point position, the user can set the eyelet towards the centre of the workspace by means of a user defined rotation about a horizontal axis as shown in the (left part of Fig. 4).

In order to have a strictly constant output point from which the length of the cable can be computed using the distance between this point and the attachment point on the mobile platform, the last part should feature a pseudosphere generated by a circle with a null radius. This is obviously not possible as it would severely
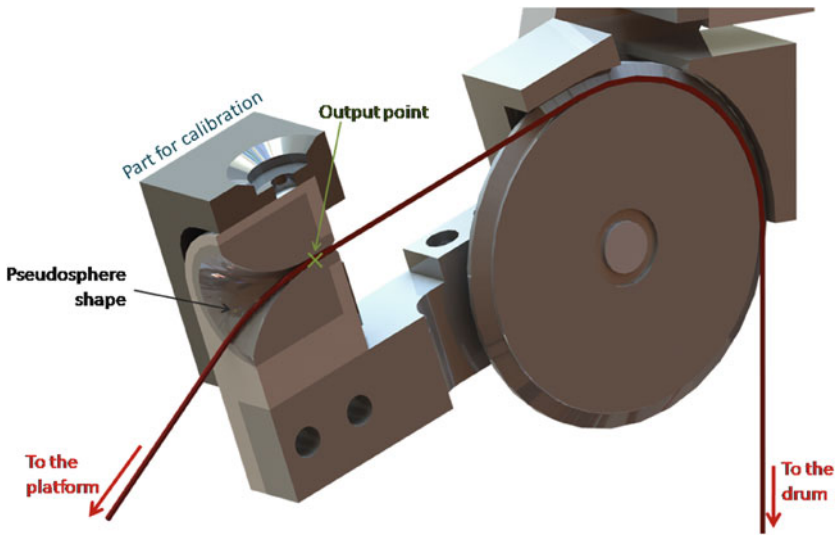
Fig. 5 Cut CAD view of the eyelet in the pulley assembly showing the elements of the eyelet

damage the cable when it runs on the eyelet. The radius has been set at 10 times the maximum cable diameter which is equal to 2 mm (corresponding to the pitch of the winch screw) that is to 20 mm. The maximum deflection angle is of 60°. With this design, the error between the distance separating the attachment point and the output point (taken as the cable length in the control law) and the actual cable length is 3.5 mm error on the cable length when the attachment point distance to the eyelet is 400 mm (the typical dimension of a platform) and the deflection of the cable at 60° from the revolution axis the pseudosphere. The error is less than 1.5 mm when this angle is 45° at the same conditions, which may happen when the workspace is square or rectangular with the posts at the corners.

Calibration of the position of the output points has been done using a laser tracker system. A specifically designed part, featuring cavities with magnets for placing the laser tracker target, is placed on the eyelet during the measures. This part is shown in Fig. 5.

4 Tested Configurations

4.1 ReelAx6: 6 Cable Suspended Triangle Configuration

The first tested configuration of the reconfigurable robot ReeAx was a suspended underconstrained configuration with 6 cables and 3 posts called ReelAx6 (Fig. 6). The mobile platform having 6 degrees of freedom (DOF), the robot was not redundantly
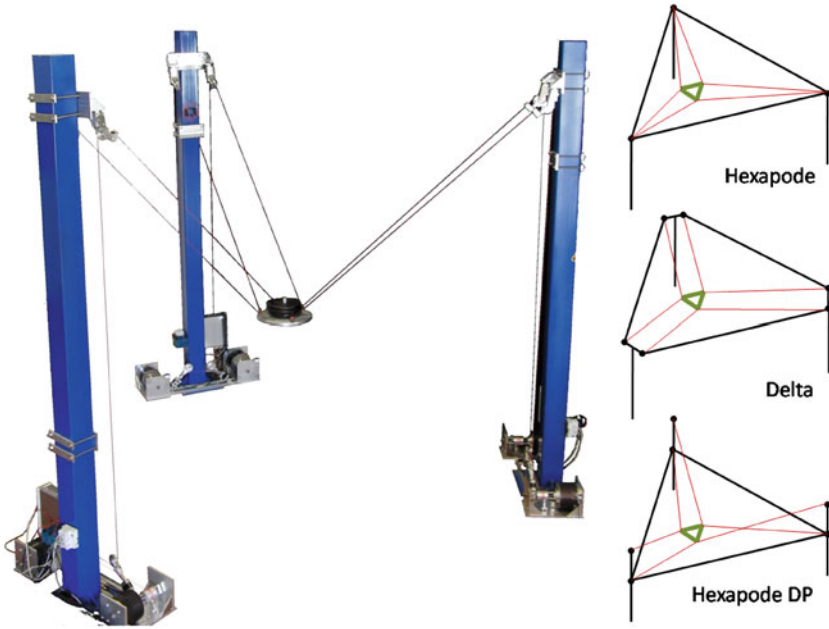
Fig. 6 ReelAx6 global view (*left*) and the three tested configurations (*right*)

actuated. The posts are placed at the vertices of an equilateral triangle measuring 3 m on each side. Its original purpose was to compare several typical geometries of parallel kinematic machines in the case of a parallel cable-driven parallel robot with a triangular footprint and a planar platform.

ReelAx6 used the first version of the winch design (Fig. 2) and the cables were Dyneema cables. The controller was very basic allowing us only to provide waypoints to each motor. To coordinate the movements of the winches, the trajectory was thus separated into several small continuous parts.

4.2 ReelAx 2D Paint: Redundant Fully Constrained Planar 2-DOF

The first reconfiguration of ReelAx occurred for a joint experimentation with the Ecole des Beaux-Arts, during which art students were to use new technologies to carry out creative art. The goal of the experiment was to reproduce famous paintings using a parallel cable-driven robot, which led us to change the design of ReelAx6 into a planar fully constrained design. The mobile platform was working in the vertical plane delimited by two posts from the ReelAx6 configuration (Fig. 7).
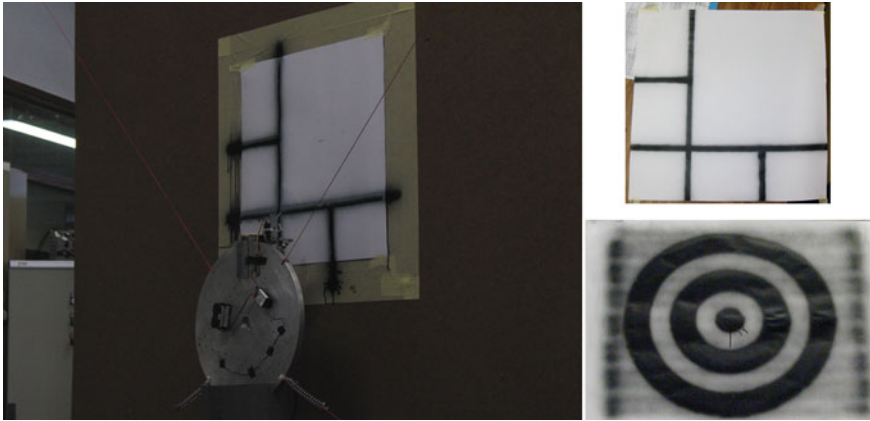
Fig. 7 View of the 2D paint configuration during operation. *Right pictures* show works painted using the robot, inspired by original works by Mondrian and Jasper Johns

Paint was delivered to the platform through an umbilical, and the operation of the paint spray gun was carried out remotely by the user.

In order to deal with the redundancy using the drives that, at this time, were not able to carry out torque control on the motors, the bottom cables have been attached to the mobile platform using springs. The flexibility thereby added allowed the use of the same basic control strategy as in ReelAx6.

4.3 Media-TIC: Redundant Fully-Constrained 6-DOF

ReelAx has also been reconfigured with an additional post and two winches in order to deal with redundantly actuated parallel cable robots. Cables are now steel cables, and the two added winches have been designed with the new version shown in Fig. 3.

The corresponding cable robot prototype has been called ReelAx8. The goal of the first studied configuration was to validate the ReelAx8 design with control laws that have been developed in the state of the art. The configuration chosen for these primary tests was a fully constrained 8 cable configuration (Fig. 8).

The goal of this research was also to validate the control laws foreseen to be used in a parallel cable-driven robot to be installed on the facade of an emblematic building of the city of Barcelona in Spain, the Media-TIC building. This project is currently in waiting for the construction permits to carry on the installation of the robot.

The control law that has been selected for its simplicity was developed by Lafourcade [11] for the SACSO robot, integrates two control parameters: the geometric target position, for following the trajectory, and the desired mean tension in the cables. In the case of the Media-TIC robot, the energy consumed is provided
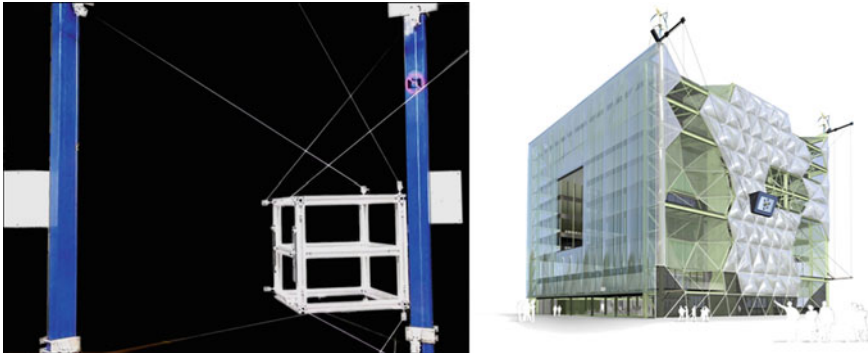
Fig. 8 *Left* the ReelAx8 fully-constrained configuration under testing. *Right* artist view of the Media-TIC building with a parallel cable-driven robot installed on one of its facades

by windmills: the mean tension parameter is therefore used to increase the lateral stiffness of the robot when wind is blowing to resist effects of gusts, which also increases the energy consumption. When wind is low, the energy consumption has to be decreased and the lateral stiffness is lower.

4.4 ReelAx8: CoGiRo

In the framework of the CoGiRo ANR project [12], an example of application has been suggested for the design of a parallel cable robot prototype, namely the transportation of loads over about 10 m, with optimization of the design to have the best robustness to non-centered loads. This leads us to the ReelAx8–CoGiRo design shown in Fig. 9 [13]. The robot overall occupied space measures $4 \times 3 \times 3$ m^3 (L × l × h), while its platform is a cube measuring 400 mm in edge, weighting 6.2 kg. It is actuated with Ø1 mm steel cables.

This ReelAx8 design has since been used to perform preliminary tests, notably of control laws, in prevision of the large size CoGiRo prototype shown in the bottom image of Fig. 9.

The final design of the CoGiRo prototype is a 16 m long, 12 m large, 6 m high cable-driven parallel robot, which should be able to lift a 500 kg payload at 2 m above the ground within a 10×8 m^2 rectangle. It is actuated by Ø4 mm cables, and features a self-supporting frame made of aluminium truss elements. The robot mobile platform is a cube measuring 1 m on the side. This design can cope with payload off-centered by 0.275 m, which is the best performance among 20738 configurations studied.
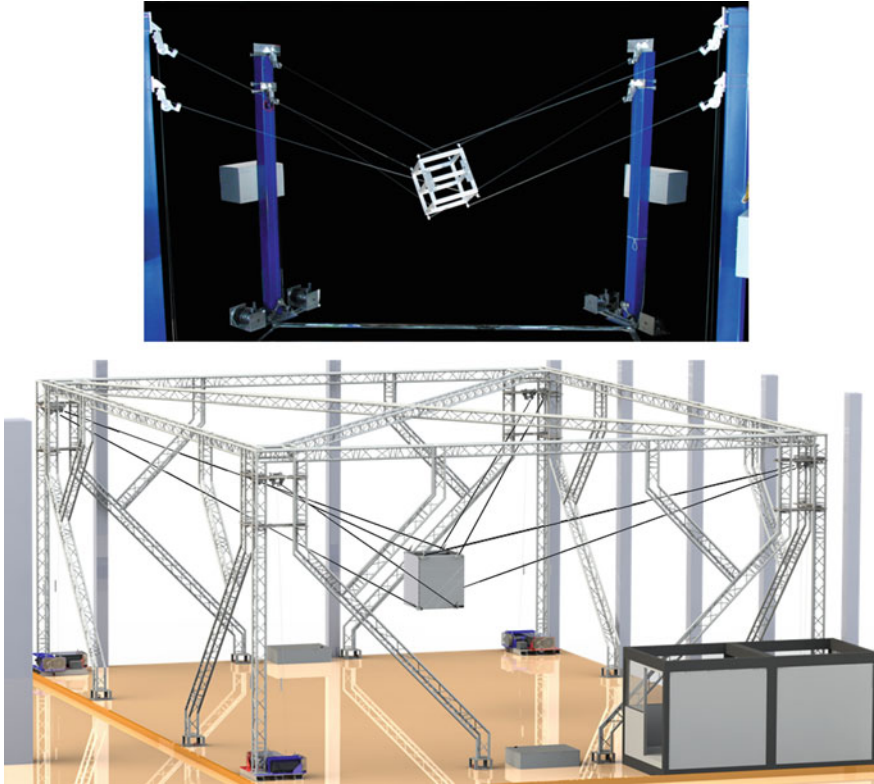
Fig. 9 *Top* ReelAx8 in a suspended redundantly actuated configuration (8 cables, 6 DOF), a preparation for the CoGiRo prototype shown in the *bottom* CAD image

4.5 ReelAx8 Light

A specific test on ReelAx8 related to the research topics of the ANR project CoGiRo has been carried out by changing the platform and checking the corresponding modifications of the robot. The main modification was to use a very light platform, in order to enhance the effects of sagging. It was made of balsa wood, and weights only 160 g, while the weight of all the cables deployed at the test position was around 140 g (Fig. 10). As a reminder, the weight of the platform in the original version of ReelAx8 was 6.2 kg.

The test carried out both with the normal and the light platform was to measure the local stiffness of the robot by pulling with a calibrated force on the platform in various directions and measuring the induced displacements in the same directions. Further work includes the development of a cable model including the effect of sagging in order to correlate with these results, based on the measurement of the sagging curve of a single cable.
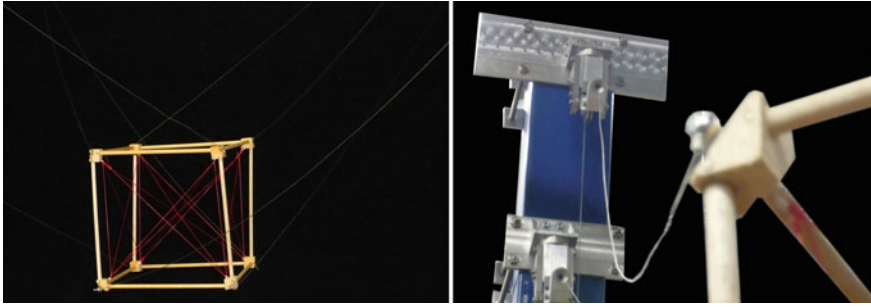
Fig. 10 Views of the ReelAx8 robot with very the light platform. The *right picture* shows a view in the line of sight between an attachment point and the corresponding output point, showing the sagging of the cable

5 Conclusion

This paper presented the LIRMM-Tecnalia reconfigurable parallel cable-driven robot called ReelAx. The robot main characteristics, e.g. footprint, mobile platform geometry and drawing point layout can be modified, making it particularly suitable for studying new configurations or novel control laws as well as various application scenarios. The main components of ReelAx were presented in some technical details together with the various configurations of ReelAx tested so far.

Ongoing and future works are mainly focused on the ReelAx8–CoGiRo suspended redundantly-actuated configuration. The control of such a redundant under- constrained parallel cable-driven robot configuration is a challenging task. We thus plan to test various control schemes and to compare their performances and relative advantages. We also plan to make ReelAx8 perform pick-and-place tasks across its large workspace by embedding a gripper onto its mobile platform.

References

1. Kawamura, S., Choe, W., Tanaka, S., Pandian, S.R.: Development of an ultrahigh speed robot FALCON using wire drive system. In: IEEE International Conference on Robotics and Automation, Nagoya (1995). doi:10.1109/ROBOT.1995.525288
2. Albus, J., Bostelman, R., Dagalakis, N.: The NIST robocrane. J. Robotic Syst. **10**(5), 702–724 (1993)
3. Tadokoro, S., Verhoeven, R., Hiller, R., Takamori, T.: A portable parallel manipulator for search and rescue at large-scale urban earthquakes and an identification algorithm for the installation in unstructured environments. In: IEEE/RSJ International Conference on Intelligent Robots and Systems, Kyongju (1999)

4. Merlet, J.-P.: Kinematics of the wire-driven parallel robot MARIONET using linear actuators. In: IEEE International Conference on Robotics and Automation, Passadena (2008)

5. Dewdney, P., Nahon, M.A., Veidt, B.: The large adaptive reflector: a giant radio telescope with an aero twist. Can. Aeronaut. Space J. **48**(4), 239–250 (2002)

6. SkyCam. http://skycam.tv/

7. SpyderCam. 2012. http://spydercam.com/

8. Lafourcade, P., Llibre, M., Reboulet, C.: Design of a parallel wire-driven manipulator for wind tunnels. In: Gosselin, M., Ebert-Uphoff, I. (eds.) Workshop on Fundamental Issues and Future Research Directions for Parallel Mechanisms and Manipulators, pp. 187–194, Quebec City (2002)

9. Hiller, M., Fang, S., Mielczarek, R., Verhoeven, R., Franitza, D.: Design, analysis and realization of tendon-based parallel manipulators. Mech. Mach. Theory **40**(4), 429–445 (2005). doi:10.1016/j.mechmachtheory.2004.08.002

10. Pott, A.: An algorithm for real-time forward kinematics of cable-driven parallel robots. In: Lenaršiš, J., Stanišič, M. M. (eds.) Advances in Robot Kinematics: Motion in Man and Machine, vol. 8, pp. 529–538. Springer, Heidelberg, (2010). doi:10.1007/978-90-481-9262-5_57

11. Lafourcade, P.: Contribution à l'étude de manipulateurs parallèles à câbles, application à la conception d'une suspension active pour soufflerie. Ph. D. thesis, ONERA-DCSD, Toulouse (2004)

12. CoGiRo Project. http://www2.lirmm.fr/cogiro/

13. Riehl, N.: Modélisation et conception de robots parallèles à cêbles de grande dimension. Ph.D. thesis, UniversitÃ Montpellier II, Montpellier (2011)

Integration of a Parallel Cable-Driven Robot on an Existing Building Façade

Jean-Baptiste Izard, Marc Gouttefarde, Cedric Baradat, David Culla and Damien Sallé

Abstract In order to use a cable-driven parallel robot to inspect an existing surface, a straightforward solution consists in fixing the robot components on this surface. In most cases, however, there are conditions that limit these fixations, for example structural reasons since the frame of the surface has probably not been specifically calculated to withstand the forces generated by the parallel cable-driven robot. In the particular case of inspection of the façade of a building, civil engineering specifications apply, which may drastically reduce the engineering possibilities from the point of view of the parallel cable-driven robot designers. This paper introduces a detailed example of implementation of a parallel cable-driven robot on the Media-TIC building located in Barcelona in Spain. In this highly technological building, the main façade parallel cable-driven robot in intended to work as a sensor for monitoring the environment, but also as an interface between the building and its occupiers. The various constraints—due to normative, structural and aesthetic reasons—that were tackled are described in the paper, along with the elected detailed design of the robot that complies with these constraints.

1 Introduction and Previous Art

Parallel cable-driven robots are well-known to have a potentially very large workspace since very long cable lengths can easily be wound on winch drums. This advan-

J.-B. Izard(✉) · C. Baradat
Tecnalia France, MIBI, 672 rue du Mas de Verchant, 34000 Montpellier
Montpellier, France
e-mail: jeanbaptiste.izard@tecnalia.com

M. Gouttefarde
LIRMM - UMR 5506 - CC 477, 161 rue Ada, 34095 Montpellier Cedex 5
Montpellier, France

D. Culla · D. Sallé
Tecnalia, Mikeletegi Pasealekua, 7, 20009 – San Sebastian Gipuzkoa, Spain

tageous unusual property enables large-scale applications such the one consisting in setting up a parallel cable-driven robot on the façade of a building. During the construction phase of the building, as a temporary tool clamped to the structure of the building, it would be possible to safely and accurately manipulate large windows and panels to install them on the façade, with full control of the rotational degrees of freedom. Moreover, on the finished building, a vertical parallel cable-driven robot gliding on its façade would be able to perform remote visual inspection or cleaning. It may be used as a dynamic local weather station, measuring illumination at different positions on the façade to mitigate sun shade systems, but also pollution and CO_2 levels. In addition, a vertical façade cable-driven robot may also be useful for pest bird scaring and to serve as a dynamic interface with the building's intelligence for the public.

Installation of such a device must respond to particular specifications as they are fixed to a structure that is not necessarily originally purposed to that use. The sidewalk below the façade may also have to be kept free from being impaired, which leads to extra caution when designing the robot in order to avoid failure that could cause harm to nearby pedestrians.

Cable-driven camera systems for sport and entertainment, such as the SkyCam [1] and SpyderCam [2] systems, are typical examples of possible integration of a parallel cable-driven robot on an existing structure, which is not specifically equipped for such an installation. In these particular cases, the drawing points for the 4 cables supporting the camera tilt and pan system are strapped to the building roof main structure as high as achievable above the winches. This solution is suitable due to the low forces that generate these systems as compared to structural forces in the building. Being in action above the public, these systems are designed with very high security factor, from 8 to 12.

The MARIONET-Crane developed by INRIA [3, 4] as a demonstrator of a search and rescue robot is an example similar to the SkyCam and SpiderCam systems, as it is installed on structures that are not meant for that use. However, MARIONET-Crane has more degrees of freedom as it uses 6 cables. The winches are installed around the intervention site, typically on overlooking buildings, and held in place by ballast weight.

SkyCam, SpyderCam and MARIONET-Crane solutions are typically fitted for horizontal low height workspaces, in suspended under-constrained configurations. In the case of a vertical façade parallel cable-driven robot, the most drastic constraint is to reach as much of the façade surface as achievable, including high height. The robot must also be able to counteract forces perpendicular to the façade, even though the footprint of the robot along this direction is required to be much smaller than the dimensions of the building. In other words, transversal stiffness is a major issue.

Overconstrained planar cable-driven robot designs with 3 or 4 cables have been suggested in the state of art as well, which is the typical design needed for moving a platform across a surface [5]. This fully constrained design has been chosen for several research prototypes later on [6–8]. When running on a plane in two dimensions, these designs run on a flat horizontal surface, with gravity supplying the necessary stability on the transversal axis; when the surface is vertical, a device forces the plat-

Fig. 1 Views of the Media-TIC building. *Left*: SE and SW façades; *Right*: SE and NE façades. Credits: José Miguel Hernandez, Iwan Baan

form on the surface to solve the stiffness issue. In the specific issue of the Media-TIC building, the façade is too fragile and irregular for the platform to run on it, making the overconstrained planar design unfitted with this application.

In the present paper, we discuss the different specifications that have been set to a low-profile façade parallel cable-driven robot intended to be installed on the Media-TIC building in Barcelona, Spain. The elected design is then introduced.

1.1 Presentation of the Media-TIC Building

Owned by El Consorci, running the Zona Franca in Barcelona, the Media-TIC building has been designed by the Cloud9 architect agency under the direction of Enric Ruiz-Geli. It is a highly technological building, with a strong focus on new technologies and concepts for achieving zero energy building at reasonable cost. The building itself will run as an incubator for SMEs on new media technologies and TICs. It is placed in an area under the control of 22@Barcelona project by the city of Barcelona. This project features specific incentives for installing pilot tests of innovative solutions to be run within the district, through the 22@Urban Lab.

It is first characterized by an innovative structural design. The main structure of the building is a large steel gantry, covered with glass and ETFE cushions. Instead of being built from the ground to the top, the floors are hanged to the gantry, which liberates space both at the floors, where there is no pillar but simply cables, and at the lobby, which operates as a very wide open volume. The whole structure has been covered with a bioluminescent paint that gives it a faint glow in the night.

This gantry and hung design, enhanced by the beams running a pattern on the south-eastern façade that is driven by the strain due to the wind, give the whole structure a distributed aspect. This focus on distribution has been declined by the architect in every system of the building, from structure to energy and sensors (Figs. 1 and 2).
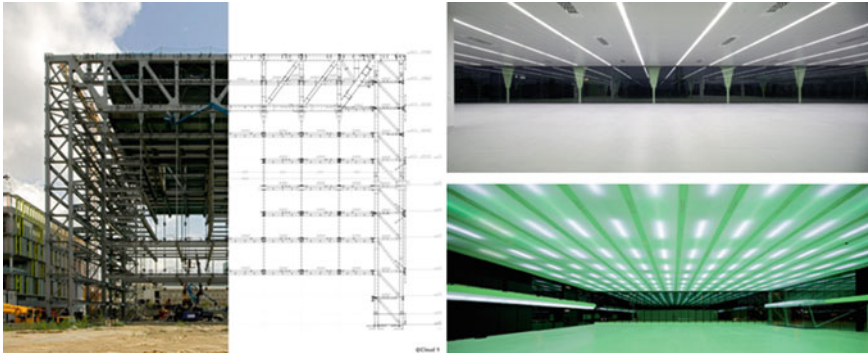
Fig. 2 *Left*: View of the gantry during construction. It is still visible on the NE façade. *Right up*: inside view of one of the floors. *Right bottom*: inside view of the lobby. Credits: Cloud9, Iwan Baan, Luis Ros

Indeed, the whole building is fitted with sensors, for example presence sensors that light the way of occupiers along their path. In addition, the south-eastern façade is fitted with 104 multilayer ETFE cushions, meant for mitigating sunlight, controlled by a pneumatic system based on a light flux sensor, based on an Arduino platform addressable by Ethernet that is individual for each cushion. This results in a dynamic control of the façade. On the other hand, the south-western façade is protected by another series of ETFE cushions, filled with oil mist in order to decrease heat brought by sunlight. Both of these technologies have been patented for the purpose of the Media-TIC building, and have resulted in a 20 % increase of the energy efficiency of the building.

The Media-TIC building makes extensive use of the highly effective urban heat and cooling system set in place in the 22@ district. Solar panels on the roof are a final asset to make the building 60 % more efficient in CO_2 emissions than the average building in Barcelona.

Granular sensor and control throughout the building, as well as different heat mitigation systems and different sources of energy, are some other different ways for the architect to stick to the concept of a "distributed building".

2 Specification

Tecnalia got in contact with the architect cabinet, Cloud9, in order to install a vertical fully constrained cable-driven parallel robot on the south-eastern façade as illustrated in Fig. 3 As it was important not to distort the aesthetics and concepts of the building just as much as making the robot safe for the public and the building, the specifications include both safety and dimensioning constraints on the one hand and aesthetic constraints on the other hand.
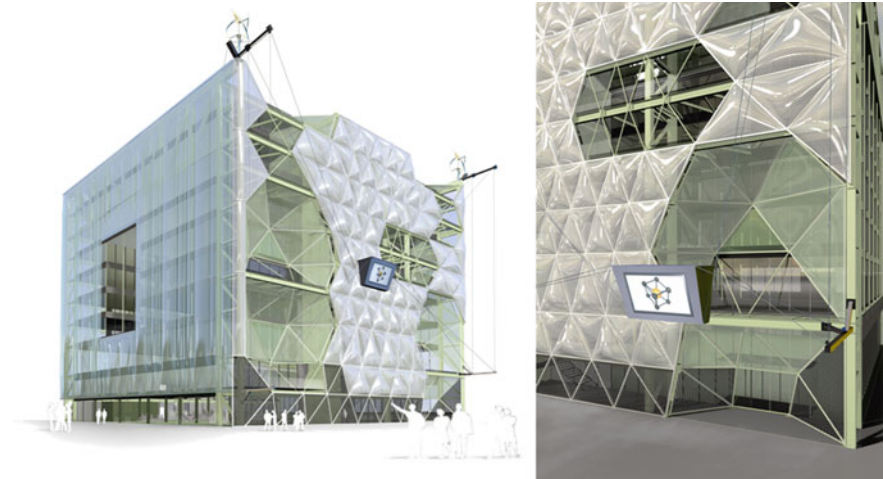
Fig. 3 Previews of the Media-TIC building with the cable-driven robot

2.1 Tasks

The main application for which the first drafts of the robot have been designed for is to be used as a weather station monitoring CO_2 level, pollution level, temperature, humidity and light level, and as an interface between the public and the building itself. The goal according to the architect was to prove the building's intelligence, by showing data such as energy consumption of the building and data from the weather station sensors.

In addition to these tasks, the robot is foreseen to be used for visual inspection of the façade using a camera. It also proved valuable to the operator of the building that the functioning of the robot would effectively scare bird pests that could degrade the façade.

2.2 Workspace Limits

The limits of the workspace have been set accordingly to the tasks to be carried out. It has been agreed that the robot's interface task should be carried out at the building's terraces spread across the façade. The workspace should therefore include positions in front of each terrace, except the ones situated at the top floor since the tensions in the robot's cables are expected to rise dramatically at these positions.

In addition, every structure that holds the auxiliary systems of the robot has to fit within the building's dedicated volume, which is 37 m high by 43 m wide, and protruding out of the façade by at most 5 m.
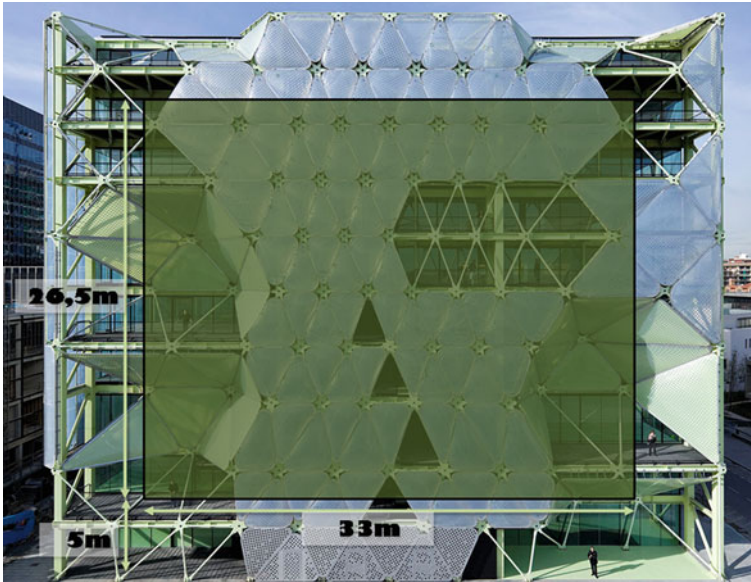
Fig. 4 Desired workspace of the parallel cable-driven robot on the layout of the Media-TIC façade

As a result, the workspace has been set to be 33 m wide centered on the building's width by 26 m high, starting 5 m above the ground as depicted in Fig. 4 The robot mobile platform should be able to keep a constant orientation throughout the workspace while carrying its payload.

2.3 Building Related Constraints

In order for the building to support the forces applied by the parallel cable-driven robot, the posts to which are attached the pulleys driving the cables to the nacelle (mobile platform) should be fixed to the main frame of the building's gantry. They may be attached by clamping, welding or drilling holes in the gantry for screws. Considering the forces that will support the posts and their direction (in mean directed towards the middle of the workspace), they should be fixed at the points where horizontal and vertical beams of the gantry are fixed together. The exact validation of the structure of the posts will be carried out by the same civil engineering company that dimensioned the Media-TIC gantry.

The winches should be placed somewhere where it is out of reach of the public, preferably on the façade to avoid long cable circulation around the building. In order to facilitate the integration of the control electronics of the robot, they should all be placed at the same position.

The robot should withstand the same wind figures than the building itself, which is a peak wind at 160 km/h, generating up to 1,3 kN of load on 1 m² of surface of the building. Considering that the forces on the nacelle and the cables will be considerably high in such a wind, it has been agreed that the robot will not operate when wind is higher than 50 km/h, which is the case 5 % of the year, resulting in a set wind load of 140 N/m². It should therefore withstand this wind speed when operating, and wind speed up to 160 km/h when at rest.

A cradle should be built somewhere on the façade to fix the robot's nacelle when it is not operating. This nacelle cradle will have to support the loading of the robot when at rest, such as wind load. It will also be used for robot initialization.

Finally, it is important that the robot comply with the safety constraints of the building. Indeed, there are 4 ETFE triangular cushions on the façade that serve as smoke vents, opening wide to ensure correct ventilation of the escape stairs of the building during a fire alarm event. These smoke vents protrude from the façade surface by 3 m It takes 3 s for the smoke vents to reach their open position. During such an event, the robot should be able to go back safely to its cradle without interfering with the smoke vents.

2.4 Norms

Since the robot will be built above the public footway in front of the building, we chose to comply with restrictive standards according to DIN 5692: Entertainment technology—Flying systems. This standard requires a security factor of 10 in structural system of the robot, force sensors monitoring continuously the tensile forces in the cables and a routine in the control loop that stops the robot when a maximum force is reached, and finally a double brake system on the winches.

2.5 Aesthetic and Conceptual Integration to the Building

The parallel kinematics principles on which a parallel cable-driven robot operates are related to the distribution principle put forward by the architect during the conception of the Media-TIC building. Such features proved to be a major asset for the architect to accept the design and seize it to integrate it fully to his building. Fitting to the main principles that directed the design of Media-TIC is indeed an important step when dealing with building with such a level of conceptual design.

It is just as much important to avoid that the robot has a bad visual impact on the façade, especially because the south-eastern façade on which it is installed is the most visible. In this respect, a parallel cable-driven robot has inherent advantages since the façade is run across by cables which have a low visual impact.

Since the building aims at being self-sufficient in energy, it is important for the robot to share this characteristic to fit with the rest of the building. On Media-TIC, this

translates into additional wind generators that have to be installed. These wind generators will provide the power needed for the robot, knowing that its speed will have to be different depending on how much energy has been harvested with the windmills in order to match with their actual production. The nacelle, which is equipped with electronic equipment (cameras, lighting, screen, wireless communications, etc.), will also be equipped with solar panels in order to compensate for its consumption.

In order to keep a low visual impact at the level of the terraces, it has been chosen that the interface between the robot and the public should be a soft interface. The typical example would be sending text messages to the robot to have it come to one specific terrace, or to carry out a path on the façade, or to send specific information about the building.

On the other hand, the architect has put forward the fact that the elements of the robot—nacelle, posts and structure—should not be hidden by choosing elements visually similar to those of the building structure: different colors and patterns from the ones used for the building should be chosen for these elements.

3 Technical Description of the Elected Design

3.1 General Layout

In order to keep out from the cushions covering the façade, the pulley's positions have been set at 1 and 5 m away from the façade. There are two cables at each of the four corners of the workspace. The centre point of the robot nacelle will move nominally 3 m away from the façade.

As mentioned above, the main concern being the lateral stiffness of the robot against wind to avoid that the nacelle hits the building when a wind gust occurs, a fully constrained design has been chosen. As explained later on, a state of the art control law will allow changing the robot stiffness and power consumption in function of the wind by modulating inner constraints in the robot (Fig. 5).

The layout of the fixing points of the cables on the nacelle has been chosen accordingly to this constraint. The robot's nacelle precise design has not yet been defined, as there are still theoretical developments and tests underway to choose the best configuration when dealing with this constraint. The goal is to find a good compromise between having a reasonably high stiffness in all directions (and especially in the critical building transverse direction) and at the same time avoiding cable interferences in the workspace. The first simulations and the test on the real prototype have been carried out with a parallelepiped platform with a cable at each vertex. Another configuration featuring two cables attached at each vertex of a tetrahedron has been successfully tested in the simulations program. In addition, the pulley's positions will be designed so that they may be placed in different positions on the beam once the robot has been built.
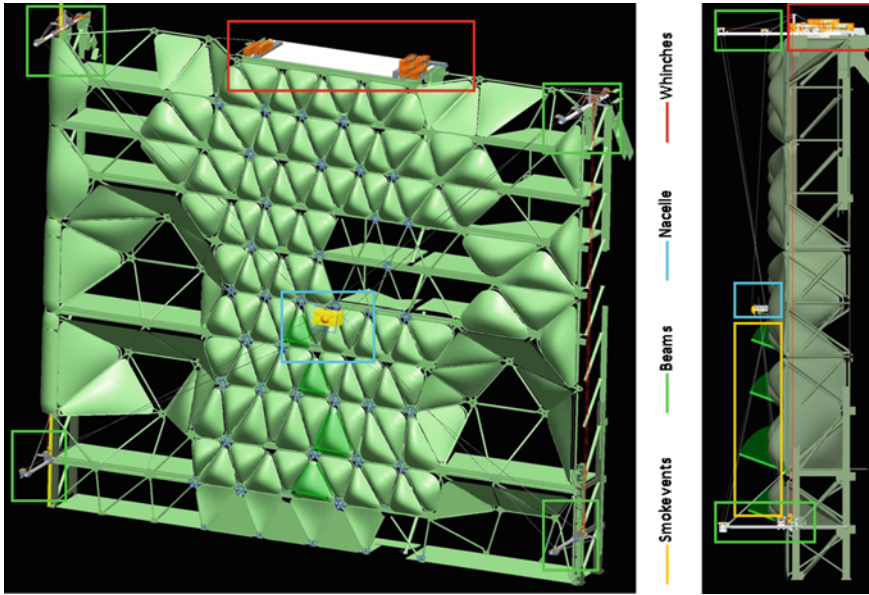
Fig. 5 General CAD view of the parallel cable-driven robot on the Media-TIC façade. Colored boxes indicate the position of the different subsystems. Nacelle is shown in parked position
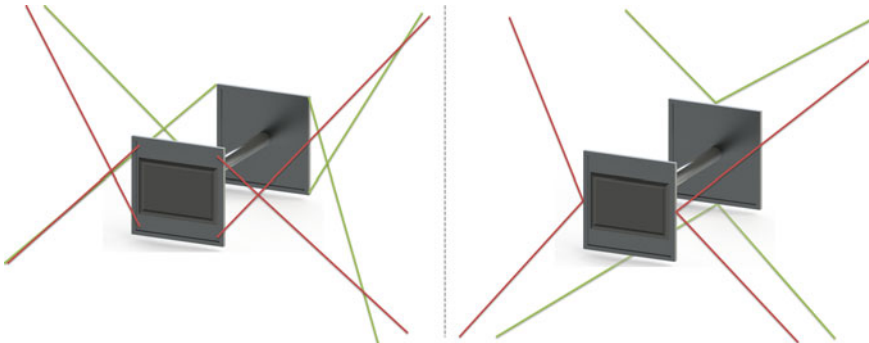
Fig. 6 CAD view of the preliminary designs of the nacelles. Right figure shows the parallelepiped nacelle, left figure shows the tetrahedron nacelle. Front panel cables are attached to the back drawing points, while back panel cable are to the front drawing points

Figure 5 shows the arrangement of cables on the platform that have been studied so far. The nacelle dimensions have been selected to keep a low profile against wind transversal to the façade. Fixing points are 2 m away on the horizontal axis parallel to the façade, 1 m away on the vertical axis and 1.5 m wide on the horizontal transverse axis. In the nacelle, a 0.5 m diameter cylinder will include all the hardware (Fig. 6).

The issue with the smoke vents has been dealt with using the following strategy. When a fire alarm occurs, the centre point of the nacelle slides outward to the building

by 1.5 m, letting it avoid the smoke vents by 0.5 m. The deployment of the smoke vent takes 3 s: considering the winch speeds, the robot is able to reach the safe position before the smoke vents are deployed. The nacelle is then moved and docked safely to its cradle once the smoke vents are opened.

The cradle of the nacelle will be positioned at one of the balconies of the building. In order to dock to it, the nacelle will have to slide closer to the façade, the position of the cradle has therefore been set in function of the position of the elements of the façade in the way, in particular the smoke vents. The cradle itself will be able to open and close to leave way for the nacelle when the robot operates.

3.2 Dimensioning

Considering the different systems to be carried in the nacelle, its mass has been evaluated at maximum 200 kg. Primary calculations taking into account platform mass, cable mass and wind load on both the platform and the cable lead to consider 10 kN as the maximum force in each cable and a steel cable diameter of 12 mm (with a 10x security factor against breaking) to reach every point in the workspace considered in the specification section. The cable construction is standard 6x36 construction with a metallic 7x7 core, and therefore generates rotation when pulled, but shows low torsional stiffness as well.

The resulting wrench transmitted from the posts to the structure has been evaluated at maximum 50 kNm of torque and 63 kN of force for each of the posts.

Nacelle speed has been set to 1.5 m/s in order to limit issues on the winches due to high cable linear speed. As a result, the motor power needed for each cable is 15 kW. At most, the installation will have to be supplied 30 kW at a time, which means the windmills will have to generate power at their nominal level of 3 kW for 10 hours before 1 hour of operation at full current can be carried out.

3.3 Control Scheme

A control architecture that is able to take into account the actuation redundancy has been set up, tested and validated through simulation. Its validation took place when it has been successfully implemented on a real robot prototype.

The objective of this control law is to take into account the redundancy during the movements of the robot to prevent any cable from sagging under low tension. A hybrid position / force control law has been set up, based on research carried out by Lafourcade [9]. It consists in synthesizing a command of the cable tension integrating two parts: one generating movement of the nacelle, $\tau_{\mathbf{range}}$, and another one making sure that all the cables are under tension during movement, $\tau_{\mathbf{kernel}}$. The first part generating movement can be obtained by a control law in the operational space or in the joint space. The second part, ensuring tension in every cable, is derived by
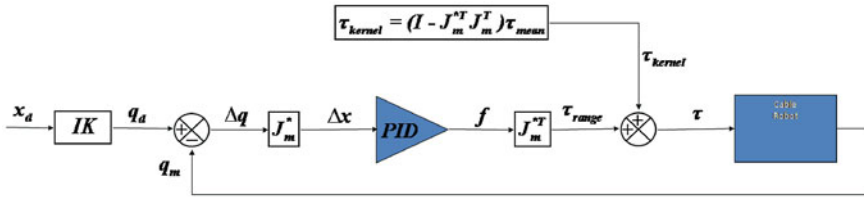
Fig. 7 Implementation of the control law with τ_{range} being generated in the operational space

projecting a mean desired cable tension on the kernel of the matrix $\mathbf{J}_m^T$ linking the cable tensions with the external wrench applied to the nacelle.

Preliminary results in stiffness estimation of fully constrained parallel cable-driven robots suggest that, with the layout of the Media-TIC robot, its transverse stiffness is directly linked to the mean cable tension. As a result, the control law set in place may be used to increase the stiffness of the parallel cable-driven robot during days when wind is blowing, with a tradeoff on the total power required for operation. During days with low wind, the robot will operate with a lower mean cable tension. This will lead to a lower transversal stiffness and a lower energy consumption for a given nacelle speed, in line with the concept of Media-TIC (Fig. 7).

3.4 Robot Subsystems

4 Winches

Winch motors have been chosen among the B&R motor range to deliver the appropriate power. The 8LSA85 motor has been chosen, featuring up to 72 Nm at 2,000 rpm, and 94 Nm at stall. It drives the 292 mm primary diameter drum with a reduction ratio of 1:16, which leads to a maximum cable speed of 1,9 m/s.

In addition to the constraint of having a security factor of 10, in order to comply with the DIN 56921 standards, the winches must be equipped with two current loss brakes, one of which being connected directly on the drum. One of these brakes is included in the 8LSA85 motor. The second brake is a double rotor elevator brake rated at 800 Nm for each rotor.

The length of cable reeled in and out is monitored via the rotation of the spool using an absolute rotary position sensor. In addition, the winch is fitted with limit switches. In order to avoid unreeling the cable when applying negative tensions in the cable, rollers are maintaining the cable in place on the drum using springs.

Winches are powered using the ACOPOSmulti range from B&R, both gathering data from the sensors and driving the motors, linked together and to a central field computer featuring the control loop through a POWERLINK field bus.
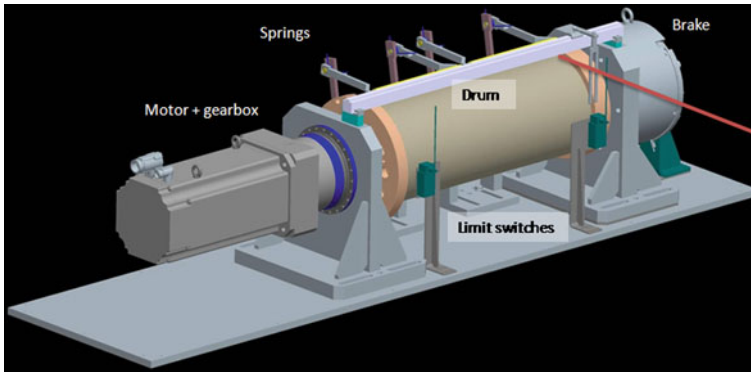
Fig. 8 CAD view of a winch
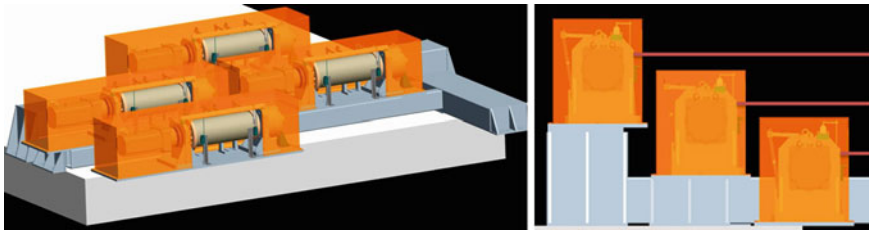
Fig. 9 Arrangement of the winches on the roof of the building

Finally, the drums are enclosed in boxes to prevent weather damage, since they are installed in open air on the roof of the building. They are placed so that there is no interference between the different cables and the winches (Figs. 8 and 9).

5 Cable Circulation

With the winches on the roof of the building, the cables must be directed from there to the positions of the pulleys at the four corners of the façade. The circulation must also include a force sensing system, giving the tension in each cable. The force sensor will be a shear stress sensor placed on the last fixed pulley of the circulation. Stress sensors will be monitored using B&R X67 hardware specially designed for remotely placed sensors, addressed via POWERLINK.

The upper beams, supporting the pulleys for the cables attached to the nacelle by the top, redirect all the cables from the winches to the pulleys and to the lower beams. Force sensors for the upper cables are placed on the pulley directing the cable from the drum to the winches. The fixed pulleys for the lower cables are not instrumented. Cable tendons are placed to limit the bending of the beam under load.
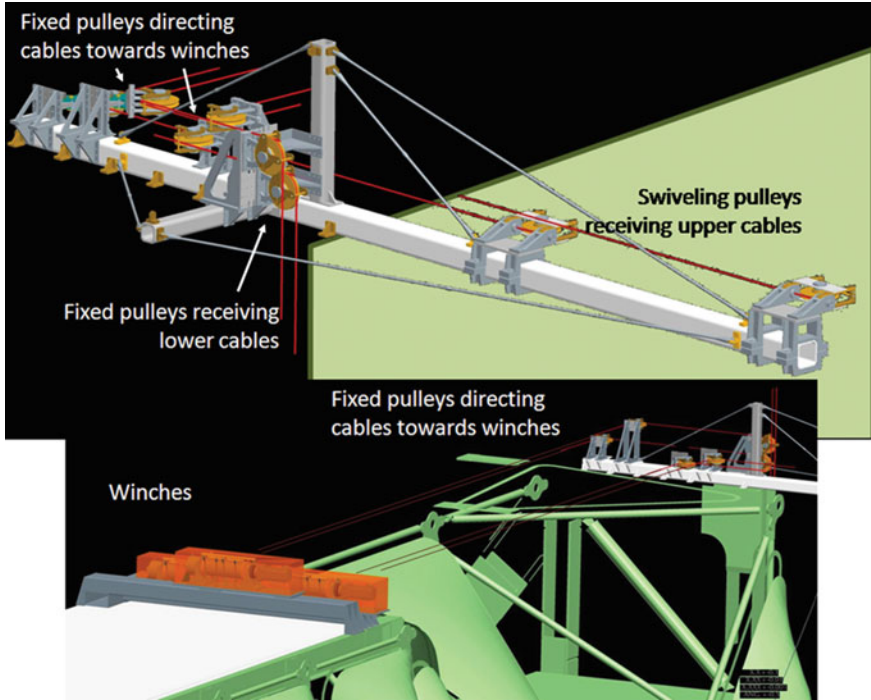
Fig. 10 Upper beam arrangements of the different pulleys. *Up*: arrangement of the upper left beam, upper right beam being symmetric. *Down*: circulation of cable between the winches and the *upper right beam*

The lower beams direct the cables from the upper beams to the output pulleys. The fixed pulleys on the lower beams are equipped with force sensors. Once again, cable tendons are fixed between the beam and the structure of the building to avoid unacceptable bending of the beams (Figs. 10 and 11).

As shown in Fig. 12, the output pulleys are assembled on a bearing whose axis is collinear to the axis of the cable coming from the fixed pulleys. The cable runs through one of the bearings. Here we are taking advantage of the low stiffness of the cable, due to the 6x36+7x7 construction, which might not be possible with a non-rotating cable. The pulley orientation is determined by the direction on which the cable pulls. The cable is kept in place in the pulley by rods at the exit of the pulley.

The block in itself is clamped to the beam. It will allow keeping on with the optimal configuration determination through simulations and tests, and constructing the most optimal configuration when the robot will be ready for start-up.
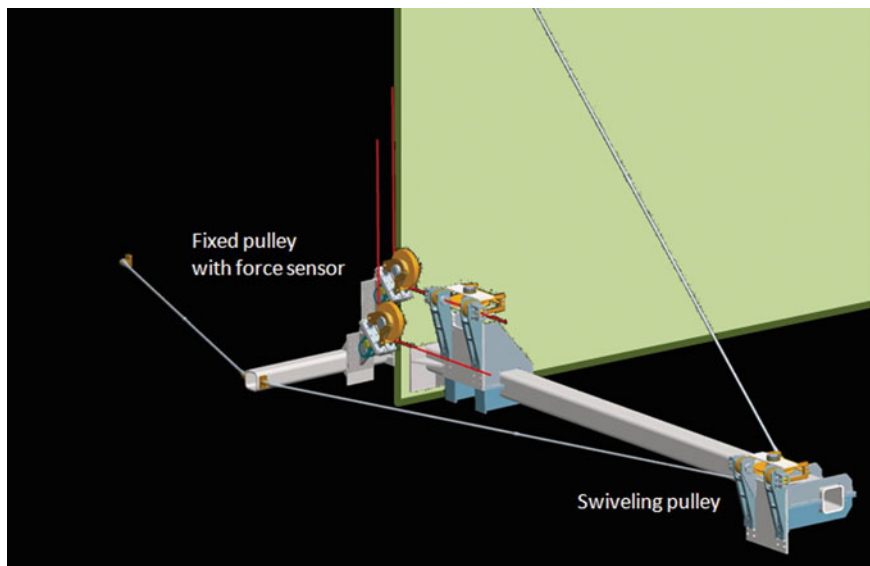
Fig. 11 *Lower left beam. Lower right beam* is symmetric

6 Nacelle

As explained above in this paper, the detailed configuration of the nacelle has not yet been chosen. However, the global shape of the platform has been determined with the goal of limiting the force due to the pressure of the wind. The nacelle will also feature several electronic hardware items, such as a computer with GPRS connection, batteries, lightings, screen, speakers, weather sensors and cameras partly powered by solar panels. The nacelle cradle will allow recharging the batteries when the nacelle is docked. All of these items are housed in a 50 cm diameter cylinder and fixed on a central axis, to which will be fixed as well the structural beams holding the cables.

7 Conclusion

This paper presented the implementation of a parallel cable-driven robot on the façade of the Media-TIC building located in the city of Barcelona, Spain. This robot is intended to work as a sensor for monitoring the environment and also as an interface between the building and its occupiers and visitors. Various constraints, due to normative, structural and aesthetic reasons, were described along with the elected detailed design of the robot that complies with them. One of the main technical issues is to design a parallel cable-driven robot with a lateral stiffness sufficient to withstand forces due to the wind. Here, this has been achieved by means of an appropriate layout of the cables in a fully constrained configuration. Besides, the selected control
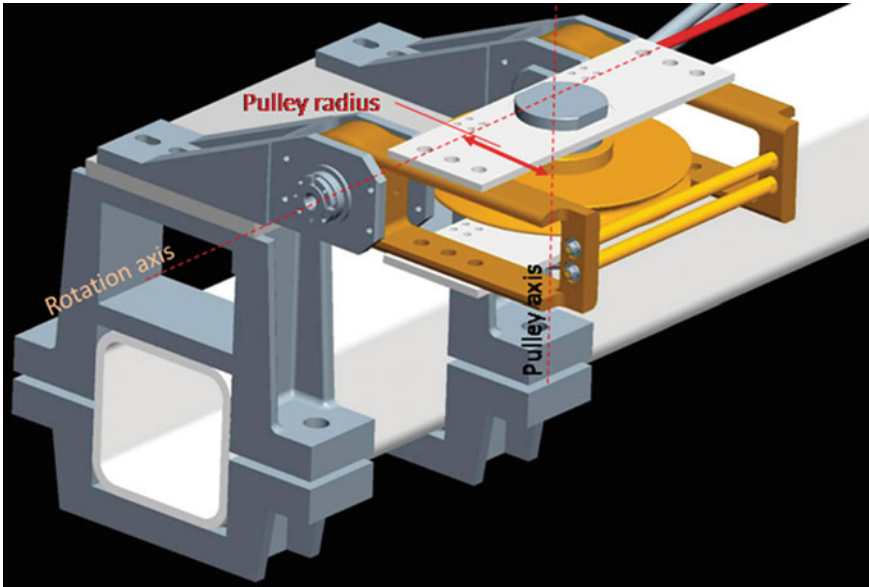
Fig. 12 Close view of the swiveling output pulley
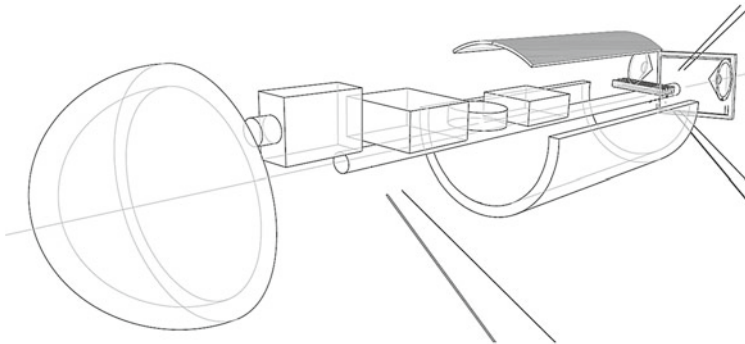
Fig. 13 View of the internal arrangement of the nacelle. Credits: Cloud9

law is able to modify the robot stiffness with a tradeoff between stiffness and energy consumption.

The robot has not yet been realized nor installed on the building façade. Indeed, we are still currently waiting for the construction permits to carry on with the installation of the robot.

participation to its design. The contribution of the company B&R to the project with the design of the system control is also greatly acknowledged.

References

1. SkyCam: http://skycam.tv/
2. SpyderCam: (2012). http://spydercam.com/
3. Merlet, J.-P.: Kinematics of the wire-driven parallel robot MARIONET using linear actuators. In: IEEE International Conference of Robotics and Automation, Passadena, CA, USA (2008)
4. Merlet, J.-P., Daney, D., Winch, A., Needs, A.A.: A portable, modular parallel wire crane for rescue operations. In: IEEE International Conference on Robotics and Automation. pp. 2834–2839, Anchorage, AK, USA (2010). doi:10.1109/ROBOT.2010.5509299
5. Ming, A., Higuchi, T.: Study on multiple degree-of-freedom positioning mechanism using wires. II: Development of a planar completely restrained positioning mechanism. 3, Tokyo, Japan : Japan Society for Precision Engineering. Int. J. Jpn. Soc. Precis. Eng. **28**, 235–242 (1991)
6. Gouttefarde, M., Gosselin, M.: Analysis of the wrench-closure workspace of planar parallel cable-driven mechanisms. IEEE Trans. Robot. **22**(3), 434–445 (2006)
7. Ottaviano, E., Ceccarelli, M., Paone, A., et Carbone, G.: A low-cost easy operation 4-cable driven parallel manipulator. In: IEEE International Conference on Robotics and Automation, pp. 4008–4013. Barcelona, Spain (2005). doi:10.1109/ROBOT.2005.1570734
8. Hiller, M., Fang, S., Mielczarek, R., Verhoeven, R., Franitza, D.: Design, analysis and realization of tendon-based parallel manipulators. 4, s.l. : Elsevier, Mechanism Mach. Theor. **40**, 429–445 (2005). doi:10.1016/j.mechmachtheory.2004.08.002
9. Lafourcade, P., Zheng, Y.-Q. and Liu, X.-W.: Stiffness analysis of wire-driven kinematic manipulators. In: 11th World Congress in Mechanism and Machine Science, China Machine Press, Tianjin, China (2004)

Part IV
Design and Components

Use of Passively Guided Deflection Units and Energy-Storing Elements to Increase the Application Range of Wire Robots

Joachim von Zitzewitz, Lisa Fehlberg, Tobias Bruckmann and Heike Vallery

Abstract   Since few years, wire robots are making their way into industrial application. Besides the continuation of research in the fields of kinematics and dynamics modeling, control, workspace analysis, and design, new challenges like robustness, energy efficiency and maturity arise due to practical requirements. This holds especially true for the actuation and deflection components of the system. In the past, a wide range of actuation and deflection concepts were presented. Within this contribution, at first known ideas of deflection concepts are reviewed and compared. In the following, a new deflection concept using passively guided skids is presented which homogenizes the load capabilities of a wire robot over its workspace. Subsequently, new approaches optimizing the energy consumption based on the installation of counterweights and pre-stressed springs are discussed. Using those passive elements, not only static pre-tension can be generated but, in the case of using springs, also dynamic motions can be boosted by using the eigenmotions of the oscillator consisting of the end effector and the attached springs. The paper describes both

J. von Zitzewitz (✉)
Center for Neuroprosthetics and Brain Mind Institute, EPFL Lausanne,
1015 Lausanne, Switzerland
e-mail: joachim.vonzitzewitz@epfl.ch

J. von Zitzewitz · H. Vallery
Sensory-Motor Systems (SMS) Lab, ETH Zurich, 8092 Zurich, Switzerland

L. Fehlberg · T. Bruckmann
Chair of Mechatronics, University Duisburg-Essen, 47057 Duisburg, Germany
e-mail: lisa.fehlberg@uni-due.de

T. Bruckmann
e-mail: tobias.bruckmann@uni-due.de

H. Vallery
Kalifa University, Abu Dhabi, United Arab Emirates
e-mail: heike.vallery@kustar.ac.ae

the theoretical background as well as simulation results for eigenmotion utilization showing that the concept is capable of drastically reducing wire forces generated by the active components, i.e. the motors, for a given task.

1 Introduction

Wire robotics is a re-emerging research field in robotics: A large number of prototypes was presented in the last decade of the past century. Apparently, only a small number of these prototypes have made their way to practical applications. Possible reasons are manifold, reaching from the difficult controllability up to the comparably low precision induced by the uni-laterally constraining and inherently elastic wires, which replace the stiff conventional robot arms.

During the last five to eight years, a renaissance of practical applications can be found, most of which were proceeded by an extensive theoretical preparative work. In more recent research projects, the focus is increasingly put on a major advantage of wire robots: their easy reconfigurability. This property emerges from the modular usability of the three main components of a wire robot: the actuation unit, the deflection unit, and the wire.

A large variety of these three components has been presented in the literature, wherein especially the deflection units are mainly used as modular components. These units, which guide the wire from the actuation unit into the workspace, are no longer considered as units mounted to a fixed position, meaning, that the robot has a permanent configuration. Rather, their number as well as their position have become adaptable in order to configure the robot for different tasks [1, 2]. The proper robot configuration (i.e., the arrangement of the deflection units and the platform connection points) influences the workspace size as well as the achievable end-effector dynamics and wrench considerably.

These two parameters, workspace size and end-effector wrench, depend on a second variable: the dimensioning of the actuation unit. In contrast to rigid-linked robots, an increase in actuator power does not only influence the producible end-effector wrench but also the workspace size: This property emerges from the fact that, in case of fully constrained, over-actuated wire robots, a minimum pre-tension has to be maintained in all wires. At the borders of the workspace, the maintenance of this pre-tension in certain wires requires high counter forces in other wires which is often the main limitation of the workspace.

Within this paper, extended concepts for the modular use of the two above-mentioned components, actuation units and deflection units, are elaborated while investigations on proper wires are subject to future research. For the deflection units, a review on their different utilization in known wire robots is presented. Subsequently, a new concept is presented which is supposed to close a gap in wire robotics as it allows to keep the wire forces homogeneous over large workspace areas.

The concept for the robot actuation is extended to passive units which are used to relieve the active units, i.e. the motors. After summarizing a recent application
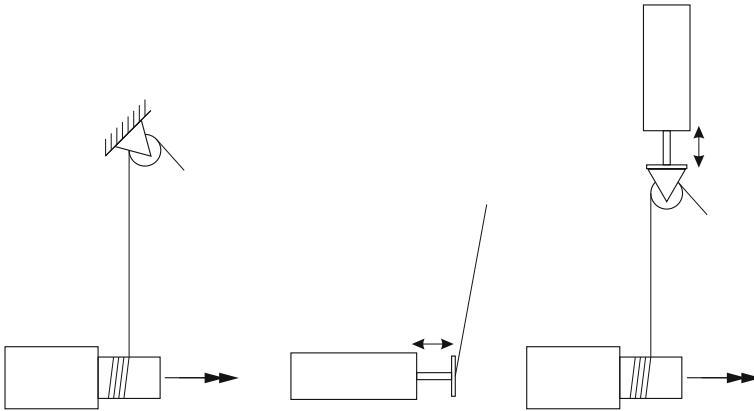
Fig. 1 Current concepts for deflection units: actuated drum and fixed deflection unit (*left*); linear actuation unit and wire with constant length (*middle*); actuated drum and actuated deflection unit (*right*)

involving counterweights, new concepts for the integration of springs are presented. These springs can either be used to relieve the motors in general or their characteristics are optimized for single tasks or trajectories.

Both concepts remarkably increase the usability of wire robots and, thereby, extend their applicability for new groups of applications.

2 Use of Deflection Units: Review and New Concept

In the following sections, the term *deflection unit* is referring to the device which guides the wire into the workspace.

Various designs for deflection units has been presented in the literature: simple rings or holes (made from low friction materials, e.g. ceramics) [3, 4] guiding the wires into the workspace are preferred to facilitate kinematic calculations, but they bare the disadvantage of higher friction and, as a consequence, increased wear compared to other solutions. Swivel castors are the logical option to overcome this problem; they are implemented in several wire robots, e.g. the IPANEMA [5]. Their geometrical description can be found in the literature [6]. Further designs involving static pulleys and/or rollers have been presented over the past years [7, 8].

However, the following section will not focus on design issues of the proper deflection unit. Rather, the different use of deflection units within the actuation concept of wire robots, independent of their design, will be discussed, as this aspect has a major influence on the properties and capabilities of the robots.

2.1 Fixed Deflection Units

In most cases, deflection units are mounted to a fixed point (Fig. 1, left). They guide the wire from this point into the workspace where its free end is connected to the end effector. In certain concepts, the position of the deflection unit can be freely chosen along the frame structure of the wire robot in order to make the robot more versatile and adaptable to different tasks [1, 2].

This concept is the mechanically most simple and probably the best investigated solution. A major disadvantage is the limited workspace with heterogeneous, pose dependent load capabilities.

2.2 Actuated Deflection Units with Constant Wire Lengths

In a concept presented by Maeda et al. [9], reinterpreted by Bruckmann et al. [10], actuation units changing the wire lengths are completely omitted. Instead, wires with constant lengths are connected to linear actuators (Fig. 1, middle).

Also this concept has the advantage of mechanical simplicity, especially concerning the wire guidance. Furthermore, this arrangement turned out to be more energy efficient compared to rotary actuators with drums, as the actuation units only have to exert the component of the wire force tangential to the linear unit [10]. However, the required linear drives are often mechanically complex modules. They introduce large friction—potentially leading to control problems—and the choice of commercially available types is much smaller compared to rotary motors. As a further disadvantage, the highly limited workspace of this option has to be mentioned.

2.3 Actuated Deflection Units

Normally, the change of the wire lengths or the position of the deflection points determine the pose of the end effector. However, also the combination of both has been applied in one project [4] to manoeuvre a tablet horizontally in space: In order to fully define the pose of an inertial body hanging on wires, at least six wires are required. When omitting wires, the body's position is no longer fully defined unless other actuated degrees of freedom are integrated. In the application mentioned before, the drive trains enables both the change of wire length by actuated winch units and the active positioning of the deflection unit. As this solution requires less wires, collision with other wires and objects inside the workspace become less probable.

A similar concept has been applied recently to address the collision problem [2]: In an interactive application with a human user standing inside the robot's workspace, the free ends of two actuated wires (variable lengths l_1 and l_2) were connected to a third wire with a constant length l_3 at the point **P** (Fig. 2). The free end of the third
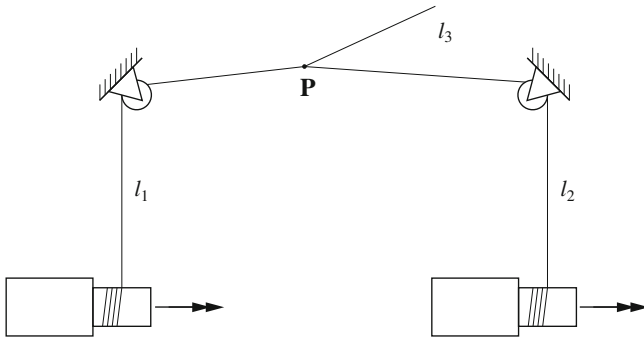
Fig. 2 Two actuated wires manipulating the deflection point of a third wire

wire was connected to the end effector grasped by a human subject. The change
of the two active wire lengths resulted in a movement of **P**. This movement was
used to avoid collision between the third wire and the subject. The point **P** could be
interpreted as an actuated deflection point with a more complex movement range.
Alternatively, a pulley could be mounted at the end of one active wire, deflecting the
second wire.

The concept of movable deflection points could also be applied to an over-actuated
wire robot in order to increase the workspace size of the robot. However, this solution
is the mechanically most complex version compared to the other concepts presented
above.

2.4 New Concept: Passively Guided Deflection Units

All concepts mentioned above have one clear disadvantage: their load capabilities
vary strongly depending on the end-effector pose inside the workspace. This results
from the increasingly inhomogeneous distribution of wire force vectors when the
end effector is moved away from its central pose towards the outer workspace zones.
This disadvantage can be compensated by actuated deflection points as they were
presented in Sect. 2.3, but this solution is costly due to its high mechanical complexity.

We suggest a new concept where the deflection units are neither fixed nor actuated;
instead, they move passively, while being connected to each other, and potentially
subjected to additional passive constraints.

In an exemplary planar case, a single force vector acts on a moving attachment
point at an object or human W (Fig. 3). Two winches are used, and two deflection
units (pulleys) are combined and constitute a trolley running on a linear guide. To
minimize the mass m_T of this trolley, given that distances between deflection units
could be large, the units can be mounted on two separate carts that are connected by a
cable. This is possible because the force between carts will always be tensile. A single
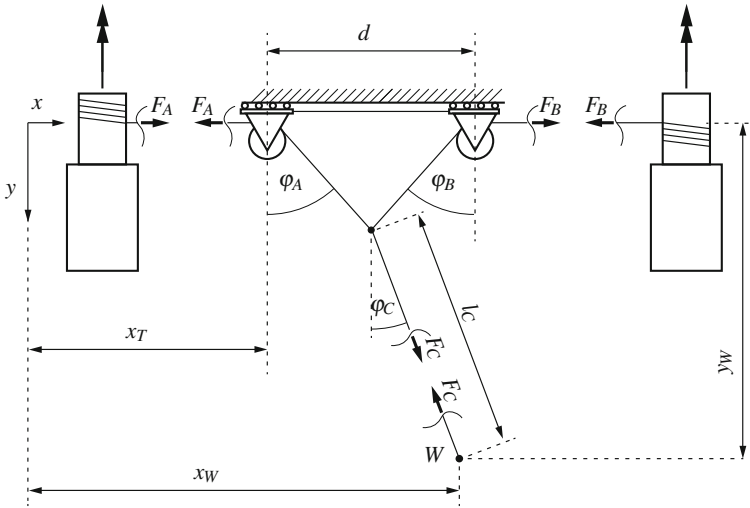
Fig. 3 Inter-connected passive deflection units enlarge the achievable workspace; the object or human subject is connected at point W

wire of length l_C connects the node to the attachment point W on the moving object or human. A configuration similar to this, but extended to the three-dimensional case, is currently being realized in an overhead support device for gait training.

We now assume that the endpoint W moves along a given trajectory $\mathbf{w} = (x_W, y_W)^T$, with $y_W > 0$, and that the force acting on W is to be controlled. This force is defined by its magnitude F_C and the angle φ_C. In the chosen Cartesian coordinate system, y points downward and x points to the right, in direction of the rail.

Geometry defines how the wire angles φ_A, φ_B, φ_C, and the trolley position x_T are related:

$$(y_W - l_C \cos \varphi_C) \tan \varphi_A + l_C \sin \varphi_C = x_W - x_T \tag{1}$$

$$(y_W - l_C \cos \varphi_C)(\tan \varphi_A + \tan \varphi_B) = d. \tag{2}$$

Force equilibrium on the node defines the relationships between the wire forces F_A, F_B, F_C, and the angles:

$$-F_A \sin \varphi_A + F_B \sin \varphi_B = -F_C \sin \varphi_C. \tag{3}$$

$$F_A \cos \varphi_A + F_B \cos \varphi_B = F_C \cos \varphi_C \tag{4}$$

Given a current trolley position x_T and wire forces F_A and F_B, the algebraic Eqs. (1–4) define the magnitude F_C and the angle φ_C of the output force vector (as well as the angles φ_A and φ_B).

The inverse problem, as necessary for control purposes, is to find appropriate reference wire forces $\hat{F}_A$ and $\hat{F}_B$ in function of a reference force $\hat{F}_C$ at the endpoint, and a reference angle $\hat{\varphi}_C$. The winches can then be used to track the desired wire forces $\hat{F}_A$ and $\hat{F}_B$.

If the deflection units were fixed, as in classical configurations, the solution would be found easily using the same equations, but the direction of the realizable output force would be constrained by the relationship

$$x_W - x_T - d < y_W \tan \hat{\varphi}_C < x_W - x_T \tag{5}$$

with fixed x_T. The range of possible angles thus depends strongly on the position of W and on the distance d between deflection units. Increasing the workspace by increasing d would automatically lead to higher wire forces F_A and F_B, which is undesirable.

The movable deflection units solve this issue and allow almost arbitrary positions x_W of the endpoint along the x direction, only constrained by space limitations in the building or by maximum allowable wire length. However, the control task of commanding appropriate wire forces is less straightforward, because of the under-actuated nature of the system. The trolley moves under the influence of the wire forces, according to the equation of motion:

$$m_T \ddot{x}_T = -F_A + F_B + F_C \sin \varphi_C. \tag{6}$$

One simple solution, which is efficient for low trolley mass, is to control based on static equilibrium: For constant wire forces F_A and F_B, the trolley will approach its equilibrium position, defined by the left side of (6) being equal to zero. Then, an additional algebraic relationship for the reference forces results:

$$\hat{F}_A - \hat{F}_B = \hat{F}_C \sin \hat{\varphi}_C. \tag{7}$$

This equation, combined with (1–4), with forces replaced by reference forces, allows the realization of a simple controller without static error: The system of five algebraic equations can be solved for $\hat{F}_A$ and $\hat{F}_B$ (and angles, and trolley position), given only $\hat{F}_C$ and $\hat{\varphi}_C$. For the equations to be solvable with non-negative forces, the commanded angle can theoretically take any value within the interval $-\pi/2 < \hat{\varphi}_C < \pi/2$. The smaller the mass of the movable deflection units is, the faster the trolley will approach its static equilibrium.

3 Combining Motors and Passive, Energy-Storing Elements

Apart from the deflection concept, the way how the wires are tensed has a considerable influence on the capabilities of a wire robot. In common wire robots, the wire tension is applied by all sorts of actuators. The most common type of actuators are electrical motors of both, rotary and linear type.

Fig. 4 The SOMNOMAT, an
actuated bed platform for sleep
research: Counterweights on
additional wires (highlighted
as *dashed lines*) partially
compensate the high platform
weight
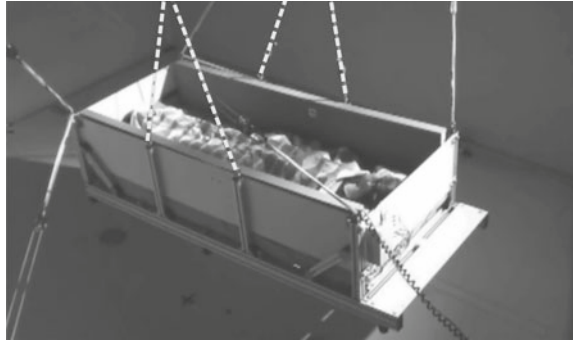
Independent from the actuation concept, the active unit always exerts unidirectional torques or forces, as wires represent unilateral constraints. As a consequence, only half of the actuator's power spectrum is utilized in common wire robots.

This section presents possibilities how to overcome these shortcomings and how to increase the wrench of wire robots by using passive energy-storing elements.

3.1 Use of Single Springs or Counterweights

The minimum requirement for an end effector to work in n degrees of freedom without end-effector wrenches is to have at least $n + 1$ wires attached to it [11, 12]. However, one of these wires could be tensed by a passive energy-storing element. In the literature, applications can be found where an active actuation unit is replaced by a spring [13, 14]. The pre-tension of this spring determines the producible end-effector wrench.

A further challenge in robotic handling applications is the often high gravitational load induced by the proper robot structure as well as the end-effector load. While the structural load is usually negligible in wire robots, the end-effector load can significantly limit the robot's range of motion.

An example is the SOMNOMAT, a tendon-driven platform with six degrees of freedom used for sleep research [15]. In the SOMNOMAT, motorized drums were used as actuation units. These motorized drums are parts of a modular wire-robot concepts [2] and were by far too small-dimensioned to lift or even move the total platform weight of 140 kg. By attaching wires connected to counterweights which partially compensate the high platform weight, the application became realizable with the minimal number of seven actuation units (Fig. 4).

Fig. 5 Pre-tensing of the actuation unit with an inertial mass directly connected to the drum
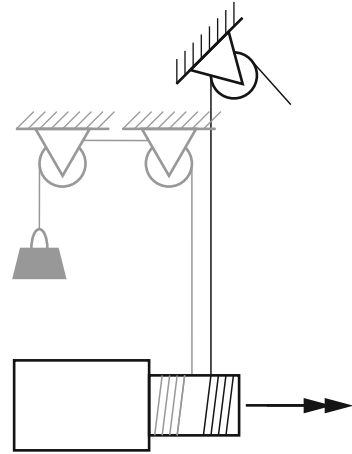
3.2 Constant Pre-Tension of Actuation Units

As pointed out in the introduction of this section, the power spectrum of actuators is not fully exploited in wire robots, because the actuators only pull on the wires. In addition, the actuation units have to produce a minimum pre-tension F_{pre} in each wire when the system is over-actuated. This pre-tension does not contribute to any force or torque at the end-effector and, therefore, further diminishes the robot's wrench for a given actuator size.

This shortcoming can be compensated by pre-tensing the actuator—and therefore the wire—with the force:

$$F_{pre,const} = F_{pre} + F_{act,max} \tag{8}$$

with $F_{act,max}$ as the maximum static force the actuator can produce. Due to this pre-tension, the static load capabilities of the actuator is more than doubled. An option to realize this pre-tension is to attach a passive, energy-storing element directly to the actuated drum (Fig. 5). The drum length hardly has to be extended for this, as one wire is unwound when the other one is wound on.

To minimize the maximal motor torques, $F_{pre,const}$ could also be set to a value between the minimal and the maximal actuator torque required for a specific task on each actuator:

$$F_{pre,const} = F_{task,min} + \frac{F_{task,max} - F_{task,min}}{2} \tag{9}$$

3.3 Energy Minimization—Utilization of Eigenmotions

In the preceding sections, passive elements were used to increase the overall load capacities of wire robots. In the following section, we want to highlight how the dimensioning of these elements can be further fine-tuned dependent on the task to be realized.

3.3.1 Idea

An approach to minimize the energy consumption of a robot is to add passive elements to the robotic structure such that the eigenmotion of the robotic structure is close to the desired task-specific trajectory. The utilization of eigenmotions of course implies that the robot is transformed into an oscillator by adding elastic elements such as springs to the structure. Examples in the literature have shown that the integration of roughly-dimensioned springs can already release active units for tasks within a specific frequency spectrum [16].

The idea of utilizing the robot's eigenmotions has been presented by Uemura et al. [17]. They present the idea of attaching springs with adjustable stiffness to the axes of a serial robot. The spring stiffness and its equilibrium angle were adjusted such that the robot's eigenmotions were close to a previously specified trajectory describing a periodic movement. This idea is transferred herein to wire robots in the following paragraphs.

A cyclic trajectory of the robot's end effector in task space coordinates is described by the n-dimensional vector $\mathbf{x}(t)$. When neglecting frictional effects and the motor inertia, the following wrench has to be produced by the actuators to move an end effector along $\mathbf{x}(t)$:

$$\mathbf{w}_{EE} = \mathbf{M} \cdot \ddot{\mathbf{x}} \tag{10}$$

with $\mathbf{M}$ as the n-dimensional inertia matrix of the end effector.

Assuming that a number of $m \in \mathbb{N}$ springs with adjustable spring constant k_i and the initial length $l_{0,i}$, $i = 1, 2, \ldots, m$, are attached serially to the actuation unit, the wrench $\mathbf{w}_s$ produced by these springs can be described by

$$\mathbf{w}_s = \mathbf{A}^T \cdot [k_1 \cdot (l_1 - l_{0,1}) \ldots k_m \cdot (l_m - l_{0,m})]^T \tag{11}$$

with $\mathbf{A}$ as the pose-dependent structure matrix of the wire robot and with l_i, k_i, and $l_{0,i}$ as the actual length, the spring constant, and the unloaded length of the i-th spring, respectively.

Under the given assumptions, the actuator has to produce the following wrench $\mathbf{w}_a$ to move the end effector along $\mathbf{x}$:

$$\mathbf{w}_a = \mathbf{w}_{EE} - \mathbf{w}_s \tag{12}$$

Fig. 6 Assembly of a planar wire robot with deflection points $A_{1...3}$ and point mass m moving along a cyclic trajectory (*grey*)
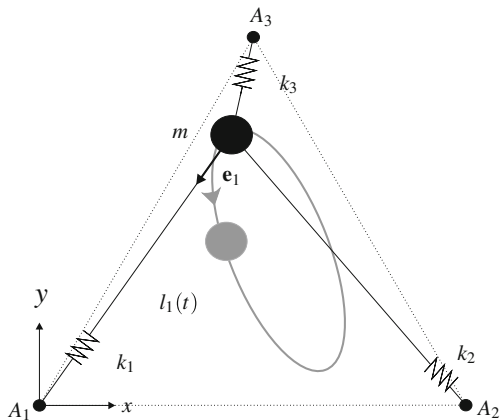
The goal is to tense the springs in such a way that the required actuator power is minimized for the given task. In other words, the oscillator consisting of the end effector and the springs should be dimensioned such that the eigenmotion of the end effector supports the desired cyclic movement optimally. Knowing the trajectory in advance, this dimensioning can be done off-line and is not critical concerning calculation time. According to [17], this is reached by minimizing the following expression

$$J(\mathbf{k}, \mathbf{l_0}) = \int_{i \cdot T}^{(i+1) \cdot T} \mathbf{w}_a^T \mathbf{w}_a dt \tag{13}$$

with $k = [k_1, k_2, \ldots, k_m]$ and $l_0 = [l_{0,1}, l_{0,2}, \ldots, l_{0,m}]$.

3.3.2 Example

The utilization of the eigenmotions in a wire robot will be demonstrated on a planar wire robot (Fig. 6).

Three wires are attached to a point-shaped end effector with a mass of $m = 1$ kg. The deflection points of the wires, A_1, A_2, A_3, form an equilateral triangle. The position vectors of these points are denoted by $\mathbf{a}_1 = [0, 0]$, $\mathbf{a}_2 = [10, 0]$, and $\mathbf{a}_3 = [5, 8.66]$. The coordinate system is located in A_1.

In a first step, the purely passive spring system is considered. Therefore, the wires are replaced by springs with adjustable stiffnesses k_1, k_2, k_3 and relaxed spring lengths $l_{0,1}, l_{0,2}, l_{0,3}$. Practically, this can be realized by a clock spring tensing a winch which coils the wires. The sum vector of wire forces caused by the springs is $\mathbf{F}_{pre} = F_{pre_1}\mathbf{e}_1 + \cdots + F_{pre_m}\mathbf{e}_m$ with an absolute value of F_{pre} and $e_i, i = 1, 2, \cdots, m$, as the unit vectors in direction of the wires.

Now, k_i and $l_{0,i}$ should be chosen such that the springs optimally support an end-effector movement along a predefined cyclic trajectory, meaning that (13) is

minimized. The following trajectory definition was chosen, describing a periodic movement, consisting of two superimposed movements: A basic elliptic movement with a frequency f_1 and amplitudes a and b, and a second superimposed oscillation with the eightfold frequency f_2 and an amplitude of 1 % of a:

$$\mathbf{x}(t) = \begin{bmatrix} a_0 + a\cos(\phi)\cos(2\pi f_1 t) - b\sin(\phi)\sin(2\pi f_1 t) + \frac{a}{100}\cos(\phi)\cos(2\pi f_2 t) \\ b_0 + a\sin(\phi)\cos(2\pi f_1 t) + b\cos(\phi)\sin(2\pi f_1 t) + \frac{a}{100}\sin(\phi)\cos(2\pi f_2 t). \end{bmatrix}$$

(14)

The basic elliptic trajectory is rotated by ϕ. The center point of the equilateral triangle formed by deflection points A_i, $i = 1, 2, 3$, does not coincide with the center point $[a_0, b_0]$ of the ellipse. In this example, the following parameters are used: $f_1 = 0.5\,\text{Hz}$, $f_2 = 4\,\text{Hz}$, $a_0 = 5.7\,\text{m}$, $b_0 = 3.5\,\text{m}$, $a = 3\,\text{m}$, $b = 1.2\,\text{m}$, $\phi = 14.5\,\text{deg}$.

Neglecting frictional effects and the inertia of the drums and motors, $\mathbf{w}_a$ can be calculated for this system as follows:

$$\mathbf{w}_a(t) = \underbrace{m\ddot{\mathbf{x}}(t)}_{\mathbf{w}_{EE}} - \underbrace{\mathbf{A}^T(\mathbf{x}(t))[\, k_1(l_1(t) - l_{0,1})\, k_2(l_2(t) - l_{0,2})\, k_3(l_3(t) - l_{0,3})\,]^T}_{\mathbf{w}_S}$$

(15)

where m and $\ddot{\mathbf{x}}(t)$ are given and the structure matrix $\mathbf{A}^T$ can be calculated by

$$\mathbf{A}^T(\mathbf{x}(t)) = [\mathbf{e}_1(t)\, \mathbf{e}_2(t)\, \mathbf{e}_3(t)]$$

(16)

with

$$\mathbf{v}_i(t) = \mathbf{a}_i - \mathbf{x}(t) \quad \text{vector of the wire } i$$
$$l_i(t) = \|\mathbf{v}_i(t)\|_2 \quad \text{length of the wire } i$$
$$\mathbf{e}_i(t) = \frac{\mathbf{v}_i(t)}{l_i(t)} \quad \text{unit vector of the wire } i$$

for $i = 1, \ldots, 3$.

For the evaluation of (13), the expression $\mathbf{w}_a^T \mathbf{w}_a(t)$ can be calculated as

$$\mathbf{w}_a^T \mathbf{w}_a(t) = s_1(t) - 2m s_2(t) + s_3(t)$$

(17)

with

$$s_1(t) = m^2 \|\ddot{\mathbf{x}}(t)\|_2^2$$
$$s_2(t) = \sum_{i=1}^{3} \ddot{\mathbf{x}}(t)^T \mathbf{e}_i(t) \underbrace{k_i(l_i(t) - l_{0,i})}_{:=F_{pre_i}(t)}$$

(18)

$$s_3(t) = \sum_{i=1}^{3} \left[\left(\mathbf{e}_i(t)^T \begin{bmatrix} F_{pre_i}(t) \\ 0 \end{bmatrix} \right)^2 + \left(\mathbf{e}_i(t)^T \begin{bmatrix} 0 \\ F_{pre_i}(t) \end{bmatrix} \right)^2 \right]$$
$$+ 2[\mathbf{e}_1(t)^T \mathbf{e}_2(t) + \mathbf{e}_1(t)^T \mathbf{e}_3(t) + \mathbf{e}_2(t)^T \mathbf{e}_3(t)]$$

where only the passive system is assumed.

Discretizing t with a sampling rate of 0.001 s the value of $J(\mathbf{k}, \mathbf{l_0})$ for the evaluation of (13) can be calculated e.g. by using trapezium rule with $iT = 0$ and $iT + T = 2$. The objective function of the optimization is defined by $J(\mathbf{k}, \mathbf{l_0})$.

The optimization of the spring parameters k_i and $l_{0,i}, i = 1, 2, 3$, can be performed by minimizing $J(\mathbf{k}, \mathbf{l_0})$, e.g. with the MATLAB® function fmincon given the following boundary conditions:

$$0 \le k_i \le \infty, \quad i = 1, 2, 3$$
$$1 \le l_{0,i} \le \min_{0 \le t \le 2} (l_i(t)), \quad i = 1, 2, 3 \tag{19}$$
$$F_{pre_i}(t) \ge 5 \quad i = 1, 2, 3$$

ensuring only positive spring constants, positive spring forces defined by a positive difference $(l_i(t) - l_{i,0})$ for any $0 \le t \le 2$, a minimal spring length of 1 m, and a predefined minimum wire force of 5 N at any time. The optimization is started using the initial value $\mathbf{x}_0 = [1.5\ 4.8\ 16\ 2\ 2\ 2]$ for $\mathbf{k}$ and $\mathbf{l_0}$ fulfilling the defined boundary conditions. It converges delivering the following parameters

$$\mathbf{k}_{opt} = [k_{opt_1} k_{opt_2} k_{opt_3}] = [2.68\ 2.91\ 4.38] \tag{20}$$

$$\mathbf{l}_{0_{opt}} = [l_{opt_{0,1}} l_{opt_{0,2}} l_{opt_{0,3}}] = [1.91\ 1\ 1]. \tag{21}$$

Using these values, the forces of the hereby defined springs can be calculated as

$$\mathbf{F}_{pre,opt}(t) = \sum_{i=1}^{3} F_{pre,opt_i}(t) \mathbf{e}_i(t) \tag{22}$$

with

$$F_{pre,opt_i}(t) = k_{i_{opt}} (l_i(t) - l_{0,i_{opt}}), i = 1, 2, 3. \tag{23}$$

Looking at the magnitude of the spring forces F_{pre,opt_i} for each spring over one cycle (Fig. 7), it can be observed that the prescribed minimal wire force is maintained in all wires.

The resulting force produced by the just dimensioned springs $\mathbf{F}_{pre,opt}$ counteract the inertial forces caused by the low frequent platform movement while the high frequent inertial forces cannot be compensated (Fig. 8).

To discuss the quality of the optimization result, first a purely active system is modeled where only actuators have to keep the platform on the desired cyclic
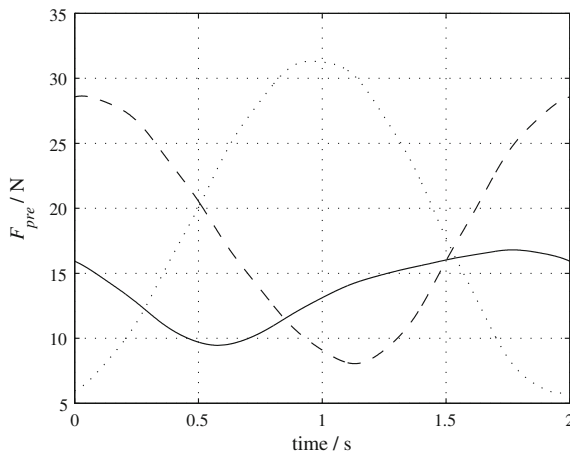
Fig. 7 Forces produced by the optimized springs (*solid*: spring 1; *dashed*: spring 2, *dotted*: spring 3
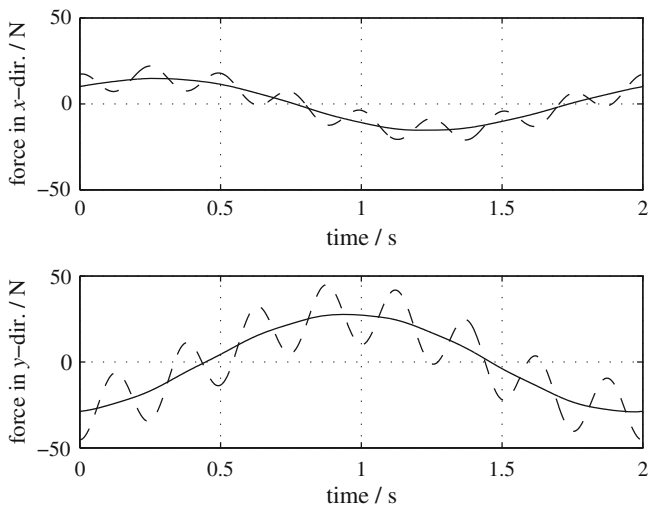
Fig. 8 Inertial force of the platform (*dashed line*) and inverted sum of forces produced by the springs (*solid line*) in x- and y-direction

trajectory. The following equation describes the dynamic system neglecting friction and actuator masses:

$$\mathbf{A}^{T}(\mathbf{x}(t))\mathbf{F}_{act}(t) = m\ddot{\mathbf{x}}(t). \tag{24}$$

Here, the unknown forces $\mathbf{F}_{act}$ have to be determined for any $t \in [0, 2]$. Since this system is underdetermined but has to maintain the wire force limits, again an optimization problem with boundary conditions can be specified. A quadratic opti-
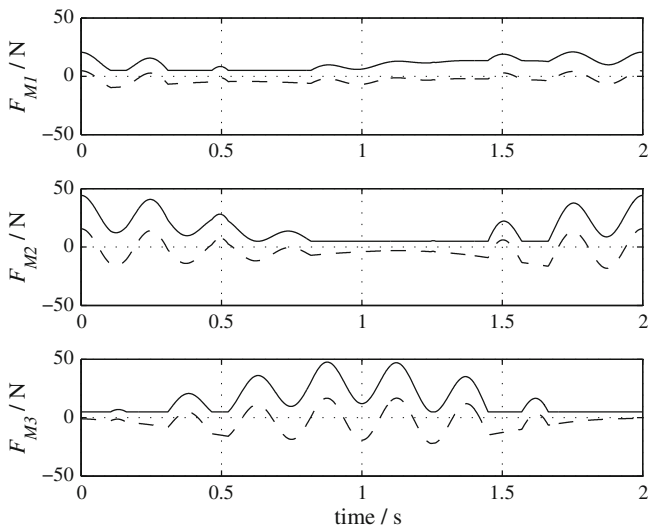
Fig. 9 Required actuator force without springs (*solid line*) and with springs (*dashed line*) (F_{Mi}: force produced by the motor placed at point $A_i, i = 1 \ldots 3$)

mization criterion is chosen which warrants continuity of the single wire forces [12]:

$$\min \|\mathbf{F}_{act}\|_2$$

subject to

$$\mathbf{A}^T \ \mathbf{F}_{act} = m\ddot{\mathbf{x}}(t)$$
$$\mathrm{F}_{min} \leq \mathbf{F}_{act} \leq \mathrm{F}_{max} \tag{25}$$

where $\mathbf{F}_{act} \in \mathbb{R}^m$ denotes the m tendon forces to be optimized. As for the springs, the minimal wire force F_{min} was set to 5 N, an upper bound F_{max} was not set.

Finally, the hybrid system combining the springs and the active system is modeled and allows the evaluation of the effects of the springs. Therefore, the required actuator forces of the purely active system $\mathbf{F}_{act}$ are compared to the actuator forces of the hybrid system $\mathbf{F}_{diff}$ which can be calculated by

$$\mathbf{F}_{diff}(t) = \mathbf{F}_{act}(t) - \mathbf{F}_{pre,opt} \tag{26}$$

It can be observed that the springs considerably reduce the amount of required actuator force by factors between 2.8 (motor 2) and 4.4 (motor 1) (Fig. 9). In the hybrid system, all motors apply positive and negative forces.

4 Conclusion and Outlook

Wire robots are probably the most suitable robotic subgroup to be used as modular, reconfigurable systems. The advantage of this modularity is the relatively simple adaptability to other tasks. This advantage can be further increased by utilizing different kinds of deflection concepts as well as the integration of passive elements in parallel or serial to the actuators.

Regarding the choice of the deflection concept for a given task, clear design rules can hardly be given. If a task cannot be realized with the minimum number of wires required for the given number of degrees of freedom, the increase of the number of used wires might already be sufficient, while the deficits of certain concepts disqualify them in advance for other tasks. The herein presented approach of using passively guided deflection units nicely demonstrates these aspects: The given task could probably be realized with other deflection concepts. However, these concepts would require more powerful actuation units and/or a larger frame, e.g. in case of fixed deflection units, which might not be feasible under given circumstances.

As for the wire deflection, several approaches exist to extend the actuation concepts and, thereby, the range of realizable applications. For example, the use of passive, energy-storing elements in the actuation concept does not only compensate in certain cases for the disadvantageous use of uni-directionally loaded motors in classical wire robots. Furthermore, these elements can relieve the motors from static and dynamic end-effector load. Simple applications have already proven the feasibility and advantages of using counterweights or springs in wire robots. The more sophisticated, task-specific methods such as the eigenmotion approach presented in this paper have a large impact on the energy consumption and load capabilities of a robot. In the presented example, we had to add a secondary, high-frequent oscillation to the basic elliptic movement to be able to demonstrate the effects of the additional springs: Despite the arbitrary position of the trajectory in the workspace, the oscillator, i.e. the combination of the springs and the end effector, could almost optimally follow the cyclic trajectory without any interference of the motors. In a next step, the load induced by the proper motor inertia and frictional effects will be integrated into the eigenmotion approach.

The third basic component of wire robots has not been discussed within this paper: The proper wire. In the literature, its choice is commonly explained with the need for types with a maximum load-to-weight ratio. Model-based compensation is normally applied to deal with unavoidable effects like elongation due to elasticity. In contrast, the utilization e.g. of these elastic effects for different control modes has not been discussed yet. In this context, over-actuated wire robots are a unique robotic subgroup: The adjustable pre-tension of wire robots allows to change the properties of the robot in a wide range, from an elastic to a comparatively stiff structure. This adaptability does not require any hardware adaptation but might allow to operate a given wire robot in different, complementary control modes, from sensitive force control to precise position control. This research field, combined with the presented options for deflection units and actuation units might considerably widen the task

spectrum for wire robots and, thus, allow to occupy some of the numerous application niches where rigid-link robotics comes to its limits.

References

1. Merlet, J.-P.: Marionet, a family of modular wire-driven parallel robots. In: Lenarcic, J., Stanisic, M.M. (eds.) Advances in Robot Kinematics: Motion in Man and Machine, pp. 53–61. Springer, Netherlands (2010)
2. von Zitzewitz, J., Rauter, G., Steiner, R., Brunschweiler, A., Riener, R.: A versatile wire robot concept as a haptic interface for sport simulation. In: Proceedings of the 2009 IEEE International Conference on Robotics and Automation (ICRA), pp. 313–318. Kobe, Japan, 12–17 May 2009.
3. Fang, S.: Design, modeling and motion control of tendon-based parallel manipulators. VDI Fortschritts-Bericht, 2005.
4. Faschinger, F., von Zitzewitz, J., Pernkopf, F.: Ein paralleler, 8-achsiger Seilroboter mit grossem Arbeitsraum als Handlingapplikation. In: Proceedings of Internationales Forum Mechatronik, pp. 218–228. Linz, Austria, 2006.
5. Pott, A., Meyer, C., Verl, A.: Large-scale assembly of solar power plants with parallel cable robots. Robotics (ISR). In: 2010 41st International Symposium on and 2010 6th German Conference on Robotics (ROBOTIK), pp. 1–6, June 2010.
6. Bruckmann, T., Mikelsons, M., Brandt, T., Hiller, M., Schramm, D.: Wire Robots Part I + II Kinematics, Analysis and Design–Dynamics. Control and Application. I-Tech Education and Publishing, Vienna (2008)
7. Mayhew, D. Bachrach, B., Rymer, W.Z., Beer, R.F.: Development of the Macarm–a novel cable robot for upper limb neurorehabilitation. In: Proceedings of the 9th International Conference on Rehabilitation Robotics (ICORR), pp. 299–302, June, July 2005.
8. von Zitzewitz, J., Rauter, G., Vallery, H., Morger, A., Riener, R.: Forward kinematics of redundantly actuated, tendon-based robots. In: Proceedings of the IEEE/RSJ International Conference on Intelligent Robots and Systems (IROS), pp. 2289–2294, 2010.
9. Maeda, K., Tadokoro, S., Takamori, T., Hiller, M., Verhoeven, R.: On design of a redundant wire-driven parallel robot warp manipulator. In: Proceedings fo the 1999 IEEE International Conference on Robotics and Automation, vol. 2, pp. 895–900, 1999.
10. Bruckmann, T. Sturm, C., Wildan, L.: Wire robot suspension systems for wind tunnels, wind tunnels and experimental fluid dynamics research, Dr. Jorge Colman Lerner and Dr. Ulfilas Boldes (ed.), ISBN: 978-953-307-623-2, InTech. http://www.intechopen.com/articles/show/title/wire-robot-suspension-systems-for-wind-tunnels (2011)
11. Kawamura, S., Ida, M., Wada, T.: Development of a virtual sports machine using a wire drive system–a trial of virtual tennis. In: Proceedings of the IEEE/RSJ International Conference on Intelligent Robots and Systems (IROS), pp. 111–116. Pittsburgh, 1995.
12. Verhoeven, R.: Analysis of the workspace of tendon-based Stewart platforms. Ph.D. Thesis, Duett, Universittsbibliothek Duisburg, 2004.
13. Lawrence, D.A., Pao, L.Y., Aphanuphong, S.: Bow spring/tendon actuation for low cost haptic interfaces. In: First Joint Eurohaptics Conference and Symposium on Haptic Interfaces for Virtual Environment and Teleoperator Systems, pp. 157–166, March 2005.
14. von Zitzewitz, J., Wolf, P., Novakovic, V., Wellner, M., Rauter, G., Brunschweiler, A., Riener, R.: A real-time rowing simulator with multi-modal feedback. Sports Technol. **1**(6), 257–266 (2009)
15. Omlin, X., von Zitzewitz, J., Rauter, G., Morger, A., Achermann, P., Riener, R.: Robotic platform to investigate the effects of vestibular stimulation on sleep. In: 19. Jahrestagung der Deutschen Gesellschaft fr Schlafforschung und Schlafmedizin (DGSM), 2011.

16. Vallery, H., Duschau-Wicke, A., Riener, R.: Hiding robot inertia using resonance. In: Engineering in Medicine and Biology Society (EMBC), 2010 Annual International Conference of the IEEE, pp. 1271–1274, 31 Sept 4 2010.
17. Uemura, M., Kawamura, S.: Resonance-based motion control method for multi-joint robot through combining stiffness adaptation and iterative learning control. In: IEEE International Conference on Robotics and Automation, ICRA '09, pp. 1543–1548, May 2009.

Use of High Strength Fibre Ropes in Multi-Rope Kinematic Robot Systems

Jens C. Weis, Björn Ernst and Karl-Heinz Wehking

Abstract   High strength fibre ropes are facing a strongly increasing interest for rope driven applications. Basic characteristics such as strength are already competitive or even outperforming wire ropes; however other limitations still prevent their full reliable industrial use. One particular application where the advantages of high strength fibre ropes do have an extraordinary important effect on the usability of the application is the use in robot systems with multi-rope kinematics. Basic requirements of these systems are (among others) high accuracy paired with a high efficiency, which means high process velocities as well as high accelerations and decelerations. Many tests have already been conducted to simulate a wide range of load settings—however up to date testing of fibre ropes in high speed usage is still mostly missing. This article describes the state of the art of high strength fibre rope usage in material handling, discusses advantages and disadvantages of these ropes and points out the most important challenges for research and improvement of rope driven robot systems.

1 Introduction

At present high strength fibre ropes are already used as high efficient suspension elements and are therefore a good choice for a wide range of applications, such as manufacturing processes or materials handling processes. Conventional materials handling systems driven by wire ropes are coming to their limits with regards to high process speeds and minimisation of process times, so there is a significant trend towards establishment of high strength fibre ropes in these applications where low weight, high strength and low inertia are basic prerequisites. Analyses focusing

J. C. Weis (✉) · B. Ernst · K.-H. Wehking
Institute of Mechanical Handling and Logistics (IFT), Universität Stuttgart,
Stuttgart, Germany
e-mail: Jens.Weis@ift.uni-stuttgart.de

on behaviour of high strength fibre ropes at high dynamic usage are not available up to today, so obviously there is demand to research on their dynamic resistance. Fast loading, changing loads, load oscillations and the influences on related rope characteristics (e.g. bending fatigue) also need to be analysed and for later use in practice.

One example from the field of materials handling processes are robot systems which are born by multi-rope kinematics. For an effective and economic use of these systems high accelerations and velocities (i.e. low process times) are mandatory. As these robot systems also need a high positioning precision it is obvious that focusing on these applications allows development of basic fundamentals regarding the design of configurable large-scale rope kinematics for rope-born robots as well as for further rope applications.

2 High Strength Fibre Rope Research

2.1 State of Research

Standards for design and testing of high strength fibre ropes in service are available at present and even partially defined in different national and international standards [1–4]. However, to date almost all of these are dealing with basics only and most of them have been developed for maritime use and are limited to this scope only. These standards usually address testing of the ultimate break load UBL, possible weight and modulus test methods as well as handling suggestions, but they do not cover lifetime estimations or prediction methods. Additional influences which might result from high-dynamic usage (e.g. additional friction, heat buildup and wear) are so far not considered and are therefore usually taken into account by using high safety factors which are based on experience.

Since there are so many different fields of applications for high strength fibre ropes, it seems generally not possible to define one material or construction which would suit every application so a variety of rope materials and rope constructions is usually suitable to meet the specific needs of a particular application [5]. Regarding the application of robot systems with multi-rope kinematics this situation results in excessive experimental work in order to obtain reliable data about the long-term behaviour of the ropes used under combined loading and with respect to highly dynamic influences as well as to define reliable and safe discard criteria. Figure 1 gives a schematic overview on the current state of high strength fibre rope research with respect to different deterioration mechanisms and system parameters of high strength fibre ropes [6]. As can be seen (among others) is that the influence of velocity and acceleration on rope life is almost fully unknown.

It can be summarized that—despite multiple research and industrial based efforts— to date there is a lack of knowledge in the field of fibre rope technology. Many challenges and questions still remain to be solved and answered.
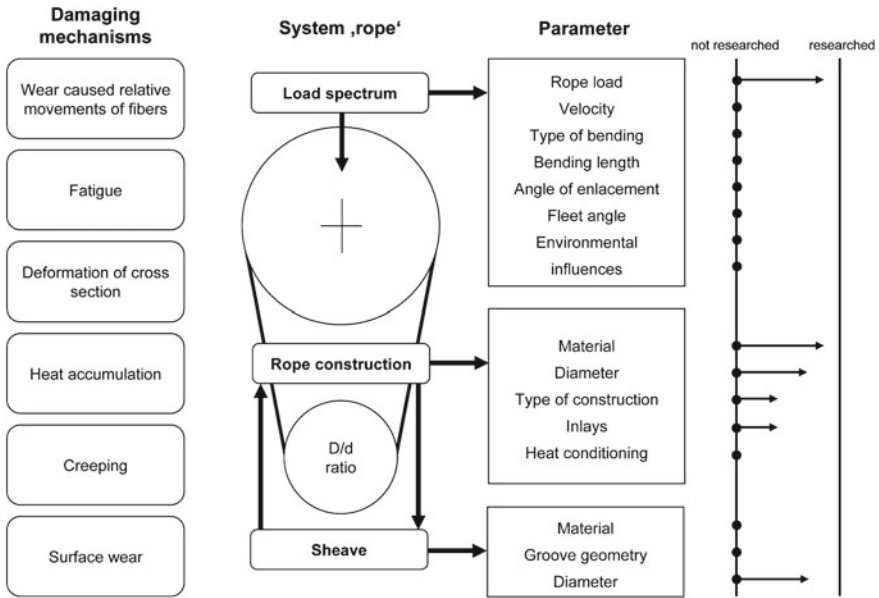
Fig. 1 Damaging mechanisms and system parameters at running fibre ropes (analog [6])

2.2 High Strength Fibre Ropes

High strength fibre ropes comprise different characteristics depending on their basic material(s), their construction and their manufacturing processes.

Typical characteristics of high strength fibre ropes include small diameter, low specific weight, low stretch, torque balance (depending on construction) with good bend-over-sheave fatigue life as well as outstanding tension-tension fatigue life. Table 1 additionally gives a general understanding of the material properties of different synthetic fibres [7]. Regarding the physical properties and the material characteristics shown in Table 1 especially high strength fibre ropes might seem to be of excellent suitability for the intended use in robot systems with multi-rope kinematics. Compared to wire ropes one of the main advantages of high strength fibre ropes may be seen in the fact that these show no need of (re-)lubrication and may therefore be used in many applications where this requirement is essential. The main disadvantages of high strength fibre ropes (compared to wire ropes) may at the time be seen in a low sensitivity against high temperatures, low lateral stiffness and a lack of standardised discard criteria.

Table 1 Matrix of comparison of material properties of different synthetic fibres [7]

Material grade of high-strength synthetic fibres	[E]	PA Polyamide PA 6.6 PA 6	PES Polyester	PP Polypropylene	HMPE High-molecular polyethylene	Aromatic-Polyamide (Aramide)	PBO (Zylon)	LCP Aromatic polyester (Vectran)
Trade name		Perlon, Nylon, Nylsuisse Enkalon	Diolen, Trevira, Dacron, Tersuisse	Hostaien Softlene, Leolene	Dyneema, Sektra	Twaron, Kevlar, Technora	Zylon	Vectran
Fibre count breaking load or breaking length in km	cN/tex	65–85	60–85	more than 47	280–400	200–250	370	220–250
Tensile strength	N/mm^2	741–969	741–969	300–500	2,688–3,648	2,880–3,600	5,624	3,102–3,525
Breaking elongation	%	12–25	10–20	15–25	3.8	2–4	2.5	3.3
Density	kg/dm^3	1.14	1.38	0.91	0.95–0.96	1.44	1.52	1.41
Moisture expansion	%	5–10	=0	=0	=0	=0	5	=0
Absorbtion of water/humidity	%	1–7	0.5–2	0	0	2–5	0.6	1
Melting point	°C	215 250	260	165	150	480	650	330
Light resonance		Good	Very good	Only good if equipped	Good	Moderate up to poor	Poor	Poor
Chemical resistance		Acidic unresistant, stable to weak bases	Acidic resistant but alkail unresistant	Acidic and alkali-resistant	Resistant apart from strength oxidant	Acidic and alkali-resistant	Acidic and alkali-resistant	Acidic and alkali-resistant (apart from dissolver)
Other negative properties		Hardening due to atmospheric influence	Unresistant to shear strength	Low abrasion resistance	Low creep rupture strength, creeping approx. 15 % of MBL	Low shear strength and weak resistance up to low temperatures	Loses relevant tensile strength due to weathering and absorbtion of humidity	
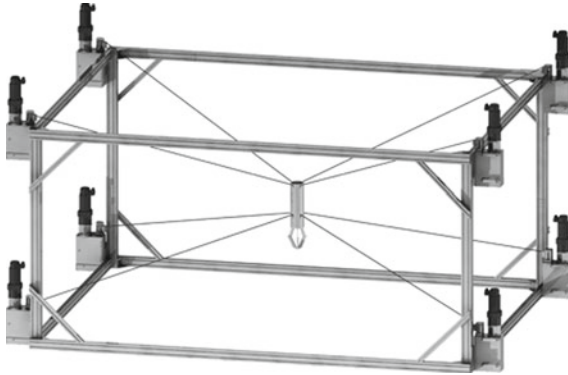
Fig. 2 Prototype of the rope-driven robot [8]

Fig. 3 HMPE fibre rope as used in the rope-driven robot (*scaled*)

2.3 Robot Systems with Multi-Rope Kinematics

Figure 2 shows the prototype of a multi-rope robot system built up at 'Fraunhofer Institute of Manufacturing, Engineering and Automation IPA' [8]. In this system the 'rope drive' comprises of eight similar winches which control eight suspension high strength fibre ropes which are connected to a picker. Coming from the winch, each rope passes two deflection sheaves and is then connected to the picker via a special end termination. When passing over the winch and the sheaves each of these ropes is paid out, bent, deflected and twisted in different angles and directions; thus, due to alternating payloads carried by the picker as well as these different angles and directions each rope obviously faces different loadings.

In the prototype shown at Fig. 2 high strength fibre ropes which consist of ultrahigh molecular weight polyethylene (UHMWPE) and a twelve braid strand construction with a nominal diameter of 2.5 mm and a minimum break load (MBL) of 5.8 kN were selected, see Fig. 3.

In this development stage the primary goal was the initial determination of the functionality of the system; testings did not include fatigue life testing (i.e. bending fatigue) of the used high strength fibre ropes.

3 High Strength Fibre Rope Testing

3.1 General

In the following chapters several possibilities and exemplary results of high strength fibre rope tests coming from so called 'running applications' conducted at the Institute of Mechanical Handling and Logistics (IFT) are described and summarized. The

questions raised with regards to dynamic behavior and fatigue life characteristics of the high strength fibre ropes as they will occur in service of the described robot system (bending fatigue life, deterioration of UBL, tension- tension fatigue life, accelerations and velocities) have not been answered and quantified before. As described above these parameters are significant with regards to positioning accuracy of the picker and minimization of picking time as well as safety and economical service of the system (i.e. availability), which directly depends upon the proper functionality of all of the used high strength fibre ropes [9]. Thus, multiple tests are to be conducted before a high strength fibre rope may be approved for use in a particular application, especially if high safety against partial or complete failure of the system is required. Therefore, attention should be paid to the following [10]:

- specific strength and specific weight,
- bending fatigue life (cyclic bend over sheave performance CBOS),
- abrasion resistance,
- cutting performance,
- actuator performance (i.e. spooling behaviour, traction characteristics, etc),
- temperature and environmental boundary conditions,
- rope end terminations,
- discard criteria ,
- inspection intervals and inspection procedures.

3.2 Standard Cyclic Bend Over Sheave Testing (CBOS)

Analyses of the static strength behaviour of high strength fibre ropes are to date state of research (see Sect. 2.3). If high strength fibre ropes are not only tensile loaded, but bent over sheaves additionally or are stored on winches they are usually bent from straight state to bent state and back to straight state cyclically. When undergoing this bending process the single fibres and strands of the rope face alternating loadings regarding tension stress, bending stress and lateral pressure.

The determination and prediction of the lifetime of running high strength fibre ropes is limited to specific use in the industrial fields of lifting applications, offshore technology and mining [11]. Contributions determining the influences of the multiple, superposed stresses in the strands and fibres have been conducted by several authors but predominantly in the field of maritime applications, see e.g. Hobbs [12] and van Leeuwen [13]. Next to the stresses a use of high strength fibre ropes in 'running' applications is only possible because the strands and fibres move relatively against each other. Obviously, these relative movements between fibres and strands are constrained by friction and therefore lead to different types of surface wear.

Due to this surface wear of strands and fibres even an explicit appraisal of single fibre stresses would not provide reliable information regarding the lifetime of the strand (and the rope) to be expected in a specific application, even with defined load scenarios.

Fig. 4 CBOS testing machine for small rope diameters at the Institute of Mechanical Handling and Logistics, Stuttgart (IFT)
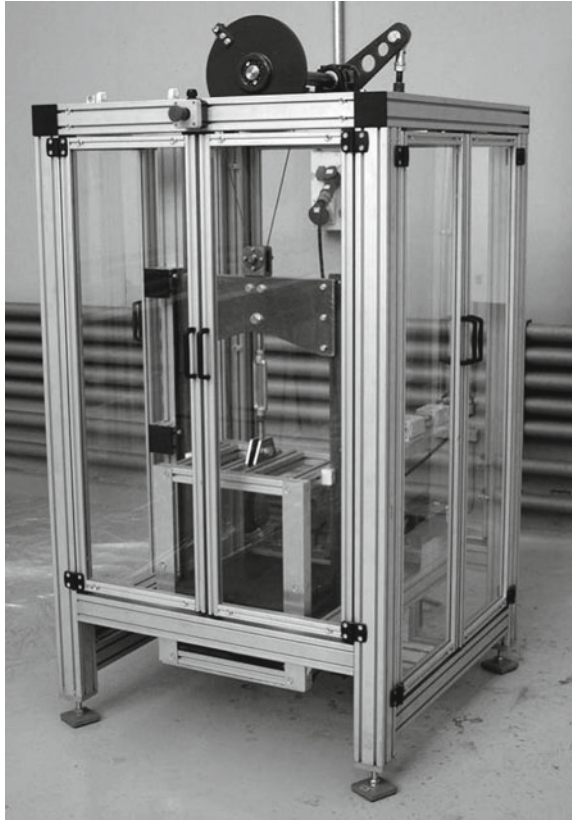
So today, the lifetime of high strength fibre ropes can be only determined with good precision in cyclic bend over sheave testing (CBOS). Figure 4 shows a typical CBOS test rig for the determination of the rope lifetime (i.e. bending cycles) under defined loading and bending conditions. This bending fatigue machine consists of a driven steel made deflection sheave and a changeable test sheave. It performs an oscillating movement with a predetermined stroke so the test rope changes from straight to bent and back to a straight state. The rope is therefore loaded by homogeneous bending cycles. The rope force is induced by a constant weight which is directly connected to the test sheave.

Systematic testing of running high strength fibre ropes at IFT started in 1997. In these CBOS tests the bending fatigue life characteristics and other behaviour relevant for the use of these ropes in practical service were investigated [14–17]. The results of the CBOS testings performed with a high strength fibre rope are displayed in Fig. 5 in a double logarithmic diagram [17]. The abscissa (x-axis) gives the specific (i.e. diameter-related) rope force, the ordinate (y-axis) the number of bending cycles until breakage. As can be seen, the bending fatigue life of the rope is

reduced significantly if the rope force is increased at a constant D/d ratio. Figure 5 also gives the number of bending cycles to breakage of wire ropes which are known for their good bending fatigue life. It can be seen that at a comparably small D/d ratio of ten the bending fatigue life of the tested high strength fibre rope outperforms both wire rope constructions remarkably; this shows the general pertinence of high strength fibre ropes for use in running applications under certain conditions.

As can be seen from the diagram, if the specific rope force exceeds approximately $300\,\text{N/mm}^2$ the bending fatigue life until breakage of the rope is decreased disproportionally high. In the field of wire ropes this area, where the fatigue caused breakage of the rope turns into a forced rupture, is usually called 'Donandt- point' [18].

The CBOS test results gained at constant (low) speeds are fundamental data for later comparisons regarding additional influences such as high dynamics and parametric dimensioning of rope drives and rope drive components such as sheaves and winches. With a sufficient data basis of CBOS tests lifetime diagrams for several kinds of high strength fibre rope may be generated (compare Fig. 5).

3.3 Analysis Methods

The number of bending cycles to breakage and to the point of discard both depend on multiple parameters (i.e. rope load, D/d ratio, groove design, coating etc.). An appropriate method to analyse experimental bending fatigue test results and to gain a usable approach for the lifetime prediction is by use of multiple regression analyses. This method has proven to be very effective yet accurate and is widely established in the field of wire ropes.

For the high strength fibre ropes used in the robot system described above no dimensioning references (based on statistically determined large-scale studies as available in the field of wire ropes) are available. Based on single CBOS test series a lifetime formula based on multiple regression analysis for the determination of the number of bending cycles until breakage of the rope for small and medium diameter-related loads was generated, see Eq. 1 [14, 16]

$$\lg \overline{N} = b_0 + b_1 \lg \frac{S d_0^2}{d^2 S_0} + b_2 \lg \frac{D}{d} + b_3 \frac{S d_0^2}{d^2 S_0} \lg \frac{D}{d} \tag{1}$$

The estimated average number of bending cycles until breakage N is be calculated as function of the applied load S and the D/d ratio of rope and sheave. The unified load S_0 and the unified diameter d_0 are used to keep the equation non-dimensional in the sense of bending cycles until breakage of the rope. The regression coefficients b_i derive from the regression analysis of the experimental CBOS test results.

The results of the multiple regression analyses should be compared to the experimental results and analysed subsequently with statistical means. In wire rope research, the subsequent analysis of the performed regression calculations by means of coefficient of determination and standard deviation has proven to be effective [18].
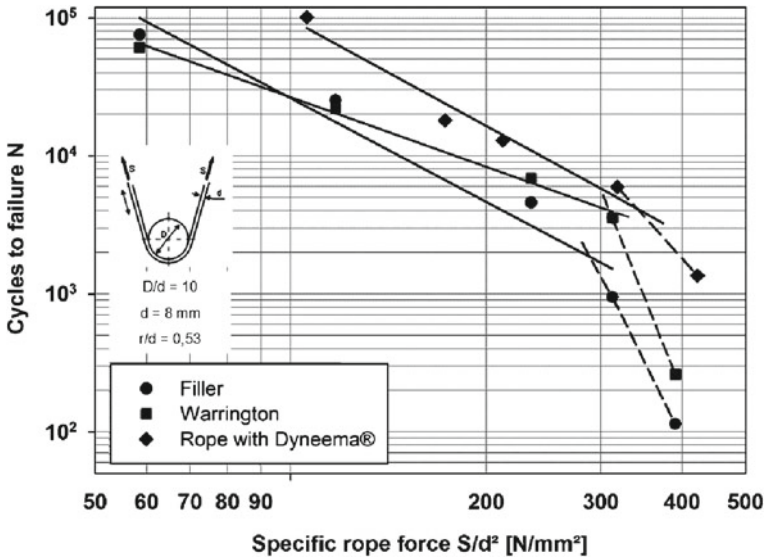
Fig. 5 Bending fatigue life of high strength fibre ropes and wire ropes [13]

The coefficient of determination describes the quality of the regression approach which was used for the analysis of the experimental test results, the standard deviation is used to analyse the degree of scatter of the experimental test results with regards to the chosen regression approach. In wire rope research, the logarithmic Gaussian distribution has proven to describe the failure probability of wire ropes with high accuracy [18].

3.4 Influence of High Accelerations and Velocity on Bending Fatigue Life

High accelerations and velocities of ropes in running applications are at present known only for steel wire ropes used in catapult systems (e.g. in fair rides such as [19] or on military aircraft carriers) but have not been quantified before. Sloan [20] exemplarily monitored the influence of the test speed during CBOS testing on the bending fatigue life of high strength fibre ropes. It can clearly be seen that an increase in cycling speed results in a significant decrease of the bending fatigue life of the tested high strength fibre rope, see Fig. 6.

With regards to the multi-rope robot system discussed above, an increase in velocity (i.e. decrease of process time) will also increase friction and wear. Taking into account the inertia of the picker, high tensile stresses and bending stresses in the ropes and significant rope elongations will make sophisticated controlling necessary

Fig. 6 Influence of test speed on the lifetime of a fibre rope [20]
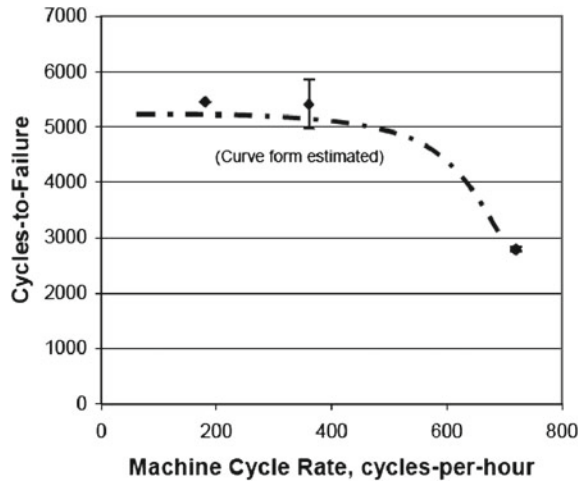
in order to realize the required positioning accuracy of the picker. It is obvious that accelerations and velocities exert significant influence on the fatigue life of the used fibre ropes; this should be taken into account as early as possible, ideally already in the planning stage of the system with regards to reliability, availability and economic usage. Further research which focuses specifically on the suspension elements with regards to dynamic influences is recommended.

3.5 Major Trends

In the last years remarkable improvements in the bending performance of high strength fibre ropes in running applications where gained. Compared to steel wire ropes the bending performance at small D/d ratios is even better than for steel wire ropes [10]. IFT continuously tests bending fatigue life of high strength rope constructions in systematic CBOS testing series. Figure 7 exemplarily describes the trends of improvement of bending fatigue life of HMPE- fibre ropes (d = 8 mm) from 2007 to 2012. A remarkable increase of the bending fatigue life (i.e. bending cycles until breakage)—even for small D/d—ratios can be found.

Currently there are many efforts to optimize fibre rope constructions for use in running applications (e.g. [21, 22]). For example, a research project at the University of Chemnitz (Germany) called 'InnoZug' is at the time generating experimental, scientific knowledge on lifetime and wear mechanisms of non-coated high strength fibre ropes of several materials and constructions [23]; another research project at the University of Aachen (Germany) called 'Smart Rope' aims to develop a rope monitoring system which is capable of communicating the state of degradation of the rope in service [24]. The storage of fibre ropes on drums in single layer spooling is currently state of research [25], but as was found at the University of Clausthal

CBOS tests at high strength fiber ropes with HMPE fibers
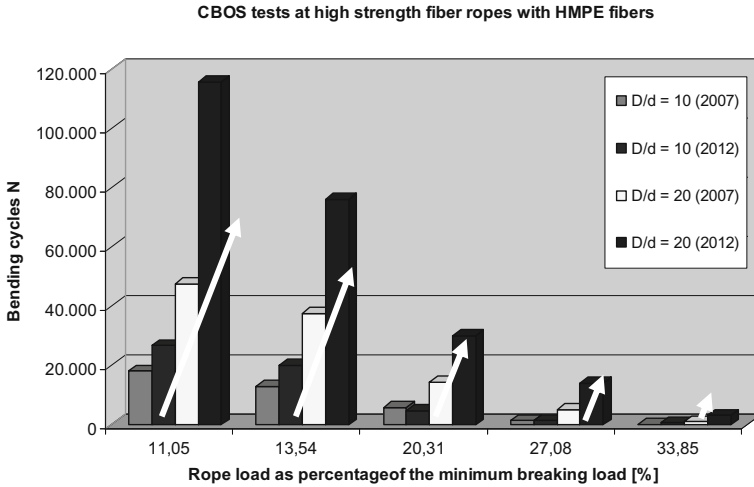
Fig. 7 Improvement of CBOS fatigue life from 2007 to 2012

(Germany) that there are specific requirements of the storage unit (i.e. winch) to be taken into account while used with fibre or fibre-cored rope constructions because of their low lateral stiffness [26]. A research project performed at IFT which investigates the usability of high strength fibre ropes for lifting in automated rack feeders is currently in its final phase. Within this research the focus is laid on the lifetime of the high strength fibre ropes with special interest on the elements of the rope drive (sheaves, winch, end terminations) with the goal to replace wire ropes the benefit of smaller engines, drive trains and outer dimensions of the systems.

Bending fatigue testing (especially CBOS testing) has shown to be the fundamental basis for validation of the choice of the right high strength fibre rope. Depending on the intended application, other influences need to be addressed and validated additionally (tension-tension testing, etc).

4 New Test Rig for Bending Fatigue Testing at High Accelerations

As described above high process accelerations/decelerations and velocities of the picker in the robot system result in bending and tension-tension loading of the used high strength fibre ropes.

In the first stage the primary focus was laid on the bending fatigue life of the high strength fibre ropes used in the system. As discussed, tension-tension fatigue life of the ropes needs to be addressed as well. Furthermore, high frictional loadings occur at the sheaves and winches between ropes and grooves. These cause premature
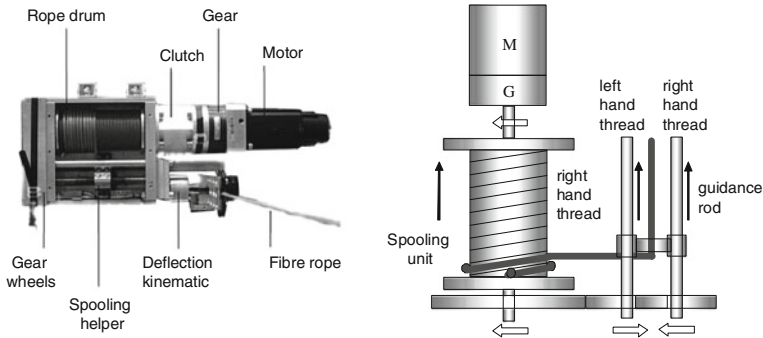
Fig. 8 Elements of the fibre rope winches (analog [8])

deterioration of the surfaces of the ropes which result in reductions of the ultimate break loads and premature levels of discard.

Figure 8 shows one of the winches as they are used in the robot system [8]. Each of the eight winches of the robot system consists of rope drum, drive chain, spooling helper and a special rope deflection sheave. The rope is spooled in single layer and guided via a customized deflection kinematic.

To evaluate the overall behaviour of the high strength fibre rope in the system the mere simulation of the spooling behaviour is not sufficient. For a precise determination of these (and other) mechanisms a new test rig was found to be necessary which is developed at IFT, see Fig. 9. In this test rig four winches for storage of the rope are attached at the upper end. The high strength fibre ropes run from the winches over a deflection sheave and back to the top where they are fixed via special end terminations, resulting in a double reeving. A test weight which is guided by slide bearings provides a constant, defined rope load during testing. As can be seen from the drawing, four high strength fibre ropes may be tested simultaneously for sufficient analyses of combined parameters.

Further details are included in order to make the test rig as versatile as possible regarding variation of test conditions and test parameters. Due to its design and dimensioning accelerations up to $10 \, \text{m/s}^2$ may be realized which is approximately five times higher than accelerations in conventional lifting applications. For realization of these accelerations a minimum overall height of ten meters was found to be necessary. The test rig characteristics are summarized as following:

- variable load carrier for simulation of high tensile loads
- variable stroke / lifting height
- high modularity of the test rig components
- parallel testing of multiple ropes
- automatic visual monitoring of the rope condition
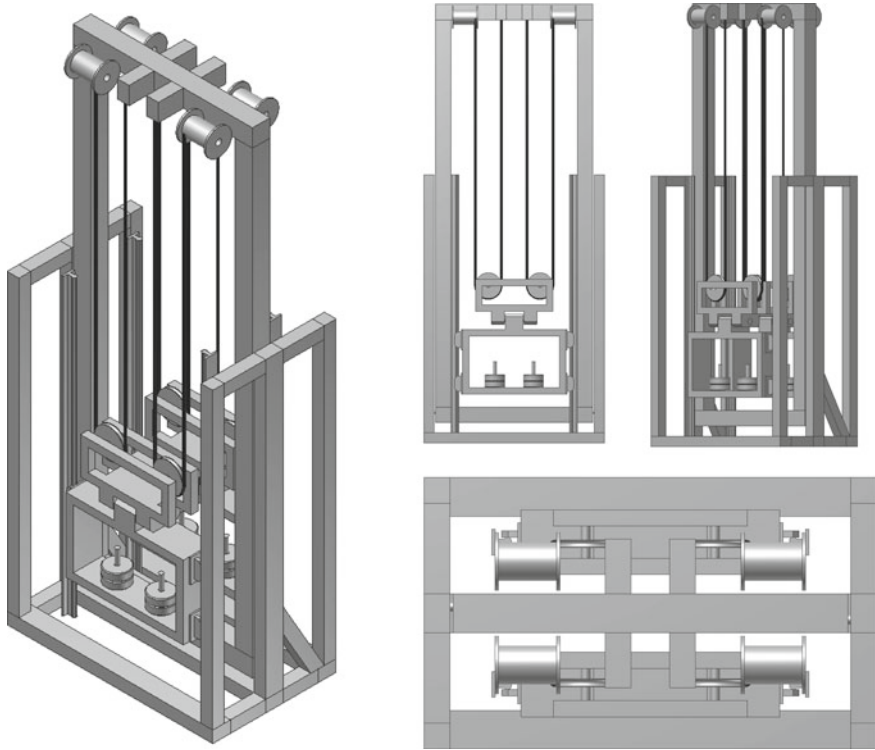
Fig. 9 Test rig for testing of accelerated high strength fibre ropes (schematic)

5 Summary

At present numerous endeavors are noticeable to establish lightweight high strength fibre ropes in running rope applications which comprise highly dynamic characteristics, such as in manufacturing processes and materials handling processes. Of course multiple other material handling applications can be found, but the robot system with multi-rope kinematics as described above seems one of the most potential applications for use of high strength fibre ropes. On the first prototype of this system multiple functional tests were conducted. However, additional expertise and experimental data of the fatigue life of the used high strength fibre ropes used in this application need to be gathered. This data and expertise is determined by means of fundamental experimental research—bending fatigue testing and tension-tension fatigue testing have proven to be adequate means to gain experience with regards to long term characteristics such as bending fatigue life, tension-tension fatigue life and resistance to high-dynamic influences of running high strength fibre ropes.

Wear has to be seen as crucial factor regarding the bending fatigue life of the high strength fibre ropes. Precise analysis methods of the actual fibre rope condition

in service are mandatory for safe and reliable definition of service intervals and to guarantee a sufficient positioning accuracy required by the system over its lifetime.

In order to determine their long-term performance under high accelerations a new test rig is built. With this test rig basic fundamental approaches are analysed and quantified. Based on the experimental results gained thorough analyses are conducted to determine further parameters such as friction behaviour, wear, temperature as well as influence of contaminants etc. under laboratory conditions.

Furthermore, application-specific deterioration parameters are to be identified and reliable indicators for a safe level of discard are to be defined. Thus, sufficient recommendations for dimensioning and scaling regarding economic and ecological aspects may be defined and a sufficient lifetime and availability in service of the system may be achieved. The rope drive elements such as sheaves and winches for storage of rope, deflection systems and end terminations are optimised.

The long term goal of the basic and fundamental research work described is to establish high strength fibre ropes also in other rope drive applications as a substitute of steel wire ropes or to make the realization of new rope drives and systems possible.

References

1. Recommended Practice for Design and Analysis of Stationkeeping Systems for Floating Structures, API RP 2SK, 2nd Edn, December 1996.
2. Fibre ropes - High modulus polyethylene - 8-strand braided ropes, 12-strand braided ropes and covered ropes. ISO 10325, 2009.
3. Faserseile: Beschreibung, Auswahl und Bemessung. VDI 2500, 1990.
4. Fibre ropes - Determination of certain physical and mechanical properties ISO 2307, 2005.
5. Simeon Whitehill, A.: Handbook of oceanographic winch, wire and cable technology. 3rd Edn, Chapter 3 High Strength Fibre Ropes. OCE 9942973, 2001.
6. Heinze, T.: Dimensionieren je nach Einsatzfall. In: Hebezeuge und Fördermittel 51 Nr.6 (2011).
7. Winter, S., Finckh-Jung, A., Wehking, K.-H.: Research and development of a new termination for high-tensile fibre ropes. In: Proceedings of the OIPEEC Conference: Safe use of ropes. College Station, Texas, USA 165–180 (2012).
8. Pott, A.: Cable-driven parallel robot for automated handling of components in all dimensions. In: Fraunhofer Institute for Manufacturing Engineering and Automation. Brochure 300/354e, Stuttgart (2010).
9. Uhlmann, E., Kraft, M., Tonn, N.: Entwicklung von Werkzeugmaschinen mit Parallelkinematik unter Verwendung von Seilantrieben. In: Modellbildung, Simulation und Optimierung, S.37-62.
10. Smeets, P.: Latest developments in high performance running fiber ropes with Dyneema. In: Contribution at the 4th Stuttgart Ropedays. Stuttgart (2012).
11. Vogel, W., Wehking, K.-H.: Neuartige Maschinenelemente in der Fördertechnik und Logistik - Hochfeste, laufende Faserseile. E-journal der Wissenschaftlichen Gesellschaft für Technische Logistik WGTL, 2004.
12. Hobbs, R.E., Burgoyne, C.J.: Bending fatigue in high strength fibre ropes. Int. J. Fatigue **13**(2), 174–180 (1991).
13. van Leeuwen, J.H.: Bending fatigue behaviour of twaron aramid ropes. Proceedings of the MTS Conference, In (1990)
14. Vogel, W.: Hochfestes Faserseil beim Lauf über Seilrollen. Draht 42, 11, 814–818 (1991). englisch. WIRE 42, 5, S.455-458 (1992).

15. Wehking, K.-H.: Endurance of high-strength fibre ropes running over Pulleys. OIPEEC Round Table, Reading September, In (1997)
16. Vogel, W.: Dauerbiegeversuche an gedrehten und geflochtenen Faserseilen aus hochfesten Polyethelenfasern. Euroseil Nr. **1**, 440–442 (1999)
17. Smeets, P.J.H.M., Vlasblom, M.P., Weis, J. C.: Latest improvements in HMPE rope design for steel wire rope applications. In: Proceedings of the OIPEEC Conference: / 3rd International Stuttgart Ropedays (Innovative ropes and rope applications). Stuttgart, 99–113 (2009).
18. Feyrer, K.: Drahtseile - Bemessung, Betrieb, Sicherheit, 2nd edn. Springer Verlag, Berlin (2000)
19. High Speed Rollercoasters (10.05.2010):http://www.intaminworldwide.com/
20. Sloan, F., Nye, R., Liggett, T.: Improving Bend-over-Sheave Fatigue in fiber Ropes. Sea Technology, July (2004)
21. Bosman, R.: Entwicklung von laufenden Seilen mit Dyneema. Fachkolloquium InnoZug, Chemnitz (2010)
22. Sloan, F.: Damage mechanisms in synthetic fibre ropes. In: Proceedings of the OIPEEC Conference, : / 3rd International Stuttgart Ropedays (Innovative ropes and rope applications). Stuttgart **259–271**(2009)
23. BMBF Forschungsprojekt InnoZug (10.05.2010): http://www.innozug.de
24. BMBF Forschungsprojekt Smart Rope (10.05.2010): http://www.mstonline.de/foerderung/projektliste/detail_html?vb_nr=V3TEX038
25. Lohrengel, A.: Einflüsse der Seileigenschaften von Kunststoffseilen auf die Trommel. Fachkolloquium InnoZug, Chemnitz (2010)
26. Dietz, P.; Schwarzer, T.: Die Eigenschaften neuer Seilkonstruktionen zur Realisierung von Leichtbauseiltrieben. Institutsmitteilung Nr. 32, IMW, Clausthal- Zellerfeld (2007).

Workspace Improvement of Two-Link Cable-Driven Mechanisms with Spring Cable

Amir Taghavi, Saeed Behzadipour, Navid Khalilinasab and Hassen Zohoor

Abstract The idea of multi-body cable-driven mechanisms is an extension of the original cable robots where the moving platform is replaced by a multi-body. Cables with variable lengths are attached between the fixed base and the links of the multi-body to provide the motion. There are possible applications for such mechanisms where complex motions as well as low moving inertia are required. One of the main challenges with such mechanisms is the high chance of interference between the cables or between the cables and the links of the multi-body mechanism. This can further reduce the usable workspace. In this article, the idea of adding passive cables in series with springs (spring cable) to improve the workspace is investigated. The spring cables can be added between the multi-body and ground or between the links. The idea is applied to a two-link planar multi-body cable-driven mechanism. The wrench feasible workspace (WFW) is found using the interval analysis. The WFW is shown to improve both in shape and volume.

A. Taghavi (✉) · S. Behzadipour · N. Khalilinasab · H. Zohoor
Department of Mechanical Engineering, Sharif University of Technology,
Tehran, Iran
e-mail: amir.taghavi@yahoo.com

S. Behzadipour
e-mail: behzadipour@sharif.edu

N. Khalilinasab
e-mail: navid.khalili.n@gmail.com

H. Zohoor
e-mail: zohoor@sharif.edu

1 Introduction

Cable driven robots are mechanisms in which the end-effector is moved by controlling the lengths of the cables connected to it. The cable robots are appealing because of their structural simplicity, high stiffness, and high exerted wrench-to-weight ratio and easiness of reconfiguration. Their main drawback is their small workspace and interference of cables, so one of their key issues is their optimal design for a desired workspace and given constraints [1].

A cable driven parallel manipulator, according to its number of cables (m) and the degrees of freedom of the end-effector (n), are classified as follows [2]:

IRPMs: Incompletely Restrained Positioning Mechanisms, in which the number of cables is less than or equal to the number of the DOFs, namely,

$$m \leq n$$

IRPMs robots rely on the presence of gravity or another ballast force to determine the resulting pose of the end-effector.

CRPMs: Completely Restrained Positioning Mechanisms, in which there is an extra cable, i.e.:

$$m = n + 1$$

RRPMs: Redundantly Restrained Positioning Mechanisms, in which there are more than one extra cable:

$$m > n + 1$$

Since IRPMs use less number of cables and actuators, the probability of cable interference as well as the production cost is lowered. However, in these robots, the volume of workspace and the magnitude of the externally applied wrench of the robot are limited by the ballast force. In contrast with IRPMs, RRPMs have larger workspace but the interference of cables and production cost become more challenging.

With such classification, a number of different definitions for the workspace of such robots are introduced and studied in the literature. One of the early works is for the one of the NIST ROBOCRANE [3], Which is a realization of a Gough–Stewart platform parallel manipulator while prismatic actuators are replaced by cables. Verhoeven and Hiller [4] used "controllable workspace" defined as "the set of poses in which the robot can maintain equilibrium against all external wrenches". The statically reachable workspace is defined by Agrawal and coworkers [5] as the set of poses of the mobile platform for which the cables can balance the weight of both the platform and the payload with tension forces only. This is of particular interest for IRPMs, which rely on gravity to keep the cables taut. Dynamic workspace analysis has been introduced by Gosselin and Barrette [6] in which the motion of a moving platform is incorporated into a set of wrenches called a pseudopyramid. A more practical workspace definition is wrench feasible workspace (WFW) which is the set

Fig. 1 Schematic of multi-body cable-driven robot
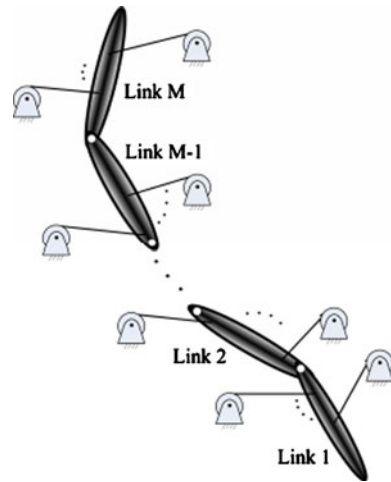
of all poses in which a specified range of external wrenches can be generated using a limited range of cable tensions [7, 8]. Wrench Closure Workspace (WCW) is a special case of WFW when both cable tension and the wrench sets are unbounded [9, 10]. The force closure workspace is the very special case of a WFW whose required set of wrenches is the whole space of wrenches and the only constraint on the cable tensions is nonnegativity [11]. Another definition that is in the literature is tensionable workspace. A pose of cable-driven mechanism belongs to tensionable workspace when it can generate any arbitrary external force/moment while maintaining tensile forces in all cables [12]. One can see that WCW, tensionable workspace, controllable workspace and force closure workspace are equivalent. They are merely dependent on the kinematics of the manipulator rather than the external loading, static or dynamic equilibrium or cable properties.

In another classification of cable robots, they are classified as single-body and multi-body cable-driven robots. In single-body cable-driven robots, all cables are attached to a rigid end-effector while in multi-body cable-driven robots; cables are attached to different links of a multi-body. An example is shown in Fig. 1, where a typical serial multi-body is driven by cables.

A possible application for multi-body cable robots is a reconfigurable robotic cell to be used for physical rehabilitation purposes. Using this concept, the human limbs are considered as multi-body systems which will be driven by cables attached to them using proper brace and shells. The cell can be easily reconfigured by changing the cable locations to provide the desired motion for the intended body part.

Determination of the workspace of cable-driven multi-body systems, due to the existence of inter-link constraints, is a problem of higher complexity. As a result, the literature on this subject is yet to be developed. Yang and coworkers proposed a kinematic design of a 7-DOF cable-driven humanoid arm with 14 cables [13]. They used force-closure method in multi-finger grasping to investigate the workspace.

Recently, two systematic approaches have been reported to determine the WCW of multi-body cable-driven mechanisms. One of them is based on Lagrange's approach in equilibrium analysis of multibody system [14] and the other one uses reciprocal screw theory [15]. They used the notion of generalized forces and Lagrange's method to eliminate the constraint forces/moments from the equilibrium equations.

In multi-body cable driven mechanisms the higher probability of interference between the cables or between the cables and the links of the multi-body and therefore smaller usable workspace is a major challenge. For example, in using cable robots in physical rehabilitation, the interference of the cables with each other or the patient's body significantly reduces the usable workspace of the robot. As a result, solutions need to be developed to improve the quality and size of their workspace before these mechanisms can find real applications.

One possible solution which is investigated in this paper is adding springs in between the links. Intuitively, it is expected that such springs help in keeping cables taut resulting in larger workspace. Also they are not expected to cause much interference with the cables as they stay close to the links of the multi-body.

In this paper the conceptual solution of adding springs to improve the WFW of a two-link cable-driven mechanism is investigated. In the following sections, a mathematical framework is developed to incorporate the springs and formulate the equilibrium of the mechanism for any number of links, cables, and spring cable. The determination of the WFW is then performed using interval analysis.

2 Kinetostatic Modeling of Cable Robots Without Spring

It is known that the workspace of cable robots is obtained from kinematics and equilibrium due to the cable tension condition. In this section, we review the kinetostatic modeling of single-body cable robot and its extension to multi-body systems.

A popular formulation of the equilibrium in single-body cable robots has the following form:

$$\mathbf{A}\boldsymbol{\tau} = \mathbf{b} \tag{1}$$

where $\boldsymbol{\tau}$ is a column vector containing the cable tensions, $\mathbf{A}$ is the structure matrix in the form of:

$$\mathbf{A}_{m \times n} = \begin{bmatrix} \mathbf{u}_1 & \dots & \mathbf{u}_m \\ \mathbf{r}_1 \times \mathbf{u}_1 & \dots & \mathbf{r}_m \times \mathbf{u}_m \end{bmatrix}$$

where $\mathbf{u}_i$ and $\mathbf{r}_i$ are unit direction vectors of the ith cable and the corresponding moment arm on the end-effector, respectively. Column vector $\mathbf{b}$ consists of external wrenches and inertia terms exerted on the end-effector. A given configuration of the robot ($\mathbf{A}$) and loading ($\mathbf{b}$) will satisfy the equilibrium and can be realized only if there is a solution for $\boldsymbol{\tau}$ in which all cable tensions are nonnegative and remain in the permissible range.

In order to extend this formulation to multi-body cable robots, we need to handle the internal joint reaction forces properly. In Newtonian method for instance, the size of matrix **A** becomes very large which is due to presence of all internal reaction forces/moments. In Lagrange's method, on the other hand, as long as the multi-body is a serial chain, the internal reaction forces/moments are eliminated and hence **A** will have the minimum size.

The general form of Lagrange's equation, if the Lagrangian can be expressed in terms of a minimal set of generalized coordinates, is:

$$\frac{d}{dt}\left(\frac{\partial L}{\partial \dot{q}_i}\right) - \frac{\partial L}{\partial q_i} = Q_i, i = 1, ..., n \tag{2}$$

where L is the Lagrangian, n is the degrees of freedom of the multi-body system, and q_i, Q_i are the generalized coordinates and generalized forces, respectively.

In a multi-body cable-driven mechanism, the contribution of cables to the dynamics is modeled as point forces applied to the links (i.e. the inertia and elastic stiffness of the cables are neglected). Therefore, Q_i's in Eq. (2) are divided into two parts: $Q_i = Q_i^c + Q_i^r$, where Q_i^c is the part pertaining to the cable forces, and Q_i^r includes all other generalized external forces/moments. The latter part together with the terms in the left hand side of Lagrange's equation can be incorporated in a vector named $\mathbf{B}_L$:

$$\mathbf{B}_L = \begin{bmatrix} \frac{d}{dt}(\frac{\partial L}{\partial \dot{q}_1}) - \frac{\partial L}{\partial q_1} - Q_1^r \\ \vdots \\ \frac{d}{dt}(\frac{\partial L}{\partial \dot{q}_{DOF}}) - \frac{\partial L}{\partial q_{DOF}} - Q_{DOF}^r \end{bmatrix} \tag{3}$$

In order to use the Lagrange's formulation, the cable forces need to be presented in generalized coordinates. Suppose that r_j is the position vector of the connection point of the jth cable to the multi-body, expressed in the fixed Cartesian frame. According to Lagrange's method, one can express Q_i^c in terms of the cable forces as:

$$Q_i^c = \sum_{j=1}^{m} (t_j \mathbf{u}_j \cdot \frac{\partial \mathbf{r}_j}{\partial q_i}) \tag{4}$$

Which can be then arranged in a matrix form as:

$$Q_i^c = \begin{bmatrix} \mathbf{u}_1 \cdot \frac{\partial \mathbf{r}_1}{\partial q_1} & \cdots & \mathbf{u}_n \cdot \frac{\partial \mathbf{r}_m}{\partial q_1} \\ \vdots & \ddots & \vdots \\ \mathbf{u}_1 \cdot \frac{\partial \mathbf{r}_1}{\partial q_{dof}} & \cdots & \mathbf{u}_n \cdot \frac{\partial \mathbf{r}_m}{\partial q_{dof}} \end{bmatrix} \begin{bmatrix} t_1 \\ \vdots \\ t_m \end{bmatrix} \tag{5}$$

Now, $\mathbf{A}_L$ and τ_L are defined according to Eq. (5) as:

$$\mathbf{A}_L = \begin{bmatrix} \mathbf{u}_1 \cdot \dfrac{\partial \mathbf{r}_1}{\partial q_1} & \cdots & \mathbf{u}_n \cdot \dfrac{\partial \mathbf{r}_m}{\partial q_1} \\ \vdots & \ddots & \vdots \\ \mathbf{u}_1 \cdot \dfrac{\partial \mathbf{r}_1}{\partial q_{dof}} & \cdots & \mathbf{u}_n \cdot \dfrac{\partial \mathbf{r}_m}{\partial q_{dof}} \end{bmatrix} \tag{6}$$

And:

$$\tau_L = \begin{bmatrix} t_1 \\ \vdots \\ t_m \end{bmatrix}$$

Consequently, the general equilibrium equations of the system given in Eq. (2), can be written in the following form:

$$\mathbf{A}_L \tau_L = \mathbf{B}_L \tag{7}$$

where $\mathbf{B}_L$ was defined in Eq. (15) and includes all the external forces (other than cables) as well as the inertia effects. Note that the left hand of Eq. (7) is a linear combination of the columns of $\mathbf{A}_L$ by the cable tensions. The columns of $\mathbf{A}_L$, according to Eq. (6), can be perceived as the cable wrenches expressed in the space of generalized coordinates.

3 Kinetostatic Modeling of Cable Robots with Spring

Spring cable in this work refers to cables that act similar to a spring. Therefore they provide a tensile force proportional to their displacement.

In multi-body cable-driven robots, spring cables can be attached between the fixed ground and one of the links. They can also connect one link to another. As mentioned above, the idea here is to investigate if they can provide an affordable solution for workspace improvement without adding redundant actuators. Using cable springs between links also decreases the probability of interference of cables with each other and the environment.

In order to model spring cables, we consider them as linear axial springs with a stiffness constant K. The generated force will then become:

$$\mathbf{F}_s = K\mathbf{u}_s \tag{8}$$

where $\mathbf{F}_s$ is the force vector of spring cable and $\mathbf{u}_s$ is the elongation vector of the spring defined as:

$$\mathbf{u}_s = (l - l_0)\mathbf{u} \tag{9}$$

where $\mathbf{u}$ is the unit direction vector of the spring cable. l and l_0 are the current and initial lengths of the spring cable, respectively.

Note that the wrenches of spring cables on cable-driven robots are determined by the configuration of the robot. Hence they are treated here as external wrench. Therefore in Newtonian approach the external wrench matrix is defined as follows:

$$\mathbf{b} = \left[\mathbf{W}_{req}\right] - \left[\begin{array}{c} \mathbf{F}_s \\ \mathbf{r}_s \times \mathbf{F}_s \end{array}\right] \tag{10}$$

In order to incorporate spring cables in our Lagrangian formulation, one needs to present the potential energy of the springs in terms of the generalized coordinates. Using linear axial spring model, the potential energy of a spring cable is:

$$V = \frac{1}{2}k\mathbf{u}_s^{\mathbf{T}}\mathbf{u}_s \tag{11}$$

where k is the stiffness coefficient of the spring. And:

$$L = T - V \tag{12}$$

As mentioned above in Eq. (3), the wrench matrix, $\mathbf{B}_L$, is dependent on the derivatives of the Lagrangian with respect to the generalized coordinate, so the elongation vector of spring cables must be expressed in terms of the generalized coordinates. This is possible since the end point of the spring cables are either on the ground and hence known or belong to the multi-body which can be determined using the forward kinematics of the multi-body.

It is clear that adding spring cables to a cable-driven mechanism does not change its WCW since the spring cables provide a bounded force. However they do change the WFW by providing bounded cable wrenches through the springs. Therefore, their impact on the WFW can be modified and optimized through the geometry and the spring coefficient which will be investigated in the following.

4 Method

As mentioned above, we need to use WFW definition. There are various analytical and numerical methods for determination of WFW in the literature. The numerical methods suffer from the discretization error as they can only handle a meshed workspace. The analytical methods are appropriate for particular types of robots and kinematics. The interval analysis method, on the other hand, provides a solution which is general and applicable to any kinematics and addresses the discretization problem as well. In this method an n-dimensional vector x is considered that denotes the pose of the end-effector. If we replace any real component of this vector with an interval, then we have a box denoted by [x]. Two sufficient conditions are then

Table 1 Parameters of single point cable-driven mechanism

τ_{min}	τ_{max}	$[b^T]$	K	L_0
1N	900 N	$([-20,20]N,[-20,20]N)$	200 N/m	0.1 m

Fig. 2 A point driven by cables. A spring cable (*red*) is added to compare the workspaces
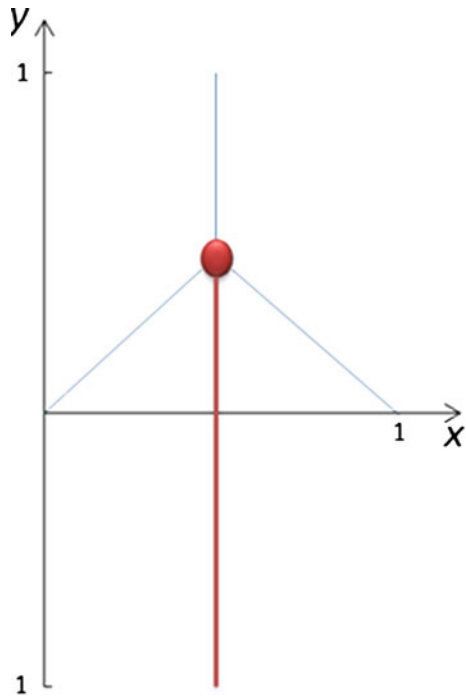
evaluated: a sufficient condition for a box of poses to be fully inside the WFW and a sufficient condition for a box of poses to be fully outside the WFW. If these two sufficient conditions aren't satisfied, the box is bisected [16]. The interval analysis method as documented well in the literature, eliminates the need for discrete meshing and therefore provide a sufficiently accurate determinations of the workspace borders. It has been also used for the design of the cable robots to fulfill a desired workspace [17, 18].

5 Results

In this section, the above formulation is implemented on a two-link planar cable-driven mechanism to show the impact of spring cable on the workspace. In our implantation, we used interval arithmetic of the INTLAB. The computation times have been obtained on a DELL XPS PC (Core 2 Duo CPU T9300, 2.50 GHz).
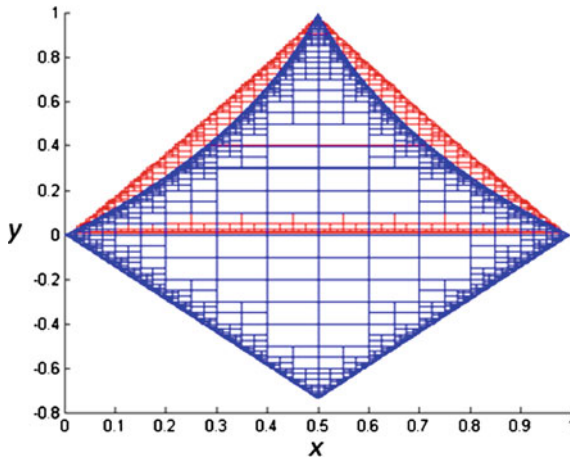
Fig. 3 Workspace of a point driven by cables with (*blue*) and without (*red*) a spring cable

Table 2 Parameter values of multi-body mechanism

Length of link 1	Location of winch 1	Location of winch 2	Location of winch 3	Location of spring on ground	
1 m	(0,3)	(1.5,-3)	(1.5,3)	(0,3)	
d_1	d_2	d_3	d_{s1}	d_{s2}	K
0.6m	0.3 m	0.8 m	0.5 m	0.5 m	100 N/m

The effects of a spring cable are intuitively understood in simple systems such as a point driven by cables on a plane. Such a point needs three cables to be fully constrained (Fig. 2). Adding a single spring cable as shown in red in the same figure has a significant impact on the workspace. For typical parameters shown in Table 1, the WFW of the mechanism is shown with and without cables in Fig. 3.

As seen in Fig. 3, the spring cable almost doubles the WFW of the mechanism as expected.

As for multi-body cable-driven mechanisms, there are two options for adding spring cables. One choice is to attach spring cables between the fixed ground and one of the links and the other one is that spring cable connects one link to another.

First, let us consider the case that the spring cable is attached between the fixed ground and link 2 as depicted in Fig. 4. Typical values were used for the parameters of mechanism as shown in Table 2.

The WFW of the mechanism with and without the spring cable are found through interval analysis and depicted in Figs. 5, 6 respectively. It is evident from the figures that the workspace is improved. The workspace has increased in terms of volume by 83 % compared to the one without the spring cable. Also it is seen that the workspace is more continuous, which is a critical aspect for robotic applications. The possibility

Fig. 4 Schematic of a two-
link mechanism with a spring
cable that is attached to ground
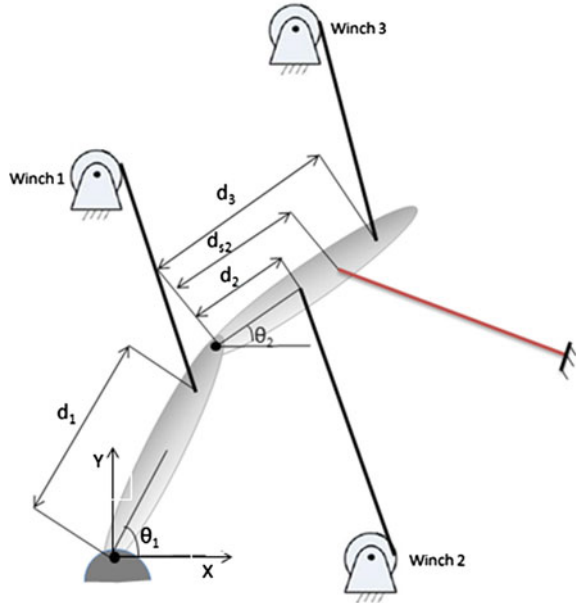
Fig. 5 Workspace of the two-
link cable-driven mechanism
without any spring cable
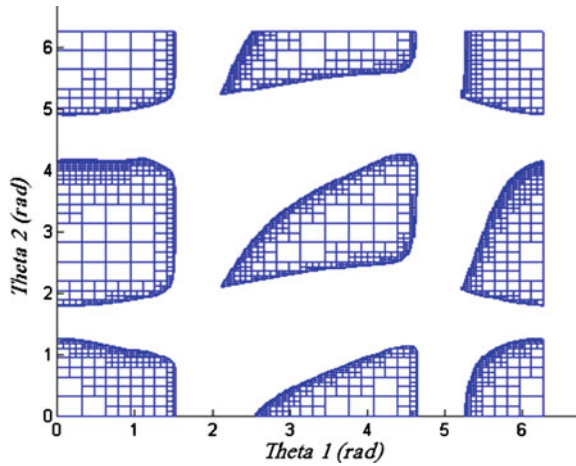
of interference, however, will increase when a spring cable is present between the
mechanism and ground.

The interference problem becomes less apparent if the spring cable doesn't con-
nect to the ground and instead goes from one link to another. A typical example is
depicted in Fig. 7.

The WFW of this mechanism is seen in Fig. 8. In terms of the workspace volume,
this mechanism shows an increase of 25 % with respect to the original mechanism.

Fig. 6 Workspace of the two-link cable-driven mechanism with a spring cable attached to ground
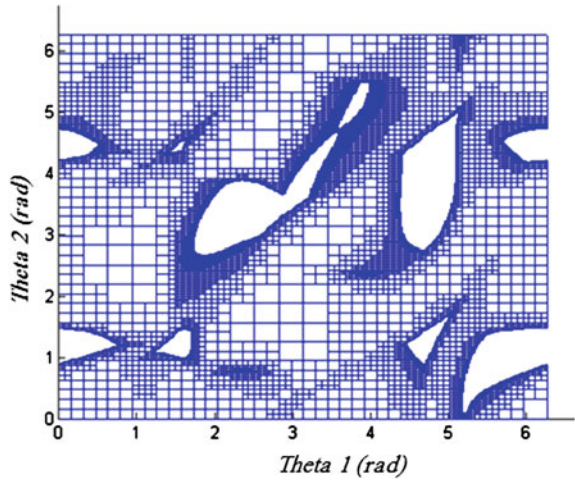
Fig. 7 Schematic of a two-link mechanism with a spring cable that is attached between the links
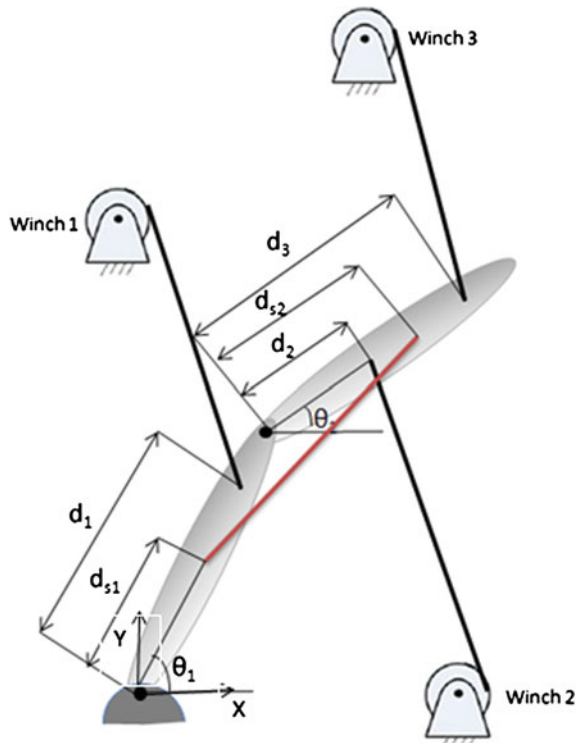
Fig. 8 Workspace of the two-link cable-driven mechanism with a spring cable attached between the links
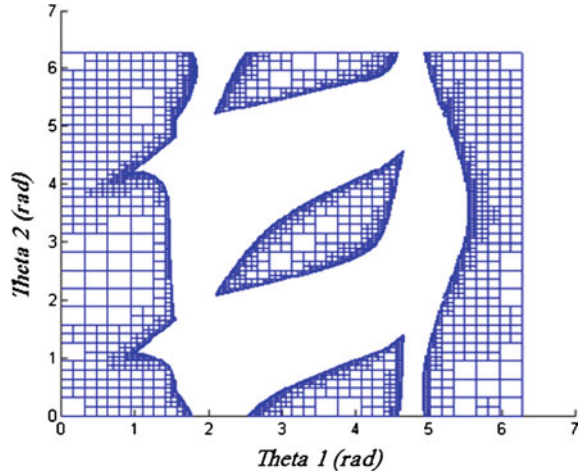
However it is about 46 % lower than the one of the previous case where the spring cable connects to the ground, the probability of cable interference, on the other hand, is decreased from the previous case. It is also interesting to note that although the workspace has some discontinuity, it consists of larger continuous parts.

6 Conclusions

In this work, a formulation is presented to study the workspace of multi-body cable-driven mechanisms with spring cables. The method was then applied to a two-link serial mechanism to investigate the impact of the spring cable on the size and shape of the workspace.

Two cases were considered: in the first one, a spring cable was attached between a link and the ground, in the second case, the spring cable was added between the two links. It is apparent that the second case has a lower possibility of cable interference. It was shown that both cases provide a more continuous workspace which is favorable for robotic application. The first case provides a larger workspace volume however it seems that the actual workspace (considering the cable interference) becomes smaller.

Based on the early results of this study, it seems adding spring cables between the links in a multi-body cable-driven mechanism has higher potentials to improve the WFW of such mechanisms. In future works, the idea will be further developed for spatial and more general mechanisms.

References

1. Jeong, J., Kim, S., Kwak, Y.: Kinematics and workspace analysis of a parallel wire mechanism for measuring a robot pose. Mechanism Mach. Theor. **31**(6), 825–841 (1999)
2. Verhoeven, R., Hiller, M., Tadokoro, S.: Workspace, stiffness, singularities and classification of tendon-driven stewart platforms. In: Lenarcic, J., Husty, M.L. (eds.) Advances in Robot Kinematics: Analysis and Control, pp. 105–114. Austria Kluwer Academic Publishers, Strobl/Salzburg (1998)
3. Albus, J., Bostelman, R., Dagalakis, N.: The nist robocrane. J. Robot. Syst. **10**(5), 709–724 (1993)
4. Verhoeven, R., Hiller, M.: Estimating the controllable workspace of tendon-based stewart platforms. In: Proceedings of 7th International Symposium on Advances in Robot Kinematics. pp. 277–284. ARK, Protoroz, Slovenia (2000).
5. Pusey, J., Fattah, A., Agrawal, S., Messina, E.: Design and workspace analysis of a 6–6 cable-suspended parallel robot. J. Mech. Mach. Theor. 761–778 (2004).
6. Gosselin, C., Barrette, G.: Kinematic analysis of planar parallel mechanisms actuated with cables. In: Proceedings of Symposium on Mechanisms, Machines and Mechatronics, pp. 41–42. Quebec, Canada (2001).
7. Bosscher, P., Riechel, A., Ebert-Uphoff, I.: Wrench-feasible workspace generation for cable-driven robots. IEEE Trans. Robot. 890–902 (2006).
8. Barette, G., Gosselin, C.: Kinematic analysis and design of planar parallel mechanisms actuated with cables. In: Proceedings of DETC'00-ASME Design Engineering Technical Conferences and Computers and Information in Engineering Conference. Baltimore, USA (2000).
9. Gouttefarde, M., Gosselin, C.: On the properties and the determination of the wrench-closure workspace of planar parallel cable-driven mechanisms. In: Proceedings of DETC'04-ASME Design Engineering Technical Conferences and Computers and Information in Engineering Conference. Salt Lake City, USA (2004).
10. Gouttefarde, M., Gosselin, C.: Analysis of the wrench-closure workspace of planar parallel cable-driven mechanisms. IEEE Trans. Robot. 434–445 (2006).
11. Pham, C., Yeo, S., Yang, G., Kurbanhusen, M., Chen, I.: Force-closure workspace analysis of cable-driven parallel mechanisms, Mech. Mach. Theor. 53–69 (2006).
12. Landsberger, S., Shanmugasundram, P.: Workspace of a parallel link crane. In: Proceedings of IMACS/SICE International Symposium on Robotics, Mechatronics and, Manufacturing Systems. pp. 479–486 (1992).
13. Yang, G., Lin, W.: Kinematic design of a 7-dof cable-driven humanoid arm: a solution-in-nature approach. In: Proceedings of the 2005 IEEE/ASME International Conference on Advanced Intelligent, Mechatronics, pp. 444–449 (2005).
14. Rezazdeh, S., Behzadipour, S.: Workspace analysis of multibody cable-driven mechanisms. ASME, J. Mech. 0210051–0210060 (2011).
15. Mustafa, S.K., Agrawal, S.K.: On the force-closure analysis of n-DOF cable-driven open chains based on reciprocal screw theory. IEEE Trans. Robot. **28**(1), 22–31 (2012)
16. Gouttefarde, M., Daney, D., Merlet, J.: Interval-analysis-based determination of the wrench-feasible workspace of parallel cable-driven robots. IEEE Trans. Robot. **27**, 1–13 (2011)
17. Bruckmann, T., Mikelsons, L., Schramm, D., Hiller, M.: Continuous workspace analysis for parallel cable-driven Stewart-Gough platforms. PAMM **7**, 4010025–4010026 (2007)
18. Bruckmann, T., Mikelsons, L., Brandt, T., Hiller, M., Schramm, D.: Design approaches for wire robots. In: Proceedings of the ASME 2009 International Design Engineering Technical Conferences and Computers and Information in Engineering Conference, ASME, International (2009).

The Constant-Orientation Dimensional Synthesis of Planar Cable-Driven Parallel Mechanisms Through Convex Relaxations

Kaveh Azizian and Philippe Cardou

Abstract The wrench-closure workspace (WCW) of cable-driven parallel mechanisms is the set of poses for which any wrench can be produced at the end-effector by a set of positive cable tensions. In this paper, we tackle the dimensional synthesis problem of finding a geometry for a planar cable-driven parallel mechanism (PCDPM) whose constant orientation wrench closure workspace (COWCW) contains a prescribed workspace. To this end, we first introduce a linear program to verify whether a given pose is inside or outside the WCW of a given PCDPM. The relaxation of this linear program over a box leads to a nonlinear feasibility problem that can only be satisfied when this box is completely inside the COWCW. We extend this feasibility problem to find a PCDPM geometry whose COWCWs include a given set of boxes. These multiple boxes may represent an estimate of the prescribed workspace, which may be obtained through interval analysis. Finally, we introduce a nonlinear program through which the PCDPM geometry is changed while maximizing the scaling factor of the prescribed set of boxes. When the optimum scaling factor is greater or equal to one, the COWCW of the resulting PCDPM contains the set of boxes. Otherwise, the COWCW generally offers a good coverage of the set of boxes.

1 Introduction

A planar parallel cable driven mechanism (PCDPM) generally consists of a moving platform (MP) and a fixed frame, which are connected with multiple cables. Each cable is wound around an actuated reel fixed to the base, and is attached to the moving platform at its other end. The cables and the moving platform are assumed to

K. Azizian (✉) · P. Cardou
Department of Mechanical Engineering, Laval University,
Quebec City, QC G1V 0A6, Canada
e-mail: kaveh.azizian.1@ulaval.ca

P. Cardou
e-mail: pcardou@gmc.ulaval.ca

be contained in the same plane. The actuated reels control the position and orientation of the moving platform in this plane by controlling the lengths of their corresponding cables.

Since the cables can be wound onto reels over long lengths, the workspace of a cable-driven mechanism can be larger than that of a conventional parallel mechanism. This is only a potential advantage, however, as the workspace of a PCDPM is further limited by the inability of cables to push on the moving platform. Indeed, there generally exist many poses inside this workspace for which the cables cannot balance all applied wrenches, because at least one of them would have to push on the platform. More formally, the wrench-closure workspace (WCW) is the set of poses for which all applied wrenches are feasible. An applied wrench is said to be feasible if it can be balanced by a set of a non-negative cable tensions. This is a special case of the wrench-feasible workspace (WFW), which is the set of poses of the moving platform for which the cables can balance any wrench of a given set of wrenches, such that the tension in each cable remains within a prescribed range.

The WCW of cable-driven parallel mechanisms has been studied in several research works. A necessary condition for the WCW to be non empty is that the number of cables be greater than the number of degrees of freedoms of the moving platform [1, 2]. This condition is necessary to avoid negative tensions in the cables. For cable-driven parallel mechanisms with more cables than the numbers of degrees of freedom of their moving platforms, the WCW depends only on the geometry of the mechanism, i.e, the locations of the attachment points on the fixed frame and on the moving platform.

Many existing works deal with the limitation of the workspace of parallel cable-driven robots induced by the unilateral nature of the forces applied by the cables on the mobile platform. Most of them propose methods allowing to determine the workspace of these robots, for instance, by means of a discretization method [3] or by a symbolic method [4]. Fattah and Agrawal [5] propose a methodology to calculate the workspace of redundant and non redundant planar cable driven robots by means of a discretization method. In their method, tensions in the cables are calculated and conditions are obtained to verify whether a reference point on the moving platform is reachable with positive tensions. Riechel and Ebert-Uphoff [6] present a means for analytically deriving the WFW for the case of a point-mass end-effector and analyze the characteristics and trends of the WFW. Some others apply the Antipodal theorem to calculate the WCW of PCDPMs [7]. All these works deal with the analysis of cable-driven parallel mechanism workspace. Very few of them tackle the difficult design problem of finding a cable-driven parallel mechanism from a prescribed workspace, i.e., the synthesis problem.

Gouteffarde et al. [8] propose an interval-analysis based approach to finding boxes guaranteed to be fully inside or fully outside of the WFW. The proposed approach can be applied to verify whether a given prescribed workspace is fully included in the WFW of a given cable driven mechanism. This is a valuable tool for the dimensional synthesis of cable driven robots, but because of its computational cost, we do not know of its application to such problems.

Hay and Snyman [9] investigated the synthesis of parallel cable-driven manipulators. They define the dexterous workspace of a PCDPM as the intersection of all constant orientation workspaces in a given set of rotation angles, while cable tensions are constrained to lie within a given set and cable lengths are greater than a given minimum. Their main goal is to maximize the area of the dexterous workspace for a given range of rotation angles by finding the locations of fixed points of the robot along a fixed rectangular frame. They begin with a randomly chosen PCDPM design and maximize the area of its dexterous workspace by varying its geometry. In this manner, they find a locally optimum configuration of the fixed points of the robot, while the locations of the attachment points on the platform have already been assumed. Therefore, this locally-optimum robot design corresponds to a dexterous workspace of maximum area, but not for a prescribed workspace.

In this paper, we seek to obtain the geometry of a PCDPM for a prescribed workspace. The main goal of this paper is to devise an efficient method for the dimensional synthesis of planar cable-driven parallel mechanisms. In order to achieve this goal, we first recall the kinetostatic model of a fully-constrained PCDPM and formally define its WCW in the following section. In Sect. 3, we introduce a linear program to verify whether a given pose is inside or outside of the WCW of a PCDPM. In Sect. 4, we modify this linear program to obtain a sufficient condition for a given box to lie inside the WCW. The developed linear program is then turned into a nonlinear non-convex feasibility problem representing the dimensional synthesis of PCDPMs in Sect. 5. In the same section, this feasibility problem is turned into a nonlinear program by introducing a scaling factor of the prescribed workspace as the objective function to be maximized. We illustrate the proposed formulations with synthesis examples throughout Sect. 5.

To this end, we resort to convex relaxations, a technique that has become popular in some fields of applied science, e.g. [10] and [11] , but has received less attention from the robotics community. Porta et al. [12] are among the only researchers who have used this technique for the analysis of robots, to the best of our knowledge.

2 Kinetostatic Model

Before searching for the geometry of a planar cable-driven parallel mechanism (PCDPM) for a prescribed wrench-closure workspace (WCW), we have to set up a precise mathematical description of the geometry of such a robot, and of its wrench-closure workspace. Such a PCDPM is schematically shown in Fig. 1. It consists of a moving platform (MP) that is connected by m cables to m fixed points A_i, $i = 1, \ldots, m$. Cable i is attached to the MP at B_i, and winds at A_i around an actuated reel. In order to analyze the motion of the MP, we have to consider two frames: the reference frame $\mathscr{A}$, which is fixed to the base, and the moving frame $\mathscr{B}$, which is attached to a reference point of the MP. The angle ϕ rotates frame $\mathscr{A}$ onto frame $\mathscr{B}$. We use the following notation for the analysis of a generic PCDPM:

Fig. 1 Sketch of an m-cable
PCDPM
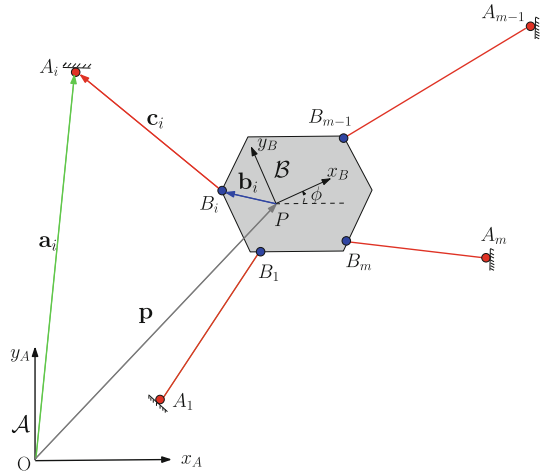
- Vector $\mathbf{a}_i \in \mathbb{R}^2$ represents the position of the actuator A_i in the fixed frame $\mathscr{A}$;
- Vector $\mathbf{b}_i \in \mathbb{R}^2$ is a constant vector and represents the position of the attachment point B_i of the ith cable in frame $\mathscr{B}$;
- Vector $\mathbf{p} \in \mathbb{R}^2$, which is expressed in $\mathscr{A}$, represents the position of the reference point P with respect to point O;
- Vector $\mathbf{c}_i$ points from B_i to A_i, and supports the ith cable.

Vector $\mathbf{c}_i$ representing the ith cable is obtained as

$$\mathbf{c}_i = \mathbf{a}_i - \mathbf{p} - \mathbf{Q}\mathbf{b}_i. \tag{1}$$

where, $\mathbf{Q}$ is the rotation matrix taking the fixed frame onto the moving frame, and can be expressed as

$$\mathbf{Q} = \mathbf{1}_{2\times 2} \, \cos\phi + \mathbf{E} \, \sin\phi, \tag{2}$$

where, $\mathbf{E} = \begin{bmatrix} 0 & -1 \\ 1 & 0 \end{bmatrix}$ and $\mathbf{1}_{2\times 2} \in \mathbb{R}^{2\times 2}$ is the 2×2 identity matrix. The wrench applied at P, the origin of the moving frame, by the ith cable is $\mathbf{v}_i = [\, \mathbf{f}_i^T \ n_i \,]^T$, where $\mathbf{f}_i$ and n_i are the force and moment about P produced by the ith cable, respectively. Since the exerted force is parallel to its corresponding cable and its related moment is perpendicular to the plane, their mathematical expressions are

$$\mathbf{f}_i = \frac{t_i}{l_i}\mathbf{c}_i, \quad n_i = \det\!\left(\left[\, \mathbf{Q}\mathbf{b}_i \ \tfrac{t_i}{l_i}\mathbf{c}_i \,\right]\right). \tag{3}$$

where l_i and t_i are the length of cable i and the tension in that cable, respectively. If we assume that points A_i and B_i do not coincide, then the wrench applied to the platform by cable i is $(t_i/l_i)\mathbf{w}_i$, with $\mathbf{w}_i$ defined as

$$\mathbf{w}_i = \begin{bmatrix} \mathbf{c}_i^T & \mathbf{c}_i^T & \mathbf{EQb}_i \end{bmatrix}^T. \tag{4}$$

Regarding the orientation angle as a constant, Eq. (4) shows that $\mathbf{w}_i$ is a function of the geometric parameters of the mechanism alone. We define the wrench matrix and tension vector of the mechanism as $\mathbf{W} = \begin{bmatrix} \mathbf{w}_1 & \mathbf{w}_2 & \dots & \mathbf{w}_m \end{bmatrix}$ and $\mathbf{t} = \begin{bmatrix} t_1/l_1 & t_2/l_2 & \dots & t_m/l_m \end{bmatrix}^T$, respectively. Defining

$$\mathbf{d}_i \equiv \mathbf{a}_i - \mathbf{Qb}_i, \ i = 1, \dots, m, \quad \mathbf{D} \equiv \begin{bmatrix} \mathbf{d}_1 & \dots & \mathbf{d}_m \end{bmatrix} \in \mathbb{R}^{2 \times m},$$

$$\mathbf{f} \equiv \begin{bmatrix} \mathbf{b}_1^T \mathbf{Q}^T \mathbf{E}^T \mathbf{a}_1 & \dots & \mathbf{b}_m^T \mathbf{Q}^T \mathbf{E}^T \mathbf{a}_m \end{bmatrix}^T \in \mathbb{R}^m, \quad \mathbf{B} \equiv \begin{bmatrix} \mathbf{b}_1 & \dots & \mathbf{b}_m \end{bmatrix} \in \mathbb{R}^{2 \times m}, \tag{5}$$

we can rewrite $\mathbf{W}$ as

$$\mathbf{W} \equiv \begin{bmatrix} \mathbf{D} - \mathbf{p}\mathbf{1}_m^T \\ \mathbf{f}^T - \mathbf{p}^T \mathbf{EQB} \end{bmatrix} \in \mathbb{R}^{3 \times m}. \tag{6}$$

We will use this compact expression of the wrench matrix to find a formulation for the synthesis problem of PCDPMs in the following sections.

The static equilibrium of the moving platform may be expressed as

$$\mathbf{Wt} + \mathbf{w}_P = \mathbf{0}_3, \tag{7}$$

in which $\mathbf{w}_P$ is the wrench applied on the MP, with its force acting at P, and is equivalent to the system of external forces and moments. These external loads may include gravity forces, for example. We can now define the WCW of PCDPMs as follows.

Definition 1 *The Wrench-Closure Workspace (WCW)*
The WCW of planar cable-driven parallel mechanisms is formally defined as the set of poses for which

$$\forall \mathbf{w}_P \in \mathbb{R}^3, \exists \mathbf{t} \in \mathbb{R}^m \mid \mathbf{t} \succ \mathbf{0}_m \text{ and } \mathbf{Wt} + \mathbf{w}_P = \mathbf{0}_3,$$

where the symbol $\succ$ denotes the componentwise strict inequality and $\mathbf{0}_3$ is the three-dimensional zero vector. In words, this workspace is the set of PCDPM postures for which any external load applied to the MP can be balanced by a set of positive cable tensions.

3 Verifying Whether a Pose Lies in the WCW of a PCDPM

In order to find a valid tension vector $\mathbf{t}$ for a given pose, we need to solve the linear system of equations given by Eq. (7). To this end, let us recall the Theorem 1 introduced in [13] in order to determine whether a given pose is inside the WCW of the mechanism.

Theorem 1 Primal WCW Membership Condition [13, 14]
A given pose is inside the WCW of a PCDPM if and only if there exists a set of cable tensions such that

$$rank(\mathbf{W}) = 3,$$
$$\mathbf{W}\mathbf{t} = \mathbf{0}_3, \quad \mathbf{t} \succ \mathbf{0}_m. \tag{8}$$

According to Theorem 1, the WCW of a PCDPM can be computed by solving the feasibility problem (8) for each pose of the MP, a result previously obtained in [13]. Therefore, the WCW of a PCDPM is the set of poses for which Eq. (8) is satisfied. We may as well use Stiemke's theorem [15] to verify whether a given pose is inside or outside the WCW. We recall this theorem as follows.

Theorem 2 Dual WCW Membership Condition [4]
A pose is outside the WCW of a PCDPM if and only if there exists a small-displacement screw $\lambda \in \mathbb{R}^3$ such that

$$\mathbf{W}^T\lambda \succeq \mathbf{0}_m, \quad \mathbf{W}^T\lambda \neq \mathbf{0}_m. \tag{9}$$

We can now introduce the following feasibility problem to calculate the WCW of a PCDPM:

$$\mathbf{W}^T\lambda \succeq \mathbf{0}_m, \quad \mathbf{1}_m^T\mathbf{W}^T\lambda = 1. \tag{10}$$

where $\mathbf{1}_m = \begin{bmatrix} 1 \ 1 \ \cdots \ 1 \end{bmatrix}^T \in \mathbb{R}^m$. Indeed, problems (9) and (10) are equivalent, since under the constraint $\mathbf{W}^T\lambda \succeq \mathbf{0}_m$ having $\mathbf{1}_m^T\mathbf{W}^T\lambda = 1$ is equivalent to having $\mathbf{W}^T\lambda \neq \mathbf{0}_m$. Hence, if problem (10) admits a feasible solution then the given pose is outside of the WCW and if it does not then the pose is inside. Hence, this equation can be used to estimate the WCW of a given PCDPM by discretizing the examined region. This linear feasibility problem is the corner stone to the proposed formulation of the dimensional synthesis of PCDPMs.

4 Verifying Whether a Box Lies in the Constan-Orientation WCW

The formulations developed in the previous sections provide us with the proper tools to address our main concern: the dimensional synthesis of PCDPMs. We wish to determine whether a given small box lies completely inside the constant-orientation WCW of a given PCDPM. To this end, notice that the problem (10) can be turned into a phase-one problem as in the following Lemma.

Lemma 1 Linear Program WCW Membership Condition
Consider the linear program [1]

---

[1] Because of space constraints, the proof will be provided upon request.

$$
\begin{aligned}
\delta^* = \; maximize \quad & \delta, \\
subject\ to \quad & \mathbf{W}^T \lambda \succeq \mathbf{0}_m, \\
& \mathbf{1}_m^T \mathbf{W}^T \lambda \ge \delta, \\
over \quad & \lambda\ and\ \delta.
\end{aligned}
\tag{11}
$$

Then, we have

$$
\delta^* = \begin{cases} +\infty & \text{if the pose lies outside the WCW,} \\ 0 & \text{otherwise.} \end{cases}
\tag{12}
$$

Consider now a box $\mathscr{B}$ with lower-left and upper-right corners $\underline{\mathbf{p}}$ and $\overline{\mathbf{p}}$, respectively, i.e., $\mathscr{B} = \{\mathbf{p} \in \mathbb{R}^2 : \underline{\mathbf{p}} \preceq \mathbf{p} \preceq \overline{\mathbf{p}}\}$. In order to find a necessary condition for $\mathscr{B}$ to be outside of the COWCW, we substitute Eq. (6) in problem (11), we let $\mathbf{p}$ in the decision variables of the problem, and we constrain it inside $\mathscr{B}$. This leads to

$$
\begin{aligned}
maximize \; & \delta, \\
subject\ to \; & \mathbf{0}_m \preceq \mathbf{D}^T \mu - \mathbf{1}_m \mathbf{p}^T \mu + \mathbf{f}\mu_0 - \mathbf{B}^T \mathbf{Q}^T \mathbf{E}^T \mathbf{p}\mu_0, \\
& \delta \le \mathbf{1}_m^T \mathbf{D}^T \mu - m\mathbf{p}^T \mu + \mathbf{1}_m^T \mathbf{f}\mu_0 - \mathbf{1}_m^T \mathbf{B}^T \mathbf{Q}^T \mathbf{E}^T \mathbf{p}\mu_0, \\
& \underline{\mathbf{p}} \preceq \mathbf{p} \preceq \overline{\mathbf{p}},
\end{aligned}
\tag{13}
$$

where $\lambda \equiv [\mu^T \quad \mu_0]^T$. Considering $\mathbf{p}$, the operation-point position as an optimization variable, while the MP orientation $\mathbf{Q}$ remains constant, we obtain a nonlinear optimization problem. This problem provides us with a tool to find a necessary condition for a box to be outside of the COWCW, i.e., a condition that is necessarily met by any box $\mathscr{B}$ outside the COWCW, but that may also be met by some boxes that are partly or completely inside this workspace. The approach consists in relaxing the constraints of problem (13), which makes it easier for a pose to be excluded from the COWCW. To this end, let us define the variables $\nu \equiv \mu_0 \mathbf{p}$ and $\eta \equiv \text{diag}(\mu)\mathbf{p}$, which represent the bilinear terms in Eq. (13), when considering $\mathbf{p}$, μ and μ_0 as decision variables. For the sake of this analysis, let us assume that the signs of μ_0 and μ are known in advance, and label them $\sigma_0 \equiv \text{sgn}(\mu_0)$ and $\sigma \equiv \text{sgn}(\mu)$, where $\text{sgn}()$ represents the signum function. Knowing the signs of μ_0 and μ, we can generate the following bounds on ν and η:

$$
\sigma_0 \underline{\mathbf{p}}\mu_0 \preceq \sigma_0 \nu \preceq \sigma_0 \overline{\mathbf{p}}\mu_0, \quad \text{diag}(\sigma)\text{diag}(\underline{\mathbf{p}})\mu \preceq \text{diag}(\sigma)\eta \preceq \text{diag}(\sigma)\text{diag}(\overline{\mathbf{p}})\mu.
\tag{14}
$$

When treating σ_0 and σ as constants, the set formed by Eq. (14) represents a convex polyhedron, which approximates the non-convex surfaces of Eq. (4). Therefore, replacing the latter with the former, we obtain a *convex relaxation* of Eq. (4). This approximation converges to the exact relationship as the size of box $\mathscr{B}$ becomes infinitesimal. This approach is called the reformulation-linearization technique (RLT), and was originally proposed by Sherali and Tuncbilek [16]. Hence, the relaxed form of problem (13) is

$$
\begin{aligned}
\text{maximize} \quad & \delta, \\
\text{subject to} \quad & \mathbf{D}^T \mu - \mathbf{1}_m \mathbf{1}_2^T \eta + \mathbf{f}\mu_0 - \mathbf{B}^T \mathbf{Q}^T \mathbf{E}^T \nu \succeq \mathbf{0}_m, \\
& \mathbf{1}_m^T \mathbf{D}^T \mu - m \mathbf{1}_2^T \eta + \mathbf{1}_m^T \mathbf{f}\mu_0 - \mathbf{1}_m^T \mathbf{B}^T \mathbf{Q}^T \mathbf{E}^T \nu \geq \delta, \\
& \sigma_0 \underline{\mathbf{p}}\mu_0 \preceq \sigma_0 \nu \preceq \sigma_0 \overline{\mathbf{p}}\mu_0, \\
& \text{diag}(\sigma)\text{diag}(\underline{\mathbf{p}})\mu \preceq \text{diag}(\sigma)\eta \preceq \text{diag}(\sigma)\text{diag}(\overline{\mathbf{p}})\mu, \\
& \sigma_0 = \text{sgn}(\mu_0), \quad \sigma = \text{sgn}(\mu)
\end{aligned}
\tag{15}
$$

The only non-convex constraints in problem (15) are the last two equalities. However, these equalities yield exactly eight possible combinations of σ_0 and σ, which are the solutions to

$$
\sigma_0^2 = 1 \quad \text{and} \quad \text{diag}(\sigma)^2 = \mathbf{1}_{2\times 2}.
\tag{16}
$$

Let us label these solutions $\sigma_{0,j}$ and σ_j, $j = 1, \ldots, 8$. As a result, the solution to problem (15) is the maximum of the outcomes of the eight resulting linear programs. This leads to Lemma 2.

Lemma 2 *Linear Sufficient Conditions for a Box to Lie Inside the COWCW Consider the eight distinct linear programs*

$$
\begin{aligned}
\text{maximize} \quad & \delta_j, \\
\text{subject to} \quad & \mathbf{G}_j \xi_j \preceq \mathbf{0}_{m+9}, \\
\text{over} \quad & \xi_j,
\end{aligned}
\tag{17}
$$

$j = 1, \ldots, 8$ *where*
$\mathbf{G}_j \equiv \begin{bmatrix} \mathbf{g}^T & 1 \\ \mathbf{R}_j^T & \mathbf{0}_{m+24} \end{bmatrix} \in \mathbb{R}^{(m+9)\times 8}$, $\mathbf{g} \equiv \begin{bmatrix} -\mathbf{1}_m^T \mathbf{A}^T & -\mathbf{1}_m^T \mathbf{f} & \mathbf{1}_m^T \mathbf{B}^T \mathbf{Q}^T \mathbf{E}^T & m\mathbf{1}_2^T \end{bmatrix}^T \in \mathbb{R}^7$,

$\mathbf{R}_j \equiv \begin{bmatrix} -\mathbf{D}^T & -\mathbf{f} & \mathbf{B}^T \mathbf{Q}^T \mathbf{E}^T & \mathbf{1}_m \mathbf{1}_2^T \\ \mathbf{0}_{2\times 2} & \sigma_{0,j}\underline{\mathbf{p}} & -\sigma_{0,j}\mathbf{1}_{2\times 2} & \mathbf{0}_2 \\ \mathbf{0}_{2\times 2} & -\sigma_{0,j}\overline{\mathbf{p}} & \sigma_{0,j}\mathbf{1}_{2\times 2} & \mathbf{0}_2 \\ \text{diag}(\sigma_j)\text{diag}(\underline{\mathbf{p}}) & \mathbf{0}_2 & \mathbf{0}_{2\times 2} & -\text{diag}(\sigma_j) \\ -\text{diag}(\sigma_j)\text{diag}(\overline{\mathbf{p}}) & \mathbf{0}_2 & \mathbf{0}_{2\times 2} & \text{diag}(\sigma_j) \end{bmatrix}^T \in \mathbb{R}^{7\times(m+8)}$, *and*

$\xi_j \equiv \begin{bmatrix} \mu_j^T & \mu_{0,j} & \nu_j^T & \eta_j^T & \delta_j \end{bmatrix}^T \in \mathbb{R}^8$. *Then, the given box $\mathscr{B} = \{\mathbf{p} \in \mathbb{R}^2 : \underline{\mathbf{p}} \preceq \mathbf{p} \preceq \overline{\mathbf{p}}\}$ is fully inside the COWCW if all of the problems (17), $j = 1, \ldots, 8$, yield zero.*[2]

Figure 2 shows an example of the effect of the proposed convex relaxation on the estimated COWCW. The parameters of the considered PCDPM are given in Table 1, and the corresponding geometry appears in the foreground of Fig. 2. This example is drawn from Stump and Kumar [4]. We calculate the real constant-orientation wrench-closure workspace (COWCW) of this mechanism for $\phi = 0.02$ rad by discretising the examined region into several points and solving problem (10) for each of them. Upon partitioning the plane into boxes instead of points and solving the relaxed problem (17) for each box, we obtain a contracted COWCW. In this figure the real COWCW is represented by a cloud of points, while the contracted COWCW is the

---

[2] The proof was omitted because of space constraints.

Fig. 2 Contracted and real COWCW of a PCDPM
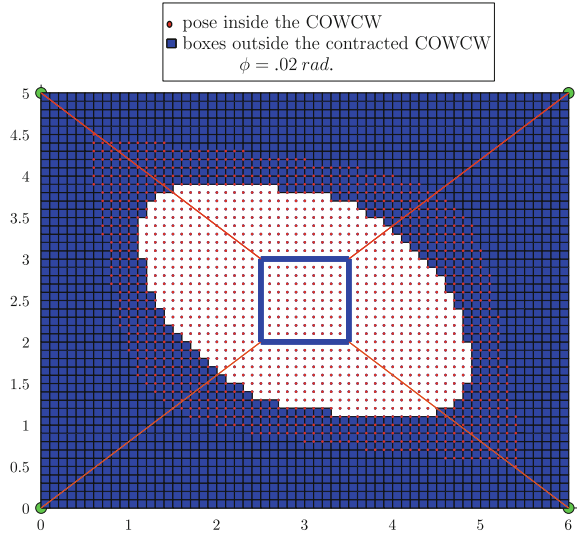
Table 1 Geometric parameters of the assumed PCDPM

i	1	2	3	4
$\mathbf{a}_i^T$	[0 0]	[6 0]	[6 5]	[0 5]
$\mathbf{b}_i^T$	[−.5 − .5]	[.5 − .5]	[.5 .5]	[−.5 .5]

negative of the area covered with boxes. As can be seen from this figure, relaxing the constraints results in an underestimation of the COWCW. In this example, we used square boxes with edge lengths of 0.1. Smaller boxes would have lead to a better estimate of the COWCW, as the convex relaxation (14) then forms a tighter approximation of (4).

As they were obtained in problem (17) the inequality constraints can always be satisfied by choosing $\xi_j = \mathbf{0}_8$. For the purpose of later assembling them, we would like these constraints to be feasible only if a given box is fully inside the WCW. To this end, we compute the Lagrange dual [17] of problem (17) and eliminate one of the decision variables by substitution of one of the constraints. This leads to following feasibility problem.

$$\text{satisfy} \quad \mathbf{R}_j \mathbf{y}_j + \mathbf{g} = \mathbf{0}_7, \quad \mathbf{y}_j \succeq \mathbf{0}_{m+8}, \quad j = 1, \ldots, 8, \tag{18}$$

over $\mathbf{y}_j \in \mathbb{R}^{m+8}$, which represents the vector of Lagrange multipliers.

Problem (18) is equivalent to its primal problems (17) but it is feasible when problem (17) yields zero $\forall J \in \{1, \ldots, 8\}$, and infeasible when problem (17) is unbounded for any $J \in \{1, \ldots, 8\}$. This is the primal-dual relationship occurs in linear programming [18]. Equation (18) may now be regarded as a single feasibility problem of 56 linear equations into $8m + 64$ non-negative variables and we can turn our attention to the synthesis problem.

5 A Formulation for the Problem of Synthesizing a PCDPM

Problems (18) serve as a building brick to formulate the dimensional synthesis of PCDPMs. Suppose we are interested in finding a PCDPM geometry whose constant-orientation WCW contains a given box $\mathscr{B}$. In order to solve this problem we introduce the nonlinear feasibility problem

$$
\begin{aligned}
\text{satisfy} \quad & \mathbf{R}_j \mathbf{y}_j + \mathbf{g} = \mathbf{0}_7, \quad j = 1, \ldots, 8, \\
& \mathbf{y}_j \succeq \mathbf{0}_{m+8}, \quad j = 1, \ldots, 8, \\
& \underline{\mathbf{a}} \preceq \mathbf{a}_i \preceq \overline{\mathbf{a}}, \quad \underline{\mathbf{b}} \preceq \mathbf{b}_i \preceq \overline{\mathbf{b}}, i = 1, \ldots, m, \\
\text{over} \quad & \mathbf{y}_j \in \mathbb{R}^{m+8}, \mathbf{a}_i \in \mathbb{R}^2, \quad \mathbf{b}_i \in \mathbb{R}^2.
\end{aligned}
\tag{19}
$$

Here, $\underline{\mathbf{a}}$, $\overline{\mathbf{a}}$, $\underline{\mathbf{b}}$ and $\overline{\mathbf{b}}$ are lower and upper bounds on the positions of the base and MP attachments points, which would otherwise be drawn to infinity during the solution process. Problem (19) is a nonlinear feasibility problem with $12m + 64$ variables and 56 equality constraints. If it exists, the associated solution yields a PCDPM geometry whose COWCW is guaranteed to include the prescribed box $\mathscr{B}$. On the other hand, the absence of a solution to this problem does not imply that there is no possible PCDPM geometry containing $\mathscr{B}$. Hence, this method lacks practicality, since failing to obtain a feasible solution does not provide any information regarding a *good* but *not perfect* geometry. For this reason introducing an objective function is thought to be more attractive to the designer. This is the main concern of the next section.

5.1 A Nonlinear Program for the Constant-Orientations Dimensional Synthesis of PCDPMs

Suppose we are given a box and we want to find the geometry of a PCDPM whose COWCW includes this box. Evidently, if we use a scaled version of this box in problem (19) and can find a geometry of a PCDPM whose COWCW allows for a scaling factor above one, then the original problem is solved. Quite naturally, the idea is to consider the scaling factor as an objective to be maximized. If, at the optimum point this factor is smaller than one, then the designer is left with the best infeasible solution.

This scaling process is depicted in Fig. 3 for a prescribed box. The box $\mathscr{B}'$ with dashed lines is the scaled image of the smaller one with solid lines. The scaling factor is s and the scaling point is C. From this figure we can obtain the lower-left and upper-right coordinates of the scaled box $\mathscr{B}'$ as

$$
\underline{\mathbf{p}}' = \mathbf{p}_c + s(\underline{\mathbf{p}} - \mathbf{p}_c) \quad \text{and} \quad \overline{\mathbf{p}}' = \mathbf{p}_c + s(\overline{\mathbf{p}} - \mathbf{p}_c),
\tag{20}
$$

where $\underline{\mathbf{p}}$ and $\underline{\mathbf{p}}$ are the lower-left and upper-right coordinates of the original box $\mathscr{B}$. Vector $\mathbf{p}_c$ and scalar s represent the position of the scaling point C and the scaling

Fig. 3 A scaled box and its
corresponding parameters
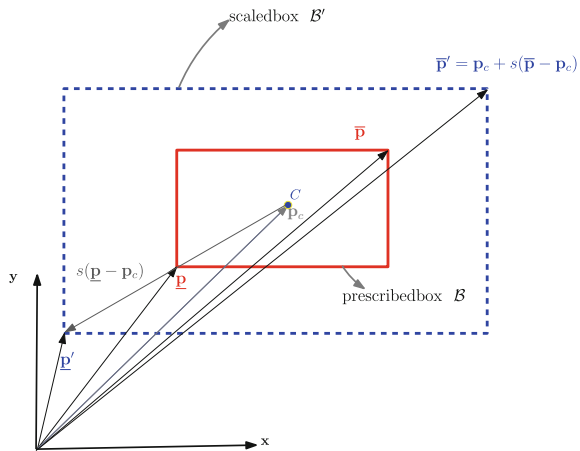
factor, respectively. If we consider the centroid of the box as the scaling point, then $\mathbf{p}_c = \frac{1}{2}(\overline{\mathbf{p}} + \underline{\mathbf{p}})$.

We now turn the feasibility problem (19) into a nonlinear program where $\mathbf{R}'_j$ is obtained by substituting $\overline{\mathbf{p}}'$ and $\underline{\mathbf{p}}'$ for $\overline{\mathbf{p}}$ and $\underline{\mathbf{p}}$, respectively, in the expression of $\mathbf{R}_j$ given in problem (17). Moreover, to ensure that $\underline{\mathbf{p}}'$ and $\overline{\mathbf{p}}'$ remain the lower left and upper-right corners of the scaled box, we constrain the scaling factor s to non-negative real numbers.

$$
\begin{aligned}
\text{maximize} \quad & s \\
\text{subject to} \quad & \mathbf{R}'_j \mathbf{y}_j + \mathbf{g} = \mathbf{0}_7, \\
& \underline{\mathbf{p}}' - \mathbf{p}_c - s(\underline{\mathbf{p}} - \mathbf{p}_c) = \mathbf{0}_2, \\
& \overline{\mathbf{p}}' - \mathbf{p}_c - s(\overline{\mathbf{p}} - \mathbf{p}_c) = \mathbf{0}_2, \\
& \underline{\mathbf{a}} \preceq \mathbf{a}_i \preceq \overline{\mathbf{a}}, \quad \underline{\mathbf{b}} \preceq \mathbf{b}_i \preceq \overline{\mathbf{b}}, \quad i = 1, \ldots, m, \\
& \mathbf{y}_j \succeq \mathbf{0}_{m+8}, \quad j = 1, \ldots, 8, \quad s \geq 0, \\
\text{over} \quad & \mathbf{y}_j \in \mathbb{R}^{m+8}, \quad \mathbf{a}_i \in \mathbb{R}^2, \quad \mathbf{b}_i \in \mathbb{R}^2, \quad s \in \mathbb{R}.
\end{aligned}
\tag{21}
$$

We illustrate this formulation with a synthesis example in the following section.

Example I: Constant Orientation WCW for a Given Box

Figure 4 shows an illustrative example of the results obtained through the solution of problem (21) or, more accurately, through the computation of one of its local optima. The assumed upper and lower bounds for the geometry of the mechanism and the lower-left and upper-right coordinates of the given box that need to be inside of the constant orientation WCW for the rotation angle $\phi = 0$ are given in Table 2. The number of cables is set to $m = 4$, which is the minimum for a WCW to exist.

Fig. 4 Geometry obtained for a PCDPM with four cables and constant orientation for a given box

Rotation angle, $\phi = 0$
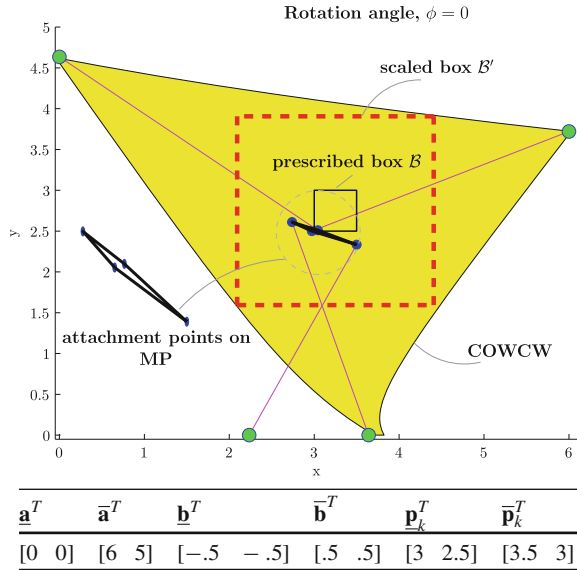
Table 2 Assumed parameters

$\underline{\mathbf{a}}^T$	$\overline{\mathbf{a}}^T$	$\underline{\mathbf{b}}^T$	$\overline{\mathbf{b}}^T$	$\underline{\mathbf{p}}_k^T$	$\overline{\mathbf{p}}_k^T$
[0 0]	[6 5]	[−.5 − .5]	[.5 .5]	[3 2.5]	[3.5 3]

In order to reach a local optimum, we need to begin with an initial guess on the decision variables. We consider the values reported in Table 1 as this initial guess of the PCDPM geometry, while we choose $\mathbf{y}_{j,0} = \mathbf{0}_{m+8}$, $j = 1, \ldots, 8$, and $s_0 = 0$ for the remaining variables. The prescribed box which is to be magnified while remaining fully in the COWCW appears in solid black lines and the scaled box is in dashed red lines. A local optimum to problem (21) is geometry are shown in Table 3. This PCDPM design was computed by using the *fmincon* function of Matlab 7.6.0 *R*2008*a* with its default *active-set* algorithm. This algorithm solves nonlinear programs by sequential quadratic programming (SQP). For this example, it takes 12.52 s to obtain the result by using a desktop computer equipped with an Intel(R) Core(TM)2 CPU 6400 @ 2.13 GHz, and 4 GB RAM. Figure 5a and b show respectively the evolution of the scaling factor and the geometry of the robot from the initial guess to the final local optimum. The optimum value of the scaling factor is $s^* = 4.6298 \geq 1$, which means that the scaled box and the original box are both inside the resulting COWCW. This may be verified from Fig. 4, where the scaled box is drawn in thick dashed lines, while the original box is in solid lines. The corresponding COWCW also appears on this figure, and is seen to contain the scaled box, as required. Notice that we applied the method proposed in [4] with the algorithm proposed in [19] in order to calculate the WCW, which is represented by the grey region in the figure.

In the foregoing examples, we assumed a constant orientation angle to perform the dimensional synthesis of PCDPMs. Although one may think of applications, e.g., in haptics [20], where the MP should undergo pure translations while being able to apply moments, in general, the MP is required to rotate and translate in the plane. Therefore, we have to investigate the synthesis problem for different orientations as well. This is the topic of the next section.

Table 3 Obtained geometry

i	1	2	3	4
$\mathbf{a}_i^T$	[2.2339 0.0000]	[3.6406 0.0000]	[6.0000 3.7216]	[0.0000 4.6358]
$\mathbf{b}_i^T$	[0.5000 -0.1669]	[-0.2600 0.1097]	[-0.0277 -0.0008]	[0.0434 0.0102]
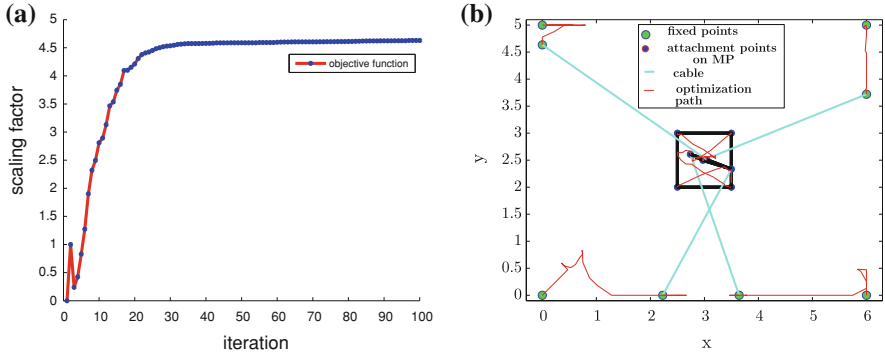
Fig. 5 Variations of optimization variables during the solving procedure. **a** Scaling factor. **b** Geometry of the robot

5.2 The Dimensional Synthesis of PCDPMs for Different MP Orientations

We show that formulation (21) can be developed to find the geometry of a PCDPM whose WCW includes a given box for different orientation angles. In order to solve such a problem, we discretize along the ϕ axis, i.e., we combine the nonlinear programs (21) defined for a set of fixed orientation angles. Evidently, this increases the number of constraints and variables. More precisely, if the number of the fixed orientation angles is n, then the nonlinear program representing the dimensional synthesis problem is

$$
\begin{aligned}
\text{maximize} \quad & s \\
\text{subject to} \quad & \mathbf{R}_{k,j}\mathbf{y}_{k,j} + \mathbf{g}_k = \mathbf{0}_7, \\
& \mathbf{p}'_k - \mathbf{p}_c - s(\underline{\mathbf{p}}_k - \mathbf{p}_c) = \mathbf{0}_2, \\
& \overline{\mathbf{p}}'_k - \mathbf{p}_c - s(\overline{\mathbf{p}}_k - \mathbf{p}_c) = \mathbf{0}_2, \\
& \underline{\mathbf{a}} \preceq \mathbf{a}_i \preceq \overline{\mathbf{a}}, \quad \underline{\mathbf{b}} \preceq \mathbf{b}_i \preceq \overline{\mathbf{b}}, \quad i = 1, \ldots, m, \\
& s \geq 0, \\
& \mathbf{y}_{k,j} \succeq \mathbf{0}_{m+8}, \quad j = 1, \ldots, 8, \quad k = 1, \ldots, n, \\
\text{over} \quad & \mathbf{y}_{k,j} \in \mathbb{R}^{m+8}, \quad \mathbf{a}_i \in \mathbb{R}^2, \quad \mathbf{b}_i \in \mathbb{R}^2, s \in \mathbb{R}.
\end{aligned}
\tag{22}
$$

Notice that to construct the matrix $\mathbf{R}_{k,j}$ and vector $\mathbf{g}_k$ we must substitute the corresponding orientation angle ϕ_k in Eq. (17). Problem (22) is a nonlinear, non-convex

Table 4 Obtained geometry for different orientation angles

i	1	2	3	4
$\mathbf{a}_i^T$	[0.0000 0.0000]	[5.1281 0.0000]	[6.0000 5.0000]	[0.0000 5.0000]
$\mathbf{b}_i^T$	[0.3729 -0.5000]	[-0.2570 -0.1436]	[-0.1238 -0.1244]	[0.1690 0.3179]
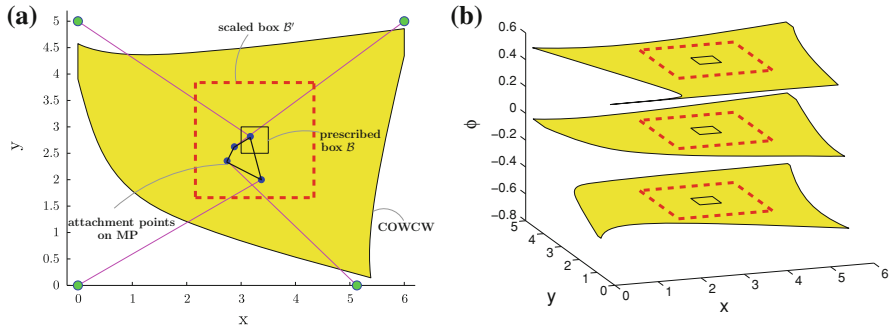
Fig. 6 Geometry and COWCWs obtained for a PCDPM with four cables for the prescribed box.
a Geometry obtained with COWCW for $\phi = 0$. **b** COWCWs with the prescribed and the resulting
scaled boxes

program with $(8m+64)n+4m+1$ variables, $60n$ equality, and $(8m+64)n+8m+1$
inequality constraints. We illustrate the results with the following example.

Example II: A Prescribed Box at Different Orientations

Suppose we have a given box with the same coordinates as in Example I. We seek a
PCDPM whose three constant-orientation wrench-closure workspaces correspond-
ing respectively to $\phi_1 = -\frac{\pi}{6}$, $\phi_2 = 0$ and $\phi_3 = \frac{\pi}{6}$, include this box. We set the
lower and upper bounds on the geometry to the values given in Table 2 and the initial
guess is the same as the one displayed in Fig. 4. We use the "trust-region-reflective"
algorithm of Matlab to solve the problem (22), which is called through the fmin-
con command. This is a gradient based method which is generally faster than other
methods, provided that the derivatives are specified by the user. Using the machine
mentioned in Example I, *fmincon* yields $s^* = 4.3568$ and the obtained geometry
is shown in Table 4 after a computation time of 161.3 s. This geometry and the cor-
responding constant orientation WCW for $\phi = 0$ are depicted in Fig. 6a. Figure 6b
shows the COWCWs corresponding to the chosen values of ϕ, the prescribed boxes,
and their scaled version. One can easily verify that all of these COWCWs include
the scaled version of the given box. In this section and the previous one, we devel-
oped formulations to find the geometry of a PCDPM whose WCW includes a given
box. The proposed approach can be used to synthesize PCDPMs for non-rectangular
prescribed workspaces which are approximated by multiple boxes. Such an approx-

imation is obtainable through the interval analysis [21]. However, we are forced to omit the corresponding example because of space constraints.

6 Conclusions

A method for the constant-orientation dimensional synthesis of planar parallel cable driven mechanisms (PCDPMs) was proposed. To achieve this goal, an optimization problem was first introduced to verify whether a given pose is inside the wrench closure workspace (WCW) of a given PCDPM. We then relaxed this problem over a box in the workspace, which lead us to a sufficient condition for this box to be inside the constant-orientation WCW of a given PCDPM. These mathematical conditions allowed the formulation of a nonlinear program in which the scale of the prescribed workspace is maximized while being constrained inside the COWCW of the PCDPM. The robot geometry being included in the decision variables of the nonlinear program, this optimization problem is thus a tool for the dimensional synthesis of PCDPMs. The value of the scaling factor at the optimum indicates whether the prescribed box is inside the constant orientation WCW. It was shown that the proposed approach can be applied to prescribed workspaces that cover several fixed orientations.

A natural sequence of this work is the extension of the proposed method to three-dimensional boxes covering the x, y and ϕ dimensions of a PCDPM workspace. We would also like to devise a method for globally solving the resulting nonlinear optimization problem. To this end, we are contemplating the use of a branch-and-bound technique. Extending the proposed method may provide a formulation for the dimensional synthesis of spatial CDPMs as well. Finally, our intuition is that the same approach could be applied to the dimensional synthesis of conventional rigid-link mechanisms. All these ideas will be topics of further reports.

References

1. Kurtz, R., Hayward, V.: Dexterity measure for tendon actuated parallel mechanisms. In: IEEE International Conference on Advanced Robotics, pp. 1141–1146. Pisa, Italy (1991).
2. Ming, A., Higuchi, T.: Study on multiple degree-of-freedom positioning mechanism using wires (part 1) concept, design and control. Int. J. Jpn. Soc. Precis. Eng. **28**(2), 131–138 (1994)
3. Pham, C.B., Yeo, S.H., Yang, G., Kurbanhusen, M.S., Chen, I.-M.: Force-closure workspace analysis of cable-driven parallel mechanisms. Mech. Mach. Theory **41**, 53–69 (2006)
4. Stump, E., Kumar, V.: Workspaces of cable-actuated parallel manipulators. ASME J. Mech. Des. **128**(1), 159–167 (2006)
5. Fattah, A., Agrawal, S.: On the design of cable-suspended planar parallel robots. ASME J. Mech. Des. **127**(5), 1021–1028 (2005)
6. Riechel, A.T., Ebert-Uphoff, I.: Force-feasible workspace analysis for underconstrained, point-mass cable robots. In: IEEE Internatlonal Conference on Robotics and Automation, pp. 4956–4962, New Orleans, LA, USA (2004).

7. McColl, D., Notash, L.: Extension of antipodal theorem to workspace analysis of planar wire-actuated manipulators. In: Proceedings of 5th IFToMM International, Workshop, pp. 9–16. (2009).
8. Gouttefarde, M., Daney, D., Merlet, J.P.: Interval-analysis-based determination of the wrench-feasible workspace of parallel cable-driven robots. IEEE Trans. Robotics **27**(1), 1–13 (2011)
9. Hay, A.M., Snyman, J.A.: Optimization of a planar tendon-driven parallel manipulator for a maximal dextrous workspace. Eng. Optim. **37**(3), 217–236 (2005)
10. Kolev, K., Cremers, D.: Continuous ratio optimization via convex relaxation with applications to multiview 3d reconstruction. In: IEEE Computer Society Conference on Computer Vision and Pattern Recognition, vol. 1, pp. 1858–1864. Miami, Florida, USA (2009).
11. Cafieri, S., Lee, J., Liberti, L.: On convex relaxations of quadrilinear terms. J. Glob. Optim. **47**(4), 661–685 (2010)
12. Porta, J., Rose, L., Thomas, F.: A linear relaxation technique for the position analysis of multiloop linkages. IEEE Trans. Robotics **25**(2), 225–239 (2009)
13. Graham, T., Roberts, R., Lippitt, T.: On the inverse kinematics, statics, and fault tolerance of cable-suspended robots. J. Rob. Syst. **15**(10), 581–597 (1998)
14. Gouttefarde, M., Gosselin, C.: Analysis of the wrench-closure workspace of planar parallel cable driven mechanisms. IEEE Trans. Robotics **22**(3), 434–445 (2006)
15. Dantzig, G., Thapa, M.: Linear Programming: Theory and Extensions. Springer, New York (2003)
16. Sherali, H., Tuncbilek, C.H.: A reformulation-convexification approach for solving nonconvex quadratic programming problems. J. Glob. Optim. **7**, 1–31 (1995)
17. Boyd, S., Vandenberghe, L.: Convex Optimization. Cambridge University Press, Cambridge (2004)
18. Bazarra, M., Sherali, H., Shetty, C.: Nonlinear Programming. Wiley Interscience, New Jersy (2006)
19. Dubé, D., Cardou, P.: Tracer rapidement l'espace des poses polyvalentes (EPP) d'un manipulateur parallèle plan à entraînement par câbles sous Matlab. REPARTI Workshop, In (2010)
20. Gosselin, C., Poulin, R., Laurendeau D.: A planar parallel 3-dof cable-driven haptic interface. In: Proceedings of the 12th World Multi-Conference on Systemics, Cybernetics and Informatics, pp. 266–271. Orlando, Florida, USA (2008).
21. Cloud, M.J., Moore, R.E., Kearfott, R.B.: Introduction to Interval Analysis. Siam, Philadelphia (2009)

Part V
Kinematics and Interval Methods

Feasible Kinematic Sensitivity in Cable Robots Based on Interval Analysis

Seyed Ahmad Khalilpour, Azadeh Zarif Loloei, Hamid D. Taghirad and Mehdi Tale Masouleh

Abstract The kinematic sensitivity has been recently proposed as a unit-consistent performance index to circumvent several shortcomings of some notorious indices such as dexterity. This paper presents a systematic interval approach for computing an index by which two important kinematic properties, namely feasible workspace and kinematic sensitivity, are blended into each other. The proposed index may be used to efficiently design different parallel mechanisms, and cable driven robots. By this measure, and for parallel manipulators, it is possible to visualize constant orientation workspace of the mechanism where the kinematic sensitivity is less than a desired value considered by the designer. For cable driven redundant robots, the controllable workspace is combined with the desired kinematic sensitivity property, to determine the so-called feasible kinematic sensitivity workspace of the robot. Three case studies are considered for the development of the idea and verification of the results, through which a conventional planar parallel manipulator, a redundant one and a cable driven robot is examined in detail. Finally, the paper provides some hints for the optimum design of the mechanisms under study by introducing the concept of minimum feasible kinematic sensitivity covering the whole workspace.

S. A. Khalilpour (✉) · A. Z. Loloei · H. D. Taghirad
Advanced Robotics and Automated Systems, Faculty of Electrical and Computer
Engineering, K. N. Toosi University of Technology, 16315-1355 Tehran, Iran
e-mail: khalilpour@kntu.ac.ir

A. Z. Loloei
e-mail: zarif@kntu.ac.ir

H. D. Taghirad
e-mail: taghirad@kntu.ac.ir

M. Tale Masouleh
Faculty of Modern Science and New Technology, University of Tehran, at Tehran, Iran
e-mail: m.t.masouleh@ut.ac.ir

1 Introduction

Cable driven redundant parallel manipulators (CDRPMs) consist of a moving platform which is connected by the means of actuated cables to the base. Redundancy is an inherent requirement for CDRPMs due to the fact that cables can only pull but cannot push the moving platform. Thus, in a non-singular posture, the moving platform can perform n Degree-Of-Freedom (DOF) provided that at least $n + 1$ cables are used. CDRPMs are special design of parallel manipulators (PMs) that heritage the advantages of PMs such as high acceleration and high load carrying capability and at the same time, have alleviated some of their shortcomings, such as restricted workspace. Due to the several eminent features of CDRPMs, they have stimulated the interest of many researchers and they are becoming the state-of-the-art in many real applications, such as telescope [1], haptic interface [2], motion trackers [3], rescue robotics [4], metrology [5], rehabilitation [6], sport training [7], heavy load transportation [8] and surgery [9]. However there are still some gap to fill in the kinematic properties of such mechanisms, such as workspace and kinematic sensitivity, which is the concerns of this paper.

The workspace of CDRPM are investigated upon different perspectives and different types of workspace are proposed in the literature. In short, four different types of workspace have been introduced: (1) Wrench feasible workspace [10], (2) Dynamic workspace [11], (3) Static workspace [12] and (4) Controllable workspace [13]. In this paper, more emphasis is placed on the controllable workspace which represents the most general feasible workspace. Controllable workspace pertains at finding the set of poses (position and orientation) of the moving platform in which any wrench can be generated by the moving platform while cables are all in tension.

Extensive presence of singular points in PMs and the challenge to obtain and avoid them is one of the major drawbacks of this kind of mechanisms. In the design of PMs, usually kinematics performance indices are used to reduce the singularities and to improve the performance of the mechanism under study. Most popular indices are Yoshikawa manipulability [14] and the dexterity indices [15], which entail some limits and as stated in [16], seems to have not drawn a consensus among the robotics community. The latter problem relies on the impossibility to define a single invariant metric for the special Euclidean group, i.e., the Jacobian matrices are nonhomogeneous. To circumvent the latter problem, recently two different indices named point-displacement and rotational kinematic sensitivities are proposed which their meaning is thought to be clear and definite to the designer of a robotic manipulator [17]. These indices provide tight upper bounds on the magnitudes of the end-effector rotations and point-displacements, respectively under a unit-magnitude array of actuated-joint displacement [18].

The kinematic analysis requires a suitable framework in order to propose a proper and systematic method. The mathematical framework of this paper is based on interval analysis [19], using the intlab package [20]. There are host of advantages relevant to using interval analysis as an alternative numerical method in order to obtain practically competent results for the analysis of kinematic properties of

robotics mechanical systems [21]. In this paper. our interest toward applying interval analysis to the kinematic analysis can be summarized as follows [22]: (1) In contrast to many other intelligent mathematical tools which would result in a lengthy computation process and may converge to a local optimum, interval analysis is not a *black box*, since it requires to combine heuristics and numerical concepts to make it more effective, (2) It allows to find all the solutions with inequalities within a given search space [23, 24] (3) For two and three-dimensional problems one can see the evolution of the solutions and to monitor the procedure in order to have better insight into the problem, (4) It allows to take into account uncertainties in the model of the robot and (5) For the problem in which infinity norm are involved, interval analysis may solve the problem more efficiently rather than other methods since infinity norm is a non-analytical function and consequently mathematical operations are not tractable.

This paper aims at introducing a more practical workspace for the CDRPMs in which the kinematic sensitivity is also taken into account while computing the controllable workspace. To this end, upon blending these two concepts, a new workspace is introduced which is referred to as *Feasible Kinematic Sensitivity* (FKS) and can be also regarded as a performance index. FKS pertains at finding a part of controllable workspace in which the kinematic sensitivity is less that a desired value. As it is the case for kinematic sensitivity and controllable workspace, the mathematical framework to obtain the FKS of a given PM is based on interval analysis and, to do so, a systematic approach is proposed.

The remainder of this paper is organized as follows. First, interval analysis is reviewed and the general concepts are introduced. Then based on the work presented in [18], the general idea of kinematic sensitivity is reviewed. The paper follows by exploring the concept of kinematic sensitivity by means of interval analysis upon proposing some systematic algorithms where it is applied to 3-R͟PR PM and 4-R͟PR redundant PM. Then the interval formulation of the controllable workspace is investigated for 3-DOFs CDRPMs with four cables. As the central subject of this paper, FKS workspace is introduced and examined for the case studies. Finally, the paper concludes with some remarks to provide some insight to the optimum synthesis of CDRPMs.

2 Background Materials

2.1 Interval Analysis

Interval analysis is amongst the numerical methods proposed in the literature that allows to safely solve the problem, and to obtain a guaranteed result. The basic principles of interval analysis are simple, where efficient implementation requires a high expertise level. In interval analysis, one deals with intervals of numbers instead of the numbers themselves [19]:

$$[x] = [\underline{x}, \overline{x}] = \{x | x \in R, \underline{x} \leq x \leq \overline{x}\} \tag{1}$$

where $\underline{x}$ is the left endpoint and $\overline{x}$ is the right endpoint of the interval. By an n-dimensional interval vector, we mean an ordered n-tuple of intervals:

$$\mathbf{X} = (X_1, \ldots, X_n) \tag{2}$$

In interval analysis all variables are independently investigated [25]. Thus the output range of interval function could be wider than the function span, but certainly the answer region lies within the output range. Therefore applying interval analysis has its own difficulties, but on the other hand the answer it gives is guaranteed, meaning that negligible errors that result from mathematical operations such as rounding and estimation, are not present. In this paper, interval analysis is not introduced in detail, since it is beyond the scope of this study and reader are referred to [25, 26] for a more comprehensive detail. It should be noted that all the interval algorithms proposed in this paper are implemented in Matlab which uses the INTLAB package supporting interval calculations.

2.2 Kinematic Sensitivity Indices

Kinematic sensitivity is defined as the maximum error that occurs in the Cartesian workspace as a result of bounded errors in the joint space ($\|\rho\| \leq 1$). In order to obtain consistent unit indices, two indices have been defined in [16]:

$$\sigma_{r_c,f} \equiv \max_{\|\rho\|_c=1} \|\phi\|_f \quad \text{and} \quad \sigma_{p_c,f} \equiv \max_{\|\rho\|_c=1} \|\mathbf{p}\|_f \tag{3}$$

in which, $\rho \in \mathbb{R}^n$ represents small actuator displacements and $x = [\mathbf{p}, \phi]$ stands for the pose of the end-effector. Moreover, $c = \{2, \infty\}$ and $f = \{2, \infty\}$ are respectively the types of norm for which the constraint and the objective are expressed. From the results obtained from [18], it can be inferred that two situations may correctly represent the kinematic sensitivity, which will be used for the purposes of this paper: (1) The constraint and objective functions are both expressed using ∞-norms ($c = f = \infty$) and (2) The constraint and objective functions are expressed respectively with ∞ and 2-norms ($c = \infty$, $f = 2$).

3 Investigation of Kinematic Sensitivity of Non-redundant Planar Parallel Mechanisms

This section is devoted entirely to an overview on the computation of the kinematic sensitivity of non-redundant planar PM based on the results reported in [17, 18, 27] and, as a case study, the so-called 3-R$\underline{P}$R is considered.[1] As pointed out previously,

---

[1] Here and throughout this paper, R and P stands respectively for a revolute and prismatic joint where the underlined joint is actuated.

Fig. 1 A 3-R̲PR parallel
manipulator. Taken from [18]

Fig. 1 A 3-R̲PR parallel manipulator. Taken from [18]
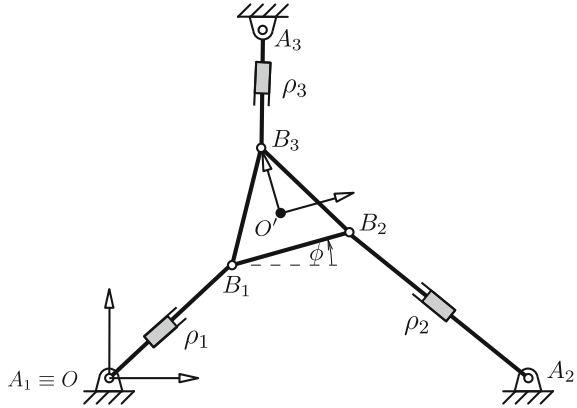
the two different situations explained above, i.e., ($c = f = \infty$ and $c = \infty$ and $f = 2$), are considered for computing the kinematic sensitivity. Although the concepts presented in this section is to the majority of intents and purposes the same as the one presented in [18], it provides for the first time, the framework to compute the kinematic sensitivity by using interval analysis. More specifically, the main objective of this section is to lay down the essential for the rest of the paper by introducing an interval-based algorithm which leads to obtain a region within the workspace of the mechanism, referred to as *feasible kinematic sensitivity workspace*, where the kinematic sensitivity is less than a given value, σ_d. It is worth noting that the computation of the constant-orientation workspace, reachable area of the moving platform for a given orientation of the moving platform and given stroke of actuator, is integrated in the proposed algorithm. As a geometrical point of view, the constant-orientation workspace of a 3-R̲PR PM can be made equivalent to the intersection of six circles, arisen from the minimum and maximum stroke of the prismatic actuators. This can be readily obtained using interval analysis and due to its simplicity, the details of such calculations are skipped in this paper. Furthermore, here and throughout this paper, for the sake of brevity, the constant-orientation workspace is referred to as workspace.

Figure 1 represents schematically a 3-R̲PR PM performing 3-DOF where the pose of the end-effector is denoted by (x, y, ϕ). Both fixed and moving platforms are considered as equilateral triangles that are encompassed by circles with radius 1 and 5, respectively, where the center of each triangle is coincidence on the circumambient circles centers. As it will be discussed latter on, from the results presented in [28] having equilateral triangles for the fixed base and moving platform results in a circle for the singularity curve which considerably optimizes the singularity-free workspace and is a definite asset in the practice. The Jacobian matrix, **K**, with respect to the pose of the mechanism, (x, y, ϕ), may be written in an interval form, [**K**], as:

Table 1 Pseudo-code for the calculation of the interval vertices of the polyhedron in a non-redundant parallel manipulator

---

Function: Compute-Vertex-Nonredundant([K])

```
t=1
for i₁=1:2
    for i₂=1:2
        ⋮
        for iₘ₋₁=1:2
            [temp]=[1,(−1)^i₁,(−1)^i₂,...,(−1)^{iₘ₋₁}]ᵀ
            [Vertices(t)]=verifylss([K],[temp])
            t=t+1
        end
        ⋮
    end
end
```

$$[\mathbf{K}] = \mathbf{K}([x], [y], [\phi]), \qquad \mathbf{K} = \begin{bmatrix} n_{1x} \text{ and } n_{1y} & (\mathbf{b}_1 \times \mathbf{n}_1) \cdot \mathbf{k} \\ n_{2x} \text{ and } n_{2y} & (\mathbf{b}_2 \times \mathbf{n}_2) \cdot \mathbf{k} \\ n_{3x} \text{ and } n_{3y} & (\mathbf{b}_3 \times \mathbf{n}_3) \cdot \mathbf{k} \end{bmatrix} \qquad (4)$$

In the above, $\mathbf{b}_i$, $i = 1, 2, 3$, denotes the position vector of point B_i in the fixed frame, and the unit vector along the ith prismatic joint direction is denoted by $\mathbf{n}_i = [n_{i_x}, n_{i_y}, 0]^T$. For a more comprehensive information regarding the kinematic properties of these kind of PMs, readers are referred to [18, 27].

3.1 Kinematic Sensitivity with ∞-norms on Constraint and Objective Function

In this case, since dealing with $c = \infty$ for the constraint, the constraint inequality $\|\rho\|_\infty \leq 1$ can be replaced by $\|\mathbf{Kx}\|_\infty \leq 1$, from the Jacobian relation. Inequality $\|\mathbf{Kx}\|_\infty \leq 1$ stands for a polyhedron with 2^n vertices in $\mathbb{R}^n$ where n represents the DOF of the PMs under study. The first step toward calculating the kinematic sensitivity for both ∞− or 2−norm consists of obtaining the vertices of the latter polyhedron, which can be done by solving the inequality $[\mathbf{K} - \mathbf{K}^T] \leq \mathbf{1}$. By using interval formulation of the Jacobian matrix, the intervals in which each vertices of the polyhedron is bounded, can be computed. Therefore the combination of all the interval vertices leads to interval formulation of the polyhedron. From the fact that the polyhedrons are symmetric with respect to the origin, calculation of half of them is sufficient. The pseudo-codes given in Table 1, provides the logic in changing the intervals of these vertices. Note that, the function `verifylss([A], [B])` in the

pseudo-codes given in Table 1 is a function of intlab toolbox that solves the system of equations $[A].[X] = [B]$, in which $[A]$ and $[B]$ are interval matrices and $[X]$ is a interval vector.

In the case of a 3-RPR PM, the number of vertices of the hexahedron is $2^3 = 8$ and because of being symmetric the calculation of four vertices is sufficient. As a geometric stand point, in this case, using interval analysis to calculate the kinematic sensitivity can be made equivalent to the map of the vertices to a cube that their dimensions in all the Cartesian directions are equal to the width of the calculated interval of the corresponding vertex. Re-formulating the relations obtained in [18] for the point-displacement and rotational kinematic sensitivities, when $c = f = \infty$, for a given position in the specified interval in the direction of the pose of the mechanism, leads to the following for the maximum point-displacement and rotational kinematic sensitivities:

$$\max \sigma_{p\infty,\infty} = \max_{i=1,\ldots,4}(\mathrm{mag}([X_i]), \mathrm{mag}([Y_i])) \tag{5}$$

$$\max \sigma_{\phi\infty,\infty} = \max_{i=1,\ldots,4}(\mathrm{mag}([\phi_i])) \tag{6}$$

where mag($\cdot$), for its interval argument, computes the distance of the farthest point in the interval from the coordinates origin. Furthermore, X_i, Y_i, ϕ_i constitute the elements of the vectors [Vertices(t)] obtained from the pseudo-code presented in Table 1. Similarly, the minimum kinematic sensitivity of the inner points of the interval is also calculated by:

$$\min \sigma_{p\infty,\infty} = \max_{i=1,\ldots,4}(\mathrm{mig}([X_i]), \mathrm{mig}([Y_i])) \tag{7}$$

$$\min \sigma_{\phi\infty,\infty} = \max_{i=1,\ldots,4}(\mathrm{mig}([\phi_i])) \tag{8}$$

where mig($\cdot$), for its interval argument, stands for the distance of the nearest point in the interval from the coordinates origin.

Table 2 provides the pseudo-code describing the interval formulation to obtain the maximum and minimum kinematic sensitivity, Eqs. (5–8), where $[x_t]$ and $[y_t]$ stands for the workspace of the mechanism, L_{in} and L_{out} represent the desired and undesired intervals of the workspace regarding to the criteria fixed for the kinematic sensitivity, σ_d, respectively. Moreover, L_{neg} involves the bound intervals, calculated according to the ε value. If the maximum value of kinematic sensitivity in the related interval is less than the desired value, σ_d, the interval is certainly inside the desired region and the function feasible ($[V]$, σ_d) will return a value as one. Moreover, if the minimum value of kinematic sensitivity in the related interval is certainly more than the desired value, the interval is out of the desired region and the function out ($[V]$, σ_d) will be activated. In the case that the workspace of the end-effector is not sufficiently small for the kinematic sensitivity of the points to have a similar behavior, the region should be split up into two intervals, in such a way that for the new intervals one of the functions feasible($[V]$, σ_d) or out($[V]$, σ_d) becomes active. The interval

Table 2 The proposed pseudo-code for the calculations of minimum and maximum kinematic sensitivity in the workspace

Input:$([x_t],[y_t],\phi,\varepsilon,\sigma_d)$
Output: (L_{in},L_{out},L_{neg})

```
L ← ([xₜ],[yₜ])
while L ≠ ∅
    [K]=Compute-Jacobian-Matrix([X],[Y],φ)
    [V]=Compute-Vertex-non-redundant([K])
    if Feasible ([V],σd) then
        Lin ← ([X],[Y])
    else if Out([V],σd) then
        Lout ← ([X],[Y])
    else if size([X],[Y]) ≥ ε then
        L ← Bisect ([X],[Y])
    else
        Lneg ← ([X],[Y])
    end if
end while
```


Fig. 2 Point-displacement FKS, the inside (*green*) region, of a 3-R$\underline{P}$R PM with $c = f = \infty$ and $\sigma_d = 0.35$ for $\phi = 45$. The *dashed lines* represent the boundary of the workspace
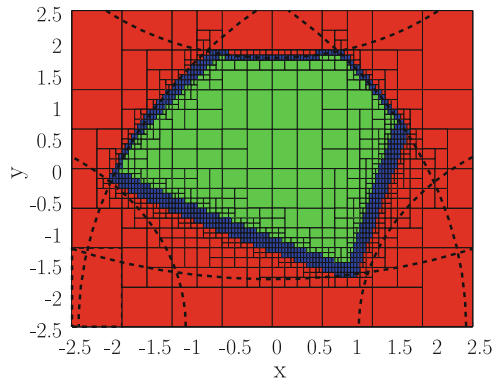
bisecting sequence pursues to the points that the remained intervals becomes small enough with respect to ε.

Figures 2 and 3 represent respectively the point-displacement and rotational kinematic sensitivity upon applying Eq. (5–8) and the pseudo-code presented in Table 2 for a given orientation of the moving platform, $\phi = \frac{\pi}{4}$. In the latter figures, the inside (green) region indicates a region that the 3-R$\underline{P}$R PM of Fig. 1 has a kinematic sensitivity less than 0.35 and the outside (red) region corresponds to the region with kinematic sensitivity greater than 0.35. As it can be observed from the forgoing figures, the outside (red) region is separated by the dark (blue) boxes from the inside (green) one which means that interval analysis was not able to reach to a conclusion for these boxes. These boxes represent the boundary of the FKS and it could be small as possible upon increasing the iteration. From the results obtained in [28], since the

Fig. 3 Rotational FKS, the
inside (*green*) region, of a
3-RPR PM with $c = f = \infty$
and $\sigma_d = 0.35$ for $\phi = 45$.
The *dashed lines* represent the
boundary of the workspace
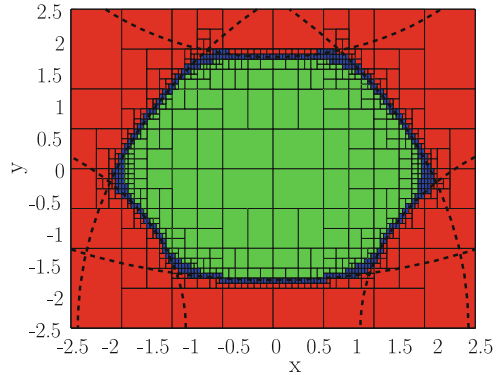
fixed and moving frame are equilateral, it can be also confirmed that the singularity
curve is a circle centers at $(0, 0)$ with a radius of 4.3507 for the 3-RPR PM under
study. As it can deduced form Fig. 3, the green region is inside the singularity cir-
cle and consequently is singularity-free. This leads to have a conservative but safer
constant-orientation workspace which is singularity-free.

3.2 Kinematic Sensitivity with ∞ norm for the Constraint and 2-norm for the Objective Function

As aforementioned, for the calculation of the maximum and minimum of the kine-
matic sensitivity for this case, i.e., $c = 2$ and $f = \infty$, one should find the vertices of
the polyhedron which was fully described in the previous section. From the results
presented in [18], the kinematic sensitivity for $c = 2$ and $f = \infty$ in the interval form
can be formulated as follows:

$$\max \sigma_{p_{\infty,2}} = \max_{i=1,...,4} (\mathrm{mag}(\sqrt{X_i{}^2 + Y_i{}^2})) \tag{9}$$

$$\min \sigma_{p_{\infty,2}} = \max_{i=1,...,4} (\mathrm{mig}(\sqrt{X_i{}^2 + Y_i{}^2})) \tag{10}$$

In this specific PM where the mechanisms performs only one rotational DOF
then the rotational kinematic sensitivity with ∞ and two-norm are identical. Figure 4
illustrates the point-displacement FKS, where σ_d is less than 0.35 (Fig. 5).

Fig. 4 Point displacement
FKS, the inside (*green*) region,
of a 3-R$\underline{P}$R PM with $c = \infty$,
$f = 2$ and $\sigma_d = 0.35$ for
$\phi = 45$. The *dashed lines*
represent the boundary of the
workspace
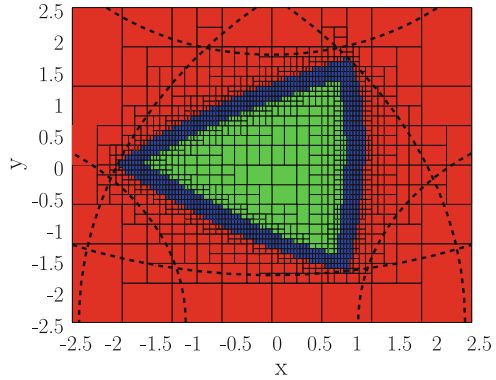
Fig. 5 A 4-R$\underline{P}$R planar
CDRPM
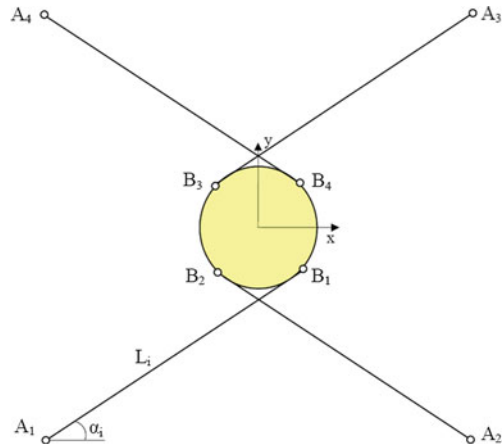
4 Investigation of Kinematic Sensitivity of Redundant Robots

From the study conducted in [18], it reveals that when computing the kinematic
sensitivity for redundant PM with respect to the ∞-norm constraint, the number of
hyperplanes increases and further confines polyhedral of constraint which is sought
at the outset. In fact appending redundant rows to the Jacobian matrix of the mech-
anism, will result into omission of farther vertices of constraint polyhedron and the
mechanism kinematic sensitivity reduces significantly. The latter implies avoiding
singular configurations within the workspace which can be regarded as a must for the
design of a PMs. Using the pseudo-code of Table 3, one can determine the interval
vertices of the hyperplanes in a redundant state. Once the interval vertices are gen-
erated with respect to the latter pseudo-code, the calculation of kinematic sensitivity
is accomplished in a maneuver akin to the non-redundant PM explained in Sect. 3.
The output of this function (interval vertices) are valid when the product of the rest
of the Jacobian matrix rows and the computed vertices vector, is a subset of interval

Table 3 The Pseudo-code for the calculations of interval vertices of polyhedron of constraint in a redundant robot

Function: Vertices=Compute-Vertex-Redundant([K])

$t = 1$
for $j_1 = 1 : n - (m - 1)$
  for $j_2 = j_1 + 1 : n - (m - 2)$
    ⋮
      for $j_m = j_{m-1} + 1 : n$
        $[K_n] = [[K_{j_1}], [K_{j_2}], \ldots, [K_{j_m}]]$
        $[K_w] = [K]$ without column $[K_n]$
        $[KnVertices]$=Compute-Vertex-Nonredundant($[K_n]$)
        for 1:number of vertices of *KnVertices*
          $[vertex]$=each of vertices of *KnVertices*
          if $-1 \leq mid([K_w]) \times mid([vertex]) \leq 1$
            vertices(t)=*vertex*
            t=t+1
          end
        end
      end
  ⋮
  end
end


Fig. 6 Point-displacement FKS, the inside (*green*) region, of a 4-R<u>P</u>R PM with $c = f = \infty$ and $\sigma_d = 0.35$ for $\phi = \frac{\pi}{6}$. The *dashed lines* represent the boundary of the workspace
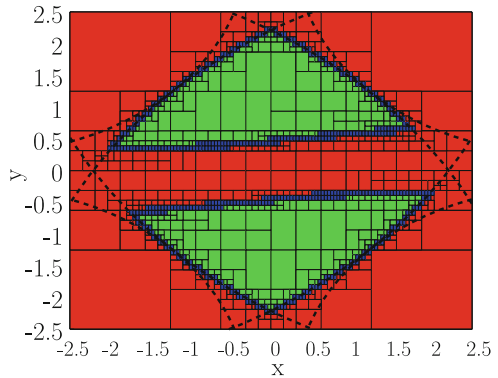
$[-1, 1]$. For the reason of dependency in interval analysis, the latter multiplication may result in an interval which could be wider than actual interval. Thus instead of multiplying the intervals, it is recommended to multiply the midpoints of the intervals in order to validate the computed vertices. In the pseudo-code of Table 3, n and m represent respectively number of active joints and number of DOFs in the robot workspace.

Fig. 7 Rotational FKS, the inside (*green*) region, of a 4-RPR PM with $c = f = \infty$ and $\sigma_d = 0.35$ for $\phi = \frac{\pi}{6}$. The *dashed lines* represent the boundary of the workspace
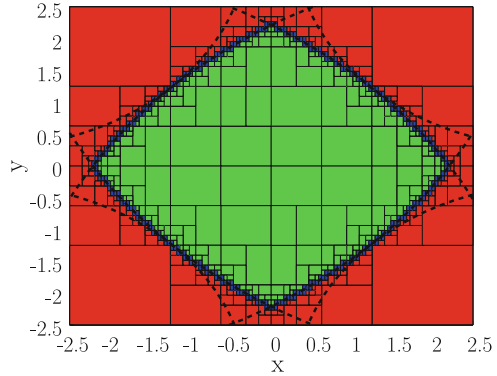
Fig. 8 Point-displacement FKS, the inside (*green*) region, of a 4-RPR with $c = \infty$ and $f = 2$ and $\sigma_d = 0.3$ with $\phi = \frac{\pi}{6}$. The *dashed lines* represent the boundary of the workspace
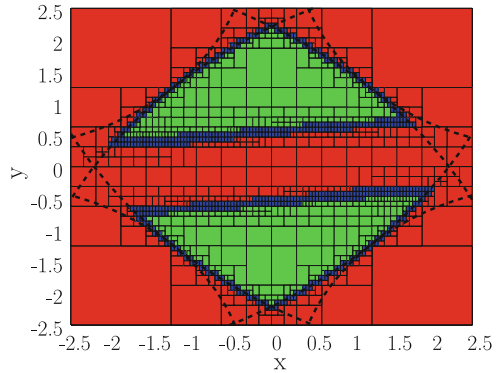
Figures 6, 7 and 8 represent respectively point-displacement and rotational FKS of a redundant PM, in which the fixed and moving attachment points lie respectively on squares encompassed by circles 1 and 5 m. The inside green region has a kinematic sensitivity less than 0.3, $\sigma_d = 0.3$. It should be noted that, considering $\sigma_d = 0.35$, similar to the previous section, leads to cover the whole workspace. From the latter, it can be concluded that in order to benefit from the the whole workspace, the kinematic sensitivity of the mechanisms under study should be equal to $\sigma_d = 0.35$. The foregoing statement relates the workspace and design parameters to the kinematic sensitivity, a performance index, which open some avenues toward the optimum design of PMs.

5 Feasible Kinematic Sensitivity in CDRPMs

The unidirectional constraint imposed by cables causes the workspace analysis of CDRPMs to be always a crucial step in the design. As aforementioned, among several types of workspace introduced in the literature for CDRPMs, the controllable workspace is considered in this paper [13]. For the controllable workspace analy-

Table 4 The proposed pseudo-code for the calculations of FKS controllable workspace of CDRPMs

---

Input:$([x_t], [y_t], \phi, \varepsilon, \sigma_d)$
Output: $(L_{in}, L_{out}, L_{neg})$

$L \leftarrow ([x_t], [y_t])$
while $L \neq \emptyset$
   $[K]$=Compute-Jacobian-Matrix$([X], [Y], \phi)$
   $[V]$=Compute-Vertex- redundant$([K])$
   $[\Delta]$=Compute-all Delta's $([X], [Y], \phi)$
   if Feasible $([V], \sigma_d)$ and all Δ are positive then
      $L_{in} \leftarrow ([X], [Y])$
   else if Out$([V], \sigma_d)$ or one Δ is negative then
      Lout$\leftarrow ([X], [Y])$
   else if size$([X], [Y]) \geq \varepsilon$ then
      L $\leftarrow$ Bisect $([X], [Y])$
   else
      $L_{neg} \leftarrow ([X], [Y])$
   end if
end while

---

sis, the analytic method proposed in [29] is used. In this method, a set of external wrenches is introduced and called *fundamental wrenches* which provides a physical interpretation of controllable workspace. Moreover, an analytical method is developed to determine the controllable workspace of redundant CDRPMs based on the so-called fundamental wrenches. The proposed method is generally applicable to any cable manipulators with any redundant cables as long as its Jacobian matrix is of full rank. The set of fundamental wrenches for a cable manipulator with one degree of redundancy refers to a set of $n + 1$ vectors; each of them is equal to an opposite direction of column vector of Jacobian transpose as [29]:

$$\mathbf{A} = -\mathbf{J}^T = [\mathbf{A}_1 | \mathbf{A}_2 | ... | \mathbf{A}_{n+1}]_{n \times (n+1)}, \quad \mathbf{w}_f = -\mathbf{A}_i, \ i = 1, ..., n+1 \qquad (11)$$

In which $\mathbf{A}$ and $\mathbf{J}$ denote the structural and Jacobian matrix, respectively, and $\mathbf{w}_f$ is the fundamental wrench vector. According to the proposed theorem in [29], the controllable workspace can be obtained when all the determinant of the following matrix are positive.

$$\Delta_{ij} = \det[\mathbf{A}_1 ... \mathbf{A}_{j-1} - \mathbf{w}_i \mathbf{A}_{j+1} ... \mathbf{A}_{i-1} \mathbf{A}_{i+1} ... \mathbf{A}_{n+1}], \quad i = 1, ..., n+1, \ i \neq j \tag{12}$$

In the pseudo-code given in Table 5, the combination method to obtain the FKS controllable workspace is shown. The approach is similar to the interval formulation of kinematic sensitivity in redundant manipulator, however, the constraint of controllable workspace is added at each iteration (Table 4).

Table 5 Computation time for the calculation of various kinematic sensitivity indices, for all cases $c = 2$

Robot type	Kinematic sensitivity	Norm of f	ε	Search area	Computation time (s)
3-R$\underline{P}$R	Point-displacement	∞	0.05	6.25	764
3-R$\underline{P}$R	Rotational	∞	0.05	6.25	418
3-R$\underline{P}$R	Point-displacement	2	0.05	6.25	1348
4-R$\underline{P}$R	Point-displacement	∞	0.05	6.25	815
4-R$\underline{P}$R	Rotational	∞	0.05	6.25	513
4-R$\underline{P}$R	Point-displacement	2	0.05	6.25	1128
CDRPM	Feasible kinematic sensitivity	∞	0.1	25.0	1783

Fig. 9 Controllable workspace, the *green* region, of a planar CDRPM with 4 cables
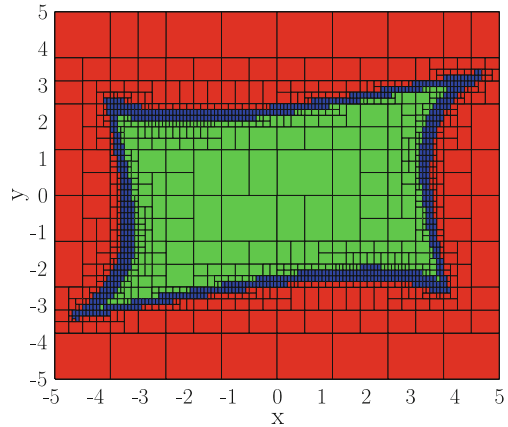
In Fig. 9, the inside (green) region illustrates the controllable workspace, while in Fig. 10, the inside (green) region represents the FKS workspace. In fact, this region is produced from blending controllable workspace and the area that has desired kinematic sensitivity, i.e. $\sigma_d = 0.3$. As it can be clearly seen from these figures, the interval analysis approach is capable to effectively combine two required kinematics characteristics in order to determine a suitable workspace for the robot. The volume of FKS may be used as a suitable measure for optimal design of such manipulators. In order to compare the computational cost of different methods, Table 4 summarizes the required time to calculate all the cases explained in the paper which are performed on a laptop computer with Core i7 CPU and 1.6 GHz clock time. From Table 5 it can be concluded that, due to the high computational time, FKS is more suitable for analyzing a given structure. Thus the computational time associated to FKS would be a major deterrent for optimization purposes. Current research is conducted to develop a suitable index for such optimization routine, and to reduce the computational cost.

Fig. 10 FKS, the *green* region, of a 4-R$\underline{\text{P}}$R CDRPM with $c = \infty$ and $f = 2$ and $\sigma_d = 0.3$ with $\phi = \frac{\pi}{6}$
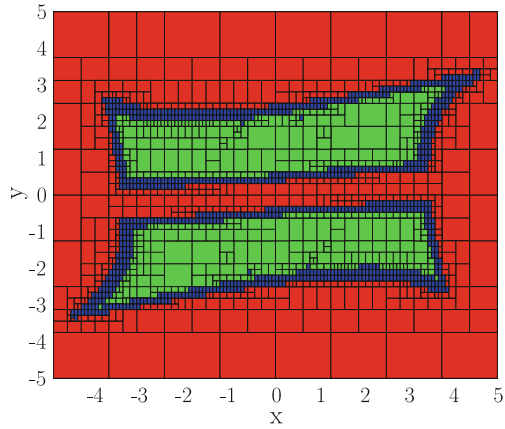
6 Conclusions

This paper proposed a framework for the computation of feasible kinematic sensitivity, a more practical constant-orientation workspace in which the kinematic sensitivity is less than a given value, by means of interval analysis. The feasible kinematic sensitivity for both point-displacement and rotation motion was explored. From the previous studies conducted on kinematic sensitivity, a judicious combination of the norms were used to express accurately the function and constraint expressions of the optimization problem corresponding to the kinematic sensitivity analysis. For the workspace of planar parallel mechanisms the constant-orientation workspace was used, while in the case of cable driven parallel manipulators, the controllable workspace was considered. As it is discussed in the paper, for a given design, a minimum feasible kinematic sensitivity value can be associated for which it can cover the whole workspace. Thus, ongoing works of this study includes to use of the minimum feasible kinematic sensitivity, set by the designer, as an optimization criteria to the end of optimum synthesis of the mechanism for which the minimum feasible kinematic sensitivity is known.

References

1. Su, Y., Duan, B., Nan, R., Peng, B.: Development of a large parallel-cable manipulator for the feed-supporting system of a next-generation large radio telescope. J. Rob. Syst. **18**(11), 633–643 (2001)
2. Dominjon, L., Perret, J., Lécuyer, A.: Novel devices and interaction techniques for human-scale haptics. Visual Comput. **23**(4), 257–266 (2007)
3. Geng, Z., Haynes, L.: Kinematic configuration of a stewart platform and its application to six degree of freedom pose measurements. Rob. Comput. Integr. Manuf. **11**(1), 23–34 (1994)

4. Tadokoro, S., Verhoeven, R., Hiller, M., Takamori, T.: A portable parallel manipulator for search and rescue at large-scale urban earthquakes and an identification algorithm for the installation in unstructured environments. In: Proceedings of the International Conference on Intelligent Robots and Systems (IROS'99), vol. 2, pp. 1222–1227 (1999).

5. Williams II, R., Albus, J., Bostelman, R.: 3D cable-based cartesian metrology system. J. Rob. Syst. **21**(5), 237–257 (2004)

6. Rosati, G., Gallina, P., Masiero, S.: Design, implementation and clinical tests of a wire-based robot for neurorehabilitation. IEEE Trans. Neural Syst. Rehabil. Eng. **15**(4), 560–569 (2007)

7. Morizono, T., Kurahashi, K., Kawamura, S.: Realization of a virtual sports training system with parallel wire mechanism. In: Proceedings of the IEEE International Conference on Robotics and Automation (ICRA' 97), vol. 4, pp. 3025–3030 (1997).

8. Higuchi, T., Ming, A., Jiang-Yu, J.: Application of multi-dimensional wire cranes in construction. In: Proceedings of the 5th International Symposium on Robotics in, Construction (ISRC88), pp. 661–668 (1988).

9. Hamid, S., Simaan, N.: Design and synthesis of wire-actuated universal-joint wrists for surgical applications. In: Proceedings of the IEEE International Conference on Robotics and Automation (ICRA'09), pp. 1807–1813 (2009).

10. Ebert-Uphoff, I., Voglewede, P.: On the connections between cable-driven robots, parallel manipulators and grasping. In: Proceedings of the IEEE International Conference on Robotics and Automation (ICRA'04), vol. 5, pp. 4521–4526 (2004).

11. Barrette, G., Gosselin, C.: Determination of the dynamic workspace of cable-driven planar parallel mechanisms. J. Mech. Des. **127**, 242 (2005)

12. Fattah, A., Agrawal, S., et al.: On the design of cable-suspended planar parallel robots. J. Mech. Des. **127**, 1021 (2005)

13. Verhoeven, R., Hiller, M.: Estimating the controllable workspace of tendon-based stewart platforms. Advances in Robot Kinematics, pp. 277–284. Kluwer Academic Publishers, Portoroz (2000).

14. Yoshikawa, T.: Analysis and control of robot manipulators with redundancy. In: Proceedings of the First International Symposium Robotics Research, pp. 735–747. MIT Press Cambridge, MA (1984).

15. Salisbury, J., Craig, J.: Articulated hands. Int. J. Rob. Res. **1**(1), 4–17 (1982)

16. Cardou, P., Bouchard, S., Gosselin, C.: Kinematic-sensitivity indices for dimensionally non-homogeneous jacobian matrices. IEEE Trans. Rob. **26**(1), 166–173 (2010)

17. Saadatzi, M., Tale Masouleh, M., Taghirad, H., Gosselin, C., Cardou, P.: On the optimum design of 3-RPR parallel mechanisms. In: Proceedings of the 19th Iranian Conference on, Electrical Engineering (ICEE'11), pp. 1–6 (2011).

18. Saadatzi, M., Masouleh, M., Taghirad, H., Gosselin, C., Cardou, P.: Geometric analysis of the kinematic sensitivity of planar parallel mechanisms. Trans. Can. Soc. Mech. Eng. **35**(4), 477 (2011)

19. Moore, R.: Interval Analysis, vol. 60. Prentice-Hall, Englewood Cliffs (1966)

20. Rump, S.: Intlab-interval laboratory. Citeseer (1998).

21. Hao, F., Merlet, J.: Multi-criteria optimal design of parallel manipulators based on interval analysis. Mech. Mach. Theory **40**(2), 157–171 (2005)

22. Merlet, J.: Interval analysis and robotics. Rob. Res. 147–156 (2011).

23. Merlet, J.: Solving the forward kinematics of a gough-type parallel manipulator with interval analysis. Int. J. Rob. Res. **23**(3), 221–235 (2004)

24. Oetomo, D., Daney, D., Shirinzadeh, B., Merlet, J.: Certified workspace analysis of 3RRR planar parallel flexure mechanism. In: Proceedings of the IEEE International Conference on Robotics and Automation (ICRA'08), pp. 3838–3843 (2008).

25. Moore, R., Kearfott, R., Cloud, M.: Introduction to interval analysis. Society for Industrial Mathematics, Philadelphia (2009)

26. Jaulin, L.: Applied Interval Analysis: with examples in parameter and state estimation, robust control and robotics, vol. 1. Springer Verlag, UK (2001)

27. Saadatzi, M., Tale Masouleh, M., Taghirad, H., Gosselin, C., Teshnehlab, M.: Multi-objective scale independent optimization of 3-rpr parallel mechanisms. In Proceedings of the IFToMM, In (2011)
28. Husty, M., Gosselin, C.: On the singularity surface of planar 3-rpr parallel mechanisms. Mech. Based Des. Struct. Mach. **36**(4), 411–425 (2008)
29. Loloei, A.Z., Taghirad, H.: Trans. Can. Soc. Mech, Eng (2012)

Solving the Direct Geometrico-Static Problem of 3-3 Cable-Driven Parallel Robots by Interval Analysis: Preliminary Results

Alessandro Berti, Jean-Pierre Merlet and Marco Carricato

Abstract This paper studies the direct geometrico-static analysis of under-constrained cable-driven parallel robots with 3 cables. The task consists in finding all equilibrium configurations of the end-effector when the cable lengths are assigned. An interval-analysis-based procedure is proposed to numerically find the real solutions of the problem for a robot of generic geometry. Three equation sets obtained by different approaches are implemented in the problem-solving algorithm and a comparison between the main merits and drawbacks of each one of them is reported.

1 Introduction

Cable-driven parallel robots (CDPRs) employ cables in place of rigid-body extensible legs in order to control the end-effector pose. CDPRs strengthen classic advantages characterizing closed-chain architectures versus serial ones, like reduced mass and inertia, a larger payload to robot weight ratio, high dynamic performances, etc., while providing peculiar advantages, such as a larger workspace, reduced manufacturing and maintenance costs, ease of assembly and disassembly, high transportability, and superior modularity and reconfigurability.

A. Berti (✉) · M. Carricato
Department of Mechanical Engineering (DIEM), University of Bologna, Bologna, Italy
e-mail: alessandro.berti10@unibo.it

M. Carricato
e-mail: marco.carricato@unibo.it

J.-P. Merlet
COPRIN Project, French National Institute for Research in Computer Science
and Control (INRIA), Sophia-Antipolis, France
e-mail: jean-pierre.merlet@sophia.inria.fr

A CDPR is *fully-constrained* if the pose of the end-effector is completely determined when actuators are locked and, thus, all cable lengths are assigned. A CDPR is, instead, *under-constrained* if the end-effector preserves some degrees of freedom (dofs) once actuators are locked [2, 16]. This occurs either when the end-effector is controlled by a number of cables n smaller than the number of dofs that it possesses with respect to the base or when some cables become slack in a fully-constrained robot. The use of CDPRs with a limited number of cables is justified in several applications (such as, for instance, rescue, service or rehabilitation operations [14, 18, 19]), in which the task to be performed requires a limited number of controlled freedoms (only n dofs may be governed by n cables) or a limitation of dexterity is acceptable in order to decrease complexity, cost, set-up time, likelihood of cable interference, etc. Furthermore, a theoretically fully-constrained CDPR may operate, in appreciable parts of its geometric workspace, as an under-constrained robot, namely when a full restraint of the end-effector may not be achieved because it would require a negative tension in one or more cables. Even though the above considerations motivate a careful study of under-constrained CDPRs, little research was conducted on them [1–7, 10, 15, 21].

A major challenge in the kinetostatic analysis of under-constrained CDPRs comes from the fact that, when the cable lengths are assigned, the end-effector is still movable, so that the actual configuration is determined by the applied forces. Accordingly, *loop-closure* and *mechanical-equilibrium equations* must be simultaneously solved and displacement analyses, which are aimed at determining the overall robot configuration when a set of n variables is assigned, become *geometrico-static problems* [2]. These are considerably more complex than displacement analyses of rigid-link parallel manipulators [11].

Only recently Carricato and Merlet [2] proposed a general methodology for the kinematic, static and stability analysis of general under-constrained *n-n* CDPRs, i.e. manipulators in which a fixed base and a mobile platform are connected to each other by n cables, with $n \leq 5$ and with cable exit points on the base and anchor points on the platform being distinct. A successful implementation of this methodology, based on exact-arithmetic elimination procedures, allowed the direct geometrico-static problem (DGP) of the 3-3 CDPR to be solved [3]. A least-degree univariate polynomial in the ideal generated by the equations governing the problem was found and the DGP of the 3-3 CDPR was proven to admit at the most 156 solutions in the complex field. However, the approach used in [3] has the following drawbacks.

- Elimination by exact-arithmetic-based procedures requires equations with rational coefficients. However, when geometrical parameters are approximated by rationals having large integer denominators and numerators, the size of the coefficients may become extremely large and very difficult to manage. In addition, solving high-order polynomials in a reliable way may be difficult, as the calculation of coefficients is very sensitive to numerical errors.
- It is not possible to incorporate constraints on the unknowns, so that all roots (both complex and real, regardless of the tension sign) must be calculated and then post-processed in order to discard unfeasible ones.

Effective alternatives are provided by approaches based on floating-point arithmetic, such as homotopy continuation or interval analysis. In this paper, a method based on interval analysis is proposed. This computing technique was shown to be very efficient in solving the direct kinematics of rigid-link parallel robots [12], but its efficiency is strictly related to the heuristics incorporated in the problem-solving algorithm. The computation time for a given problem may vary from a few seconds, if the right heuristics are adopted, to several hours with a poor implementation.

This paper is organized as follows. Section 2 provides basic notions of interval analysis. Section 3 presents the geometrico-static model of the 3-3 CDPR and it discusses three different formulations of the equations governing the DGP. Section 4 describes the structure of the code and the procedures incorporated therein. Section 5 presents the results obtained from case studies. Section 6 draws some conclusions.

2 Interval Analysis

A short introduction to interval analysis is presented in the following. More informations may be found in [9, 17].

The *real interval* $X = [\underline{x}, \overline{x}]$ is defined as the set of real numbers y such that $\underline{x} \leq y \leq \overline{x}$. The *width* of the interval is $\overline{x} - \underline{x}$ and its *mid-point* is $(\overline{x} + \underline{x})/2$. An *interval vector* $\mathbf{X}$, also called a *box*, is a list of intervals. The mid-point of a box is the vector whose components are the mid-points of its interval components.

If $f(\mathbf{x})$ is a function in n unknowns, with $\mathbf{x} = [x_1, x_2, \ldots, x_n]$, and $\mathbf{B} = [X_1, X_2, \ldots, X_n]$ is a box comprising an interval for each unknown, an interval evaluation $F(\mathbf{B})$ of f over $\mathbf{B}$ is an interval $[\underline{F}, \overline{F}]$ such that, for any $\mathbf{x} \in \mathbf{B}$, $\underline{F} \leq f(\mathbf{x}) \leq \overline{F}$. There are many ways to implement an interval evaluation of a function but the simplest one is the *natural evaluation*, in which each arithmetic operation and elementary mathematical function is substituted by an interval equivalent. For example, if $f(x) = x^2 - 2x + 1$ and $X = [4, 5]$, the natural evaluation of f over X is:

$$f([4, 5]) = [4, 5]^2 - 2[4, 5] + 1 = [16, 25] - [8, 10] + [1, 1] = [7, 18] \quad (1)$$

It is worth emphasizing that the bounds provided by the natural evaluation of f are not exact: the upper (lower) bound may be larger (lower) than the actual maximum (minimum) of the function image, namely $f(\mathbf{B}) = \{f(\mathbf{x})|x \in \mathbf{B}\} \subseteq F(\mathbf{B})$. Ordinarily, the overestimation decreases with the width of the box over which f is evaluated, and there are cases and methods that allow one to get bounds as tight as possible.

The following properties hold:

- if $0 \notin [\underline{F}, \overline{F}]$, then there is no value of $\mathbf{x}$ such that $f(\mathbf{x}) = 0$ (Property A);

- the bounds of F are exactly the minimum and the maximum of $f(\mathbf{B})$ when f may be expressed so as to contain a single occurrence of each unknown x_i $(i = 1, \ldots, n)$ (Property B);
- interval evaluation may be implemented on a computer in a 'guaranteed' way, by taking into account numerical round-off errors;
- interval arithmetic is not restricted to algebraic functions, but it may be used for all mathematical functions of engineering relevance.

The structure of a generic interval-analysis-based algorithm to solve a system of n equations in n unknowns is as follows. Let $\mathbf{B}_1 = [X_1, X_2, \ldots, X_n]$ be a box and $\mathbf{f} = [f_1(\mathbf{x}), f_2(\mathbf{x}), \ldots, f_n(\mathbf{x})] = \mathbf{0}$ a vector equation to be solved within $\mathbf{B}_1$. $\mathcal{L}$ is a list of boxes, initially set as $\mathcal{L} = \{\mathbf{B}_1\}$. An index i, initialized to 1, indicates which box $\mathbf{B}_i$ in $\mathcal{L}$ is currently being processed, while N denotes the number of boxes in $\mathcal{L}$. $\mathcal{S}$ is another list, initially empty, storing the solutions. The interval evaluation of f_j over $\mathbf{B}_i$ is denoted as $F_j(\mathbf{B}_i)$, with $j = 1, \ldots, n$. A key component of the algorithm is the evaluation operator $\mathcal{E}$, which takes a box $\mathbf{B}_i$ as an input and it returns:

- 1, if both the width of $F_j(\mathbf{B}_i)$ is smaller than a given threshold ε and $F_j(\mathbf{B}_i)$ includes 0 for any j; in this case, $\mathbf{B}_i$ is deemed a solution and it is stored in $\mathcal{S}$;
- -1, if $F_j(\mathbf{B}_i)$ does not include 0 for at least one j;
- 0, otherwise.

Another key component is the filter operator $\mathcal{F}$, which takes a box as an input and it returns:

- -1, if there is no solution in the input box;
- a box smaller than the input one, if the filter determines that the removed part of the input box cannot contain a solution;
- the input box, otherwise.

The overall algorithm proceeds along the following steps:

1: $i = 1$, $\mathcal{L} = \{\mathbf{B}_1\}$, $\mathcal{S} = \{\}$, $N = 1$;
2: if $i > N$, then return $\mathcal{S}$;
3: if $\mathcal{F}(\mathbf{B}_i) = -1$, then $i = i + 1$, go to 2, else $\mathbf{B}_i = \mathcal{F}(\mathbf{B}_i)$;
4: compute $\mathcal{E}(\mathbf{B}_i)$

    a) if $\mathcal{E}(\mathbf{B}_i) = -1$, then $i = i + 1$, go to 2;
    b) if $\mathcal{E}(\mathbf{B}_i) = 1$, then add $\mathbf{B}_i$ to $\mathcal{S}$, $i = i + 1$, go to 2;
    c) if $\mathcal{E}(\mathbf{B}_i) = 0$, select a variable x_k and bisect X_k in the middle point, create two new boxes $\mathbf{B}_i'$ and $\mathbf{B}_i''$ from $\mathbf{B}_i$, replace $\mathbf{B}_i$ with $\{\mathbf{B}_i', \mathbf{B}_i''\}$ in $\mathcal{L}$, $N = N+1$, $i = i + 1$, go to 2.

The above algorithm always terminates, since the size of a box always decreases after a bisection. Provided that the new boxes emerging from a bisection are put at the top of the list, there is usually no problem of memory storage. The efficiency of the algorithm mainly depends on the effectiveness of the operators $\mathcal{E}$ and $\mathcal{F}$, and thus on the heuristics adopted to implement them. In Sect. 4, some important tools of interval analysis are presented, which drastically reduce the computation time.
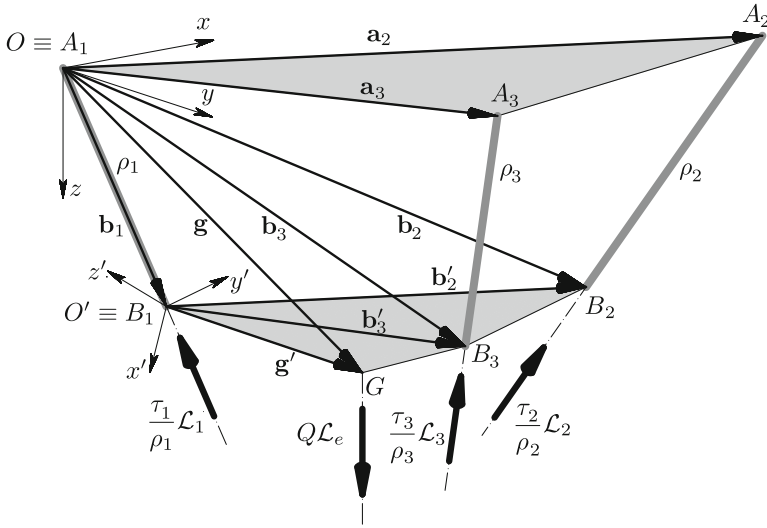
Fig. 1 Geometric model of a cable driven parallel robot with three cables

3 Geometrico-Static Model

A mobile platform is connected to a fixed base by 3 cables. The ith cable ($i = 1, 2, 3$) exits from the base at point A_i and it is connected to the platform at point B_i (Fig. 1). The platform is acted upon by a force of constant magnitude Q applied at point G, e.g. the platform weight acting through its center of mass. This force is described as a 0-pitch wrench $Q\mathcal{L}_e$, where $\mathcal{L}_e$ is the normalized Plücker vector of its line of action.

$Oxyz$ is a Cartesian coordinate frame attached to the base in O, whereas $O'x'y'z'$ is a Cartesian frame appended to the moving platform in O'. Without loss of generality, the coordinate frames are chosen in such a way that $O \equiv A_1$, $O' \equiv B_1$, the z axis is directed as $\mathcal{L}_e$, point A_2 lies in plane xz and point B_2 lies in plane $x'z'$. By this choice, the position vectors of points A_1, A_2, A_3, B_1, B_2, B_3 and G in $Oxyz$ and of points B_1, B_2, B_3 and G in $O'x'y'z'$ may be respectively expressed as

$$
\begin{aligned}
&\mathbf{a}_1 = [0, 0, 0]^T, \quad \mathbf{a}_2 = [a_{2x}, 0, a_{2z}]^T, \quad \mathbf{a}_3 = [a_{3x}, a_{3y}, a_{3z}]^T, \\
&\mathbf{b}_1 = [x_1, y_1, z_1]^T, \quad \mathbf{b}_2 = [x_2, y_2, z_2]^T, \quad \mathbf{b}_3 = [x_3, y_3, z_3]^T, \quad \mathbf{g} = [g_x, g_y, g_z]^T, \\
&\mathbf{b}_1' = [0, 0, 0]^T, \quad \mathbf{b}_2' = [b_{2x}', 0, b_{2z}']^T, \quad \mathbf{b}_3' = [b_{3x}', b_{3y}', b_{3z}']^T, \quad \mathbf{g}' = [g_x', g_y', g_z']^T,
\end{aligned}
\tag{2}
$$

with a_{ij}, b_{ij}' and g_j' ($i = 1, 2, 3; j = x, y, z$) being known geometric parameters and x_i, y_i, z_i ($i = 1, 2, 3$) and g_j ($j = x, y, z$) being variables describing the platform pose.

3.1 Fundamental Geometric and Static Equations

If ρ_i is the assigned length of the ith cable (taken as strictly positive), when *all* cables are *active* (i.e. in tension) the set of geometrical constraints imposed on the platform comprises 3 relations, namely

$$\|\mathbf{b}_i - \mathbf{a}_i\|^2 = \rho_i^2, \quad i = 1, 2, 3. \tag{3}$$

Since the platform has 6 dofs, its pose is ultimately determined by mechanical equilibrium. The normalized Plücker vector of the line associated with the ith cable is $\mathcal{L}_i/\rho_i$, where, in axis coordinates, $\mathcal{L}_i = [(\mathbf{a}_i - \mathbf{b}_i); \mathbf{p}_i \times (\mathbf{a}_i - \mathbf{b}_i)]$ and $\mathbf{p}_i$ is any vector from an arbitrarily-chosen reference point P (called, for brevity, *moment pole*) to the cable line. Accordingly, the wrench exerted by the ith cable on the platform is $(\tau_i/\rho_i)\mathcal{L}_i$, with τ_i being a positive scalar representing the intensity of the cable tensile force. Static equilibrium may then be expressed as

$$\underbrace{[\mathcal{L}_1 \; \mathcal{L}_2 \; \mathcal{L}_3 \; \mathcal{L}_e]}_{\mathbf{M}(P)} \begin{bmatrix} \tau_1/\rho_1 \\ \tau_2/\rho_2 \\ \tau_3/\rho_3 \\ Q \end{bmatrix} = \mathbf{0}, \tag{4}$$

with $\tau_i \geq 0$, $i = 1, 2, 3$.

When a direct geometrico-static problem (DGP) is solved, the cable lengths are assigned. Accordingly, Eqs. (3) and (4) form a coupled system of 9 relations whose unknowns are the platform-pose variables, grouped in the array $\mathbf{X}$, and the cable tensions, grouped in the array $\boldsymbol{\tau}$. The efficiency of the interval-analysis-based problem-solving algorithm is strictly related to the complexity of these relations. In particular, the occurrences of the same variable in each equation should be limited as much as possible (Property B). In this perspective, the most suitable choice of the *parameterization of the platform pose* and of the *formulation of the static constraints* is extremely important. These issues are discussed in the following sections.

3.2 Parameterization of the Platform Pose

The platform pose $\mathbf{X}$ is described by 9 variables, namely the components of the position vectors $\mathbf{b}_1$, $\mathbf{b}_2$ and $\mathbf{b}_3$ in the $Oxyz$ frame (Fig. 1). These variables are not independent, but they must satisfy the following geometrical constraints:

$$
\begin{aligned}
(x_2 - x_1)^2 + (y_2 - y_1)^2 + (z_2 - z_1)^2 - \|\mathbf{b}_2'\|^2 &= 0 \\
(x_3 - x_1)^2 + (y_3 - y_1)^2 + (z_3 - z_1)^2 - \|\mathbf{b}_3'\|^2 &= 0 \\
(x_3 - x_2)^2 + (y_3 - y_2)^2 + (z_3 - z_2)^2 - \|\mathbf{b}_3' - \mathbf{b}_2'\|^2 &= 0 \; .
\end{aligned}
\tag{5}
$$

By this parameterization, the relationships in Eq. (3) assume the form

$$x_1^2 + y_1^2 + z_1^2 - \rho_1^2 = 0$$
$$(x_2 - a_{2x})^2 + y_2^2 + (z_2 - a_{2z})^2 - \rho_2^2 = 0 \qquad (6)$$
$$(x_3 - a_{3x})^2 + \left(y_3 - a_{3y}\right)^2 + (z_3 - a_{3z})^2 - \rho_3^2 = 0$$

and the position vector of G in $Oxyz$ may be expressed as

$$\mathbf{g} = \mathbf{b}_1 + \alpha(\mathbf{b}_2 - \mathbf{b}_1) + \beta(\mathbf{b}_3 - \mathbf{b}_1) + \gamma[(\mathbf{b}_2 - \mathbf{b}_1) \times (\mathbf{b}_3 - \mathbf{b}_1)] , \qquad (7)$$

where α, β and γ are known constants obtained by solving the system

$$\alpha \, \mathbf{b}_2' + \beta \, \mathbf{b}_3' + \gamma \, (\mathbf{b}_2' \times \mathbf{b}_3') - \mathbf{g}' = \mathbf{0} . \qquad (8)$$

Accordingly, by choosing O as the moment pole, matrix $\mathbf{M}(P)$ in Eq. (4) may be explicitly written as

$$\mathbf{M}(O) = \begin{bmatrix} x_1 & x_2 - a_{2x} & x_3 - a_{3x} & 0 \\ y_1 & y_2 & y_3 - a_{3y} & 0 \\ z_1 & z_2 - a_{2z} & z_3 - a_{3z} & -1 \\ 0 & -a_{2z}y_2 & a_{3y}z_3 - a_{3z}y_3 & -g_y \\ 0 & a_{2z}x_2 - a_{2x}z_2 & a_{3z}x_3 - a_{3x}z_3 & g_x \\ 0 & a_{2x}y_2 & a_{3x}y_3 - a_{3y}x_3 & 0 \end{bmatrix} \qquad (9)$$

and static equations become

$$x_1 \frac{\tau_1}{\rho_1} + (x_2 - a_{2x}) \frac{\tau_2}{\rho_2} + (x_3 - a_{3x}) \frac{\tau_3}{\rho_3} = 0 \qquad (10a)$$

$$y_1 \frac{\tau_1}{\rho_1} + y_2 \frac{\tau_2}{\rho_2} + \left(y_3 - a_{3y}\right) \frac{\tau_3}{\rho_3} = 0 \qquad (10b)$$

$$z_1 \frac{\tau_1}{\rho_1} + (z_2 - a_{2z}) \frac{\tau_2}{\rho_2} + (z_3 - a_{3z}) \frac{\tau_3}{\rho_3} - Q = 0 \qquad (10c)$$

$$-a_{2z}y_2 \frac{\tau_2}{\rho_2} + \left(a_{3y}z_3 - a_{3z}y_3\right) \frac{\tau_3}{\rho_3} - Qg_y = 0 \qquad (10d)$$

$$(a_{2z}x_2 - a_{2x}z_2) \frac{\tau_2}{\rho_2} + (a_{3z}x_3 - a_{3x}z_3) \frac{\tau_3}{\rho_3} + Qg_x = 0 \qquad (10e)$$

$$a_{2x}y_2 \frac{\tau_2}{\rho_2} + \left(a_{3x}y_3 - a_{3y}x_3\right) \frac{\tau_3}{\rho_3} = 0 \qquad (10f)$$

Equations (5), (6) and (10) form a square system of 12 scalar relations in the 12 variables grouped in the array

$$\mathbf{Y} = [\mathbf{X}^T, \boldsymbol{\tau}^T]^T = [x_1, y_1, z_1, x_2, y_2, z_2, x_3, y_3, z_3, \tau_1, \tau_2, \tau_3]^T . \qquad (11)$$

The polynomial relations in Eqs. (5) and (6) have degree 2 in $\mathbf{X}$, whereas the relations in Eq. (10) have degree 2 in $\mathbf{X}$, degree 1 in $\boldsymbol{\tau}$ and total degree 2 in $\mathbf{Y}$.

The described parameterization of the platform pose, which uses 9 variables, is redundant, since a minimal representation is achieved by only 6 variables (cf. [3]). However, the redundant parameterization is preferred here, since it yields simpler lower-order polynomials, which prove to be stabler and more efficient when interval analysis methods are implemented to solve them. In fact, by property B (Sect. 2), using simpler expressions is valuable even at the price of introducing a larger number of variables, in order to limit overestimation in interval evaluation.

3.3 Formulation of the Static Constraints

The DGP requires simultaneously solving the relations emerging from both the geometrical and the static constraints. According to Sect. 3.2, these constraints may be set up as a system of 12 equations having $\mathbf{Y}$ as unknown, namely Eqs. (5), (6) and (10). These equations are implemented in the first solution routine (called *R1*).

The number of unknowns may be decreased by eliminating cable tensions. By observing that Eq. (10) is linear in τ_1, τ_2 and τ_3, 3 linearly independent relationships may be selected within the system, say (10a), (10d) and (10e), and solved for the tensions. The expressions this way calculated may be substituted back into Eqs. (10b), (10c), (10f), thus forming a system of 3 equations in $\mathbf{X}$ only, namely Eqs. (10b'), (10c') and (10f'). The system implemented in the second solution routine (*R2*) comprises these relationships, together with Eqs. (5) and (6). The resulting system comprises 9 equations in 9 unknowns (i.e. $\mathbf{X}$).

An alternative, more elaborated, strategy to eliminate cable tensions, presented in [3], may be designed by observing that Eq. (4) admits a solution only if

$$\text{rank}\,[\mathbf{M}(P)] \leq 3\,. \tag{12}$$

Hence, by setting all 4×4 minors of $\mathbf{M}(P)$ equal to zero and by conveniently changing the moment pole, a large set of linearly independent relations only comprising the platform-pose variables may be derived, i.e.

$$p_k\,(\mathbf{X}) = 0, \quad k = 1 \ldots N_p, \tag{13}$$

where N_p is an integer significantly larger than the number N_X of variables contained in $\mathbf{X}$. For the DGP to admit a solution, the above equations must be dependent, though in a non-linear way. When complemented with Eqs. (5) and (6), Eq. (13) allows the pose $\mathbf{X}$ to be directly solved. The price paid for the elimination of cable tensions is that the polynomials comprised in Eq. (13) are much more involved than those in

Eq. (10). In particular, they have a higher degree, more terms and more complicated coefficients. A partial simplification is obtained as follows [3].

Since the moment vector of the first column of $\mathbf{M}(O)$ is zero (Eq. 9), setting $\det \mathbf{M}_{j456,1234}(O) = 0$[1], for $j = 1\ldots 3$, yields

$$[x_1, y_1, z_1]^T \det \mathbf{M}_{456,234}(O) = (\mathbf{b}_1 - \mathbf{a}_1) \det \mathbf{M}_{456,234}(O) = \mathbf{0} . \qquad (14)$$

Since $(\mathbf{b}_1 - \mathbf{a}_1)$ may not vanish by assumption $(\rho_1 \neq 0)$, Eq. (14) provides

$$\det \mathbf{M}_{456,234}(O) = 0 . \qquad (15)$$

Two analogous equations may be obtained by conveniently changing the moment pole, namely

$$\det \mathbf{M}_{456,134}(A_2) = 0, \qquad (16)$$

$$\det \mathbf{M}_{456,124}(A_3) = 0. \qquad (17)$$

The system of equations implemented in the third solution routine (*R3*) is formed by Eqs. (5), (6) and (15)–(17).

Interval-analysis methods require each variable to be comprised between a lower and an upper bound. In the equation set implemented in *R1*, cable tensions appear as unknowns, so that lower and upper bounds for τ_1, τ_2 and τ_3 may be conveniently specified. In particular, the lower bound may be conveniently set equal to 0, to avoid solutions with negative cable tension. The upper bound may be chosen, instead, on the basis of the maximum tensile strength of the cables. Conversely, in the equation sets implemented in *R2* and *R3*, cable tensions do not appear as unknowns and they cannot be directly bounded. As a consequence, *R2* and *R3* find all solutions contained in a purely geometrical search domain and then they isolate those with properly-bounded cable tensions by a suitable test added in the filter operator $\mathcal{F}$.

4 The Problem-Solving Algorithm

The problem-solving code was developed by using the C++ library ALIAS [13], which contains interval-analysis-based algorithms developed by the INRIA team COPRIN.

---

[1] The notation $\mathbf{M}_{hij,klm}(O)$ denotes the block matrix obtained from rows h, i and j, and columns k, l and m, of $\mathbf{M}(O)$.

4.1 Code Structure

The structure outlined hereafter is common to all routines *R1*, *R2* and *R3* and it follows the scheme presented in Sect. 2.

The main procedure initially retrieves, from convenient text files, the geometric data of the manipulator, the search domain and the configuration parameters of the ALIAS functions incorporated into the code. The operations successively performed by the algorithm may be resumed as follows. At the generic ith step, a first filter $\mathcal{F}_1$, which implements the 2B method (described in Sect. 4.4.1), tries to shrink, or even eliminate, the current box $\mathbf{B}_i$. After that, the evaluation operator $\mathcal{E}$ tests if $\mathbf{B}_i$ may contain solutions or not. If the test is negative, the box is discarded. If the test is positive and the width of the box is smaller than a given threshold ε, $\mathbf{B}_i$ is deemed to be a solution and it is added to the solution list $\mathcal{S}$. If the test is positive, but the width of the box is larger than ε, another filter $\mathcal{F}_2$, which implements the 3B method (described in Sect. 4.4.2), is applied to further contract the box and then $\mathbf{B}_i$ is bisected. The adopted bisecting strategy consists in splitting the variable having the largest width.

4.2 Domain Initialization

The first step of the code consists in initializing the search domain. The starting intervals for the unknowns in $\mathbf{X}$ may be easily determined by observing that $\mathbf{b}_1$, $\mathbf{b}_2$ and $\mathbf{b}_3$ have to lie inside the spheres centered, respectively, in A_1, A_2 and A_3 and having radii ρ_1, ρ_2 and ρ_3. For *R1*, initial bounds for cable tensions may be established as explained in Sect. 3.3.

4.3 Evaluation Operator

The evaluation operator $\mathcal{E}$ is implemented by means of the ALIAS procedure `Solve_General_Gradient_Interval` (SGGI). If the Jacobian matrix of the system to be solved exists and it may be computed, SGGI improves interval evaluation of functions by conveniently using gradients and by taking advantage of possible monotonicities [9]. SGGI also uses Moore theorem [17] to determine if a unique solution exists in a given box, in which case Krawczyk method is applied to compute the solution [13]. In addition, the *inflation method* [13] is used to increase the width of the box in which the computed solution remains unique, thus working as a filter for neighboring boxes.

4.4 Filtering Operators

The performances of the algorithm largely depend on the filter operators $\mathcal{F}_1$ and $\mathcal{F}_2$. Their basic operation is described hereafter.

4.4.1 Filter $\mathcal{F}_1$: the 2B Method

The 2B filter consists in rewriting each equation as the equality of two terms, thus determining if the interval evaluations of both terms are consistent and, if not, using consistency to improve the width of the interval for one or more unknowns.

Let, for instance, the equation $x^2 - 2x + 1 = 0$ be considered. By introducing the new variable $X = x^2$, the original equation may be re-written as $X = 2x - 1$. Now, let $\left[\underline{u}, \overline{u}\right]$ be the interval evaluation of $2x - 1$. If $\overline{u} > 0$, then the inverse function of X indicates that x should lie in $\left[-\sqrt{\overline{u}}, \sqrt{\overline{u}}\right]$ and, by this information, the current interval of x may be updated. If $\underline{u} > 0$, the inverse function of X shows that x should lie outside $\left[-\sqrt{\underline{u}}, \sqrt{\underline{u}}\right]$: if the range of x is included in this interval, then there is no solution to the equation in the current box.

This process may be repeated for each unknown in the equation and for a number of runs depending on the rate of contraction obtained for each interval.

4.4.2 Filter $\mathcal{F}_2$: the 3B Method

By this approach, the range $X_j = \left[\underline{x}_j, \overline{x}_j\right]$ for one variable x_j in a given box $\mathbf{B}_i$ is replaced by $\left[\underline{x}_j, \underline{x}_j + \delta\right]$, where δ is an arbitrary small number, while the ranges for the other variables remain unchanged. Then, the algorithm tests whether, for the new ranges, the system may have some solution, either by using the 2B method and/or by evaluating the equations. If the answer is negative, the range for x_j in the box $\mathbf{B}_i$ is changed to $\left[\underline{x}_j + \delta, \overline{x}_j\right]$. The process is then repeated on the new range, but the width of the test interval is now doubled, i.e. the algorithm tests the interval $\left[\underline{x}_j, \underline{x}_j + 2\delta\right]$. The process is repeated until the no-solution test is no longer satisfied. Within the 3B filter, the 2B method may also be applied to update the range for all unknowns.

The same process may be repeated on the right side of the interval, by trying to decrease the upper bound of X_j (in this case, the interval test is $\left[\overline{x}_j - \delta, \overline{x}_j\right]$).

4.5 Parallel Implementation

Most interval-analysis-based algorithms are appropriate for a distributed implementation. Indeed, processing a given box does not generally depend on the processing

of the other boxes in the list. The implementation may be as follows. A master computer manages the list and it sends a box to a slave computer. The slave executes the algorithm, by performing a few bisections. Then, it returns the remaining boxes to the master and it waits for a new box to process. Such a scheme may be easily implemented in a network of workstations. The decrease of computation time will be, in general, less than proportional to the number of slaves, due to the overhead of the data transmission between the master and the slaves.

This approach may also take advantage of modern multi-core CPU architectures. By following this scheme and by using POSIX thread libraries, a distributed implementation of the DGP code was prepared and used on a single workstation with a multi-core CPU. In the first step, an instance of $\mathcal{E}$ generates a few boxes and it stores them in the list $\mathcal{L}$. Then, a number of threads equal to the number of CPUs is created, with each one taking a box from $\mathcal{L}$. A local instance of $\mathcal{E}$ performs an assigned number of bisections and it appends the generated boxes to $\mathcal{L}$. The solutions found, if any, are appended to the solution list $\mathcal{S}$. Even though implementing this algorithm on a single machine is not as effective as a distributed implementation over a computer network, the results are quite good. In the following, the routines incorporating the parallel-computing scheme are denoted by an asterisk (*).

4.6 Routine Configuration

The main configuration parameters of each routine are reported hereafter.
R1:

- The equations to be solved are Eqs. (5), (6) and (10a)–(10f).
- The 2B filter is applied to Eqs. (5), (6), (10a)–(10c) and (10f).
- The 3B filter is applied to all equations of the system.
- Positive-tension configurations are found by suitably configuring the initial search domain.

R2:

- The equations to be solved are Eqs. (5), (6) and Eqs. (10b$'$), (10c$'$) and (10f$'$).
- The 2B filter is applied to Eqs. (5), (6) and (10b$'$). Applying the 2B filter to the other equations appears to be inconvenient in terms of computation time.
- The 3B filter is applied only to Eqs. (5) and (6), since Eqs. (10b$'$), (10c$'$) and (10f$'$) are too complex and they would excessively raise the computational burden.
- Positive-tension configurations are obtained by introducing, in filter $\mathcal{F}_1$, a simplification procedure that calculates tensions from Eqs. (10a), (10d) and (10e) and discards the boxes in which positive tensions do not appear.

R3:

- The equations to be solved are Eqs. (5), (6) and (15)–(17).
- The 2B filter is applied to Eqs. (5), (6) and (15).

Table 1 Geometric parameters, search domain and solutions for Example 1

Data	$\mathbf{a}_2 = [10, 0, 0]^T$ $\mathbf{a}_3 = [0, 12, 0]^T$ $(\rho_1, \rho_2, \rho_3) = [7.5, 10.0, 9.5]Q = 1$										
	$\mathbf{b}_2' = [1.41, 0, 0]^T$ $\mathbf{b}_3' = [0.71, 0.71, 1]^T$ $\mathbf{g}' = [0.71, 0.71, 0]^T$										
Search domain	x_1	y_1	z_1	x_2	y_2	z_2	x_3	y_3	z_3	τ_1	τ_2	τ_3
	-7.5	-7.5	-7.5	0	-10	-10	-9.5	2.5	-9.5	0	0	0
	7.5	7.5	7.5	20	10	10	9.5	21.5	9.5	2	2	2
Results	x_1	y_1	z_1	x_2	y_2	z_2	x_3	y_3	z_3	τ_1	τ_2	τ_3
	1.682	3.674	6.318	2.800	4.126	5.580	1.933	5.060	6.193	0.546	0.326	0.550
	1.379	4.481	5.854	2.623	3.904	5.507	1.535	3.834	4.606	0.684	0.305	0.614
	2.787	4.995	4.851	3.511	6.151	4.478	4.200	4.959	4.800	0.289	0.787	0.912
	3.515	4.063	5.233	2.475	3.244	5.732	2.260	4.630	5.553	0.526	0.511	0.581
	3.603	5.329	3.857	2.233	4.976	3.863	3.224	3.968	3.916	0.590	0.783	0.956
	1.344	3.471	6.511	2.397	3.329	5.578	1.359	4.259	5.337	0.676	0.251	0.486

- The 3B filter is applied to Eqs. (5) and (6).
- Positive-tension configurations are obtained as in *R2*.

5 Discussion of Results

5.1 Performances and Possible Improvements

Extensive numerical investigation was performed to test the efficiency and robustness of the code, as well as to show the performances of the different routines that were implemented. Two meaningful examples are reported in Sect. 5.2.

R1 is the only routine that offers the possibility to specify cable-tension bounds in the initial search domain. It is particularly stable, even though not particularly fast. *R2* is usually faster than *R1*, mainly because of the reduced number of unknowns incorporated in the static-equation formalization. However, the system of equations on which *R2* relies often become 'nearly' singular and this produces very high computation times, making this routine unreliable. Choosing different sets of relationships in Eqs. (10) to calculate cable tensions does not seem to improve the routine performances. *R3* is stable and reliable. For ordinary robot geometries, such that the base is larger than the platform and cable lengths position the platform well within the workspace, *R3* is usually faster than *R1*, whereas when the base and the platform have similar dimensions *R1* is more efficient than *R3*.

A number of possible improvements may be conceived in order to enhance the efficiency of the code. In particular, the evaluation operator $\mathcal{E}$ may be improved by using Kantorovitch theorem [20] instead of Moore's one, to verify if a single solution exists in a given box. Kantorovitch theorem should speed up computation, especially for simple equations such as those implemented in *R1*. Furthermore, the 2B filter $\mathcal{F}_1$ may be enhanced by introducing additional tests based on larger sets of relations

Table 2 Geometric parameters, search domain and solutions for Example 2

| Data | | $\mathbf{a}_2 = [10, 0, 0]^T$ $\mathbf{a}_3 = [0, 12, 0]^T$ $(\rho_1, \rho_2, \rho_3) = [7.5, 10.0, 9.5]$ $Q = 1$ | | | | | | | | | | |
| | | $\mathbf{b}_2' = [9.90, 0, 0]^T \mathbf{b}_3' = [4.98, 4.98, 7]^T$ $\mathbf{g}' = [4.98, 4.98, 0]^T$ | | | | | | | | | | |

Search domain	x_1	y_1	z_1	x_2	y_2	z_2	x_3	y_3	z_3	τ_1	τ_2	τ_3
	−7.5	−7.5	−7.5	0	−10	−10	−9.5	2.5	−9.5	0	0	0
	7.5	7.5	7.5	20	10	10	9.5	21.5	9.5	2	2	2
Results	x_1	y_1	z_1	x_2	y_2	z_2	x_3	y_3	z_3	τ_1	τ_2	τ_3
	5.537	4.500	0.771	3.925	−1.862	7.722	−1.787	6.214	7.320	0.682	0.660	0.545
	3.131	−1.218	6.705	1.220	4.679	−1.013	4.909	8.500	7.341	0.766	0.655	0.494
	−1.423	1.949	7.101	7.949	4.796	8.532	4.475	3.646	−0.666	0.581	0.567	0.481
	−0.760	0.132	7.460	8.658	2.254	9.645	1.979	9.527	8.957	0.226	0.427	0.385
	−3.982	6.248	1.166	5.434	8.889	−0.368	1.724	8.892	8.810	0.140	0.261	1.065

Table 3 Computation times for Example 1

Routine	*R1*	*R2*	*R3*	*R1**	*R2**	*R3**
Example 1	202	97	101	136	66	72

Table 4 Computation times for Example 2

Routine	*R1*	*R2*	*R3*	*R1**	*R2**	*R3**
Example 2	21	–	63	15	–	47

chosen from the minors of matrix **M** (cf. Eq. 9). Indeed, when dealing with interval analysis, additional equations may allow lower computation times to be attained, as they enrich the set of available tests that may be used to exclude portions of the domain from the solution search. Another possible improvement may be obtained by using Rohn extremal test [8] in order to check if **M** is rank-deficient or not. This variants will be implemented in an upgraded version of the code. This will also be able to filter stable equilibrium configurations among the admissible ones (cf. [2]).

5.2 Examples

The results reported in the following examples were obtained by a personal computer Toshiba® with processor Intel® Core i7 CPU M620, 2.67 GHz, equipped with 2 cores and 4 threads. All lengths are expressed in meters and the load applied on the platform is in newtons. For both examples, the threshold ε defined in Sect. 4.1 is set equal to 0.001, whereas the parameter δ of the 3B filter discussed in Sect. 4.4.2 is set equal to 0.01. The geometric parameters, the search domains and the solutions found are reported in Tables 1 and 2, whereas Tables 3 and 4 list the computation times (in seconds) required by the tested routines. In Example 1, drawn from [3] the base is considerably larger than the platform, as it is likely to occur in practice, whereas in Example 2 the dimensions of the two links are almost the same, so that (at the equilibrium) the cables are almost parallel. Although the latter example has little practical interest, it emphasizes that, when the system of equations adopted in *R2* approaches a singularity, computation time increases exponentially. Equilibrium configurations found for Example 1 are shown in Fig. 2.

6 Conclusions

This paper applied interval-analysis methods to solve the direct geometrico-static problem of cable-driven parallel robots with 3 cables. The task consists in finding all equilibrium configurations of the end-effector when the cable lengths are assigned. The problem is challenging, since loop-closure and equilibrium equations must be solved simultaneously.
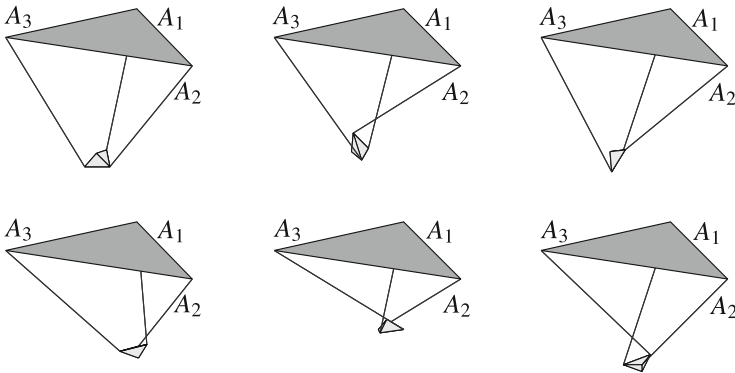
Fig. 2 Solutions of Example 1

The algorithm searches for all real solutions within a predetermined domain, whose frontier is computed so as to ensure that all possible solutions are enclosed within. The domain is subdivided into regions. An evaluation operator verifies if a region contains a solution, whereas some filter operators exclude portions which cannot contain roots. Regions whose assessment is uncertain are bisected and further assessed. The code is able to discard solutions in which one or more cables are subject to negative tensile forces.

Interval analysis requires great experience to be implemented with success and choosing the right heuristics has a dramatic impact on the effectiveness of this tool. The evaluation operator adopted in the current version performs a sharper interval evaluation of functions by using gradients and by taking into account possible monotonicities. The filter operators are based on the 2B and 3B consistency methods, which significantly reduce the number of boxes processed and, thus, the computation time. Interval analysis has a structure that is appropriate for parallel implementation. Accordingly, a distributed version of the algorithm was presented that takes advantage of modern multi-core CPUs. Finally, three equation sets emerging from different formalizations of the static equilibrium were implemented and a comparison between their main advantages and disadvantages was reported.

The results obtained by the numerical experimentation conducted so far are promising. The code is robust and reliable, and it is able to find all solutions of the problem for a generic geometry within a few minutes. The code has wide margins of improvement, by enhancing the implemented heuristics. In this perspective, a number of refinements were identified that should significantly enhance the computation efficiency and that will be implemented in an upgraded version of the code.

References

1. Abbasnejad, G., Carricato, M.: Real solutions of the direct geometrico-static problem of under-constrained cable-driven parallel robots with 3 cables: a numerical investigation. Meccanica (2012). doi:10.1007/s11012-012-9552-3
2. Carricato, M., Merlet, J.P.: Geometrico-static analysis of under-constrained cable-driven parallel robots. In: Lenarčič, J., Stanišić, M.M. (eds.) Advances in Robot Kinematics: Motion in Man and Machine, pp. 309–319. Springer, Dordrecht (2010)
3. Carricato, M., Merlet, J.P.: Direct geometrico-static problem of under-constrained cable-driven parallel robots with three cables. In: Proceedings of the 2011 IEEE International Conference on Robotics and Automation, pp. 3011–3017. Shanghai, China (2011)
4. Carricato, M., Merlet, J.P.: Inverse geometrico-static problem of under-constrained cable-driven parallel robots with three cables. In: Proceedings of the 13th World Congress in Mechanism and Machine Science, pp. 1–10, Paper No. A7-283. Guanajuato, Mexico (2011)
5. Collard, J.F., Cardou, P.: Computing the lowest equilibrium pose of a cable-suspended rigid body. Optim. Eng. (2012). doi:10.1007/s11081-012-9191-5
6. Fattah, A., Agrawal, S.K.: On the design of cable-suspended planar parallel robots. ASME J. Mech. Des. **127**(5), 1021–1028 (2006)
7. Heyden, T., Woernle, C.: Dynamics and flatness-based control of a kinematically undetermined cable suspension manipulator. Multibody Syst. Dyn. **16**(2), 155–177 (2006)
8. Jansson, C., Rohn, J.: An algorithm for checking regularity of interval matrices. SIAM J. Matrix Anal. Appl. **20**(3), 756–776 (1999)
9. Jaulin, L.: Applied Interval Analysis: with Examples in Parameter and State Estimation, Robust Control and Robotics, vol. 1. Springer, Berlin (2001)
10. Jiang, Q., Kumar, V.: The direct kinematics of objects suspended from cables. In: Proceedings of the ASME 2010 International Design Engineering Technical Conferences, vol. 2A, pp. 193–202, Paper no. DETC2010-28036. Montreal, Canada (2010)
11. McCarthy, J.M.: 21st century kinematics: synthesis, compliance, and tensegrity. ASME J. Mech. Robot. **3**(2), 020201/1–020201/3 (2011)
12. Merlet, J.P.: Solving the forward kinematics of a Gough-Type parallel manipulator with interval analysis. Int. J. Robot. Res. **23**(3), 221–235 (2004)
13. Merlet, J.P.: ALIAS-C++. http://www-sop.inria.fr/coprin/logiciels/ALIAS/ALIAS-C++/ALIAS-C++.html (2007)
14. Merlet, J.P., Daney, D.: A portable, modular parallel wire crane for rescue operations. In: Proceedings of the 2010 IEEE International Conference on Robotics and Automation, pp. 2834–2839. Anchorage, USA (2010)
15. Michael, N., Kim, S., Fink, J., Kumar, V.: Kinematics and statics of cooperative multi-robot aerial manipulation with cables. In: Proceedings of the ASME 2009 International Design Engineering Technical Conferences, vol. 7A, pp. 83–91, paper no. DETC2009-87677. San Diego, USA (2009)
16. Ming, A., Higuchi, T.: Study on multiple degree-of-freedom positioning mechanism using wires—Part 1: concept, design and control. Int. J. Japan Soc. Precis. Eng. **28**(2), 131–138 (1994)
17. Moore, R., Bierbaum, F.: Methods and Applications of Interval Analysis, vol. 2. Society for Industrial Mathematics (1979)
18. Rosati, G., Gallina, P., Masiero, S.: Design, implementation and clinical tests of a wire-based robot for neurorehabilitation. IEEE Trans. Neural Syst. Rehabi. Eng. **15**(4), 560–569 (2007)
19. Surdilovic, D., Zhang, J., Bernhardt, R.: STRING-MAN: wire-robot technology for safe, flexible and human-friendly gait rehabilitation. In: Proceedings of the 2007 IEEE International Conference on Rehabilitation Robotics, pp. 446–453. Noordwijk, The Netherlands (2007)
20. Tapia, R.: The Kantorovitch theorem for Newton's method. Am. Math. Monthly **78**(1.ea), 389–392 (1971)

21. Yamamoto, M., Yanai, N., Mohri, A.: Trajectory control of incompletely restrained parallel-wire-suspended mechanism based on inverse dynamics. IEEE Trans. Robot. **20**(5), 840–850 (2004)

Direct Geometrico-Static Analysis of Under-Constrained Cable-Driven Parallel Robots with 4 Cables

Marco Carricato and Ghasem Abbasnejad

Abstract This paper studies the direct geometrico-static problem of under-constrained parallel robots suspended by 4 cables. The task consists in determining the end-effector pose and the cable tensions when the cable lengths are assigned. The problem is challenging, because kinematics and statics are coupled and they must be solved simultaneously. An effective elimination procedure is presented that provides the complete solution set, thus proving that, when all cables are in tension, 216 potential solutions exists in the complex field. A least-degree univariate polynomial free of spurious factors is obtained in the ideal governing the problem and solutions are numerically computed via both an eigenvalue formulation and homotopy continuation. Equilibrium configurations with slack cables are also considered.

1 Introduction

Cable-driven parallel robots (CDPRs) employ cables in place of rigid-body extensible legs in order to control the end-effector pose. A CDPR is *fully-constrained* if the end-effector pose is completely determined when actuators are locked and, thus, all cable lengths are assigned. Conversely, a CDPR is *under-constrained* if the end-effector preserves some freedoms once actuators are locked. This occurs either when the end-effector is controlled by a number of cables smaller than the number of degrees of freedom (dofs) that it possesses with respect to the base or when some cables become slack in a fully-constrained robot [9]. The use of CDPRs with a limited number of

---

M. Carricato (✉)· G. Abbasnejad
Department of Mechanical Engineering (DIEM) and
Center for Health Sciences and Technologies (CIRI HST),
University of Bologna, Bologna, Italy
e-mail: marco.carricato@unibo.it

G. Abbasnejad
e-mail: ghasem.abbasnejad2@unibo.it

cables is justified in several applications, in which the task to be performed requires
a limited number of controlled freedoms (only n dofs may be governed by n cables)
or a limitation of dexterity is acceptable in order to decrease complexity, cost, set-up
time, likelihood of cable interference, etc. While a rich literature exists for fully-
constrained CDPRs (see, for instance, [2, 4, 6, 7, 9, 10, 16, 20, 21, 23, 25, 26, 33,
34, 36, 38, 39], little research was conducted on under-constrained robots [1, 11,
12, 18, 22, 24, 30, 41].

A major challenge in the kinetostatic analysis of under-constrained CDPRs con-
sists in the intrinsic coupling between kinematics and statics [31]. Indeed, while in
a fully-constrained CDPR the pose of the end-effector is exclusively determined by
the geometrical constraints imposed by cable lengths, in an under-constrained robot,
when the actuators are locked and the cable lengths are assigned, the end-effector is
still movable, so that the actual pose is determined by the applied forces. Accordingly,
loop-closure and *mechanical-equilibrium equations* must be simultaneously solved
and displacement analyses become *geometrico-static problems* [9]. These are signif-
icantly more complex than displacement analyses of fully-constrained manipulators
and their solution is a pending challenge in current kinematics [27].

By taking advantage of the methodology presented in [9], this paper studies the
direct geometrico-static problem (DGP) of 4-4 CDPRs (the inverse problem is pre-
sented in [8]). The locution 4-4 CDPR denotes a parallel robot in which a fixed base
and a mobile platform are connected to each other by 4 cables, with cable exit points
on the base and anchor points on the platform being distinct. Cables are treated as
inextensible and massless, and the platform is acted upon by a *constant force*, e.g.
gravity. The aim of the DGP is to determine the platform pose and the cable ten-
sions, when the cable lengths are assigned. The following issues, which are classic
challenges in robot analysis [35], are specifically dealt with:

1. determination of the number of solutions in the (zero-dimensional) algebraic
   variety defined by the problem polynomial equations;
2. reduction of the problem to a single equation in one unknown;
3. numerical computation of the solution set;
4. identification of a specific geometry providing the maximal number of distinct
   real-valued solutions.

In all numerical examples presented in the text, measures are given in SI units.

2 Geometrico-Static Model

A mobile platform is connected to a fixed base by 4 cables (Fig. 1). The ith cable
exits from the base at point A_i and it is connected to the mobile platform at point
B_i. The cable length is ρ_i, with $\rho_i > 0$. $Oxyz$ is a Cartesian coordinate frame
fixed to the base, with $\mathbf{i}$, $\mathbf{j}$ and $\mathbf{k}$ being unit vectors along the coordinate axes and $\mathbf{k}$
being oriented along the downward vertical. $Gx'y'z'$ is a Cartesian frame attached
to the end-effector, with $\mathbf{i}'$, $\mathbf{j}'$ and $\mathbf{k}'$ being the corresponding unit vectors along the
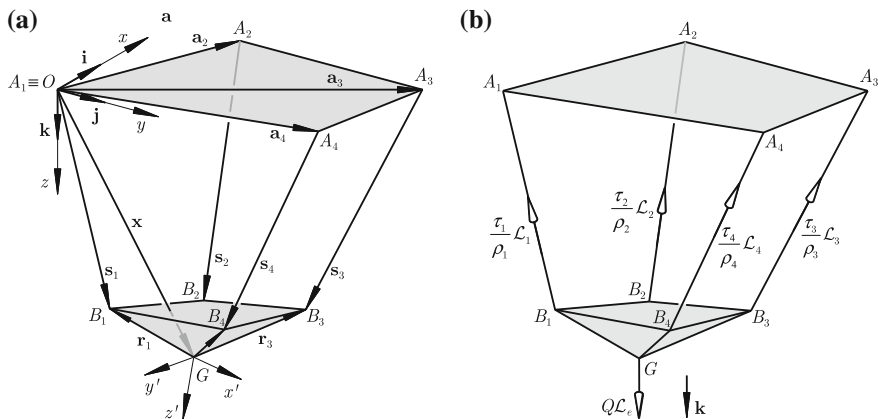
Fig. 1 A cable-driven parallel robot with 4 cables: **a** geometric model; **b** static model

coordinate axes. Without loss of generality, O is chosen to coincide with A_1 and G is assumed to be the platform center of mass. The platform posture is described by $\mathbf{X} = [\mathbf{x}^T; \boldsymbol{\Phi}^T]^T$, where $\mathbf{x} = [x, y, z]^T$ is the position vector of G in the fixed frame and $\boldsymbol{\Phi}$ is the array grouping the variables parameterizing the platform orientation with respect to $Oxyz$. If Rodrigues parameters are adopted, i.e. $\boldsymbol{\Phi} = [e_1, e_2, e_3]^T$, the rotation matrix $\mathbf{R}$ between the mobile and the fixed frame is

$$\mathbf{R}(\boldsymbol{\Phi}) = \mathbf{I}_3 + 2(\tilde{\boldsymbol{\Phi}} + \tilde{\boldsymbol{\Phi}}\tilde{\boldsymbol{\Phi}})/(1 + e_1^2 + e_2^2 + e_3^2), \tag{1}$$

where $\tilde{\boldsymbol{\Phi}}$ denotes the skew-symmetric matrix associated with the operator $\boldsymbol{\Phi}\times$. For the sake of brevity, the following symbols are also introduced:

$$\mathbf{a}_i = A_i - O, \quad \mathbf{r}_i = B_i - G = \mathbf{R}(\boldsymbol{\Phi})\mathbf{b}_i, \quad \mathbf{s}_i = B_i - A_i = \mathbf{x} + \mathbf{r}_i - \mathbf{a}_i,$$

where $\mathbf{b}_i$ is the position vector of B_i in $Gx'y'z'$.

The platform is acted upon by the vertical gravity force $Q\mathbf{k}$, applied at G. This force is described as a 0-pitch wrench $Q\mathscr{L}_e$, where $\mathscr{L}_e$ is the normalized Plücker vector of its line of action. The normalized Plücker vector of the line associated with the ith cable is $\mathscr{L}_i/\rho_i$, where, in axis coordinates, $\mathscr{L}_i = -[\mathbf{s}_i; \mathbf{p}_i \times \mathbf{s}_i]$ and $\mathbf{p}_i$ is any vector from an arbitrarily-chosen reference point P (called for brevity *moment pole*) to the cable line. So, the wrench exerted by the ith cable on the platform is $(\tau_i/\rho_i)\mathscr{L}_i$, with τ_i being a positive scalar representing the intensity of the cable tensile force.

When *all* cables of the robot are in tension, the set $\mathcal{C}$ of geometrical constraints imposed on the platform comprises 4 relations in $\mathbf{X}$, i.e.

$$||\mathbf{s}_i||^2 = ||\mathbf{x} + \mathbf{R}(\boldsymbol{\Phi})\mathbf{b}_i - \mathbf{a}_i||^2 = \rho_i^2, \quad i = 1\ldots 4. \tag{2}$$

By subtracting the first relation from both the second and the third one, and by clearing the denominator $1 + e_1^2 + e_2^2 + e_3^2$, the following equations are obtained:

$$q_1 := H_{200}x^2 + H_{020}y^2 + H_{002}z^2 + H_{100}x + H_{010}y + H_{001}z + H_{000} = 0, \quad \text{(3a)}$$

$$q_2 := I_{100}x + I_{010}y + I_{001}z + I_{000} = 0, \quad \text{(3b)}$$

$$q_3 := J_{100}x + J_{010}y + J_{001}z + J_{000} = 0, \quad \text{(3c)}$$

$$q_4 := K_{100}x + K_{010}y + K_{001}z + K_{000} = 0, \quad \text{(3d)}$$

where all coefficients H_{kmn}, I_{kmn}, J_{kmn} and K_{kmn} are quadratic functions in $\boldsymbol{\Phi}$.

As only 4 geometrical restraints are enforced, the platform preserves 2 dofs, with its pose being determined by static equilibrium. This may be written as

$$\sum_{i=1}^{4} \frac{\tau_i}{\rho_i}\mathscr{L}_i + Q\mathscr{L}_e = \underbrace{\left[\mathscr{L}_1 \ \mathscr{L}_2 \ \mathscr{L}_3 \ \mathscr{L}_4 \ \mathscr{L}_e \right]}_{\mathbf{M}(P)} \begin{bmatrix} (\tau_1/\rho_1) \\ (\tau_2/\rho_2) \\ (\tau_3/\rho_3) \\ (\tau_4/\rho_4) \\ Q \end{bmatrix} = \mathbf{0}, \quad \text{(4)}$$

where $\tau_i \geq 0$, $i = 1 \ldots 4$, and $\mathbf{M}(P)$ is a 6×5 matrix depending on the moment pole P, other than on the platform pose. By setting $\mathscr{L}_i = - [\mathbf{s}_i; \ (B_i - P) \times \mathbf{s}_i]$ and $\mathscr{L}_e = [\mathbf{k}; \ (G - P) \times \mathbf{k}]$, $\mathbf{M}(P)$ has the form

$$\mathbf{M}(P) = \begin{bmatrix} -\mathbf{s}_1 & -\mathbf{s}_2 & -\mathbf{s}_3 & -\mathbf{s}_4 & \mathbf{k} \\ (P - B_1) \times \mathbf{s}_1 & (P - B_2) \times \mathbf{s}_2 & (P - B_3) \times \mathbf{s}_3 & (P - B_4) \times \mathbf{s}_4 & (G - P) \times \mathbf{k} \end{bmatrix}. \quad \text{(5)}$$

After clearing denominators, the polynomials involved in Eq. (4) have total degree 3 in $\mathbf{X}$ and degree 1 in $\boldsymbol{\tau}$.

Equations (3)–(4) amount to 10 scalar relations in 10 variables, namely $\mathbf{x}$, $\boldsymbol{\Phi}$ and τ_i, $i = 1 \ldots 4$. Cable tensions may be eliminated from the set of unknowns by the approach proposed in [9]. Indeed, Eq. (4) holds only if

$$\text{rank}\,[\mathbf{M}(P)] \leq 4, \quad \text{(6)}$$

namely if $\mathscr{L}_1$, $\mathscr{L}_2$, $\mathscr{L}_3$, $\mathscr{L}_4$ and $\mathscr{L}_e$ are linearly dependent. By setting all 5×5 minors of $\mathbf{M}(P)$ equal to zero and by conveniently varying P, a large set of linearly independent relations that do not contain cable tensions may be obtained, i.e.

$$p_k(\mathbf{X}) = 0, \quad k = 1 \ldots N_p, \quad \text{(7)}$$

where N_p is an integer significantly greater than two (two is the number of relations that must be joined to Eq. (3) in order to obtain a square system of 6 equations in $\mathbf{X}$). For the DGP to admit a solution, the relations in Eq. (7) must be dependent, though

in a non-linear way. Formulating equilibrium constraints via Eq. (7) is particularly beneficial when variable-elimination strategies are pursued that take advantage of the abundance of linearly independent relations that this approach provides, such as methods based on Groebner bases or Sylvester's dialytic approach [10, 11].

When $P \equiv A_1$, all equations emerging by setting the 5×5 minors of $\mathbf{M}$ equal to zero, namely[1]

$$p_1 := \det \mathbf{M}_{23456}(A_1) = 0, \tag{8a}$$
$$p_2 := \det \mathbf{M}_{13456}(A_1) = 0, \tag{8b}$$
$$p_3 := \det \mathbf{M}_{12456}(A_1) = 0, \tag{8c}$$
$$p_4 := \det \mathbf{M}_{12356}(A_1) = 0, \tag{8d}$$
$$p_5 := \det \mathbf{M}_{12346}(A_1) = 0, \tag{8e}$$
$$p_6 := \det \mathbf{M}_{12345}(A_1) = 0, \tag{8f}$$

are linearly independent. Conversely, the relations obtained by letting $P \equiv A_i$, $i = 2 \ldots 4$, are linearly dependent on those in Eq. (8), so that they may be discarded. Nine additional linearly independent equations may be obtained by letting $P \equiv B_i$, $i = 1 \ldots 4$, i.e.

$$p_7 := \det \mathbf{M}_{23456}(B_1) = 0, \tag{9a}$$
$$p_8 := \det \mathbf{M}_{13456}(B_1) = 0, \tag{9b}$$
$$p_9 := \det \mathbf{M}_{12456}(B_1) = 0, \tag{9c}$$
$$p_{10} := \det \mathbf{M}_{23456}(B_2) = 0, \tag{9d}$$
$$p_{11} := \det \mathbf{M}_{13456}(B_2) = 0, \tag{9e}$$
$$p_{12} := \det \mathbf{M}_{12456}(B_2) = 0, \tag{9f}$$
$$p_{13} := \det \mathbf{M}_{23456}(B_3) = 0, \tag{9g}$$
$$p_{14} := \det \mathbf{M}_{13456}(B_4) = 0, \tag{9h}$$
$$p_{15} := \det \mathbf{M}_{12456}(B_5) = 0, \tag{9i}$$

and two more by letting $P \equiv G$, i.e.

$$p_{16} := \det \mathbf{M}_{23456}(G) = 0, \tag{10a}$$
$$p_{17} := \det \mathbf{M}_{13456}(G) = 0. \tag{10b}$$

All polynomials p_j, $j = 1 \ldots 17$, have degree 6 in $\boldsymbol{\Phi}$, degree 3 in $\mathbf{x}$ and total degree 9 in $\mathbf{X}$. No other linearly independent relations in $\mathbf{X}$ may be obtained from the minors of $\mathbf{M}(P)$ by varying the moment pole.

---

[1] The notation $\mathbf{M}_{hijkl}(P)$ denotes the block matrix obtained from rows h, i, j, k and l of $\mathbf{M}(P)$.

3 Problem-Solving Algorithm

Solving the DGP of the 4-4 CDPR requires solving, simultaneously, both the equations emerging from the geometrical constraints and those inferred from static equilibrium. As in the case of the robot suspended by 3 cables [10], this problem is significantly more complex than the forward kinematics of the general Gough–Stewart manipulator, a difficult task that attracted the interest of researchers for several years [28]. The forward kinematics of the Gough–Stewart robot is governed by six equations analogous to the point-to-point distance relations in Eq. (3), one of which is equivalent to Eq. (3a) and five more to Eq. (3b)–(3d). Two of the latter equations, which have degree 3 in **X**, are replaced, in the 4-4 CDPR, by a set of relations of degree 9 in **X**, thus making the problem significantly more complicated. In the following, the four challenges mentioned at the end of the Introduction are taken on.

3.1 Number of Solutions in the Complex Field

Let $\langle J \rangle$ be the ideal generated by the polynomial set $J = \{q_1, q_2, q_3, q_4, p_1, \ldots, p_{17}\}$. As mentioned in Sect. 2, q_1, q_2, q_3 and q_4 have, respectively, degree 4, 3, 3 and 3 in **X**, whereas all other generators in J have degree 9 in the same variables. In general, 1,576 monomials in **X** are involved. In order to ease numeric computation via a computer algebra system, namely the *Groebner Package* provided within the software *Maple*$_{15}$, all geometric parameters of the 4-4 robot are assigned generic *rational* values. Accordingly, $\langle J \rangle \subset \mathbb{Q}[\mathbf{X}]$, where $\mathbb{Q}[\mathbf{X}]$ is the set of all polynomials in **X** with coefficients in $\mathbb{Q}$. All Groebner bases are reduced and are computed with respect to graded reverse lexicographic monomial orders (grevlex, in brief). The lexicographic monomial order is particularly suitable to solve systems of polynomial equations, for it provides polynomial sets whose variables may be eliminated successively. However, the Groebner bases that it produces tend to be very large and thus, even for problems of moderate complexity, they have little chance to be actually computed. Conversely, the graded reverse lexicographic order produces bases that are endowed with no particular structure suitable for elimination purposes, but it provides more efficient calculations.

In general, a Groebner basis $G[J]$ of $\langle J \rangle$ with respect to grevlex(**X**), with variables ordered so that $z > y > x > e_1 > e_2 > e_3$, may be computed in a fairly expedited way. A key factor for the efficiency of such a computation is the *abundance of generators* available in J, which greatly simplifies and speeds up calculation (a feature already pointed out in [15]). Numerical tests showed that the fastest computation is achieved by exploiting the first 19 generators in J, i.e. $\{q_1, q_2, q_3, q_4, p_1, \ldots, p_{15}\}$. The computation of $G[J]$ for the exemplifying 4-4 robot whose dimensions are reported in Table 2 requires roughly 18 min on a PC with a 2.67 GHz Intel Xeon processor and 4 GB of RAM. If only 6 generators are used, computation time is 4 times higher and,

most important, spurious solutions are introduced in the solution set (this is because only two minors of **M** are used out of six).

Once $G[J]$ is known, the normal set of $\langle J \rangle$ may be easily computed, namely (in vector format)

$$\mathbf{N}[J] = \left[1, e_3, e_2, e_1, x, y, z, e_3^2, e_2 e_3, \ldots, e_1 e_2 e_3^2 x, e_1 e_2 e_3^2 y \right]^T. \quad (11)$$

Since $\mathbf{N}[J]$ comprises 216 monomials, this is also the number of complex roots (including multiplicities) in the algebraic variety V of $\langle J \rangle$ [37] and, thus, the order of the least-degree univariate polynomials comprised in $\langle J \rangle$.

3.2 Least-Degree Univariate Polynomial

A univariate polynomial of degree as high as 216 has, in practice, no use for the actual calculation of the solutions of the DGP, since its order makes it almost unmanageable under the numerical point of view. However, the computation of this polynomial provides a challenging benchmark to test the effectiveness of the elimination method presented in [10] and, for this reason, it is pursued here. The method encompasses three steps:

1. first, a Grobner basis G is calculated with respect to an efficient monomial order (see Sect. 3.1);
2. then, a subset of the original unknowns is eliminated by computing, by way of the FGLM algorithm [19], a Groebner basis G_l of a suitable elimination ideal $\langle J_l \rangle$;
3. finally, a least-degree univariate polynomial devoid of extraneous factors is computed by applying a dialytic elimination similar to that presented in [15] to the polynomials of G_l.

The above method allowed a 156th-degree univariate polynomial to be successfully computed in the ideal governing the DGP of the 3-3 CDPR, when other approaches either failed or proved to be excessively onerous in terms of computational burden. The DGP of the 4-4 CDPR provides an even harder challenge.

In the following, the techniques at the basis of the second and the third step are presented and the application of the method to the problem at hand is described.

3.2.1 Computation of Elimination Ideals

If $\mathbf{X}_l$ is a list of l variables in $\mathbf{X}$ and $\mathbf{X} \backslash \mathbf{X}_l$ is the (ordered) relative complement of $\mathbf{X}_l$ in $\mathbf{X}$, a monomial order $>_l$ on $\mathbb{Q}[\mathbf{X}]$ is of l-elimination type provided that any monomial involving a variable in $\mathbf{X}_l$ is greater than any monomial in $\mathbb{Q}[\mathbf{X} \backslash \mathbf{X}_l]$. If $G_{>l}[J]$ is a Groebner basis of $\langle J \rangle$ with respect to $>_l$, then $G[J_l] := G_{>l}[J] \cap \mathbb{Q}[\mathbf{X} \backslash \mathbf{X}_l]$ is a basis

Table 1 Structure of the Groebner bases of the elimination ideals of $\langle J \rangle$

$G[J_l]$	$\mathbf{X} \backslash \mathbf{X}_l$	N_l	Degrees of the generators in $\mathbf{X} \backslash \mathbf{X}_l$	No. of monomials with variables in $\mathbf{X} \backslash \mathbf{X}_l - \{w\}$, $w \in \mathbf{X} \backslash \mathbf{X}_l$
$G[J]$	$[z, y, x, e_1, e_2, e_3]$	195	3(3), 4(5), 5(158), 6(29)	230, 232, 232, 271, 224, 195
$G[J_1]$	$[y, x, e_1, e_2, e_3]$	147	5(36), 6(111)	185, 180, 181, 160, 147
$G[J_2]$	$[x, e_1, e_2, e_3]$	111	5(1), 7(99), 8(11)	127, 127, 117, 111
$G[J_3]$	$[e_1, e_2, e_3]$	61	8(1), 10(60)	66, 61, 61
$G[J_4]$	$[e_2, e_3]$	21	20(15), 21(6)	22, 21
$G[J_5]$	$[e_3]$	1	216(1)	–

of the lth elimination ideal $\langle J_l \rangle := \langle J \rangle \cap \mathbb{Q}[\mathbf{X} \backslash \mathbf{X}_l]$ [14]. The l-elimination monomial order implemented in *Maple* is a product order that induces grevlex orders on both $\mathbb{Q}[\mathbf{X}_l]$ and $\mathbb{Q}[\mathbf{X} \backslash \mathbf{X}_l]$. The FGLM algorithm [19] may be conveniently used to convert $G[J]$ from grevlex ($\mathbf{X}$) to $>_l$, so that $G[J_l]$ may be readily isolated from $G_{>l}[J]$.

The structure of $G[J_l]$ with respect to grevlex ($\mathbf{X} \backslash \mathbf{X}_l$), as obtained by the FGLM algorithm, is illustrated in Table 1 for $l = 0 \ldots 5$. Column 3 reports the number N_l of generators in $G[J_l]$, column 4 provides the degree in $\mathbf{X} \backslash \mathbf{X}_l$ of such generators (in parentheses, the number of generators having a given degree is specified), and column 5 reports, for each variable $w \in \mathbf{X} \backslash \mathbf{X}_l$, the number of monomials in $G[J_l]$ having variables in $\mathbf{X} \backslash \mathbf{X}_l - \{w\}$. By computing elimination ideals via the FGLM algorithm, a least-degree polynomial in one variable may be theoretically obtained. However, the elimination task is computationally very expensive and time consuming. The 'deeper' the elimination process (i.e. the fewer the variables in $\mathbf{X} \backslash \mathbf{X}_l$), the longer the time necessary to perform the computation and, mainly, the larger the amount of memory that is required. The latter issue is particularly critical and, even when the robot geometry is elementary and thus the coefficients of the polynomials in J simple, the complete elimination is out of reach for an ordinary computer.

3.2.2 Dialytic Elimination

Dhingra et al. [15] presented a method that computes a least-degree univariate polynomial from a Groebner basis without deriving elimination ideals. The method is based on the identification of a subset $H[J]$ of $G[J]$ and a variable $w \in \mathbf{X}$ such that the number of generators in $H[J]$ equals the number of monomials in the variables of $\mathbf{X} - \{w\}$ appearing in the polynomials of $H[J]$. This way, $H[J]$ (which may coincide with $G[J]$) may be set up as a square system of homogeneous linear equations in the monomials of $\mathbf{X} - \{w\}$, whose coefficients only depend on w. A Sylvester-type eliminant matrix may, thus, be constructed and a resultant in w computed.

For the problem at hand, $G[J]$ contains 195 generators and, by choosing $w = e_3$ (e_3 is the 'smallest' variable in the monomial ordering chosen to compute $G[J]$), the number of monomials in $\mathbf{X} - \{e_3\}$ is exactly equal to 195 (Table 1). According to Dhingra et al.'s approach, the resultant in w may thus emerge from the expansion

of a 195×195 eliminant matrix. However, the size of this matrix is too big for the expansion to be performed (computation time is, in this case, the critical issue).

A feasible alternative emerges by observing that dialytic elimination may be applied to the Groebner basis of *any* elimination ideal of $\langle J \rangle$. Indeed, Table 1 shows that, if w is the smallest variable in $\mathbf{X} \backslash \mathbf{X}_l$, $G[J_l]$ comprises a number of monomials in $\mathbf{X} \backslash \mathbf{X}_l - \{w\}$ which is equal to N_l for *all* values of l. For instance, the Groebner basis $G[J_3]$ of $\langle J \rangle \cap \mathbb{Q}[e_1, e_2, e_3]$ with respect to grevlex(e_1, e_2, e_3) comprises 61 polynomials (1 of degree 8 in $\boldsymbol{\Phi}$ and 60 of degree 10 in $\boldsymbol{\Phi}$), including 61 monomials in e_1 and e_2. It follows that, if w is assigned the role of 'hidden' variable, the generators of $G[J_l]$ may be set to zero in the following form:

$$\mathbf{T}(w) \, \mathbf{E}_w = \left(\sum_{k=0}^{u} w^k \mathbf{B}_k \right) \mathbf{E}_w = \mathbf{0}, \tag{12}$$

where u is the highest power of w in $G[J_l]$, $\mathbf{B}_k$ is a $N_l \times N_l$ numeric matrix, $\mathbf{T}(w)$ is a matrix polynomial of degree u in w, and $\mathbf{E}_w$ is a N_l-dimensional vector comprising all monomials in $G[J_l]$ having variables in $\mathbf{X} \backslash \mathbf{X}_l - \{w\}$. Accordingly, the desired resultant, free from extraneous polynomial factors, may be obtained as

$$\det \mathbf{T}(w) = \sum_{h=0}^{216} L_h w^h = 0, \tag{13}$$

with the coefficients L_h only depending on the input data, i.e. the robot geometry and the cable lengths.

The advantage gained by applying a dialytic step to a Groebner basis $G[J_l]$ with $l > 0$ emerges from the data presented in Table 2. The table reports, for an exemplifying 4-4 CDPR, the CPU time required to compute grevlex bases for the elimination ideals of $\langle J \rangle$, with $l = 0 \ldots 5$, on the PC mentioned in Sect. 3.1. In particular, the third column reports the CPU time $T_{G[J_l]}$ required to obtain $G[J_l]$ from $\langle J_{l-1} \rangle \cap \mathbb{Q}[\mathbf{X} \backslash \mathbf{X}_l]$ by the FGLM algorithm, whereas the fourth column reports the CPU time $T_{\langle J \rangle \cap \mathbb{Q}[e_3]}$ required to calculate $\langle J \rangle \cap \mathbb{Q}[e_3]$ by applying dialytic elimination to $G[J_l]$, for $l = 0 \ldots 4$. As expected, the higher l is (i.e. the more variables are eliminated), the more demanding the FGLM elimination proves to be. In particular, the last elimination ideal cannot be computed, due to excessive memory usage. Conversely, the computation time of the dialytic step decreases with l, since it depends on the dimension of $\mathbf{T}(w)$. For the example at hand, $\langle J \rangle \cap \mathbb{Q}[e_3]$ cannot be computed from $G[J_l]$, with $l = 0 \ldots 2$, due to excessive computation time. Instead, a univariate polynomial in e_3 may be successfully computed from either $G[J_3]$ or $G[J_4]$. The more 'efficient' computation is obtained by eliminating $\{x, y, z\}$ by the FGLM algorithm and $\{e_1, e_2\}$ by the dialytic step ($18 + 237 + 702 + 598 + 348 \approx 1,900 \, \text{min}$).

It emerges from the above result that the hybrid approach presented in [10], which eliminates a subset of variables by the FGLM algorithm and then applies Dhingra et al.'s method on the Groebner basis of the corresponding elimination ideal, provides a

Table 2 Computation time to obtain Groebner bases of the elimination ideals of $\langle J \rangle$ for the robot with $\mathbf{a}_2 = [9; 0; 1]$, $\mathbf{a}_3 = [11; 9; 0]$, $\mathbf{a}_4 = [-2; 8; -1]$, $\mathbf{b}_1 = [-2; -1; -1]$, $\mathbf{b}_2 = [1; -2; 0]$, $\mathbf{b}_3 = [2; 1; -1]$, $\mathbf{b}_4 = [0; 2; -1]$, $(\rho_1, \rho_2, \rho_3, \rho_4) = (6, 7, 8, 9)$ and $Q = 1$

l	$\langle J_l \rangle$	$T_{G[J_l]}$ (min)	$T_{\langle J \rangle \cap \mathbb{Q}[e_3]}$ (min)
0	$\langle J \rangle$	18	...
1	$\langle J \rangle \cap \mathbb{Q}[y, x, e_1, e_2, e_3]$	237	...
2	$\langle J \rangle \cap \mathbb{Q}[x, e_1, e_2, e_3]$	702	...
3	$\langle J \rangle \cap \mathbb{Q}[e_1, e_2, e_3]$	598	348
4	$\langle J \rangle \cap \mathbb{Q}[e_2, e_3]$	1,077	68
5	$\langle J \rangle \cap \mathbb{Q}[e_3]$	...	–

profitable strategy to compute high-order least-degree univariate polynomials. This strategy may succeed when alternative methods either fail or prove to be too onerous in terms of computational burden.

3.3 Numerical Computation of the Solution Set

For the numeric solutions of the problem to be actually calculated, several options may be considered.

3.3.1 Eigenvalue Formulation

One approach, which relies on a prior computation of a Groebner basis, is based on the properties of the normal set $\mathbf{N}[J]$ of $G[J]$ [13, 32]. Let the polynomial $w\eta_h$ be considered, with $w \in \mathbf{X}$ and with η_h being the hth monomial in $\mathbf{N}[J]$. If r_h is the remainder on division of $w\eta_h$ by $G[J]$, r_h is a linear combination of monomials in $\mathbf{N}[J]$, i.e. $r_h = \sum_{k=1}^{216} a_{hk}\eta_k$, with a_{hk} being a constant coefficient. Since $r_h - w\eta_h$ belongs to $\langle J \rangle$, it must vanish on V. By assembling all equations of this kind that may be obtained for $h = 1 \ldots 216$, one has

$$(\mathbf{A}[J, w] - w\mathbf{I}) \mathbf{N}[J] = \mathbf{0}, \tag{14}$$

where $\mathbf{A}[J, w] = [a_{hk}]$ is a 216×216 numeric matrix called *multiplication matrix* for w and $\mathbf{I}$ is the 216×216 identity matrix. Equation (14) is a linear eigenvalue problem,[2] which may be accurately solved in a fast way. Since the first 7 entries of $\mathbf{N}[J]$ are 1, e_1, e_2, e_3, x, y, z (see Eq. 11), a unique solution in $\mathbf{X}$ emerges from each eigenvector $\mathbf{N}_h$ as

---

[2] The 216th-degree characteristic polynomial associated to the eigenvalue problem (14) provides a theoretical way to compute the resultant in w. However, under a practical viewpoint, expanding a 216×216 matrix is even less effectual than applying Dhingra et al.'s method to $G[J]$.

Table 3 Real solutions with nonnegative cable tensions of the DGP of the robot reported in Table 2

No.	(e_1, e_2, e_3)	(x, y, z)	$(\tau_1, \tau_2, \tau_3, \tau_4)$	$\mathbf{H}_r$
1	$-7.8443, -19.3444, 2.2184$	$4.5660, 3.2683, 0.8375$	$1.25, 1.54, 0.94, 1.24$	$<>$
2	$-24.7302, 0.7581, -1.9562$	$4.4681, 4.1679, 0.9753$	$0.84, 1.12, 1.13, 1.29$	$<>$
3	$0.0350, -0.0540, 0.1114$	$4.5175, 3.6961, 5.9635$	$0.75, 0, 0.62, 0$	$>$

$$e_{1,h} = \frac{N_{h,2}}{N_{h,1}}, \ e_{2,h} = \frac{N_{h,3}}{N_{h,1}}, \ e_{3,h} = \frac{N_{h,4}}{N_{h,1}}, x_h = \frac{N_{h,5}}{N_{h,1}}, \ y_h = \frac{N_{h,6}}{N_{h,1}}, \ z_h = \frac{N_{h,7}}{N_{h,1}}. \tag{15}$$

For the example reported in Table 2, computing $\mathbf{A}[J, e_3]$ requires roughly 16s and calculating its eigenvalues a few tenth of second. Once a robot configuration is found, cable tensions may be obtained by any subset of 4 linearly independent relations chosen within Eq. (4). Clearly, a real configuration proves *feasible* only if therein cable tensions are *nonnegative* and the configuration is *stable*. Stability may be assessed by way of the reduced Hessian $\mathbf{H}_r$ defined in [9]. In this paper, the symbols $>$, $\geq$, $<$, $\leq$ and $<>$ denote, respectively, a positive-definite, a positive-semidefinite, a negative-definite, a negative-semidefinite and an indefinite matrix. For the example reported in Table 2, only 8 out of the 216 solutions are real and, among them, only 2 have positive tension in all cables. They are listed in the first two rows of Table 3. Interestingly, no one of them is stable. This means that, when the assigned cable lengths are fed-in to the robot actuators, the end-effector necessarily moves to a rest configuration in which some cable is slack. Indeed, further investigation (Sect. 4) shows that a single feasible configuration exists, in which only two cables are taut. This configuration is reported in the third row of Table 3.

3.3.2 Homotopy Continuation

An alternative to the method described in Sect. 3.3.1 is provided by homotopy continuation [37]. If no information is *a priori* known about the roots of $\langle J \rangle$, the DGP of the 4–4 robot may be cast, on the basis of the degree of the polynomials contained in J, into the larger family of all polynomial systems made up by 1 quartic, 3 cubics and 2 equations of degree 9 on $\mathbf{X} \in \mathbb{P}^6$. By counting solutions at infinity, a general member of this family, e.g. $J_{red} = \{q_1, q_2, q_3, q_4, p_4, p_5\}$, has a number of isolated roots equal to the minimal multi-homogeneous Bezout number [40]. This is also the number of paths tracked by the homotopy-continuation software used in this paper, i.e. *Bertini* [3]. By searching all possible multi-homogenizations, the minimal Bezout number emerges when $\mathbf{X}$ is partitioned as $[\{x, y, z\}, \{e_1, e_2, e_3\}]$ and it is equal to 2,160.[3] Computation converges in a robust way, but it is slow. This is due to the

---

[3] The partition $[\{x, y, z\}, \{e_1, e_2, e_3\}]$ also provides the fastest computation of $\langle J \rangle \cap \mathbb{Q}[e_3]$ by the hybrid elimination approach proposed in Sect. 3.2. This observation confirms the heuristic advanced in [10] to determine which variables may be most conveniently eliminated by the FGLM procedure before attempting the final dialytic step.

complexity of the polynomials emerging from Eq. (6), which have several hundreds of terms and a considerable degree. For the robot whose geometric parameters are given in Table 2, *Bertini* computes the finite solutions of J_{red} in roughly 100 min. Furthermore, since only 2 relations are selected within Eq. (7) (e.g. p_4 and p_5) to form, together with Eq. (3), a square system of 6 equations in 6 unknowns, only two minors of $\mathbf{M}(P)$ out of six are used and spurious solutions, for which some unused minors do not vanish, are introduced.

Due to this limitations, the formulation of static equilibrium via Eq. (4) is preferable for the application of homotopy-continuation methods. Indeed, even though Eqs. (3) and (4) amount to 10 scalar relations in 10 variables, they comprise simpler lower-order polynomials, which prove to be stabler when numerical methods are implemented to solve them. In fact, by partitioning variables as $[\{\mathbf{x}\}, \{\boldsymbol{\Phi}\}, \{\boldsymbol{\tau}\}]$ in order to obtain the best multi-homogenization, *Bertini* tracks 3,600 paths, but it converges to the 216 solutions of the example referred to in Table 2 in roughly 9 min. Computation is, thus, much faster than by the previous formulation and no extraneous roots are introduced. This formulation is also advantageous compared with the eigenproblem reported in Sect. 3.3.1, whose overall performance depends on the duration of the Groebner-basis computation (based on exact arithmetic). While the latter time considerably increases with the complexity of the rational coefficients of the polynomials in J, the time required by homotopy continuation varies in a far less relevant way, since real-value geometric parameters are directly handled in floating-point arithmetic.

It is worth emphasizing that all procedures described above are aimed at solving the DGP of the 4-4 CDPR under the assumption that no information is known about the number of roots in $\mathbb{C}^6$. Once the latter information is known, however, a more efficient continuation technique may be used to solve practical cases. Indeed, the complete family of all DGPs of 4-4 CDPRs lies in a 28-dimensional parameter space, parametrized by the geometric quantities $\mathbf{a}_i$, $\mathbf{b}_i$ and ρ_i, $i = 1\ldots 4$. Accordingly, when the 216 isolated roots of a generic robot are known, *parameter-homotopy continuation* may be applied to find the solutions for any other member of the family [37]. In this case, only 216 paths need to be tracked and paths corresponding to solutions at infinity are avoided. By this approach, *Bertini* converges to the 216 solutions of the example reported in Table 2 in roughly 2.7 min.

Another possibly very efficient approach relies on techniques based on interval analysis [29]. This method brings about the significant advantage of easily incorporating constraints on the cable-tension sign in the calculation (there is no need to compute all possible solutions of the problem, in order to, successively, sort out only those that are real and for which cable tensions are nonnegative), as well as uncertainties in the parameter values (e.g. due to manufacturing tolerances or measuring errors), physical bounds on variable ranges (e.g. due to hardware limits and/or user restraints), additional geometric constraints (e.g. due to interference problems), etc. Preliminary results concerning the application of interval analysis to the DGP of under-constrained CDPRs are reported in [5].

3.4 Number of Real-Valued Solutions and Feasible Configurations

The 216 solutions computed by the methods presented in Sect. 3.3 may be complex or real, but only the latter have physical interest. By varying the robot parameters in $\mathbb{R}^{28}$, the count of real roots varies. Since there may be roots in the solution set that always remain complex, the maximal number of real solutions may be smaller than 216. Determining a tight bound for this count is a challenging task.

By a continuation procedure originally proposed by Dietmaier [17] and recently adapted by the authors to the DGP of under-constrained CDPRs [1], sets of 4-4 CDPR parameters for which the DGP provides at the most 98 real configurations were found so far. A numerical example is reported in Table 4. For the sake of brevity, only the 20 real configurations for which no cable tension is negative are listed (rows 1-20). Among these, only 5 are stable and, thus, feasible. The robot also admits 19 equilibrium configurations with one or more slack cables (Sect. 4), but only the configuration with a single cable in tension is stable. The equilibrium configurations with slack cables are listed in Table 4 in rows 21-39.

4 Equilibrium Configurations with Unloaded Cables

When cable lengths are assigned as inputs, nothing ensures, *a priori*, that when the platform reaches its stable equilibrium pose all cables are under tension. Accordingly, the final pose may be *either* a DGP solution for the current 4-4 CDPR *or* a valid pose for any one of the m–m CDPRs (with $m < 4$) that may be derived from the initial 4-4 robot. Accordingly, the overall solution set must be obtained by solving the DGP for *all* possible constraint sets $\{||\mathbf{s}_j|| = \rho_j, j \in \mathcal{W}\}$, with $\mathcal{W} \subseteq \{1, 2, 3, 4\}$ and card($\mathcal{W}$) ≤ 4, and by retaining, for each solution set, only the solutions for which $||\mathbf{s}_k|| < \rho_k$, $k \notin \mathcal{W}$. In general, this amounts to solving 15 DGPs, namely 1 DGP with 4 cables in tension, 4 DGPs with 3 cables in tension, 6 DGPs with 2 cables in tension and 4 DGPs with 1 cable in tension.

The example reported in Table 3 is particularly interesting. In this case, in fact, even though the robot exhibits a geometry with no apparent special features, it has a single feasible configuration, with only two cables in tension (i.e. cables 1 and 3). All real solutions with four or three cables in tension prove to be unstable. The numerical investigation conducted so far showed that cases like this are likely to occur. This shows the importance of computing the *complete* solution set of the DGP, thus including configurations with unloaded cables.

Table 4 Real solutions with nonnegative cable tensions of the DGP of the robot with $\mathbf{a}_2 = [-0.76054; 0; 0.90931]$, $\mathbf{a}_3 = [-0.71646; 0.68047; 0.07970]$, $\mathbf{a}_4 = [0.02574; 0.70420; 0.87389]$, $\mathbf{b}_1 = [16.54820; 0; 0]$, $\mathbf{b}_2 = [17.16360; 0.77720; 0]$, $\mathbf{b}_3 = [16.22250; 0.75153; 0.76874]$, $\mathbf{b}_4 = [17.38600; 0.09567; 0.81726]$, $(\rho_1, \rho_2, \rho_3, \rho_4) = (1; 1.01493; 1.12171; 1.138230)$ and $Q = 1$

No.	(e_1, e_2, e_3)	(x, y, z)	$(\tau_1, \tau_2, \tau_3, \tau_4)$	$\mathbf{H}_r$
1	2.4620, 0.0475, −0.0432	−16.9518, 0.3857, 1.2564	33.4, 5.0, 11.6, 28.2	<>
2	−2.0125, 1.9489, −5.8751	12.0236, 8.2020, −7.3775	86.8, 10.7, 87.2, 6.7	<>
3	3.4339, 1.7412, 1.2351	−8.6254, −13.1378, −4.6438	110.1, 19.1, 109.6, 0.1	<>
4	0.0738, −0.1895, −1.2345	2.9456, 16.8817, −1.2941	7.5, 14.6, 16.3, 19.7	>
5	−1.6115, −1.8141, 0.4874	−0.6584, −16.1920, −3.9850	30.5, 35.3, 2.6, 14.1	<>
6	18.0137, 31.2651, 7.0149	7.9403, −13.9345, −1.5605	13.7, 2.4, 26.7, 23.4	>
7	−30.8489, −70.8600, −12.4272	10.9162, −11.7819, −1.5808	10.7, 3.3, 26.9, 26.4	<>
8	1.2141, −0.0295, −0.1205	−16.9142, 2.8593, 1.8060	17.2, 12.2, 10.7, 17.4	>
9	−0.5383, 0.3499, −1.1452	0.1154, 16.5864, −2.7129	37.5, 31.3, 14.1, 3.1	<>
10	−0.0318, −0.0510, −0.7501	−5.4425, 16.2821, −1.3011	18.9, 25.7, 6.7, 16.4	<>
11	−0.0278, −0.0559, −0.8455	−3.5374, 16.7826, −1.2996	16.0, 21.9, 8.7, 15.7	>
12	0.0096, −0.0960, −0.9984	−0.7053, 17.1315, −1.3024	11.8, 17.8, 11.7, 16.6	<>
13	0.4639, 0.0205, −0.0400	−17.4454, 1.1046, 0.9309	1.7, 35.8, 31.1, 14.5	<>
14	−0.0400, −1.3814, 2.6631	13.1849, −8.2555, −3.5470	10.2, 30.8, 33.8, 3.4	<>
15	0.0216, −0.3513, −2.5343	11.7477, 12.0239, −1.5488	6.1, 7.2, 29.0, 26.8	<>
16	−19.8826, 49.6758, −38.5605	13.5491, 8.6097, −4.8587	28.1, 3.9, 11.0, 25.3	<>
17	4.2385, −14.6735, 8.9676	14.7575, 6.2950, −4.8534	26.1, 8.1, 6.4, 27.3	<>
18	7.2409, −22.7365, 15.5123	14.5027, 6.8246, −4.8518	25.6, 6.7, 8.2, 25.2	>
19	0.3745, −0.3751, −0.5197	−8.4164, 14.8582, −3.7949	0.3, 93.0, 19.3, 94.8	<>
20	1.7383, −8.0398, 7.1664	15.5137, 2.5875, −4.9518	17.1, 9.7, 11.3, 16.2	<>
21	0.9523, 0.4239, 0.4062	−12.3637, −11.4946, 0.3181	17.5, 32.7, 40.2, 0	<>
22	−19.4314, −11.2612, −2.2585	−8.8424, −13.7747, −3.1139	38.2, 25.6, 24.3, 0	<>
23	−1.3911, −0.9981, −1.3884	−0.6505, 0.0967, −15.7689	0.9, 0.5, 0.1, 0	<>
24	0.7069, −0.9954, 0.6999	0.0593, 0.6494, −15.7714	0.6, 0.1, 0, 0.7	<>
25	−0.4757, −2.4789, 0.7972	11.7905, −8.3803, −7.7523	18.4, 89.9, 0, 90.9	<>
26	1.1059, −0.4337, −0.4269	−12.0838, 12.4460, 0.8943	32.0, 19.8, 0, 40.4	<>
27	−0.6663, −0.9927, −0.6711	−0.6538, −0.0188, −15.7639	0.7, 0.7, 0, 0.1	<>
28	6.0629, 9.1687, 2.9878	6.2292, −14.7313, −1.6233	17.0, 0, 32.0, 25.3	<>
29	1.4778, −1.0031, 1.4794	−0.0563, 0.6494, −15.7795	0.8, 0, 0.1, 0.6	<>
30	0.2912, −0.5223, −1.2952	4.4079, 16.6051, −1.7581	0, 17.6, 26.6, 33.7	<>
31	−1.0000, −0.9928, −0.9928	−0.7603, −0.0000, −15.7806	0.9, 0.7, 0, 0	<>
32	−1.0000, −0.4268, −0.4268	−12.3088, −0.0000, −11.4377	29.4, 28.9, 0, 0	<>
33	89.7786, 2.3211, 93.2252	−0.0681, 0.0647, −16.2418	4.4, 0, 4.2, 0	<>
34	1.0886, −1.0054, 1.0840	0.0267, 0.7293, −15.7880	0.8, 0, 0, 0.7	<>
35	3.6274, −3.6215, 1.3794	0.5191, 14.2028, −9.2843	33.4, 0, 0, 32.9	<>
36	0.2707, −0.2549, 0.9012	−1.6557, −13.8183, −8.3698	0, 34.3, 34.8, 0	<>
37	0.0333, −0.9915, −0.0050	−0.1382, 0.5574, −16.2520	0, 4.0, 0, 4.1	<>
38	−0.7058, −3.8044, −3.8528	14.6876, 1.1730, −7.0336	0, 0, 34.7, 34.3	<>
39	−, −, −	−0.7165, 0.6805, 17.4595	0, 0, 1, 0	>

5 Conclusions

This paper studied the kinematics and statics of under-constrained cable-driven parallel robots with 4 cables, in crane configuration. For such robots, kinematics and statics are coupled and they must be solved simultaneously. This poses major challenges, since displacement analysis problems gain remarkable complexity with respect to those of analogous 6-dof rigid-link robots.

The direct geometrico-static problem (DGP), which aims at determining the platform pose and the cable tensions once the cable lengths are assigned, was effectively worked out and the complete solution set was determined, including cases in which not all cables are in tension. Equilibrium configurations with slack cables are particularly important, since for a given robot they may be feasible (i.e. stable) and the end-effector may switch across them, due to inertia forces or external disturbances.

By the innovative hybrid elimination method presented in [10], a least-degree univariate polynomial was numerically obtained in the ideal governing the problem when the four cables are in tension, thus showing that, in this case, 216 solutions exist in the complex field. The DGP of the 4-4 CDPR provided a meaningful benchmark to test the effectiveness of this elimination approach. The potential solutions of the problem (namely, those obtained before imposing the constraints concerning the cable-tension sign and stability) were numerically computed by both an eigenvalue formulation and homotopy continuation. The problem of identifying a general 4-4 robot with the highest number of *real* equilibrium configurations was also addressed and preliminary results were reported.

References

1. Abbasnejad, G., Carricato, M.: Real solutions of the direct geometrico-static problem of under-constrained cable-driven parallel robots with 3 cables: a numerical investigation. Meccanica (2012). doi:10.1007/s11012-012-9552-3
2. Alikhani, A., Behzadipour, S., Vanini, S.A.S., Alasty, A.: Workspace analysis of a three DOF cable-driven mechanism. ASME J. Mech. Robotics **1**(4), 041005/1–7 (2009)
3. Bates, D.J., Hauenstein, J.D., Sommese, A.J., Wampler, C.W.: Bertini: Software for numerical algebraic geometry. Available at http://www.nd.edu/~sommese/bertini
4. Behzadipour, S., Khajepour, A.: Stiffness of cable-based parallel manipulators with application to stability analysis. ASME J. Mech. Des. **128**(1), 303–310 (2006)
5. Berti, A., Merlet, J.P., Carricato, M.: Solving the direct geometrico-static problem of 3–3 cable-driven parallel robots by interval analysis: preliminary results. In: Proceedings of the 1st International Conference on Cable-Driven Parallel Robots. Stuttgart, (2012)
6. Bosscher, P., Riechel, A.T., Ebert-Uphoff, I.: Wrench-feasible workspace generation for cable-driven robots. IEEE Trans. Robotics **22**(5), 890–902 (2006)
7. Bouchard, S., Gosselin, C., Moore, B.: On the ability of a cable-driven robot to generate a prescribed set of wrenches. ASME J. Mech. Robotics **2**(1), 011010/1–10 (2010)
8. Carricato, M., Abbasnejad, G., Walter, D.: Inverse geometrico-static analysis of under-constrained cable-driven parallel robots with four cables. In: Lenarčič, J., Husty, M. (eds.) Advances in Robot Kinematics. Springer, Dordrecht (2012)

9. Carricato, M., Merlet, J.P.: Geometrico-static analysis of under-constrained cable-driven parallel robots. In: Lenarčič, J., Stanišic, M.M. (eds.) Advances in Robot Kinematics: Motion in Man and Machine, pp. 309–319. Springer, Dordrecht (2010)

10. Carricato, M., Merlet, J.P.: Direct geometrico-static problem of under-constrained cable-driven parallel robots with three cables. In: Proceedings of the 2011 IEEE International Conference on Robotics and Automation, pp. 3011–3017. Shanghai, (2011)

11. Carricato, M., Merlet, J.P.: Inverse geometrico-static problem of under-constrained cable-driven parallel robots with three cables. In: Proceedings of the 13th World Congress in Mechanism and Machine Science, pp. 1–10, Paper No. A7_283. Guanajuato, (2011)

12. Collard, J.F., Cardou, P.: Computing the lowest equilibrium pose of a cable-suspended rigid body. Optimization and Engineering (2012). doi:10.1007/s11081-012-9191-5

13. Corless, R.M.: Gröbner bases and matrix eigenproblems. ACM SIGSAM Bull. **30**(4), 26–32 (1996)

14. Cox, D., Little, J., O'Shea, D.: Ideals, Varieties, and Algorithms. Springer, New York (2007)

15. Dhingra, A.K., Almadi, A.N., Kohli, D.: A Gröbner-Sylvester hybrid method for closed-form displacement analysis of mechanisms. ASME J. Mech. Des. **122**(4), 431–438 (2000)

16. Diao, X., Ma, O.: Force-closure analysis of 6-dof cable manipulators with seven or more cables. Robotica **27**(2), 209–215 (2009)

17. Dietmaier, P.: The Stewart–Gough platform of general geometry can have 40 real postures. In: Lenarčič, J., Husty, M.L. (eds.) Advances in Robot Kinematics: Analysis and Control, p. 16. Kluwer Academic Publishers, Dordrecht (1998)

18. Fattah, A., Agrawal, S.K.: On the design of cable-suspended planar parallel robots. ASME J. Mech. Des. **127**(5), 1021–1028 (2006)

19. Faugère, J.C., Gianni, P., Lazard, D., Mora, T.: Efficient computation of zero-dimensional Gröbner bases by change of ordering. J. Symb. Comput. **16**(4), 329–344 (1993)

20. Ghasemi, A., Eghtesad, M., Farid, M.: Workspace analysis for planar and spatial redundant cable robots. ASME J. Mech. Robotics **1**(4), 044502/1–6 (2009)

21. Gouttefarde, M., Daney, D., Merlet, J.P.: Interval-analysis-based determination of the wrench-feasible workspace of parallel cable-driven robots. IEEE Trans. Robotics **27**(1), 1–13 (2011)

22. Heyden, T., Woernle, C.: Dynamics and flatness-based control of a kinematically undetermined cable suspension manipulator. Multibody Syst. Dyn. **16**(2), 155–177 (2006)

23. Hiller, M., Fang, S., Mielczarek, S., Verhoeven, R., Franitza, D.: Design, analysis and realization of tendon-based parallel manipulators. Mech. Mach. Theory **40**(4), 429–445 (2005)

24. Jiang, Q., Kumar, V.: The direct kinematics of objects suspended from cables. In: Proceedings of the ASME 2010 International Design Engineering Technical Conferences, vol. 2, pp. 193–202, Paper No. DETC2010-28036. Montreal, (2010)

25. Kawamura, S., Kino, H., Won, C.: High-speed manipulation by using parallel wire-driven robots. Robotica **18**(1), 13–21 (2000)

26. Lau, D., Oetomo, D., Halgamuge, S.: Wrench-closure workspace generation for cable driven parallel manipulators using a hybrid analytical-numerical approach. ASME J. Mech. Des. **133**(7), 071004/1–10 (2011)

27. McCarthy, J.M.: 21st century kinematics: synthesis, compliance, and tensegrity. ASME J. Mech. Robotics **3**(2), 020201/1–3 (2011)

28. Merlet, J.P.: Parallel Robots. Springer, Dordrecht (2006)

29. Merlet, J.P.: Interval analysis for certified numerical solution of problems in robotics. Int. J. Appl. Math. Comput. Sci. **19**(3), 399–412 (2009)

30. Michael, N., Kim, S., Fink, J., Kumar, V.: Kinematics and statics of cooperative multi-robot aerial manipulation with cables. In: Proceedings of the ASME 2009 International Design Engineering Technical Conference, vol. 7, pp. 83–91, Paper No. DETC2009-87677. San Diego, (2009)

31. Ming, A., Higuchi, T.: Study on multiple degree-of-freedom positioning mechanism using wires–Part 1: concept, design and control. Int. J. Jpn. Soc. Precis. Eng. **28**(2), 131–138 (1994)

32. Möller, H.M.: Gröbner bases and numerical analysis. In: Buchberger, B., Winkler, F. (eds.) Gröbner Bases and Applications, London Mathematical Society Lecture Note Series, vol. 251, pp. 159–178. Cambridge University Press, Cambridge (1998)

33. Perreault, S., Gosselin, C.M.: Cable-driven parallel mechanisms: application to a locomotion interface. ASME J. Mech. Des. **130**(10), 102301/1–8 (2008)
34. Pusey, J., Fattah, A., Agrawal, S., Messina, E.: Design and workspace analysis of a 6–6 cable-suspended parallel robot. Mech. Mach. Theory **39**(7), 761–778 (2004)
35. Raghavan, M., Roth, B.: Solving polynomial systems for the kinematic analysis and synthesis of mechanisms and robot manipulators. ASME J. Mech. Des. **117**(2B), 71–79 (1995)
36. Rosati, G., Zanotto, D., Agrawal, S.K.: On the design of adaptive cable-driven systems. ASME J. Mech. Robotics **3**(2), 021004/1–13 (2011)
37. Sommese, A.J., Wampler, C.W.: The Numerical Solution of Systems of Polynomials Arising in Engineering and Science. World Scientific Publishing, Singapore (2005)
38. Stump, E., Kumar, V.: Workspaces of cable-actuated parallel manipulators. ASME J. Mech. Des. **128**(1), 159–167 (2006)
39. Su, Y.X., Duan, B.Y., Nan, R.D., Peng, B.: Development of a large parallel-cable manipulator for the feed-supporting system of a next-generation large radio telescope. J. Robotic Syst. **18**(11), 633–643 (2001)
40. Wampler, C.W.: Bezout number calculations for multi-homogeneous polynomial systems. Appl. Math. Comput. **51**(2–3), 143–157 (1992)
41. Yamamoto, M., Yanai, N., Mohri, A.: Trajectory control of incompletely restrained parallel-wire-suspended mechanism based on inverse dynamics. IEEE Trans. Robotics **20**(5), 840–850 (2004)

Implementing Extended Kinematics of a Cable-Driven Parallel Robot in Real-Time

Valentin Schmidt and Andreas Pott

Abstract   This paper describes the implementation of extended pulley kinematics for parallel cable robots. An algorithm for the extended kinematics taking into account cable pulleys is discussed and implemented in real-time. This solution uses an iterative solver which can be computationally costly, depending on convergence. The convergence was tested for a specific geometry and successfully implemented on the cable robot IPAnema. Accuracy of both the standard and extended kinematics were tested according to the ISO 9283 standard. The Absolute accuracy was measured to be 22.32 mm for the standard and 17.50 mm for the extended kinematics which shows some improvement. A method for testing accuracy of orientations is also introduced.

1 Introduction

The kinematics of cable robots and indeed all [14] parallel robots have been subject of research for a number of years. While inverse kinematics are trivial, forward kinematics are much more difficult to solve, especially within computational constraints such as real-time capability. In general, the forward kinematics of parallel robots can have 40 real solutions [1], which are numerically difficult to compute directly [2]. Other methods, more practical to implement, are thus consistent topics of research. Some rely on changing geometry [12], others on interval methods [7], and also on numerical optimization methods [3, 10].

With the increasing research on cable robots, and an ever increasing number of prototypes, precise information regarding achievable accuracy and methods of improvement have become more important. While accuracy and repeatability values

V. Schmidt (✉) · A. Pott
Fraunhofer Institute for Manufacturing Engineering and Automation IPA, Stuttgart, Germany
e-mail: Valentin.Schmidt@ipa.Fraunhofer.de

A. Pott
e-mail: Andreas.Pott@ipa.Fraunhofer.de

Fig. 1 IPAnema Winch showing the drum and cable guiding system. As the cable exits the winch it is passed through a pulley which also has a vertical hinge. This hinge allows the pulley to orientate towards the platform anchor point. In other words, the anchor point is always in the same plane as the pulley
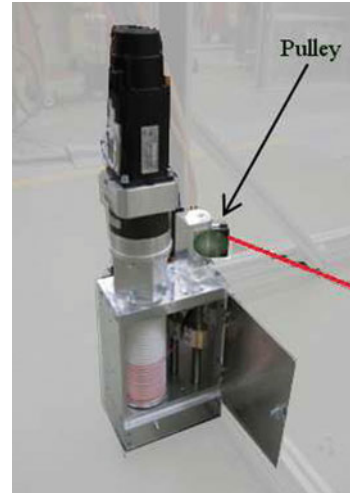
achieved in the past are good, performance can still be improved. Methods include continuous calibration and inclinometers [4], general geometric calibration [8], and external sensors such as an expensive non-contact laser scanning system for Cartesian metrology used by the NIST Robocrane [13].

Robot kinematic models, both forward and inverse kinematics, have a direct impact on accuracy. Previous implementations [10] have usually assumed perfect points as base and platform connections. In practice cables are often guided along a pulley as shown in Fig. 1.

Taking into account of such pulleys in kinematics has been shown in existing models [9], but such models have yet to be implemented in real-time.

Real-time calculations pose a frequent challenge for forward kinematics especially when optimization methods are used whose convergence is not guaranteed. Hence research into convergence and computation time has been conducted [15].

In this paper an algorithm that takes winch pulleys into account is reviewed and implemented in a real-time environment. To evaluate this implementation experiments into the accuracy and repeatability of the IPAnema robot were performed. These lead to marginal improvements. An angular variation test which can be applied to any parallel machine is also introduced to evaluate the accuracy of the two kinematic models against each other.

2 Robot Architecture

The algorithms were tested on the cable robot IPAnema, constructed at the laboratories of the Fraunhofer IPA. Figure 2 shows the IPAnema cable robot, in the configuration during the experiment. The numbers indicate the winch positions, and the
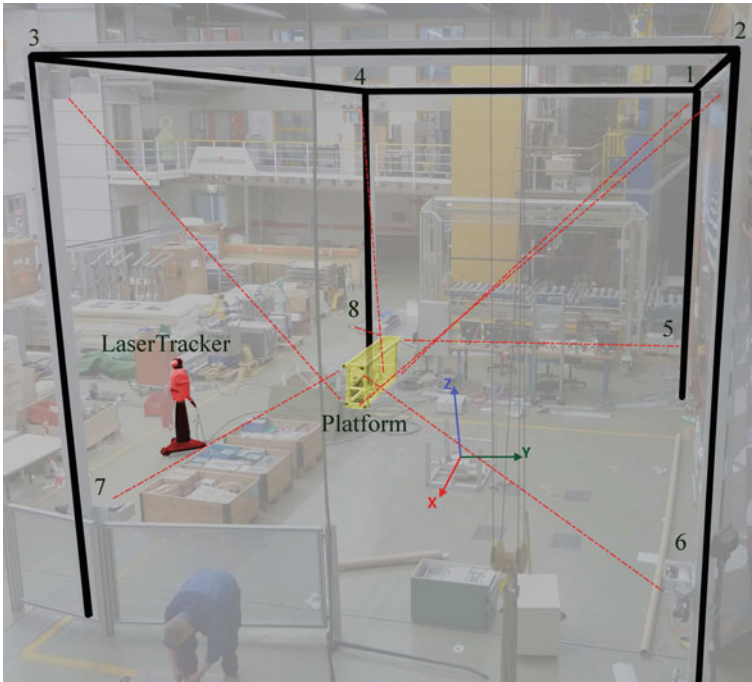
**Fig. 2** The Robot IPAnema pictured with the Leica LaserTracker

Table 1 Robot geometrical parameters: base vector $\mathbf{a}_i$ and platform vector $\mathbf{b}_i$

Cable i	Base vector $\mathbf{a}_i$ in (m)			Platform vector $\mathbf{b}_i$ in (m)		
	x	y	z	x	y	z
1	[−4.277	2.950	4.604]^T	[−0.653	0.201	−0.085]^T
2	[4.335	2.951	4.480]^T	[0.641	0.196	−0.102]^T
3	[4.029	−2.736	4.609]^T	[0.639	−0.052	−0.092]^T
4	[−3.967	−2.733	4.737]^T	[−0.634	−0.117	−0.058]^T
5	[−4.346	2.902	0.515]^T	[−0.759	0.200	0.410]^T
6	[4.255	2.925	0.372]^T	[0.763	0.192	0.402]^T
7	[3.952	−2.766	0.424]^T	[0.756	−0.014	0.406]^T
8	[−4.033	−2.766	0.573]^T	[−0.750	−0.012	0.423]^T

connecting cables are highlighted in red. In this exact configurations the dimensions
(Table 1) were measured.

The dimensions were determined very accurately using a Leica LaserTracker.
With this optical device the absolute position of a reflector can be determined with
an accuracy of $\pm 15\,\mu\text{m} + 6\,\mu\text{m/m}$.

Fig. 3 Standard kinematik description
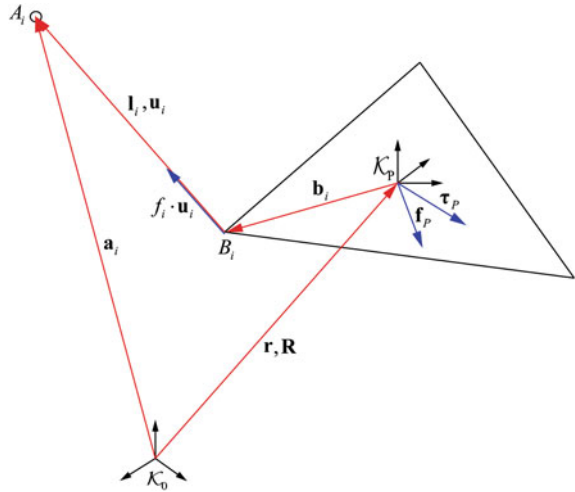
3 Extended Kinematics for Cable Driven Robots

For reference, the basic kinematic algorithms are quickly introduced. On Fig. 3 the position of anchor points on the base and the robot platform are described by vector $\mathbf{a}_i$ and $\mathbf{b}_i$ respectively, and give the rope vector $\mathbf{l}_i$ for a given pose. The platform vectors $\mathbf{b}_i$ are in the coordinate system of the platform which is defined by the Cartesian vector $\mathbf{r}$ and rotation matrix $\mathbf{R}$. Since the length of the cables in the standard kinematic model is $l_i = \|\mathbf{l}_i\|_2$ simple vector algebra yields

$$\mathbf{a}_i - \mathbf{r} - \mathbf{R}\mathbf{b}_i = \mathbf{l}_i \qquad (1)$$

$$\|\mathbf{a}_i - \mathbf{r} - \mathbf{R}\mathbf{b}_i\|_2 = l_i \qquad (2)$$

$$\text{for i} = 1, \ldots, \text{m}.$$

This suffices for the general computation of inverse kinematics under the assumption that all cable connections are ideal points. This is also the basis for the standard forward kinematics used in [10]. Here, m functions

$$\Psi_i \, (\mathbf{l}, \mathbf{r}, \mathbf{R}) = (\|\mathbf{a}_i - \mathbf{r} - \mathbf{R}\mathbf{b}_i\|_2)^2 - l_i^2 \qquad (3)$$

$$\text{for } i = 1, \ldots, m.$$

are combined to give

$$\phi \, (\mathbf{l}) = \min_{\mathbf{r}, \mathbf{R}} \sum_{i=0}^{m} \Psi_i \, (\mathbf{l}, \mathbf{r}, \mathbf{R}), \qquad (4)$$

which will minimize $\mathbf{r}$, $\mathbf{R}$ for a given length vector $\mathbf{l} = [l_1, \ldots, l_m]^T$. In very simple terms, this is almost equivalent to considering the pre-tensed cables as linear springs and minimizing their potential energy. Further factors such as cable stiffness need to be taken into account for this to truly apply, but in principle the approach would be almost identical.

To solve the forward kinematic problem, a Levenberg-Marquardt (LM) optimization algorithm is used which can be found in [5]. This solver minimizes the objective function $\phi(\mathbf{l})$ from (4) by iterative procedure

$$\left(\mathbf{J}(\mathbf{l}) \mathbf{J}^T(\mathbf{l}) + \mu \mathbf{I} \right) \mathbf{h} = -\mathbf{J}^T(\mathbf{l}) \phi(\mathbf{l}). \tag{5}$$

Where μ is a damping parameter, $\mathbf{J}(\mathbf{l})$ is the Jacobian of $\phi(\mathbf{l})$ in dimension x, y, z and rotation angles a, b, c

$$\mathbf{J}(\mathbf{l}) = \begin{bmatrix} \frac{\partial \Psi_1}{\partial x} & \cdots & \frac{\partial \Psi_m}{\partial x} \\ \frac{\partial \Psi_1}{\partial y} & \cdots & \frac{\partial \Psi_m}{\partial y} \\ \frac{\partial \Psi_1}{\partial z} & \cdots & \frac{\partial \Psi_m}{\partial z} \\ \frac{\partial \Psi_1}{\partial a} & \cdots & \frac{\partial \Psi_m}{\partial a} \\ \frac{\partial \Psi_1}{\partial b} & \cdots & \frac{\partial \Psi_m}{\partial b} \\ \frac{\partial \Psi_1}{\partial c} & \cdots & \frac{\partial \Psi_m}{\partial c} \end{bmatrix}^T \tag{6}$$

and $\mathbf{h}$ is each consecutive step. This does not guarantee a solution, but has shown good results in practice at very fast computational speeds. The lack of guaranteed solution is a severe impact on real-time capability. For this reason a maximum number of iteration steps (currently 100 steps) is implemented. This does not guarantee a solution, but ensures that there exists a guaranteed maximum computation time. In practice this maximum has not been reached, and the algorithm runs robustly in real time.

The extended kinematics takes into account of the pulley mechanism illustrated in Fig. 1. Where the equation for the length of cable i now reads

$$l_i = \theta_i r_p + l_{fi}. \tag{7}$$

Here the angle θ_i and the direct length from pulley exit point C_i to the platform anchor point $\mathbf{B}_i$ are used to determine total cable length. $\mathbf{B}_i$ is needed in the global coordinate frame simply

$$\mathbf{B}_i = \mathbf{r} + \mathbf{R} \mathbf{b}_i. \tag{8}$$

There are many ways which can yield the parameters for (7) using basic trigonometry on the triangles formed by points: M_i, B_i, C_i and A_i (origin of coordinate system $\mathcal{K}_A$ denoted by vector $\mathbf{a}_i$). The one derived in [11] is applied here.

This evaluation was used in the implementation of both forward and inverse kinematics, but deviates from the in [11] proposed method, in that it does not use

transformation matrices to find the necessary lengths but only the vector $\mathbf{k}_{Az}$ defined by the winch coordinate system. This is necessary to fulfill the real-time constraints, which need the equations to be evaluated as efficiently as possible. Eliminating evaluation of the angle of rotation of the pulley mechanism around axis k_{Az} and subsequent matrix evaluations is expected to give faster computations. This is done by evaluating the vector $\mathbf{m}_i$ by

$$\mathbf{m}_i = \mathbf{a}_i + r_p \hat{\mathbf{w}} \tag{9}$$

where $\mathbf{w}$ is a vector from the origin of $\mathcal{K}_A$ in the direction of M_i which is found by

$$\mathbf{w} = (\mathbf{k}_{Az} \times (\mathbf{B}_i - \mathbf{a}_i)) \times \mathbf{k}_{Az}. \tag{10}$$

Hence

$$d_i = \|\mathbf{B}_i - \mathbf{m}_i\|_2 \tag{11}$$

and b_z is the distance from $\mathbf{m}_i$ to $\mathbf{B}_i$ along $\mathbf{k}_{Az}$ given by

$$b_z = \|\mathbf{k}_{Az} \cdot (\mathbf{B}_i - \mathbf{a}_i)\|_2 \tag{12}$$

which helps to find

$$l_{fi} = \sqrt{r_p^2 \times b_z^2} \tag{13}$$

and finally

$$\theta_i = \arccos \frac{l_{fi}}{d_i} + \arccos \frac{b_z}{d_i}. \tag{14}$$

This gives us all the dimensions needed to evaluate the inverse kinematics for each cable using Eq. (7).

As the same method is used for the forward kinematics, the extended forward kinematics simply replacing $\|\mathbf{a}_i - \mathbf{r} - \mathbf{R}\mathbf{b}_i\|_2$ in Eq. (4) with the evaluation in Eq. (7) to give $\tilde{\Psi}_i$ which yields

$$\tilde{\phi}(\mathbf{l}) = \min_{\mathbf{r},\mathbf{R}} \sum_{i=0}^{m} \tilde{\Psi}_i \left(\mathbf{l}, \mathbf{r}, \mathbf{R}, \mathbf{k}_{Az}, r_p\right). \tag{15}$$

The initial guess for the LM optimizer is identical to the interval based method proposed in [10]. The full equation is implemented in the programming language c results in >50 lines of source code and the analytic Jacobian matrix >150, and is therefore not provided here (Fig. 4).
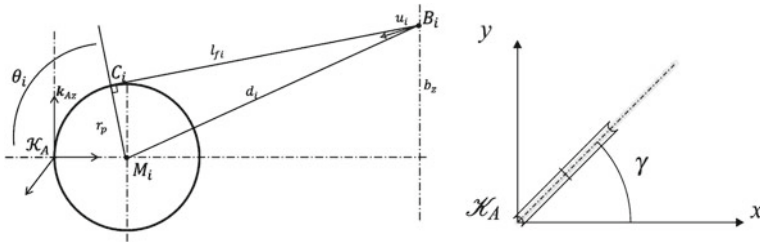
Fig. 4 Kinematics of cable i

4 Validation

4.1 Computation and Convergence

To test real-time capability of this algorithm, it was first simulated on a desktop PC. This simulation used the geometric parameters measured for the accuracy evaluation, shown in Table 1.

The radius of the pulley was assumed to be identical for each winch and measured at $r_p = 21$ mm. The orientation of the winches can be seen in Fig. 2 and was assumed to be aligned perfectly with the axes. This means winches 1 and 5 were pointing in the negative x direction, winches 2 and 6 in the positive x direction, and winches 3, 4, 7, and 8 in the negative y direction.

For three different magnitudes of noise (0.1, 0.5 and 1 mm) the simulation was conducted for 5,000 positions chosen at random in the presumed workspace of the robot.

The continuous re-evaluation of the Eq. (15) through the LM solver poses the greatest risk for real-time capability of the algorithm. Depending on the number of iterations this can involve very many computations. Hence, the number of iterations of the LM solver is evaluated. Figure 5 shows the number of iterations for each simulated position. These are slightly worse than the results for the standard kinematics shown in [10], but are generally very reasonable, rarely exceeding 20 iterations, even for 1 mm noise. A few times the maximum number of iterations of 100 was reached, but these were most likely poses at the edge or beyond the workspace.

For this comparison it is important to note that convergence is very dependent on geometry and individual poses. Especially poses with big orientation differences are often at the edge of the workspace and will increase the number of necessary iterations.

The average position error of the platform shown in Fig. 6 was almost identical to that seen for the standard model, and is in the same order of magnitude as the noise error applied to the cables.

When using the analytically derived Jacobian matrix, the calculations times on a desktop pc ranged between 80 and 130 μs per evaluation. While this does not guarantee real-time capability, it is a good indication that this algorithm can be run

(a)

(b)

(c)
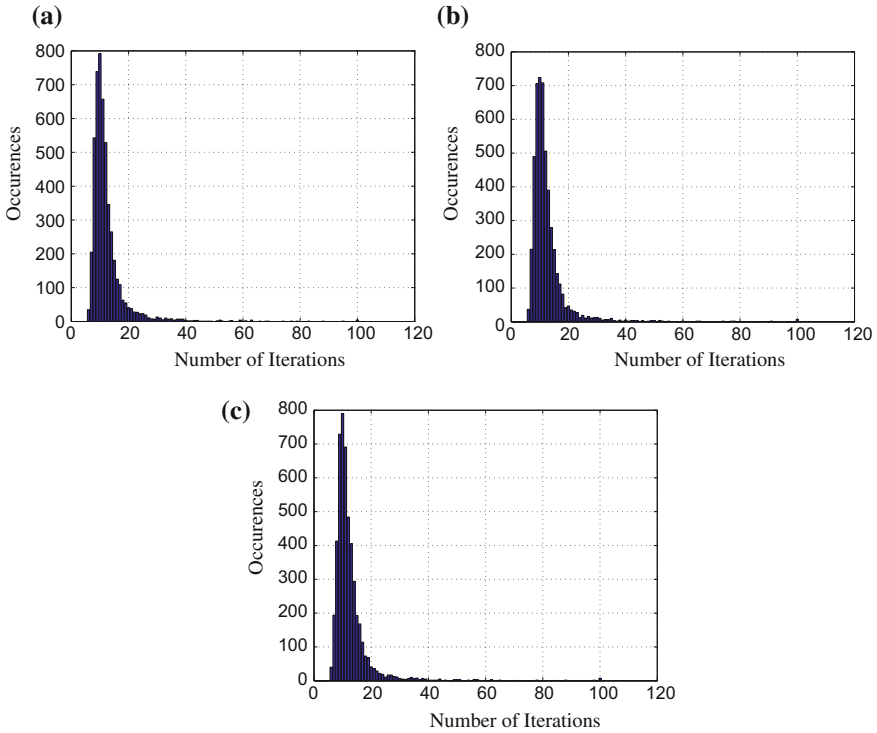
Fig. 5 Histograms showing number of iterations for forward kinematics optimizer. **a** Noise of 0.1 mm, **b** Noise of 0.5 mm, **c** Noise of 1 mm

in real-time. The test in practice proved successful, and so accuracy and repeatability measurements could be made. In fact, so far the algorithm running on the actual robot experienced no missed steps, when poses and trajectories of the robot were within the workspace.

4.2 Accuracy and Repeatability

The same LaserTracker used to determine the robot dimensions, was used to measure the accuracy and repeatability. Both kinematic models were tested in the exact same environment. Neither LaserTracker or the robot was moved, after the dimensions $(\mathbf{a}_i, \mathbf{b}_i)$ were established. The reflector denoting the origin of both the global (at the platform home position) and the platform coordinate system was not altered throughout the experiment. This significantly increases the precision of the results as any systematic errors will be the same for both sets of data. Any calibrating of the
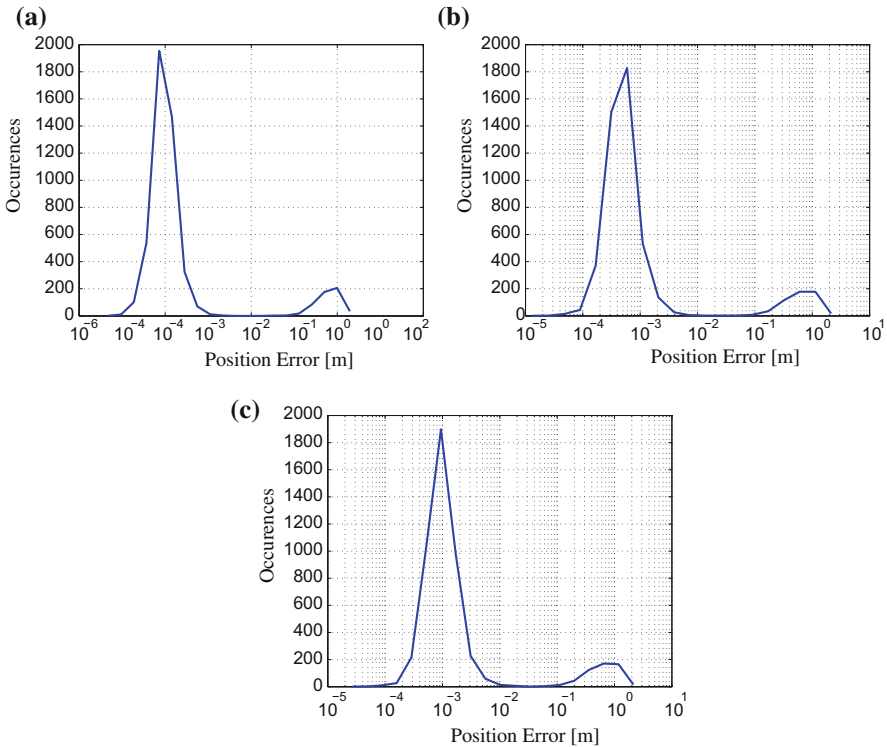
Fig. 6 Histograms showing number of iterations for forward kinematics optimizer. **a** Noise of 0.1 mm, **b** Noise of 0.5 mm, **c** Noise of 1 mm

LaserTracker would cause inaccuracies, as the measurement of reference points can add many forms of error to the calculations.

Accuracy and Repeatability were measured according to the ISO 9283 standard. Hence each pose was measured with 30 repetitions and through the same approach trajectory. The standard also defines testing conditions, which were adhered to. The calculations for the can be found in [6]. All poses had the same orientation of $a = b = c = 0$.

As expected, the absolute accuracy was improved for the extended kinematic algorithm, but the repeatability stayed very much the same. Table 2 shows the results for the extended kinematic to be on average an improvement of roughly 21 %. Unfortunately this is lower than was hoped, and for some poses little to no improvement was seen. This indicates that other inaccuracies play an equally important role. The elasticity in the cables, or the inaccuracies in the drive chain of each winch would therefore provide an equal positioning error of the same magnitude ≈5 mm.

Table 2 Absolute positioning accuracy of standard and extended kinematics

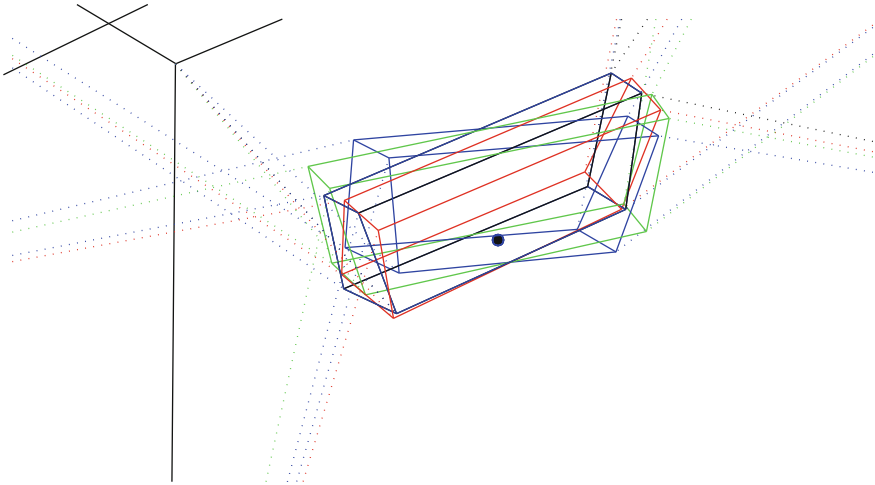| Pose in (mm)			Standard kinematics (mm)	Extended kinematics (mm)
x	y	z		
[0,	−1000,	1000]	11.2867	11.9711
[−800,	−1000,	1000]	11.6281	12.4002
[−800,	1000,	1000]	24.5868	17.7851
[800,	1000,	1000]	21.8419	17.8160
[800,	−1000,	1000]	12.1822	15.1232
[−800,	1000,	2500]	37.8695	21.6268
[800,	1000,	2500]	35.2317	21.0895
[800,	−1000,	2500]	24.0249	21.5672
[−800,	−1000,	2500]	21.9880	18.9035
[0,	1000,	1000]	22.5879	16.6677
Average:			22.3228	17.4950

Table 3 Repeatability of pose for standard and extended kinematics

Pose in (mm)			Standard kinematics (mm)	Extended kinematics (mm)
x	y	z		
[0,	−1000,	1000]	0.6472	0.8713
[−800,	−1000,	1000]	0.5530	0.8137
[−800,	1000,	1000]	0.7931	0.6726
[800,	1000,	1000]	0.7131	0.5677
[800,	−1000,	1000]	0.4130	0.5095
[−800,	1000,	2500]	0.7690	0.4123
[800,	1000,	2500]	0.7753	0.4112
[800,	−1000,	2500]	0.3559	0.3057
[−800,	−1000,	2500]	0.6080	0.2601
[0,	1000,	1000]	0.3076	0.2257
Average:			0.5935	0.5050

4.2.1 Angular Variation Test

Another test that was conducted was on the orientation accuracy. Since the platform origin was consistently measured, when the platform orientation is changed but the position x, y, z is not, this origin should not move. This concept is illustrated in Fig. 7 where the origin indicated by the thick dot is identical for four different orientations. This test can be implemented on any parallel kinematic machine, provided one can measure the origin about which the platform rotations are defined easily (Table 3).

Thirty different orientations were tested with angles ranging in the ranges $-5° < a, b, c < 5°$. Then the same calculations as for repeatability, as in the previous section, was used to evaluate the discrepancy in position between the

Fig. 7 Four orientations with the identical origin for the platform coordinate system at pose [0, 0, 1,000]

Table 4 Deviation in position at a change in orientation		Standard kinematics	Extended kinematics
	Average	2.6287	2.1099

different orientations. Table 4 shows that although there is a slight improvement for the extended kinematics, this is only 0.5 mm and therefore very marginal.

5 Conclusion

This paper presented the successful implementation of extended forward kinematics taking into account winch pulleys in a real-time system. In addition to providing the basic algorithm which can be implemented for any given robot structure provided it is theoretically overconstrained and has a reasonable workspace.

The algorithm is based on a LM optimizer which uses the Jacobian of objective function $\phi()$ the to determine a solution. The successful operation of the IPAnema robot with this extended kinematic proves the applicability, and real-time capability.

Tests were conducted to investigate the improvement on accuracy through the use of extended kinematics. As expected absolute accuracy was improved while the relative accuracy remained similar. While there were measurable improvements, these were not as good as initially hoped. This means other imprecisions, inaccuracies, uncertainties in the robot have a similar impact, on the absolute accuracy, as the pulley mechanism. In addition a novel test was introduced and conducted to inves-

tigate orientational accuracy. This showed only marginal improvements when using extended kinematics.

To further improve the accuracy of the cable robot IPAnema, other factors need to be considered such as the elasticity of the cables. This can be the subject of ongoing research.

References

1. Dietmaier, P.: The stewart-gough platform of general geometry can have 40 real postures. In: ARK, pp. 7–16. Kluwer Academic Publishers, Salzburg (1998)
2. Husty, M.L.: An algorithm for solving the direct kinematic of stewart-gough-type platforms. Mech. Mach. Theory **31**(4), 365–380 (1996)
3. Jeong, J.W., Soo, H.K., Yoon, K.K.: Design and kinematic analysis of the wire parallel mechanism for a robot pose measurement. In: Proceedings of IEEE International Conference on Robotics and Automation, vol. 4, pp. 2941–2946. (1998) doi:10.1109/ROBOT.1998. 680740.http://ieeexplore.ieee.org/stamp/stamp.jsp?arnumber=680740
4. Joshi, S.A., Surianarayan, A.: Calibration of a 6-dof cable robot using two inclinometers. In: Performance Metrics for Intelligent Systems, pp. 3660–3665. Gaithersburg, Taipei (2003)
5. Lourakis, M.: levmar: Levenberg-marquardt nonlinear least squares algorithms in C/C++. www. ics.forth.gr/lourakis/levmar/ (Jul. 2004). Accessed on 10 Okt. 2011
6. ISO 9283 1998-04: Manipulating industrial robots—Performance criteria and related test methods (1998)
7. Merlet, J.P.: Solving the forward kinematics of a gough-type parallel manipulator with interval analysis. Int. J. Robot. Res. **23**(3), 221–235 (2004)
8. Miermeister, P., Pott, A.: Auto calibration method for cable-driven parallel robots using force sensors. In: Lenarčič,J., Husty, M. (eds.) Procceedings of the 13th International Symposium Advances in Robot Kinematics. Springer, Berlin (2012)
9. Miermeister, P., Pott, A.: Modelling and real-time dynamic simulation of the cable-driven parallel robot ipanema. In: European Conference on Mechanism Science (EuCoMeS 2010), pp. 471–478. Cluj-Napoca (2010)
10. Pott, A.: An algorithm for real-time forward kinematics of cable-driven parallel robots. In: 12th International Symposium on Advances in Robot Kinematics. Springer, Verlag (2010)
11. Pott, A.: Influence of pulley kinematics on cable-driven parallel robots. In: Lenarčič, J., Husty, M. (eds.) Procceedings of the 13th International Symposium Advances in Robot Kinematics. Springer, Berlin (2012)
12. Thomas, F., Ottaviano, E., Ros, L., Ceccarelli, M. (eds.): Uncertainty model and singularities of 3–2–1 wire-based tracking systems. Kluwer Academic Publishers, Caldes de Malavalla (2002)
13. Williams II, R.L., Snyder, B.M., Albus, J.S., Bostelman, R.V.: Seven-dof cable-suspended robot with independent metrology (2004)
14. Williams II, R.L.: Planar cable-suspended haptic interface: Design for wrench exertion (1999)
15. Yang, C., Huang, Q., Ogbobe, P., Han, J.: Forward kinematics analysis of parallel robots using global newton-raphson method. In: Second International Conference on Intelligent Computation Technology and Automation, 2009. ICICTA'09, vol. 3, pp. 407–410 (2009) doi:10.1109/ ICICTA.2009.564

Part VI
Calibration and Identification

An Identification Methodology for 6-DoF Cable-Driven Parallel Robots Parameters Application to the INCA 6D Robot

Ryad Chellal, Edouard Laroche, Loïc Cuvillon and Jacques Gangloff

Abstract This paper proposes a methodology for the identification of the combined kinematic and dynamic parameters of a 6-Degrees of Freedom (6-DoF) Cable-Driven Parallel Robots (CDPRs) model. This methodology aims to ensure that the errors on the kinematic parameters do not affect the performances of the dynamic parameters estimation step. The proposed methodology has been implemented on a 6-DoF INCA robot. The identified model fits the system behaviour with good accuracy, and should then be used for the synthesis and analysis of kinematic and dynamic position / vision control strategies.

1 Introduction
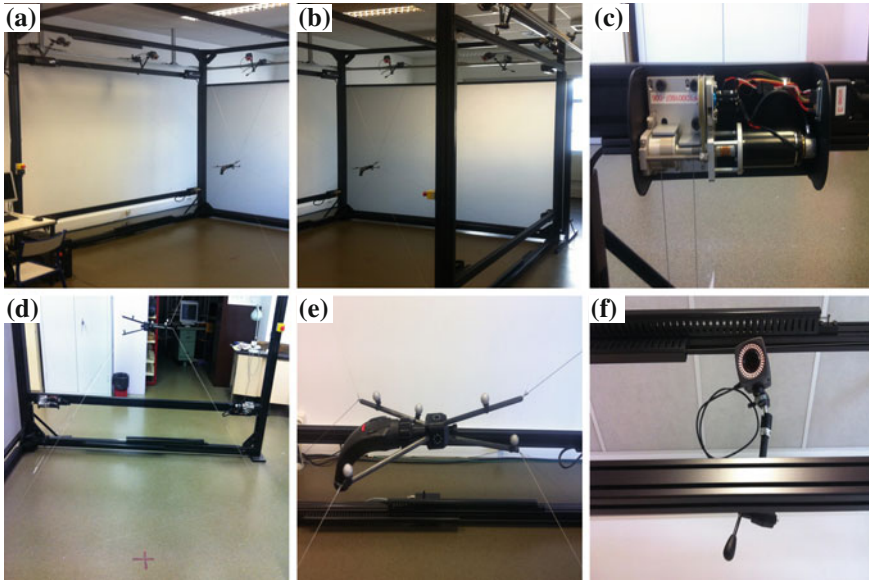
1.1 Parallel Cable-Driven Robots

The CDPRs are parallel robot manipulators in which the end-effector or also platform is connected to the base via cables, its movement resulting from the winding and unwinding of the cables around pulleys actuated by motors.

Compared to serial and parallel conventional manipulator robots actuated by rigid links, cable-actuated robots benefit from interesting features: they can reach a very large kinematic workspace, achieve movements at higher speeds due to the low total mass of the structure in movement, and also provide a modular or adjustable geometry to satisfy the performances of the performed tasks.

However, for cable-actuated robots, the cables can only exert tensile forces (positive tensions) [1]. This introduces static constraints in addition to the purely kinematic constraints present on the rigid link actuated parallel robots.

R. Chellal (✉) · E. Laroche · L. Cuvillon · J. Gangloff
LSIIT (UDS/UMR CNRS/INSAS), Strasbourg University,
Pole API bd S. Brand, 67400 Illkirch, Strasbourg, France
e-mail: ryad.chellal@lsiit-cnrs.unistra.fr

Fig. 1 Parallel cable-driven robot INCA 6D. **a** Cubic kinematic workspace (View 1). **b** Cubic kinematic workspace (View 2). **c** Motor (Maxon DC motor 148877) and the CDU/CBU mechanisms. **d** Driving/Balancing cables, balancing springs and pulleys. **e** End-effector. **f** Infrared camera

This type of robots is used in two major applications depending on the size of the kinematic workspace on which they operate:

- Applications with a small kinematic workspace: this is typically, the case of haptic interfaces in virtual reality.
- Applications with a large kinematic workspace: where they are used to move cameras over long distances, on sites of sport matches or shows.

1.2 Haptic Interface INCA

The INCA robot (Fig. 1), developed by the Haption company,[1] is a haptic interface with force feedback specifically designed to test the manipulation of objects in virtual reality environments. In the 3D version using 4 cables, only the forces are solicited for the translational motions. The 6D version with 8 cables considered here, can also render the moments for the rotational motions.

In the present work, the INCA robot is used as a manipulator to address the problems of the manipulation of cable-driven robots.

The INCA 6D robot has a $3 \times 3 \times 3$ m^3 cubic configuration kinematic workspace (Fig. 1a, b), where each of the 8 motors (Fig. 1c) is placed on one of the 8 vertices of

---

[1] See the website: http://www.haption.com/site/index.php/fr/ for an illustration.

the cube. Each of the 8 driving cables is attached from the driving winch of a Cable Driving Unit (CDU) (mechanism for storing and winding/unwinding the driving cables (Fig. 1c)) to the end-effector (Fig. 1e) through a pulley which represents the output point of the driving cable (Fig. 1d).

Each of the 8 balancing cables is attached from the balancing winch of a Cable Balancing Unit (CBU) (mechanism for storing and winding/unwinding the balancing cables (Fig. 1c)) to a balancing spring (Fig. 1d) by a pulley, in order to ensure a pretension in the driving cables when no torques are applied, and also to maintain a continuous variation of the cable tensions when the motors are powered.

The sensors available on the system are:

- Interoceptive sensors: 8 optical encoders to measure the angular positions of the motors, 8 angular potentiometers for initial calibration of the robot pose, and 8 current sensors to measure the effective currents of the motors.
- Exteroceptive sensors: 6 infra-red cameras (Fig. 1f) fixed around the robot, allow the pose (position and orientation) reconstruction of objects defined by their own geometry inside the kinematic workspace, that is specified by a system of passive markers (see Fig. 1e for the end-effector markers). This vision system will be used soon to perform a visual servoing positioning task with the INCA 6D robot.

1.3 Problematic and Content of the Paper

This paper proposes a methodology to identify the combined kinematic and dynamic parameters of a model of 6-DoF CDPRs, that has been validated experimentally on the INCA robot on its 6D version.

Firstly, we expose the structure of a physical model for the 6-DoF CDPRs based on plausible assumptions for this type of system.

Secondly, we describe a methodology to identify separately the kinematic and dynamic parameters, requiring the measurement of the motors angular positions (measured by optical encoders) and the end-effector pose (provided from a system of cameras). That methodology should allows us to reject the influence of errors on the kinematic parameters from the dynamic parameters estimation stage. The existent methods and their correspondent resolving algorithms to estimate the robot parameters are briefly introduced.

Finally, the identification results are compared to the experimental data to validate the proposed identification methodology. Problems that we encountered to improve the accuracy of the model are also mentioned.

2 Physical Model

2.1 Modelling Assumptions

We differentiate most of the works that considered linear cables [2–4] from the works on very long cables size taking into account the geometry of non-linear cables [5–7].

In our case, the model is intended for the synthesis and analysis of control laws to achieve high bandwidths of the end-effector. So assumptions are necessary in order to obtain a model of a reasonable complexity:

- Given the size of the INCA 6D robot, it is considered that the cables are massless to allow them to remain linear, and perfectly stiff or rigid (without elongation). So inertias and linear spring stiffness of the cables can be ignored. The problems of vibrations of cable manipulators due to cable flexibilities are investigated in [8, 9].
- We consider an uniform winding / unwinding of the cables. The potential problems of the winding / unwinding of cables using the CDU mechanisms were examined in [3], to minimise the dynamic effect of the cables between the CDU and the pulley on the system dynamic model.

2.2 Kinematics Modelling

2.2.1 Position Kinematics

A position kinematic mapping function is needed to relate the end-effector pose $X_e = [P_e \ \Phi_e]^T$ (including the position P_e and orientation Φ_e) to the motors angular positions vector $\theta = [\theta_1 \ \theta_2 \ \dots \ \theta_n]^T$.

The cable length $L_i = \| \ O_i E_i \ \|_2$ can be calculated by the Euclidean norm between the position P_{E_i} of the moving attachment point E_i of the driving cable i to the end-effector, and the position P_{O_i} of the fixed vertex O_i (Fig. 2a):

$$L_i = f_i(X_e) = \| \ P_{E_i} - P_{O_i} \ \|_2 = \| \ P_e + r_i - P_{O_i} \ \|_2 \qquad (1)$$

in which $r_i = O_e E_i$ is the radius vector of the attachment point E_i (Fig. 2a). This radius expressed in a chosen reference frame R_o can be calculated knowing the rotation matrix $^o R_e$ between R_o and the frame attached to the end-effector R_e where the radius $^e r_i$ is constant such as: $^o r_i = {}^o R_e \, {}^e r_i$.

The rotation matrix $^o R_e$ can be decomposed into three successive pure rotations Roll-Pitch-Yaw (R-P-Y) [10, 11] of angles (ϕ_r, ϕ_p, ϕ_y) respectively around the principal axes (X_o, Y_o, Z_o) of R_o. Under this minimal representation of the orientation,
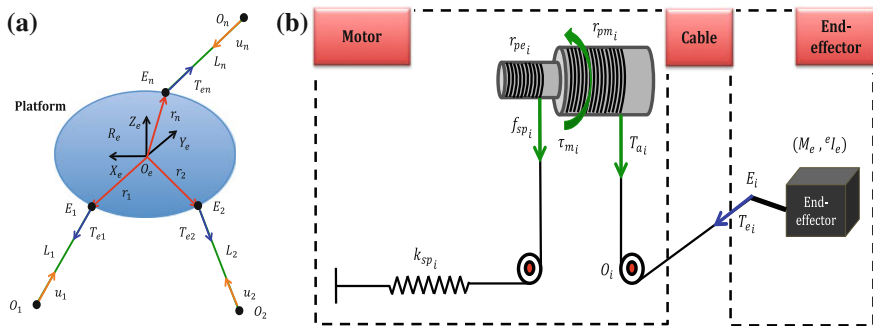
Fig. 2 Diagrams of the 6-DoF CDPRs. **a** Kinematics/Statics diagram of the 6-DoF CDPRs. **b** Dynamics diagram of the 6-DoF CDPRs with additional CBU of the INCA 6D robot

the relationship between $^{o}R_e$ and $\Phi_e = [\phi_r \ \phi_p \ \phi_y]^T$ is:

$$
{}^{o}R_e = \begin{bmatrix} c_y c_p & c_y s_p s_r - s_y c_r & c_y s_p c_r + s_y s_r \\ s_y c_p & s_y s_p s_r - c_y c_r & s_y s_p c_r - c_y s_r \\ -s_p & c_p s_r & c_p c_r \end{bmatrix} \tag{2}
$$

with $s_k = \sin \phi_k$ and $c_k = \cos \phi_k$, k standing for r, p or y.

Defining the reference of the motor position $\theta_{io} = 0$ from the initial pose of the end-effector $X_{eo} = [P_{eo} \ \Phi_{eo}]^T$, that by convention increases / decreases during the winding/unwinding of the driving cable i around its associate driving winch of radius r_{pm_i}, the motor angular position θ_i is given by:

$$
\theta_i = -\Delta L_i \, / \, r_{pm_i} = -(L_i - L_{io}) \, / \, r_{pm_i} \tag{3}
$$

where the initial cable length L_{io} is deduced by Eq. (1) from the initial pose X_{eo}.

Hence the Inverse Position Kinematic Model (IPKM) is given by:

$$
\theta = f_\theta(Xe) = -R_{pm}^{-1} \, (L - L_o) = -R_{pm}^{-1} \, (f(X_e) - f(X_{eo})) \tag{4}
$$

with the cables lengths vector $L = [L_1 L_2 \dots L_n]^T$ and the diagonal matrix of the driving winches radius $R_{pm} = \mathrm{diag}(r_{pm_1}, \dots, r_{pm_n})$.

2.2.2 Velocity Kinematics

A velocity kinematic mapping allows to relate the end-effector velocity $V_e = [v_e \ w_e]^T$ (including the linear v_e and angular w_e velocities) to the motors angular velocities vector $\dot{\theta} = [\dot{\theta}_1 \ \dot{\theta}_2 \ \dots \ \dot{\theta}_n]^T$.

The time derivative of the Eq. (1), provides the well-know inverse kinematics Jacobian matrix J defined for conventional parallel robots [12] as follows:

$$\dot{L} = J(X_e)\, V_e \tag{5}$$

where $\dot{L} = [\dot{L}_1\ \dot{L}_2\ \ldots\ \dot{L}_n]^T$ is the cables translational velocities vector, and the ith row J_i of the $(n \times 6)$ Jacobian matrix is expressed by:

$$J_i(X_e) = [u_i{}^T\ (r_i \times u_i)^T] \tag{6}$$

with $u_i = O_i E_i\ /\ \|\ O_i E_i\ \|$ the unit direction vector of the ith driving cable (Fig. 2a).

Therefore, we can determine the motors velocities vector $\dot{\theta}$ by taking the time derivative of the Eq. (4), leading to the Inverse Velocity Kinematic Model (IVKM):

$$\dot{\theta} = J_\theta(X_e)\, V_e = -R_{pm}^{-1}\, J(X_e)\, V_e \tag{7}$$

The angular velocity w_e can be related to the derivative of the chosen orientation representation $\dot{\Phi}_e$, using the Jacobian matrix J_{rpy}. For instance using the composition law of the angular velocities such as:

$$w_e = \begin{bmatrix} c_y\, c_p & -s_y & 0 \\ s_y\, c_p & c_y & 0 \\ -s_y & 0 & 1 \end{bmatrix} \dot{\Phi}_e = J_{rpy}\, \dot{\Phi}_e \tag{8}$$

2.3 Statics Modelling

The resultant of external wrenches F_e (including the forces f_e and moments m_e) on the center of mass O_e of the end-effector rigid body of mass M_e, are dues to both the cables tensions $T_e = [T_{e1}\ T_{e2}\ \ldots\ T_{en}]^T$ applied on the end-effector side (Fig. 2a), and the gravity acceleration G:

$$F_e = W(X_e)\, T_e + M_e\, G\, [0\ 0\ -1\ 0\ 0\ 0]^T \tag{9}$$

where $W(X_e)$ is the wrench Jacobian matrix such as: $W(X_e) = -J^T(X_e)$.

2.4 Dynamics Modelling

The CDPRs are mainly composed of 2 kinds of subsystems connected by cables (Fig. 2b):

- End-effector.
- Actuators (including the motors and the CDU / CBU loads).

First, we consider the model of each of the 2 subsystems separately, and finally formulate the CDPR systems dynamics, including the whole of the 2 subsystems considered.

2.4.1 End-Effector Dynamics

The use of the Newton-Euler dynamics formulation to the end-effector rigid body subsystem (Fig. 2b), written on the center of mass of the end-effector O_e [10, 11] gives:

$$F_e = \begin{bmatrix} M_e \, I_{3\times3} & O_{3\times3} \\ O_{3\times3} & I_e \end{bmatrix} \dot{V}_e + \begin{bmatrix} O_{3\times1} \\ w_e \times (I_e \, w_e) \end{bmatrix} = A_e \, \dot{V}_e + B_e \quad (10)$$

with :

M_e mass of the end-effector.
I_e moment of inertia tensor (inertia matrix) of the end-effector with respect to the center of mass O_e.

The moment of inertia tensor I_e expressed in R_o can be calculated from the constant moment of inertia tensor ${}^e I_e$ expressed in R_e knowing the rotation matrix ${}^o R_e$ such as: ${}^o I_e = {}^o R_e \, {}^e I_e \, {}^o R_e{}^T$.

2.4.2 Actuators Dynamics

Applying the Newton-Euler or Euler-Lagrange formulations to the ith actuator subsystem constituted by the lumped motor shaft and the driving/balancing winches (Fig. 2b), leads to the dynamic equation:

$$j_{eq_i} \ddot{\theta}_i + f_{veq_i} \ddot{\theta}_i + f_{seq_i} \, \mathrm{sign}(\ddot{\theta}_i) + k_{eq_i} \theta_i = \tau_{mi} - r_{pm_i} (T_{ai} - T_{aoi}) \quad (11)$$

where:

j_{eq_i} equivalent inertia moment of the ith actuator.
f_{veq_i}, f_{seq_i} equivalent viscous and Coulomb friction coefficients of the ith actuator.
k_{sp_i} stiffness coefficient of the ith balancing spring connected to the balancing winch via a balancing cable.

with the equivalent rotational stiffness $k_{eq_i} = k_{sp_i} \, r_{pe_i}{}^2$, r_{pe_i} being the radius of the balancing winch, and the cable pretension $T_{aoi} = k_{spr_i} \, L_{oi}$.

The applied motor torque τ_{mi} is proportional to the effective motor current i_{mi} with the electromechanical constant k_{emi}:

$$\tau_{mi} = k_{emi} \, i_{mi} \quad (12)$$

The global actuators dynamics is obtained by combining the dynamic model of
the n actuators:

$$J_{eq}\,\ddot{\theta} + F_{veq}\,\dot{\theta} + F_{seq}\,sign(\dot{\theta}) + K_{eq}\,\theta = \tau_m - R_{pm}\,(T_a - T_{ao}) \qquad (13)$$

where :

$$\begin{cases} J_{eq} &= \mathrm{diag}(j_{eq_1}, j_{eq_2}, \ldots, j_{eq_n}) \\ F_{veq} &= \mathrm{diag}(f_{veq_1}, f_{veq_2}, \ldots, f_{veq_n}) \\ F_{seq} &= \mathrm{diag}(f_{seq_1}, f_{seq_2}, \ldots, f_{seq_n}) \\ K_{eq} &= \mathrm{diag}(k_{eq_1}, k_{eq_2}, \ldots, k_{eq_n}) \end{cases} \quad \begin{cases} T_a = [T_{a1}\ T_{a2}\ \ldots\ T_{an}]^T \\ \tau_m = [\tau_{m1}\ \tau_{m2}\ \ldots\ \tau_{mn}]^T \end{cases}$$

2.4.3 System Dynamics

We now formulate the overall system dynamics, including the end-effector and the
actuators subsystems dynamics.

Under the assumption that the cables are massless, the tensions applied by the
cables on the end-effector T_e and on the actuators T_a are equal:

$$T_e = T_a = T \qquad (14)$$

Combining the relationships of the Eqs. (4), (7), (9), (10), (13) and (14) allows
us to derive the CDPR systems Direct Dynamic Model (DDM) projected in the
operational space:

$$M_x\,\dot{V}_e + B_e + F_{vx}\,V_e + F_{sx}\,sign(R_{pm}^{-1}\,J(X_e)\,V_e) + K_x\,f(X_e) + G_x = F_{ev} \qquad (15)$$

under the n constraints:
$$T(\tau_m, \theta, \dot{\theta}, \ddot{\theta}) \; > \; 0$$

where the dynamical parameters matrices projected in the operational space are:

$$\begin{cases} M_x &= A_e + J^T(X_e)\,R_{pm}^{-1}\,J_{eq}\,R_{pm}^{-1}\,J(X_e) \\ F_{vx} &= J^T(X_e)\,R_{pm}^{-1}\,F_{veq}\,R_{pm}^{-1}\,J(X_e) + J^T(X_e)\,R_{pm}^{-1}\,J_{eq}\,R_{pm}^{-1}\,\dot{J}(X_e, V_e) \\ F_{sx} &= J^T(X_e)\,R_{pm}^{-1}\,F_{seq} \\ K_x &= J^T(X_e)\,R_{pm}^{-1}\,K_{eq}\,R_{pm}^{-1} \\ G_x &= M_e\,G\,[0\,0\,-1\,0\,0\,0]^T \end{cases}$$

and the input term of virtual forces F_{ev} meaning the external forces / moments acting
on the end-effector resulting from the effective applied motors torques vector τ_m is:

$$F_{ev} = W(X_e)\,R_{pm}^{-1}\,\tau_m$$

3 Parameters Identification

We deal in this section with the problem of the parameters identification of robots, in order to improve the model accuracy.

Some related works have been done for the rigid links manipulator robots, concerning the kinematic parameters identification, we can mention [13] for the parallel robots. While the works that focused on the dynamic parameters identification were largely presented in [14] for the electromechanics systems in general and for the serial robots particularly, the case of parallel robots is addressed in [15].

Considering that the CDPRs kinematics completely defined by the Eqs. (4) and (7) is needed to compute the CDPRs dynamics in Eq. (15), the kinematic and dynamic parameters are definitively coupled into the DDM. In order to avoid the influence of the errors on the kinematic parameters from the dynamic parameters estimation stage, we propose to identify these parameters separately in 2 steps described below:

- Step 1: The kinematic parameters are first estimated using the IPKM.
- Step 2: The dynamic parameters are then estimated from the DDM, using the identified kinematic parameters.

3.1 Kinematic Parameters Identification

In order to obtain an accurate kinematic positioning of the end-effector through the kinematic workspace, the vector of the kinematic parameters x_K to be identified, can be estimated leading to $\widehat{x}_K$ by minimising the following kinematic identification error criterion $E(x_K)$ defined for a number of samples N_s at a sampling time T_s:

$$E(x_K) = \sum_{i=1}^{n} \sum_{k=1}^{N_s} e_{ik}(x_k) = \sum_{i=1}^{n} \sum_{k=1}^{N_s} (\theta_{ik} - \widehat{\theta}_{ik}(x_K))^2 \qquad (16)$$

with:

$e_{ik}(x_K) = e_i(t = k\,T_s, x_K)$ kinematic identification error.
$\theta_{ik} = \theta_i(t = k\,T_s)$ motor position measurements.
$\widehat{\theta}_{ik}(x_K) = \widehat{\theta}_i(t = k\,T_s, x_K)$ motor position estimations using the IPKM.

The problem of the minimisation of Eq. (16) criterion is typically a non-linear least squares optimisation problem, with the objective function $E(x_K)$. This problem could be solved iteratively using a numerical algorithms such as: gradient descent, Gauss-Newton or Levenberg-Marquardt in a more common version.

3.2 Dynamic Parameters Identification

The identification of the dynamical parameters of robots is a difficult problem, since the dynamic of these Multiple-Input Multiple-Output (MIMO) systems is generally non-linear and their multiple states are coupled.

An identification methodology for robots have been studied in [14], and can be classified according to the error chosen as the validation criterion:

- Validation on the input error: which is based on the Inverse Dynamic Model (IDM) written in a linear form according to the parameters to be identified.
- Validation on the output error: which is based on the DDM.

In order to obtain an accurate dynamic positioning of the end-effector through the kinematic workspace, the use of the output error validation seems to be an obvious choice. Hence, the vector of the dynamic parameters x_D to be identified, can be estimated leading to $\widehat{x}_D$ by minimising the following dynamic identification error criterion $E(\widehat{x}_K, x_D)$, defined in the operational space in term of end-effector posture:

$$E(\widehat{x}_K, x_D) = \sum_{i=1}^{6} \sum_{k=1}^{N_s} e_{ik}(\widehat{x}_K, x_D) = \sum_{i=1}^{6} \sum_{k=1}^{N_s} (X_{eik} - \widehat{X}_{eik}(\widehat{x}_K, x_D))^2 \quad (17)$$

or also in the joint space in term of motors positioning:

$$E(\widehat{x}_K, x_D) = \sum_{i=1}^{n} \sum_{k=1}^{N_s} e_{ik}(\widehat{x}_K, x_D) = \sum_{i=1}^{n} \sum_{k=1}^{N_s} (\theta_{ik} - \widehat{\theta}_{ik}(\widehat{x}_K, x_D))^2 \quad (18)$$

with:

$e_{ik}(\widehat{x}_K, x_D) = e_i(t = k\, T_s, \widehat{x}_K, x_D)$	dynamic identification error.
$X_{eik} = X_{ei}(t = k\, T_s)$	end-effector pose measurement.
$\widehat{X}_{eik}(\widehat{x}_K, x_D) = \widehat{X}_{ei}(t = k\, T_s, \widehat{x}_K, x_D)$	end-effector pose estimation using the DDM.
$\theta_{ik} = \theta_i(t = k\, T_s)$	motor position measurements.
$\widehat{\theta}_{ik}(\widehat{x}_K, x_D) = \widehat{\theta}_i(t = k\, T_s, \widehat{x}_K, x_D)$	motor position estimations using the DDM and IPKM.

The problem of the minimisation of Eqs. (17) and (18) criterion is also a non-linear least squares optimisation problem, with the objective function $E(\widehat{x}_K, x_D)$. This problem could be solved iteratively using the same algorithms mentioned for the kinematic parameters estimation. However, the identified vector of the dynamic parameters resulting from the optimisation problem, requires many integrations of the DDM over a fairly long time interval and is therefore very demanding in computation time (Fig. 3).

(a)

(b)
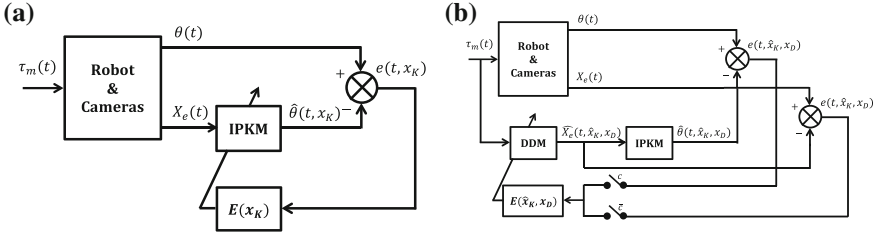
Fig. 3 Parameters identification schemes. **a** Kinematic parameters identification scheme. **b** Dynamic parameters identification scheme with the validation on output error

4 Experimental Results

Here we apply the proposed identification methodology to the INCA 6D cable-driven parallel robot.

The performance of the identification method is quantified by evaluating the fit on the outputs.[2]

4.1 Initial Values of the Parameters

The reference frame R_o is placed at the center of the kinematic workspace (Fig. 4a), and the frame attached to the end-effector R_e is chosen initially parallel with R_o (R_e // R_o, see Fig. 4b).

Each motor is controlled in current and the current loop can be modelled by a continuous first order transfer function $G_i(s)$ with a time constant τ_i between the desired current I_{di} and the effective motor current I_{mi}:

$$G_i(s) = \frac{I_{mi}(s)}{I_{di}(s)} = \frac{1}{1 + \tau_i \, s}$$

The initial values of the kinematic (see Fig. 4) and dynamic parameters of the INCA 6D robot, known by design or calculated, are given in the Table 1. The dynamic parameters related to the actuators are assumed to be identical for each of them. These parameters have been used in the simulations, and also to initialise the vector of the estimated parameters during the kinematic and dynamic identification steps.

---

[2] For the ith output of a MIMO system of input vector u ($dim(u) = N_u$) and output vector y ($dim(u) = N_y$) along a set of N_s samples by:

$$FIT_i(\%) = \left(1 - \frac{\sum_{i=1}^{N_y} \sum_{k=1}^{N_s} (y_{ik} - \widehat{y}_{ik})^2}{\sum_{i=1}^{N_y} \sum_{k=1}^{N_s} (y_{ik} - \bar{y}_i)^2} \right) \times 100$$

where $\widehat{y}$ is the estimation of the output vector y and $\bar{y}_i$ the average of the ith output y_i.
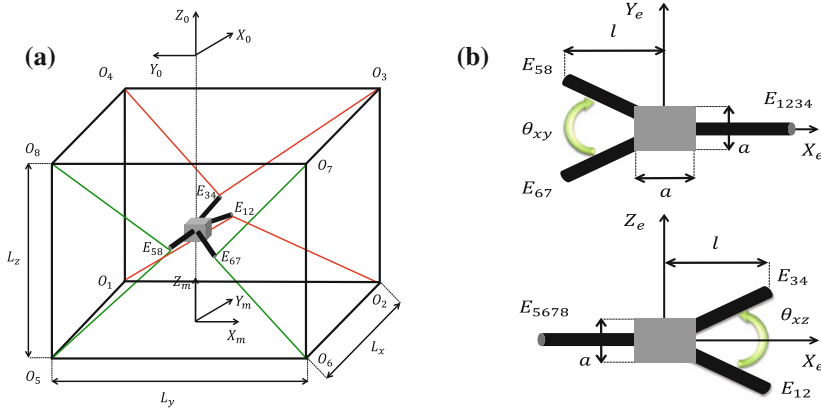
Fig. 4 Kinematic workspace parameters. **a** Kinematic workspace parameters. **b** End-effector parameters

About the Coulomb friction f_{seq} parameter, it is evaluated by powering each motor separately with a time-ramp signal of desired current, that increases starting from the initial value $I_{min} = 0$ A to the final value $I_{max} = 3$ A with a unit slope, while the other motors are controlled to 0 A. Noting the minimum value of the current that produces a motion of the end-effector, the Coulomb friction coefficient is then calculated by the linear relation Eq. (12) between the Coulomb friction torques f_{seq} and motor currents i_m using the gain constant k_{em}. The measured values of the Coulomb friction lead to the ratio $\tau_{mmax}/f_{seq} \simeq 100$, where τ_{mmax} is the maximum torque that could be applied by the motors.

4.2 Identification of the Kinematic Parameters

4.2.1 Experimental Data for the Kinematic Identification

In order to evaluate the validity of the kinematic parameters through the entire kinematic workspace, we performed 8 different tests. Each of the Test i consists in moving the end-effector (in an initial pose identical for the 8 tests) on the direction of the ith motor by applying to it a time-step signal of desired current, of an amplitude $I = 1$ A, while the other motors are controlled to 0 A. We noted at the end of each test, the final rotation angles of the motors, as well as the final pose of the end-effector.

The motors positions are collected at a sample rate $T_e = 1$ ms, and the end-effector poses at a sample rate $T_c = 4$ ms.

Table 1 Initial and estimated values of the kinematic and dynamic parameters of the INCA 6D robot

| Kinematic parameters	Initial values	Estimated values
L_x (m)	2.53	2.50
L_y (m)	2.8	2.75
L_z (m)	3	3.05
a (mm)	41	idem
l (mm)	153	153
θ_{xy} (^{o})	70	63
θ_{xz} (^{o})	24	21.6
r_{pe} (mm)	6	idem
r_{pm} (mm)	17.5	17.5
Dynamic parameters	Initial values	Estimated values
M_e (g)	0.1569	0.2895
$^eI_{exx}$ (g·m^2)	$4.9691 \cdot 10^{-3}$	$1.4904 \cdot 10^{-4}$
$^eI_{eyy}$ (g·m^2)	$6.9127 \cdot 10^{-3}$	$2.0736 \cdot 10^{-4}$
$^eI_{ezz}$ (g·m^2)	$6.9127 \cdot 10^{-3}$	$2.0736 \cdot 10^{-4}$
$^eI_{exy}$ (g·m^2)	0	idem
$^eI_{eyz}$ (g·m^2)	0	idem
$^eI_{exz}$ (g·m^2)	0	idem
j_{eq} (g·m^2)	$2.9110 \cdot 10^{-5}$	$3.8795 \cdot 10^{-5}$
$f_{v_{eq}}$ ((N·m)/(rad/s))	$3.1 \cdot 10^{-3}$	$6.6779 \cdot 10^{-5}$
$f_{s_{eq}}$ ((N·m)/(rad/s))	$1.8 \cdot 10^{-3}$	$4.4 \cdot 10^{-3}$
k_{sp} (N/m)	16	14.45
k_{em} ((N·m)/A)	$60.3 \cdot 10^{-3}$	idem
τ (ms)	1.3	idem

4.2.2 Estimated Kinematic Parameters

Applying the kinematic identification scheme presented previously on Fig. 3a, the kinematic parameters are estimated iteratively using the Levenberg-Marquardt method solving the non-linear least squares optimisation problem of Eq. (16).

In the Table 1, the achieved estimates of the chosen kinematic parameters to be identified are given. The kinematic parameters a and r_{pe} were maintained at their known values, because they are not involved in the kinematics modelling.

The comparison between the angular positions of the motors estimations issued from the IPKM, and the experimental identification data is shown in the Fig. 5.

In the first column of the Table 2, the corresponding numerical values of the fit on the motors positions are provided.
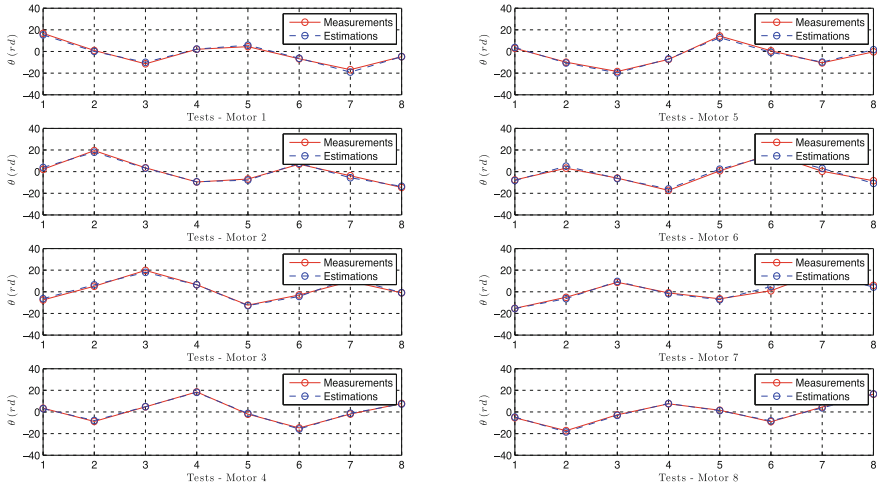
Fig. 5 Experimental and estimated motor position trajectories of the kinematic identification step

4.3 Identification of the Dynamic Parameters

4.3.1 Experimental Data for the Dynamic Identification

The choice of the excitation trajectories is an important point for the identification procedure. Indeed, the parameters estimation of a model that is structurally identifiable may be impossible to achieve if the data are not rich enough. The excitation trajectories are constrained to contain both slow (for friction and stiffness) and high (for inertia) dynamics.

For the particular case of the CDPRs, the trajectories should be also large enough to avoid a slack behaviour of the cables by maintaining positive cable tensions, and sufficiently slow not to amplify the vibrations of the cables.

In the case shown, the motor current signals are chosen as decoupled Pseudo-Random Binary Sequence(s) (PRBS(s)). For the identification trajectory, the low level $I_{d\,min} = 0$ A and high level $I_{d\,max} = 1$ A of the signals are adjusted to respect the constraints on the cable tensions. The high frequency of the frequency band $[0 - f_{max}]$ was set to $f_{max} = 1$ Hz, during a time interval $[0–5$ s$]$.

A cross validation is performed with different PRBS trajectories of parameters described in the Table 2, in order to test the influences on the estimates, depending on the changes in the PRBS signal parameters. Are investigated the changes in: the frequency band f_{max} (Val(b)), the current levels $I_{d\,min}$ and $I_{d\,max}$ (Val(c)), and both current levels with frequency band (Val(d)). The validation trajectory Val(a) is the identification trajectory extension taken during $[5–10$ s$]$. And the trajectories of validation Val(e) and Val(f) are used to evaluate the model accuracy in case of non-negligible cable vibrations observed during the experimentations from this trajectories frequency.

Table 2 Identification results by evaluating the fit on the motors positions, according to different parameters of the SBPA excitation trajectories

SBPA parameters		Dynamic ident	Dynamic val(a)	Dynamic val(b)	Dynamic val(c)	Dynamic val(d)	Dynamic val(e)	Dynamic val(f)
I_{min} (A)		0	0	0	0.5	0.5	0	0.5
I_{max} (A)		1	1	1	1.5	1.5	1	1.5
f_{max} (Hz)		1	1	2	1	2	5	5
Motors	Kinematic ident	Dynamic ident	Dynamic val(a)	Dynamic val(b)	Dynamic val(c)	Dynamic val(d)	Dynamic val(e)	Dynamic val(f)
Motor 1	88.60	91.20	92.55	84.79	86.10	90.15	83.26	82.24
Motor 2	88.19	85.09	88.02	84.79	81.41	86.83	69.92	69.35
Motor 3	85.75	88.22	89.09	82.65	81.55	82.65	80.45	77.88
Motor 4	92.92	93.88	93.39	88.20	85.70	89.14	79.32	74.11
Motor 5	88.90	86.85	84.72	77.91	82.05	82.60	79.90	79.66
Motor 6	84.08	93.62	92.02	87.15	85.39	89.32	81.26	75.88
Motor 7	83.44	90.26	90.46	83.73	85.99	88.82	82.97	81.98
Motor 8	95.08	85.67	87.79	82.09	84.27	86.96	70.91	71.98
Average	88.37	89.35	89.75	83.91	84.06	87.06	78.50	76.64

The motor currents and positions are collected at a sample rate $T_e = 1$ ms. The motor torques are computed using the linear relationship Eq. (12) from the motor currents. In order to avoid the noise in the measurements, the motors currents can also be estimated from the desired currents using the transfer function $G_i(s)$.

4.3.2 Estimated Dynamic Parameters

Applying the dynamic identification scheme presented previously in Fig. 3b (with $c = 1$), the dynamic parameters are estimated iteratively using also the Levenberg-Marquardt method solving the non-linear least squares optimisation problem of Eq. (18).

In the Table 1, the achieved estimates of the chosen dynamic parameters to be identified are given. The dynamic parameters k_{em} and τ are maintained at their known values, which have been confirmed by additional experimentations. The non-diagonal components of the moment of inertia are set to: $^eI_{exy} = {}^eI_{eyz} = {}^eI_{exz} = 0$ g·m^2, and the diagonal components $^eI_{eyy}$ and $^eI_{ezz}$ are forced to be equal ($^eI_{ezz} = {}^eI_{eyy}$), because of the geometric symmetry of the end-effector.

The comparison between the angular positions of the motors estimations issued from the DDM and IPKM, and the experimental identification data is shown in the Fig. 6.

In the second column of the Table 2, the corresponding numerical values of the fit on the motors positions for the identification trajectory are provided. Whereas the valued of the fit for the cross-validation trajectories are given in the column 3 to 8.
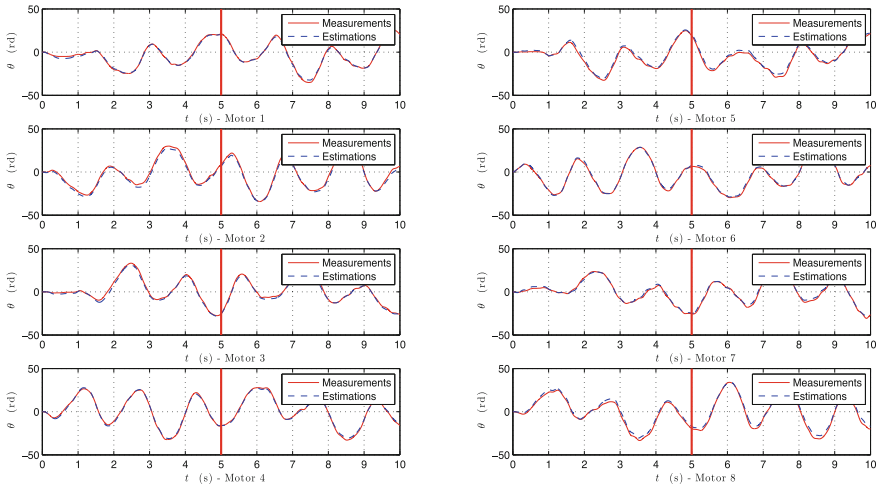
Fig. 6 Experimental and estimated motor position trajectories of the dynamic identification step

5 Conclusion and Perspectives

This paper presented a methodology for the identification of the combined kinematic and dynamic model parameters of a 6-DoF CDPRs, where the kinematic parameters are first estimated to avoid the influences of the errors on the kinematic parameters from the step of the dynamic identification.

The method has been successfully experimented on the INCA 6D robot, to reach an improved inputs-outputs behaviour of the model according to the experimental data. The proposed methodology provides a good fit on the motors output positions between the model and experimentations, and the estimated values of both the kinematic and dynamic parameters remain close from their initial guessed values, except for the viscous friction term. The validity of the identified model remains good even when the cables are subject to non-negligible vibrations, as could be observed on the validations with higher frequency trajectories.

Our perspectives in this work, are to investigate the dynamic identification step by the study of the cable flexibilities influences on the modelling. For this, in a close future, the pose reconstruction task will be available in real-time to be included in the dynamic identification scheme, where the pose information given by the 6 infra-red cameras evaluates the model error in term of end-effector posture.

Further works will involve the synthesis and analysis of kinematic and dynamic position / vision control strategies to achieve high bandwidths and reach a high speed motions, while maintaining positive tensions in the cables.

References

1. Ebert-Uphoff, I., Voglewede, P.A.: On the connections between cable-driven robots, parallel manipulators and grasping. IEEE International Conference on Robotics and Automation, New Orleans, LA, In (2004)
2. Williams, R.L., Gallina, P.: Translational planar cable-direct- driven robots. J. Intell. Rob. Syst. **37**, 69–96 (2003)
3. Pham, C.B., Yang, G., Yeo, S.H.: Dynamic analysis of cable-driven parallel mechanisms. IEEE/ASME International Conference on Advanced Intelligent Mechatronics, Monterey, CA, USA, In (2005)
4. Behzadipour, S., Sohi, M.A.: Antagonistic stiffness in cable-driven mechanisms. IFToMM World Congress, Besançon, France, In (2007)
5. Korayem, M.H., Bamdad, M., Saadat, M.: Workspace analysis of cable-suspended robots with elastic cable. IEEE Internatioanl Conference on Robotics and Biomimetics, Sanya, China, In (2007)
6. Riehl, N., Gouttefarde, M., Krut, S., Baradat, C., Pierrot, F.: Effects of non-negligible cable mass on the static behavior of large workspace cable-driven parallel mechanisms. International Conference on Robotics and Automation, Kobe, Japan, In (2009)
7. Riehl, N., Gouttefarde, M., Baradat, C., Pierrot, F.: On the determination of cable characteristics for large dimension cable-driven parallel mechanisms. International Conference on Robotics and Automation, Anchorage, AK, USA, In (2010)
8. Sunil, Y.Z., Agrawal, K., Piovoso, M.J.: Coupled dynamics of flexible cables and rigid end-effector for a cable suspended robot. American Control Conference, Minneapolis, MN, USA, In (2006)
9. Diao, X., Ma, O.: Vibration analysis of cable-driven parallel manipulators, Multibody Sys. Dyn. **21**(4), 347–360 (2009)
10. Spong, M.W., Vidyasagar, M.: Robot Dynamics and Control. Wiley, New York (1989)
11. Dombre, E.: Khalil. Modélisation identification et commande des robots, Hermès, W. (1999)
12. Merlet, J.P.: Les robots parallèles, Hermès (1997).
13. Yu, D., Chen, W., Li, H.: Kinematic parameter identification of parallel robots for semi-physical simulation platform of space docking mechanism. Mechanics **17**(5), 2029–6983 (2011)
14. Gautier, M., Poignet, P.: Identification en boucle fermée par modèle inverse des parameètres physiques de systèmes mlécatroniques. J. Europeén des Systeèmes Automatisés **36**(3), 465–480 (2002)
15. Poignet, P., Ramdani, N., Vivas, O.A.: Robust estimation of parallel robot dynamic parameters with interval analysis. IEEE Conference on Decision and Control, Maui, HI, USA, In (2003)

Differential Kinematics for Calibration, System Investigation, and Force Based Forward Kinematics of Cable-Driven Parallel Robots

Philipp Miermeister, Werner Kraus and Andreas Pott

Abstract In this paper the differential kinematics for cable-driven robots is derived and the use for calibration, system investigation and a force based forward kinematics is shown. The Jacobians for each part of the kinematic chain are derived with respect to the platform pose and the most important system parameters. Beside the consideration of geometrical quantities, the differential relations between non-geometrical quantities such as cable stiffness and cable forces are determined. The decomposition in the most fundamental Jacobians allows to analyse and compute more complex relations by reassembling the Jacobians as needed. This approach allows more insight in the system behavior and enables the reuse of the individual modules. The purpose of this paper is to provide the framework and the key equations and to show the use for calibration, force based forward kinematics and system analysis as well as for control purposes.
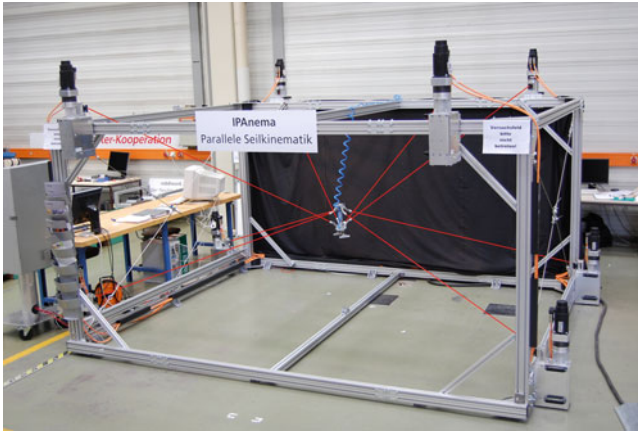
P. Miermeister (✉) · W. Kraus · A. Pott
Fraunhofer Institute for Manufacturing Engineering and Automation IPA,
Nobelstrasse 12, 70569 Stuttgart, Germany
e-mail: philipp.miermeister@ipa.fraunhofer.de

W. Kraus
e-mail: werner.kraus@ipa.fraunhofer.de

A. Pott
e-mail: andreas.pott@ipa.fraunhofer.de

Fig. 1 Cable-driven parallel robot demonstrator at Fraunhofer IPA

1 Introduction

Cable-driven parallel robots, here simply called cable robots, are parallel kinematic machines mainly consisting of a platform, cables and winches. The cables connect the platform to the winches which control the platform pose by changing the cable length. In recent years, cable robots got lots of attention due to their advantages over serial kinematic robots and conventional parallel kinematic robots with rigid links [1, 4]. On the one side, cable robots inherit the properties of parallel kinematic robots as for instance high stiffness, payload and very good precision. On the other side, they outperform conventional parallel kinematics with regards to flexibility, workspace and speed, because the cables allow ultra light weight constructions in nearly arbitrary large areas. The winches can be easily attached to solid structures as steel frames or walls and allow to change the robot configuration in a short time. The applications for cable robots include pick and place tasks, video recording for sport events as well as virtual reality simulators. It is also possible to invert the principle of actuation by exchanging the motors with passive positioning sensors which allows the cable robot to be used as metrology system (Fig. 1).

All the tasks need an accurate robot model in order to provide good results. The correct model parametrization can be obtained by a calibration procedure. For an overconstrained cable robot with more than six cables it is possible to use the redundant information for auto-calibration which allows to avoid expensive external metrology equipment. A solely kinematic description of cable robots may not be sufficient for tasks such as auto-calibration, because cable elongation caused by cable forces is not negligible. The inclusion of cable forces in the robot model demands the consideration of the system stiffness and the implementation of an extended forward kinematics that regards cable forces. The calibration, stiffness computation, and forward kinematics as well as system analysis and controller development demand

the knowledge of differential relations of geometrical and non-geometrical quantities. This paper describes the differential kinematics of cable-driven parallel robots as well as the differential relations of some non-geometrical quantities such as the cable stiffness and platform mass. The derived relations are used for calibration, stiffness analysis and the implementation of an extended force based forward kinematics which regards the cable forces and cable elongation and therefore allows to compute the platform pose more accurately than a solely geometrical forward kinematics.

At first, the kinematics of the cable robot is described. Then the most basic relations of the geometrical and force related quantities are derived. Later, the use for calibration and stiffness analysis is shown and a force based forward kinematics is implemented.

2 Robot Kinematics

The cable robot consists of m cables connecting the platform to the winches which in turn are attached to a rigid base. The platform pose is described by the generalized coordinates

$$\mathbf{x} = \begin{bmatrix} \mathbf{r}^{\mathrm{T}} & \mathbf{d}^{\mathrm{T}} \end{bmatrix}^{\mathrm{T}} \tag{1}$$

where $\mathbf{r}$ and $\mathbf{d}$ refer to the platform position and orientation, respectively. Considering the base coordinates $\mathbf{a}_i$ and the cable attachment points at the platform described by $\mathbf{b}_i$, the kinematic loop for a single drive chain reads

$$\mathbf{l}_i = \mathbf{a}_i - \mathbf{r} - \mathbf{R}_{0\mathrm{P}}(\mathbf{d})\mathbf{b}_i, \tag{2}$$

where $\mathbf{l}_i$ refers to the cable vector and $\mathbf{R}_{0\mathrm{P}}$ is the rotation matrix between the platform frame $\mathcal{K}_{\mathrm{P}}$ and the inertial frame $\mathcal{K}_0$ shown in Fig. 2. Considering the cables as massless elements in an ideal tightened state without elongation and sagging it is possible to compute the actuator variables $\mathbf{q}_\theta = \begin{bmatrix} \theta_1 & \cdots & \theta_m \end{bmatrix}^{\mathrm{T}}$ for a given platform pose $\mathbf{x}$ using the analytically and uniquely solvable inverse kinematics

$$\mathbf{q}_\theta = \mathbf{h}(\mathbf{p}, \mathbf{x}, \mathbf{x}_0) = \mathbf{q}_{\mathrm{N}}(\mathbf{x}) - \mathbf{q}(\mathbf{x}_0), \tag{3}$$

where $q_{\mathrm{N},i}(\mathbf{x}) = \left\| \mathbf{l}_{\mathrm{N},i} \right\|_2$ denotes the nominal controlled cable length, $\mathbf{x}_0$ describes the initial configuration, and $\mathbf{p}$ relates to the system parametrization. The corresponding forward kinematics

$$\mathbf{x} = \mathbf{h}^{-1} = \mathbf{f}(\mathbf{p}, \mathbf{q}_\theta) \tag{4}$$

has to be solved numerically and provides multiple solutions [3]. Both Eqs. (3) and (4) are fundamental to the solution of various problems such as the development of controllers. Deriving the actuator variable $\mathbf{q}_\theta$ with respect to the platform pose $\mathbf{x}$ and using the kinetostatic principle one gets the following relation
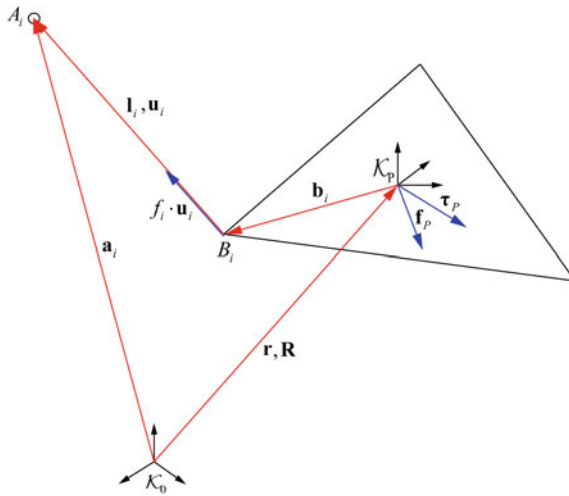
Fig. 2 Robot kinematics

$$\frac{d\theta(\mathbf{x})}{d\mathbf{x}} = \frac{d\mathbf{q}(\mathbf{x})}{d\mathbf{x}} = \mathbf{J}_{qx} = -\mathbf{AP} \tag{5}$$

therein

$$\mathbf{A}^{\mathrm{T}} = \begin{bmatrix} {}_{(0)}\mathbf{u}_1 & \cdots & {}_{(0)}\mathbf{u}_m \\ {}_{(0)}\mathbf{b}_1 \times {}_{(0)}\mathbf{u}_1 & \cdots & {}_{(0)}\mathbf{b}_m \times {}_{(0)}\mathbf{u}_m \end{bmatrix} \tag{6}$$

corresponds to the well known *structure matrix* $\mathbf{A}^{\mathrm{T}}$ [6]. The subscript (0) refers to the coordinate system in which the vector is described. Matrix $\mathbf{P}$ depends on the parametrization of the rotation and expresses the relation between the geometrical and analytical Jacobian matrix. For quaternions, matrix $\mathbf{P}$ can be computed as in [5].

3 Differential Relations of Kinematic Quantities

The kinematic loop of a cable-driven parallel robot as shown in Fig. 2 and the associated differential kinematics is used in many algorithms. Especially the differential relations of the platform pose $\mathbf{x}$ with respect to the associated platform vectors $\mathbf{b}$, the cable vectors $\mathbf{l}$ as well as the actuator variables $\mathbf{q}_\theta$ are of interest for many applications. In the following, the pose related Jacobians for the geometrical quantities are derived.

3.1 Pose Related Derivatives of Robot Kinematics

An infinitesimal change of the platform motion can be describe by

$$\delta\mathbf{x} = \begin{bmatrix} \delta\mathbf{r} & \mathbf{w}_\delta \end{bmatrix}^{\mathrm{T}} \tag{7}$$

where $\delta\mathbf{r}$ is the virtual platform displacement and $\mathbf{w}_\delta$ is the angular displacement vector. The angular displacement vector is similar to the angular velocity vector when rotation is derived with respect to time. The angular displacement uniquely describes the infinitesimal rotation of a body and is independent of the underlying parametrization $\mathbf{d}$ of the rotation. The relation between the virtual rotation and a specific parametrization is given by

$$\mathbf{w}_\delta = \mathbf{P}\delta\mathbf{d}. \tag{8}$$

The cable attachment points B_i on the platform are changing with respect to the inertial frame according to the virtual motion of the platform. Introducing the position vector $\mathbf{r}_{B,i} = \mathbf{r} + \mathbf{R}_{0P}\mathbf{b}_i$ to a single attachment point B_i one can compute the virtual displacement by

$$\delta\mathbf{r}_{B,i} = \mathbf{J}_{Bx,i}\delta\mathbf{x}, \tag{9}$$

$$\mathbf{J}_{Bx,i} = \frac{\partial\mathbf{r}_{B,i}}{\partial\mathbf{x}} = \begin{bmatrix} \mathbf{E} & \mathbf{J}_{b\psi,i} \end{bmatrix}\mathbf{T} \tag{10}$$

with

$$\mathbf{J}_{b\psi,i} =_{(0)} -\tilde{\mathbf{b}}_i. \tag{11}$$

and the transformation matrix

$$\mathbf{T} = \begin{bmatrix} \mathbf{E} & \mathbf{0} \\ \mathbf{0} & \mathbf{P} \end{bmatrix}. \tag{12}$$

The tilde operator in Eq. (11) relates to a screw symmetric matrix which fulfills relation

$$\tilde{\mathbf{b}}\mathbf{u} = \mathbf{b} \times \mathbf{u}. \tag{13}$$

For a kinematic loop where A_i is regraded as fixed point, the derivative of a single cable vector $\mathbf{l}_i$ with respect to the platform pose $\mathbf{x}$ can be computed by

$$\delta\mathbf{l}_i = \frac{d\mathbf{l}_i}{d\mathbf{x}}\delta\mathbf{x} = \frac{d\mathbf{r}_{B,i}(\mathbf{x})}{d\mathbf{x}}\delta\mathbf{x} = \mathbf{J}_{Bx,i}\delta\mathbf{x} \tag{14}$$

and therefore the Jacobian reads

$$\mathbf{J}_{lx,i} = \mathbf{J}_{Bx,i}. \tag{15}$$

In case of a more advanced kinematic model which includes the winch pulley to compute the cable length, one has to consider the influence of the attachment point B_i on the pulleys rotation and tilt angle. In the following only the simplified inverse kinematics model is assumed.

The change in the cable length q_i follows from

$$\delta q_i = \frac{\mathbf{l}_i^{\mathrm{T}} \frac{\mathrm{d}}{\mathrm{d}\mathbf{x}} \mathbf{l}_i}{\|\mathbf{l}_i\|_2} \delta \mathbf{x} = \mathbf{u}_i^{\mathrm{T}} \frac{\mathrm{d}\mathbf{l}_i}{\mathrm{d}\mathbf{x}} \delta \mathbf{x}. \tag{16}$$

where the Jacobian is defined as

$$\mathbf{J}_{\mathrm{qx},i} = \mathbf{u}_i^{\mathrm{T}} \mathbf{J}_{\mathrm{lx},i}. \tag{17}$$

One can see that the change in the cable length q_i is the projection of $\delta \mathbf{l}_i$ on the cables' unit vector $\mathbf{u}_i$. The derivative of the unit vector itself with respect to $\mathbf{x}$ reads

$$\delta \mathbf{u}_i = \|\mathbf{l}_i\|_2^{-2} \left(\frac{\partial \mathbf{l}_i}{\partial \mathbf{x}} \|\mathbf{l}_i\|_2 - \mathbf{l}_i \frac{\partial \|\mathbf{l}_i\|_2}{\partial \mathbf{x}} \right) \delta \mathbf{x}. \tag{18}$$

Further computation and the use of Eq. (17) yields

$$\delta \mathbf{u}_i = q_i^{-2} \left(\mathbf{J}_{\mathrm{lx},i} q_i - \mathbf{l}_i \otimes \mathbf{u}_i \mathbf{J}_{\mathrm{lx},i} \right) \delta \mathbf{x}. \tag{19}$$

Separating $\mathbf{J}_{\mathrm{lx},i}$ yields

$$\delta \mathbf{u}_i = \mathbf{J}_{\mathrm{ul},i} \mathbf{J}_{\mathrm{lx},i} \delta \mathbf{x} \tag{20}$$

where the 3×3 Jacobian $\mathbf{J}_{\mathrm{ul}}$ describes the mapping $\delta \mathbf{l} \to \delta \mathbf{u}$ from the cable vector to the unit vector with

$$\mathbf{J}_{\mathrm{ul},i} = q_i^{-1} \mathbf{E} - q_i^{-2} \mathbf{l}_i \otimes \mathbf{u}_i. \tag{21}$$

Mappings between the geometrical quantities can be described by multiplying the corresponding Jacobians

$$\delta \mathbf{x} \xrightarrow{\mathbf{J}_{\mathrm{Bx}}} \delta \mathbf{r}_{\mathrm{B},i} \xrightarrow{\mathbf{E}} \delta \mathbf{l}_i \xrightarrow{\mathbf{J}_{\mathrm{ul}}} \delta \mathbf{u}_i. \tag{22}$$

3.2 Parameter Related Derivatives of Robot Kinematics

Parameter related derivatives are of interest for calibration and system investigation. The associated Jacobians allow to determine the influence of the parameters on the robot geometry. The main geometrical parameters are the cable outlet points A_i described by the vector $\mathbf{a}_i$ and the cable attachment points at the platform denoted by the local platform vector $\mathbf{b}_i$. For a cable robot with m cables, the kinematic equations depend on $6m$ geometrical parameters which are combined in the geometrical

parameter vector

$$\mathbf{p}_G = \begin{bmatrix} \mathbf{a}_1^T \ \mathbf{b}_1^T \ \cdots \ \mathbf{a}_m^T \ \mathbf{b}_m^T \end{bmatrix}^T. \tag{23}$$

The derivative of a single cable vector with respect to the geometrical parameters $\mathbf{p}_G$ yields

$$\delta \mathbf{l}_i = \mathbf{J}_{\text{lpG},i} \delta \mathbf{p}_G \tag{24}$$

where

$$\mathbf{J}_{\text{lpG},i} = \frac{\partial \mathbf{l}_i}{\partial \mathbf{p}_G} = \begin{bmatrix} \mathbf{0}_{3\times 6(i-1)} \ \mathbf{E}_{3\times 3} \ -\mathbf{R}_{0P} \ \mathbf{0}_{3\times 6(m-i)} \end{bmatrix}_{3\times 6m}. \tag{25}$$

The derivative of a single unit vector

$$\delta \mathbf{u}_i = \mathbf{J}_{\text{upG},i} \delta \mathbf{p} \tag{26}$$

is closely related to the derivative of the cable vector. The corresponding $3 \times 6m$ Jacobian can be computed by consideration of Eqs. (25) and (21) so that

$$\mathbf{J}_{\text{upG},i} = \frac{\partial \mathbf{u}_i(\mathbf{l}_i(\mathbf{p}_G))}{\partial \mathbf{p}_G} = \frac{\partial \mathbf{u}_i}{\partial \mathbf{l}_i} \frac{\partial \mathbf{l}_i}{\partial \mathbf{p}_G} = \mathbf{J}_{\text{ul},i} \mathbf{J}_{\text{lpG},i}. \tag{27}$$

The derivative of the cable length with respect to the geometrical parameters $\mathbf{p}_G$ yields

$$\delta q_i = \mathbf{J}_{\text{qpG},i} \delta \mathbf{p}_G, \tag{28}$$

where the Jacobian for a single drive chain i reads

$$\mathbf{J}_{\text{qpG},i} = \frac{\partial h_i}{\partial \mathbf{p}_G} = \begin{bmatrix} \mathbf{0}_{1\times 6(i-1)} \ \mathbf{u}_i^T \ -\mathbf{u}_i^T \mathbf{R}_{0P} \ \mathbf{0}_{1\times 6(m-i)} \end{bmatrix}_{1\times 6m}. \tag{29}$$

For the later described force model one has to consider the difference between the actual cable length and the nominal cable length $\Delta \mathbf{q} = \mathbf{q}(\mathbf{x}) - \mathbf{q}_N(\mathbf{x}_0, \mathbf{q}_\theta)$ where Δq_i depends on the actual state $\mathbf{x}$ and the initial state $\mathbf{x}_0$ which both depend on the parameter set $\mathbf{p}$. The influence of the geometrical parameters on the actual configuration as well as the initial configuration can be regarded by computing the difference between the current and the initial Jacobian

$$\mathbf{J}_{\Delta\text{qpG}} = \frac{\partial (\mathbf{q} - \mathbf{q}_N)}{\partial \mathbf{p}_G} = \mathbf{J}_{\text{qpG}} - \mathbf{J}_{\text{qpG0}}, \tag{30}$$

$$\delta \Delta \mathbf{q} = \mathbf{J}_{\Delta\text{qpG}} \delta \mathbf{p}_G. \tag{31}$$

4 Force Equations

A solely kinematic model does not regard cable forces and therefore is inaccurate since the elongation of the cables is not considered in the kinematic equations. A model that regards the cable forces can be obtained by adding two additional force equations to the geometrical model.

The first equation (32) describes the static cable behavior by computing the cable forces with respect to the cable elongation. The second equation (35) describes the platform wrench resulting form the cable forces and external forces such as gravitation. Equation (35) can be used to find a static force equilibrium where the platform is at rest. Here a simplified linear spring model

$$\mathbf{f} = \mathbf{K}\mathbf{Q}^{-1}\Delta\mathbf{q}(\mathbf{x}, \mathbf{q}_\theta) \tag{32}$$

is used to describe the cable elasticity where $\mathbf{K} = \mathrm{diag}(\mathbf{k})$ is the specific stiffness matrix and $\mathbf{Q} = \mathrm{diag}(\mathbf{q})$ is a $m \times m$ diagonal matrix containing the cable lengths. Vector

$$\Delta\mathbf{q} = \mathbf{q}(\mathbf{x}) - \mathbf{q}_N(\mathbf{x}_0, \mathbf{q}_\theta) \tag{33}$$

represents the difference between the actual cable length $\mathbf{q}$ and the nominal cable length $\mathbf{q}_N$. The nominal cable length is obtained by the solely geometrical robot model and depends on the initial configuration as well as the current actuator states

$$\mathbf{q}_N = \mathbf{q}_0 + \mathbf{q}_\theta + \mathbf{q}_{\theta,\mathrm{off}} \tag{34}$$

where $\mathbf{q}_{\theta,\mathrm{off}}$ is an initial cable offset, which allows to define an initial force state with $\Delta\mathbf{q}_0 = \mathbf{q}_{\theta,\mathrm{off}}$. Taking cable forces into account, the platform can be described as a free floating body whose static force equilibrium is described by constraint

$$\mathbf{g}(\mathbf{x}) = \mathbf{A}^\mathrm{T}(\mathbf{p}, \mathbf{x})\mathbf{f}(\mathbf{q}_\theta, \mathbf{x}) + \mathbf{w}_g(\mathbf{x}) = \mathbf{0}. \tag{35}$$

Damping effects are neglected in the cable model, because only the static behavior is of interest.

4.1 Pose Related Derivatives of the Force Equations

For calibration, force based forwards kinematics and the investigation of the system stiffness, it is necessary to compute the pose related derivatives of the force equations. The derivative of Eq. (35) with respect to the platform pose yields

$$\mathbf{J}_{gx} = \frac{d\mathbf{g}(\mathbf{x})}{d\mathbf{x}} = \frac{d\mathbf{A}^\mathrm{T}(\mathbf{x})}{d\mathbf{x}}\mathbf{f}(\mathbf{x}) + \mathbf{A}^\mathrm{T}(\mathbf{x})\frac{d\mathbf{f}(\mathbf{x})}{d\mathbf{x}} + \frac{d\mathbf{w}_g(\mathbf{x})}{d\mathbf{x}}. \tag{36}$$

The derivative of the first expression in Eq. (36) reflects the influence of changing force directions caused by the platform displacement and rotation. The derivative yields

$$\mathbf{J}_{\text{Ax}} = \frac{\mathrm{d}}{\mathrm{d}\mathbf{x}} \left(\mathbf{A}(\mathbf{x})^{\text{T}} \right) \mathbf{f}(\mathbf{x}) = \sum_{i=1}^{m} \frac{\mathrm{d}}{\mathrm{d}\mathbf{x}} \left(\mathbf{v}_{\text{A},i}(\mathbf{x})^{\text{T}} \right) f_i(\mathbf{x}) \tag{37}$$

where $\mathbf{v}_{\text{A},i}$ is the i-th column vector of the structure matrix $\mathbf{A}^{\text{T}}$. For a single drive train i one gets

$$\mathbf{J}_{\text{Ax},i} = \frac{\partial}{\partial \mathbf{x}} (\mathbf{A}_i^{\text{T}}(\mathbf{x})) \left[\begin{array}{c} \mathbf{J}_{\text{ux},i} \\ -\tilde{\mathbf{u}}_i \mathbf{J}_{\text{bx},i} + \tilde{\mathbf{b}}_i \mathbf{J}_{\text{ux},i} \end{array} \right]. \tag{38}$$

The derivative of the force vector yields

$$\mathbf{J}_{\text{fx}} = \frac{\mathrm{d}\mathbf{f}(\mathbf{x})}{\mathrm{d}\mathbf{x}} = -\mathbf{K}\mathbf{Q}_{\text{N}}\mathbf{Q}^{-2}\mathbf{A}\mathbf{P} \tag{39}$$

which describes the change of the cable forces caused by the platform displacement where $\mathbf{Q}_{\text{N}} = \text{diag}(\mathbf{q}_{\text{N}})$. Deriving the platform wrench yields

$$\mathbf{J}_{\text{wx}} = \frac{\mathrm{d}}{\mathrm{d}\mathbf{x}} \mathbf{w}_{\text{g}}(\mathbf{x}) = mg \left[\mathbf{0} \left(-\frac{\mathrm{d}}{\mathrm{d}\mathbf{x}} b_{g,y} \right)^{\text{T}} \left(\frac{\mathrm{d}}{\mathrm{d}\mathbf{x}} b_{g,x} \right)^{\text{T}} \mathbf{0} \right]^{\text{T}} \tag{40}$$

where the local platform vector $\mathbf{b}_{\text{g}}$ describes the point of action of the gravitational force.

5 Application

## 5.1 Forward Kinematics Under the Consideration of Cable Forces

For an exclusively kinematic model, forward kinematics is used to compute a valid pose which fulfills the kinematic constraints (2). Similarly, it is possible to find a static pose $\mathbf{x}$ which fulfills constraint Eq. (35). Finding a static pose from a given initial pose $\hat{\mathbf{x}}$ with $\hat{\mathbf{g}} = \mathbf{g}(\hat{\mathbf{x}}) \neq \mathbf{0}$ is a nonlinear optimization problem. For small deviations $\Delta \mathbf{x}$ it is possible to linearize Eq. (35) around the equilibrium point $\mathbf{x}_{\text{eq}}$ so that

$$\mathbf{g}(\mathbf{x} + \Delta \mathbf{x}) \approx \mathbf{g}(\mathbf{x})|_{\mathbf{x}_{\text{eq}}} + \left. \frac{\mathrm{d}\mathbf{g}(\mathbf{x})}{\mathrm{d}\mathbf{x}} \right|_{\mathbf{x}_{\text{eq}}} \Delta \mathbf{x}. \tag{41}$$

Introducing the residual function

$$\mathbf{r}(\mathbf{x}) = \hat{\mathbf{g}} - \mathbf{g}(\mathbf{x}), \tag{42}$$
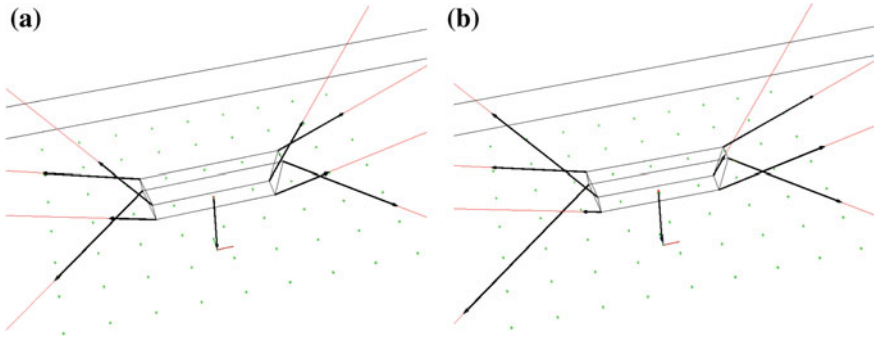
Fig. 3 Visualization of the cable forces computed by the force based forward kinematics. **a** Initial force distribution. **b** Force distribution when cable $i = 1$ was wound up by $5\,\text{cm}$

the static pose fulfilling Eq. (35) can be found by minimizing the objective function

$$\mathbf{x}_{\text{eq}} = \min_{\mathbf{x}} \left(\frac{1}{2}\mathbf{r}(\mathbf{x})^{\text{T}}\mathbf{r}(\mathbf{x}) \right). \tag{43}$$

Under consideration of linearization (41) and Eq. (42) one gets

$$\mathbf{r} = \Delta\mathbf{g} - \mathbf{J}_{\text{gx}}\Delta\mathbf{x}. \tag{44}$$

where the minimal solution can be computed by solving the well known normal equation

$$\mathbf{J}_{\text{gx}}^{\text{T}}\mathbf{J}_{\text{gx}}\Delta\mathbf{x} = \mathbf{J}_{\text{gx}}^{\text{T}}\Delta\mathbf{g}. \tag{45}$$

The force based forward kinematics for instance can be used to investigate the platform behavior with respect to the system stiffness as shown in Figs. 3 and 4. At the beginning of the simulation, the nominal values for the cable lengths are computed. Then the force based forward kinematics computes a valid static pose starting from an initial pose $\mathbf{x}_0$. Thereafter, the length of the cable $i = 1$ is iteratively reduce by $10\,\text{cm}$. The force based forward kinematics is used to compute the new platform pose and corresponded force distribution during each iteration step.

5.2 Calibration

For calibration it is important to know the differential relations of the geometrical and non geometrical parameters that are subject to calibration. In general, the calibration task consists of multiple parts [2]. At first, a kinematic model of the robot has to be established and those geometrical parameters have to be identified that have the most influence on the pose error. This goes along with pose selection [7] in order to find
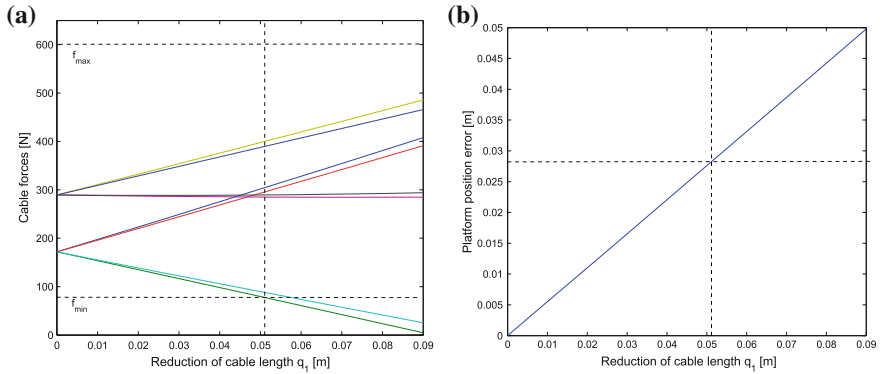
Fig. 4 Influence of the changing cable length on the platform position and cable lengths during pose measurement. **a** Cable force with respect to changing cable length $-\Delta_{q1}$. The *bold blue line* indicates cable $i = 1$. **b** Platform position error with respect to changing cable length $-\Delta_{q1}$

a well conditioned identification matrix which reflects the sensitivity with respect to parametric errors.

For a solely geometrical calibration, the most influential parameters are the platform vectors **b** and the winch position vectors **a**. The associated parameter vector for a cable robot with m cables is

$$\mathbf{p}_\text{G} = \left[\, \mathbf{a}_1^\text{T} \; \mathbf{b}_1^\text{T} \; \cdots \; \mathbf{a}_m^\text{T} \; \mathbf{b}_m^\text{T} \,\right]^\text{T}. \tag{46}$$

Since cable robots with $m > 6$ cables are overconstrained, it is possible to use the redundant cables for auto-calibration. Six independent cables define the platform pose while $m - 6$ dependent cables are used to measure the pose and compare the measurements. The relation of the associated dependent actuator variables $\mathbf{q}_{\theta,\text{D}}$ and independent actuator variables $\mathbf{q}_{\theta,\text{I}}$ is described by the forward kinematics

$$\mathbf{q}_{\theta,\text{D}} = \mathbf{h}_\text{D}(\mathbf{p}_\text{D}, \mathbf{x}(\mathbf{p}_\text{I}, \mathbf{q}_{\theta,\text{I}}), \mathbf{x}(\mathbf{p}_\text{I})). \tag{47}$$

The aim of the calibration procedure is to minimize the error between the model and the actual robot which is expressed by the residual function

$$\mathbf{r}(\mathbf{p}) = \mathbf{q}_{\theta,\text{M}} - \mathbf{q}_{\theta,\text{D}}(\mathbf{p}) \tag{48}$$

where $\mathbf{q}_{\theta,\text{M}}$ relates to the measured actuator variables. The minimal solution for the associated objective function

$$\mathbf{p}_\text{opt} = \min_{\mathbf{p}}(\underbrace{\frac{1}{2}\mathbf{r}(\mathbf{p})^\text{T}\mathbf{r}(\mathbf{p})}_{\mathbf{g}(\mathbf{p})}). \tag{49}$$

can be found by solving the associated least squares problem

$$\mathbf{J}_{qp}^{T}\mathbf{J}_{qp}\Delta\mathbf{p} = \mathbf{J}_{qp}^{T}\mathbf{r} \tag{50}$$

with

$$\mathbf{J}_{qp} = \frac{d\mathbf{r}(\mathbf{p})}{d\mathbf{p}} = \frac{d\mathbf{h}_{D}(\mathbf{p}_{D}, \mathbf{x}(\mathbf{p}_{I}, \theta_{I}), \mathbf{x}_{0}(\mathbf{p}_{I}))}{d(\mathbf{p}_{D}, \mathbf{p}_{I})} = \left[\mathbf{J}_{qpD} \; -\mathbf{J}_{qxD}\mathbf{J}_{qxI}^{-1}\mathbf{J}_{qpI} \right] \tag{51}$$

and

$$\mathbf{J}_{qpD} = \frac{\partial\mathbf{h}(\mathbf{p}_{D}, \mathbf{x}, \mathbf{x}_{0})}{\partial\mathbf{p}_{D}}, \mathbf{J}_{qpI} = \frac{\partial\mathbf{h}(\mathbf{p}_{I}, \mathbf{x}, \mathbf{x}_{0})}{\partial\mathbf{p}_{I}} \tag{52}$$

$$\mathbf{J}_{qxD} = \frac{\partial\mathbf{h}(\mathbf{p}_{D}, \mathbf{x}, \mathbf{x}_{0})}{\partial\mathbf{x}}, \mathbf{J}_{qxI} = \frac{\partial\mathbf{h}(\mathbf{p}_{I}, \mathbf{x}, \mathbf{x}_{0})}{\partial\mathbf{x}}. \tag{53}$$

The inverse of $\mathbf{J}_{qxI}$ can be computed only in the sense of least squares when quaternions are used to describe the rotation. This can be avoided using relation (17) from which follows

$$\mathbf{J}_{qDpI} = \mathbf{J}_{qxD}\mathbf{J}_{qxI}^{-1}\mathbf{J}_{qpI} = \mathbf{A}_{D}\mathbf{A}_{I}^{-1}\mathbf{J}_{qpI}. \tag{54}$$

The influence of the parameter variation on the measured cable length of a selected pose k can now be expressed using matrix notation

$$\mathbf{r}(\mathbf{p})^{(k)} = \underbrace{\left[\mathbf{J}_{qpD}^{(k)} \; -\mathbf{J}_{qDpI}^{(k)} \right]}_{\mathbf{J}_{H}^{(k)}} \underbrace{\begin{bmatrix} \Delta\mathbf{p}_{D} \\ \Delta\mathbf{p}_{I} \end{bmatrix}}_{\Delta\mathbf{p}}. \tag{55}$$

Now, with Eq. (55) one can build the identification matrix and use the Levenberg–Marquardt or Newton algorithm to find the optimal parameter set $\mathbf{p}_{opt}$ by minimizing the objective function $\mathbf{g}(\mathbf{p})$ in Eq. (49). The Levenberg–Marquardt algorithm starts with a first initial guess and then converges to the optimal parameter set as shown in Fig. 5b. In each step the parameters are adjusted and the robot frame and the platform geometry are changed as shown in Fig. 5a. The change in the parameter set causes the platform to move in a new position which can be computed by solving the forward kinematics in each iteration step. Using a force based forward kinematics as previously described allows to regard the cable elasticities and to identify the force related model parameters such as the cable stiffness and platform mass.

5.3 System Stiffness

The system stiffness of a cable-driven parallel robot is relevant for the analysis of the system behavior and the development of control algorithms. It largely depends on

(a)

(b)
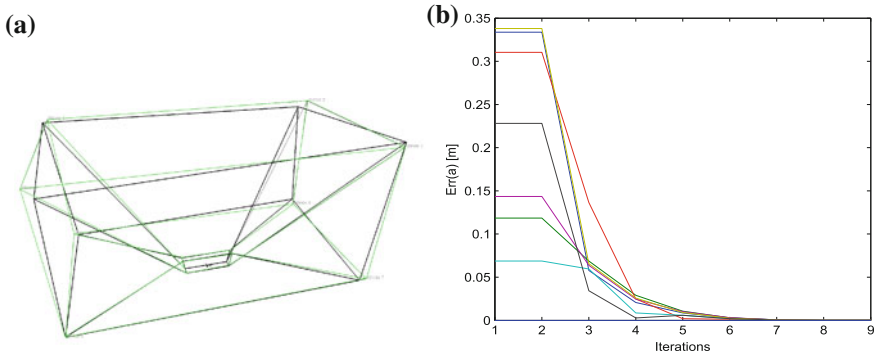
Fig. 5 Robot calibration procedure. **a** Erroneous robot model (*green*) and the actual robot frame (*black*). **b** Convergence behavior of the winch position vectors

the current platform position and also can be changed by altering the cable forces. The cable force vector $\mathbf{f}$ depends on the nominal cable length $\mathbf{q}_N$ which itself is controlled by the actuator variable $\mathbf{q}_\theta$ as denoted in Eq. (32). Considering that the cable forces not only depend on the actuator variables but also on the platform pose, one gets the derivative with respect to the actuator variables by

$$\delta\mathbf{f} = \frac{d\mathbf{f}(\mathbf{x}(\mathbf{q}_\theta))}{d\mathbf{q}_\theta}\delta\mathbf{q}_\theta = \left(\frac{\partial\mathbf{f}}{\partial\mathbf{q}_\theta} + \frac{\partial\mathbf{f}}{\partial\mathbf{x}}\frac{\partial\mathbf{x}}{\partial\mathbf{q}_\theta}\right)\delta\mathbf{q}_\theta \tag{56}$$

Implicit differentiation of force constraint (35) yields

$$\frac{d\mathbf{g}(\mathbf{x}(\mathbf{q}_\theta))}{d\mathbf{q}_\theta} = \frac{\partial\mathbf{g}(\mathbf{q}_\theta, \mathbf{x}, \mathbf{x}_0)}{\partial\mathbf{q}_\theta} + \frac{\partial\mathbf{g}(\mathbf{q}_\theta, \mathbf{x}, \mathbf{x}_0)}{\partial\mathbf{x}}\frac{\partial\mathbf{x}}{\partial\mathbf{q}_\theta} = \mathbf{0} \tag{57}$$

and therefore the mapping of the actuator variable $\mathbf{q}_\theta$ on the platform pose $\mathbf{x}$ while staying on the constraint manifold $\mathbf{g}$ yields

$$\delta\mathbf{x} = \frac{\partial\mathbf{x}}{\partial\mathbf{q}_\theta}\delta\mathbf{q}_\theta. \tag{58}$$

with

$$\frac{\partial\mathbf{x}}{\partial\mathbf{q}_\theta} = -\frac{\partial\mathbf{g}(\mathbf{q}_\theta, \mathbf{x})}{\partial\mathbf{x}}^{-1}\frac{\partial\mathbf{g}(\mathbf{q}_\theta, \mathbf{x})}{\partial\mathbf{q}_\theta}. \tag{59}$$

Now the relation between the cable forces $\mathbf{f}$ and the actuator variable $\mathbf{q}_\theta$ can be described by substituting (59) and (56) resulting in

$$\delta\mathbf{f} = \left(\frac{\partial\mathbf{f}}{\partial\mathbf{q}_\theta} - \frac{\partial\mathbf{f}}{\partial\mathbf{x}}\frac{\partial\mathbf{g}(\mathbf{q}_\theta, \mathbf{x})}{\partial\mathbf{x}}^{-1}\frac{\partial\mathbf{g}(\mathbf{q}_\theta, \mathbf{x})}{\partial\mathbf{q}_\theta}\right)\delta\mathbf{q}_\theta \tag{60}$$

Deriving force equation (32) with respect to the actuator variable $\mathbf{q}_\theta$ one gets

$$\mathbf{J}_{f\theta} = \frac{\partial \mathbf{f}}{\partial \mathbf{q}_\theta} = -\mathbf{KQ}^{-1}. \tag{61}$$

The partial derivative of Eq. (35) yields

$$\left(\underbrace{\frac{\partial}{\partial \mathbf{q}_\theta} \left(\mathbf{A}(\mathbf{x})^{\mathrm{T}} \right) \mathbf{f}(\mathbf{q}_\theta, \mathbf{x})}_{0} + \mathbf{A}(\mathbf{x})^{\mathrm{T}} \frac{\partial \mathbf{f}(\mathbf{q}_\theta, \mathbf{x})}{\partial \mathbf{q}_\theta} \right) = \mathbf{A}(\mathbf{x})^{\mathrm{T}} \frac{\partial \mathbf{f}(\mathbf{q}_\theta, \mathbf{x})}{\partial \mathbf{q}_\theta} \tag{62}$$

where the first part becomes zero since changes in the direction of the cable vector do not influence the structure matrix and the dependency of $\mathbf{x}(\mathbf{q}_\theta)$ is separately considered in Eq. (57). Using the matrix notation one can write

$$\delta \mathbf{f} = \mathbf{K}_{\mathrm{fq}} \delta \mathbf{q}_\theta \tag{63}$$

where

$$\mathbf{K}_{\mathrm{fq}} = \left(\mathbf{J}_{\mathrm{fq}} - \mathbf{J}_{\mathrm{fx}} \mathbf{J}_{\mathrm{gx}}^{-1} \mathbf{A}^{\mathrm{T}} \mathbf{J}_{\mathrm{fq}} \right) \tag{64}$$

is stiffness matrix in the joint space. The equation can be used for the investigation of the system stiffness and controller development.

6 Conclusion

In this paper the differential relations between geometrical and non-geometrical quantities were derived. Then the use for calibration, a force based forward kinematics and the investigation of system stiffness was shown. The decomposition of the kinematic relations allows more insight in the system properties and simplifies the implementation of algorithms that are making use of the Jacobians, because the individual components can be reused in different contexts.

References

1. Hiller, M., Fang, S., Mielczarek, S., Verhoeven, R., Franitza, D.: Design, analysis and realization of tendon-based parallel manipulators. Mech. Mach. Theory **40**, 429–445 (2005)
2. Hollerbach, J.M., Wampler, C.W.: The calibration index and taxonomy for robot kinematic calibration methods. Int. J. Robot. Res. **15**, 573–591 (1996)

3. Husty, M.L.: An algorithm for solving the direct kinematic of stewart-gough-type platforms. Mech. Mach. Theory **31**, 365–380 (1996)
4. Merlet, J.P., Daney, D.: A new design for wire-driven parallel robot. In: 2nd International Congress, Design and Modelling of mechanical systems. Monastir (2007).
5. Schiehlen, W., Eberhard, P.: Technische Dynamik, Modelle f"ur Regelung und Simulation. Teubner (1986).
6. Verhoeven, R.: Analysis of the workspace of tendon-based stewart platforms. Ph.D. thesis, University of Duisburg-Essen (2004).
7. Verl, A., Boye, T., Pott, A.: Measurement pose selection and calibration forecast for manipulators with complex kinematic structures. CIRP Ann.-Manuf. Technol. 57, 425–428 (2008).

Part VII
Control

Experimental Performance of Robust PID Controller on a Planar Cable Robot

Mohammad A. Khosravi and Hamid D. Taghirad

Abstract In this paper dynamic analysis and experimental performance of robust PID control for fully-constrained cable driven robots are studied in detail. Since in this class of manipulators cables should remain in tension for all maneuvers through their whole workspace, feedback control of such robots becomes more challenging than conventional parallel robots. To ensure that all the cables remain in tension, a corrective term is used in the proposed PID control scheme. In design of PID control it is assumed that there exist bounded norm uncertainties in Jacobian matrix and in all dynamics matrices. Then a robust PID controller is proposed to overcome partial knowledge of robot, and to guarantee boundedness of tracking errors. Finally, the effectiveness of the proposed PID algorithm is examined through experiments and it is shown that the proposed control structure is able to provide suitable performance in practice.

1 Introduction

Cable driven parallel manipulators (CDPMs) are a special class of parallel robots in which the rigid extensible links are replaced by actuated cables. In a CDPM the end-effector is connected to the base by a number of active cables. While the cables length is changing, the end-effector is manipulated toward the desired position and orientation. Cable driven robots have some advantages compared to that of conventional robots. Using cables as an alternative to rigid links enables cable robots

M. A. Khosravi(✉) · H. D. Taghirad
Advanced Robotics and Automated Systems, Industrial Control Center of Excellence,
Faculty of Electrical and Computer Engineering,
K. N. Toosi University of Technology, P.O. Box 6315-1355, Tehran, Iran
e-mail: m.a.khosravi@dena.kntu.ac.ir

H. D. Taghirad
e-mail: taghirad@kntu.ac.ir

to be used for very large workspace applications such as large adaptive reflector and SkyCam [1, 2]. Because of negligible mass and inertia of cables, they are suitable for high speed applications. Moreover, they can achieve some useful properties such as transportability and ease of assembly/disassembly, reconfigurability and economical structure and maintenance [3]. Consequently, CDPMs are exceptionally suitable to be used in many applications such as, handling of heavy materials [4], high speed manipulation [5, 6], cleanup of disaster areas [7], rapidly deployable rescue robots, and access to remote location and working in hazardous environment [8].

Using cables in the structure of the robot, however, introduces new challenges in the study of CDPMs. Cables can only apply tensile forces, therefore, the cables must be kept in tension in the whole workspace of the robot [9]. In order to fulfill this requirement, usually fully constrained structures are considered for a cable robot [7]. This kind of robots is being analyzed in this paper.

In comparison to the large amount of papers reported on the control of conventional robots, relatively few papers are reported on the control of CDPMs. However, many control schemes which are developed for serial or parallel robots, may be adapted for CDPMs. Lyapunov based control [6, 10], computed torque method [10, 11], sliding mode [12] and PD control [13] are some control algorithms being used in the control of CDPMs. The goal of this paper is to develop a position control algorithm based on PID, and verify its robustness against modeling uncertainties. This algorithm is formulated in task space and uses a corrective term to ensure that all the cables remain in tension.

The structure of this paper is as follows. In Sect. 2 kinematics and dynamics of CDPMs are studied in detail. Dynamic equations of actuators are obtained and incorporated in overall dynamics of the system. Section 3 describes the control algorithm of the system and according to upper bounds on dynamical terms, control gains are tuned such that the robust stability of the system is guaranteed. Finally, to show the effectiveness of proposed control algorithm experimental results for a planar cable driven robot are detailed in Sect. 4.

2 Kinematics and Dynamics Analysis

2.1 Kinematics Analysis

Cable driven robot is a closed kinematic chain mechanism whose end-effector is connected to the base by a number of actuated cables. The kinematics notation of a general cable driven robot with n cables is shown in Fig. 1. In this figure $\mathbf{l}_i$ denotes the vector along i'th cable and has the same length as the cable. The length of the i'th cable is denoted by l_i. $\mathbf{S}_i$ denotes the unit vector along the i'th cable from the base to the end-effector. A_i and B_i denote the attachment points of the i'th cable on the base and end-effector, respectively. The positions of the attachment points A_i and B_i are represented by vectors $\mathbf{a}_i$, $\mathbf{b}_i$, respectively. Obviously, $\mathbf{a}_i$ is a constant vector in the

Fig. 1 Kinematic schematic of a general CDRPM
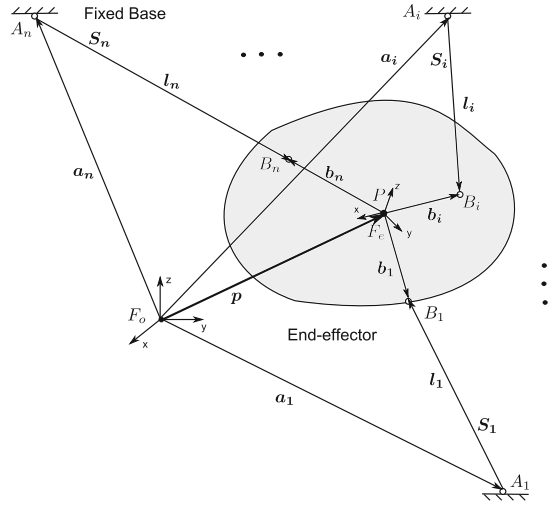
base frame F_o and $\mathbf{b}_i$ is a constant vector in the end-effector frame F_e. The origin of the end-effector frame F_e is fixed at a reference point P, the end-effector center of mass, which is used to define the position vector of the end-effector $\mathbf{p}$. Based on the kinematics notation defined in Fig. 1 the position of the end-effector may be written as:

$$\mathbf{p} = \mathbf{a}_i + \mathbf{l}_i - \mathbf{b}_i \, (i = 1, 2, \cdots, n) \tag{1}$$

where all vectors are represented in the base frame F_o. As a result

$$l_i^2 = [\mathbf{p} - \mathbf{a}_i + \mathbf{b}_i]^T \cdot [\mathbf{p} - \mathbf{a}_i + \mathbf{b}_i] \tag{2}$$

Differentiate this equation with respect to time, and rewrite it into matrix form as:

$$\dot{\mathbf{L}} = \tilde{\mathbf{J}} \mathbf{t} \tag{3}$$

in which,

$$\tilde{\mathbf{J}} = \begin{bmatrix} \mathbf{S}_1 & \mathbf{S}_2 & \cdots & \mathbf{S}_n \\ \mathbf{b}_1 \times \mathbf{S}_1 & \mathbf{b}_2 \times \mathbf{S}_2 & \cdots & \mathbf{b}_n \times \mathbf{S}_n \end{bmatrix}^T \tag{4}$$

and, $\dot{\mathbf{L}} = \begin{bmatrix} \dot{l}_1, \dot{l}_2, \cdots, \dot{l}_n \end{bmatrix}^T$, and $\mathbf{t} = \begin{bmatrix} \dot{\mathbf{p}}, \boldsymbol{\omega} \end{bmatrix}^T = \begin{bmatrix} \dot{\mathbf{p}}_x, \dot{\mathbf{p}}_y, \dot{\mathbf{p}}_z, \omega_x, \omega_y, \omega_z \end{bmatrix}^T$. The matrix $\tilde{\mathbf{J}}$ is the Jacobian matrix corresponding to the general cable robot, $\dot{\mathbf{p}}$ denotes the velocity vector of point P; $\boldsymbol{\omega}$ denotes angular velocity of the end-effector, and $\mathbf{t}$ represents the twist vector in $\mathbb{R}^6$, which consists of the linear and angular velocities of the end-effector.

Fig. 2 Dynamics schematic of a general CDRPM
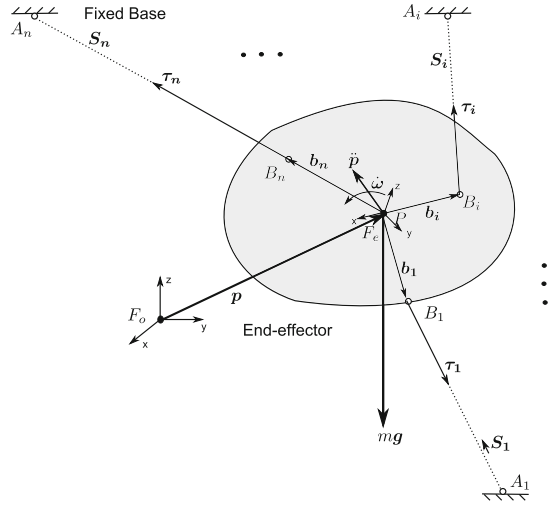
2.2 Dynamics Analysis

For a typical cable robot the mass of the cables is extremely smaller than that of the end-effector, and can therefore be neglected. By this assumption the dynamics model of the robot reduces to that of the end-effector. Based on the dynamics notation given in Fig. 2, when all the cables are in tension the equations of motion can be derived using Newton-Euler laws [14].

$$\begin{bmatrix} m\mathbf{I} & \mathbf{0}_{3\times3} \\ \mathbf{0}_{3\times3} & \mathbf{I}_P \end{bmatrix} \begin{bmatrix} \ddot{\mathbf{p}} \\ \dot{\boldsymbol{\omega}} \end{bmatrix} + \begin{bmatrix} \mathbf{0}_{3\times1} \\ \boldsymbol{\omega} \times \mathbf{I}_P\boldsymbol{\omega} \end{bmatrix} + \begin{bmatrix} -m\mathbf{g} \\ \mathbf{0}_{3\times1} \end{bmatrix} = -\tilde{\mathbf{J}}^T\boldsymbol{\tau} \tag{5}$$

in which, m denotes mass of the end-effector; $\mathbf{I}_P$ denotes inertia tensor of the end-effector about point P in F_o frame; $\mathbf{g}$ denotes the gravity acceleration vector; $\boldsymbol{\tau} = [\tau_1, \tau_2, \cdots, \tau_n]$ denotes the vector of cable forces and τ_i denotes the cable force value in the i'th cable.

Consider $\mathbf{x} = [x_p, y_p, z_p, \alpha, \beta, \gamma]^T$ as generalized coordinates vector, in which $\boldsymbol{\theta} = [\alpha, \beta, \gamma]^T$ is the vector of Euler angles. With this definition the rotation matrix $^{F_o}\mathbf{R}_{F_e}$ can be written in term of roll-pitch-yaw Euler angels,

$$^{F_o}\mathbf{R}_{F_e} = \begin{bmatrix} c\beta c\gamma & c\gamma s\alpha s\beta - c\alpha s\gamma & c\alpha c\gamma s\beta + s\alpha s\gamma \\ c\beta s\gamma & c\alpha c\gamma + s\alpha s\beta s\gamma & -c\gamma s\alpha + c\alpha s\beta s\gamma \\ -s\beta & c\beta s\alpha & c\alpha c\beta \end{bmatrix} \tag{6}$$

where c and s denotes shorthand writings for sin and cos functions, respectively. Furthermore, the angular velocity of the end-effector can be written as,

$$\boldsymbol{\omega} = \mathbf{E}\dot{\boldsymbol{\theta}}, \quad \dot{\boldsymbol{\theta}} = \left[\dot{\alpha}, \dot{\beta}, \dot{\gamma}\right]^T \tag{7}$$

in which,

$$\mathbf{E} = \begin{bmatrix} c\beta c\gamma & -s\gamma & 0 \\ c\beta s\gamma & c\gamma & 0 \\ -s\beta & 0 & 1 \end{bmatrix}$$

Thus, one can write,

$$\dot{\mathbf{L}} = \mathbf{J}\dot{\mathbf{x}} \tag{8}$$

in which,

$$\mathbf{J} = \tilde{\mathbf{J}} \begin{bmatrix} \mathbf{I}_{3\times 3} & \mathbf{0}_{3\times 3} \\ \mathbf{0}_{3\times 3} & \mathbf{E} \end{bmatrix} \tag{9}$$

With this notation, the equations of motion can be written in the terms of $\mathbf{x}$. After some manipulation these equations can be derived in an explicit form as,

$$\mathbf{M}(\mathbf{x})\ddot{\mathbf{x}} + \mathbf{C}(\mathbf{x}, \dot{\mathbf{x}})\dot{\mathbf{x}} + \mathbf{G}(\mathbf{x}) = -\mathbf{J}^T \boldsymbol{\tau} \tag{10}$$

in which,

$$\mathbf{M}(\mathbf{x}) = \begin{bmatrix} m\mathbf{I}_{3\times 3} & \mathbf{0}_{3\times 3} \\ \mathbf{0}_{3\times 3} & \mathbf{E}^T \mathbf{I}_P \mathbf{E} \end{bmatrix} \tag{11}$$

$$\mathbf{C}(\mathbf{x}, \dot{\mathbf{x}}) = \begin{bmatrix} \mathbf{0}_{3\times 3} & \mathbf{0}_{3\times 3} \\ \mathbf{0}_{3\times 3} & \mathbf{E}^T \mathbf{I}_P \dot{\mathbf{E}} + \mathbf{E}^T (\mathbf{E}\dot{\boldsymbol{\theta}})_\times \mathbf{I}_P \mathbf{E} \end{bmatrix} \tag{12}$$

$$\mathbf{G}(\mathbf{x}) = \begin{bmatrix} -m\mathbf{g} \\ \mathbf{0}_{3\times 1} \end{bmatrix} \tag{13}$$

2.3 Overall Robot Dynamics

In this section overall dynamics of the cable robot considering actuators dynamics is obtained. In practice a robot is always experiencing friction and disturbance forces. Therefore, we can reformulate the manipulator dynamics as

$$\mathbf{M}(\mathbf{x})\ddot{\mathbf{x}} + \mathbf{C}(\mathbf{x}, \dot{\mathbf{x}})\dot{\mathbf{x}} + \mathbf{G}(\mathbf{x}) + \mathbf{F}_d\dot{\mathbf{x}} + \mathbf{F}_s(\dot{\mathbf{x}}) + \mathbf{T}_d = -\mathbf{J}^T \boldsymbol{\tau} \tag{14}$$

with $\mathbf{x}$ as the generalized coordinates vector, $\boldsymbol{\tau}$ as the vector of cable forces, $\mathbf{F}_d$ as the coefficient matrix of viscous friction and $\mathbf{F}_s$ as a Coulomb friction term. $\mathbf{M}(\mathbf{x})$ denotes the mass matrix, $\mathbf{C}(\mathbf{x}, \dot{\mathbf{x}})$ denotes the Coriolis/centripetal matrix, and $\mathbf{G}(\mathbf{x})$ denotes the gravity vector which are defined in previous section. $\mathbf{J}$ is the jacobian matrix of the robot and $\mathbf{T}_d$ denotes disturbance, which may represent, any modeling

uncertainty. The robot dynamics may be written as

$$\mathbf{M}(\mathbf{x})\ddot{\mathbf{x}} + \mathbf{N}(\mathbf{x}, \dot{\mathbf{x}}) = -\mathbf{J}^T \boldsymbol{\tau} \tag{15}$$

where

$$\mathbf{N}(\mathbf{x}, \dot{\mathbf{x}}) = \mathbf{C}(\mathbf{x}, \dot{\mathbf{x}})\dot{\mathbf{x}} + \mathbf{G}(\mathbf{x}) + \mathbf{F}_d \dot{\mathbf{x}} + \mathbf{F}_s(\dot{\mathbf{x}}) + \mathbf{T}_d \tag{16}$$

It should be noted that the dynamic model is valid only when $\boldsymbol{\tau} \geq 0$ and $\mathbf{J}$ is nonsingular. On the other hand, the actuators dynamics is represented by

$$\mathbf{I}_m \ddot{\mathbf{q}} + \mathbf{D}\dot{\mathbf{q}} - r\boldsymbol{\tau} = \mathbf{u} \qquad \boldsymbol{\tau} \geq 0 \tag{17}$$

in which, $\mathbf{q}$ denotes motors angular position vector, $\mathbf{I}_m$ denotes actuator moments of inertia matrix, $\mathbf{D}$ denotes a diagonal positive definite matrix which represents actuator viscous friction, r denotes the radius of pulleys, $\boldsymbol{\tau}$ denotes the cable tension vector and $\mathbf{u}$ denotes the motor torque vector. As for the position reference, define all $\mathbf{q}$ to be zero when the end-effector centroid is located at the central position. From this configuration positive angle $\mathbf{q}$ will cause a change $\Delta \mathbf{L}$ in cable lengths, therefore, we have:

$$\Delta \mathbf{L} = r\mathbf{q} = \mathbf{L} - \mathbf{L}_0 \Rightarrow \mathbf{q} = r^{-1}(\mathbf{L} - \mathbf{L}_0) \tag{18}$$

where $\mathbf{L}_0$ is the initial length vector at $\mathbf{x} = 0$. Differentiate this equation and use manipulator Jacobian relation $\dot{\mathbf{L}} = \mathbf{J}\dot{\mathbf{x}}$ to write:

$$\dot{\mathbf{q}} = r^{-1}\dot{\mathbf{L}} = r^{-1}\mathbf{J}\dot{\mathbf{x}} \ , \ \ \ddot{\mathbf{q}} = r^{-1}\mathbf{J}\ddot{\mathbf{x}} + r^{-1}\dot{\mathbf{J}}\dot{\mathbf{x}} \tag{19}$$

Use Eqs. (19), (17) and (14) with some manipulations one may reach to:

$$\mathbf{M}_{eq}(\mathbf{x})\ddot{\mathbf{x}} + \mathbf{N}_{eq}(\mathbf{x}, \dot{\mathbf{x}}) = \mathbf{J}^T \mathbf{u} \tag{20}$$

in which,

$$\begin{cases} \mathbf{M}_{eq}(\mathbf{x}) = r\mathbf{M}(\mathbf{x}) + r^{-1}\mathbf{J}^T \mathbf{I}_m \mathbf{J} \\ \mathbf{C}_{eq}(\mathbf{x}, \dot{\mathbf{x}}) = r\mathbf{C}(\mathbf{x}, \dot{\mathbf{x}}) + r^{-1}\mathbf{J}^T \mathbf{I}_m \dot{\mathbf{J}} \\ \mathbf{N}_{eq}(\mathbf{x}, \dot{\mathbf{x}}) = r\mathbf{N}(\mathbf{x}, \dot{\mathbf{x}}) + r^{-1}\mathbf{J}^T \mathbf{I}_m \dot{\mathbf{J}}\dot{\mathbf{x}} + r^{-1}\mathbf{J}^T \mathbf{D}\mathbf{J}\dot{\mathbf{x}} \end{cases} \tag{21}$$

In this formulation, actuator dynamics is included and transformed into task space by Jacobian matrix, which is a projection from cable length space to task space.

3 Robust PID Control of Cable Driven Robot

In this section we propose a robust PID controller based on the nominal model of the system. In the design procedure of the controller we suppose that the dynamical matrices such as $\mathbf{M}_{eq}(\mathbf{x})$, $\mathbf{C}_{eq}(\mathbf{x}, \dot{\mathbf{x}})$, etc are all uncertain and we have only some

information about their bounds. Furthermore, we suppose that the end-effector position $\mathbf{x}$ is accurately measured in real time. In contrast, it is assumed that the attachment points are not precisely implemented in practice. Therefore, we have to use an uncertain jacobian matrix $\hat{\mathbf{J}}$ obtained from the uncertain installation of the attachment points. The control law is designed based on these bounds and assumptions to satisfy some robust stability conditions.

Recall dynamic model of the system (20), in presence of uncertainties in all dynamical terms, it can be shown that [15]:

$$\underline{m} \leq \|\mathbf{M}_{eq}(\mathbf{x})\| \leq \overline{m} \quad ; \quad \|\mathbf{C}_{eq}(\mathbf{x}, \dot{\mathbf{x}})\| \leq \xi_{C_{eq}} \|\dot{\mathbf{x}}\| \tag{22}$$

$$\|\mathbf{G}_{eq}(\mathbf{x})\| \leq \xi_{g_{eq}} \quad ; \quad \|\mathbf{F}_d \dot{\mathbf{x}} + \mathbf{F}_s(\dot{\mathbf{x}})\| \leq \xi_{f0} + \xi_{f1} \|\dot{\mathbf{x}}\| \tag{23}$$

$$i_{m1}\mathbf{I} \leq \mathbf{I}_m \leq i_{m2}\mathbf{I} \quad ; \quad d_1\mathbf{I} \leq \mathbf{D} \leq d_2\mathbf{I} \tag{24}$$

in which $\underline{m}, \overline{m}, \xi_{C_{eq}}, \xi_{g_{eq}}, \xi_{f0}, \xi_{f1}, i_{m1}, i_{m2}, d_1$, and d_2 are some positive real constants. Moreover, if the disturbances are bounded, for a positive constant ξ_t one may write:

$$\|\mathbf{T}_d\| \leq \xi_t \tag{25}$$

Now choose a controller for the system consist of a PID control law and a corrective term $\mathbf{Q}$, as following:

$$\mathbf{u} = \hat{\mathbf{J}}^\dagger \left[\mathbf{K}_V \dot{\mathbf{e}} + \mathbf{K}_P \mathbf{e} + \mathbf{K}_I \int_0^t \mathbf{e}(s)ds \right] + r\mathbf{Q} = \hat{\mathbf{J}}^\dagger \mathbf{K}\mathbf{y} + r\mathbf{Q} \tag{26}$$

in which,

$$\mathbf{e} = \mathbf{x}_d - \mathbf{x} \tag{27}$$

$$\mathbf{K} = [\mathbf{K}_I \quad \mathbf{K}_P \quad \mathbf{K}_V] \tag{28}$$

$$\mathbf{y} = \left[\int_0^t \mathbf{e}^T(s)ds \quad \mathbf{e}^T \quad \dot{\mathbf{e}}^T \right]^T \tag{29}$$

and, $\hat{\mathbf{J}}^\dagger$ denotes the pseudo-inverse of $\hat{\mathbf{J}}^T$. In this controller structure the corrective term $\mathbf{Q}$ spans the null space of $\hat{\mathbf{J}}^T$ and must satisfy

$$\hat{\mathbf{J}}^T \mathbf{Q} = \mathbf{0} \tag{30}$$

The vector $\mathbf{Q}$ is used in the control structure to ensure that all cables remain in tension in the whole workspace. Moreover, this term increases the stiffness of the system. The estimated matrix $\hat{\mathbf{J}}^T$ obtained from inaccurate installation of the

attachment points is assumed to be bounded by:

$$\|\mathbf{I} - \mathbf{J}^T \hat{\mathbf{J}}^\dagger\| \leq \delta_1, \qquad \|\mathbf{J} - \hat{\mathbf{J}}\| \leq \delta_2 \tag{31}$$

By implementation of this control law **u**, in the system dynamics represented by (20), the closed loop system error dynamics may be written as:

$$\dot{\mathbf{y}} = \mathbf{A}\mathbf{y} + \mathbf{B}\Delta\mathbf{A} \tag{32}$$

in which,

$$\mathbf{A} = \begin{bmatrix} \mathbf{0} & \mathbf{I}_6 & \mathbf{0} \\ \mathbf{0} & \mathbf{0} & \mathbf{I}_6 \\ -\mathbf{M}_{eq}^{-1}\mathbf{K}_I & -\mathbf{M}_{eq}^{-1}\mathbf{K}_P & -\mathbf{M}_{eq}^{-1}\mathbf{K}_V \end{bmatrix}, \quad \mathbf{B} = \begin{bmatrix} \mathbf{0} \\ \mathbf{0} \\ \mathbf{M}_{eq}^{-1} \end{bmatrix} \tag{33}$$

and

$$\Delta\mathbf{A} = \mathbf{N}_{eq}(\mathbf{x}, \dot{\mathbf{x}}) + \mathbf{M}_{eq}\ddot{\mathbf{x}}_d + (\mathbf{I} - \mathbf{J}^T\hat{\mathbf{J}}^\dagger)\mathbf{u}_1 + r(\hat{\mathbf{J}}^T - \mathbf{J}^T)\mathbf{Q} \tag{34}$$

It is fully elaborated in [15], that the positioning error represented by (32) is uniformly ultimately bounded (UUB) provided that the control gains are selected from a suitable feasible set. Furthermore, it is shown that if the control gains $\mathbf{K}_P, \mathbf{K}_v$, and $\mathbf{K}_I$ are chosen large enough, the feasibility conditions are easily satisfied. The proof of these conditions are based on Lyapunov stability analysis for the uncertain system. In this paper we leave the theoretical details of the proposed method, and verify the performance of the closed-loop system through experiments.

4 Experimental Results

In order to verify the performance of the proposed method, it is applied to a planar cable robot. This manipulator consists of four actuated limbs and has with three degrees of freedom (x, y, ϕ), and is under investigation for high speed and wide workspace applications in K. N. Toosi University of Technology.

4.1 Experimental Setup

The planar cable robot under investigation is illustrated in Fig. 3, in which the end-effector mass is considered as m = 2.5 kg with a variation of 1 kg. Actuators are located on the vertices of a rectangle with dimension of 2.24 × 2.1 m. The block diagram of the cable robot control hardware configuration is shown in Fig. 4, in
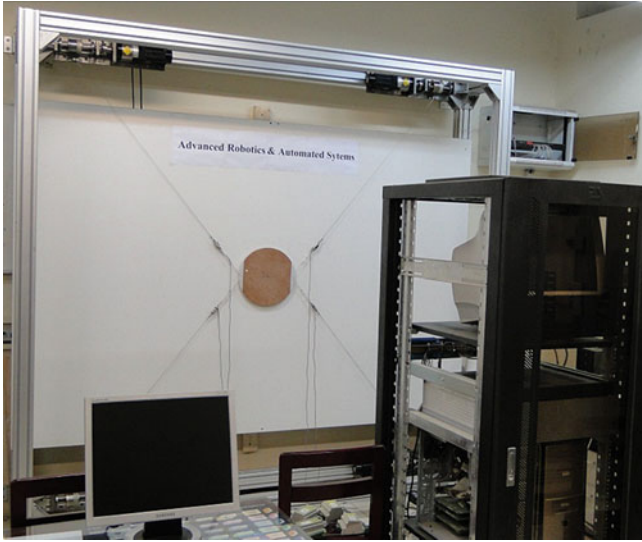
Fig. 3 The planar cable driven redundant parallel manipulator under investigation for high speed and wide workspace applications in K. N. Toosi University of Technology
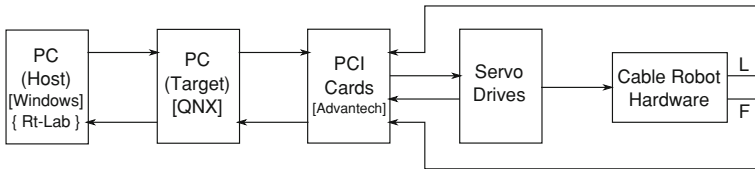
Fig. 4 Control Experimental Setup

which a real-time hardware in the loop structure is used for the experiments. The host computer serves as the user interface and enables the user to edit and modify the controller in a user friendly environment. This interface is developed in Simulink toolbox of Matlab to provide suitable environment for evaluation of different control routines on the system. The target computer is a real time processing computer which uses QNX operating system and performs real time execution of the control laws and real time communication with Input/Output channels. RT-LAB software is used as the main hardware in the loop software and uses Simulink toolbox of Matlab to easily define the required operations and compile and execute those operations in real time QNX environment [16]. The interfacing boards between the sensors, actuators and the target computer are channeled through PCI bus I/O interfaces, and are integrated with the RT-LAB and Matlab to create a real time control system.
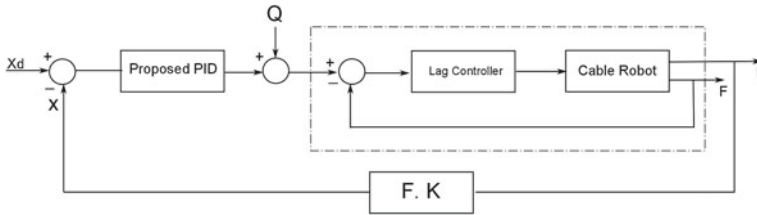
Fig. 5 Cascade control block diagram

4.2 Control Scheme

To have a good performance in position and orientation tracking, servo drives should generate the desired tensions in the cables according to the outputs of the proposed control algorithm. In other words, the servo drives should perform as ideal torque sources to be able to perform such task. Based on this fact, cascade control scheme is proposed for the experiments. The cascade control strategy uses two control loops, called as the outer and the inner loops as shown in Fig. 5.

The main goal of the outer loop which consists of the proposed PID control law is to control the position and orientation of the end-effector. Inputs of this loop are the position and orientation errors and its outputs are desired tensions in the cables. In the inner loop, the desired tensions are compared to actual tensions measured by force sensors embedded at the end-effector attachment points. TLL500 from Transducer Techniques is used as suitable force sensors in the experiments due to their relatively large measurement range and low weight. Since in practice the actual tensions can never track the desired tensions perfectly, the main purpose of using cascade scheme in control structure of the robot is to obtain a desirable bandwidth for the inner loop which is much larger than that for the outer control loop [17]. Notice that to implement the proposed control law it is assumed that the position of the end-effector is measured in task space. However, in practice and for this experiments the cable lengths are measured in the joint space, and as shown in Fig. 5, forward kinematics solution is used to find the position vector **x**. In practice, a suitable solution to forward kinematics of the robot is found in real time, by implementation of sequential quadratic programming routine (CFSQP) as an s-function in Simulink.

4.3 Results

The first set of experiments aims to generate two disjointed linear motions in translation and rotation. In x direction, it is considered to move the end-effector from the origin to $[0.2, 0, 0]^T$ and in ϕ direction it is considered to rotate the end-effector from its central position to $[0, 0, \pi/9]^T$. Furthermore, a more challenging circular profile is considered in the next experiments, to track a circular path of 0.2m about
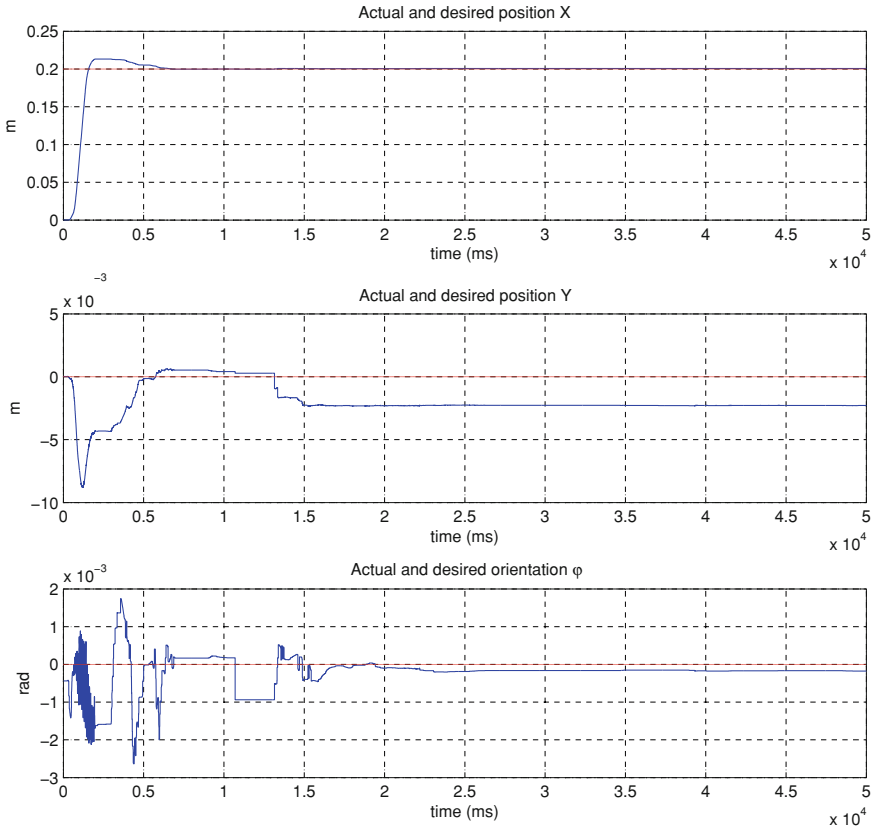
Fig. 6 Implementation results showing the actual and desired position and orientation of the end-effector for $\mathbf{x}_d = [0.2, 0, 0]^T$

the central position. For the first experiment, suppose that the home position for the end-effector is $\mathbf{x} = [0, 0, 0]^T$ in SI units and the desired end-effector position and orientation is $\mathbf{x}_d = [0.2, 0, 0]^T$. The results of implementation using proposed PID control (26) in companion to the required $\mathbf{Q}$, which ensures that all the cables are in tension, are given in Fig. 6. The controller gains are selected in the feasible stability region of the system considering modeling uncertainty bounds, as $k_P = 5000$, $k_V = 1500$, $k_I = 200$. As it is seen in this figure position and orientation outputs track the desired values very well and the steady state errors are very small and in order of 10^{-3}, while as it is shown in Fig. 7 all cables are in tension for the whole maneuver. The prescribed uniformly ultimately bounded tracking error for the control structure is verified in all three directions in this experiment.

In the second experiment, suppose that the desired orientation of the end-effector is $\mathbf{x}_d = [0, 0, \pi/9]^T$, while the same controller gains are considered. The experimental results are given in Fig. 8. As it is observed, tracking performance is very suitable and
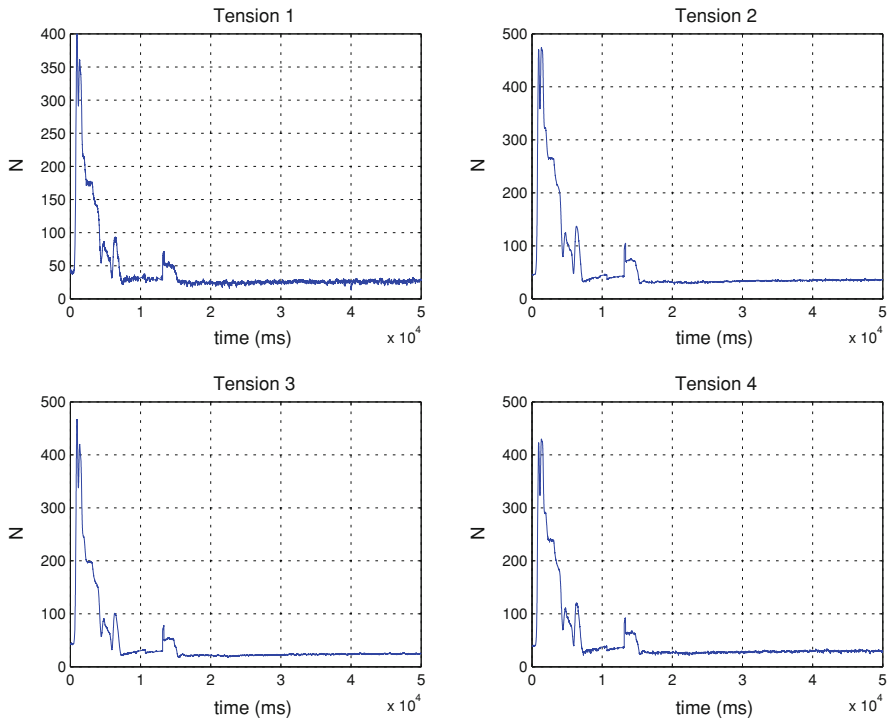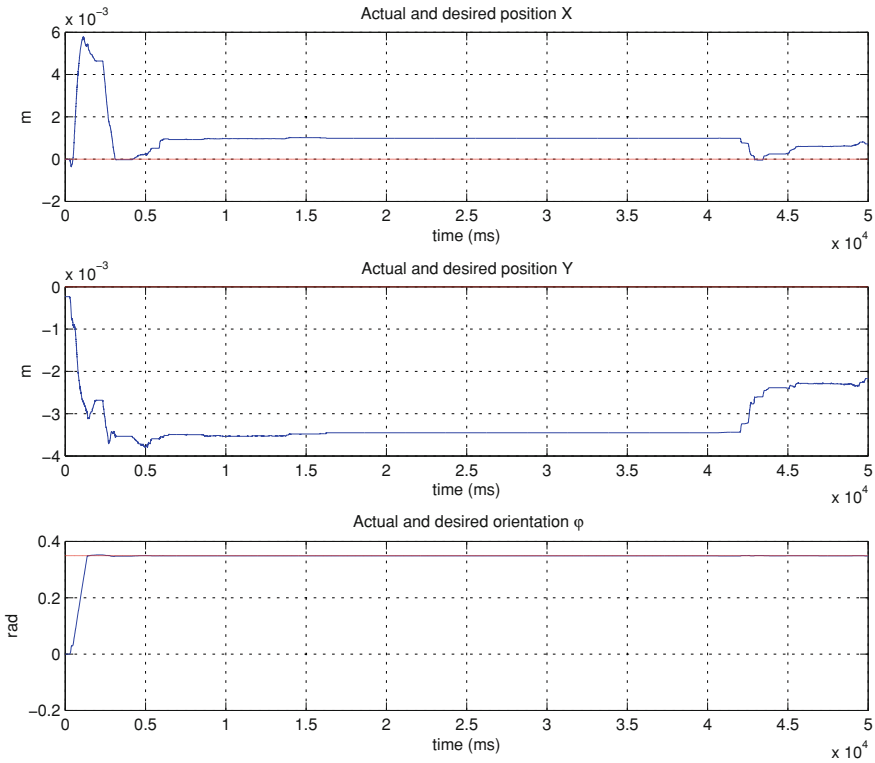
Fig. 7 Implementation results showing the cables tension for $\mathbf{x}_d = [0.2, 0, 0]^T$

the position errors in x and y directions are small and in order of 10^{-3}. Furthermore, as it is shown in Fig. 9, it is observed that all tensions in the cables for this test are also positive.

For the circular profile, the end-effector is commanded to track a circular path with radius of 0.2 m in 10 s, while attempting to maintain $\phi = 0$ in all time. The reference Cartesian positions for this experiment are $x = 0.2 \cos(0.2\pi t)$ and $y = 0.2 \sin(0.2\pi t)$. Figures 10 and 11 show the reference and actual circle and deviation of ϕ from its zero desired value. It can be seen that the proposed PID control scheme is capable to perform such maneuver, while the absolute positioning errors are relatively small. As it is seen in Fig. 11, orientation error in this test is very small and in order of 10^{-3}.

To verify the repeatability of the cable robot another experiment is performed. Repeatability of the cable robot is considered by repeating performance of a circular trajectory of the end-effector. In this experiment the trajectory is considered for eight turns, for a circle with radius of 0.2 m, while attempting to maintain zero orientation. Figure (12) shows the performance of the robot in this experiment. As it is seen in this figure the repeatability performance of the robot is far better than absolute positioning of the end effector. There are some potential sources of error in these experiments
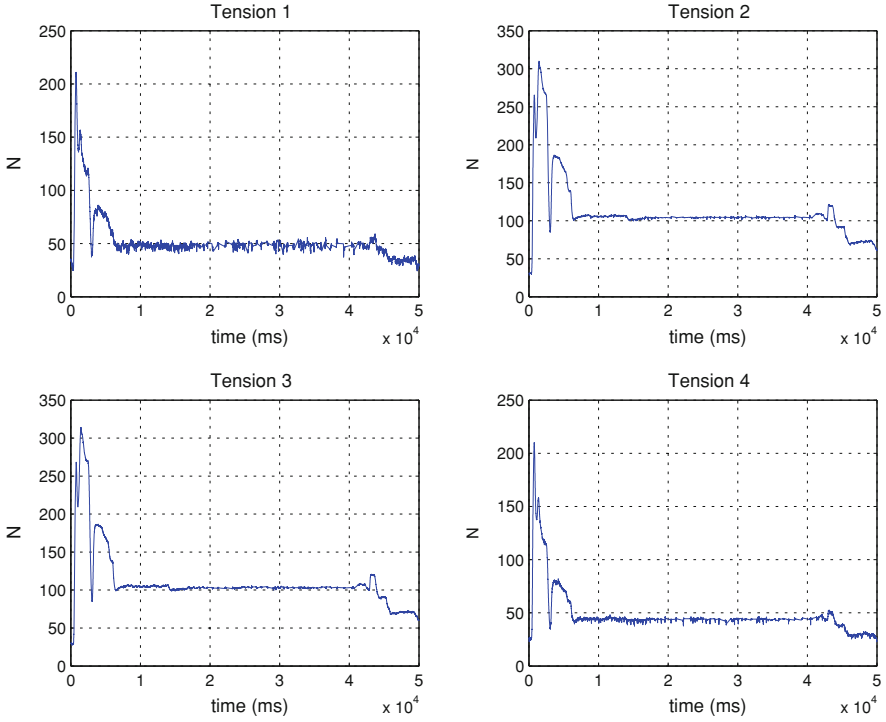
Fig. 8 Implementation results showing the actual and desired position and orientation of the end-effector for $\mathbf{x}_d = [0, 0, \pi/9]^T$

which are under current improvement. One issue is the friction and backlash in the gearing transmission of the actuators and other uncertainties that are not taken into account. Furthermore, as explained before, actual position and orientation of the end-effector are not directly measured and are computed by forward kinematics solution. This leads to a finite error in the computations which may lead to the final positioning error of the system. Furthermore, the elasticity of the cables are simply neglected in this analysis, which may lead to positioning errors, especially at high speed maneuvers.

5 Conclusions

This paper addresses the issues of dynamic analysis and control of fully constrained cable robots. According to limiting characteristics of cables that can only apply tensile forces, and in order to ensure that all the cables are in tension for all maneuvers

Fig. 9 Implementation results showing the cables tension for $\mathbf{x}_d = [0, 0, \pi/9]^T$

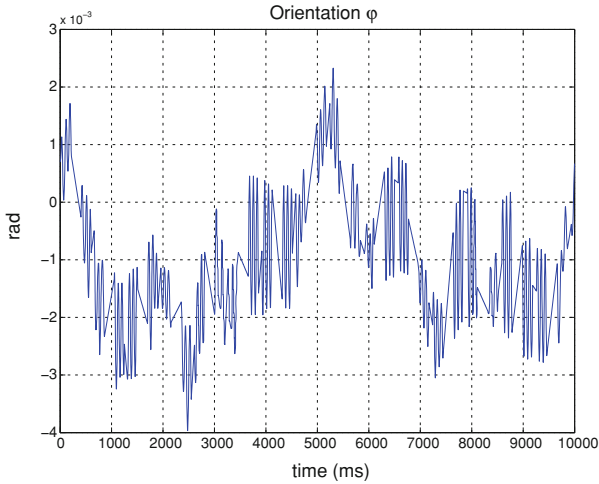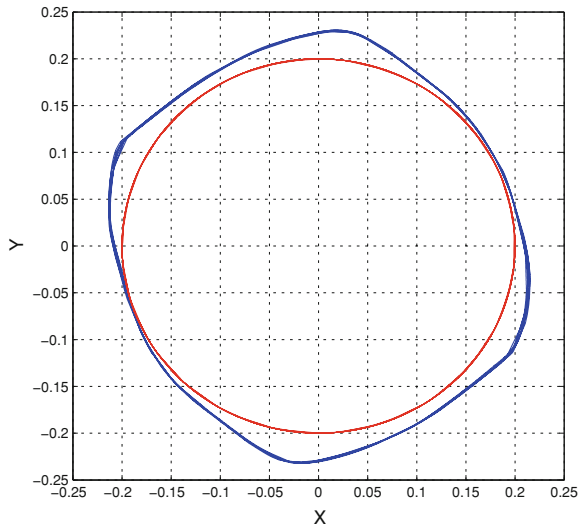**Fig. 10** Implementation results for a circular trajectory
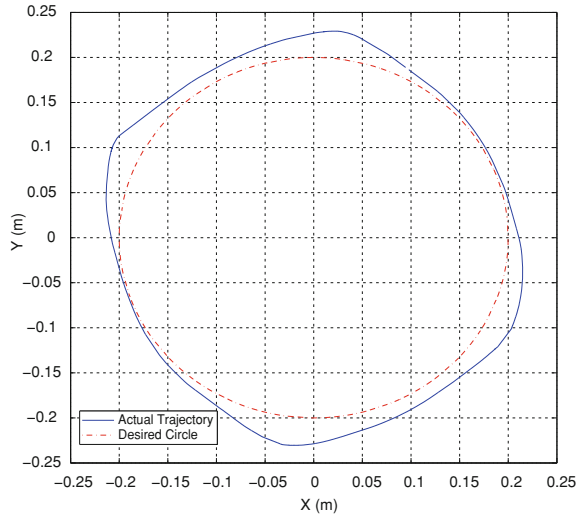
Fig. 11 Implementation results showing the rotation ϕ during circular trajectory

Fig. 12 Implementation results showing the repeatability of the cable robot

through their whole workspace, a corrective term based on null space of the Jacobian transpose is used in companion with the proposed PID algorithm. In the design of proposed PID controller it is assumed that in dynamic equations of cable robot all terms are uncertain and only some information about their upper bounds is available. A robust PID controller is proposed to overcome partial knowledge of robot, and to guarantee boundedness of tracking errors. Finally, to show the effectiveness of the proposed algorithm several experiments on a three degrees of freedom planar

cable robot are performed with different desired trajectories and suitable tracking performance for the closed loop system is reported.

References

1. Skycam, an innovative technology. http://www.skycam.tv. Oklahoma, USA (2006)
2. Taghirad, H.D., Nahon, M.A.: Kinematic analysis of a macro-micro redundantly actuated parallel manipulator. Adv. Robot. **22**(6–7), 657–687 (2008)
3. Khosravi, M.A., Taghirad, H.D.: Dynamic analysis and control of cable driven robots with elastic cables. Trans. Can. Soc. Mech. Eng. **35**(4), 543–557 (2011)
4. Bostelman, R., Albus, J., Dagalakis, N. Jacoff, A.: Applications of the NIST robocrane. In: Proceedings of the 5th International Symposium on Robotics and Manufacturing (1994)
5. Maeda, K., Tadokoro, S., Takamori, T., Hiller, M.: R. On design of a redundant wire-driven parallel robot WARP manipulator. In: Proceedings of IEEE International Conference on Robotics and Automation. Verhoeven (1999)
6. Kawamura, S., Kino, H., Won, C.: High-speed manipulation by using parallel wire-driven robots. Robotica **18**(3), 13–21 (2000)
7. Roberts, R., Graham, T., Lippitt, T.: On the inverse kinematics, statics, and fault tolerance of cable-suspended robots. J. Robot. Syst. **15**(10), 649–661 (1998)
8. Riechel, A. Bosscher, P., Lipkin, H. Ebert-Uphoff, I.: Cable driven robots for use in hazardous environments. In: Proceedings of 10th International Conference on Robotics and Remote Systems for Hazardeous Enviromnments. Gainesville (2004)
9. Behzadipour, S., Khajepour, A.: Stiffness of cable-based parallel manipulators with application to stability analysis. J. Mech. Des. **128**(1), 303–310 (2006)
10. Alp, A., Agrawal, S.: Feedback controllers with positive inputs. In: Proceedings of the American Control Conference, Cable Suspended Robots (2002)
11. Williams, R.L., Gallina P., Vadia, J.: Planar translational cable direct driven robots. J. Robot. Syst. **20**(3), 107–120 (2003)
12. Ryoek, S., Agrawal, S.: Generation of feasible set points and control of a cable robot. IEEE Trans. Robot. **22**(3), 551–558 (2006)
13. Kino, H., Yahiro, T., Takemura, F.: Robust PD control using adaptive compensation for completely restrained parallel-wire driven robots. IEEE Trans. Robot. **23**(4), 803–812 (2007)
14. Diao, X., Ma, O.: Vibration analysis of cable-driven parallel manipulators. Multibody Syst. Dyn. **21**, 347–360 (2009)
15. Khosravi, M.A., Taghirad, H.D.: Robust PID control of fully-constrained cable driven robots. Submitted to IEEE/ASME Trans. Mechatron. (2012)
16. RT-LAB version 8 User Guide. Opal-RT Company (2005)
17. Meunier, G., Boulet, B., Nahon, M.: control of an overactuated cable-driven parallel mechanism for a radio telescope application. IEEE Trans. Control Syst. Tech. **17**(5), 1043–1054 (2009)

A Preliminary Study for H_∞ Control of Parallel Cable-Driven Manipulators

Edouard Laroche, Ryad Chellal, Loïc Cuvillon and Jacques Gangloff

Abstract This paper reports preliminary investigations for H_∞ control of cable-driven parallel robot. This methodology specially suits for multi-input multi-output systems including flexible modes, which is the case of cable robots with flexible cables. A nonlinear model is first developed accounting for flexible cables for the case where actuators are speed controlled. A first method based on a rigid model is proposed as an adaptation for speed-controlled actuators of the well-known Jacobian-based method. A low-pass filter is tuned in order to increase the reachable bandwidth. The H_∞ controller is derived from a linear dynamic model. One interest is that one single controller manages both the position of the end-effector and the cable tension. The simulation results show that improvements are possible in the bandwidth thanks to the H_∞ control.

1 Introduction

Cable-driven parallel robots have several advantages that make them an attractive solution for several original application field. Thanks to their large operation range, they allow to move a camera over an operation field such as astadium (see the

E. Laroche (✉) · R. Chellal · L. Cuvillon · J. Gangloff
LSIIT laboratory, Strasbourg university and CNRS, Strasbourg, France
e-mail: Edouard.laroche@lsiit-cnrs.unistra.fr

R. Chellal
e-mail: Ryad.chellal@lsiit-cnrs.unistra.fr

L. Cuvillon
e-mail: Loic.Cuvillon@lsiit-cnrs.unistra.fr

J. Gangloff
e-mail: Jacques.Gangloff@lsiit-cnrs.unistra.fr

Cablecam company, http://www.cablecam.com/). Their low invasiveness and potentially high safety make then good candidates for interactions with human operators, such as in medical robotics [1].

When dealing with control, several items must be considered:

- As any parallel manipulator, kinematic constraints must be managed by the control law.
- Their main default is common with all the flexible manipulators: due to the elongation of the cables, a control at the joint level cannot ensure an accurate positioning of the end-effector level. Therefore, some exteroceptive sensor is necessary (see Dallej et al. for a prospective study of vision-based control of a cable-driven robot [6]).

Several approaches have been proposed in the literature for the control of cable robots. To our knowledge, the first approach for handling the cable tension was proposed by Ming and Higuchi [14]. Zi et al. consider long cables and account for their geometry to derive a fuzzy controller [22]. You et al. use a backstepping approach to control a 3-DOF cable robot [20]. Alikhani and Vali use sliding mode to control a 3 DOF suspended crane and the second Lyapunov approach to show the stability of the control scheme [2]. Diao and Ma consider a model where the flexible effects are modeled as equivalent springs and analyses the flexible modes [7] but do not consider any control solution.

H_∞ control methodology has been developed following the works of Zames and Francis [21]. It is now a standard method that is used in demanding applications and has become a standard method in aeronautics for attitude control of satellites, aircrafts or rockets with structural flexibility [17]. This methodology has been used also in Robotics for the control of flexible arms [3, 5]. To our knowledge the current paper is the first one to consider H_∞ control of cable-driven parallel robots.

The aim of this paper is to investigate the issue of controlling a cable robot with high dynamics when the flexible modes are effective. The case of a manipulator with four cables and 3 DOF is considered in simulation, assuming that measurements are available for the end-effector position and the cable tension. This model is developed in Sect. 2 in addition with an analysis of the evolution of the linearized model with respect to the parameters and the end-effector position. Then, a method based on the rigid kinematic model, adapted to the case where the actuators are speed-controlled, is proposed and evaluated in Sect. 3. The interest of using a low-pass filter in order to damp the flexible modes is evaluated. Then, in Sect. 4, the H_∞ control method is introduced and evaluated as an interesting candidate in the purpose of handling the flexible modes of the multi-input multi-output system.

Table 1 Modeling assumptions

|	
$\mathscr{H}_1$	Each motor block has the same behavior
$\mathscr{H}_2$	Rectilinear cables (neglected cable mass)
$\mathscr{H}_3$	Cables with elastic deformations
$\mathscr{H}_4$	Perfect speed-controlled winders

2 Model

2.1 Description and Assumptions

The cable robot considered herein is the 3 DOF version of the INCA robot by Haption. It is composed of four cables connected to a single point. Designed as a haptic interface, this single point is normally connected to a handle held by the operator. In the current work, the robot is considered as a manipulator intended to move the end-effector.

Assumptions given in Table 1 are necessary in order to obtain a model with reasonable complexity. As usually done, each winding system is considered to have the same behavior (assumption $\mathscr{H}_1$). Considering the reasonable size of the robot, the cable mass is considered as sufficiently low so that the cables are considered as rectilinear (assumption $\mathscr{H}_2$). In that sense, our work differs from other works that account for a non-rectilinear geometry of the cables [12, 13, 22]. Most of the works consider rigid cables (i.e. without elongation) [15, 19]. In the current research project, the model is intended to evaluate control laws with high bandwidth. Therefore, it is necessary to account for flexibilities (assumption $\mathscr{H}_3$). Under the assumption of low cable mass, the cable elongation can be considered as uniform. When considering the haptic interface, it is natural to control the winder motors in torque, allowing to compute the required force feedback. For manipulation, it is convenient to implement local speed control loops at the winder levels. As the flexibility problem is collocated, this control can be easily designed with a very high bandwidth only limited by the implementation solution. In the current work, this control is assumed to be perfect, which means that the control signals for positioning the end-effector are the winder speeds. Naturally, these signals cannot be computed independently as they must satisfy the kinematic constraints.

2.2 Inverse Rigid Kinematic Model

A schematic view of the INCA and a picture are given in Fig. 1 and the model parameters are reported in Table 2. The base frame is denoted $\mathscr{R}_b = (B, \vec{x}, \vec{y}, \vec{z})$ and is the only reference frame used in the paper. The positions of the cable ends at the winders expressed in the base frame are denoted A_i, $i = 1 \ldots 4$ and the coordinates
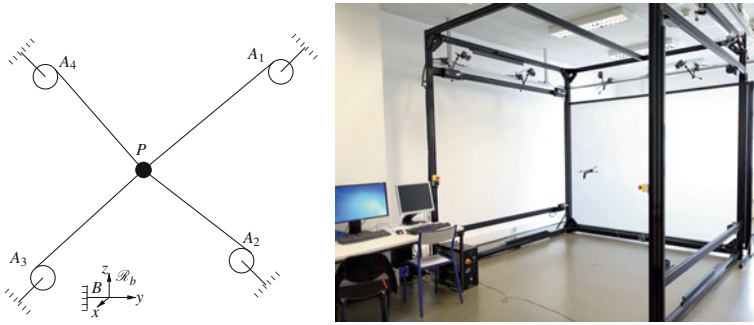
Fig. 1 Cable robot INCA. **a** Schematic view of the INCA 3DOF. **b** Picture of the INCA in a 6DOF version

Table 2 Model parameters

Parameter	Value
R	50 mm
A_i^{T} $i = 1, \ldots, 4$ (m)	$\begin{matrix} -1.5 & -1.5 & -1.5 \\ 1.5 & -1.5 & 1.5 \\ 1.5 & 1.5 & -1.5 \\ -1.5 & 1.5 & 1.5 \end{matrix}$
m	0.1 kg
g	9.8 m.s^{-2}
E	$350 \cdot 10^6$ N.m^{-3}
S	1 mm^2

of A_i are denoted q_l^i, $l = 1, 2, 3$. The end-effector is considered as a point mass located at point P with mass m and of coordinates q_l, $l = 1, 2, 3$.

The cable lengths l_i can be determined as the distance between the points A_i and P:

$$l_i = \| A_i - P \| \tag{1}$$

where $\|\cdot\|$ is the Euclidean norm.

For a rigid cable, one has $\frac{dl_i}{dt} = -R\dot{\theta}_i$ where R is the radius of the winding cylinder and assuming that a positive winding speed reduces the cable length. Remember that $\dot{\theta}$ is the control signal. The inverse kinematic rigid model allows us to compute θ from P: $\theta = \theta(P)$. The corresponding differential inverse kinematic model for the rigid model writes:

$$\dot{\theta} = J_i(\theta) \, \dot{P} \tag{2}$$

where $J_i(\theta) = \frac{d\theta(P)}{dP}$. Its entry of line k and row l writes:

$$J_i[k, l] = \frac{\partial \theta_k}{\partial q_l} = -\frac{q_l - q_l^k}{R \, l_k} \tag{3}$$

2.3 Direct Flexible Dynamic Model

2.3.1 Effector

Being assimilated as a mass-point, the dynamic equation of the end-effector is easily obtained by the first Law of Mechanics:

$$\frac{dV_P}{dt} = \frac{1}{m}F \tag{4}$$

where V_P is the 3D velocity of the end-effector ($V_P = \dot{P}$) and F is the sum of the forces applied to the end-effector.

Among the forces applied to the end-effector, we account for the tension T_i, $i = 1, \ldots, 4$ of the cables, for the gravity and for friction, resulting in:

$$F = \sum_{i=1}^{4} T_i \, s_i + \begin{bmatrix} 0 \\ 0 \\ -g \, m \end{bmatrix} - f_a \, V_P \tag{5}$$

where $\vec{s_i} = \frac{1}{l_i}\overrightarrow{A_i P}$ is the unit vector along the cable, g is the gravity acceleration and f_a is the friction ratio.

2.3.2 Winding System

Remember that each winder is considered to be perfectly controlled in speed. This enables the rejection of the friction and other perturbation that may impact the open-loop behavior.

On the INCA interface, cables are made of steel and have a diameter close to 1 mm. With a nominal length of 2 m, the resulting elongation may exceed several millimeters and may significantly affect the quality of the positioning if high accuracy at high bandwidth is required. In the current study, the specific flexibility effects due to the elongation of the cables are investigated. The idea is to show the limitations for rigid control laws and the ability of the H$_\infty$ control method to handle these flexible modes.

Some works developed for modeling winding processes can be used in order to write the model for the cable winding [11]. Let us consider the portion of cable located between points A_i and P. Its length is l_i varies with P. Let l_{0i} denote the corresponding no-load length that varies with the winding process. Denoting E the cable Young modulus Young and S its section, the cable tension is $T_i = ES\varepsilon_i$ where the elongation writes:

$$\varepsilon_i = (l_i - l_{0i})/l_{0i} \tag{6}$$

Assume that the cable is winded without any possibility to slip with respect to the wheel. During the winding process, a rotation of angle $d\theta_i$ winds a portion of

stressed cable of length $\delta l_i = R \, d\theta_i$ even if the cable length remains constant as P is also constant. From (6), the corresponding decrease of the no-load length can be established: $dl_{0i} = \delta l_i / (1 + \varepsilon_i)$. The relationship between the state variables is then:

$$\frac{dl_{0i}}{dt} = \frac{R}{1 + \varepsilon_i} \dot{\theta}_i \tag{7}$$

A very specific feature of winding systems is that the unwinding sequence has a different model from the winding sequence [11]. Indeed, if the structure of the model remains the same as (7), the ε_i must be replaced by the elongation of the stored portion of the cable. However, modeling the storage of the cable requires refinements that are considered to have a reduced impact on the dynamics. Therefore, the same model is considered for winding and unwinding in this study.

2.4 Open-Loop Behavior

The nonlinear model based on the given equations is of order 10: it relies on P (3 positions), V_P (three velocity components) and l_0 (four no-load lengths). Let X denote the state vector:

$$X = \begin{bmatrix} x & y & z & \dot{x} & \dot{y} & \dot{z} & l_{01} & l_{02} & l_{03} & l_{04} \end{bmatrix}^{\mathrm{T}}$$

The considered measurements are:

- The vector $P = \begin{bmatrix} x & y & z \end{bmatrix}^{\mathrm{T}}$ of the end-effector position in the base frame. In practice, some exteroceptive sensor must be used in order to measure P.
- The mean cable tension $T = \frac{1}{4}(T_1 + T_2 + T_3 + T_4)$. In practice, the cable tension can be estimated from the actuator currents and an estimation of the inertia and friction torque.

The measurement vector writes $Y = \begin{bmatrix} x & y & z & T \end{bmatrix}^{\mathrm{T}}$. Remember that the input vector is $\dot{\theta}$ and has four entries.

The nonlinear model given in Eqs. (4)–(7) can be written into the following general form:

$$\dot{X} = \mathbf{f}(X, \dot{\theta}, \Theta) \tag{8}$$
$$Y = \mathbf{g}(X, \dot{\theta}, \Theta) \tag{9}$$

where Θ is the parameter vector. A nonlinear simulator has been implemented that will be used in the next sections in order to evaluate the control strategies. The nonlinear equations has also been derived usingMaple in order to obtained several

(a) **(b)**
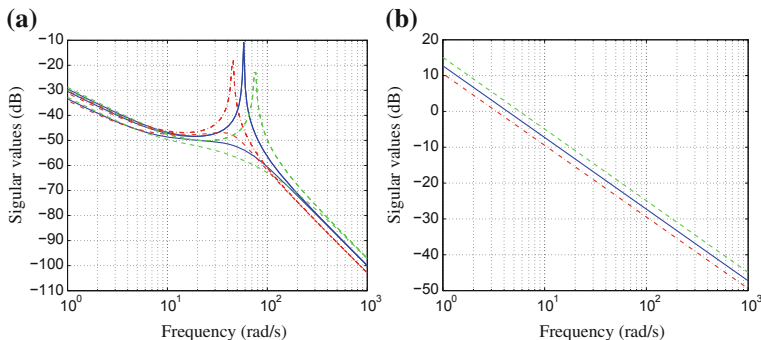
Fig. 2 Frequency behavior of the nominal model (*plain line*) and of the models obtained with **a** increase by ratio 1.4 on E and decrease by ratio 1.4 on m (*dash*); **b** decrease by ratio 1.4 on E and increase by ratio 1.4 on m (*dot-dash*). **a** Position part. **b** Tension part

linearized models:

$$\dot{X} = A_k X + B_k \dot{\theta} \tag{10}$$

$$Y = C_k X + D_k \dot{\theta} \tag{11}$$

where $A_k = \frac{\partial \mathbf{f}}{\partial X}(X_k, \mathbb{O}_{4\times 1}, \Theta_k), B_k = \frac{\partial \mathbf{f}}{\partial \dot{\theta}}(X_k, \mathbb{O}_{4\times 1}, \Theta_k), C_k = \frac{\partial \mathbf{g}}{\partial X}(X_k, \mathbb{O}_{4\times 1}, \Theta_k)$ and $D_k = \frac{\partial \mathbf{g}}{\partial \dot{\theta}}(X_k, \mathbb{O}_{4\times 1}, \Theta_k)$. The linearization has been performed for winder speeds and end-effector velocity equal to zero, and several end-effector positions, the corresponding no-load lengths being computed accordingly. Details on the state matrices are skipped for brevity.

The frequency behavior of the linearized models is reported in Figs. 2 and 3. The nominal model corresponds to the center of the workspace with the nominal values of the parameters. Its behavior is given in plain in Fig. 2. On the left-hand side are given the singular values of the transfer between $\dot{\theta}$ and P (i.e. the position part). One can see that the system exhibits a flexible mode at 60 rad/s. With three outputs and more than three inputs, the system can exhibit only three different singular values. Actually, only two distinct values are observed, due to the symmetries. In low frequency, the model behaves like an integrator with a slope of -20 dB/dec whereas in high frequency, it behaves like a double integrator with a slope of -40 dB/dec. The tension part of the model, i.e. the transfer between $\dot{\theta}$ and T is given in the right-hand side. The system behaves like a pure integrator with a slope of -20 dB/dec.

The evolution of the behavior when parameters E and m varies is also given in Fig. 2 for the central position of the end-effector. In dash is given the behavior of the system obtained with an increase of E by a ratio 1.4 and a decrease on m by the same factor. This result in an increase in the eigen-frequency of the flexible mode in the position behavior and an increase in the gain for the tension part, which is the expected evolution. The opposite evolution is observed when considering a decrease of E and an increase on m.

(a)   **(b)**
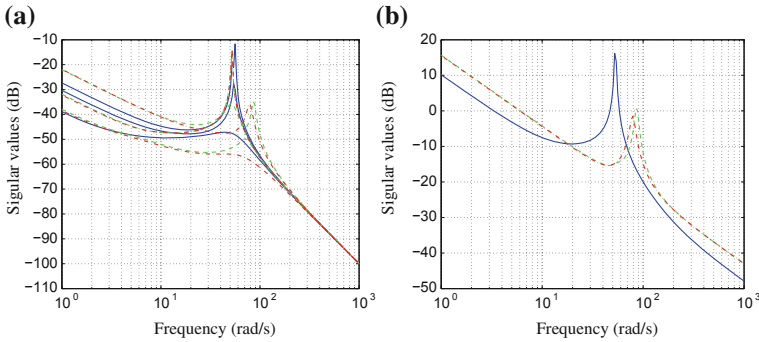
Fig. 3 Evolution of the frequency behavior with respect to the position of the end-effector (i/*plain* $x = y = z = 1$ m, ii/*dash* $x = y = -z = 1$ m, iii/*dot-dash* $x = -y = -z = 1$ m) **a** Position part. **b** Tension part

The evolution of the frequency-behavior has also been investigated when considering changes in the end-effector position. In the results reported in Fig. 3, three different positions have been considered by shifting successively x, y and z of ± 1 m. The most impressive change in the behavior is on the tension as the dissymmetry causes a peak in the frequency response. On the position part, one can see that the three singular values are now distinct.

3 Control Based on the Rigid Kinematic Model

As the aim of the study is to investigate the flexibility effects on cable robots, it is worth having a reference approach based on a rigid model.

3.1 Method

It is well known that, due to its parallel structure, the management of the cable tension require special attention [14]. When the actuators are controlled in torque, the input space can be decomposed into two subspace:

- In the null space ($u \in \ker(J_i^T)$), the torques have no effect on the end-effector motion but only affect the cable tension; therefore, this subspace is used to manage the cable tension.
- The other dimensions ($u \notin \ker(J_i^T)$) allow to manage the position of the end-effector.

When considering speed-controlled actuators, the issue slightly differs in nature. Indeed, the actuator speeds cannot be controlled independently as they must fulfill

the kinematic constraints. However, the same principle of separation between motion and tension action applies.

An exponential convergence of P towards a reference P^r is enforced by choosing $\dot{P} = k_P(P^r - P)$ where k_P is a gain that allows the user to tune the convergence speed. The rigid kinematic model (2), where J_i dimensions are 3×4, can then be used in order to compute $\dot{\theta}$ accordingly. However, this simple solution does not allow to manage the tension. This can be done by simply adding to $\dot{\theta}$ some component v that belongs to the null-space of J_i^{T}, resulting in:

$$\dot{\theta} = J_i \, \dot{P} + v \tag{12}$$

where v is any vector in $\ker(J_i^{\mathrm{T}})$. Denoting v_1 a unit vector of $\ker(J_i^{\mathrm{T}})$, the tension can be chosen in order to control the mean tension T to the reference T^r with:

$$v = k_T(T^r - T)v_1 \tag{13}$$

where k_T is a gain that allows the user to tune the convergence speed. Thanks to the first-order tension dynamics exhibited in Figs. 2b and 3b, the stability of the control scheme is guarantied. When the mean tension is perfectly controlled, v vanishes and the winder speed references satisfy the kinematic constraints.

At the center of the working space, on has $v_1 = \frac{1}{2}\begin{bmatrix} 1 & 1 & 1 & 1 \end{bmatrix}^{\mathrm{T}}$. For small displacements around this central position, v_1 can be kept constant which is the case in the results shown herein. In order to reduce the destabilizing effects of the flexible modes, a first-order low-pass filter $\frac{1}{1+\tau_f s}$ is used on the four control signals.

3.2 Results

3.2.1 Nominal Trajectories

A trajectory has been chosen for the evaluation of the performance of the controlled system (see the dashed lines in Fig. 4a, b). Imagine a cube of width $2A$ ($A = 0.25$ m in the sequel) centered in the workspace. Starting from the center, the trajectory consists in reaching one vertex ($x = y = z = A$) in 2 s and then to move along the edges successively in the x, y and z directions in 2 s each and finally to reach the center of the workspace in one second. The tension reference is piece-wise continuous, equal to 100 N before $t = 8$ s and equal to 110 N afterwards.

The trajectories obtained by simulation of the nominal model starting with a tension of 100 N, $k_P = 40$ rad/s/m, $k_T = 2$ rad/s/N and $\tau_f = 40$ ms are given in Fig. 4. One can see that both position and tension follow their reference. Notice that the change of tension reference at $t = 8$ s is properly followed and do not introduce any oscillation. Be aware that herein, only feedback action is considered
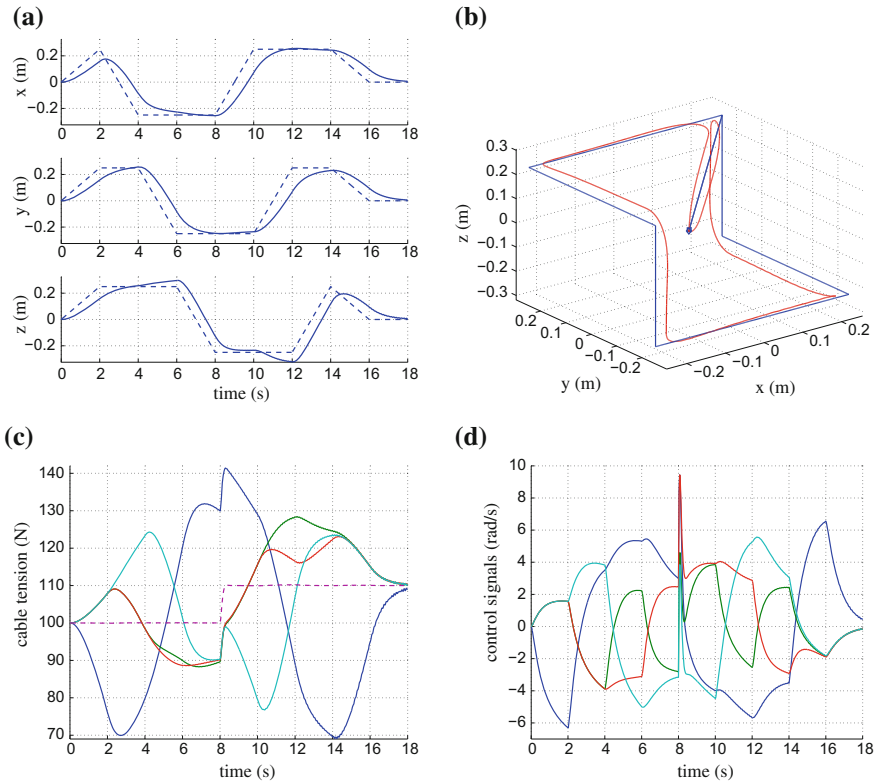
Fig. 4 Trajectories for time-domain evaluation. **a** Reference (*dash*) and actual position (*plain*). **b** 3D trajectories. **c** Cable tension (*plain*) and mean tension (*dash*). **d** Control signals (winder speeds)

for evaluation. The tracking efficiency could be improved by using some feed-forward action.

3.2.2 Filter Tuning

In order to evaluate the quality of the control, the following indicators are proposed:

- J_u is the RMS value of the control signal (more precisely, the RMS value is computed on a vector including the control signal samples of all the motors stacked in the one unique vector). As a smooth control signal is preferred, this index should be minimized.
- J_P is the mean distance between the reference position and its actual value. For good position tracking, it should be minimized.
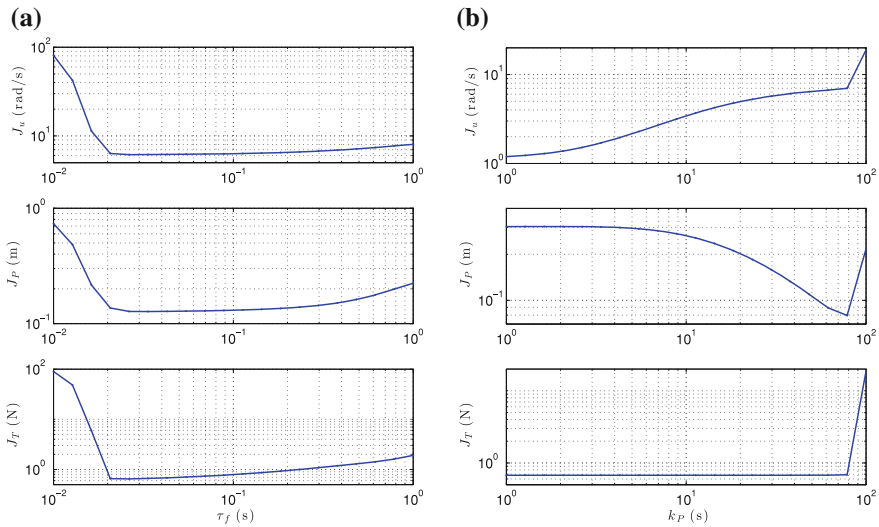
Fig. 5 Effects of the variations of the controller parameters. **a** Variation of τ_f ($k_p = 40$ rad/s/m). **b** Variation of k_p ($\tau_f = 40$ ms)

J_T is the RMS error between the actual tension and its reference value. As the previous index, it should be minimized.

For $k_P = 40$ rad/s/m and $k_T = 1$ rad/s/N, several simulations have been processed with different values of τ_f, from 10 ms to 1 s, in order to evaluate the influence of the filter tuning on the system performance. The values of the indicators defined in the previous subsection are reported in Fig. 5a. One can notice that the performance is very bad for the low values of τ_f, which clearly shows the interest of the filter ($\tau_f = 0$ corresponds to remove the filter). Actually, a more accurate look at the simulations (not included in the paper) shows that the system undergoes severe oscillations for those values. An optimal value is obtained for $\tau_f \in [20-100]$ ms. Notice that this optimum has been obtained for given values of the system and controller parameters and should be recomputed for other values of those parameters.

For a fixed value $\tau_f = 40$ ms, the metrics computed for different values of k_P logarithmically spaced in $[1-100]$ rad/s/m are reported in Fig. 5b. As expected, it appears that when k_P increases, J_u increases, J_P decreases and J_T remains constant. This observation only holds for $k_P \leq 78$ rad/s/m. For higher values of k_P, the system becomes unstable.

Fig. 6 Standard scheme for H_∞ synthesis
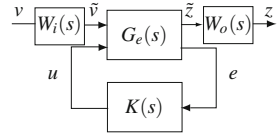
4 H_∞ Control

H_∞ control methodology allows the synthesis of LTI controllers for MIMO systems. Among the MIMO methodologies, it generally provides good results when flexible modes come into play [9, 17].

4.1 H_∞ Methodology

The general synthesis scheme for H_∞ synthesis is shown in Fig. 6. Given an extended plant $G_e(s)$ with performance channel $\tilde{v} \to \tilde{z}$ and control channel $u \to e$, the issue is to design the controller $K(s)$ such that the performance channel has a good frequency behavior in the sense that it respects some frequency templates. Assume that the weighting functions $W_i(s)$ and $W_o(s)$ are diagonal, i.e. $W_i(s) = \text{diag}\{W_{ik}\}$, $k = 1, \ldots, n_v$, and $W_o(s) = \text{diag}\{W_{ok}\}$, $k = 1, \ldots, n_v$, where n_v and n_z are the dimensions of v and z respectively. Let lft denote the linear fractional transformation.[1] If the H_∞ norm[2] of the closed-loop system $T_{zv}(s) = W_o(s) \cdot \text{lft}(G_e(s), K(s)) \cdot W_i(s)$ is less than 1, then for any SISO transfer from input #$k \in \{1, \ldots, n_v\}$ and output #$l \in \{1, \ldots, n_z\}$, one has:

$$\left| T_{\tilde{z}\tilde{v}}(j\omega) \right| \leq \frac{1}{|W_{ik}(j\omega)| \cdot |W_{ol}(j\omega)|} \tag{14}$$

where $T_{\tilde{z}\tilde{v}}(j\omega) = \text{lft}(G_e(s), K(s))$. The right-hand side of the inequality is the template.

Given $G_e(s)$, $W_i(s)$ and $W_o(s)$, the computation of $K(s)$ in order to minimize the H_∞ gain of the weighted closed-loop system can be done in several fashions. The most usual methods compute a full order controller (i.e. $K(s)$ has the same order than the augmented system $G_a(s) = \text{diag}\{W_o(s), \mathbb{I}_{n_e}\} \cdot G_e(s) \cdot \text{diag}\{W_i(s), \mathbb{I}_{n_u}\}$) as a solution of a convex optimization problem. The synthesis can be done by the resolution of Riccati [8] or LMI equations [10]. Theses algorithms are available into continuous and discrete-time versions. A reduction-order step is generally used in order to get a controller of reasonable order. More recently, the development of non-

---

[1] Let $T_{zv}(s)$ denote the transfer of the system with input v and output z. The interconnection of $G_e(s)$ and $K(s)$ presented in Fig. 6 is $T_{\tilde{z}\tilde{v}}(s) = \text{lft}(G_e(s), K(s))$.

[2] The H_∞ norm $\|G(s)\|_\infty$ of transfer $G(s)$ is the maximum singular value of $G(j\omega)$ over all the frequencies $\omega \in \mathbb{R}^+$. For single-input single-output systems, it reduced to the maximum gain.

Fig. 7 Two-bloc synthesis scheme
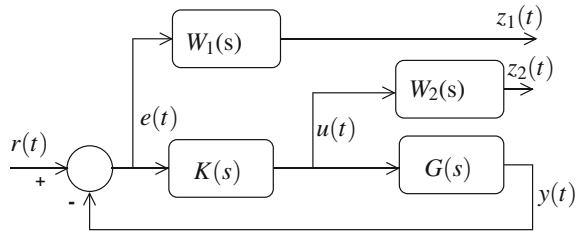
smooth optimization has been taken into profit for the development of structured and low-order controllers. Let us mention the HIFOO package [4] and the `hinfstruct` function available with recent versions of the Robust Control Toolbox [16]. In the current work, the Riccati version of the continuous-time full-order synthesis has been used. In practice, iterations are necessary on the tuning of the weighting functions in order to get the H∞ norm of the closed-loop close to 1.

4.2 Controller Synthesis

In the current case, the system has four inputs (the four winder speeds) and four measurements (the three coordinates of the end-effector position and the mean tension. Let introduce the reference signal $r = \begin{bmatrix} x^r & y^r & z^r & T^r \end{bmatrix}^{\mathrm{T}}$. When implementing the H∞ methodology, the first step consists in selecting the design scheme. The very usual two-bloc scheme presented in Fig. 7 has been chosen as it manages the most important features of the closed-loop system.[3] By choosing $W_1(s)$ such that the template $1/W_1(s)$ is a high-pass filter, the output sensitivity function $S(s) = T_{er}(s)$ is shaped in order to impose:

- the bandwidth,
- the modulus margin,
- the accuracy.

In order to distinguish between the dynamics in position and tension, $W_1(s)$ is chosen under the following shape: $W_1(s) = \mathrm{diag}\{w_{1P}(s)\,\mathbb{I}_3, w_{1T}(s)\}$ where $w_{1P}(s)$ is a SISO weighting functions for tuning the position dynamics whereas $w_{1T}(s)$ shapes the tension dynamics. The weighting function $W_2(s) = w_2(s)\,\mathbb{I}_4$ is chosen such that $1/W_2(s)$ is a low-pass filter, thus forcing the gain of $K(s)$ to decrease in high frequencies. This "roll-off" effect enforces the robustness to unmodeled dynamics and ensures a low sensitivity with respect to measurement noise.

After several iterations, the following weighting functions were selected that provided a closed loop performance close to one and satisfying results: $w_{1P} = \frac{0.5s+4}{s+0.008}$,

---

[3] The scheme of Fig. 7 is equivalent to the scheme of Fig. 6 by choosing $\tilde{v} = r$, $\tilde{z} = \begin{bmatrix} e^{\mathrm{T}} & u^{\mathrm{T}} \end{bmatrix}^{\mathrm{T}}$, $W_i(s) = \mathbb{I}_4$ and $W_o(s) = \mathrm{diag}\{W_1(s), W_2(s)\}$.

$w_{1T} = \frac{0.5s+40}{s+0.08}$, $w_2(s) = \left(\frac{0.005\,s+0.05}{0.0001\,s+1}\right)^2$. The frequency response (singular value) of the controller is given in Fig. 8 in two parts: on the left-hand side is given the part that manages the position (first three inputs); on the right-hand side is given the part that manages the tension (last input). Whereas the position part mainly behaves like a proportional controller with low-pass filter including some compensation of the flexible modes (close to 100 rad/s), the tension part behaves like a proportional-integral controller with low-pass filter.

The corresponding closed-loop transfers are given in Fig. 9. One the top plots are given the sensitivity function $T_{er} = S(s)$ that behaves like a high-pass filter thanks to the template $1/W_1(s)$. On the bottom plots are given transfer $T_{ur} = K(s)\,S(s)$ where the action of the template $1/W_2(s)$ on the roll-off effect can be seen in high frequencies.

4.3 Results

The nonlinear model has been simulated with the same reference trajectory as in Sect. 3. The corresponding trajectories are given in Fig. 10. The metrics (defined in Sect. 3.2.2) are $J_u = 7.42$ rad/s, $J_P = 79.6$ mm and $J_T = 0.82$ N. One can notice that the position and mean tension are properly controlled. The dynamics are sensibly higher than those obtained with the Jacobian-based approach (see Fig. 4) even if this latter was tuned in order to attain the fastest dynamics.

The larger dispersion observed in cable tensions (compare Figs. 4c and 10c) are directly due to the increase of the bandwidth. This drawback can be reduced by choosing smoother reference trajectories, as proposed by Trevisani [18]. But this effect is independent from the closed loop behavior which is the topic herein.

5 Conclusion

In this paper, a H_∞ controller has been designed for a cable robot and compared with a more conventional controller that neglects the flexible effects in the robot behavior. The results have clearly shown that the H_∞ methodology allows an improvement of the highest reachable bandwidth. One strong limitation of the H_∞ methodology is that is leads to a LTI controller that cannot adapt to the evolution of the behavior with respect to the position. However, the robustness of the designed controller was sufficient for an evolution in a reasonably large domain (a square of 0.5 m large in the results exhibited in the paper). For a larger workspace, some gain-scheduling approach would be necessary in order to adapt the controller behavior.
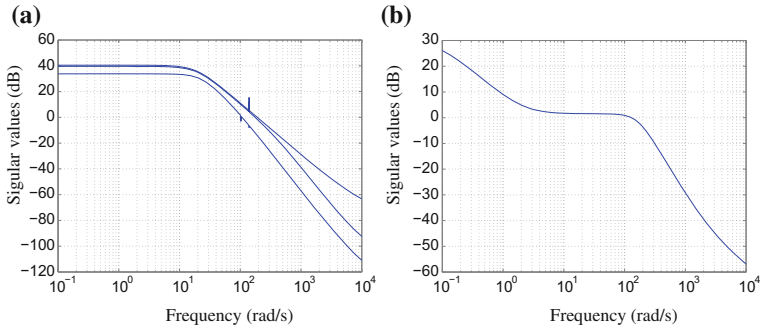
Fig. 8 H$_\infty$ controller $K(s)$. **a** Position part (three first inputs). **b** Tension part (last output)
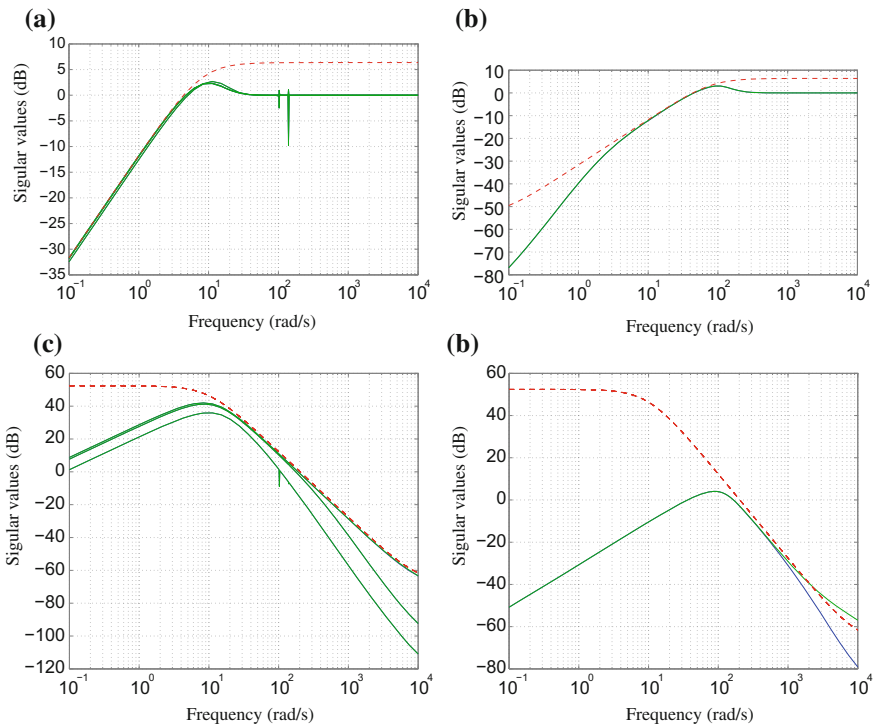
Fig. 9 Closed-loop transfer functions (*plain*) and the corresponding templates (*dash*). **a** Position part of $T_{er} = S(s)$. **b** Tension part $T_{er} = S(s)$. **c** Position part of $T_{ur} = K(s)S(s)$. **d** Tension part of $T_{ur} = K(s)S(s)$

(a)

(b)

(c)

(d)
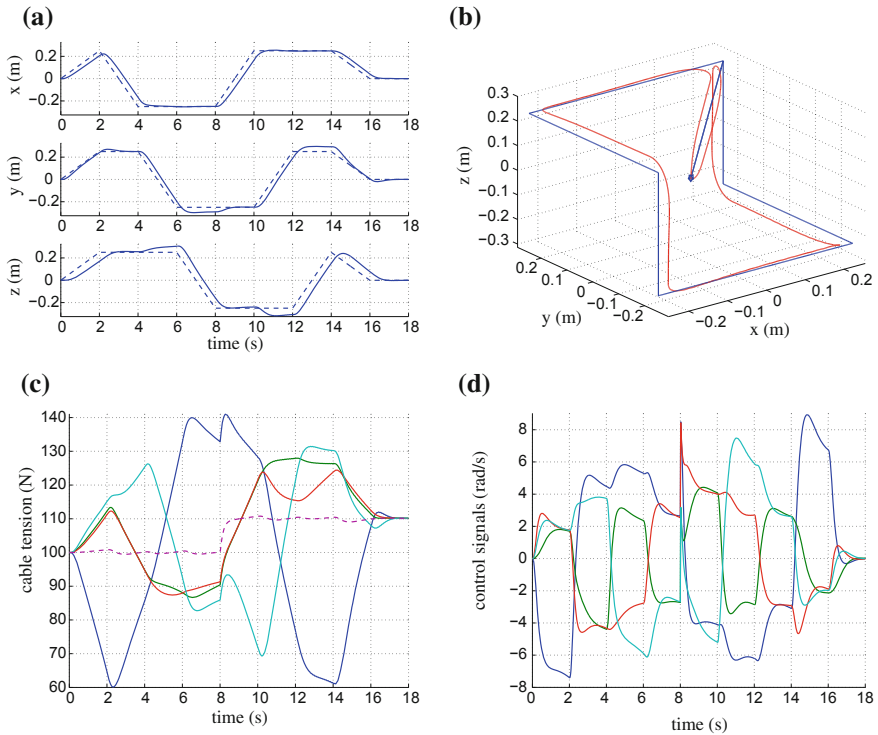
Fig. 10 Trajectories with the H_∞ controller. **a** Reference (*dash*) and actual position (*plain*). **b** 3D trajectories. **c** Cable tension (*plain*) and mean tension (*dash*). **d** Control signals (roller speeds)

References

1. Abdelaziz, S., Esteveny, L., Renaud, P., Bayle, B., Barbé, L., de Mathelin, M., Gangi, A.: Design considerations for a novel mri compatible manipulator for prostate cryoablation. Int. J. Comput. Assist. Radiol. Surg. **6**(6), 811–819 (2011)
2. Alikhani, A., Vali, M.: Modeling and robust control of a new large scale suspended cable-driven robot under input constraint. In: International Conference on Ubiquitous Robots and Ambiant Intelligence, Incheon, (2011)
3. Banavar, R., Dominic, P.: An lqg/h_∞ controller for a flexible manipulator. IEEE Trans. Control Syst. Technol. **3**, 409–416 (1995)
4. Burke, J.V., Henrion, D., Lewis, A.S., Overton, M.L.: HIFOO—a Matlab package for fixed-order controller design and h-infinity optimization. In: IFAC Symposium on Robust Control Design, Toulouse, (2006). http://www.cs.nyu.edu/overton/software/hifoo/
5. Cuvillon, L., Laroche, E., Gangloff, J., de Mathelin, M.: A mutivariable methodology for fast visual servoing of flexible manipulators moving in a restricted workspace. Adv. Robotics **26**(13), 1 (2012). http://lsiit-cnrs.unistra.fr/Publications/2012/2-CLGD12
6. Dallej, T., Gouttefarde, M., Andreff, N., Michelin, M., Martinet, P.: Towards vision-based control of cable-driven parallel robots. In: International Conference on Intelligent Robots and Systems. San Francisco, (2011)

7. Diao, X., Ma, O.: Vibration analysis of cable-driven parallel manipulators. Multibody Syst. Dyn. **21**, 347–360 (2009)
8. Doyle, J., Glover, K., Khargonekar, P., Francis, B.: State-space solutions to standard H_2 and H_∞ control problems. IEEE Trans. Autom. Control **34**(8), 831–847 (1989)
9. Duc, G., Font, S.: Commande H$_\infty$ et μ-analyse. Hermes Science Publications, Paris (1999)
10. Gahinet, P., Apkarian, P.: A linear matrix inequality approach to H$_\infty$ control. Int. J. Robust Nonlin. Control **4**(4), 421–448 (1994)
11. Koç, H., Knittel, D., de Mathelin, M.: Modeling and robust control of winding systems for elastic webs. IEEE Trans. on Control Syst. Technol. **10**, 197–208 (2002)
12. Korayem, M., Bamdad, M., Saadat, M.: Workspace analysis of cable-suspended robots with elastic cable. In: IEEE International Conference Robotics and Biomimetics, Sanya, pp. 1942–1947 (2007). doi:10.1109/ROBIO.2007.4522464
13. Kozak, K., Zhou, Q., Wang, J.: Static analysis of cable-driven manipulators with non-negligible cable mass. IEEE Trans. Robot. **22**(3), 425–433 (2006). doi:10.1109/TRO.2006.870659
14. Ming, A., Higuchi, T.: Study on multiple degree-of-freedom positioning mechanism using wire-concept, design and control (part 1). Int. J. Jpn. Soc. Precis. **28**(2), 131–138 (1994)
15. Pham, C.B., Yeo, S.H., Yang, G., Chen, I.M.: Workspace analysis of fully restrained cable-driven manipulators. Robot. Auton. Syst. **57**(9), 901–912 (2009). doi:10.1016/j.robot.2009.06.004
16. Simoes, A., Apkarian, P., Noll, D.: Nonsmooth multi-objective synthesis with applications. Control Eng. Pract. **11**(17), 1338–1348 (2009)
17. Skogestad, S., Postlethwaite, I.: Multivariable Feedback Control. Wiley, Chichester (1996)
18. Trevisani, A.: Underconstrained planar cable-direct-driven robots: a trajectory planning method ensuring positive and bounded cable tensions. Mechatronics **20**, 113–127 (2010)
19. Williams, R., Galina, P.: Translational planar cable-direct-driven robots. J. Intel. Robot. Sys. **37**, 69–96 (2003)
20. Xianqiang, Y., Weihai, C., Su, Y., Wei, X.: Dynamic control of a 3-dof cable-driven robot based on backstepping technique. In: IEEE Conference on Industrial Electronics and Applications, Beijing, (2011)
21. Zames, G., Francis, B.: Feedback, minimax sensitivity, and optimal robustness. IEEE Trans. Autom. Control **28**(5), 585–601 (1983)
22. Zi, B., Duan, B., Du, J., Bao, H.: Dynamic modeling and active control of a cable-suspended parallel robot. Mechatronics **18**, 1–12 (2008)

Trajectory Tracking for a Three-Cable Suspension Manipulator by Nonlinear Feedforward and Linear Feedback Control

Christoph Woernle

Abstract The kinematically indeterminate cable suspension manipulator CABLEV moves a payload platform in space by three spatially arranged cables with independently controllable winches. As the position of the platform is not fully determined by the lengths of the cables, undesired sway motions of the payload platform may occur. To make the payload platform track prescribed translational and rotational reference trajectories in space, a two-stage control concept is presented. A nonlinear feedforward control that exploits the flatness property of the system generates control inputs for the undisturbed motion along reference trajectories. Sway motions caused by disturbances are actively damped by a linear feedback of measured state variables enabling an asymptotically stable tracking behaviour. Experimental results from the prototype system CABLEV are shown.

1 Introduction

Cable suspension manipulators support a payload platform in space by several spatially arranged cables with computer-controlled winches. The winches are mounted either fixed or on movable trolleys. Compared to conventional cranes, not only the translational motion of the payload can be controlled but also its orientation.

Cable suspension manipulators can be classified with respect to mobility and statics, see Table 1. The kinematically parallel suspension of a platform by a system of cables is *kinematically determinate* if the position of the payload platform is geometrically defined by the actual lengths of the tense cables. It is *kinematically indeterminate* if the platform is (finitely or infinitesimally) movable while the cable lengths are kept constant. The suspension is *statically determinate* if the cable forces

C. Woernle (✉)
University of Rostock, Rostock, Germany
e-mail: woernle@uni-rostock.de

Table 1 Kinematic and static determinateness
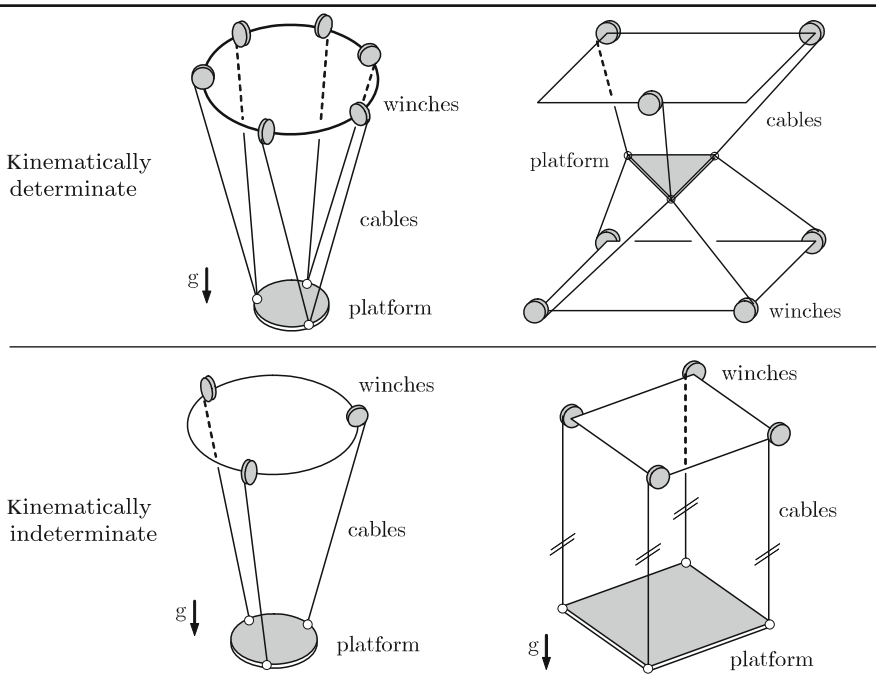
can be calculated by means of the six (static or dynamic) equilibrium conditions for the platform only, otherwise it is *statically indeterminate*.

A payload platform suspended by six cables in analogy to a Gough-Stewart platform is kinematically and statically determinate as long as all cables are kept under tension by the gravity force [1, 4]. With more than six cables the platform is, in general, kinematically determinate but statically indeterminate. Examples are shown in [3, 9, 12, 13]. A platform suspended by less than six cables is kinematically indeterminate. Three-cable suspensions as described in [2, 10, 17] are, in general, statically determinate. A platform suspension with four parallel cables is statically indeterminate. Workspaces and singularities are investigated in [15].

In this contribution the kinematically indeterminate cable suspension manipulator CABLEV is described (Fig. 1). It was developed at University of Rostock as a prototype system to validate control concepts [7, 8, 10]. Its payload platform is supported by three cables with winches mounted on trolleys that move them on a common gantry.

The design of the cable guidance system allows kinematically defined inclinations of the cables (Fig. 2). In order to detect the sway motions of the platform, the inclination angle of each cable in one vertical plane is measured by means of a precise potentiometer. The measurement axes are differently orientated in order to provide three independent signals. There exists a singular position where the normals of the
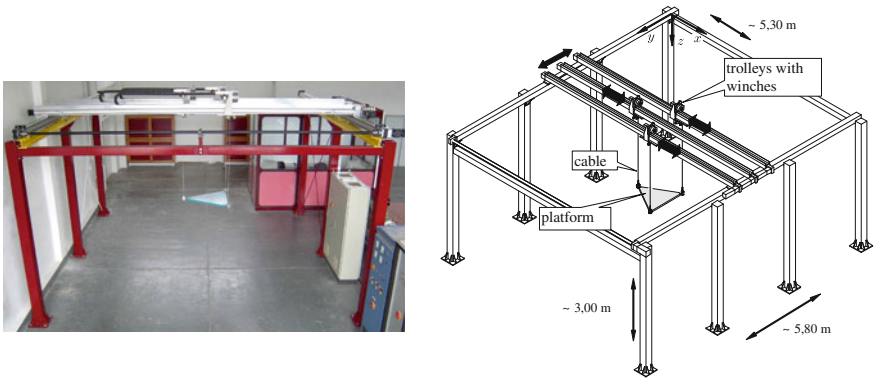
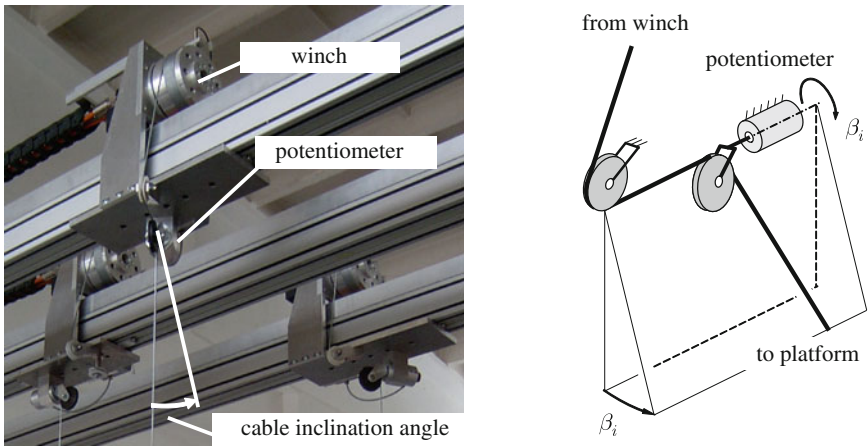**Fig. 1** Cable suspension manipulator CABLEV

Fig. 2 Cable guidance system with measurement of the cable inclination angles β_i in one vertical plane at each trolley

three measurement axes intersect in a common point that is, however, beyond the relevant workspace.

Trajectory tracking control of the payload platform is achieved by means of the concept of flat systems according to [6]. A flat system has the property that the state variables and the control inputs can be algebraically expressed in terms of the so-called flat output and a finite number of time derivatives of the flat output. Its application to kinematically indeterminate manipulators represents a generalization of computed-torque control. The control forces are algebraically calculated from the desired trajectories of the payload platform and their time derivatives up to the fourth order leading to a feedforward control strategy.

As successfully demonstrated by experiments with CABLEV, flatness-based feed-forward control provides exact motions of the platform along desired trajectories as

long as there are no unknown disturbances, e.g., wind forces, acting on the platform [7, 8, 10]. To counteract these effects, a feedback of measured actual state-space variables is needed. For flat systems, trajectory tracking control by exact state-space linearization with nonlinear state feedback can be achieved according to [5]. This type of feedback control of CABLEV is described in [7, 8]. In this paper a less complex control architecture with linear state feedback is described. It can be applied under the assumption that the feedforward control already ensures motions in the neighborhood of the reference trajectory [7].

The contribution is organized as follows. First, the flatness-based feedforward control of CABLEV is briefly reviewed. Based on the linearized equations of motion, a linear state-space controller is developed. A measurement model that calculates the actual platform position from measured cable inclination angles is described. Simulations show the effects of combined nonlinear feedforward and linear feedback control.

2 Dynamic Model of Cablev

The dynamic model of CABLEV is formulated in differential-algebraic form [16]. It comprises the dynamic differential equations of the drives and the payload platform and the algebraic constraint equations between the coordinates. The model is used to derive the feedforward and feedback control laws.

2.1 Coordinates

The independently controllable robot coordinates $\boldsymbol{p} \in \mathbb{R}^7$ are the gantry displacement p_{g0}, the trolley displacements p_{gi}, $i = 1, 2, 3$, and the cable lengths p_{ci}, $i = 1, 2, 3$, (Fig. 3)

$$\boldsymbol{p} = \begin{bmatrix} \boldsymbol{p}_g \\ \boldsymbol{p}_c \end{bmatrix} \quad \text{with} \quad \boldsymbol{p}_g = \begin{bmatrix} p_{g0} \ p_{g1} \ p_{g2} \ p_{g3} \end{bmatrix}^T, \quad \boldsymbol{p}_c = \begin{bmatrix} p_{c1} \ p_{c2} \ p_{c3} \end{bmatrix}^T. \quad (1)$$

The platform coordinates $\boldsymbol{y}_p \in \mathbb{R}^6$ describe the spatial position and orientation of the platform-fixed coordinate system $\mathcal{K}_p$ relative to the inertial system $\mathcal{K}_0$ by, for example, three Cartesian coordinates r_x, r_y, r_z of the origin of $\mathcal{K}_p$ and three Bryan angles $\varphi_1, \varphi_2, \varphi_3$,

$$\boldsymbol{y}_p = \begin{bmatrix} \boldsymbol{r} \\ \boldsymbol{\varphi} \end{bmatrix} \quad \text{with} \quad \boldsymbol{r} = \begin{bmatrix} r_x & r_y & r_z \end{bmatrix}^T, \quad \boldsymbol{\varphi} = \begin{bmatrix} \varphi_1 & \varphi_2 & \varphi_3 \end{bmatrix}^T. \quad (2)$$
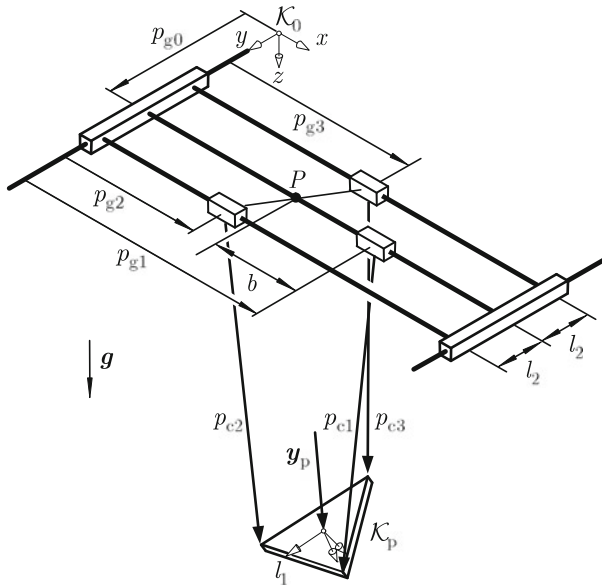
Fig. 3 Coordinates of CABLEV [8]

To describe sway motions of the payload platform with three degrees of freedom, three sway coordinates $\boldsymbol{\eta}$ are defined as a subset of the platform position vector $\boldsymbol{y}_p$ from (2) according to

$$\boldsymbol{\eta} = [r_x \quad r_y \quad \varphi_3]^T. \tag{3}$$

The spatial velocity $\dot{\boldsymbol{s}}_p$ of the platform relative to $\mathcal{K}_0$ comprises the translational and angular velocity of $\mathcal{K}_p$ (coordinates of $\boldsymbol{\omega}$ in $\mathcal{K}_p$),

$$\dot{\boldsymbol{s}}_p = \begin{bmatrix} \boldsymbol{v} \\ \boldsymbol{\omega} \end{bmatrix} \quad \text{with} \quad \boldsymbol{v} = \begin{bmatrix} \dot{r}_x & \dot{r}_y & \dot{r}_z \end{bmatrix}^T, \quad \boldsymbol{\omega} = \begin{bmatrix} \omega_x & \omega_y & \omega_z \end{bmatrix}^T, \tag{4}$$

whereby $\boldsymbol{s}_p$ are quasi-coordinates defined as differentials only. The relation between $\dot{\boldsymbol{y}}_p$ and $\dot{\boldsymbol{s}}_p$ is then given by the kinematical differential equation

$$\begin{bmatrix} \dot{\boldsymbol{r}} \\ \dot{\boldsymbol{\varphi}} \end{bmatrix} = \begin{bmatrix} \boldsymbol{I} & \boldsymbol{0} \\ \boldsymbol{0} & \boldsymbol{H}_\omega(\boldsymbol{\varphi}) \end{bmatrix} \begin{bmatrix} \boldsymbol{v} \\ \boldsymbol{\omega} \end{bmatrix}$$
$$\rightarrow \dot{\boldsymbol{y}}_p = \boldsymbol{H}(\boldsymbol{y}_p) \qquad \dot{\boldsymbol{s}}_p \tag{5}$$

with the identity matrix $\boldsymbol{I}$. The second row in (5) is the kinematic differential equation related to the Bryan angles.

Fig. 4 Geometric constraints
between y_p and p [8]

$|c_i| = p_{ci}$,
$i = 1, 2, 3$
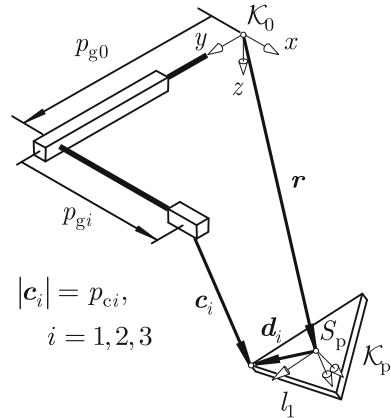
2.2 Implicit Constraints

The coordinates p and y_p fulfil implicit constraint equations that are needed at the
position, velocity, and acceleration levels [16].

Position level. Assuming three longitudinally stiff and tense cables, there exist
three implicit constraints between robot coordinates p and platform coordinates y_p
according to Fig. 4,

$$g_i(y_p, p) \equiv c_i^2(y_p, p) - p_{ci}^2 = 0, \quad i = 1, 2, 3, \quad \text{or} \quad g(y_p, p) = 0. \quad (6)$$

The cable vectors c_i are expressed in $\mathcal{K}_0$ by

$$
\begin{aligned}
c_1 &= r + {}^P T \, {}^P d_1 - (p_{g0} \, e_y + p_{g1} \, e_x), \\
c_2 &= r + {}^P T \, {}^P d_2 - ((p_{g0} + l_2) \, e_y + p_{g2} \, e_x), \\
c_3 &= r + {}^P T \, {}^P d_3 - ((p_{g0} - l_2) \, e_y + p_{g3} \, e_x),
\end{aligned}
\quad (7)
$$

with the distance l_2 between the rails and the constant vector coordinates of the
platform-fixed vectors ${}^P d_i$ in $\mathcal{K}_p$, the transformation matrix ${}^P T(\varphi)$ from $\mathcal{K}_p$ to $\mathcal{K}_0$,
and the unit vectors of $\mathcal{K}_0$, $e_x = [1 \; 0 \; 0]^T$, $e_y = [0 \; 1 \; 0]^T$.

Velocity level. For the equations of motion the Jacobian matrices associated to
the constraints (6) are needed. The total time derivatives of (6) are

$$\dot{g}_i \equiv 2 c_i^T \dot{c}_i - 2 p_{ci} \dot{p}_{ci} = 0, \quad i = 1, 2, 3, \quad (8)$$

with the time derivatives of the cable vectors $\dot{c}_i = \dot{r} + \dot{d}_i - (\dot{p}_{g0} \, e_y + \dot{p}_{gi} \, e_x)$. With the
angular velocity of the platform ω, the time derivative of the platform-fixed vectors
d_i is $\dot{d}_i = \tilde{\omega} \, d_i$, whereby the vector product is written with the Tilde operator,
$\tilde{\omega} \, d_i \,\hat{=}\, \omega \times d_i$. By this, the time derivative of the constraints at the velocity level (8)

can be written as

$$\dot{g} \equiv [\ \boldsymbol{G}_{sv}\ \ \boldsymbol{G}_{s\omega}\ ]\begin{bmatrix} \boldsymbol{v} \\ \boldsymbol{\omega} \end{bmatrix} + [\boldsymbol{G}_{pg}\ \ \boldsymbol{G}_{pc}]\begin{bmatrix} \dot{\boldsymbol{p}}_g \\ \dot{\boldsymbol{p}}_c \end{bmatrix} = \boldsymbol{0}$$
$$\rightarrow \boldsymbol{G}_s(\boldsymbol{y}_p,\ \boldsymbol{p}_g)\quad \dot{\boldsymbol{s}}_p\ +\boldsymbol{G}_p(\boldsymbol{y}_p,\quad \boldsymbol{p})\ \dot{\boldsymbol{p}}\ =\boldsymbol{0} \tag{9}$$

with the constraint matrices

$$\boldsymbol{G}_s = 2\begin{bmatrix} \boldsymbol{c}_1^T \big| -\boldsymbol{c}_1^T\,\tilde{\boldsymbol{d}}_1 \\ \boldsymbol{c}_2^T \big| -\boldsymbol{c}_2^T\,\tilde{\boldsymbol{d}}_2 \\ \boldsymbol{c}_3^T \big| -\boldsymbol{c}_3^T\,\tilde{\boldsymbol{d}}_3 \end{bmatrix} \in \mathbb{R}^{3,6}, \tag{10}$$

$$\boldsymbol{G}_p = -2\begin{bmatrix} \boldsymbol{c}_1^T\,\boldsymbol{e}_y\ \ \boldsymbol{c}_1^T\,\boldsymbol{e}_x & 0 & 0 & p_{c1} & 0 & 0 \\ \boldsymbol{c}_2^T\,\boldsymbol{e}_y & 0 & \boldsymbol{c}_2^T\,\boldsymbol{e}_x & 0 & 0 & p_{c2} & 0 \\ \boldsymbol{c}_3^T\,\boldsymbol{e}_y & 0 & 0 & \boldsymbol{c}_3^T\,\boldsymbol{e}_x & 0 & 0 & p_{c3} \end{bmatrix} \in \mathbb{R}^{3,7}. \tag{11}$$

Acceleration level. The total time derivative of the velocity constraints (9) yields the implicit constraints at the acceleration level

$$\ddot{g} \equiv \boldsymbol{G}_s\,\ddot{\boldsymbol{s}}_p + \boldsymbol{G}_p\,\ddot{\boldsymbol{p}} + \boldsymbol{\gamma} = \boldsymbol{0}\quad \text{with}\quad \boldsymbol{\gamma}(\boldsymbol{y}_p,\boldsymbol{p},\dot{\boldsymbol{s}}_p,\dot{\boldsymbol{p}}) = \dot{\boldsymbol{G}}_s\,\dot{\boldsymbol{s}}_p + \dot{\boldsymbol{G}}_p\,\dot{\boldsymbol{p}}. \tag{12}$$

2.3 Kinematic Redundancy and Output Variables

With seven robot coordinates $\boldsymbol{p}$ from (1) and six platform coordinates $\boldsymbol{y}_p$ from (2), the system is kinematically redundant. In addition to $\boldsymbol{y}_p$ a seventh output y_0 can be controlled that is here defined as the residual of the implicit control constraint

$$g_0(\boldsymbol{p}) \equiv y_0 = p_{g1} - \tfrac{1}{2}\,(p_{g2} + p_{g3}) - b = 0,\quad b = \text{const.} \tag{13}$$

According to Fig. 3, this constraint requires that the intersection point P between the line through the outer trolleys and the intermediate rail has the constant distance b to the inner trolley. Thus, the shape of the triangle whose vertices are the three trolleys is constrained.

The seven outputs $\boldsymbol{y}$ of the system are then composed of the six platform coordinates $\boldsymbol{y}_p \in \mathbb{R}^6$ from (2) and the additional output y_0 from (13),

$$\boldsymbol{y} = \begin{bmatrix} \boldsymbol{y}_p^T & y_0 \end{bmatrix}^T \in \mathbb{R}^7. \tag{14}$$

The outputs at the velocity level are here defined as quasi-coordinates with the platform velocities $\dot{s}_p \in \mathbb{R}^6$ from (4) and $\dot{y}_0$,

$$\dot{s} = \begin{bmatrix} \dot{s}_p^T & \dot{y}_0 \end{bmatrix}^T \in \mathbb{R}^7. \tag{15}$$

2.4 Dynamic Equations

The dynamic equations of CABLEV are composed of the equations of the payload platform, the equations of the drive system (gantry, trolleys, winches), and the constraint equations.

2.4.1 Platform Dynamics

The dynamic platform equations consist of the kinematic differential equation (5), the constraints (6), and the six kinetic differential equations

$$\begin{bmatrix} m\boldsymbol{I} & \boldsymbol{0} \\ \boldsymbol{0} & \boldsymbol{\Theta} \end{bmatrix} \begin{bmatrix} \dot{v} \\ \dot{\omega} \end{bmatrix} = \begin{bmatrix} \boldsymbol{0} \\ -\widetilde{\omega}\,\boldsymbol{\Theta}\,\omega \end{bmatrix} + \begin{bmatrix} \boldsymbol{f}^e \\ \boldsymbol{\tau}^e \end{bmatrix} + \begin{bmatrix} \boldsymbol{G}_{sv}^T \\ \boldsymbol{G}_{s\omega}^T \end{bmatrix} \begin{bmatrix} \lambda_1 \\ \lambda_2 \\ \lambda_3 \end{bmatrix} \tag{16}$$

$$\rightarrow \quad \boldsymbol{M}_s \qquad \ddot{\boldsymbol{s}}_p \quad = \quad \boldsymbol{k}_s^c(\dot{\boldsymbol{s}}_p) \quad + \boldsymbol{k}_s^e(\boldsymbol{y}_p, \dot{\boldsymbol{s}}_p) + \boldsymbol{G}_s^T(\boldsymbol{y}_p, \boldsymbol{p}_g) \quad \boldsymbol{\lambda}$$

with the constant mass matrix $\boldsymbol{M}_s \in \mathbb{R}^{6,6}$ containing the platform mass m and the inertia tensor $\boldsymbol{\Theta} \in \mathbb{R}^{3,3}$ with respect to the center of gravity S_p represented in coordinates of $\mathcal{K}_p$, the generalized gyroscopic forces $\boldsymbol{k}_s^c \in \mathbb{R}^6$, the generalized applied forces $\boldsymbol{k}_s^e \in \mathbb{R}^6$ (e.g., gravity force), and the minimal coordinates of the cable forces $\boldsymbol{\lambda} \in \mathbb{R}^3$ (Lagrange multipliers).

2.4.2 Drive System Dynamics

For the gantry, the trolleys, and the winches, the equations of motion are formulated in terms of the robot coordinates $\boldsymbol{p}$,

$$\boldsymbol{M}_p \ddot{\boldsymbol{p}} = \boldsymbol{B}_p \boldsymbol{u} + \boldsymbol{G}_p^T(\boldsymbol{y}_p, \boldsymbol{p})\,\boldsymbol{\lambda}, \tag{17}$$

with the mass matrix $\boldsymbol{M}_p \in \mathbb{R}^{7,7}$ and the control inputs

$$\boldsymbol{u} = \begin{bmatrix} \boldsymbol{u}_g \\ \boldsymbol{u}_c \end{bmatrix} \quad \text{with} \quad \boldsymbol{u}_g = \begin{bmatrix} u_{g0} & u_{g1} & u_{g2} & u_{g3} \end{bmatrix}^T, \quad \boldsymbol{u}_c = \begin{bmatrix} u_{c1} & u_{c2} & u_{c3} \end{bmatrix}^T. \tag{18}$$

The control inputs are the drive forces of the gantry u_{g0} and the trolleys u_{gi}, $i = 1, 2, 3$ and the winch torques u_{ci}, $i = 1, 2, 3$. The constant matrix $\boldsymbol{B}_p \in \mathbb{R}^{7,7}$ in (17) projects $\boldsymbol{u}$ onto the directions of the robot coordinates $\boldsymbol{p}$. For the dynamic simulation of CABLEV, the kinetic Eq. (16) and (17) and the constraint Eq. (12) yield the accelerations $\ddot{\boldsymbol{s}}_p$ and $\ddot{\boldsymbol{p}}$ and the cable force coordinates $\boldsymbol{\lambda}$, whereby the positions and the velocities have to be consistent with the constraints (6) and their first-order time derivatives (9).

3 Flatness-Based Feedforward Control

Flatness of the considered system means that the control inputs $\boldsymbol{u}$ as well as all internal variables, like the state variables $\boldsymbol{x}$ or the cable force coordinates $\boldsymbol{\lambda}$, can be algebraically expressed in terms of the control outputs $\boldsymbol{y}$ and the time derivatives of the outputs up to a finite order. In particular, the system is flat if its dynamics can be inverted according to $\left(\frac{d^n y}{dt^n} \hat{=} y^{(n)} \right)$

$$\boldsymbol{u} = \phi_u(\boldsymbol{y}, \dot{\boldsymbol{y}}, \ldots, \boldsymbol{y}^{(\alpha+1)}), \qquad \boldsymbol{x} = \phi_x(\boldsymbol{y}, \dot{\boldsymbol{y}}, \ldots, \boldsymbol{y}^{(\alpha)}), \tag{19}$$

whereby $\alpha \in \mathbb{N}$ is a finite natural number [6]. This property leads directly to a feedforward control law that moves the platform along sufficiently smooth trajectories. Control of conventional rigid-link manipulators by inverse dynamic algorithms (computed torque) is a special case of flatness-based feedforward control. For CABLEV, the inversion of the system dynamics according to (19) can be done in two steps that are described next: the so-called *generalized inverse kinematics* and the *inverse dynamics* [8, 10].

3.1 Generalized Inverse Kinematics

In the first step of the system inversion the robot coordinates $\hat{\boldsymbol{p}}$ are calculated in terms of the prescribed outputs $\hat{\boldsymbol{y}}$ from (14) and the output derivatives $\dot{\hat{\boldsymbol{s}}}, \ddot{\hat{\boldsymbol{s}}}$ from (15). This can be illustrated as follows: For a given position $\hat{\boldsymbol{y}}_p$ and velocity $\dot{\hat{\boldsymbol{s}}}_p$ of the platform, the robot coordinates $\hat{\boldsymbol{p}}$ and the cable force coordinates $\hat{\boldsymbol{\lambda}}$ are calculated in such a way that the platform is subjected to the desired acceleration $\ddot{\hat{\boldsymbol{s}}}_p$. Hereby the maximum value of the vertical downward acceleration $\ddot{\hat{r}}_z$ in vector $\ddot{\hat{\boldsymbol{s}}}_p$ is the gravity acceleration g, thus $\ddot{\hat{r}}_z < g$. In the special case of a given rest position of the platform, thus $\hat{\boldsymbol{y}}_p$ with $\dot{\hat{\boldsymbol{s}}}_p = \ddot{\hat{\boldsymbol{s}}}_p = \boldsymbol{0}$, the variables $\hat{\boldsymbol{p}}$ and $\hat{\boldsymbol{\lambda}}$ are calculated in such a way that the given position $\hat{\boldsymbol{y}}_p$ is a static equilibrium position.

With (16), (6), and (13), a set of ten nonlinear equations is available to calculate the ten unknowns $\hat{\boldsymbol{p}} \in \mathbb{R}^7$ and $\hat{\boldsymbol{\lambda}} \in \mathbb{R}^3$ for given $\hat{\boldsymbol{y}}, \dot{\hat{\boldsymbol{y}}}, \ddot{\hat{\boldsymbol{y}}}$:

$$(16): \boldsymbol{G}_s^T(\hat{\boldsymbol{y}}_p, \hat{\boldsymbol{p}}_g)\hat{\boldsymbol{\lambda}} = \boldsymbol{M}_s\,\ddot{\hat{\boldsymbol{s}}}_p - \boldsymbol{k}_s^c(\dot{\hat{\boldsymbol{s}}}_p) - \boldsymbol{k}_s^e(\hat{\boldsymbol{y}}_p, \dot{\hat{\boldsymbol{s}}}_p) \left.\begin{array}{c} \\ \\ \end{array}\right\}$$

$$(6): \hspace{2.5cm} \boldsymbol{g}(\hat{\boldsymbol{y}}_p, \hat{\boldsymbol{p}}) = \boldsymbol{0} \hspace{2cm} \Bigg\} \, . \hspace{1cm} (20)$$

$$(13): \hspace{2.5cm} g_0(\hat{\boldsymbol{p}}) \equiv y_0 = 0$$

The platform velocities $\dot{\hat{\boldsymbol{s}}}_p$ and the accelerations $\ddot{\hat{\boldsymbol{s}}}_p$ can be expressed in terms of the output derivatives $\dot{\hat{\boldsymbol{y}}}_p$ and $\ddot{\hat{\boldsymbol{y}}}_p$ by means of (5). The numerical solution of (20) by a Newton-Raphson algorithm yields

$$\hat{\boldsymbol{p}} = \boldsymbol{\phi}(\hat{\boldsymbol{y}}, \dot{\hat{\boldsymbol{s}}}, \ddot{\hat{\boldsymbol{s}}}), \qquad \hat{\boldsymbol{\lambda}} = \boldsymbol{\phi}_\lambda(\hat{\boldsymbol{y}}, \dot{\hat{\boldsymbol{s}}}, \ddot{\hat{\boldsymbol{s}}}). \tag{21}$$

A good initial guess for $\hat{\boldsymbol{p}}$ is available from the preceding time step. The function (21) is called generalized inverse kinematics as a generalization of the inverse kinematics transformation for rigid robots.

3.2 Inverse Dynamics

The second step of the system inversion is the calculation of the physical control forces $\boldsymbol{u}$ in terms of $\hat{\boldsymbol{p}}$. They are obtained directly by solving (17) with respect to $\boldsymbol{u}$, leading to $\boldsymbol{u} = \boldsymbol{u}(\hat{\boldsymbol{p}}, \dot{\hat{\boldsymbol{s}}}, \ddot{\hat{\boldsymbol{s}}}, \hat{\boldsymbol{\lambda}})$. Thus, the first and second order time derivatives of the generalized inverse kinematics (21) are needed, too. Altogether a feedforward control law is obtained that calculates $\boldsymbol{u}$ for output trajectories $\hat{\boldsymbol{y}}(t)$ specified up to the fourth-order time derivative

$$\boldsymbol{u} = \boldsymbol{\phi}_u(\hat{\boldsymbol{y}}, \dot{\hat{\boldsymbol{s}}}, \ddot{\hat{\boldsymbol{s}}}, \hat{\boldsymbol{s}}^{(3)}, \hat{\boldsymbol{s}}^{(4)}). \tag{22}$$

The inverse system model (22) makes the platform track a desired spatial trajectory $\hat{\boldsymbol{y}}(t)$ under ideal conditions, i.e., exact mechanical model, no disturbance forces, and consistent initial conditions. However, it is computationally expensive as the first and second-order derivatives of the generalized inverse kinematics from (21) is needed according to (22), see Fig. 5.

In practice, the computational amount can be reduced. CABLEV is actuated by electric motors with reduction gears of high ratio that tend to linearize and to decouple the dynamics of the drive axes. This justifies well the use of individual cascaded axis controllers that make the actual robot coordinates $\boldsymbol{p}$ follow the sequence of values $\hat{\boldsymbol{p}}$ calculated by means of the generalized inverse kinematics (21). To further improve the tracking behaviour, the velocities $\dot{\hat{\boldsymbol{p}}}$ can be calculated by differentiation of (20) and added to the velocity inputs $\boldsymbol{v}_c$, $\boldsymbol{v}_g$ of the axis controllers. This feedforward control scheme has been successfully verified by experiments [7, 10].
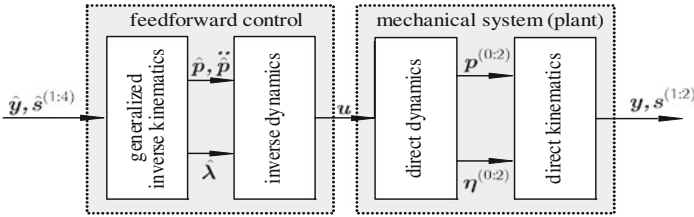
Fig. 5 Flatness-based feedforward control for CABLEV [8]

4 Feedback Control

For active damping of sway motions of the platform, a feedback of actual state variables is provided that is superimposed to the previously described feedforward control. The idea is to achieve sway control by appropriate motions of the four gantry/trolley coordinates $\boldsymbol{p}_g$ but not by changes of the cables lengths $\boldsymbol{p}_c$. A similar approach was used by Sawodny et al. [14] for trajectory control of an overhead crane. For controller design a linear state-space model of CABLEV with velocity-controlled axes according to Fig. 5 is derived. It is based on the linearized equations of motion that describe small motions in the vicinity of an equilibrium position of the platform. With measured cable inclination angles $\hat{\boldsymbol{\beta}}$ in one vertical plane according to Fig. 2, a kinematic forward transformation calculates the actual platform position $\boldsymbol{y}_p$ that are needed to feed back actual states for path following control.

4.1 Linearized Sway Motion Model

To apply established methods for linear control design, linearized equations of motion are formulated as ordinary differential equations in terms of small deviations $\Delta\boldsymbol{\eta}$ of the sway coordinates defined by (3) from an equilibrium position $\boldsymbol{\eta}_E$ of the platform. For that purpose the differential-algebraic equations (5), (6), (16) describing the sway motion are linearized and transferred into ordinary differential equations by eliminating the cable force coordinates $\boldsymbol{\lambda}$ and introducing the independent sway coordinates $\Delta\boldsymbol{\eta}$. The linearized sway dynamics model is then obtained as

$$\boldsymbol{M}_\eta\,\Delta\ddot{\boldsymbol{\eta}} + \boldsymbol{C}_\eta\,\Delta\boldsymbol{\eta} = \boldsymbol{B}_1\,\Delta\boldsymbol{p}_g + \boldsymbol{B}_2\,\Delta\ddot{\boldsymbol{p}}_g. \tag{23}$$

The coefficient matrices $\boldsymbol{M}_\eta \in \mathbb{R}^{3,3}$, $\boldsymbol{C}_\eta \in \mathbb{R}^{3,3}$, $\boldsymbol{B}_1 \in \mathbb{R}^{3,4}$, $\boldsymbol{B}_2 \in \mathbb{R}^{3,4}$ are constant for a certain reference position. The control inputs for the mechanical system are the reference velocities $\boldsymbol{v}_g$ of the axis velocity controllers. The dynamic transfer behavior from the reference velocities $\boldsymbol{v}_g$ to the actual velocities $\Delta\dot{\boldsymbol{p}}_g$ of the gantry/trolleys appearing in (23) is approximated by a first order dynamics,

$$T \, \Delta \ddot{\boldsymbol{p}}_{\mathrm{g}} + \Delta \dot{\boldsymbol{p}}_{\mathrm{g}} = \boldsymbol{v}_{\mathrm{g}}, \tag{24}$$

with time constants $\boldsymbol{T} = \mathrm{diag}(T_1, \dots, T_4)$.

Introducing the state vector

$$\boldsymbol{x}_{\mathrm{sway}} = \begin{bmatrix} \Delta \boldsymbol{\eta} \\ \Delta \dot{\boldsymbol{\eta}} \\ \Delta \boldsymbol{p}_{\mathrm{g}} \\ \Delta \dot{\boldsymbol{p}}_{\mathrm{g}} \end{bmatrix} \in \mathbb{R}^{14} \quad \text{with} \quad \Delta \boldsymbol{\eta} = \begin{bmatrix} \Delta r_x \\ \Delta r_y \\ \Delta \varphi_3 \end{bmatrix}, \Delta \boldsymbol{p}_{\mathrm{g}} = \begin{bmatrix} \Delta p_{\mathrm{g}1} \\ \Delta p_{\mathrm{g}2} \\ \Delta p_{\mathrm{g}3} \\ \Delta p_{\mathrm{g}4} \end{bmatrix}, \tag{25}$$

the reference velocities $\boldsymbol{v}_{\mathrm{g}}$ as inputs and the sway coordinates as outputs, $\boldsymbol{y}_{\mathrm{sway}} = \Delta \boldsymbol{\eta}$, Eqs. (23), (24) can be brought into standard state-space form

$$\dot{\boldsymbol{x}}_{\mathrm{sway}} = \boldsymbol{A} \, \boldsymbol{x}_{\mathrm{sway}} + \boldsymbol{B} \, \boldsymbol{v}_{\mathrm{g}}, \qquad \boldsymbol{y}_{\mathrm{sway}} = \boldsymbol{C} \, \boldsymbol{x}_{\mathrm{sway}}. \tag{26}$$

4.2 Kinematic Measurement Model

For anti-sway control the actual sway coordinates $\boldsymbol{\eta}$ from (3) and their time derivatives $\dot{\boldsymbol{\eta}}$ have to be measured and fed back. According to (2), they are a subset of the platform coordinates $\boldsymbol{y}_{\mathrm{p}}$ that are, however, not measured directly. Instead, the seven robot coordinates $\boldsymbol{p} = [\boldsymbol{p}_{\mathrm{g}} \ \boldsymbol{p}_{\mathrm{c}}]^{\mathrm{T}}$ and the measured cable inclination angles

$$\boldsymbol{\beta} = [\beta_1 \ \beta_2 \ \beta_3]^{\mathrm{T}} \tag{27}$$

in one vertical plane according to Fig. 2 are available for measuring the platform position.

With these measured coordinates, the platform coordinates $\boldsymbol{y}_{\mathrm{p}}$ are calculated by kinematic forward transformation. Together with the three non-measured cable inclination angles $\overline{\boldsymbol{\beta}}$ in the second vertical plane, nine loop closure conditions are obtained by cuts at the spherical joints at the platform vertices according to Fig. 6,

$$\boldsymbol{h}_i(\boldsymbol{p}, \boldsymbol{\beta}, \overline{\boldsymbol{\beta}}, \boldsymbol{y}_{\mathrm{p}}) \equiv \boldsymbol{r}_{P_i}(p_{\mathrm{g}0}, p_{\mathrm{g}i}, \beta_i, \overline{\beta}_i, p_{ci}) - \boldsymbol{r}_{P'i}(\boldsymbol{y}_{\mathrm{p}}) = \boldsymbol{0}, \quad i = 1, 2, 3. \tag{28}$$

This is a set of nine nonlinear equations for the calculation of the unknowns $\boldsymbol{y}_{\mathrm{p}} \in \mathbb{R}^6$ and $\overline{\boldsymbol{\beta}} \in \mathbb{R}^3$ for known values of $\boldsymbol{p}$ and $\boldsymbol{\beta}$, whereby $\overline{\boldsymbol{\beta}}$ is not needed in the sequel.

The sway velocities $\dot{\boldsymbol{\eta}}$ can be calculated from the time derivative of (28) yielding a system of nine linear equations for the unknowns $\dot{\boldsymbol{y}}_{\mathrm{p}}$ and $\dot{\overline{\boldsymbol{\beta}}}$ for known $\dot{\boldsymbol{p}}$ and $\dot{\boldsymbol{\beta}}$,
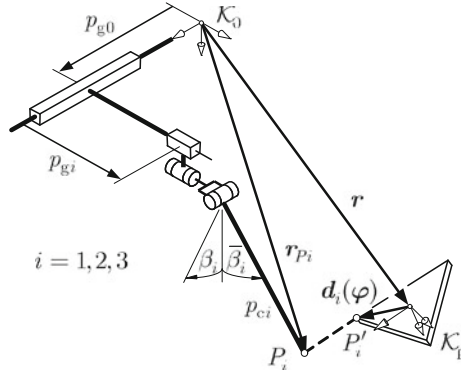
Fig. 6 Kinematic measurement model for CABLEV

$$\underbrace{\begin{bmatrix} L_{\mathrm{p}} & L_{\beta} & L_{\overline{\beta}} & L_y \end{bmatrix}}_{L(\boldsymbol{p},\ \boldsymbol{\beta},\ \overline{\boldsymbol{\beta}},\ \boldsymbol{y}_{\mathrm{p}})} \begin{bmatrix} \dot{\boldsymbol{p}} \\ \dot{\boldsymbol{\beta}} \\ \dot{\overline{\boldsymbol{\beta}}} \\ \dot{\boldsymbol{y}}_{\mathrm{p}} \end{bmatrix} = \boldsymbol{0}. \tag{29}$$

4.3 Linear State-Space Controller

The sway dynamics (26) is stabilized by a linear state feedback

$$\bar{v}_{\mathrm{g}} = -\boldsymbol{R}\, x_{\mathrm{sway}}. \tag{30}$$

applied on the inputs of the individual axis velocity controllers. The structure of the obtained feedback control with decoupled PI axis controllers is shown in Fig. 7. Here, the diagonal matrices $\boldsymbol{K}_{\mathrm{c}}$ and $\boldsymbol{K}_{\mathrm{g}}$ contain the motor constants and gear ratios.

The feedback gain matrix $\boldsymbol{R} \in \mathbb{R}^{4,14}$ in (30) is here determined by LQR design. Since the linear feedback (30) is only designed for the dynamics of CABLEV in the vicinity of an equilibrium position in the workspace, an increasing decline of the control behaviour is expected if the platform moves away from this position. Though simulation results show a good robustness of the controller, the control behavior can be improved if the feedback gains are calculated in dependency on varying parameters like the cable length [7, 14]. For trajectory tracking control, the small deviations $\Delta \boldsymbol{\eta}$, $\Delta \dot{\boldsymbol{\eta}}$, $\Delta \boldsymbol{p}_{\mathrm{g}}$, $\Delta \dot{\boldsymbol{p}}_{\mathrm{g}}$ in x_{sway} are referred to the values of the corresponding variables from the reference trajectory.
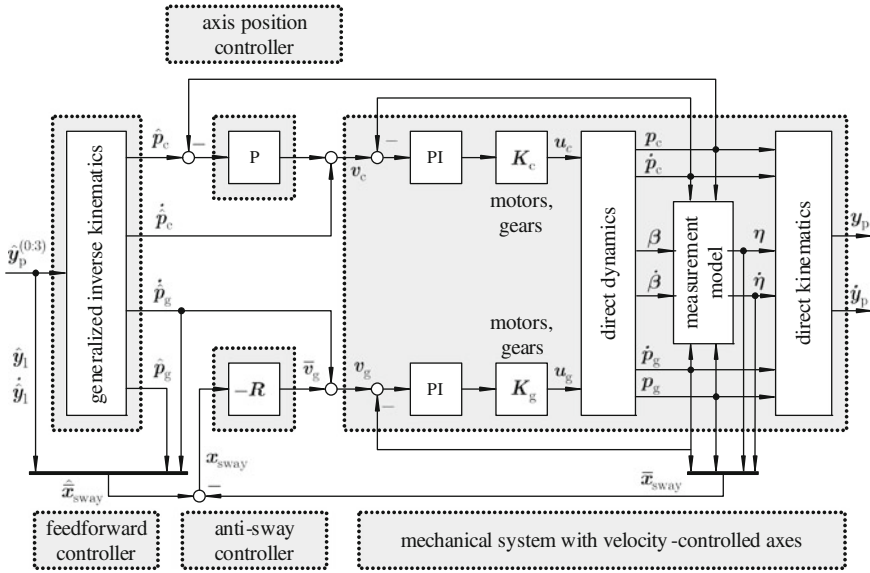
Fig. 7 Trajectory tracking feedback control for CABLEV

5 Experimental Result

As an experimental result, a closed-loop trajectory in the vertical xz-plane in combination with a rotation of the platform with an angle $\varphi_3 = 30°$ around the vertical axis is considered in Fig. 8. The platform is at rest in the initial and final positions of the trajectory. To demonstrate the effect of the trajectory tracking control, the Bryan angles of the initial platform position deviate by 10° each from the reference trajectory. Figure 8a–c shows that the measured actual cable inclination angles $\beta_i(t)$ track relatively well the values $\hat{\beta}_i(t)$ calculated by the feedforward control. The deviations between $\hat{\beta}_i(t)$ and $\beta_i(t)$ in the initial phase are caused by the initial values of the platform being not consistent with the reference trajectory. Figure 8d–f shows the platform coordinates $r_x(t)$, $r_z(t)$, and $\varphi_3(t)$ that are calculated by means of the measurement model (28) from the measured actual cable inclination angles $\beta_i(t)$ and from the actual robot coordinates $p(t)$ (not represented here). The corresponding tracking errors $e_{r_x}(t)$, $e_{r_z}(t)$, and $e_{\varphi_3}(t)$ (right-hand axes) tracking errors of about 4 cm for the horizontal coordinate r_x, about 1 cm for the vertical coordinate r_z, and about 2° for the rotation angle φ_3.
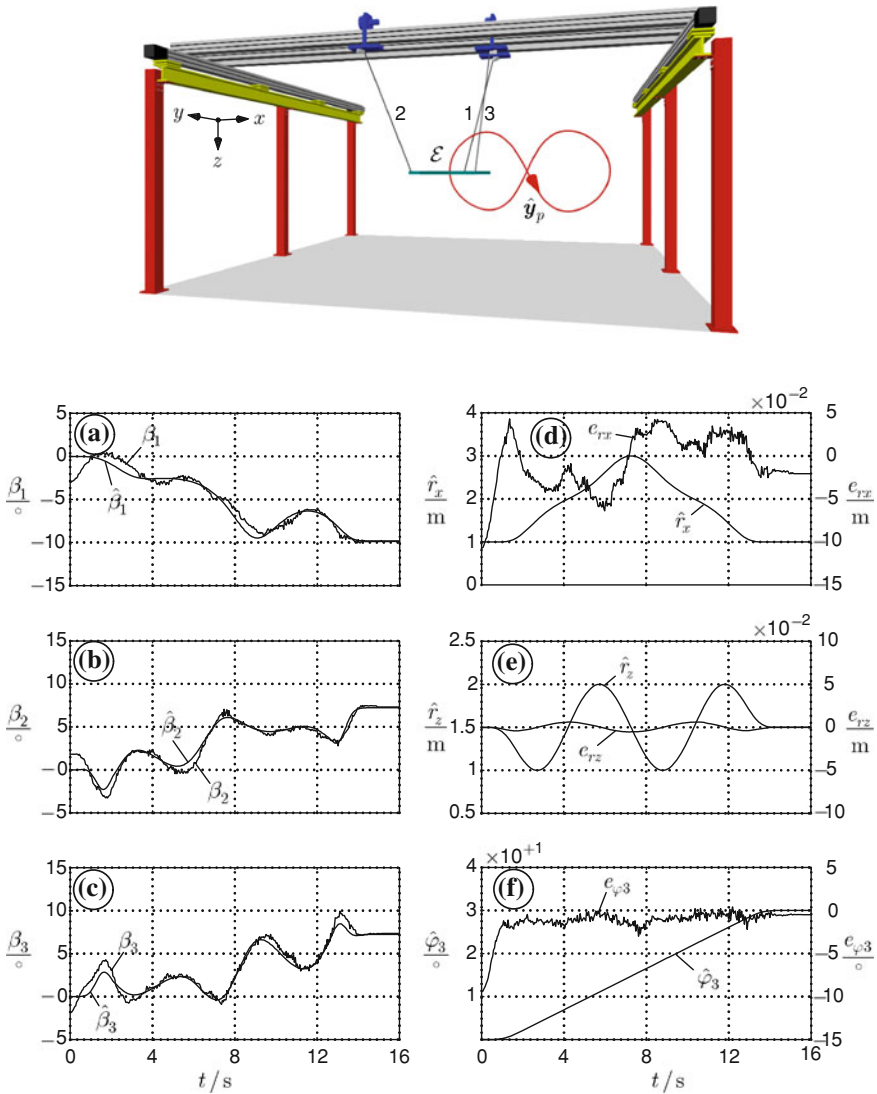
Fig. 8 Experimental result for tracking a spatial trajectory with initial disturbance

6 Conclusion

A trajectory tracking control for the kinematically indeterminate three-cable suspension manipulator CABLEV is theoretically and experimentally presented. It consists of a flatness-based nonlinear feedforward control and a superimposed linear feedback control. A critical issue for the trajectory tracking control is a sufficiently precise

measurement of the actual motion parameters of the platform, especially the velocity needed for the state-space controller. In the described investigations, the velocity was obtained by finite differences of the cable inclination sensors (potentiometers) that underlies several disturbance effects. An improvement can be achieved by platform-fixed inertial sensors (accelerometers and gyros) that are aided by complementary position sensors, here the cable inclination angles, as shown in [11].

References

1. Alp, A., Agrawal, S.: Cable suspended robots: feedback controllers with positive inputs. Proceedings of the American Control Conference, Anchorage, AK, USA, In (2002)
2. Arai, T., Osumi, B.: Three wire suspension robot. Ind. Robot **19**, 17–22 (1992)
3. Bruckmann, T., Hiller, M., Schramm, D.: An active suspension system for simulation of ship maneuvers in wind tunnels. In: Pisla, D., et al. (eds.) New Trends in Mechanism Science: Analysis and Design, pp. 529–544. Springer, Berlin (2010)
4. Dagalakis, N., Albus, J., Wang, B.L., Unger, J., Lee, J.: Stiffness study of a parallel link robot crane for shipbuilding applications. ASME J. Offshore Mech. Arct. Eng. **111**, 183–193 (1991)
5. Delaleau, E., Rudolph, J.: Control of flat systems by quasi-static feedback of generalized states. Int. J. Control **71**, 745–765 (1998)
6. Fliess, M., Lévine, J., Martin, P., Rouchon, P.: Flatness and defect of nonlinear systems: introductory theory and examples. Int. J. Control **51**, 1327–1361 (1995)
7. Heyden, T.: Bahnregelung eines seilgeführten Handhabungssystems mit kinematisch unbestimmter Lastführung. Fortschrittberichte VDI, Reihe 8, Band 1100. VDI-Verlag, Düsseldorf (2006).
8. Heyden, T., Woernle, C.: Dynamics and flatness-based control of a kinematically undetermined cable suspension manipulator. Multibody Syst. Dyn. **16**, 155–177 (2006)
9. Hiller, M., Fang, S., Mielczarek, S., Verhoeven, R., Franitza, D.: Design, analysis and realization of tendon-based parallel manipulators. Mech. Mach. Theory **40**, 429–445 (2005)
10. Maier, T.: Bahnsteuerung eines seilgeführten Handhabungssystems–Modellbildung, Simulation und Experiment. Fortschrittberichte VDI, Reihe 8, Band 1047. VDI-Verlag, Düsseldorf (2004).
11. Meinicke, A.: Kalibrierung von Inertialmessystemen ind Integrierte Navigation zur Lageregelung eines Mehrseilkrans. Ph.D. Thesis, Universität Rostock (2009).
12. Miermeister, P., Pott, A.: Modelling and real-time dynamic simulation of the cable-driven parallel robot IPAnema. In: Pisla, D., et al. (eds.) New Trends in Mechanism Science: Analysis and Design, pp. 353–360. Springer, Berlin (2010)
13. Ming, A., Higuchi, T.: Study on multiple degree-of-freedom positioning mechanisms using wires (parts 1 and 2). Int. J. Jpn. Soc. Precis. Eng. 28, 131–138 and 235–242 (1994).
14. Sawodny, O., Aschemann, H., Lahres, R., Hofer, E.: Tracking control for automated bridge cranes. In: Tzafestas, S. (ed.) Advances in Manufacturing, pp. 310–320. Springer, Berlin (1999)
15. Verhoeven, R., Hiller, M., Tadokoro, S.: Singularities and classification of tendon-driven stewart platforms. In: Lenarčič, J., Husty, M. (eds.) Advances in Robot Kinematics: Analysis and Control, pp. 105–114. Kluwer Academic Publishers, Amsterdam (1998)
16. Woernle, C.: Mehrkörpersysteme. Springer, Berlin (2011)
17. Yamamoto, M., Yanai, N., Mohri, A.: Trajectory control of incompletely restrained parellel-wire-suspended mechanism based on inverse dynamics. IEEE Trans. Robot. **20**, 840–850 (2004)

Part VIII
Dynamics Modeling

Geometric Stiffness Analysis of Wire Robots: A Mechanical Approach

Dragoljub Surdilovic, Jelena Radojicic and Jörg Krüger

Abstract This paper presents a mechanical approach for the modelling of wire robots dynamics considering the effects of structural elasticity. The mechanical wires represent critical flexible elements of a wire robot that are responsible for elastic deformations and vibrations of the entire structure. A comprehensive elastodynamic analysis plays a crucial role in wire-robot synthesis and control. Especially in the large-span systems, the elastic deformations and vibrations may be characterized by relatively low frequencies and high amplitudes causing undesirable behaviour. The paper considers coupled 6D deformations of the common wire-robot platform in both over- and under-constrained wire robot structures. Special emphasis is on the *geometric stiffness* matrix that is dependent on wire tension and which has been derived following a rigorous mechanical approach analysing the motion of the entire system and specific components. The geometric stiffness matrix in wire robots plays a crucial role in stabilization of the wire robot, such as in active stiffening and damping of unacceptable vibration effects. The decomposition of both spatial elastic wire and geometric stiffness matrices on virtual elemental springs has been applied to provide a physical insight and better understanding of the wire robot elastic behaviour. Several examples illustrate the theoretical analysis.

Keywords Wire-robots elastic deformations · Geometric stiffness · Stiffness decomposition · Screw-analysis

D. Surdilovic (✉) · J. Radojicic · J. Krüger
Department of Robotics and Automation, Fraunhofer Institute for Production Systems
and Design Technology IPK-Berlin, Pascalstr. 8-9, 10587 Berlin, Germany
e-mail: dragoljub.surdilovic@ipk.fraunhofer.de

1 Introduction

The *wire-robots* (the term also used: cable driven parallel robots) have been recently addressed in numerous researches focusing on their advantages for implementing large spans, fast moving, lightweight and heavy-duty active spatial mechanisms. In comparison to a more general class of cable robots (e.g. spatial advanced robotized crane systems), the wire robots, especially the so called over-constrained structures, offer benefits to apply and control wire over-tension by wire pulling forces and thus to perform more precise and robust pose and motion control in spite of the external dynamic perturbations and excitations (e.g. wind, inertia etc.). However, due to the relatively large dimensions and inevitable elasticity inherent in robot cables, the wire robots are prone to vibrations. Thereby the common platform can perform complex coupled 6D oscillations, particularly in case of abrupt motion changes. The motion planning of wire-robots cannot be similar to that of the convenient industrial robots performed separately from system dynamic i.e. quasi-static analysis considerations, such as planning of tension free or wrench feasible working spaces etc. Therefore, elastodynamic analysis of wire robots becomes essential in trajectory planning, as well as during system design and control development.

The wire-robot stiffness analysis has been recently the subject of several studies taking into account the particular features of wire robots. The conventional wire-robot elasticity i.e. stiffness analysis completely neglects or considers a slight dependence of the stiffness matrix from the wire tension (pre-stress). The seminal studies on the wire robot elastic deformations have been performed within ROBOCRANE project [1]. The applied approach has been based on static analysis and linearized stiffness matrix computation in both wire and Cartesian space (so called *spatial stiffness* matrix). Since the nominal length of the wires has been changed due to tension force induced
dilatations (relevant in large-span systems), a slight dependence of the spatial stiffness matrix from the wire tension (less than $<0.5\,\%$ according [2]) has been reported when real wire lengths have been considered. A more exact non-linear stiffness analysis is based on wire robot Jacobian mapping [2]. Diao and Ma [3] have considered elemental longitudinal and transversal vibrations of elastic wires around quasistatic platform equilibrium. They have accented the dominance of longitudinal wire vibration contribution to the platform oscillations over negligible transversal effects (less than $2\,\%$). The wire-stiffness has been in [4] included in the dynamic models of the elastic robots, derived using Lagrange-formalisms and introducing additional lumped wire longitudinal elastic coordinates. Based on this model a simple PD position plus tension controller including gravity compensation has been synthesized to ensure stable trajectory tracking.

However, as known from the theory of elasticity, a cable when subjected to large longitudinal tension expresses an increased transversal stiffness. This type of nonlinear behaviour in elastic structures related to second-order geometry effects due to deformation and complex load of a body (e.g. buckling effects of thin beam under axial compression force) has been referred to as *geometric-stiffness* in static and

dynamic deformation analysis, *or p-delta effect* in civil structural engineering [5]. The geometric stiffness matrix depends on the external loads and may be either positive or even negative definite, increasing or reducing the structural stiffness (e.g. buckling of rods). In convenient robotic systems the geometric stiffness effects have been firstly analysed by Chen and Kao [6], which referred this effect to as *conservative congruence transformation* (CCT) between joint and Cartesian stiffness matrices. The CCT in robotic system with dominate joint-elasticity is related to the variations of robot Jacobian (Hessian) matrix during infinitesimal elastic displacements and external loads. However, the practical relevance of the CCT in industrial robotic systems, considering relatively stiff joints (transmissions), considerably rigid structures and relatively small loads is still not clear.

Studies on parallel robots stiffness matrix analysis have also attracted considerable interest [7]. In order to analyse stability of Stewart-Gough platform preloaded by internal forces, Svinin et al. [8] have initially considered geometric stiffness effects in parallel robot structures. Motivated by this work Behzadipour and Khajepour [9, 10] have recently analysed the influence of cable tension on spatial stiffness and stabilization of cable robots. The authors have refereed this effect to as *antagonistic variable stiffness*. Similar analysis of a specific wire robot developed for wind-tunel testing has been reported in [11]. Recently Arsenault [12] has analysed the influence of wire preloads on increasing stiffness matrix of a planar 3DOF cable-driven robot based on linearization of the state-equilibrium equations. This model was utilized in the paper to analyse stability and optimize the robot workspace under cable pre-stress conditions.

All the above mentioned researches, however, have analysed geometric-stiffness based on equivalence with parallel robots assuming wires attached at specific points in the space. Thereby particular wire-robot motion effects occurring in commonly applied pulley elements (e.g. due to pulley rolling and wire coil) have been neglected. In this paper we will derive geometric stiffness of a general wire-robot system taking also into account the pulley motion effects. The stiffness analysis will be based on both an exact mechanical approach, and the screw-theory [13]. Using the stiffness matrix decomposition, the influence of geometric stiffness on the entire spatial stiffness and dynamic vibrations will be analysed and illustrated with practical wire-robots examples. It will be shown that wire-tension, i.e. geometric stiffness plays a considerable role in stabilization and reduction of undesired vibration effects even in under-constrained robot structures.

2 Kinematic Analysis

In Fig. 1, a general model of wire-robot with n-wires ($i = 1, \ldots, n$) is given. In a over-constrained wire-robot structure ensuring 6DOF motion plus wires tension is $n \geq 7$. Using the notion from (Fig. 1), the position of the ith wire platform attachment point B_i is defined by

$$\mathbf{p}_i = \mathbf{a}_i + \mathbf{L}_i = \mathbf{p} + \mathbf{b}_i \tag{1}$$

Fig. 1 Wire-robot structure
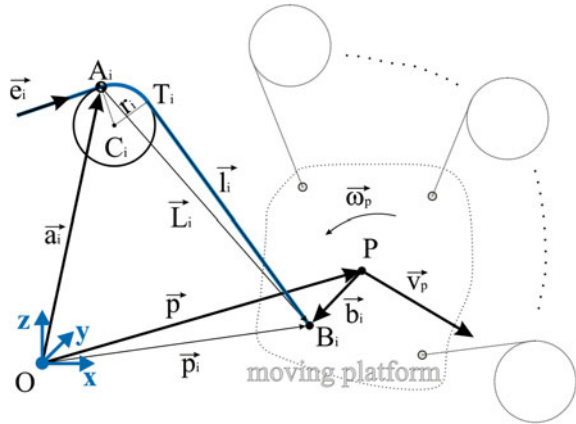
where $\mathbf{a}_i$ and $\mathbf{b}_i$ are position vectors of pulley and platform attachment points A_i and B_i wrt. base and local platform frames respectively, $\mathbf{p}$ is the position vector of the platform reference frame and

$$\mathbf{L}_i = \overrightarrow{A_i C_i} + \overrightarrow{C_i T_i} + \mathbf{l}_i \tag{2}$$

where $\mathbf{l}_i$ is the wire-length vector, while C_i and T_i denote centre of the pulley and wire tangent points (Fig. 1).

Let us analyse the wire motion during an arbitrary platform displacement. In general the wire performs a complex composite motion that can be decomposed into *transferred motion* representing the entire wire plane $\{A_i B_i C_i T_i\}$ rotation (rolling motion of the pulley) around the fixed pulley axis $\mathbf{e}_i$, and *relative motion* in the wire plane. The relative motion consists of relative translation i.e. change of the relative length in the actual cable direction (due to cable control, i.e. via a winch or linear slider mechanism that are not presented in the Fig. 1), and a relative rotation of the wire around the pulley (i.e. point T_i that represents actual pole of the velocity). Based on this analysis, differentiating (1) twice with respect to time taking into account vector differentiation rules, the expressions for absolute wire end-point velocities and accelerations are obtained

$$\mathbf{v}_i = \dot{\mathbf{p}}_i = \boldsymbol{\omega}_{e_i} \times \mathbf{L}_i + \boldsymbol{\omega}_{r_i} \times \mathbf{l}_i + \overset{*}{\mathbf{l}}_i = \mathbf{v}_p + \boldsymbol{\omega}_p \times \mathbf{b}_i \tag{3}$$

$$\mathbf{a}_i = \ddot{\mathbf{p}}_i = \boldsymbol{\varepsilon}_{e_i} \times \mathbf{L}_i + \boldsymbol{\varepsilon}_{r_i} \times \mathbf{l}_i + \boldsymbol{\omega}_{e_i} \times (\boldsymbol{\omega}_{e_i} \times \mathbf{L}_i) + \boldsymbol{\omega}_{e_i} \times (\boldsymbol{\omega}_{r_i} \times \mathbf{l}_i) + \boldsymbol{\omega}_{r_i}$$
$$\times (\boldsymbol{\omega}_{r_i} \times \mathbf{l}_i) + 2(\boldsymbol{\omega}_{e_i} + \boldsymbol{\omega}_{r_i}) \times \overset{*}{\mathbf{l}}_i + \overset{**}{\mathbf{l}}_i = \mathbf{a}_p + \boldsymbol{\varepsilon}_p \times \mathbf{b}_i + \boldsymbol{\omega}_p$$
$$\times (\boldsymbol{\omega}_p \times \mathbf{b}_i) \tag{4}$$

Fig. 2 Velocity vectors components
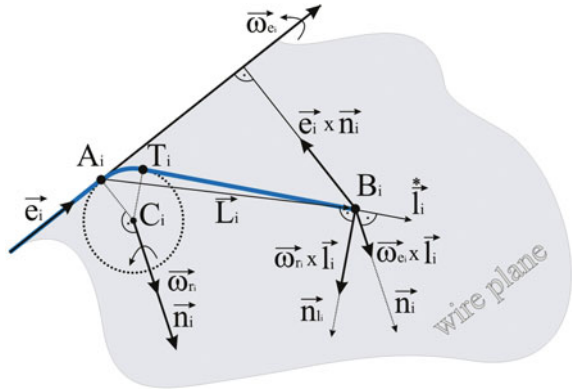
where $\boldsymbol{\omega}_{e_i}$ and $\boldsymbol{\varepsilon}_{e_i}$ denote pulley rotation velocity and acceleration around $\mathbf{e}_i$ (Fig. 2), $\boldsymbol{\omega}_{r_i}$ and $\boldsymbol{\varepsilon}_{r_i}$ relative wire rotation velocity and acceleration around wire-plane normal $\mathbf{n}_i$, $\overset{*}{\mathbf{l}}_i$ and $\overset{**}{\mathbf{l}}_i$ are linear wire relative velocity and acceleration due to cable length changes, $\mathbf{v}_p$ and $\boldsymbol{\omega}_p$, $\mathbf{a}_p$ and $\boldsymbol{\varepsilon}_p$ are platform linear and angular velocities and acceleration vectors respectively. Relative velocity components and their directions are shown in Fig. 2. The projections of the velocity and acceleration vectors (3, 4) into wire-length vector direction, defined by unit vector $\mathbf{l}_{i0} = \mathbf{l}_i/l_i$, i.e. scalar multiplication of these equations by $\mathbf{l}_{i0}$ yields the magnitudes of wire linear relative velocity

$$\overset{*}{l}_i = [\mathbf{l}_{i0}{}^T \quad -\mathbf{l}_{i0}{}^T \underline{\underline{\mathbf{b}_i}}]\, \mathbf{t}_p \tag{5}$$

where $\mathbf{t}_p = [\mathbf{v}_p{}^T \quad \boldsymbol{\omega}_p^T]^T$ is the platform twist vector, while $\underline{\underline{\mathbf{b}_i}}$ denotes *skew-symmetric* 3×3 matrix formed from the elements of the vector $\mathbf{b}_i$ in order to represent the vector product in the matrix form. Scalar multiplication of (4) by $\mathbf{l}_{i0}$ yields the magnitude of wire relative acceleration

$$\overset{**}{l}_i = \omega_{e_i}{}^2 \left[(\vec{\mathbf{e}}_i \times \vec{\mathbf{L}}_i) \cdot \vec{\mathbf{n}}_i \right] \left[(\vec{\mathbf{e}}_i \times \vec{\mathbf{n}}_i) \cdot \vec{\mathbf{l}}_{i0} \right] + \omega_{r_i}{}^2 l_i$$
$$+ \left[\mathbf{l}_{i0}{}^T \quad -\mathbf{l}_{i0}{}^T \underline{\underline{\mathbf{b}_i}} \right] \dot{\mathbf{t}}_p \quad -\mathbf{l}_{i0}{}^T \underline{\underline{\omega_p \mathbf{b}_i}} \omega_p \tag{6}$$

where the first two components represent the projections of centrifugal accelerations components (corresponding to the pulley and relative wire rotations), while the remaining parts define projections of platform tangential and centrifugal accelerations into the wire directions.

The expressions for vectors of angular pulley and wire relative rotations are obtained by scalar multiplication of (3) by vectors $\mathbf{n}_{l_i} = \mathbf{n}_i \times \mathbf{l}_{i0}$ and $\mathbf{n}_i$ respectively in terms of platform twist vector

$$\omega_{e_i} = \frac{1}{(\vec{\mathbf{e}}_i \times \vec{\mathbf{L}}_i) \cdot \vec{\mathbf{n}}_i} \left[\mathbf{n}_i{}^T \quad -\mathbf{n}_i{}^T \underline{\underline{\mathbf{b}_i}} \right] \mathbf{t}_p \tag{7}$$

$$\omega_{r_i} = \frac{1}{l_i} \left[-\mathbf{l}_{i0}{}^T \underline{\underline{\mathbf{n}_i}} \quad \mathbf{l}_{i0}{}^T \underline{\underline{\mathbf{b}_i}} \right] \mathbf{t}_p \tag{8}$$

3 Wire-Robot Jacobian and Its Time-Derivative

The relationship between relative wire velocity, defining the cable length variations, and platform twist vector is defined by the wire-robot Jacobian

$$\overset{*}{\mathbf{l}} = \mathbf{J}\mathbf{t}_p \tag{9}$$

where $\overset{*}{\mathbf{l}} = [\overset{*}{l}_1 \ldots \overset{*}{l}_i \ldots \overset{*}{l}_n]^T$ and Jacobian matrix $\mathbf{J} \in \mathfrak{R}^{n \times 6}$ is

$$\mathbf{J}^T = \begin{bmatrix} \mathbf{l}_{10} & \cdots & \mathbf{l}_{i0} & \cdots & \mathbf{l}_{n0} \\ \underline{\underline{\mathbf{b}_1}}\mathbf{l}_{10} & \cdots & \underline{\underline{\mathbf{b}_i}}\mathbf{l}_{i0} & \cdots & \underline{\underline{\mathbf{b}_n}}\mathbf{l}_{n0} \end{bmatrix} \tag{10}$$

The time derivative of wire Jacobian is obtained by differentiating (9) (the same result is obtained by substituting (7) and (8) in (6))

$$\overset{**}{\mathbf{l}} = \mathbf{J}\dot{\mathbf{t}}_p + \dot{\mathbf{J}}\mathbf{t}_p \tag{11}$$

where based on (10) is

$$\dot{\mathbf{J}}^T = \begin{bmatrix} \dot{\mathbf{l}}_{10} & \cdots & \dot{\mathbf{l}}_{i0} & \cdots & \dot{\mathbf{l}}_{n0} \\ \underline{\underline{\dot{\mathbf{b}}_1}}\mathbf{l}_{10} + \underline{\underline{\mathbf{b}_1}}\dot{\mathbf{l}}_{10} & \cdots & \underline{\underline{\dot{\mathbf{b}}_i}}\mathbf{l}_{i0} + \underline{\underline{\mathbf{b}_i}}\dot{\mathbf{l}}_{i0} & \cdots & \underline{\underline{\dot{\mathbf{b}}_n}}\mathbf{l}_{n0} + \underline{\underline{\mathbf{b}_n}}\dot{\mathbf{l}}_{n0} \end{bmatrix} \tag{12}$$

Taking into account that the time derivatives of the constant intensity vectors $\mathbf{l}_{i0}$ and $\mathbf{b}_i$ (considering an ideal rigid platform) are

$$\begin{aligned} \dot{\mathbf{l}}_{i0} &= \boldsymbol{\omega}_{e_i} \times \mathbf{l}_{i0} + \boldsymbol{\omega}_{r_i} \times \mathbf{l}_{i0} \\ \dot{\mathbf{b}}_i &= \boldsymbol{\omega}_i \times \mathbf{b}_i \end{aligned} \tag{13}$$

and substituting (7) and (8) yields

$$\dot{\mathbf{J}} = \mathbf{t}_p{}^T \otimes \mathbb{J} = \mathbf{t}_p{}^T \otimes [\mathbb{J}_1{}^T \ldots \mathbb{J}_i{}^T \ldots \mathbb{J}_n{}^T]^T \tag{14}$$

where $\mathbb{J}$ is a $n(6) \times 1(6)$ block matrix (numbers outside parenthesis define block matrix dimension, while within parenthesis the dimension of each block-matrix element has been given), $\otimes$ is the Kronecker's product (each block-element of $\mathbb{J}$ is by $\mathbf{t}_p{}^T$

multiplied) and the block element $\mathbf{J}_i \in \mathfrak{R}^{6 \times 6}$ has the form

$$\mathbf{J}_i = \begin{bmatrix} -\frac{1}{l_i}\underline{\mathbf{n}_i}\,\mathbf{l}_{i0}\mathbf{l}_{i0}{}^T\underline{\mathbf{n}_i} + \frac{1}{(\bar{\mathbf{e}}_i \times \bar{\mathbf{L}}_i)\cdot\bar{\mathbf{n}}_i}\underline{\mathbf{n}_i}\mathbf{l}_{i0}{}^T\underline{\mathbf{e}_i} & \frac{1}{l_i}\underline{\mathbf{n}_i}\mathbf{l}_{i0}\,\mathbf{l}_{i0}{}^T\underline{\mathbf{n}_i}\underline{\mathbf{b}_i} - \frac{1}{(\bar{\mathbf{e}}_i \times \bar{\mathbf{L}}_i)\cdot\bar{\mathbf{n}}_i}\underline{\mathbf{n}_i}\mathbf{l}_{i0}{}^T\underline{\mathbf{e}_i}\underline{\mathbf{b}_i} \\ -\frac{1}{l_i}\underline{\mathbf{b}_i}\underline{\mathbf{n}_i}\mathbf{l}_{i0}\,\mathbf{l}_{i0}{}^T\underline{\mathbf{n}_i} + \frac{1}{(\bar{\mathbf{e}}_i \times \bar{\mathbf{L}}_i)\cdot\bar{\mathbf{n}}_i}\underline{\mathbf{b}_i}\underline{\mathbf{n}_i}\,\mathbf{l}_{i0}{}^T\underline{\mathbf{e}_i} & \frac{1}{l_i}\underline{\mathbf{b}_i}\underline{\mathbf{n}_i}\mathbf{l}_{i0}\,\mathbf{l}_{i0}{}^T\underline{\mathbf{n}_i}\underline{\mathbf{b}_i} - \frac{1}{(\bar{\mathbf{e}}_i \times \bar{\mathbf{L}}_i)\cdot\bar{\mathbf{n}}_i}\underline{\mathbf{b}_i}\underline{\mathbf{n}_i}\mathbf{l}_{i0}{}^T\underline{\mathbf{e}_i}\underline{\mathbf{b}_i} + \underline{\mathbf{b}_i}\mathbf{l}_{i0} \end{bmatrix}$$

$$(15)$$

4 Structural and Geometric-Stiffness Matrices

The Cartesian spatial stiffness matrix relates the variations of applied forces and moments (*wrench*) to the corresponding spatial displacements (*twist*) rates of change

$$\delta\mathbf{w} = \mathbf{K}\delta\mathbf{t}$$

$$[\delta\mathbf{F}^T \quad \delta\mathbf{M}^T]^T = \begin{bmatrix} K_{xx} & K_{xo} \\ K_{xo} & K_{oo} \end{bmatrix} [\delta\mathbf{x}^T \quad \delta\mathbf{o}^T]^T \qquad (16)$$

where $\mathbf{w}$ and $\mathbf{t}$ are wrench and twist screw vectors, $\delta\mathbf{F}$ and $\delta\mathbf{M}$ are variations of Cartesian forces and moments acting on the common platform and $\delta\mathbf{x}$ and $\delta\mathbf{o}$ are corresponding relative translational and rotational displacements compatible with the constraints. The mapping between internal wire tension forces, grouped in the wire tension vector $\mathbf{f} = [f_1 \dots f_i \dots f_n]^T$ with elemental forces acting along $\mathbf{l}_{i0}$ ($i = 1, \dots, n$), and Cartesian wrench is also defined by the wire-robot Jacobian

$$\mathbf{w} = \mathbf{J}^T\mathbf{f} \qquad (17)$$

In the conventional stiffness modeling approach the Jacobian mapping has been also utilized to transform the variations of internal wire and external platform forces and moments

$$\delta\mathbf{w} = \mathbf{J}^T\delta\mathbf{f} \qquad (18)$$

Assuming light-weight wires (e.g. high strength dyneema cables) and linear elastic deformation wire model, the wire tension forces are proportional to the elastic cable longitudinal displacements

$$\delta f_i = k_i\delta l_i = \overline{k_i}/l_i\delta l_i \qquad (19)$$

where $\overline{k}$ is the specific wire cable axial stiffness for unit length $\overline{k} = EA$, E is Young's module and A the cable cross-section (for the sake of simplicity the same elastic characteristics have been adopted for each wire). Replacing the above relationship between wire length and twist variations yields the spatial wire robot stiffness matrix

$$\mathbf{K} = \overline{k}\mathbf{J}^T\overline{\mathbf{L}}\mathbf{J} \qquad (20)$$

where $\overline{\mathbf{L}} = diag(1/l_i) \in \mathfrak{R}^{n \times n}$. When instead of the nominal wire lengths l_i, the real ones after deformation have been considered $\hat{l}_i = l_i + \Delta l_i$, the stiffness matrix become dependent on the tension since the matrix $\overline{\mathbf{L}}$ takes the form $\overline{\mathbf{L}} = diag((1/l_i(1 + \mathrm{f}_i/\overline{k}))$. As mentioned above, this influence of the wire-tension is commonly negligible and becomes more expressed in systems with large-span.

However, if the changes of the wire-robot structures have been also taken into account, the correct differentiation of (17) gives external-wrench/wire-tension relationship in the variational form

$$\delta \mathbf{w} = \mathbf{J}^T \delta \mathbf{f} + \delta \mathbf{J}^T \mathbf{f} \tag{21}$$

where the variation of the Jacobian describes the structural changes during deformation. Based on (12) the Jacobian variation can be written in a block $1(6) \times n(7)$ matrix form

$$\delta \mathbf{J}^T = [\delta \mathbf{J}_1{}^T \ldots \delta \mathbf{J}_i{}^T \ldots \delta \mathbf{J}_n{}^T] \tag{22}$$

with 6×1 block elements

$$\delta \mathbf{J}_i{}^T = \begin{bmatrix} \delta \mathbf{l}_{i0} \\ \underline{\delta \mathbf{b}_i} \mathbf{l}_{i0} + \underline{\mathbf{b}_i} \delta \mathbf{l}_{i0} \end{bmatrix} \tag{23}$$

Using the screw derivatives [13] and considering the analysis of the wire motion composition (3–8), the variation of constant length vectors $\mathbf{l}_{i0}$ and $\mathbf{b}_i$ (assuming a rigid platform) may be written in the form

$$\delta \mathbf{l}_{i0} = \delta \mathbf{o}_i \times \mathbf{l}_{i0} = \delta \mathbf{o}_{e_i} \times \mathbf{l}_{i0} + \delta \mathbf{o}_{r_i} \times \mathbf{l}_{i0} = \delta o_{e_i} \mathbf{e}_i \times \mathbf{l}_{i0} + \delta o_{r_i} \mathbf{n}_i \times \mathbf{l}_{i0}$$
$$\delta \mathbf{b}_i = \delta \mathbf{o}_p \times \mathbf{b}_i \tag{24}$$

where based on expressions for angular velocities (7, 8) describing relative angular variations, the relationships between wire and platform elemental displacements is obtained in the form

$$\delta \mathbf{l}_{i0}{}^T = \frac{1}{l_i} \left[\delta \mathbf{x}_p \ \delta \mathbf{o}_p \right] \begin{bmatrix} \underline{\mathbf{n}_i} \mathbf{l}_{i0} \\ \underline{\mathbf{b}_i \mathbf{n}_i} \mathbf{l}_{i0} \end{bmatrix} \otimes \mathbf{l}_{i0}{}^T \underline{\mathbf{n}_i} + \frac{1}{(\vec{\mathbf{e}}_i \times \vec{\mathbf{L}}_i) \cdot \vec{\mathbf{n}}_i} \left[\delta \mathbf{x}_p \ \delta \mathbf{o}_p \right] \begin{bmatrix} \mathbf{n}_i \\ \underline{\mathbf{b}_i \mathbf{n}_i} \end{bmatrix} \otimes \mathbf{l}_{i0}{}^T \underline{\mathbf{e}_i} \tag{25}$$

By this means we can express the Jacobian variations (Hessian) in terms of elemental platform displacement variations. Then (22, 23) can be rewritten in the form

$$\delta \mathbf{J}_i{}^T = \underline{\mathbf{J}_i}{}^T \delta \mathbf{t}_p \tag{26}$$

where 6×6 matrix has the form

$$
\underline{\mathbf{J}}_i^T = \begin{bmatrix} -\frac{1}{l_i}\underline{\underline{\mathbf{n}_i}}\mathbf{l}_{i0}\mathbf{l}_{i0}{}^T\underline{\underline{\mathbf{n}_i}} + \frac{1}{(\bar{\mathbf{e}}_i \times \bar{\mathbf{L}}_i)\cdot\bar{\mathbf{n}}_i}\underline{\underline{\mathbf{e}_i}}\mathbf{l}_{i0}\mathbf{n}_i{}^T & \frac{1}{l_i}\underline{\underline{\mathbf{n}_i}}\mathbf{l}_{i0}\mathbf{l}_{i0}{}^T\underline{\underline{\mathbf{n}_i\,\mathbf{b}_i}} - \frac{1}{(\bar{\mathbf{e}}_i \times \bar{\mathbf{L}}_i)\cdot\bar{\mathbf{n}}_i}\underline{\underline{\mathbf{e}_i}}\mathbf{l}_{i0}\mathbf{n}_i{}^T\,\mathbf{b}_i \\ -\frac{1}{l_i}\underline{\underline{\mathbf{b}_i\mathbf{n}_i}}\mathbf{l}_{i0}\,\mathbf{l}_{i0}{}^T\underline{\underline{\mathbf{n}_i}} + \frac{1}{(\bar{\mathbf{e}}_i \times \bar{\mathbf{L}}_i)\cdot\bar{\mathbf{n}}_i}\underline{\underline{\mathbf{b}_i\mathbf{e}_i}}\mathbf{l}_{i0}\mathbf{n}_i{}^T & \frac{1}{l_i}\underline{\underline{\mathbf{b}_i\mathbf{n}_i}}\mathbf{l}_{i0}\mathbf{l}_{i0}{}^T\underline{\underline{\mathbf{n}_i\,\mathbf{b}_i}} - \frac{1}{(\bar{\mathbf{e}}_i \times \bar{\mathbf{L}}_i)\cdot\bar{\mathbf{n}}_i}\underline{\underline{\mathbf{b}_i\,\mathbf{e}_i}}\mathbf{l}_{i0}\mathbf{n}_i{}^T\,\mathbf{b}_i + \mathbf{l}_{i0}\mathbf{b}_i \end{bmatrix} \tag{27}
$$

which is equivalent to the previously derived block-matrix elements of the Jacobian time-derivative (14). Finally based on (21) and (22) yields

$$
\delta \mathbf{J}^T \mathbf{f} = (\underline{\mathbf{J}}^T \mathbf{f})\delta \mathbf{t}_p = \left(\sum_{i=1}^{n} \underline{\mathbf{J}}_i^T \mathbf{f}_i \right) \delta \mathbf{t}_p \tag{28}
$$

from which taking into account definition of the stiffness follows tension-force dependent wire-robot *geometric-stiffness matrix*

$$
\mathbf{K}_g(\mathbf{f}) = \underline{\mathbf{J}}^{\mathrm{T}}\mathbf{f} = \left(\sum_{i=1}^{n} \underline{\mathbf{J}}_i^{\mathrm{T}}\mathbf{f}_i \right) \tag{29}
$$

The total stiffness matrix is the sum of the structural and geometric stiffness matrices

$$
\mathbf{K} = \mathbf{K}_s + \mathbf{K}_g = \bar{k}\mathbf{J}^T\bar{\mathbf{L}}\mathbf{J} + \sum_{i=1}^{n} \underline{\mathbf{J}}_i^T \mathbf{f}_i \tag{30}
$$

Obviously the structural wire stiffness matrix is a symmetric positive semi-definite (PSD) matrix, while in general the geometric stiffness may be positive or negative-definite dependent on the robot position and the wire tension. As is well known, in an over-constrained wire-robot structure (with $n > 6$ wires) we can realize for the same external wrench various wire tensions utilizing Jacobian null-space and inverse force transformation

$$
\mathbf{f} = \mathbf{J}^{\#T}\mathbf{w} + \boldsymbol{\lambda} \otimes \mathbf{N} \tag{31}
$$

where $\mathbf{N}$ denotes $n \times (n-1)$ dimensional null-space (kernel) of $\mathbf{J}^T$ and $\boldsymbol{\lambda}$ represents arbitrary wire tension scaling factors. The reachable tension range of the internal wire forces defines *wrench-feasible* or *wrench-closure* wire-robot workspace where arbitrary external wrenches may be realized within some maximum load. Based on the above analysis, changing i.e. controlling the wire pre-stress, in general, provides also the possibility to vary the geometric stiffness matrix. By this means the entire wire-robot stiffness may be increased and elastic displacements of platform, caused by external wrenches, can be reduced.

The geometric stiffness matrix (26–29) consists of symmetric and asymmetric components. The stability of quasi-static force equilibrium of the platform depends on whether the entire stiffness matrix is PSD or not. That means that geometric stiffness matrix, i.e. wire pre-stress not only can contribute to increasing the entire stiffness, but also improving the stability or even destabilizing the platform in some configuration.

5 Stiffness Decomposition

In order to analyze the influence and relevance of the geometric-stiffness in wire-robotic systems it is useful to apply the eigen-screw stiffness matrix decomposition methodology [14]. According to this approach a general stiffness matrix can be decomposed into primitive components that may be interpreted as linear and/or rotational virtual springs (Fig. 3). All these virtual springs provide a possible equivalent physical realization of the wire-robot stiffness in the Cartesian space with the considered configuration. This decomposition facilitates both a better physical appreciation of the stiffness realization in wire-robotic systems, and a better understanding of how to adjust the stiffness by means of the above modeled geometric stiffness and wire-tensions.

The eigen-screws based stiffness matrix decomposition depends in general on the coordinate frame used to describe the stiffness matrix. The decomposition is based on the eigen-value matrix decomposition in which each PSD matrix with the rank m (for the spatial stiffness matrices $m \leq 6$) can be decomposed into rank-1 elemental matrices each of them can be represented in the form

$$\mathbf{K} = \sum_{i=1}^{m} \mathbf{K}_i = \sum_{i=1}^{m} k_i \mathbf{v}_i \mathbf{v}_i^{T} \tag{32}$$

where k_i ($k_i > 0$ when $\mathbf{K}$ is a PSD matrix) is a constant and $\mathbf{v}_i$ is so called *spring-wrench*. For a rank-1 $\mathbf{K}_i$ this decomposition is unique except the sign change. Each element of the decomposition (32) may be interpreted as a spatial spring consisting of a linear and torsional spring elements (Fig. 3) associated with the eigenvectors and eigenvalues of the stiffness matrix.

A modified eigenvalue decomposition of the stiffness matrix referred to as *eigen-screw* decomposition has also been proposed in [14]. This decomposition is based on the screw eigenvalue problem

$$\mathbf{K} \boldsymbol{\Delta} \mathbf{e} = \lambda \mathbf{e} \tag{33}$$

which includes a transformation matrix $\boldsymbol{\Delta}$ of screw vectors $\mathbf{e}$. The advantage of the decomposition (33) is that it is independent of the reference frame and unique.

6 Examples

In order to illustrate possibilities to shape the spatial stiffness matrix and to influence the elastic deformation, vibration and stability of the wire-robots by means of the internal pre-stress wire forces, a simple case of 4DOF planar manipulator has been considered (Fig. 4). This wire-robot structure with relatively large-span (approximately 30×30 m and maximum payload 20 kg) has been actually considered as a

Fig. 3 Stiffness decomposition
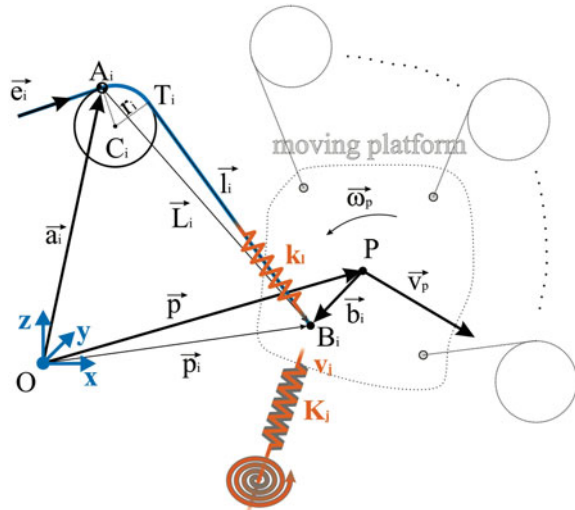
simple and fast robotic solution for inspections of planar surfaces. As is well known the main drawbacks of this robot type represent uncontrollable Cartesian DOFs: translation in the normal y direction to the plane, and rotations around x and z axes. In an ideal planar case the Jacobian and stiffness matrix have rank-3. For the considered case and almost central platform position (Fig. 4), assuming minimum wire tension of 100 N, the structural and geometric-stiffness matrix have been computed and decomposed on Cartesian eigen-stiffness. The values of structural and geometric stiffness, as well as eigen-value matrices which columns represent the directions of the eigen-spring elements in the Cartesian space and corresponding eigen-stiffness are given in (34). Obviously the structural stiffness equivalent Cartesian springs are acting only in DOFs within Jacobian rank, while the geometric stiffness matrix has the full rank and produces the stiffness effects in all directions. When the minimum tension has been increased from 100 to 1000 N, the structural stiffness remains the same, while the geometric one becomes considerably larger (35). The effects on structure stiffening also in critical uncontrollable directions: in plane normal direction and specially rotational stiffness become more expressed.

$$\mathbf{f} = [240.85 \quad 222.55 \quad 100 \quad 363.35]^T$$

$$\mathbf{K}_s = 10^4 \begin{bmatrix} 1.026 & 0 & 0 & 0 & -0.004 & 0 \\ 0 & 0 & 0 & 0 & 0 & 0 \\ 0 & 0 & 0.966 & 0 & 0.003 & 0 \\ 0 & 0 & 0 & 0 & 0 & 0 \\ -0.004 & 0 & 0.003 & 0 & 0 & 0 \\ 0 & 0 & 0 & 0 & 0 & 0 \end{bmatrix} \quad \mathbf{K}_g = \begin{bmatrix} 9.8 & 0 & -2.7 & 0 & 2.6 & 0 \\ 0 & -28.9 & 0 & 3.8 & 0 & 0.14 \\ -2.7 & 0 & 10.4 & 0 & 0.08 & 0 \\ 0 & 3.8 & 0 & 280.3 & 0 & -75.6 \\ 2.6 & 0 & 0.08 & 0 & 593.6 & 0 \\ 0 & 0.14 & 0 & -75.6 & 0 & 293.7 \end{bmatrix}$$

Fig. 4 Planar wire-robot
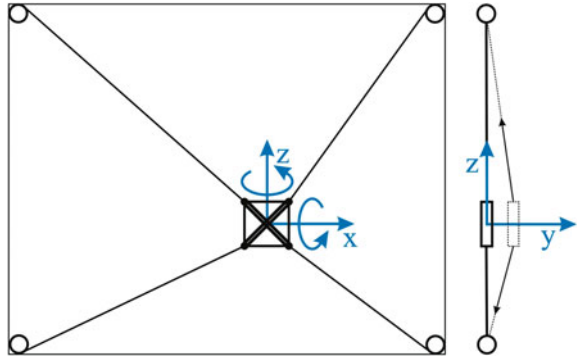
$$\mathbf{V}_s = \begin{bmatrix} -1 & 0 & 0 & 0 & 0 & 0 \\ 0 & 0 & 0 & 1 & 0 & 0 \\ 0 & 0 & 1 & 0 & 0 & 0 \\ 0 & 0 & 0 & 0 & 1 & 0 \\ 0 & 1 & 0 & 0 & 0 & 0 \\ 0 & 0 & 0 & 0 & 0 & 1 \end{bmatrix} \quad \mathbf{V}_g = \begin{bmatrix} 0 & -0.7 & -0.7 & 0 & 0 & 0 \\ 0 & 0 & 0 & -1 & 0 & 0 \\ 0 & 0.7 & -0.7 & 0 & 0 & 0 \\ 0 & 0 & 0 & 0 & 0.7 & -0.7 \\ -1 & 0 & 0 & 0 & 0 & 0 \\ 0 & 0 & 0 & 0 & 0.7 & 0.7 \end{bmatrix}$$

$$\mathbf{K}_{s\lambda} = [10257 \ 1 \ 9659 \ 0 \ 0 \ 0] \quad \mathbf{K}_{g\lambda} = [593.7 \ 12.75 \ 7.4 \ -29 \ 211 \ 362] \tag{34}$$

$$\mathbf{f} = [1140.8 \ 2327.3 \ 1000 \ 2468]^T$$

$$\mathbf{K}_g = \begin{bmatrix} 73 & 0 & -29 & 0 & 2 & 0 \\ 0 & -216 & 0 & 3 & 0 & 1 \\ -29 & 0 & 78 & 0 & 1 & 0 \\ 0 & 3 & 0 & 2104 & 0 & -824 \\ 2 & 0 & 1 & 0 & 4452 & 0 \\ 0 & 1 & 0 & -824 & 0 & 2202 \end{bmatrix} \quad \mathbf{V}_g = \begin{bmatrix} -0.7 & 0.7 & 0 & 0 & 0 & 0 \\ 0 & 0 & 0 & 0 & 0 & 1 \\ -0.7 & -0.7 & 0 & 0 & 0 & 0 \\ 0 & 0 & 0 & 0.7 & -0.7 & 0 \\ 0 & 0 & -1 & 0 & 0 & 0 \\ 0 & 0 & 0 & -0.7 & -0.7 & 0 \end{bmatrix}$$

$$\mathbf{K}_{g\lambda} = [46.5 \ 104.3 \ 4452.5 \ 2978 \ 1327 \ -216] \tag{35}$$

In the next example the influence of geometric stiffness on the vibration of the planar wire robot on (Fig. 4) has been analyzed. The robot has been positioned in the same location as in the previous case and the wire forces $\mathbf{f} = [240.85 \ 222.55 \ 100 \ 363.35]^T$ (N), which compensate for the platform weight (25 kg) and ensure the minimum wire pre-tension of 100 N have been realized. The wire pre-tension has been controlled in the null-space of the planar motion Jacobian using the robot redundancy ($n = 4$ wires for 3 DOFs of planar motion). Then a rectangular external force $F_y = 50$ N in the uncontrollable y-direction orthogonal to the motion plane has been simulated for the duration of 3 s. The simulated platform oscillations in the y direction are presented in (Fig. 5). If the minimum tension is again increased from 100 to 1000 N, the oscillation behavior (frequency, amplitude) has been considerably changed (Fig. 6) due to geometric stiffness effects (i.e. stiffening of the wire robot especially in the lateral direction and reducing deformations due to
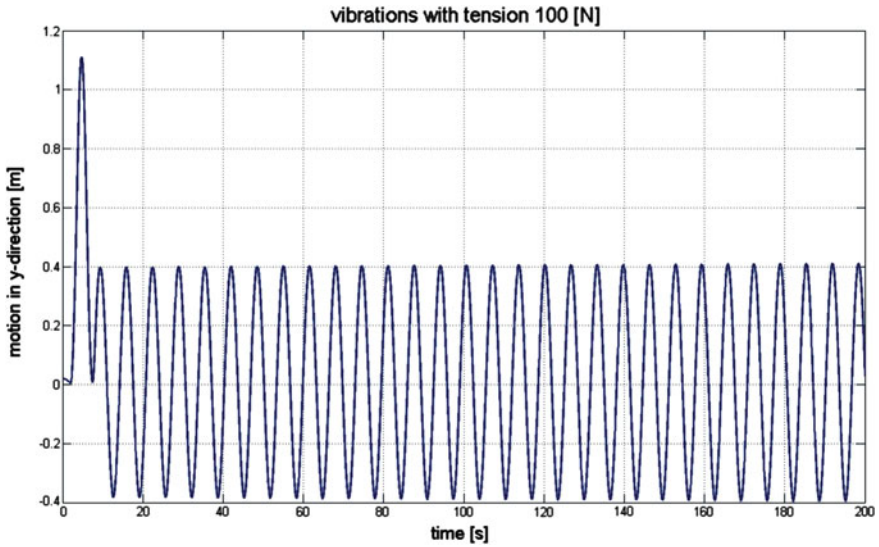
Fig. 5 Oscillation in y-direction caused by an impulse force of 50 N
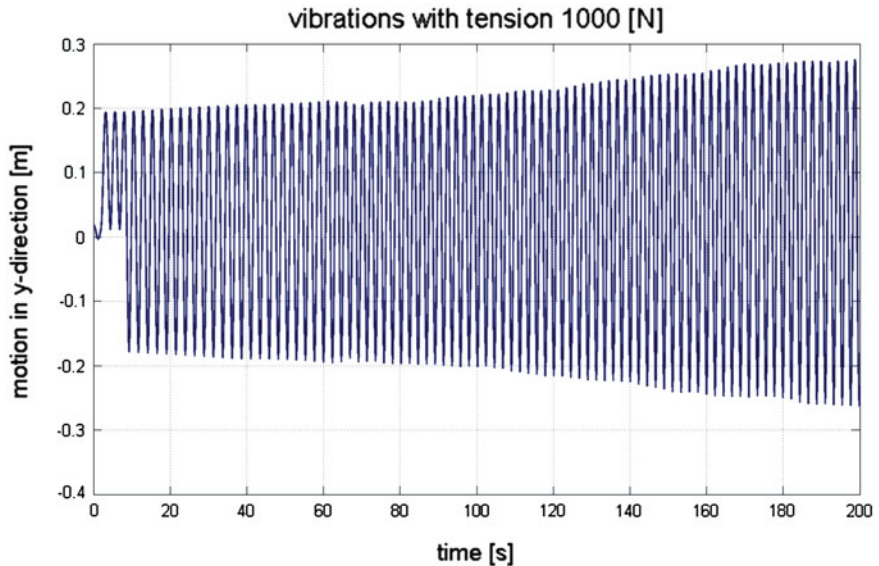
Fig. 6 Oscillations after increasing wire pre-tension

increased wire tension). Obviously the amplitude of the vibrations has been reduced by 50 % and (from 0.4 to 0.2 m) and the frequency of vibration has been increased from approximately 0.16 to 0.4 Hz in the considered simulation experiment after increasing the pre-tension. Thereby structural stiffness remains unchanged. By higher
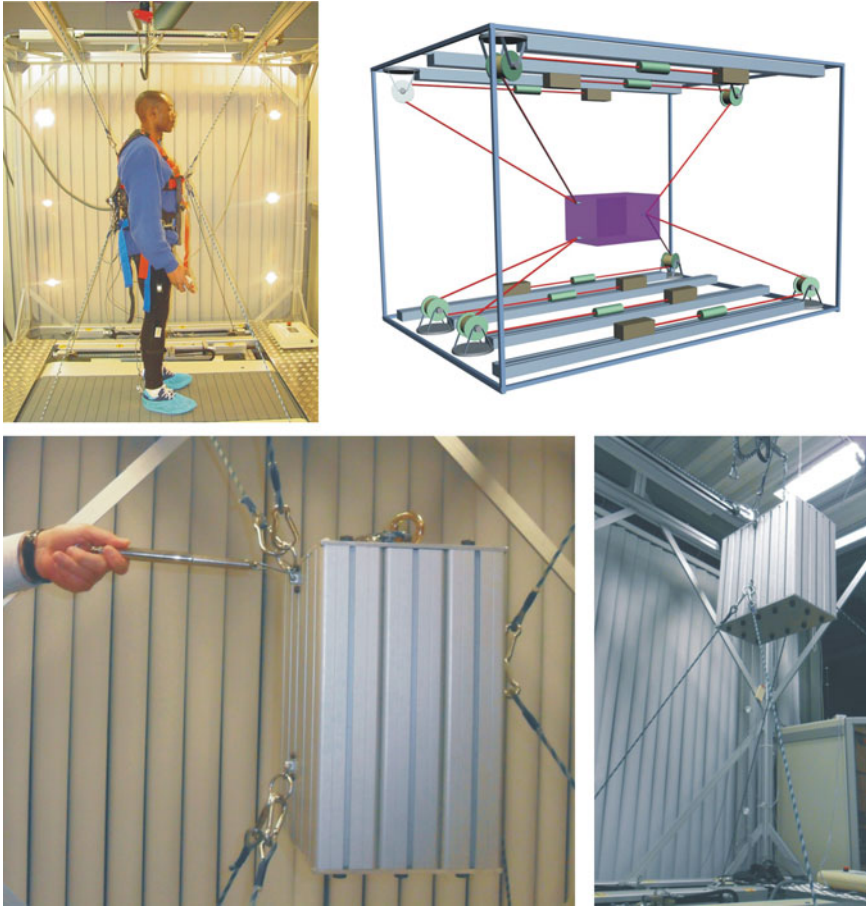
Fig. 7 STRING-MAN wire-robot

wire tensions the coupling between translational and rotational vibrations become more complex.

In the third experiment a wire-robot with $n = 7$ wires (Fig. 7) has been considered. This robot is referred to as STRING-MAN and has been initially developed to support posture-balancing and gait rehabilitation [15]. The unique feature of this robot is that the human patient body is attached to the wires as a common platform. The compliance and force control, rather than the considered stiffness effects, are essential for the interaction with a patient (see [15] for more details). In our experiments the patient (i.e. dummy) has been replaced by a box-like platform (Fig. 7). The STRING-MAN system provides an over-constrained wire-robot structure, whose corresponding structural-stiffness has the full rank. However, the initially computed and experimentally measured geometric stiffness effects have been proven again as

essential for increasing the entire robot stiffness (Fig. 7) (due to limited space more detailed results have been omitted).

7 Conclusion

This paper has presented the detailed modeling and analysis of geometric stiffness effects in general wire-robot systems with pulley elements. The spatial wire-robot stiffness plays an essential role for the precise realization of desired positions, planning and tracking of trajectories and stabilization of the common robot platform. In the conventional robotic structures the geometric stiffness (also referred to as CCT) depends on external loads and is commonly negligible in comparison to the structural stiffness of relatively rigid robotic arms and joints. In wire robotic system, however, the geometric stiffness effects are well expressed and play the crucial role for increasing the total robot stiffness and pose stabilization. The geometric stiffness in wire robots is related to the internal wire forces, which can be considerably increased (controlled) by means of the wires over-tension in the Jacobian null-space regardless of the external loads.

The derived robot geometric stiffness models can be efficiently utilized for wire-robot design and motion planning, as well as in real-time computations, e.g. in active stiffening and vibration suppression and damping algorithms. The on-going work would be focusing on more comprehensive analysis and experimental testing of the geometric stiffness for the stabilization/destabilization of wire robots in critical configurations and working conditions. The influence of geometric stiffness on vibration suppressions is also the topic of current research.

References

1. Dagalkis, N.G., Albus, J.S., Wang, B.-L., Unger, J., Lee, J.D.: Stiffness study of a parallel link robot crane for shipbuilding applications. J. Offshore Mech. Arct. Eng. **111**, 183–193 (1989)
2. Verhoeven, R., Hiller, M., Tadokoro, S.: Workspace, stiffness, singularities and classification. In: Proceedings of the 6th International Symposium on Advances in Robot Kinematics–ARK, pp. 105–114. Gerhard-Mercator-Universität-GH Duisburg, Germany (1998).
3. Diao, X., Ma, O.: Vibration analysis of cable-driven parallel manipulators. Multibody Syst. Dyn. **21**, 347–360 (2009)
4. Khosravi, M.A., Taghirad, H.D.: Dynamic analysis of cable driven robots with elastic cables. Trans. Can. Soc. Mech. Eng. **35**(4), 543–577 (2011)
5. Wilson, E.L.: Three-Dimensional Static and Dynamic Analysis of Structures. CSI, Berkley (2002)
6. Chen, S.-F., Kao, I.: Conservative congruence transformation for joint and cartesian stiffness matrices of robotic hands and fingers. Int. J. Robot. Res. **19**, 835–847 (2000)

7. Merlet, J.P.: Parallel Robots. Kluver Academic, Dordrecht (2000)

8. Svinin, M.M., Hosoe, S., Uchiyama, M.: On the stiffness and stability of Gough-Stewart platform. In: Procceding of, : ICRA, pp. 3268–3273. Seoul, Corea (2001)

9. Behzadipour, S., Khajepour, A.: Stiffness of cable-based parallel manipulators with application to stability analysis. J. Mech. Des. **128**, 303–314 (2006)

10. Azadi, M., Behzadipour, S., Faulkner, G.: Antagonistic variable stiffness elements. Mech. Mach. Theory **44**, 1746–1758 (2009)

11. Liu, X., Qiu, Y., Duan, X.: Stiffness enhancement and motion control of a 6-dof wire-driven parallel manipulator with redundant actuators for wind tunnels. In: Okamoto, S. (ed.) Wind Tunnels. InTech, Vienna (2011)

12. Arsenault, M.: Optimization of the prestress stable wrench closure workspace of planar parallel three-degree-of-freedom cable-driven mechanisms with four cables. In: Proceedingof 2010 IEEE ICRA, Anchorage, Alaska, USA, pp. 1182–1187 (2010).

13. Lipkin, H.: Time derivatives of screw with applications to dynamics and stiffness. Mech. Mach. Theory **40**(3), 259–273 (2005)

14. Huang, S., Schimmels, J.: The Eigenscrew decomposition of spatial stiffness matrices. IEEE Trans. Robot. Autom. **6**(2), 146–156 (2000)

15. Surdilovic, D., Bernhardt, R., Schmidt, T., Zhang, J.: STRING-MAN: A novel wire robot for gait rehabilitation. In: Bien, Z.Z. (ed.) Advances in Rehabilitation Robotics. Lecture Notes in Control and Information Sciences, vol. 306, pp. 413–424. Springer, Berlin (2004).

Stiffness Analysis of a Planar 2-DoF Cable-Suspended Mechanism While Considering Cable Mass

Marc Arsenault

Abstract The mass of the cables is not considered in most existing research on cable-driven mechanisms (CDM). Moreover, of those papers where cable mass is considered, few have examined its effects on mechanism stiffness. The research presented herein seeks to better understand these effects with regards to a planar two-degree-of-freedom suspended CDM. The mechanism's stiffness matrix is first developed and then used to generate mappings of intuitive stiffness indices over the workspace. The sagging of the cables under their own weight is found to heavily influence mechanism stiffness. The importance of maintaining a minimum level of cable tension to minimize the effect of cable sagging on the mechanism's stiffness and workspace is also demonstrated.

1 Introduction

A parallel cable-driven mechanism (CDM) is one where an end-effector (EE) is linked to a base by a set of cables working in parallel. By varying the lengths of the cables, the pose (i.e., position and orientation) of the EE can be controlled so as to accomplish the task at hand. Some known attributes of CDMs include the inertial properties of their moving parts, their potential to operate in very large workspaces, the ease with which they are built, transported and reconfigured as well as their relatively low cost. However, CDMs also present some interesting challenges, the most important of which is the inherent flexibility of the cables. This requires the cables to be kept taut in order to maintain the rigidity of a CDM.

M. Arsenault (✉)
Department of Mechanical and Aerospace Engineering,
Royal Military College of Canada,
Kingston K7K 7B4, Ontario, Canada
e-mail: marc.arsenault@rmc.ca

Recognizing that cables cannot push on the EE, completely restrained CDMs use $n_c > d$ cables to resist wrenches applied to the EE while maintaining tension in the cables (n_c is the number of cables while d corresponds to the quantity of degrees of freedom of the space in which the EE is operating, e.g., $d = 3$ in the plane and $d = 6$ in three-dimensional space). Meanwhile, suspended CDMs use $n_c \geq d$ cables located above the EE where the latter's weight is assumed to provide the required tension in the cables.

Much of the fundamental research on CDMs has focused on workspace determination [4, 12, 13, 23], stiffness modeling [3, 9, 22, 24], synthesis [8] and the effect of the axial flexibility of cables on kinematics [18]. However, despite the fact that research on CDMs has been ongoing for at least two decades, most of the existing literature deals with the case where cable mass is neglected. When this assumption is made, a cable can be modeled as a straight line segment linking its attachment points on the EE and base with tension being constant along its length. This simplifies the analysis of CDMs with, for instance, closed-form solutions to the inverse kinematic and static analyses being readily available. However, while the neglect of cable mass may often be justified, this is not always the case. Under the effect of its own weight, a cable will sag and deflect away from the above-mentioned straight line segment. This can have a significant impact on the performance of CDMs as well as the complexity of their analysis. Cable sagging is especially prevalent when the weight of a cable is significant with respect to its tension. Whereas completely restrained CDMs may theoretically adjust the tension of the cables to minimize the effects of cable sagging, such is not the case for suspended CDMs. For this reason, suspended CDMs are susceptible to the effects of cable sag. Some examples of suspended CDM applications where cable sagging may need to be considered include large cranes [1], reconfigurable search and rescue systems [6], building, inspection and maintenance systems for large buildings [5, 14] and receiver support systems for large radio telescopes [19].

Past research involving cables of non-negligible mass has largely been motivated by the study of structures (e.g., bridges). Closed-form solutions for the profile of a single cable subjected to varying end conditions have long been available [15]. More recently, researchers have begun to consider the effect of cable sagging on suspended CDMs. The inverse kinematic problem (IKP)[1] of CDMs while considering cable mass was shown in [17] to require the numerical solution of a non-linear set of equations. The errors in the solution of the IKP that stem from neglecting cable mass were quantified in [20] where the influence of cable weight on cable tension was also studied. Meanwhile, the effect of cable sagging on mechanism workspace was analyzed in [16, 21]. The dynamic model of a six-degree-of-freedom suspended CDM taking cable mass into account was presented in [25]. Finally, a simplified model of CDMs while considering cable mass was presented in [11] for the case of inextensible cables where the sagging remains below a specified threshold.

---

[1] The task of computing the cable rest lengths corresponding to a given pose of the EE is referred to here as the *inverse kinematic problem* though its solution also requires the consideration of the mechanism's static equilibrium equations.

It is generally desirable for suspended CDMs to resist displacements of their EE (and payload) under the effect of disturbance forces. The ability to do so is quantified by the mechanism's stiffness. When cable mass is non-negligible, the stiffness has been shown to be strongly influenced by cable sagging [17]. In fact, given a sagging cable in static equilibrium with one end fixed and the other subjected to an external force, a small increase in this force will lead to a corresponding displacement of the free end. Part of the displacement will be due to an extension (or contraction) of the cable along its length while the other will stem from a decrease (or increase) of the cable sagging. The stiffness of the cable is thus determined from a combination of its axial flexibility and the sag-induced flexibility inherent to its curved profile. The stiffness matrix of a single cable was obtained in [17]. It was then used to compare the stiffness of suspended CDMs with and without the massless cable assumption by computing natural frequencies from a linearized dynamic model. A similar cable stiffness matrix was also used in [7] in the definition of a metric to determine when cable mass should be considered.

2 Model of the Elastic Catenary

Prior to introducing the mechanism that concerns this work, it is essential to provide a description of the cable model that is used in its analysis. The cable is assumed to be homogeneous with axial elasticity and negligible flexural stiffness. These assumptions were used in [15] in the development of a model for the *elastic catenary*, the latter also having been used, for instance, in [7, 17, 20]. The unstrained cable has linear density ρ, diameter d, cross-sectional area A, length l_0. Moreover, Young's modulus for the cable's material is E and its breaking strength is $\sigma_{\max}$. The free body diagram of an elastic catenary is illustrated in Fig. 1a. One end of the cable is assumed to be fixed (i.e., A). Under the action of a tension force t applied at its free end B (and a corresponding reaction force t_0 at end A), the cable has a strained length l. In Fig. 1b, the free body diagram of a section of cable extending from end A to an arbitrary point located a distance s_0 along the unstrained cable length or, equivalently, a distance s along the strained cable length, is shown. The tension in the cable at this point is represented as t_{s_0} with the direction tangent to the cable defined by θ_{s_0}. A reference frame $X_c Y_c$ is defined with its origin at the fixed end of the cable (i.e., A) such that the cable is located entirely within the $X_c Y_c$ plane with the Y_c axis vertical. Given $\mathbf{c} = [c_x, c_y]^T$ a vector directed from A to B expressed in the $X_c Y_c$ frame, the X_c axis is chosen so that $c_x \geq 0$.

Static equilibrium equations applied to the cable yield:

$$t_{0_x} = t_x, \quad t_{0_y} = \rho g l_0 - t_y \tag{1}$$

where $t_{0_x} = t_0 \cos \theta_0$, $t_{0_y} = t_0 \sin \theta_0$, $t_x = t \cos \theta$ and $t_y = t \sin \theta$. Moreover, $w_c = \rho g l_0$ is the weight of the cable and g is the gravitational acceleration. Based on the existing model for the elastic catenary [15], the coordinates of a point located

(a)   **(b)**
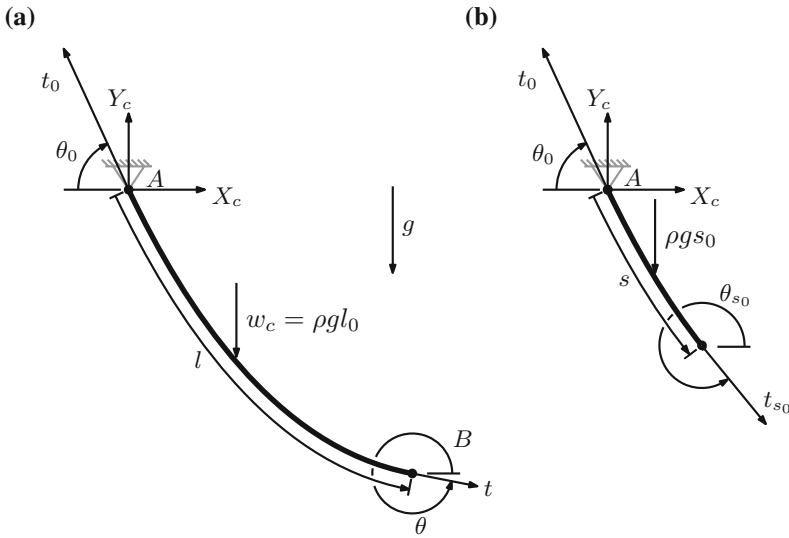
Fig. 1 Free body diagram of an elastic catenary: **a** entire cable, **b** element of cable

a distance s_0 along the unstrained cable length, expressed in the $X_c Y_c$ frame, are given by[2]:

$$x(s_0) \quad = \frac{t_x s_0}{k'} + \frac{t_x}{\rho g} \ln \left\{ \frac{t_y - \rho g(l_0 - s_0) + \sqrt{t_x^2 + \left[t_y - \rho g(l_0 - s_0) \right]^2}}{t_0 - t_{0_y}} \right\} \quad (2)$$

$$y(s_0) = \frac{t_y s_0}{k'} + \frac{\rho g s_0}{k'} \left(\frac{s_0}{2} - l_0 \right) + \frac{1}{\rho g} \left\{ \sqrt{t_x^2 + \left[t_y - \rho g(l_0 - s_0) \right]^2} - t_0 \right\} \quad (3)$$

where $k' = EA$. Setting $s_0 = l_0$ in these equations yields:

$$c_x = \frac{t_x l_0}{k'} + \frac{t_x}{\rho g} \ln \left(\frac{t + t_y}{t_0 - t_{0_y}} \right), \quad c_y = \frac{t_y l_0}{k'} - \frac{\rho g l_0^2}{2k'} + \frac{1}{\rho g}(t - t_0) \quad (4)$$

It should be recognized in the above equations that, once (1) is considered, the cable profile equations as well as the components of vector **c** are expressed only in terms of the external force applied at B as well as the mechanical properties of the cable.

Aside from having a curved profile, the elastic catenary also has a varying tension along its length. The tension at a given point in the cable, located at s_0, is [15]:

$$t_{s_0} = \sqrt{t_x^2 + \left[t_y - \rho g(l_0 - s_0) \right]^2} \quad (5)$$

---

[2] In the interest of brevity, the details regarding the development of the model for the elastic catenary are not included in this paper.

It is useful to identify the minimum and maximum tensions along the cable since these will be used later in the computation of the mechanism's workspace. The maximum tension will always occur at the cable's highest point while the minimum tension will occur at its lowest point. In order to understand this, one may first observe from the static equilibrium of the cable (refer to Fig. 1) that the horizontal component of tension is constant throughout the cable. Meanwhile, the vertical component of tension will be maximal at the cable's highest point since the largest portion of the cable weight is being supported there. Equivalently, a minimum will be attained at the lowest point since none of the cable weight is being supported there. In determining the minimum tension, one must consider whether the cable profile droops below the lowest of its two end points (such as the cable joining A_2 and P in Fig. 2). This will be the case if the vertical component of the cable tension at the lowest cable end, A or B, is positive. If such drooping occurs, the minimum tension is t_x since the tangent to the cable profile at its lowest point is horizontal. The procedure for determining the minimum and maximum tensions in a cable is summarized in Algorithm 1. It is noted that the treatment presented here is slightly more general than in [21], where it was assumed that the highest point in the cable is always located at the end of the cable that is attached to ground (i.e., $c_y \leq 0$). This would only remain the case for any arbitrary configuration of the mechanism if the attachment points to ground are all at the same elevation.

```
% Highest cable point is A:        % Highest cable point is B:
if c_y ≤ 0 then                     else
   t_max = t0                          t_max = t
   % Cable droops below B:             % Cable droops below A:
   if t_y > 0 then                     if t0_y > 0 then
      t_min = t0_x = t_x                  t_min = t0_x = t_x
   % Lowest cable point is B:          % Lowest cable point is A:
   else                                else
      t_min = t                           t_min = t0
   end                                 end
                                    end
```

One of the main focuses of this paper is the stiffness analysis of a suspended CDM. The stiffness of a cable can be interpreted here as its ability to resist displacements of its free end (i.e., B) upon the application of disturbance forces to it. As was previously mentioned in Sect. 1, the stiffness of a cable with non-negligible mass will be influenced by its axial flexibility as well as its sag-induced flexibility. This is represented as a 2×2 matrix $\mathbf{K}_c$ representing the stiffness of a single cable such that:

$$\delta \mathbf{t} = \mathbf{K}_c \delta \mathbf{c} \tag{6}$$

where $\mathbf{t} = [t_x, t_y]^T$. The compliance matrix $\mathbf{C}_c$ of a single cable, previously derived in [17], is first computed by differentiating (4) with respect to t_x and t_y, i.e.,

$$\mathbf{C}_c = \begin{bmatrix} C_{c11} & C_{c12} \\ C_{c21} & C_{c22} \end{bmatrix} = \begin{bmatrix} \partial c_x/\partial t_x & \partial c_x/\partial t_y \\ \partial c_y/\partial t_x & \partial c_y/\partial t_y \end{bmatrix} \tag{7}$$
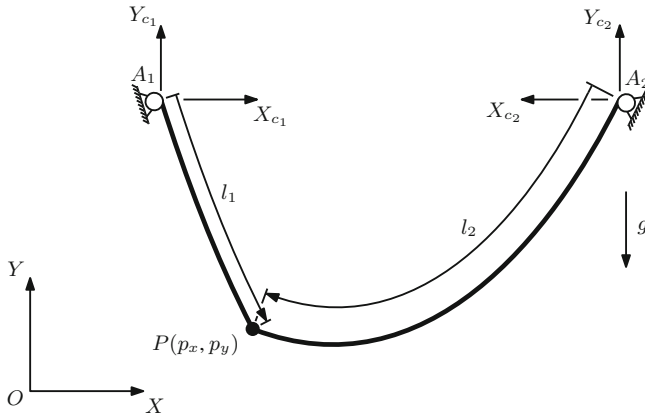
Fig. 2 Diagram of the planar 2-DoF suspended CDM

where expressions for t_0, t, t_{0_x} and t_{0_y} in terms of t_x and t_y are first substituted into (4) from (1) while taking into account the fact that $t_0 = \sqrt{t_{0_x}^2 + t_{0_y}^2}$ and $t = \sqrt{t_x^2 + t_y^2}$. The elements of the compliance matrix are thus found as:

$$C_{c_{11}} = \frac{l_0}{k'} + \frac{1}{\rho g} \ln\left(\frac{t+t_y}{t_0-t_{0_y}}\right) + \frac{t_{0_x}^2}{\rho g}\left[\frac{1}{t(t+t_y)} - \frac{1}{t_0(t_0-t_{0_y})}\right] \tag{8}$$

$$C_{c_{12}} = C_{c_{21}} = \frac{t_x}{\rho g}\left(\frac{1}{t} - \frac{1}{t_0}\right), \quad C_{c_{22}} = \frac{l_0}{k'} + \frac{1}{\rho g}\left(\frac{t_{0_y}}{t_0} + \frac{t_y}{t}\right) \tag{9}$$

The cable's stiffness matrix may then be obtained as $\mathbf{K}_c = \mathbf{C}_c^{-1}$.

3 Kinematic and Static Analysis of the 2-DoF Planar Suspended CDM

A diagram of the planar two-degree-of-freedom (2-DoF) suspended CDM analyzed in this work is shown in Fig. 2. It consists of a point mass EE, represented by point P, that is linked to ground by cables attached to points A_1 and A_2. By actuating the rest lengths of these cables (i.e., l_{0_1} and l_{0_2}) the position of the EE can be controlled. Moreover, under the effect of the combined mass of the EE and payload, m, as well as its own mass, the ith cable has a sagged profile with a strained length l_i ($i = 1, 2$).

A reference frame XY is defined as being attached to ground with its origin at O. Reference frames $X_{c_i}Y_{c_i}$ are also defined for each of the two cables according to the approach described in Sect. 2 for the X_cY_c frame of Fig. 1. The positions of A_i and P in the XY reference frame are given by vectors $\mathbf{a}_i = [a_{i_x}, a_{i_y}]^T$ and $\mathbf{p} = [p_x, p_y]^T$ directed from O to A_i and P, respectively.

3.1 Inverse Kinematic Problem

The IKP of suspended CDMs while considering cable mass has previously been solved [17, 20]. In the particular case considered here, the mechanism's IKP consists of finding the required rest lengths l_{0_1} and l_{0_2} so that the EE is at the position given by $\mathbf{p}$. The ends of the ith cable are constrained to A_i and P. Vector $\mathbf{c}_i = [c_{i_x}, c_{i_y}]^T$, directed from A_i to P and expressed in the $X_{c_i} Y_{c_i}$ reference frame, is computed as:

$$\mathbf{c}_i = \mathbf{Q}_i^T (\mathbf{p} - \mathbf{a}_i) \tag{10}$$

The rotation matrix bringing the XY frame parallel to the $X_{c_i} Y_{c_i}$ frame is:

$$\mathbf{Q}_i = \begin{bmatrix} \mathrm{sgn}(p_x - a_{i_x}) & 0 \\ 0 & 1 \end{bmatrix} \tag{11}$$

where $\mathrm{sgn}(\cdot)$ represents the algebraic sign of the argument. Sequentially setting $\mathbf{c} = \mathbf{c}_i$ for each of the two cables and substituting into (4), a total of four cable profile equations needing to be satisfied in the solution to the IKP are generated. Ultimately, these equations are expressed in terms of t_i, θ_i and l_{0_i}, where t_i and θ_i, for the ith cable, are equivalent to t and θ in Fig. 1a. Two additional equations are required in order to solve for these six unknowns. These arise from the static equilibrium equations of the mechanism's EE, i.e.,

$$\mathbf{W}\mathbf{t}_c + \mathbf{w} = \mathbf{0} \tag{12}$$

where $\mathbf{w} = [0, -mg]^T$ is net wrench applied to the EE by the combined weight of the EE and payload, $\mathbf{t}_c = [t_1, t_2]^T$ is a vector containing the tensions of each cable at P, and $\mathbf{W} = [-\mathbf{Q}_1\mathbf{n}_1, -\mathbf{Q}_2\mathbf{n}_2]$ with $\mathbf{n}_i = [\cos\theta_i, \sin\theta_i]^T$. The task of solving the IKP of the mechanism thus becomes that of computing a solution to a set of six non-linear equations in six unknowns. The system of equations can be written as $\mathbf{f}(\mathbf{x}) = \mathbf{0}$ where $\mathbf{f}$ is a vector formed by the above-described non-linear equations and $\mathbf{x}$ is a vector containing the six unknowns (i.e., $\mathbf{x} = [l_{0_1}, l_{0_2}, t_1, t_2, \theta_1, \theta_2]^T$). In addition to satisfying this system of equations, constraints related to the application as well as to the mechanical properties of the mechanism are also considered. Cable tensions are limited to $t_{\min_c} \leq t_i \leq t_{\max_c}$ while, optionally, cables may also be prevented from drooping beneath the EE in order to limit interferences with objects in the mechanism's workspace. Mathematically, the latter constraint translates to $-\pi/2 \leq \theta_i \leq 0$.

In order to solve the IKP, a numerical approach is required and the Newton–Raphson method was chosen here as it was found to perform acceptably.[3] Even so, additions to the basic form of the Newton–Raphson algorithm were made in order to improve its performance and increase the probability of it finding a proper

---

[3] It is recognized that other algorithms may be more efficient in solving this problem. However, it is not an aim of this work to attempt to identify them.

solution to the mechanism's IKP. In this light, two continuation schemes were used to mitigate the issue of providing the algorithm with an initial guess that is sufficiently close to the solution. In the first continuation scheme, the initial guess $\mathbf{x}_0$ was found from the solution to the IKP (without continuation) for a pose $\mathbf{p}_0$ of the EE where convergence is easy to achieve. The IKP of the mechanism is then solved with the Newton–Raphson algorithm for poses of the EE that gradually move toward the final desired pose, i.e.,

$$\mathbf{p}_j = \mathbf{p}_0 + \left(\frac{j}{N}\right)(\mathbf{p} - \mathbf{p}_0), \quad j = 1, 2, \ldots, N \tag{13}$$

where N is the number of steps used in the continuation scheme. The initial guess for each continuation step is taken as the solution from the prior step. In the second continuation scheme, the initial guess $\mathbf{x}_0$ is obtained from the closed-form solution to the IKP of the mechanism with its EE at $\mathbf{p}$ when cable mass is neglected. The numerical solution to the IKP while considering cable mass is then solved for gradually increasing values of the cable density, i.e.,

$$\rho_j = \left(\frac{j}{N}\right)\rho, \quad j = 1, 2, \ldots, N \tag{14}$$

where, once again, the initial guess for a given step is taken as the solution to the previous one. The IKP was programmed to attempt, as necessary, each of these continuation schemes, in the order they are presented here, first with $N = 10$ and then with $N = 100$, until a solution is found. Both continuation schemes were deemed desirable since EE poses were encountered for which only one scheme was successful in solving the IKP.

In addition to the use of continuation schemes, damping was also added to the Newton–Raphson algorithm. The latter is known to search for an acceptable solution by iteratively generating (supposedly) better estimates of the true solution as $\mathbf{x}_{k+1} = \mathbf{x}_k + \Delta\mathbf{x}_k$ with

$$\Delta\mathbf{x}_k = -\mathbf{J}(\mathbf{x}_k)^{-1}\mathbf{f}(\mathbf{x}_k) \tag{15}$$

where $\mathbf{J}(\mathbf{x}) = \partial\mathbf{f}(\mathbf{x})/\mathbf{x}$ is the numerically-estimated Jacobian matrix of the non-linear system of equations. In this work, $\max(|f_q(\mathbf{x})|) \leq \varepsilon$ was used as the stop criteria where $f_q(\mathbf{x})$ is the qth element of $\mathbf{f}(\mathbf{x})$ ($q = 1, 2, \ldots, 6$) and $\max(\cdot)$ is the maximum of the values in the argument. Since the Newton–Raphson algorithm considers only first order terms in its calculation of $\Delta\mathbf{x}_k$, it is not necessarily the case that $\max(|f_q(\mathbf{x}_{k+1})|) < \max(|f_q(\mathbf{x}_k)|)$. Moreover, the bounds imposed on the cable tensions as well as the constraint restricting cable drooping may be violated at a given $\mathbf{x}_{k+1}$. Given a solution estimate $\mathbf{x}_{k+1}$, $\mathbf{f}(\mathbf{x}_{k+1})$ is computed along with $t_{\min_i}$ and $t_{\max_i}$ (based on Algorithm 1). If $\max(|f_q(\mathbf{x}_{k+1})|) > \max(|f_q(\mathbf{x}_k)|)$ or one of the constraints is violated, damping is used to compute a new estimate to the IKP solution as:

$$\mathbf{x}_{k+1} = \mathbf{x}_k + \eta\Delta\mathbf{x}_k \tag{16}$$

where $\eta \leq 1$. This is repeated for a diminishing series of values of η until either all conditions are met or all values have been attempted (values of η of 1, 0.5, 0.25 and 0.1 were used).

3.2 Workspace Computation

The wrench feasible workspace (WFW), as described in [10], is considered here and consists of the set of poses of a CDM where it may generate all wrenches within a required set while maintaining its cables in tension. Additional constraints, such as cable tensions belonging to a specified range, may also be considered. The required wrench set is chosen here to consist only of the wrench needed to offset the combined weight of the EE and payload. As such, a given EE pose is considered to be part of the WFW in this work if the following conditions are satisfied:

- The mechanism is in static equilibrium (i.e., (12) is satisfied).
- The kinematic constraints related to the cable profile equations are satisfied for each mechanism cable (i.e., (4) is satisfied).
- The cable tensions remain within the specified range (i.e., $t_{\min_i} \leq t_{\min_c} \leq t_{\max_i}$).
- None of the cables droop below the EE.[4]

These conditions are the same that are required for a given pose of the EE to admit a solution to its IKP. The WFW of the mechanism is thus estimated numerically by discretizing the Cartesian space into a point cloud representing poses of the EE and verifying, for each pose, whether a solution to the IKP exists. An estimate of the WFW is thus obtained as a set of points. In Sect. 4, the WFW is represented (for aesthetic reasons) as an area of the Cartesian space enclosed by a boundary. However, it is understood that not all points within this area have been verified as being within the mechanism's WFW. Notwithstanding, the method used here is deemed acceptable given the objectives of evaluating the stiffness properties of the mechanism.

3.3 Computation of the Stiffness Matrix and Stiffness Indices

The stiffness matrix of the mechanism, $\mathbf{K}$, relates small disturbances in the force applied to the EE to corresponding deflections of the latter, i.e., $\delta\mathbf{w} = \mathbf{K}\delta\mathbf{p}$. In order to develop an expression for $\mathbf{K}$, one may, referring to (12), rewrite the static equilibrium of the EE in a given pose as:

$$\mathbf{w} = \sum_{i=1}^{2} \mathbf{Q}_i \mathbf{t}_i \qquad (17)$$

---

[4] This condition is optional.

where $\mathbf{t}_i = t_i \mathbf{n}_i$ is the equivalent of $\mathbf{t}$ for the ith cable. Linearization of this equation yields:

$$\delta\mathbf{w} = \sum_{i=1}^{2} \mathbf{Q}_i \delta\mathbf{t}_i \tag{18}$$

Moreover, substitution of (6), applied to the ith cable, leads to:

$$\delta\mathbf{w} = \sum_{i=1}^{2} \mathbf{Q}_i \mathbf{K}_{c_i} \delta\mathbf{c}_i \tag{19}$$

Finally, the linearization of (10) yields $\delta\mathbf{c}_i = \mathbf{Q}_i^T \delta\mathbf{p}$ where $\mathbf{a}_i$ is observed to be constant. Taking into account that $\mathbf{K}_{c_i} = \mathbf{C}_{c_i}^{-1}$, one finally has:

$$\delta\mathbf{w} = \left(\sum_{i=1}^{2} \mathbf{Q}_i \mathbf{C}_{c_i}^{-1} \mathbf{Q}_i^T \right) \delta\mathbf{p} \tag{20}$$

and the mechanism's stiffness matrix is:

$$\mathbf{K} = \sum_{i=1}^{2} \mathbf{Q}_i \mathbf{C}_{c_i}^{-1} \mathbf{Q}_i^T \tag{21}$$

where $\mathbf{C}_{c_i}$ for the ith cable is obtained from (7) through (9).

In order to evaluate and compare the stiffness performance of a mechanism in a given pose, it is useful to define stiffness indices having physical meaning that can be extracted from the stiffness matrix. Such indices could eventually be used, for instance, in optimizing the mechanism geometry. In the following, indices quantifying the stiffness of the mechanism along the X and Y axes (see Fig. 2). The stiffness in the X direction can be useful, for example, in determining the mechanism's resistance to displacements of its EE due to wind drag. Based on the definition of the mechanism's stiffness matrix, one may write:

$$\delta f_x = K_{11}\delta p_x + K_{12}\delta p_y, \quad \delta f_y = K_{21}\delta p_x + K_{22}\delta p_y \tag{22}$$

where K_{ij} is the element of $\mathbf{K}$ located on the ith row and the jth column. If the stiffness along the X axis is sought, one may imagine applying a small disturbance force δf_x in that direction with $\delta f_y = 0$ and measuring the corresponding deflection δp_x. Setting $\delta f_y = 0$ in the second part of (22) allows one to find $\delta p_y = -(K_{21}/K_{22})\delta p_x$. Substituting in the first part of (22), the stiffness in the X axis direction is:

$$K_x = K_{11} - \frac{K_{12}^2}{K_{22}} \tag{23}$$
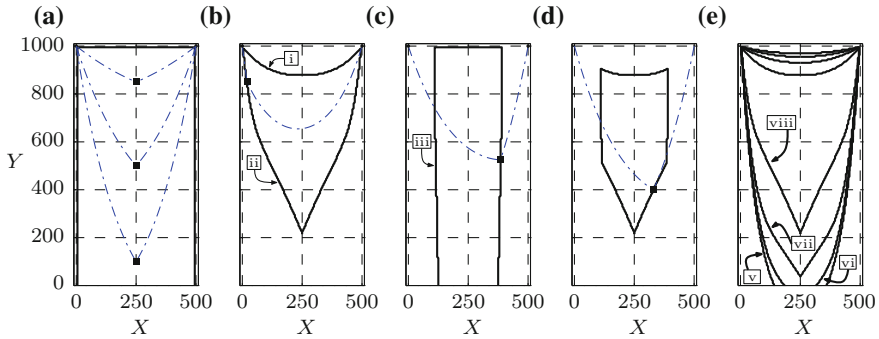
Fig. 3 Workspace of mechanism with varying constraints and varying EE/payload mass

where the fact that the stiffness matrix is symmetrical is used. Similarly, the stiffness in the Y axis direction is:

$$K_y = K_{22} - \frac{K_{12}^2}{K_{11}} \tag{24}$$

4 Results

It is sought here to investigate the effect of cable sagging on the stiffness of a planar two-cable 2-DoF suspended CDM. Based on previous works [17, 21], the mechanism is assumed to use galvanized steel cables with 7×19 thread structure and a diameter of $d = 35$ mm. These cables have a linear density $\rho = 7.5$ kg/m, a Young's modulus of $E = 200$ GPa and a maximum admissible stress of $\sigma_{max} = 180$ MPa. Using the latter value as well as a safety factor (SF) of 2, the maximum tension capable of being applied to the cables is:

$$t_{max_c} = \frac{\sigma_{max} A}{SF} = \frac{\sigma_{max}}{SF} \cdot \frac{\pi d^2}{4} \cong 87 \text{ kN} \tag{25}$$

For its part, the minimum tension to be applied to the cables is set to $t_{min_c} = 100$ N. The positions of the cable's attachment points to ground are $\mathbf{a}_1 = [0, 1000]^T$ m and $\mathbf{a}_2 = [500, 1000]^T$ m. In order to gain a better sense of the stiffness indices that are computed for the mechanism in a given pose, these will be normalized with respect to the axial stiffness of a cable having the properties listed above and a rest length of $l_0 = 1,000$ m. This yields a nominal stiffness of $K_0 \approx 200$ kN/m. The stiffness indices that will be mapped are thus $K'_x = K_x/K_0$ and $K'_y = K_y/K_0$.

Prior to analyzing the stiffness of the mechanism, it is interesting to consider the properties of its workspace. The workspace of the mechanism with $m = 5,000$ kg is plotted for different sets of constraints in Fig. 3a–d. Sample mechanism config-urations are also shown where cables appear as dash-dotted lines and the EE is

represented by a black square. When constraints on cable tensions and cable drooping are not applied, Fig. 3a, the mechanism's workspace is the same as that of an equivalent mechanism with massless cables.[5] That is to say that the workspace corresponds to the area beneath the line segment joining A_1 and A_2. When limits are applied to the cable tensions, Fig. 3b, the workspace becomes a closed area of the XY plane delimited by curves where at least one of the cables has reached its maximum tension.[6] As the EE moves upward, the tangents of the cables at the EE (i.e., $\mathbf{n}_i$) generally become increasingly aligned with the X axis and the cable tensions must increase correspondingly in order to support the EE/payload weight. This remains possible until at least one of the cables reaches its maximum tension on boundary [i] (Fig. 3b). Meanwhile, as the EE moves to the left of the horizontal centre of its workspace (i.e., $p_x = 250$ m), $\mathbf{n}_1$ becomes increasingly vertical while $\mathbf{n}_2$ approaches the horizontal. Eventually, the Y-component of $\mathbf{n}_2$ becomes positive or, equivalently, the cable droops beneath the EE and is pulling down on the latter. As the EE moves to the left, the cable attached to A_1 must thus support a larger portion of the EE/payload weight and, eventually, a portion of the other cable's weight. This increases its tension until the maximum limit is reached on boundary [ii] (Fig. 3b). As the EE moves downward, the cable lengths are longer and the actuators have to support the corresponding increase in weight. This explains why the workspace boundaries in Fig. 3b gradually taper toward $p_x = 250$ m line when moving in the negative Y axis direction. When the constraint preventing cables from drooping below the EE is applied, Fig. 3c, this removes from the workspace those regions that are furthest away from its horizontal centre. For example, when the EE is on boundary [iii] (Fig. 3c), $\mathbf{n}_2$ is horizontal. Fig. 3d shows the workspace obtained when tension limits and the constraint preventing cable drooping are considered simultaneously. Finally, Fig. 3e shows the variation in the workspace when the EE/payload weight is varied: [v] m=100 kg, [vi] m=1,000 kg, [vii] m=2,500 kg and [viii] m=5,000 kg (no constraint is applied with regards to cable drooping). Since the $t_{\max_i} \leq t_{\max_c}$ constraint is responsible for all workspace boundaries in this case, the workspace size increases as expected as the EE/payload weight decreases.

When cable mass is not considered, the stiffness of a CDM is a combination of the axial stiffness of its cables along with a stiffness due to the tension forces in the cables. For most EE poses of most mechanisms, however, the overall stiffness is largely dictated by the axial stiffness of the cables (though some exceptions exists [2]). This is observed in Fig. 4 where mappings of stiffness indices K'_x and K'_y are provided for the case where cable mass is neglected. Though the EE/payload mass, which has direct implications on the cable tensions, is varied significantly between Fig. 4a–d, the corresponding change in the mechanism stiffness is relatively small. One may also observe from these figures that throughout much of the workspace K'_x and K'_y are either close to or greater than unity. This implies that the stiffness in

---

[5] While this holds for the planar 2-DoF suspended CDM, it does not for all suspended CDMs [21].

[6] Though the minimum tension constraint (i.e., $t_{\min_c}$) does not constrain the workspace in the cases discussed here, it has the potential to do so depending on the mechanism geometry and mechanical properties.
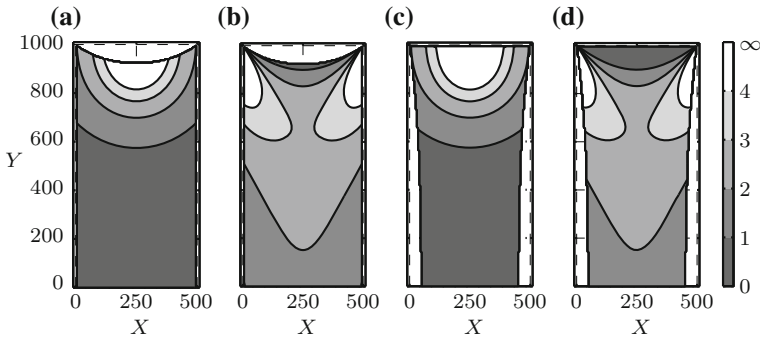
Fig. 4 Mapping of K'_x and K'_y for the case of massless cables (with cable tension limits): **a** K'_x with $m = 5,000$ kg, **b** K'_y with $m = 5,000$ kg, **c** K'_x with $m = 100$ kg, **d** K'_y with $m = 100$ kg
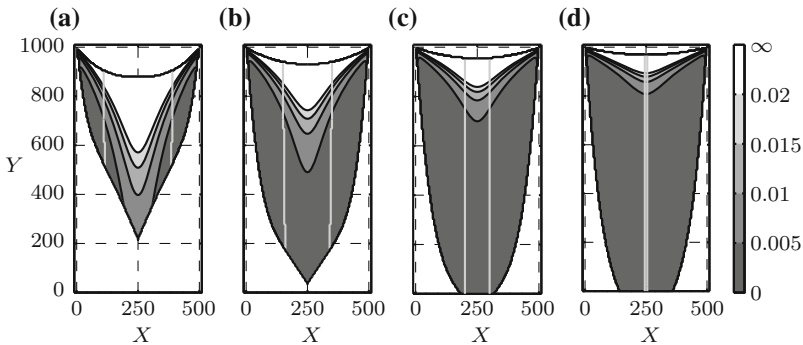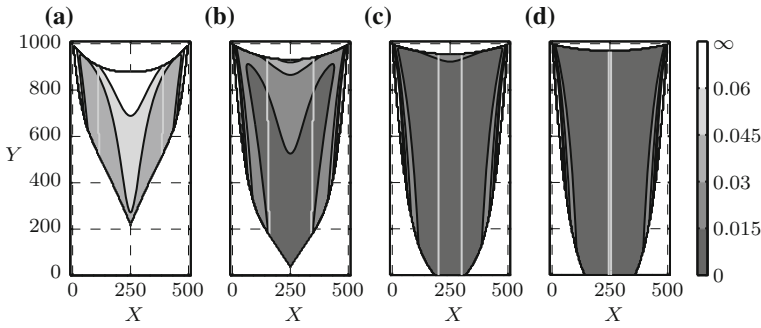

Fig. 5 Mapping of K'_x while considering cable mass (with cable tension limits): **a** $m = 5,000$ kg, **b** $m = 2,500$ kg, **c** $m = 1,000$ kg, **d** $m = 100$ kg

the respective directions are mostly on the same order of magnitude as K_0, the axial stiffness of a 1,000 m cable having the properties described earlier.

Meanwhile, mappings of K'_x and K'_y over the mechanism's workspace are plotted while taking cable mass into consideration in Figs. 5 and 6, respectively, for varying values of the combined EE/payload mass. In comparison to the results obtained for the case of massless cables, the stiffness of the mechanism is observed to be lower by approximately two orders of magnitude. This is explained by the sag-induced flexibility of a cable of non-negligible mass that combines with its axial flexibility and tension force to determine its overall stiffness. The fact that the sag-induced flexibility has a potentially considerable impact on cable (and mechanism) stiffness has previously been demonstrated [17]. Clearly, neglecting cable mass in such situations would lead to a significant overestimation of the mechanism stiffness.

Looking at Figs. 5 and 6, it may be seen that the stiffness of the mechanism is proportional to m. In fact, increasing the EE/payload mass leads to an increase in the cable tensions which reduces cable sagging and sag-induced flexibility. As such, the

Fig. 6 Mapping of K'_y while considering cable mass (with cable tension limits): **a** $m = 5,000$ kg, **b** $m = 2,500$ kg, **c** $m = 1,000$ kg, **d** $m = 100$ kg

effect of cable tensions on the stiffness of the mechanism is much greater when cable mass is considered. In a completely restrained CDM, where $n_c > d$, the effect of varying EE/payload mass on mechanism stiffness could be mitigated by strategically adjusting the level of prestress so as to maintain the cable tensions above a desired threshold and thus minimize the effect of sag-induced flexibility. This, however, is not possible for suspended CDMs.

Observing Fig. 5 leads one to conclude that K'_x increases with p_y. This is logical since having the EE closer to line $A_1 A_2$ leads to shorter cable lengths (having higher axial stiffness), higher cable tensions (for given EE/payload mass) and cables that are increasingly aligned with the X axis. The stiffness in the X direction also decreases as the EE moves away from the workspace's horizontal centre due to increased sagging in one of the cables (e.g., mechanism configuration shown in Fig. 3b). In the Y-axis direction, the stiffness also tends to increase with p_y due to shorter cable lengths and greater cable tensions. These effects overcome the increasing alignment of the cables with the Y axis as p_y is decreased. Finally, although this is not easily visible in Fig. 6, the stiffness in the Y-axis direction increases at the outer left and right boundaries of the mechanism workspace. In fact, configurations near to these boundaries have one cable that is close to vertical. Since vertical cables do not exhibit any cable sag, this leads to much higher values of K'_y.

The workspaces considered in the preparation of Figs. 5 and 6 take cable tension limits into account but do not constrain against cable drooping. However, the workspace boundaries based on the cable drooping constraint are also shown in grey in these figures. From these, one can observe that the workspace area decreases significantly with m if cable drooping is to be avoided, to the point where the workspace practically vanishes when $m = 100$ kg. This has important ramifications for mechanisms subjected to significantly varying EE/payload mass (e.g., pick and place manipulators). In essence, if a mechanism's cables are sized based on the heaviest loads it must carry, then the cables will undergo significant drooping when the payload is small (e.g., when the mechanism is preparing to pickup its payload).

5 Conclusion

Despite past research dealing with several different effects of cable mass on the performance of CDMs, very few works have discussed the implications of cable sagging on mechanism stiffness. This paper has begun to fill this void through the stiffness analysis of a planar two-cable 2-DoF suspended CDM. The solution to the mechanism's IKP was reviewed and its workspace was estimated numerically while considering both cable tension limits and cable drooping. The main contribution of the paper, however, is the development of the mechanism's stiffness matrix and the resulting stiffness analysis. The mapping of intuitive stiffness indices throughout the mechanism workspace allowed for some useful observations to be made. In particular, the results obtained confirmed the findings of previous researchers in that there is a significant drop in the stiffness of a mechanism when its cable mass is considered. This reduction in stiffness is due to the added flexibility of each cable caused by its sagging. Moreover, though the level of tension in a mechanism's cables is known to contribute to its stiffness, this effect is much more pronounced when cable mass is being considered. In fact, increased tension leads to a reduction in cable sagging which, as previously mentioned, has a significant impact on stiffness. This could be taken into consideration in the design of control algorithms for completely restrained CDMs so as to maintain cable tensions (and thus stiffness) above a given threshold. For suspended CDMs, however, this implies that stiffness would vary considerably with payload which could prove challenging for applications such as pick and place operations. For such applications, changes to the EE/payload mass also lead to variations in the size of the mechanism workspace when cables are not permitted to droop below the elevation of the EE. In fact, if cables drooping beneath the EE are to be avoided, the workspace will eventually degenerate to a curve as $m \rightarrow 0$. One approach to curtail the issues related to the variation of the payload mass in a suspended CDMs would be to make the mass of the EE sufficiently large so as to maintain minimum cable tensions at all times. However, this is clearly a less than ideal scenario since it would reduce the mechanism's maximum payload capacity. While there remains much to be learned about the effects of cable mass on the performance of CDMs, including its effects on mechanism stiffness, it is hoped that some of the observations made here for a simple mechanism will prove beneficial in the study of more complex systems.

References

1. Albus, J., Bostelman, R., Dagalakis, N.: The NIST robocrane. J. Robot. Syst. **10**(5), 709–724 (1993)

2. Arsenault, M.: Optimization of the prestress stable wrench closure workspace of planar parallel three-degree-of-freedom cable-driven mechanisms with four cables.In: Proceedings of the IEEE International Conference on Robotics and Automation (2010).
3. Behzadipour, S., Khajepour, A.: Stiffness of cable-based parallel manipulators with application to stability analysis. ASME J. Mech. Des. **128**(1), 303–310 (2006)
4. Bosscher, P., Ebert-Uphoff, I.: Wrench-based analysis of cable-driven robots. In: Proceedings of the IEEE International Conference on Robotics and Automation, pp. 4950–4955 (2004).
5. Bosscher, P., Williams II, R.L., Bryson, L.S., Castro-Lacouture, D.: Cable-suspended robotic contour crafting system. Autom. Constr. **17**(1), 45–55 (2007)
6. Bosscher, P., Williams II, R.L., Tummino, M.: A concept for rapidly-deployable cable robot search and rescue systems. In: Proceedings of the ASME International Design Engineering Technical Conferences and Computers and Information in, Engineering Conference, pp. 589–598 (2005).
7. Bouchard, S.: Géométrie des robots parallèles entraînés par des câbles. Ph.D. thesis, Université Laval (2008).
8. Bruckmann, T., Mikelsons, L., Hiller, M., Schramm, D.: Continuous workspace analysis, synthesis and optimization of wire robots. In: Proceedings of the ASME 2008 International Design Engineering Technical Conferences & Computers and Information in, Engineering Conference (2008).
9. Choe, W., Kino, H., Katsuta, K., Kawamura, S.: Design of parallel wire driven robots for ultra-high speed motion based on stiffness analysis. In: Proceedings of the Japan/USA Symposium on Flexible Automation, vol. 1, pp. 159–166 (1996).
10. Ebert-Uphoff, I., Voglewede, P.A.: On the connections between cable-driven robots, parallel manipulators and grasping. In: Proceedings of the IEEE International Conference on Robotics and Automation, pp. 4521–4526 (2004).
11. Gouttefarde, M., Collard, J.F., Riehl, N., Baradat, C.: Simplified static analysis of large-dimension parallel cable-driven robots.In: Proceedings of the IEEE International Conference on Robotics and Automation (2012).
12. Gouttefarde, M., Daney, D., Merlet, J.P.: Interval-analysis-based determination of the wrench-feasible workspace of parallel cable-driven robots. IEEE Trans. Robot. **27**(1), 1–13 (2011)
13. Gouttefarde, M., Gosselin, C.M.: Analysis of the wrench-closure workspace of planar parallel cable-driven mechanisms. IEEE Trans. Robot. **22**(3), 434–445 (2006)
14. Havlik, S.: Cable suspended manipulation robots. In: Proceedings of the 16th International Symposium on Automation and Robotics in Construction (ISARC), pp. 269–274 (1999).
15. Irvine, H.M.: Cable Structures. The MIT Press, Cambridge (1981)
16. Korayem, M., Bamdad, M., Saadat, M.: Workspace analysis of cable-suspended robots with elastic cable. In: Proceedings of the IEEE International Conference on Robotics and, Biomimetics, pp. 1942–1947 (2008).
17. Kozak, K., Zhou, Q., Wang, J.: Static analysis of cable-driven manipulators with non-negligible cable mass. IEEE Trans. Robot. **22**(3), 425–433 (2006)
18. Merlet, J.P.: Kinematics of the wire-driven parallel robot MARIONET using linear actuators. In: Proceedings of the 2008 IEEE International Conference on Robotics and Automation (2008).
19. Nan, R., Peng, B.: Chinese concept for the 1 km^2 radio telescope. Acta Astronaut. **46**(10), 667–675 (2000)
20. Riehl, N., Gouttefarde, M., Krut, S., Baradat, C., Pierrot, F.: Effects of non-negligible cable mass on the static behavior of large workspace cable-driven parallel mechanisms. In: Proceedings of the 2009 IEEE International Conference on Robotics and Automation (2009).
21. Riehl, N., Gouttefarde, M., Pierrot, F., Baradat, C.: On the static workspace of large dimension cable-suspended robots with non negligible cable mass. In: Proceedings of the ASME 2010 International Design Engineering Technical Conferences & Computers and Information in, Engineering Conference (2010).
22. Sui, C., Zhao, M.: Control of a 3-DOF parallel wire driven stiffness-variable manipulator. In: Proceedings of the IEEE International Conference on Robotics and, Biomimetics, pp. 204–209 (2004).

23. Verhoeven, R., Hiller, M.: Estimating the controllable workspace of tendon-based Stewart platforms. In: Proceedings of the 7th International Symposium on Advances in Robot Kinematics (2000).
24. Verhoeven, R., Hiller, M., Tadokoro, S.: Workspace, stiffness, singularities and classification of tendon-driven Stewart platforms. In: Proceedings of the 6th International Symposium on Advances in Robot Kinematics, pp. 105–114 (1998).
25. Zi, B., Duan, B., Du, J., Bao, H.: Dynamic modeling and active control of a cable-suspended parallel robot. Mechatronics **18**(1), 1–12 (2008)

A Modeling Method of the Cable Driven Parallel Manipulator for FAST

Rui Yao, Hui Li and Xinyu Zhang

Abstract A Five Hundred meter Aperture Spherical radio Telescope (FAST) is being built in China, and a similarity model was set up in Beijing for further study of FAST. In FAST, A six-cable driven parallel manipulator is adopted as the first level adjustable feed support system. This paper addresses the complete modeling method of the six-cable driven parallel manipulator of FAST with cable mass and elastic deformation. Comparing with the precise catenary modeling equation, modeling and solution of line equation is easier and quicker, but has modeling error for cable driven parallel manipulator. Hence, analysis and compensation method of the modeling error is studied in detail, which encourages the line equation to model and solve the six-cable driven parallel manipulator accurately. Finally, simulation and experiment have been done for supporting the modeling and error compensation methods in this paper.

1 Introduction

China is building a Five-hundred meter Aperture Spherical radio Telescope (FAST) [1]. Figure 1 shows the conceptualization of the FAST system, where the feed support system moves over the active reflector. The feed support system of FAST includes two parts: first-level adjustable feed support system, which is a six-cable driven parallel manipulator with large span that provides the coarse positioning, and a second-level adjustable feed support system (A–B rotator and a Stewart platform) that can compensate the positioning error and achieve the required accuracy. At present, a

R. Yao (✉) · H. Li · X. Zhang
National Astronomical Observatories, Chinese Academy of Sciences, Beijing 100012, China
e-mail: ryao@nao.cas.cn, lihui@nao.cas.cn

X. Zhang
Graduate University of Chinese Academy of Sciences, Beijing 100049, China
e-mail: xyzhang@nao.cas.cn
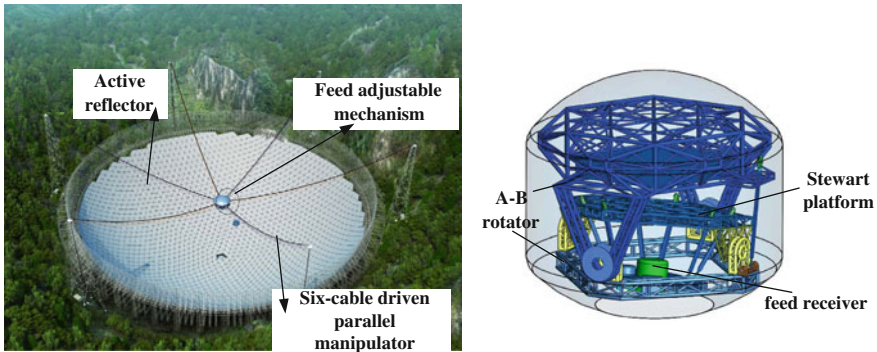
Fig. 1 Conceptual model of the FAST

similarity model of the feed support system is set up in Beijing [2]. Cable driven parallel manipulator has advantages of simple configuration, high load ability, large workspace, low price and high speed [3, 4].

For modeling cable driven parallel manipulators with large span, previous researches did plenty of work on it [5–7]. In order to get highly modeling accuracy, precise catenary equation is adopted. Comparing with the precise catenary equation, modeling and solution of simplified catenary equations are easier and quicker, which are more suitable for real-time calculation and control of cable driven parallel manipulator with large span. However, simplified catenary equations will lead to modeling error, which may not be accepted in real control [5]. So the modeling error should be analyzed and compensated in real application. This paper is expected to fill that gap.

In this paper, complete modeling equations with cable mass and elastic deformation based on the precise catenary and simplified catenary equations will be set up for the six-cable driven parallel manipulator in Sect. 2. Then, a modeling compensation method will be discussed in Sect. 3 to enhance the modeling accuracy of the simplified modeling method for the six-cable driven parallel manipulator. From experiment, the simplified modeling method with a compensation equation can satisfy control accuracy of the six-cable driven parallel manipulator.

2 Modeling of the Six-Cable Driven Parallel Manipulator with Large Span

For building the FAST, a six-cable driven parallel manipulator is adopted as the first-level adjustable feed support system, and a similarity model of the six-cable driven parallel manipulator is set up in Beijing. This section will discuss the modeling method of the six-cable driven parallel manipulator. Considering cable mass and
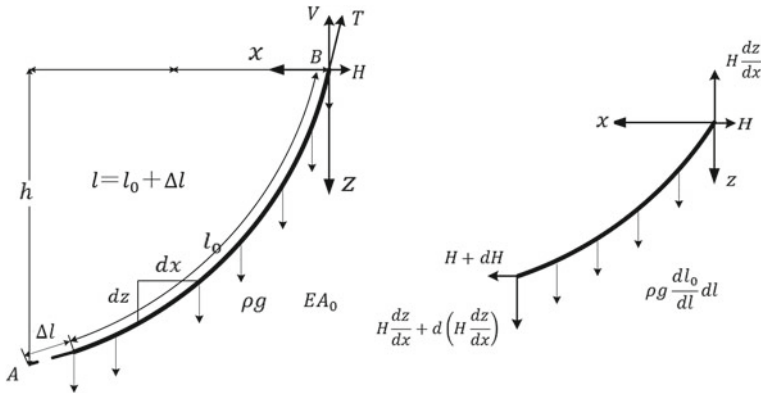
Fig. 2 Precise catenary modeling of a cable

elastic deformation, precise catenary equation and simplified catenary equations are set up in this section.

2.1 Modeling Equations of Single Cables

2.1.1 Precise Catenary Equation

For setting up a cable model with precise catenary equation, the symbols used in Fig. 2 are defined as: l_0 is the unstrained length of the cables; Δl the strain of the cable; T the tension applied to the fixed end of the cable; ρ the unstrained linear density; E the elastic modulus; A_0 the unstrained cross-sectional area; H the horizontal component of the cable tension vector and V its vertical component. Using the variables and coordinate system above, we will briefly reproduce Irvines derivation [8] in this paper.

As shown in Fig. 2 a point along the length of the strained cable can be denoted by Cartesian coordinate and. To begin with, the cable must satisfy the geometric constraint:

$$\sum x = 0 \qquad H + dH - H = 0 \tag{1}$$

$$\sum z = 0 \quad H\frac{dz}{dx} + d\left(H\frac{dz}{dx}\right) + \rho g dl_0 - H\frac{dz}{dx} = 0 \tag{2}$$

where,

$$\frac{dl}{dl_0} = \frac{T}{EA_0} + 1 \tag{3}$$

$$T = H\sqrt{1 + \left(\frac{dz}{dx}\right)^2} \tag{4}$$

From $dl = dx\sqrt{1 + \left(\frac{dz}{dx}\right)^2}$, Eq. 2 can be expressed as:

$$d\left(H\frac{dz}{dx}\right) + \rho g \frac{EA_0}{T + EA_0}dl = 0 \tag{5}$$

Assuming $\frac{dz}{dx} = p$, Eq. 5 can be written as:

$$\frac{dp}{dx} + \frac{\rho g EA_0}{H} \frac{\sqrt{1 + p^2}}{H\sqrt{1 + p^2} + EA_0} = 0 \tag{6}$$

Therefore,

$$x = -\frac{H}{\rho g}sh^{-1}\left(\frac{dz}{dx}\right) - \frac{H^2}{\rho g EA_0}\frac{dz}{dx} + c \tag{7}$$

Where,

$$sh^{-1}(x) = \ln\left(x + \sqrt{1 + x^2}\right), x \in (-\infty, +\infty) \tag{8}$$

$$x = -\frac{H}{\rho g}\ln\left(\frac{dz}{dx} + \sqrt{1 + \left(\frac{dz}{dx}\right)^2}\right) - \frac{H^2}{\rho g EA_0}\frac{dz}{dx} + c \tag{9}$$

Integrating and applying the boundary conditions as follows:

$$x = 0, z = 0$$
$$x = L, z = h \tag{10}$$

The length of cable is l, the unstrained length of the cable is l_0, and Δl represents the strain of the cable. The relationship can be expressed as: $l = l_0 + \Delta l$.

$$l = \int_0^l \sqrt{1 + \left(\frac{dz}{dx}\right)^2}dx \tag{11}$$

$$l_0 = \int \frac{1}{\frac{T}{EA_0} + 1}dl \tag{12}$$

Fig. 3 Line modeling of a
cable
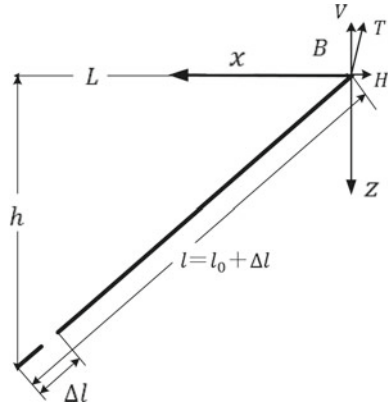
2.1.2 Line Equation

A line is shown in Fig. 3. A cable under its mass cannot remain straight. The ideal-
ization would be possible if the ends of the cable were subjected to tensions that are
predominantly larger than the effect of the cable mass or the accuracy requirement
is not high.

In Fig. 3, line equation with elastic deformation of a cable can be easily derived
as follows:

$$l = \left(h^2 + L^2\right)^{1/2} \tag{13}$$

$$T = \left(V^2 + H^2\right)^{1/2} \tag{14}$$

$$L = l\frac{H}{T} \tag{15}$$

$$h = l\frac{V}{T} \tag{16}$$

$$\Delta l = \frac{Tl}{EA_0} \tag{17}$$

where Δl is elastic deformation of the cable.

2.2 Modeling of the Six-Cable Driven Parallel Manipulator

In Fig. 4, for studying the largest radio telescope FAST, a similarity model of FAST
is set up in Beijing. The related geometric parameters of the six-cable driven parallel
manipulator in the similarity model are given in Table 1 [9].

Fig. 4 40 m diameter six-cable driven parallel manipulator

Table 1 Geometric parameters of the six-cable driven parallel manipulator

Symbol	Quantity	Value
r_a	Radius of the moving platform	0.5 (m)
r_b	Radius of cable towers distributed circle	20 (m)
h	Height of cable tower	18 (m)
d	Diameter of cable	8 (mm)
ρ	Density of cable	0.5145 (kg/m)
m_o	Mass of moving platform	213 (kg)
E	Youngs modular	1.6×10^{11} (Pa)

In Fig. 5, two coordinates are set up for the six-cable driven parallel manipulator: an inertial frame $\Re : O - XYZ$ is located at the center of the reflectors bottom. Another moving frame $\Re' : O' - X'Y'Z'$ is located at the center of the moving platform. B_i ($i = 1, 2, ..., 6$) are the connected points of the cables and cable towers, and A_j ($j = 1, 2, 3$) are the connected points of the cables and moving platform.

For analyses, the symbols used in this section are defined as: $O'^{\Re}$ is the O' expressed in the inertial frame; $B_i^{\Re}$ the vector B_i expressed in the inertial frame; $A_j^{\Re}$ the vector A_j expressed in the inertial frame; $A_j^{\Re'}$ the vector A_j expressed in the moving frame; r_b the radius of the cable towers distributed circle; r_a the radius of the moving platform; h the height of the cable tower.

According to Fig. 5, the vector of the cables can be expressed as:

$$\boldsymbol{B}_i^{\Re} = [r_b \cos((i - 1)\pi/3), r_b \sin((i - 1)\pi/3), h]^{\mathrm{T}}, \quad i = 1, 2, \ldots 6 \qquad (18)$$
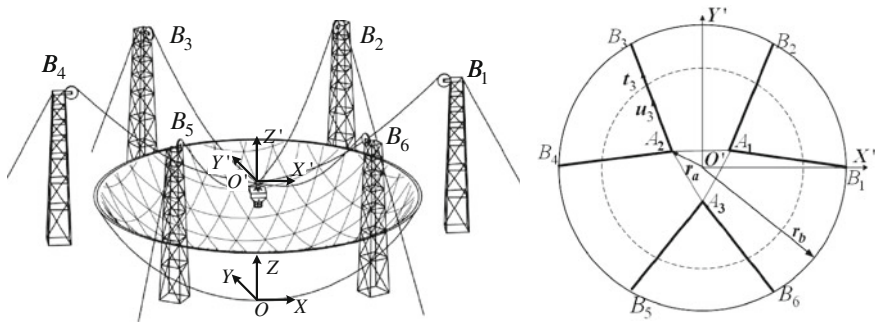
Fig. 5 Geometric parameter of the six-cable driven parallel manipulator

$$A_j^{\mathfrak{R}'} = [r_a \cos((4j-3)\pi/6), r_a \sin((4j-3)\pi/6), 0]^{\mathrm{T}}, \quad j = 1, 2, 3 \quad (19)$$

$$A_j^{\mathfrak{R}} = R \cdot A_j^{\mathfrak{R}'} - O'^{\mathfrak{R}} \quad (20)$$

where R is the coordinate-axis rotation matrix.

Assuming $L_i = A_j^{\mathfrak{R}} - B_i^{\mathfrak{R}}$, $u_i = L_i / \|L_i\|$, $r_i = A_j^{\mathfrak{R}} - O'^{\mathfrak{R}}$, static equilibrium equation of the six-cable driven parallel manipulator can be written as:

$$F = J^{\mathrm{T}} \sigma \quad (21)$$

where σ is the cable tension vector; J^{T} the tension transmission matrix of the cable driven parallel manipulator; $F \in R^n$ the wrench of the moving platform.

$$\sigma = [\sigma_1, \sigma_2, \ldots, \sigma_6]^{\mathrm{T}} \quad (22)$$

$$J^{\mathrm{T}} = \begin{pmatrix} u_1 & \cdots & u_6 \\ r_1 \times u_1 & \cdots & r_6 \times u_6 \end{pmatrix} \quad (23)$$

According to Eqs. 21–23, initial cable length and cable tension of the six-cable driven parallel manipulator can be calculated. Putting the initial cable tension into the two single cable modeling equations, the real cable length and tension can be calculated by using iterative algorithm. The cable tensions of the six-cable driven parallel manipulator should satisfy:

$$\sum_{i=1}^{6} \sigma_{ix} = 0, \ \sum_{i=1}^{6} \sigma_{iy} = 0, \ \sum_{i=1}^{6} \sigma_{iz} = 0$$

$$\sum_{i=1}^{6} M_{ix} = 0, \ \sum_{i=1}^{6} M_{iy} = 0, \ \sum_{i=1}^{6} M_{iz} = 0 \quad (24)$$

where $\sum_{i=1}^{6} \sigma_{ix}$ is the tension in X-direction of the six-cable driven parallel manipulator, and $\sum_{i=1}^{6} M_{ix}$ is the torque in X-direction of the six-cable driven parallel manipulator.

3 Modeling Error Analysis and Compensation of the Six-Cable Driven Parallel Manipulator

3.1 Modeling Error Analysis

When the terminal pose of the moving platform is at $O' = \begin{bmatrix} x, y, z, \alpha, \beta, \gamma \end{bmatrix}^{\mathrm{T}}$, the inverse kinematics equation for the six-cable driven parallel manipulator can be written as:

$$l = \Gamma\left(O'\right) \tag{25}$$

where $l = (l_1, l_2, \ldots, l_i)$ $(i = 1, 2, \ldots, 6)$ represents the cable length.

Therefore, the inverse solutions of the six-cable driven parallel manipulator by line modeling equation can be written as:

$$l_l = \Gamma_l\left(O'\right) \tag{26}$$

where l_l are the length of the cable arc calculated by the line modeling equation.

The solutions of the six-cable driven parallel manipulator based on precise catenary can be expressed as:

$$\Theta\left(l\right) = O' \tag{27}$$

So, the modeling error vector of the six-cable driven parallel manipulator by line modeling equation is:

$$\varepsilon_l = \Theta\left(l_l\right) - \mathbf{O}' \tag{28}$$

where $\varepsilon_l = \begin{bmatrix} \varepsilon x_l, \varepsilon y_l, \varepsilon z_l, \varepsilon \alpha_l, \varepsilon \beta_l, \varepsilon \gamma_l \end{bmatrix}^{\mathrm{T}}$ are the error vectors of the six-cable driven parallel manipulator caused by line modeling equation.

For meeting the modeling accuracy requirement of the six-cable driven parallel manipulator, the error compensation target can be expressed as:

$$\min\left(\sqrt{\frac{\sum_1^k \left(\varepsilon x_{line}^2 + \varepsilon y_{line}^2 + \varepsilon z_{line}^2\right)}{k}}\right), \quad k = 1, 2, \ldots \tag{29}$$

The compensation conditions are:

$$\sqrt{\varepsilon x_{line}^2 + \varepsilon y_{line}^2 + \varepsilon z_{line}^2} \leq \varepsilon_0 \tag{30}$$
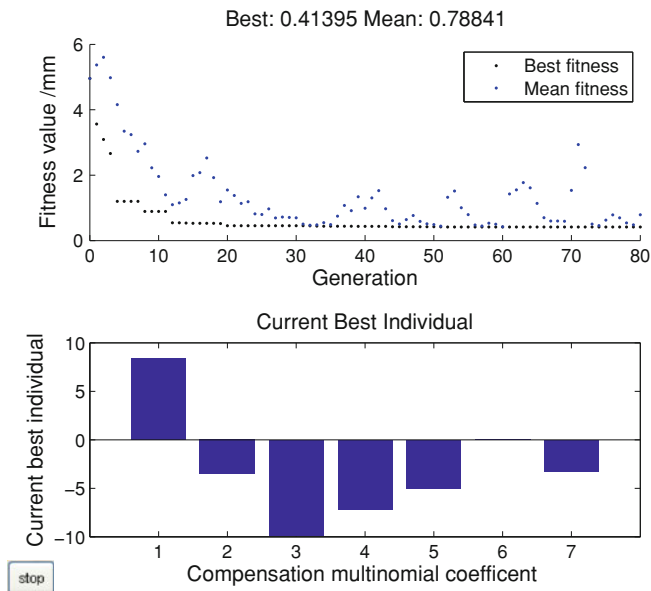
Fig. 6 Compensation polynomial coefficients of line equation

where

$$\varepsilon_{line} = \Theta \left(l_l + \boldsymbol{\varepsilon l_l} \right) - \boldsymbol{O}' \tag{31}$$

$$l_l = \Gamma_l \left(\boldsymbol{O}' \right) \tag{32}$$

$$\varepsilon_{line} = \left(\varepsilon x_{line}, \varepsilon y_{line}, \varepsilon z_{line}, \varepsilon \alpha_{line}, \varepsilon \beta_{line}, \varepsilon \gamma_{line} \right)^{\mathrm{T}} \tag{33}$$

The kinematic control accuracy of the six-cable driven parallel manipulator is Root Mean Square 10 mm (RMS 10 mm). The maximum allowed modeling error ε_0 is given as 1 mm. For meeting the modeling accuracy requirement, a modeling error compensation polynomial is introduced as Eq. 34.

$$\varepsilon l_l = f\left(L, H, h \right) = \left(a_1 \times L^2 - a_2 \times L - b_1 \times h^2 - b_2 \times h \right) \times 10^{-6}$$
$$+ \left(-c_1 \times 10^{-4} \times H^2 + c_2 \times 10^{-2} \times H - d \right) \times 10^{-6} \tag{34}$$

The compensation polynomial coefficients for the line equation can be optimized by genetic algorithm in Fig. 6. From Fig. 6, we obtain the expected error result of this modeling is about RMS 0.78841 mm.

Therefore, the compensation polynomial for the line equation is:
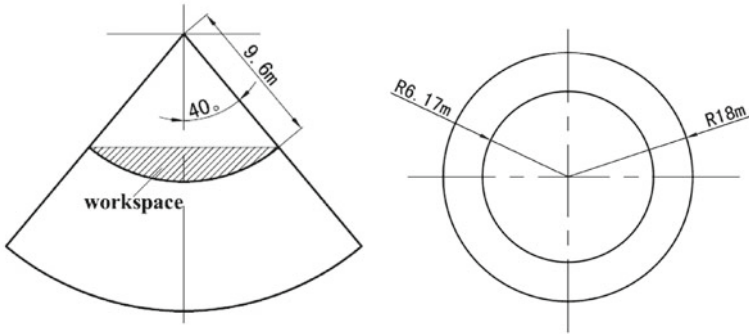
Fig. 7 Required workspace of the six-cable driven parallel manipulator

Fig. 8 Experimental
trajectories-line
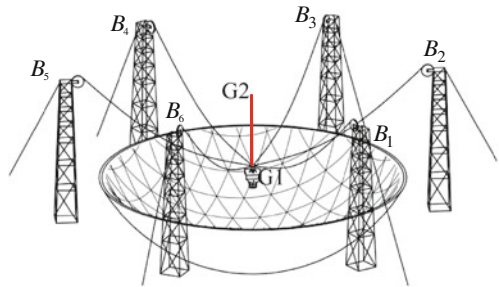
Fig. 9 Experimental
trajectories-arc
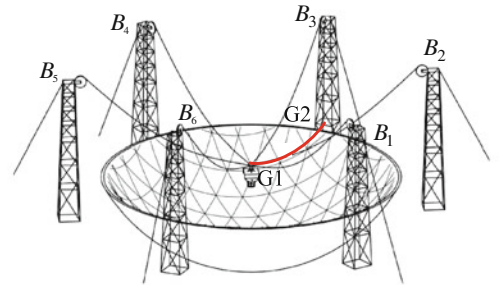
$$\varepsilon l_l = \left(8.3721 \times L^2 - 3.5328 \times L - 9.8747 \times h^2 - 7.1498 \times h\right) \times 10^{-6}$$
$$+ \left(-5.0527 \times 10^{-4} \times H^2 + 0.0894 \times 10^{-2} \times H - 3.2483\right) \times 10^{-6}$$

$$(35)$$

Fig. 10 Experimental trajectories-circle
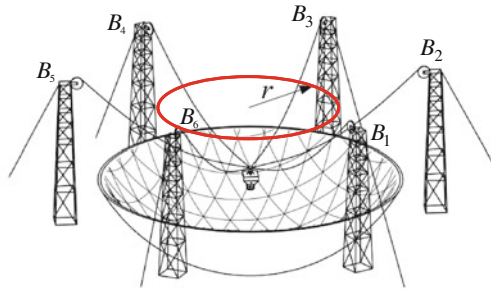
Fig. 11 Total station

3.2 Simulation and Experiment

In Fig. 7, required workspace of the six-cable driven parallel manipulator is presented as a sphere crown surface for studying the modeling error and error compensation methods.

For proving the feasibility of the error compensation method of the six-cable driven parallel manipulator, three experimental trajectories are introduced in Figs. 8, 9, 10. The three experimental trajectories are line, arc and circle respectively.

In Fig. 8, the line trajectory is from $G_1 = (0, 0, 8.4\,\text{m})$ to $G_2 = (0, 0, 9.4\,\text{m})$, and the kinematic velocity is $v = 2.3\,\text{mm/s}$.

In Fig. 9, the arc trajectory is from $G_1 = (0, 0, 8.4\,\text{m})$ to $G_2 = (2, 0, 8.7\,\text{m})$ with pose angle from $0°$ to $6°$, and the kinematic velocity is $v = 2.5\,\text{mm/s}$.

Fig. 12 Kinematic control
accuracy of line trajectory
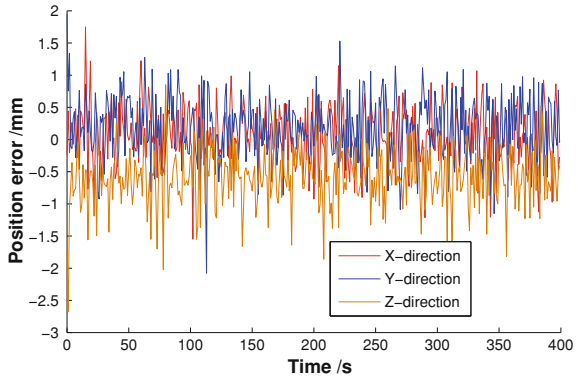
Fig. 13 Kinematic control
accuracy of arc trajectory
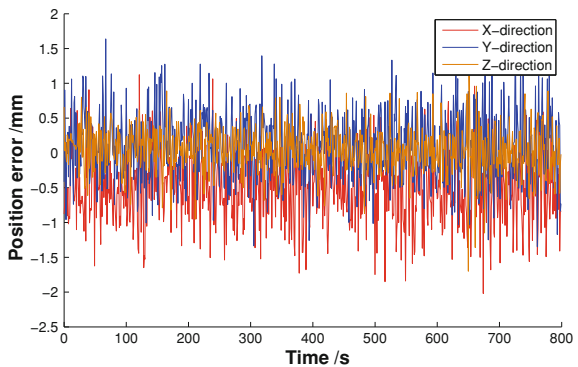
Figure 10 shows that the center of circle trajectory is at (0, 0, 8.7 m), and the radius of the circle trajectory is r = 2 m with 6° pose angle. The kinematic velocity of the circle trajectory is $v = 6.3$ mm/s .

Without kinematic control of the second feed support system, the kinematic control accuracy of the six-cable driven parallel manipulator can be measured by Total Station which is shown in Fig. 11.

The kinematic control errors of the six-cable driven parallel manipulator on the three experimental trajectories are shown in Figs. 12, 13, 14.

From Figs. 12, 13, 14, we know that the kinematic control accuracies of the six-cable driven parallel manipulator on line, arc and circle trajectories are RMS 1.001 mm, RMS 0.929 mm and RMS 1.703 mm respectively.

According to the kinematic control experiment, the accuracy of the six-cable driven parallel manipulator can meet the requirement, which proves the simplified modeling and compensation method in this paper are feasible and accurate.

Fig. 14 Kinematic control accuracy of circle trajectory
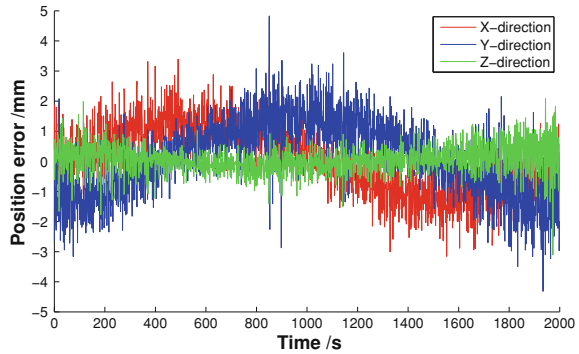
4 Conclusions

This paper addressed the modeling method of a six-cable driven parallel manipulator with large span in FAST. Considering the cable mass and elastic deformation, completely modeling equations are derived in detail based on precise and simplified catenary equations. The modeling error of the six-cable driven parallel manipulator caused by simplified catenary equations is analyzed, and a modeling error compensation method is studied. Taking the similarity model as example, error compensation polynomial coefficients are optimized by genetic algorithm. Finally, the experiment result indicates that the modeling and error compensation method in this paper can satisfy kinematic accuracy.

References

1. Nan, R.D.: Five hundred meter aperture spherical radio telescope (FAST). Sci. China Ser. G Phys. Mech. Astron. **49**(2), 129–148 (2006).
2. Yao, R., Tang, X.Q., Wang, J.S.: Cable tension analysis and optimization of radio telescope feed support system (in Chinese). Prog. Nat. Sci. **19**(11), 1211–1229 (2009)
3. Fang, S., Frantiza, D., Torlo, M., et al.: Motion control of a tendon-based parallel manipulator using optimal tension distribution. IEEE/ASME Trans. Mechatron. **9**(9), 561–568 (2004)
4. Hiller, M., Fang, S.Q.: Design, analysis and realization of tendon-based parallel manipulators. Mech. Mach. Theory **40**, 429–445 (2005)
5. Qu, L., Tang, X.Q., Yao, R.: Error analysis and compensation of cable driven parallel manipulator for the forty-meter aperture radio telescope (in Chinese). High technol. lett. **20**(4), 303–308 (2010)
6. Taghirad, H.D., Nahon, M.A.: Forward kinematics of a macro-micro parallel manipulator, pp. 1–6. IEEE/ASME International Conference Advanced Intelligent, Mechatronics (2007)
7. Lambert, C., Nahon, M., Chalmers, D.: Implementation of an aerostat positioning system with cable control. IEEE/ASME Trans. Mechatron. **12**(2), 32–40 (2007)

8. Irivne, H.: Cable Structures, pp. 16–20 MIT Press, Massachusetts (1981).
9. Nan, R.D.: Structure for supporting the feedback cabin of the FAST. Technical Report, National Astronomical Observatories Chinese Academy of Science (2005)

Cable Vibration Analysis for Large Workspace Cable-Driven Parallel Manipulators

Jingli Du, Wen Ding and Hong Bao

Abstract Cable-driven parallel manipulator is one of the best solutions for large workspace applications. But when long-span cables are involved the effect of cable vibration on the positioning precision of the end-effector should be carefully evaluated since these cables are prone to vibration, degrading the performance of manipulators. In this paper a dynamic model of cable-driven parallel manipulators is presented where each cable is divided into several elements to account for cable vibration. A simple linear cable element is presented where nodal force is related to both nodal position and element length to involve the effect of cable length variation. Numerical examples are presented to demonstrate the effect of cable vibration. The results show that it is necessary to take into consideration cable dynamics for manipulators operating at high speed and vibration of cables can shorten their corresponding chord length.

Keywords Cable-driven manipulator · Cable vibration · Finite element method · Dynamics

1 Introduction

Cable-driven parallel manipulators (CDPMs) possess nearly all the merits of conventional parallel manipulators and have several advantages [1]: (1) the minimum moving inertia, (2) the potential large workspace, (3) to be less expensive and easier to build, transport, and reconfigure. Therefore, CDPMs have found their applications in many fields, such as material handling, haptics, multi-dimensional cranes and high speed manipulation.

J. Du (✉) · W. Ding · H. Bao
Key Laboratory of Electronic Equipment Structure Design of Ministry of Education,
Xidian University, Xi'an, Shaanxi 710071, China
e-mail: jldu@mail.xidian.edu.cn

For applications where extremely large workspace is demanded, CDPMs seem to be one of the best solutions due to their large workspace, low construction cost and ease of construction. Traditional manipulators with serial or parallel structures are impractical for these applications since the required workspace is far larger than what the traditional manipulators can provide.

Many difficult problems are faced in the mechanical design of CDPMs since cables can only apply tensile forces. CDPMs must work in such a state that all cables are tensioned, and their structure will collapse as soon as cables lose their tension. Nowadays, many efforts on the control of CDPMs lay the emphasis on guaranteeing cables work in tension [2, 3]. Nevertheless, few works focus on the dynamic characteristics of cables themselves and their effect on the operation precision of the end-effector. However, it can be easily understood that cables' dynamics is significant to the operation precision for these large workspace applications. It is pointed out in [4] that vibration of cables and, as a result, that of the end-effector were observed during very slow movements of a CDPM with the dimension 50 m.

Though the effect of cable dynamics on CDPMs does not attract enough attention, dynamic characteristics of cables have been widely researched in other fields. Wang and Luo developed a closed-form solution for rigid-body motions of two-dimensional traveling cables with a nonlinear geometrical constraint, which showed that the rigid-body motions of cables were always stable [5]. Terumichi et al. studied the nonstationary vibration of a string with time-varying length, whose end was attached to a mass-spring system [6]. This model could be employed to analytically study the dynamics of elevators. Wang et al. investigated three dimensional underwater vibrations of a geometrically nonlinear cable with time-dependent length [7]. These researches emphasized the influence of cables' axial motion due to the variation of cable length on their dynamic behaviors.

Zhang et al. investigated coupled dynamics between flexible cables and rigid end-effector in cable-driven manipulators. They assumed cables were massless and the longitudinal vibration about their desired configuration was accounted for [8]. Meunier et al. presented a cable model where cables were modeled as lumped masses connected with spring and damper elements [9]. This model works well. However, change of cable length was added only to the first element of each cable, which bounded the cable length. Du et al. presented a dynamic model for CDPMs where cable length varies slowly [4]. This model could be further simplified. For CDPMs in many large workspace applications, deployable and retractable velocity of cable length is not very rapid; therefore, cables' axial motion has negligible effect on their vibration. In this case a simpler model can be employed.

In this paper we present a very simple dynamic model of CDPMs which can effectively describe the dynamic behaviors of cables and can be efficiently solved. In the model each cable is divided into the same count of linear elements, whose stiffness matrices are computed easily. The model can be directly employed to further research vibration suppression and trajectory tracking performance of control strategies.

Fig. 1 A linear cable element
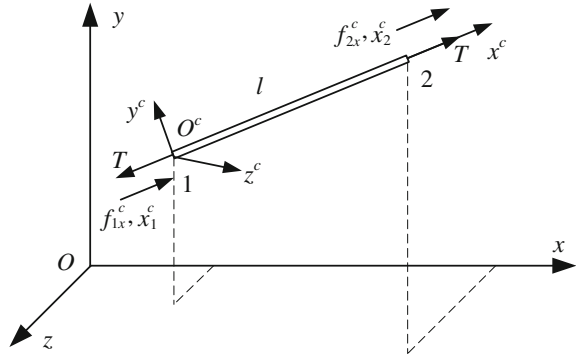
2 Finite Elements for Cables

In many applications cables are treated as linear elements that can only be tensioned but not compressed. Here this commonly used linear element is modified in a nature way where element length is also considered as a variable to account for cable length variation. Illustrated in Fig. 1 is a tensioned linear element with modulus of elasticity E, cross section area A and unstressed length l, which is a one-dimensional element. A local frame $O^c x^c y^c z^c$ is attached to the element with the x^c axis aligning with it. The element is subjected to tensile forces T at nodes 1 and 2 directed along the x^c axis. Nodes 1 and 2 are located at x_1^c and x_2^c on the x^c axis of the local element frame, respectively.

The relationship between tensile force and nodal position plus element length can be easily obtained as follow:

$$T = \frac{EA}{l}(x_2^c - x_1^c - l) \tag{1}$$

Here nodal position instead of nodal displacement is employed in (1) to facilitate the description of cable configuration during movement of CDPMs. Thus, the nodal force can be expressed as

$$\begin{cases} f_{1x}^c = -T = \frac{EA}{l}(x_1^c - x_2^c + l) \\ f_{2x}^c = T = -\frac{EA}{l}(x_1^c - x_2^c + l) \end{cases} \tag{2}$$

Equation (2) is rewritten in matrix form

$$f^c = k_c^c x^c + k_s^c l \tag{3}$$

where

$$f^c = \begin{bmatrix} f_{1x}^c & f_{2x}^c \end{bmatrix}^T, \quad x^c = \begin{bmatrix} x_1^c & x_2^c \end{bmatrix}^T,$$

$$k_c^c = \frac{EAc}{l} \begin{bmatrix} 1 & -1 \\ -1 & 1 \end{bmatrix}, \quad k_s^c = \frac{EAc}{l} \begin{bmatrix} 1 \\ -1 \end{bmatrix} \tag{4}$$

and

$$c = \begin{cases} 1 & \text{for } x_2^c - x_1^c > l \\ 0 & \text{otherwise} \end{cases} \tag{5}$$

is introduced to account for the fact that cable can only be tensioned but not com-
pressed. *EA/l* is the stiffness coefficient of the element which varies with element
length. However, this stiffness coefficient is independent of nodal position, and under
the assumption that all elements belonging to the same cable of CDPMs are of the
same length these elements are of the same stiffness coefficient. This assumption is
practically significant since all elements for the same cable being of the same length
can facilitate the dynamics analysis of CDPMs. Thus, for given cable lengths during
the movement of CDPMs stiffness coefficients can be easily determined.

In order to achieve the dynamics equations of CDPMs, the stiffness Eq. (3) must
be transformed into the global frame. Denote the nodal position of nodes 1 and 2 by
$x_1 = [x_1 \ y_1 \ z_1]^T$ and $x_2 = [x_2 \ y_2 \ z_2]^T$ in the global frame, respectively, and
introduce the transformation matrix

$$T = \begin{bmatrix} c_x & c_y & c_z & 0 & 0 & 0 \\ 0 & 0 & 0 & c_x & c_y & c_z \end{bmatrix} \tag{6}$$

where $c_x = (x_2 - x_1)/d$, $c_y = (y_2 - y_1)/d$, $c_z = (z_2 - z_1)/d$, and $d = ||x_2 - x_1||$
is the stressed element length. And then, the global matrices for k_c^c and k_s^c can be
obtained as follows

$$k_c = T^T k_c^c T, \quad k_s = T^T k_s^c \tag{7}$$

Thus, (3) can be written in the global frame as

$$f = k_c x + k_s l \tag{8}$$

where f is the vector of nodal force, and x the vector of nodal position in the global
frame.

The subscript j indicating cable number is omitted in the above equations, and it
is understood that these equations are applicable to all cables in CDPMs.

3 Dynamics Equation of CDPMs

Using the linear element derived in the above section, we can investigate the dynamic
behaviour of CDPMs, especially, the influence of cable vibration on the position
precision of the end-effector. In this paper only dynamics of CDPMs with pure

Fig. 2 Spatial discretization of a cable in CDPMs
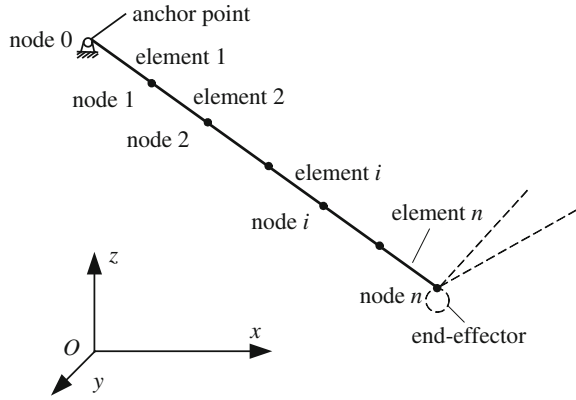
translational DOFs, namely the end-effector is reduced to a mass point, is investigated since we focus on the dynamics of cables.

All cables are divided into the same count of elements for simplicity, say n elements, as shown in Fig. 2. For each cable, the node 0 is fixed at the anchor point and the node n is attached on the end-effector, and all elements are of the same unstressed length, which is $l(t) = L_c(t)/n$ where $L_c(t)$ is the time-varying length of the corresponding cable.

All cables connect to a common node where the end-effector locates. The global nodal force can be obtained by using a standard assembling procedure of the finite element method with the element stiffness equation in (8):

$$F = \sum k_c x + \sum k_s L = K_c X + K_s L \qquad (9)$$

where Σ is the assembly operator of the finite element method, and F, X and L represent the nodal force, nodal position and element length of the cables in CDPMs, respectively.

We suppose the gravity of cables is negligible compared with their tensions, thus the dynamics equation of cables of CDPMs is readily written as

$$M_c \ddot{X} + F = M_c \ddot{X} + K_c X + K_s L = Q \qquad (10)$$

where Q is external load on cable nodes resulted from the reaction force of anchor points and the end-effector. The damping item is not accounted for. The mass matrix M_c also varies with element length, here a lumped mass matrix is used and it is easy to compute.

4 Solution of Dynamics Equation

4.1 Initial State of CDPMs

To numerically solve the dynamics equation of CDPMs their initial configuration needs to be determined beforehand. We assume CDPMs start to move from a static state. Therefore, the static analysis of CDPMs is presented here briefly. In this process, each cable is treated as a linear spring which can only be tensioned. The static equation of CDPMs constrained with m cables can be expressed as

$$G = -J^T \tau \tag{11}$$

where $\tau = [\tau_1, \tau_2, \ldots, \tau_m]$ is the vector of cable tension to resist external load, and G is the vector of gravity term of the end-effector including payloads. J is the Jacobian matrix defined as

$$J^T = [\mathbf{u}_1, \mathbf{u}_2, \cdots, \mathbf{u}_m] \tag{12}$$

in which $\mathbf{u}_j\,(j = 1, 2, \ldots, m)$ is the unit vector along the jth cable directed from the end-effector to the anchor node.

The solution to (11) depends on the number of cables. In the case where the cable number is more than the DOFs of the end-effector, (11) is an underdetermined system of equations and has an infinite number of solutions if $J^T J$ is invertible. In this case, the general solution to cable tensions can be written as

$$\tau = \tau_0 + N(J^T)\mathbf{s} \tag{13}$$

in which τ_0 is the minimal norm solution of (11) derived using the pseudo inverse of matrix J^T and is expressed as

$$\tau_0 = -J(J^T J)^{-1}G, \tag{14}$$

$N(J^T)$ is the null space of J^T and s is an undetermined vector of the dimension m–Rank(J^T). For $\tau > 0$ CDPMs can rest with a given pose. Properly choosing s can easily make $\tau > 0$ or further satisfy other requirements.

With given position of the end-effector, cable length can be obtained as the distance between its two ends, which is denoted by d_j, and the corresponding unstressed cable length is

$$L_{cj} = d_j/(1 + \tau_j/EA) \tag{15}$$

where τ_j is the cable tension of the jth cable, and all cables are assumed to be of the same modulus of elasticity E and cross section area A.

During simulation all elements belonging to the jth cable are supposed to be of the same unstressed length, in the initial state, this length is $l_{ij} = L_{cj}/n$, $(j = 1, 2, \ldots, m; i = 1, 2, \ldots, n)$.

4.2 Numerical Solution of Dynamics Equation

With the initial configuration of CDPMs obtained, a time integration with equal step size Δt is employed to solve the dynamics equation. For a given cable length variation we can compute the corresponding element length, which is described as $\boldsymbol{L}^{(k)} = \boldsymbol{L}(k \cdot \Delta t)$. The integration is achieved as follows:

(1) At the instant $t = 0$, each cable of CDPMs is meshed into n elements. With the external load $\boldsymbol{G}$ and the position of the end-effector given, obtain the nodal position $\boldsymbol{X}^{(0)}$, nodal velocity $\dot{\boldsymbol{X}}^{(k)} = 0$ and cable tension $\boldsymbol{\tau}^{(0)}$, and matrices $\boldsymbol{K}_c^{(0)}$, $\boldsymbol{K}_s^{(0)}$. Set $k = 0$.
(2) Compute the nodal force using (9) according to the current nodal position and element length: $\boldsymbol{F}^{(k)} = \boldsymbol{K}_c^{(k)} \boldsymbol{X}^{(k)} + \boldsymbol{K}_s^{(k)} \boldsymbol{L}^{(k)}$.
(3) Solve the nodal acceleration $\ddot{\boldsymbol{X}}^{(k)}$ using (10).
(4) Update the nodal velocity and nodal position: $\dot{\boldsymbol{X}}^{(k+1)} = \dot{\boldsymbol{X}}^{(k)} + \ddot{\boldsymbol{X}}^{(k)} \Delta t$, $\boldsymbol{X}^{(k+1)} = \boldsymbol{X}^{(k)} + \dot{\boldsymbol{X}}^{(k)} \Delta t$.
(5) Update the element length $\boldsymbol{L}^{(k+1)} = \boldsymbol{L}((k + 1) \cdot \Delta t)$.
(6) Compute $\boldsymbol{K}_c^{(k+1)}$, $\boldsymbol{K}_s^{(k+1)}$ according to the updated nodal position and element length.
(7) Set $k = k+1$, and go to (2) until reach the upper time boundary.

The accumulation operation in step 4 needs to be implemented using a numerical integration method, such as the common fourth-order Runge–Kutta method.

5 Numerical Examples

Dynamic behaviors of a typical CDPM are simulated to investigate the effect of cable vibration on the position precision of the end-effector. Shown in Fig. 3 is a 4–3 CDPM where 4 long cables move the end-effector to translate in its workspace, which serves as the prototype of a cable-driven robot camera. The dimensions are $a = 40\,\mathrm{m}$, $b = 30\,\mathrm{m}$ and $h = 10\,\mathrm{m}$. The end-effector is reduced to a point with the mass $20.0\,\mathrm{kg}$. All the cables are of the same parameters: section area $A = 5.37 \times 10^{-6}\,\mathrm{m}^2$, mass per unit length $\rho = 4.56 \times 10^{-2}\,\mathrm{kg/m}$, modulus of elasticity $E = 28.0\,\mathrm{GPa}$.

In this simulation the end-effector is demanded to track the following trajectory

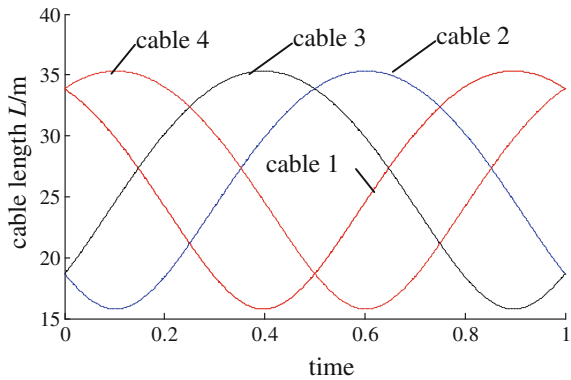$$x = R\cos(2\pi t/T),\ y = R\sin(2\pi t/T),\ z = 5 \tag{16}$$
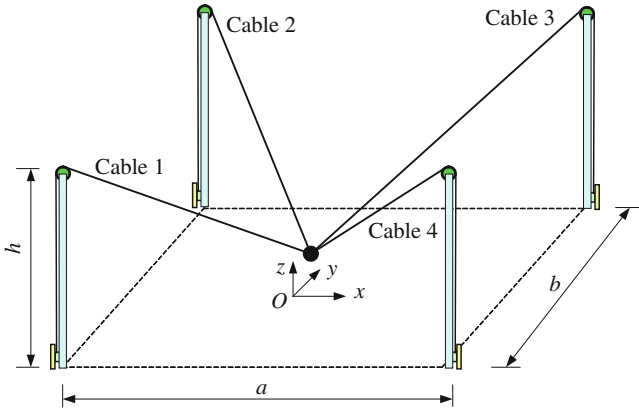
Fig. 3 A typical CDPM for large workspace application

**Fig. 4** Cable length variation for the trajectory with the duration $T = 20$ s

with different velocities where $R = 10$ m and T is the duration to finish the trajectory.

The dynamic behaviors for $T = 10$, 20, and 40 s are simulated and the corresponding velocities are 6.283, 3.142 and 1.571 m/s, respectively. A nondimensional time $\tau = t/T$ is introduced to facilitate the comparison among these results. The cable length variation to complete this trajectory for $T = 20$ s and the corresponding cable tension variation are shown in Figs. 4 and 5, respectively. Both the cable length and cable tension vary with time continuously and smoothly.

When the dynamic behavior of cables is taken into account the vibrations of the end-effector around its desired position corresponding to different velocities are shown in Fig. 6. We can see that small-amplitude high-frequency vibrations of the end-effector exist around its desired position when it moves with low velocities. The vibration amplitude increases with the increasing operation velocity. Furthermore, when the end-effector's velocity increases to a certain extent its vibration amplitude is very significant, however, its frequency decreases.

Fig. 5 Cable tension variation for the trajectory with the duration $T = 20$ s
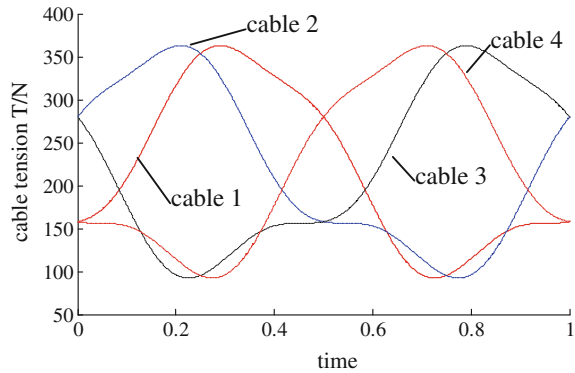
The maximal amplitude of the vibration $((\Delta x^2 + \Delta y^2 + \Delta z^2)^{1/2})$ is approximately 0.08 m when the operation velocity $v = 1.571$ m/s ($T = 40$ s). This shows that the cable vibration effect is relatively small when the manipulator moves slowly. However we find that this assumption holds only if there is no position error of the end-effector at the initial instant and the length of cables changes slowly and smoothly. Otherwise, the vibration of the manipulator can be observed obviously and it attenuates very slowly due to the low damp of cables.

The maximal vibration amplitude increases to 0.4 m for $v = 3.142$ m/s ($T = 20$ s). We can see that the amplitude increases rapidly with the operation velocity, not in a linearly way. The end-effector undergoes a large-amplitude low-frequency vibration when $v = 6.283$ m/s ($T = 10$ s). The vibration characteristic of the end-effector with high operation velocity differs from that with low velocity. The vibration amplitude is too large for the manipulator to work with this operation velocity.

Note also from the end-effector's vibration in z axis shown in Fig. 6 that the end-effector vibrates above its desired position. This phenomenon is very obvious when the operation velocity is high. This is because that cable vibrations shorten the chord length of cables, namely the distance between cable ends. This shortening effect is more significant when cables vibrate with increasing amplitude. Chord length variation with respect to its desired length for cable 1 is shown in Fig. 7. When the end-effector operates at high speed cables' chord length is significantly less than their desired length due to the vibration of cables.

Vibrations of the midpoint of cable 1 around its desired position during the movement of the end-effector for $T = 20$ s are shown in Fig. 8. The vibration amplitudes increase with the increasing operation speed of the end-effector. These vibrations change the corresponding cable tension and chord length. For CDPMs of large workspace and operating at high velocity the effect of cable vibration needs to be carefully considered to guarantee acceptable position precision.

The tension of cable 1 acted on the end-effector during the motion for different velocities is shown in Fig. 9 and tensions of other cables vary in the similar form. When the manipulator operates at low velocity, cable tension vibrates around its

Fig. 6 Vibrations of the end-effector with different operation velocities
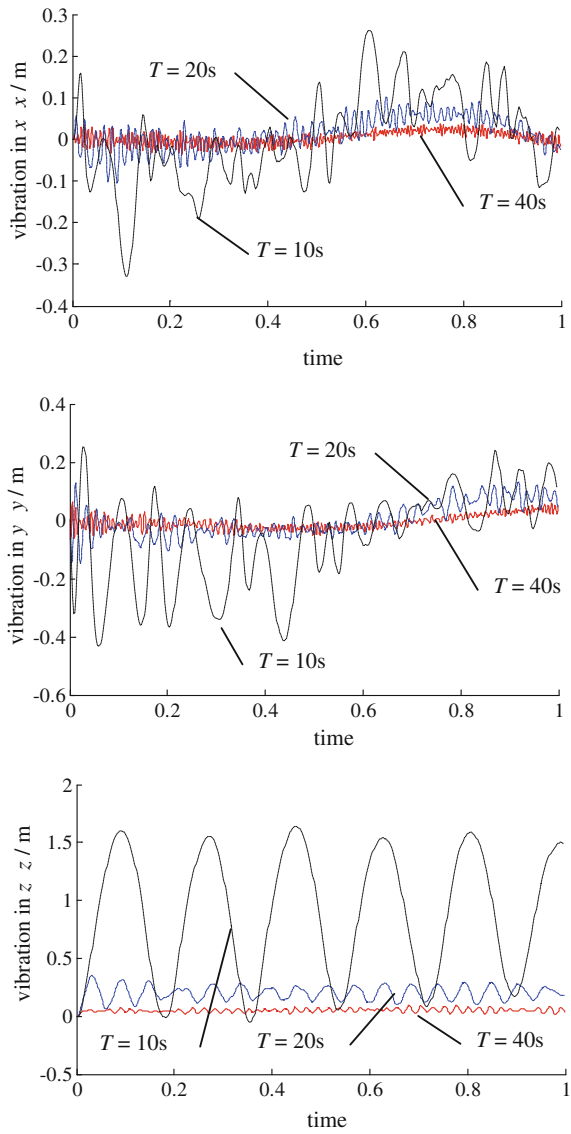
desired value, and cables are in tension state in almost all the movement. With the increasing operation velocity, cable tension vibrates more severely, and cables are in slack state with more time, and the manipulator is under-constrained with cables in these states.
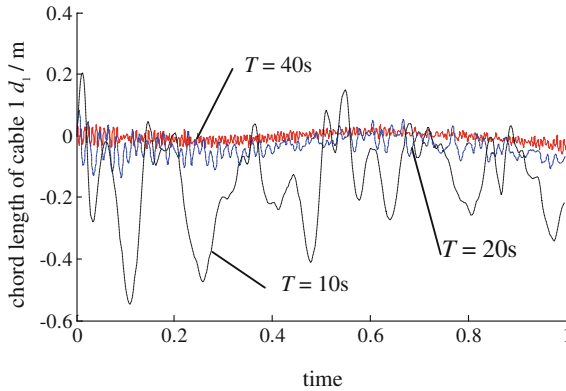
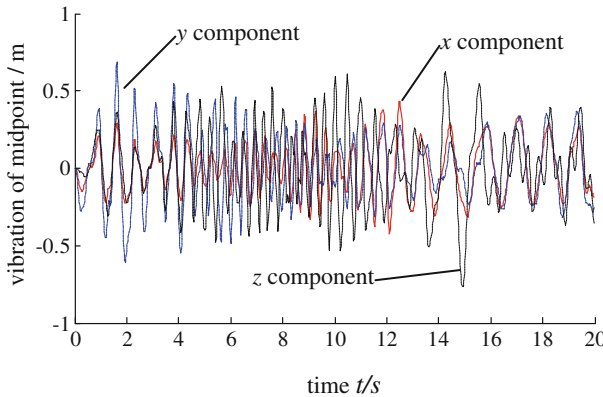**Fig. 7** Chord length variation of cable 1 for different operation velocities

Fig. 8 Midpoint vibration of cable 1 for $T = 20$ s

6 Conclusions

This paper addresses dynamic modeling of CDPMs for large workspace applications. In these manipulators cables are prone to vibration even manipulators operate at very low velocity, degrading the positioning precision of the end-effector. Many factors can cause these vibrations, such as initial position or velocity of the end-effector, wind disturbance, speed reducer backlash, and friction of cables around fixed pulleys. For these applications, modeling the dynamics of cables is of practical significance.

The dynamic model proposed here for large CDPMs is very simple; however, can imitate cable vibration effectively, which can be readily utilized to estimate the effect of cable vibrations on the positioning precision of the end-effector. Furthermore, for its simplicity, this model can be easily utilized in control design of CDPMs to

Fig. 9 Tensions in cable 1 for
different operation velocities
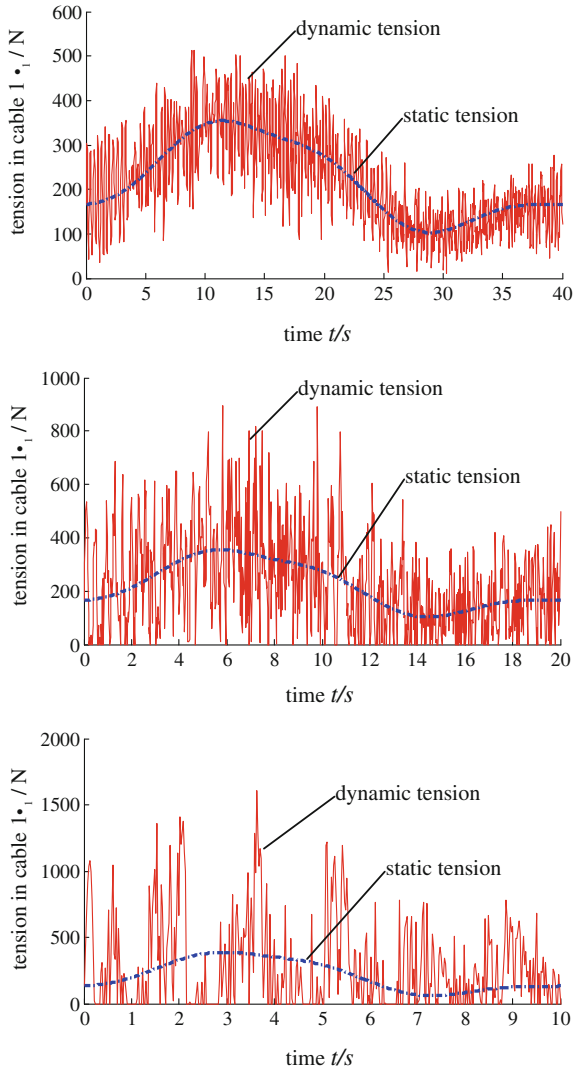
eliminate these vibrations, guaranteeing smooth motion of the manipulator with high
positioning precision.

In practice, only first two or three vibration modes of cables need to be involved in
control design for vibration suppression; therefore, each cable only needs be divided
into several nodes, leading to an acceptable model scale.

It is noted that in this dynamic model the effect of cable's axial velocity, namely
the derivative of cable length with respect to time, is not fully taken into account.
Indeed, all terms involving cable's axial velocity are omitted, thus, the dynamics of
the manipulator reduces to a structural vibration problem with a moving equilibrium

position, which is applicable to CDPMs where cable length changes not very rapidly. Cable damping effect is not involved in these simulations, which will be included in further analysis.

References

1. Gouttefarde, M., Gosselin, C.: Analysis of the wrench-closure workspace of planar parallel cable-driven mechanisms. IEEE Trans. Rob. **22**(3), 434–445 (2006)
2. Oh, S.R., Agrawal, S.K.: A reference governor based controller for a cable robot under input constraints. IEEE Trans. Control Syst. Technol. **13**(4), 639–645 (2005)
3. Fang, S., Franitza, D., Torlo, M., Bekes, F., Hiller, M.: Motion control of a tendon-based parallel manipulator using optimal tension distribution. IEEE/ASME Trans. Mechatron. **9**(3), 561–568 (2004)
4. Du, J.L., Bao, H., Cui, C.Z., Yang, D.W.: Dynamic analysis of cable-driven parallel manipulators with time-varying cable lengths. Finite Elem. Anal. Des. **48**(1), 1392–1399 (2012)
5. Wang, Y., Luo, A.C.: Dynamics of traveling, inextensible cables. Commun. Nonlinear Sci. Numer. Simul. **9**(5), 531–542 (2004)
6. Terumichi, Y., Ohtsuka, M., Yoshizawa, M., Fukawa, Y., Tsujioka, Y.: Nonstationary vibrations of a string with time-varying length and a mass-spring system attached at the lower end. Nonlinear Dyn. **12**(1), 39–55 (1997)
7. Wang, P.H., Fung, R.F., Lee, M.J.: Finite element analysis of a three-dimensional underwater cable with time-dependent length. J. Sound Vib. **209**(2), 223–249 (1998)
8. Zhang, Y., Agrawal, S.K., Piovoso, M.J.: Coupled dynamics of flexible cables and rigid end-effector for a cable suspended robot. In: Proceedings of the 2006 American Control Conference Minneapolis, June 14–16, pp. 3880–3885. Minnesota, USA (2006).
9. Meunier, G., Boulet, B., Nahon, M.: Control of an overactuated cable-driven parallel mechanism for a radio telescope application. IEEE Trans. Control Syst. Technol. **17**(5), 1043–1054 (2009)

Author Index